Conference Proceedings, Published Version

Bourban, Sébastien E.; Pham, Chi Tuân; Tassi, Pablo; Argaud, Jean-Philippe; Fouquet, Thierry; El Kadi Abderrezzak, Kamal; Gonzales de Linares, Matthieu; Kopmann, Rebekka; Vidal Hurtado, Javier (Hg.)

Proceedings of the XXVIIIth TELEMAC User Conference 18-19 October 2022

Zur Verfügung gestellt in Kooperation mit/Provided in Cooperation with:
TELEMAC-MASCARET Core Group

Verfügbar unter/Available at: https://hdl.handle.net/20.500.11970/110837

Vorgeschlagene Zitierweise/Suggested citation:
Bourban, Sébastien E.; Pham, Chi Tuân; Tassi, Pablo; Argaud, Jean-Philippe; Fouquet, Thierry; El Kadi Abderrezzak, Kamal; Gonzales de Linares, Matthieu; Kopmann, Rebekka; Vidal Hurtado, Javier (Hg.) (2022): Proceedings of the XXVIIIth TELEMAC User Conference 18-19 October 2022. Paris-Saclay: EDF Direction Recherche et Développement.

Proceedings of the

XXVIIIth TELEMAC User Conference

18-19 October 2022, Paris-Saclay

Proceedings of the

XXVIIIth TELEMAC User Conference

18 to 19 October 2022, EDF R&D, Paris-Saclay

Editorial Committee

Sébastien E. BOURBAN
Chi Tuân PHAM
Pablo TASSI
Jean-Philippe ARGAUD
Thierry FOUQUET
Kamal EL KADI ABDERREZZAK
Matthieu GONZALES DE LINARES
Rebekka KOPMANN
Javier VIDAL HURTADO

Members of the TELEMAC Consortium

ARTELIA
www.arteliagroup.com

Bundesanstalt für Wasserbau
Federal Waterways Engineering and Research Institute
www.baw.com

Centre d'études et d'expertise sur les risques,
l'environnement, la mobilité et l'aménagement
www.cerema.fr

Centre Européen de Recherche et
de Formation Avancée en Calcul Scientifique
www.cerfacs.fr

Électricité de France, Recherche & Développement,
Laboratoire National d'Hydraulique et Environnement
www.edf.com

HR Wallingford
www.hrwallingford.com

Science and Technology Facilities Council
Daresbury Laboratory
www.stfc.ac.uk

Foreword of the XXVIIIth TELEMAC User Conference

Dr Sébastien E. Bourban
October 2022

Dear TELEMAC Users,

EDF R&D is delighted to organise once again the TELEMAC User Conference in Paris – the XXVIIIth of its kind! We last hosted this annual event in 2011, which shows just how keen members of the TELEMAC community are to take on this role, whether they are private, public or academic institutions.

In 2011, we organised the TUC at our historical LNHE (National Laboratory of Hydraulics and Environment) site in Paris-Chatou, together with LHSV (Saint-Venant Hydraulics Laboratory) co-directed with Ecole Nationale des Ponts ParisTech. This time, we have chosen to host the event at our brand-new R&D campus, on the plateau of Paris-Saclay. The plateau steams with innovation and sciences: did you know? Paris-Saclay University has been ranked 1st in mathematics, three years in a row, by the Shanghai Ranking of the best universities in the world.

EDF is constantly facing strong environmental, industrial, commercial, scientific, digital transformation and regulatory challenges, at national, European and international levels, in the production of electrical energy, in all its forms. To meet these challenges, the company invests heavily in R&D, particularly in its scientific computational solvers and supercomputers. EDF R&D is continuously looking for both performance and quality of its predictions in ever more diverse fields of application, while maintaining the international reputation of its solvers as the state of the art for applied research and a standard for the industries.

TELEMAC is one of those solvers, or rather a suite of solvers covering all aspects of free surface, environmental hydraulics. For EDF, TELEMAC is both a competitive advantage and a showcase for our collective excellence: sharing TELEMAC openly and allowing participative access on an international scale makes it possible to guarantee and raise the state of the art.

In keeping with the tradition, this XXVIIIth edition of the TUC comes with a book of proceedings, nowadays published online for all to download. The editorial committee has received this year 38 articles, which you will find here included for your scientific curiosity. This book has grown over the years. Exactly 10 years ago, the last time I organised a TUC, in Oxford that time, also renowned worldwide for its academic excellence, the book counted 25 articles.

On behalf of EDF R&D and as President of the TELEMAC Consortium, I am happy to welcome you to our R&D site in Paris-Saclay for this XXVIIIth TELEMAC User Conference.

Thank you for sharing your passion with the community and thank you for your participation in this annual event.

Yours truthfully,

Dr Sébastien E. Bourban

Ingénieur Chercheur, EDF R&D LNHE / LHSV
Chef du Projet TELEMAC au Laboratoire National d'Hydraulique et Environnement /
Directeur Adjoint du Laboratoire d'Hydraulique Saint Venant
6, Quai Watier, 78400 CHATOU, France

Content

Day 1

Session 1

Numerical methods, Code coupling and Integrated systems

Session 2

Hydrodynamics, Water Works and Flow around structures

Session 3

Flash floods, Surges, Tsunamis and Extreme events

Day 2

Session 1

River, Coastal and Estuarine Sediment Transport

Session 2

River, Coastal and Estuarine Sediment Transport

Session 3

Water Quality, Biodiversity and Marine Pollution

Session 4

Data assimilation, Uncertainty and Optimisation methods

Rural area flooding digital prediction based on TELEMAC-2D

WEI Ronglian[1], CUI Zihao[1], ZHOU Lu[2], MIN Jiesheng[2]
rlwei@yuansuan.cn
[1] Zhejiang Yuansuan Technology Co., Ltd., Hangzhou, China
[2] EDF China, R&D Center, Beijing, China

Abstract – **In 2020, the Wuqiangxi Watershed, located near Hangzhou, suffered severe financial damage due to an extreme rainfall. The likelihood of such events has recently been increasing due to global warming and climate change. To address these issues, the local water conservation bureau demanded a study to dynamically forecast flood risks of the Wuqiangxi Watershed, and thus to assist in early warning as well as intervention to ensure civil protection.**

In this study, an integrated solution was proposed to fulfil the needs of the local bureau. Flood risks prediction calculation is performed by TELEMAC-2D coupled with a lumped hydrological model named Xin'anjiang (XAJ). Once heavy rainfall is detected in the weather forecast of the next 24 hours, the following simulation process is triggered: (1) The XAJ model is firstly applied to calculate the flow discharges from the upstream sub-watersheds; and (2) The computed discharges are then taken as inflows of the 2D hydrodynamic model. The rainfall-runoff process in the 2D hydrodynamic domain is simulated by the built-in SCS-CN model available in the open TELEMAC system.

This paper presents a technical focus on the process of hydraulic models deployed in flood risk prediction.

Keywords: TELEMAC-2D, Xin'anjiang model, hydrology, dynamic flood risk maps.

I. INTRODUCTION

Flash floods intensively occur during June to August in Hangzhou because of severe downpours. Chun'an County lies in a hilly area in the west of Hangzhou, and is famous for the sceneries of Qiandao Lake. The later, also known as Xin'anjiang Reservoir, is an artificial lake built for the Xin'anjiang hydropower station to retain the upper reaches of Xin'anjiang River. In July 2020, Chun'an suffered the strongest rains throughout history and the water level of Qiandao Lake reached a record-breaking point of 108.43 meters. Wuqiangxi Watershed in Chun'an County (see Figure 1), the interest area of this project, was subjected to serious flood event (see Figure 2) as a consequence of torrential flood, superimposed to the backwater effect induced by the high stage of Qiandao Lake.

The focus of this study is to demonstrate how a hydrological model namely Xin'anjiang model and TELEMAC-2D (version V8P3R1 of the open TELEMAC system) are coupled in the study to dynamically predict flood risks.

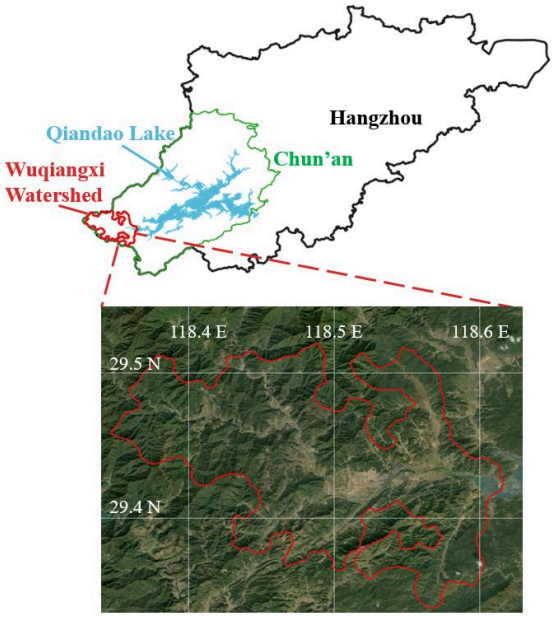

Figure 1. The location of Wuqiangxi Watershed

Figure 2. Flood event in Wuqiangxi Watershed

The first part of this article presents how the data was gathered for the study. A second part describes the model setup with the data while a third part details the calibration process and the model results.

II. DATA COLLECTION

A. Topographic data

Topographic data for Wuqiangxi Watershed consists of Digital Elevation Model (DEM) data and river cross-section data. The obtained DEM data describes the terrain with a 12.5 m resolution and consists in the ALOS PALSAR RTC

Digital Elevation Model (DEM), which was downloaded through the official website of NASA EARTH DATA [1]. The local bureau provided surveyed river cross-section data in the Wuqiangxi Watershed. The topographic data was processed as an ASCII file including three columns of data, which are longitude, latitude, and bottom elevation.

B. Precipitation and evaporation data

There are two forms of precipitation data depending on the functionality designed in the study. For the in-time forecasting, precipitation data is obtained through access to real-time weather forecast. In terms of recurrence of extreme floods, a formula recommended in a local hydrological manual [2] is implemented to reproduce, for instance, once-in-20-year, once-in-50-year, or once-in-a-century rainstorm data:

$$\mathrm{H_p}=\overline{\mathrm{H}}(\Phi_\mathrm{p} * \mathrm{C_v} + 1), \quad (1)$$

where H_p is the designed precipitation, $\bar{H}$ is the average rainfall listed in the manual, Φ_p is the coefficient of deviation of Pearson-III curve, C_v is the coefficient of variation.

The evaporation data was provided by local evaporation gauging stations.

III. MODEL DESCRIPTION

The main goal of the study is to cyclically forecast flood risks every 3 hours in order to demonstrate how simulation can be used to better assist municipalities manage flood risks. Once rainfall occurs in the weather forecast, the Xin'anjiang model (referred to as the XAJ model in the rest of this article) will be initiated to compute the runoff discharges in the upstream of Wuqiangxi Watershed. Then, the computed discharges are processed as the input of the TELEMAC-2D model. The TELEMAC-2D model performs the hydrodynamic simulation inside Wuqiangxi Watershed, subsequently a risk rating function is carried out based on output water depth and velocities [3]. This procedure will be looped every 3 hours if it rains in the next 24 hours. For other types of applications, for instance the reproduction of extreme rainstorms, the same procedure will be launched. A detailed description is presented in the following content.

A. The XAJ model

The XAJ model was applied to model the hydrological process in upstream sub-catchments of the Wuqiangxi Watershed. It is a conceptual model put forward by Professor Zhao Renjun of Hohai University in 1963 [4]. The model describes hydrological phenomena through four different levels of calculation, which are:

- evapotranspiration calculation at the first level,
- runoff generation calculation at the second level,
- runoff separation at the third level,
- flow concentration at the fourth level.

In evapotranspiration calculation, according to the characteristics of soil storage, the soil can be divided into the top, intermediate and deep layers. Those three layers are computed separately. The runoff generation calculation is based on Stored-full Runoff Theory [4], which means that runoff is not produced until the soil is saturated and thereafter runoff equals the rainfall excess without further loss. The total runoff, generated in the previous step, must be separated into its three components, *RS* surface runoff, *RG* the ground water contribution, and *RI* a contribution to interflow. In the final flow concentration level, according to the difference of flow characteristics between the hillslope and the river network, it is divided into two different processes: hillslope runoff and river network runoff.

Figure 3 shows the flow chart of the XAJ model. The inputs to the model are *P*, the measured areal mean rainfall depth (mm) and *EM*, the measured pan evaporation in the same unit. *E* is the total evapotranspiration in the watershed and Q is the discharge at the water outlet of a watershed. *E* and *Q* are the model outputs.

As previously mentioned, the XAJ model includes four processes. Each process introduces its conforming state variables, indicated in the black rectangular boxes in Figure 3. *R* is the total runoff generated by a rainfall, and *FR* is the runoff contributing area factor. *W* is the tension water storage, and consists of *WU*, *WL* and *WD*. *WU* is the top layer tension water storage; *WL* is the intermediate layer tension water storage; *WD* is the deep layer tension water storage. *EU*, *EI* and *ED* are the corresponding evapotranspiration state variables. *S* is the free water storage; *RS* is the surface runoff; *RI* is the interflow runoff; *RG* is the ground water runoff. *QS, QI* and *QG* are the respective routing flow.

In addition to those input and state variables, there are 15 parameters for a watershed when using the lag-and-route method [4]. The 15 parameters can be grouped as follows:

- Evapotranspiration parameters *K*, *UM*, *LM*, *C*.
- Runoff generation parameters *WM*, *B*, *IM*.
- Parameters of runoff separation *SM*, *EX*, *KG*, *KI*.
- Routing parameters *CG*, *CS*, *CI*, *L*.

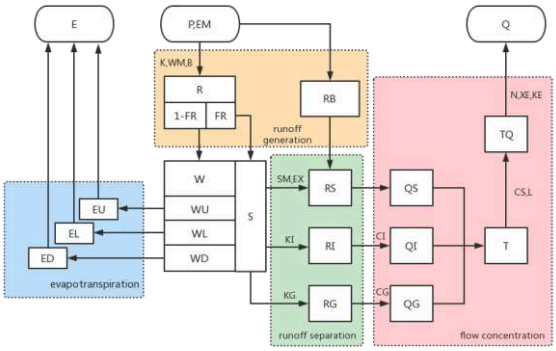

Figure 3. Flow chart of the XAJ model

1) Study area

19 rivers in Wuqiangxi Watershed were taken into account in the TELEMAC-2D model, hence 19 sub-catchments upstream were delineated based on the obtained DEM data, shown as green-shadowed areas in Figure 4.

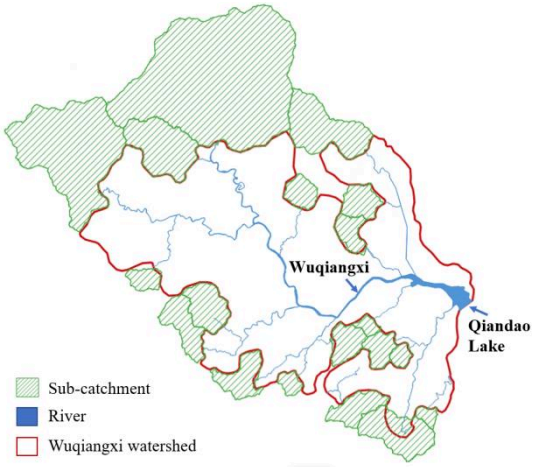

Figure 4. Layout of sub-catchments

2) Model output

The output of the XAJ model is a sequence of discharges as Table I shows. It will be converted to a liquid boundaries file for the TELEMAC-2D model. It should be noted that if the hydrological output was directly applied as the boundary file, a deviation of the input flow rate would be introduced. The output discharge per hour is an average flow rate over the time span, while TELEMAC-2D assumes a linear interpolation in time of the flow rates at each time step. It would lead to discrepancy at flood peak arrival time and consequently results in failure to timely decision-making.

Table I . Output of XAJ model

Time (h)	Q (m^3/s)
1.0	3.78
2.0	5.62
3.0	8.65
4.0	7.21
5.0	5.97
6.0	4.52

To address this issue, the corresponding time step for discharge is shifted to half hour earlier, as can be seen through the green line in Figure 5. The adjusted line is more appropriate than the original one (the red line in Figure 6). A sensitivity analysis shall be operated with regards to the adjusted time length in future work, in order to accurately characterize inflows.

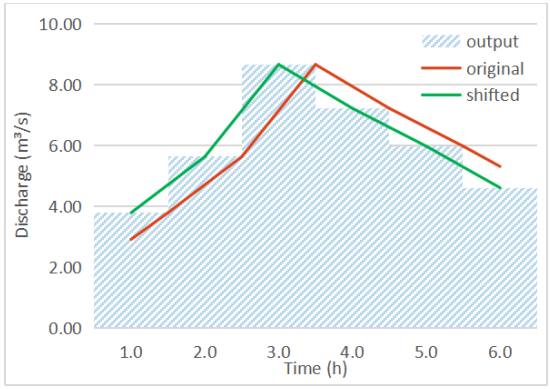

Figure 5. Adjustment of time-varying discharges as hydrodynamic input

It barely rained this summer in Hangzhou (2022); therefore, a once-in-50-year rainstorm was designed in this study and the finalized discharge time series for one branch is shown in Figure 6.

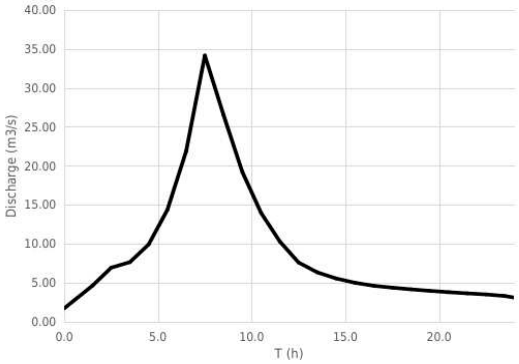

Figure 6. Finalized discharge time series for one small branch

B. Hydrodynamic model

1) Computational Mesh

The study area of the TELEMAC-2D model in Wuqiangxi Watershed is around 348 km^2. The mesh resolution ranges from 4 m in the river channel to 150 m at the outline, containing around 233,834 elements and 117,844 nodes, see Figure 7.

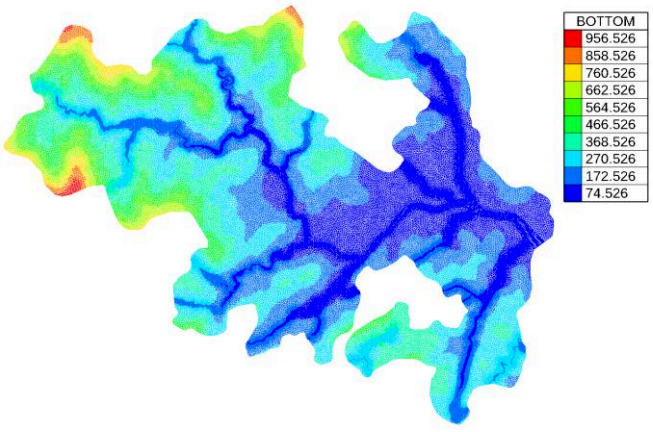

Figure 7. Computational mesh for Wuqiangxi watershed (Bottom elevation unit: m)

2) Boundary conditions

River bottom varies greatly in Wuqiangxi Watershed, as mentioned before it is a mountainous area. To tackle the potential supercritical entry warning, around 20 meters long at the inlets of 19 streams were pre-processed as flat bottom. Furthermore, test runs suggested that at least 4 nodes are required for each boundary segment to better maintain subcritical flow.

3) Initial conditions

Monthly average runoffs of sub-catchments were evaluated by the XAJ model, and then were applied as boundary conditions to spin-up the model. 48 hours of model computation were sufficient to reach a steady state. Thereafter, the last record was extracted as the initial condition for further simulations.

4) Parameters

a) Bottom friction coefficient: The land type of Wuqiangxi Watershed can be characterized as town, cropland, forest and stream. Manning friction coefficients are set with respect to land use type. The friction coefficients served in the TELEMAC-2D model are listed in Table II [5].

Table II Friction coefficient

Friction coefficient	**Land Use Type**			
	Town	***Cropland***	***Forest***	***Stream***
Manning Coefficient	10	0.075	0.18	0.04

b) Curve Number (CN): The rainfall-runoff process within the TELEMAC-2D model is modelled by the built-in Soil Conservation Service Curve Number (SCS-CA) model. In SCS-CA model, Curve Number (CN) is used to describe infiltration capacity of different soil types. By referring to the Hydrology National Engineering Handbook [6], CN values are determined according to the land use type, as shown in Table III.

Table III CN value

Curve number	**Land Use Type**			
	Town	***Cropland***	***Forest***	***Stream***
CN	95	85	73	95

IV. CALIBRATION & RESULTS

A. Calibration of the XAJ model

The original source codes of the XAJ model in this study was further developed by scientists in Yuansuan. It was calibrated with the help of historic data of two flood events in 1993 and 1994 in Chengcun, Anhui Province. The hydrologic data in Chengcun is relatively sufficient and frequently selected for verification [7]. As shown in Figure 8 & Figure 9, the hydrograph (red dash line) calculated by the XAJ model shows a good agreement with the observed data (black line), which ensures the reliability of the XAJ model used in this project.

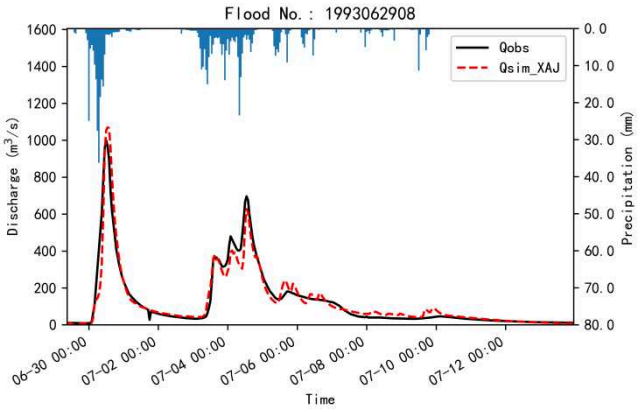

Figure 8. Results comparison for flood event in 1993

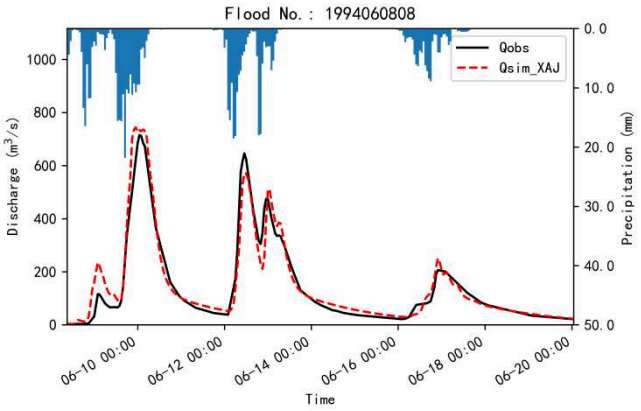

Figure 9. Results comparison for flood event in 1994

B. Hydrodynamic results

In order to compare the backwater effect induced by the high-water level of Qiandao Lake at the downstream location of Wuqiangxi Watershed, 3 scenarios were simulated and compared. For the once-in-50-year flood event, the TELEMAC-2D model was launched 3 times with different downstream water level namely:

- 104 meters - scenario 1: normal water level
- 106 meters - scenario 2: intermediate water level
- 108 meters - scenario 3: high water level

By looking into the towns adjacent to Qiandao Lake, the submerged area was evidently affected by the high stage at the Wuqiangxi outlet (see Figure 10, Figure 11 & Figure 12). The differences of water depth at one village (red dot in Figure 10, Figure 11 & Figure 12) for different scenarios are depicted in Figure 13. The hydrodynamic model took around 1.3 hours to spin-up from initial condition (104 m) to the conforming high water level condition. The water depth difference at the point of interest reached 1.3 meters between scenario 2 and scenario 1, not to mention the 2.5 meters dissimilarity between scenario 3 and scenario 1. This is aimed to demonstrate the potential danger for civilians living adjacent to Qiandao Lake and hence to suggest Qiandao Lake may not operate at high water level.

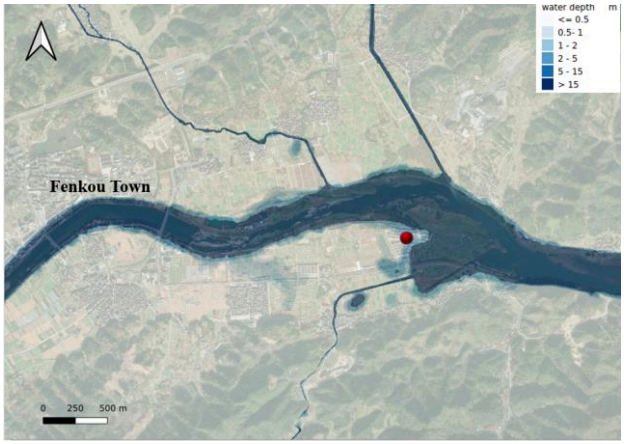

Figure 10. Water depth at Wuqiangxi downstream, outlet water level 104 m

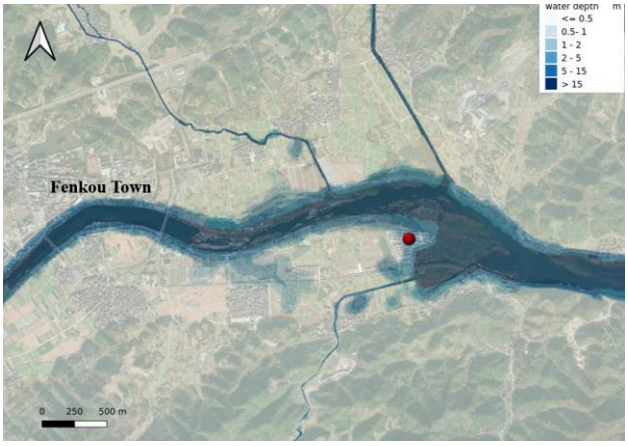

Figure 11. Water depth at Wuqiangxi downstream, outlet water level 106 m

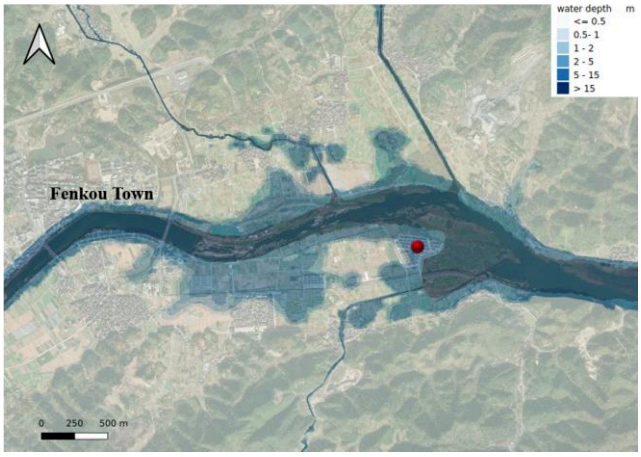

Figure 12. Water depth at Wuqiangxi downstream, outlet water level 108 m

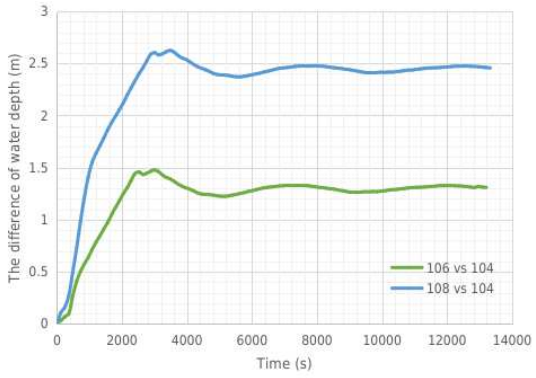

Figure 13. The difference of water depth at one village for high stage scenarios (green line: 106 m vs 104 m, blue line: 108 m vs 104 m)

V. CONCLUSION & PERSPECTIVES

It is the first time that the XAJ model and a TELEMAC-2D model are coupled to forecast flood risks in China. The results demonstrates that it is qualified to model the general flood hazard tendency in Wuqiangxi Watershed and capable to be used as a core engine dynamically forecasting flood risk and reproducing extreme flash floods.

The sensitivity analysis for shifted time step of input flow rates and the validation for hydrodynamic model have not been carried out at this stage. In the next phase of this work, the installation of water gauges in vulnerable villages in Wuqiangxi Watershed will proceed to serve the verification and validation data for both the XAJ and the TELEMAC-2D model.

ACKNOWLEDGEMENT

The authors would like to thank Sebastien Bourban and Chi-Tuan Pham at EDF R&D for their technical support during the work. The authors would also like to thank the Wuqiangxi Watershed local bureau.

REFERENCES

[1] NASA EARTH DATA, Phased Array L-band Synthetic Aperture Radar (PALSAR), https://www.earthdata.nasa.gov/sensors/palsar.

[2] Zhejiang Hydrological Authority, “Short-duration rainstorm atlas of Zhejiang province (in Chinese) ”[M], 2003.

[3] H. Udale-Clarke, D. Ramsbottom, B. Dyer, S. Wade et al., “Flood Risk Assessment Guidance for New Development”, Phase2, R&D Technical Report FD2320/TR2, October 2005.

[4] R. J. Zhao, “The Xin’anjiang model applied in China”, Journal of Hydrology, vol. 135, no. 1–4, pp. 371–381, 1992.

[5] Q. Zhang, “Research on Hydrological-Hydrodynamic Model and Its Application in Flash Flood Forecasting,” MA thesis, Qsinghua University, May 2019.

[6] V. Mockus, National engineering handbook. US Soil Conservation Service: Washington, DC, USA, 4, 1964.

[7] C. Zhang, R. J. Wang, Q. X. Meng, “Calibration of Conceptual Rainfall-Runoff Models Using Global Optimization”, Advances in Meteorology, pp. 1-12, 2015.

Simulation of urban waterlogging with TELEMAC-2D/SWMM coupled model

Lemin HE[1], Hanyu ZHAN[1], Tingyu DAI, Lu ZHOU[2], Jiesheng MIN[2]
lmhe@yuansuan.cn, Hangzhou, China
[1]: Zhejiang Yuansuan Technology Co., Ltd., Hangzhou, China
[2]: EDF China, R&D Centre, Beijing, China
lmhe@yuansuan.cn

Abstract – **Urban waterlogging caused by rainstorm has occurred more frequently in many cities of China these years. In 2021, "July·20th" torrential rain hit Zhengzhou, the capital city of Henan province, resulting in a serious waterlogging disaster, causing heavy casualties and economic losses, and exposing the weaknesses of the design and construction of the city's drainage system in case of heavy rain.**

Detailed numerical simulation is a key technology for predicting and mitigating the urban waterlogging problems. On the basis of the city of Kaifeng, Henan province, as a case study, this work aims to analyse the spatiotemporal distribution of waterlogging and assess its risk for each district in the city. In this study, a waterlogging simulation model considering the city's digital elevation model (DEM), the non-uniform surface friction and infiltration, and the drainage system is proposed and tested to obtain the spatiotemporal distribution of the water depth and water velocity on the ground of the urban areas. The 2D hydrodynamics module TELEMAC-2D (of the open TELEMAC system) is used to simulate the surface water flow and is then coupled with SWMM (Storm Water Management Model) to simulate the flow in the underground water drainage system taking into account pumps, regulating sluice and so on.

A rainfall data from 2021.08.28 to 2021.08.29 is used to validate the model. The spatial distribution of high-risk areas obtained by the model is generally in agreement with the registered logs provided by the city's bureau of urban management.

Keywords: Urban Waterlogging, SWMM, TELEMAC-2D

I. INTRODUCTION

In 2021, the now sadly famous "July·20th" torrential rain hit Henan province. In the cities of Zhengzhou, Kaifeng, Xinxiang, Zhoukou and Jiaozuo (see Figure 1), ten national meteorological observation stations broke the historical extreme value of daily rainfall [1]. According to the data of Kaifeng meteorological station, from July 20th to 21st, the maximum accumulated precipitation in 48 hours was 354.7 mm, which has reached 56.5% of the annual average precipitation of 627.5mm in Kaifeng [2]. The heavy rain caused heavy casualties and economic losses [3], and exposed some weaknesses of the design and construction of the city's drainage system as well as the requirement to upgrade flood control schemes to face more and more unusual weather.

With now increasingly frequent extreme weather and weak drainage system capacity, urban waterlogging prevention is facing severe challenges. In order to meet the challenges, a numerical simulation method was used to predict the urban water distribution.

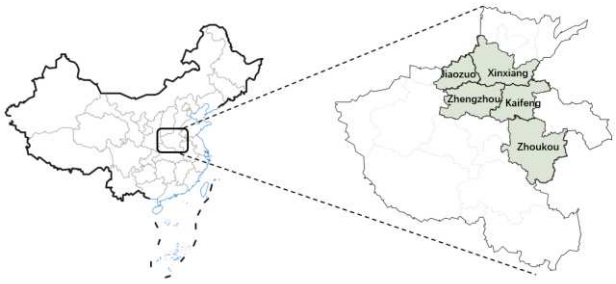

Figure 1. Position of Henan province in China

There are many software packages available commercially and non-commercially with varying degrees of complexity to simulate stormwater runoff quantities and qualities. Deepak Singh Bisht used Storm Water Management Mode (SWMM) and MIKE URBAN to simulate the flood inundation scenarios and provides an insight into the importance of 2D model to deal with location-specific flooding problems [4]. Guoru H proposed a 1D-2D coupled urban flood simulation model based on InfoWorks ICM to obtain disaster-causing factor data by simulating the flood process under the rainstorm return periods of 1 a, 5 a, and 50 a. SWMM is used to simulate the runoff and design of an efficient drainage system [5]. Since, SWMM is a 1D pipe flow model and does not simulate urban surface flood extent and inundation depth, a TELEMAC-2D model was used to complement SWMM's limitations.

This paper presents the TELEMAC-2D/SMWM coupled model specifically constructed for urban water logging simulation in Kaifeng urban district. Its aim is to build a model that can predict future waterlogging in real time.

Section II introduces the study area and presents the setup of the model, including precipitation data access and rainstorm design method, SWMM pipe flow model setup, TELEMAC-2D overland flow model setup and coupling mode of the two models. Section III presents the typical case

verification results and highlights some error analysis. Section IV finally concludes this work with some further perspectives.

II. STUDY AREA AND METHODS

A. Study area

Kaifeng is in the hinterland of Central China, on the south bank of the Yellow River. The terrain is flat and relatively low compared to the Yellow River. Kaifeng has a monsoon climate of medium latitudes with four distinct seasons. The annual average precipitation is 627.5 mm, and the precipitation is mostly concentrated during the summer, more specifically in July and August [1].

The urban district of Kaifeng City is considered as the study area in this paper. As shown in Figure 2, the area was defined according to the density of population and it is centred on Kaifeng ancient City Wall, reaching Lian-Huo Expressway in the north, Jinming Avenue in the west, Huaxia Avenue in the south, and Qingshui River in the east. The total area is about 77.4 km^2.

The 2D mesh is made of 310,671 nodes and 612,177 triangular elements, refined in built-up areas and river. The elements sizes vary from 20 m for the largest elements to 5 m for the smallest ones.

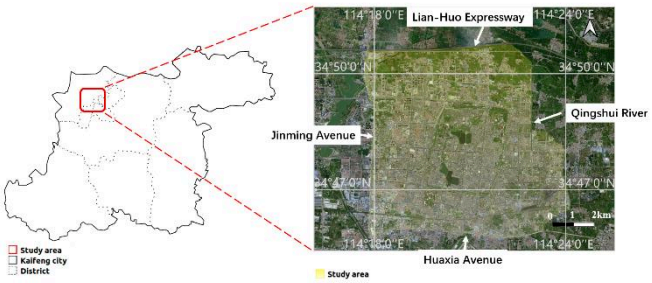

Figure 2. Study area

A. Data resources

The data resources used for the simulation were from reliable and authoritative public data or from Kaifeng City Administration Bureau.

Topographic data includes Digital Elevation Model (DEM) and building contour data. The DEM data were collected by the Advanced Land Observing Satellite (ALOS) launched from Japan on January 24, 2006. Phased Array L-band Synthetic Aperture Radar (PALSAR) data was used by the Satellite to receive the reflection from the ground to acquire elevation information. The horizontal and vertical accuracy of the data can reach 12.5 m, and the data is public data [6]. The building contour data was obtained from Open Street Map [7]. The data includes the position coordinates and height of the building.

Land use data was obtained from Map World on National Platform for Common Geospatial Information Services [8]. The data was used to distinguish different areas such as water system, green land, roads and buildings.

Pipe network data was obtained from Kaifeng City Administration Bureau. The data consists of spatial position, dimensions and elevations of manholes, pipelines and outlets.

Historical meteorological data was selected from daily observation precipitation dataset of Chinese national meteorological stations released by China Meteorological Administration [9].

Positions prone to waterlogging, water depth data caused by the historical rainfall, as well as underpass data consist of spatial position, width, length and depth were obtained from Kaifeng City Administration Bureau.

B. Precipitation and Rainstorm data

The precipitation data is a dynamic input for the simulation and can be directly used as input to the simulation in the form of a precipitation data file. We can generate the rain file in the following two ways: precipitation data access and rainstorm design.

- *Precipitation data access*: the calculation access to the real-time rainfall forecast data API, and the precision of the precipitation data file is determined according to the weather forecast precision. Usually, the rainfall forecast precision is hourly for the next 24 hours and daily for the next seven days.
- *Rainstorm design*: was based on the rainfall return period, e.g., 50 years, 100 years, and so on. Heavy rainstorms have long return periods, while light rain events have short return periods. The storm intensity equation was used to simulate rainfall of different intensities. The storm intensity equation was derived based on local rainfall records for many years:

$$q = \frac{5075(1 + 0.61lgP)}{(t + 19)^{0.92}} \quad (1)$$

where q is rainfall intensity in L/s·ha2, P is the return period in years and t is rainfall duration in minutes.

The most used definition of rainstorm intensity is the average rainfall of a continuous rainfall period, which can be computed using the following formula:

$$i = \frac{h}{t} \quad (2)$$

where i is the rainfall intensity (mm/min), t is the duration of the rainfall event (min), and h is the total rainfall (mm).

Therefore, the unit conversion of q based on the definition of i is:

$$q = \frac{L}{s \cdot ha} = \frac{10^6 mm^3}{\frac{1}{60} \cdot min \cdot 10^4 m^2} = 0.006 \cdot i \quad (3)$$

and:

$$i = \frac{847525(1+0.61\lg P)}{(t+19)^{0.92}} \quad (4)$$

We simulated a rainfall series with an accuracy of one minute using the Chicago hyetograph based on the storm intensity formula [10] .

$$i(t)=\begin{cases}\dfrac{847525(1+0.61\lg P)\left[\frac{(1-0.92)t}{r}+19\right]}{\left(\frac{t}{r}+19\right)^{0.92+1}} & \text{if } t<t_{peak}\\ \dfrac{847525(1+0.61\lg P)\left[\frac{(1-0.92)t}{1-r}+19\right]}{\left(\frac{t}{1-r}+19\right)^{0.92+1}} & \text{if } t\geq t_{peak}\end{cases} \quad (5)$$

where i is the rainfall intensity in mm/min, P is the return period in years and r is proportion coefficient of the rain peak.

C. *The SWMM pipe flow model*

SWMM simulates the runoff quantity generated from a sub-catchment during simulation period along with the discharge of the closed pipes. Developed primarily for urban areas, the model is able to simulate water volume and quality from a single event or a long-term continuous simulation through the catchment [11]. In this study, SWMM is used to simulate the drainage process by the underground pipe network.

In order to account for the infiltration losses, SWMM has three different schemes to choose from, i.e., Horton Model, Green–Ampt model and curve number scheme, while the flow routing can be carried out using steady wave routing, kinematic wave routing and dynamic wave routing [11]. In the present study, curve number scheme for infiltration losses and dynamic wave routing for flow routing were used.

In SWMM, the manhole was set as the junction and the pipeline was set as the conduit. The sub-catchment is the hydrologic unit of the land. In the overland part, the runoff is computed by using the curve number scheme infiltration model. The sub-catchment is connected to a junction to deliver the runoff to the underground pipe network, and the junction is connected by the link to deliver the water to another junction or outlet.

1) Junction properties

Junction properties consist of elevation of junction invert depth from ground to invert elevation, and pond area.

- *Elevation and depth*: the value is directly obtained from the pipe network data.
- *Pond area*: The ALLOW_PONDING analysis option needs to be turned on. The purpose is that the overflow water from the manhole can be temporarily stored in pond, so as to ensure the conservation of the total flow volume. The pond area is set as the area of the corresponding sub-catchment area.

2) Conduits properties

Conduit properties consist of upstream node, downstream node, conduit length, offset of conduit, roughness parameter in Manning's equation.

- Upstream node, downstream node, conduit length, offset of conduit: their value is obtained from the pipe network data.
- Roughness parameter in Manning's equation: The friction coefficient is determined according to the engineering manual [12], and the specific value is shown in the following table:

Table I Roughness parameter of different conduit material

Conduit material	***Concrete***	***Brick***	***PVC***	***GRP***
Roughness parameter	0.014	0.001	0.009	0.0084

3) Sub-catchment properties

Properties associated with a sub-catchment in SWMM are rain gage, outlet, area, width, slope, percent of land area which is impervious, roughness parameter in Manning's equation for impervious area and for pervious area.

- *Rain gage*: Precipitation time series generated in part C was set as rain gage input.
- *Area*: According to the position of junction and Theissen polygon principle, the shape of sub-catchment area is automatically generated. Then, the obviously unreasonable shape of the sub-catchment shape was manually adjusted according to the satellite map, and the area of the shape was counted as the area in SWMM.
- *Outlet*: The sub-catchment shape is generated according to the position of each junction. Therefore, the sub-catchment forms a one-to-one correspondence with the junction, and we can use the corresponding junction as an outlet.
- *Width*: In the SWMM simulation, the time and process curves of overland runoff production depend on the width of the sub-catchment, which is the ratio of the area to the length of the overland flow. Since the length of overland flow is difficult to determine accurately, in this study, the width of the sub-catchment is taken as the square root of the sub-catchment area.
- *Slope*: The slope can affect the rate of overland water flowing into the pipe network system in SWMM. The average slope of sub-catchment area can be obtained according to the DEM data.
- *Percent of land area which is impervious*: To be consistent with the TELEMAC-2D setup, we consider the entire study area to be pervious, so this parameter is set to 0% for all sub-catchment area.
- *Roughness parameter in Manning's equation for pervious area*: According to the land use data, we determined whether the features of each sub-catchment was road and building, green land or water system. Then set the Manning friction coefficient of the corresponding area according to relevant engineering manuals or relevant literature. In this study, the specific coefficients are consistent with the settings in TELEMAC-2D. The

roughness parameter is subjected to change during the calibration process.

- *CN number*: Similarly to the roughness parameter, we first determined the land properties of the sub-catchment and then set the corresponding CN value according to relevant engineering manuals or literature.

4) Outlet properties

The outlet is an outfall node which is final downstream boundary of the drainage system. The corresponding water stage elevation is set according to the value from the pipe network data.

According to the above definitions, the SWMM model obtained is shown in Figure 3.

Figure 3. SWMM model in ths study

Figure 4 is the water depth simulation result of a pipeline. In the figure, we see a longitudinal view of the pipe and manhole, with the light blue colour representing the water in the pipe and manhole and the dark blue line representing the water head. It can be seen that most of the water head is below the elevation of the manhole. But the head of manhole No. 1197 exceeded the top elevation, and the water would enter the pond to be stored. When there is a free volume in the manhole, the water flows back from the pond.

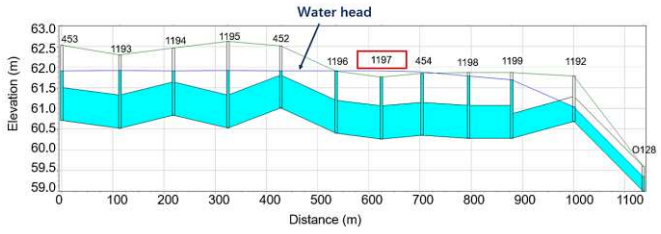

Figure 4. Water elevation profile of Node 453-O128

D. TELEMAC-2D surface flow model

The surface flow process was simulated using TELEMAC-2D. In surface flow simulation, it is necessary to consider the barrier effect of land elevation, the resistance due to friction, the absorption effect of the land, and the drainage process of the pipe network. For the drainage process, TELEMAC-2D and SWMM need to be coupled, and this will be described in detail in Part F. After considering all the factors above, TELEMAC-2D was used to solve the Saint-Venant shallow-water equations, to obtain the important variables e.g., water depth, velocity, and flowrate.

5) Elevation

In the simulation of urban waterlogging, elevation has an important effect on water flow. However, the accuracy of DEM data obtained is 12.5m*12.5m, which is not enough to describe the elevation of buildings. Therefore, we made fine adjustments to the DEM data, and modified the DEM data using the obtained information of building contour, location and subsidence depth of underpass, so as to reflect the overland characteristic.

Firstly, we performed low-pass smoothing on the DEM data. The "noise" band with higher frequency in the DEM raster is filtered out, which mainly contains the elevation information of buildings. The low-pass smoothing allowed us to create a DEM raster files that does not contain building elevations.

The building contour data which was obtained from Open Street Map includes the position and height information of the building. We modified the DEM raster file by using the building contour data which is a vector file that contains the building height attributes and position information. The elevation of the building part was changed to the height of the building plus the original ground elevation.

In addition, as shown in Figure 5, we found that the overpass elevation was recorded in the DEM instead of the ground elevation. The subsidence channel area is prone to waterlogging, so the deviation of elevation will have a great impact on the simulation results and risk prediction. We obtain the underpass data, which consists in spatial position, width, length and depth from Kaifeng City Administration Bureau. Based on these data, the DEM raster was further manually modified. The final DEM raster is shown in Figure 6.

Figure 5. An underpass in Kaifeng

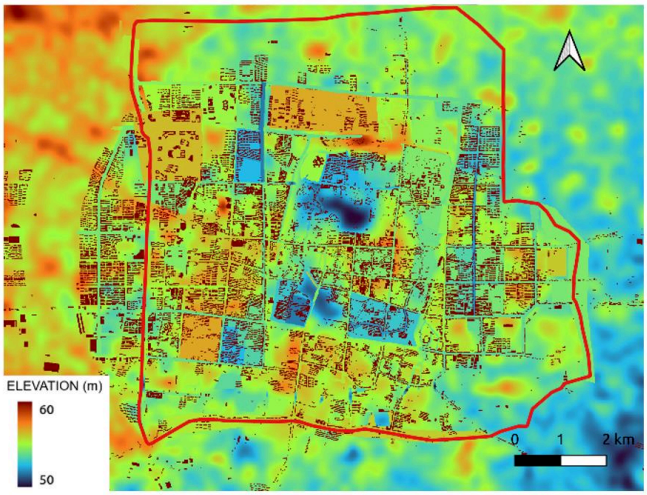

Figure 6. Modification of urban DEM

6) Bottom friction

Hydraulic roughness is roughness in fluid dynamics. Different land cover types with different surface roughness have different resistivity during urban waterlogging process. When simulating waterlogging in flood area model, different roughness values are given for different land use types. Its value can be related to the Manning coefficient, as shown in:

$$V=\frac{k}{n}R_h^{2/3}\cdot S^{1/2} \quad (6)$$

Where V is the velocity; K is the conversion constant and its value is 1 for the SI units; n is the Manning's n roughness coefficient, which reflects the influence of pipe and channel wall roughness on water flow, and we need to determine the value of the coefficient; R_h is the hydraulic radius and S is the slope.

Land use data was obtained from Map World on National Platform for Common Geospatial Information Services. The data was used to distinguish different areas such as water system, green land, road and building.

As shown in the Figure 7, we outline the study area, green land and water system area according to the satellite map. Since the study area is the urban district of Kaifeng City, it is considered that all the areas belong to the road and building area except the green land and water system. After determining the shape of each domain, we set the specific Manning friction coefficient according to the relevant literature [16], as shown in Table II. It should be noted that these values are not the final coefficients, and in future research, we will use the ADAO module of the SALOME platform, also linked to the TELEMAC system, to adjust the coefficients automatically [13].

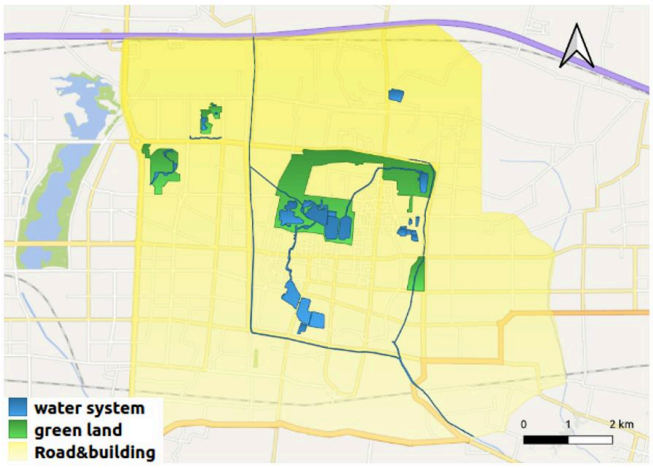

Figure 7. Shape of different feature land

Table II Friction coefficient of different features

Features	***Water system***	***Green land***	***Road & building***
Friction coefficient	0.015	0.5	0.06

7) Infiltration

In order to simulate the runoff process in the study area and take into account the inhomogeneity of land feature, a Soil Conservation Service Curve Number (SCS-CN) model was used in this study. The SCS-CN model is an empirical model developed by the Environmental Protection Agency (EPA) of the United States by analysing rainfall and runoff data of small watersheds in different regions. The model is mature and widely used [14][15]. It represents the natural law of rainfall and runoff and is very suitable for areas lacking data. The SCS-CN model has a simple structure, and the comprehensive parameter CN (Curve Number) value is used to represent the runoff production capacity of different land features. The CN is a dimensionless parameter, and the main influencing factors include soil type, land use, hydrological conditions and soil water content condition. Based on the principle of water balance and certain assumptions, the relationship between rainfall and runoff volume is:

$$Q=\frac{(P-\lambda S)^2}{P+(1-\lambda)S} \quad (7)$$

$$S=25.4\times\left(\frac{1000}{CN}-10\right) \quad (8)$$

where, P is the potential maximum runoff; S is the potential maximum retention after runoff begin.

Similarly to the way of setting the friction coefficient, as shown in Figure 7, we delimit different areas according to land properties. Then, we determined the specific CN value according to the literature [16] and engineering manual [6] shown in Table III, and used ADAO to calibrate the CN value.

Table III CN value of different land features

Features	*Water system*	*Greenland*	*Road & building*
CN value	98	61	95

E. Coupling

Based on urban GIS data, rainfall data, pipe network data, the SWMM pipe network model is constructed. The drainage flowrate of each manhole was obtained, and it was input into the TELEMAC-2D model. Similarly, the TELEMAC-2D model is established according to the urban geographic elevation data, land use data and rainfall data. Combined with the simulation results of the SWMM model, the water depth and water velocity over time are simulated by TELEMAC-2D. Figure 8 shows a schematic of the coupling data flow.

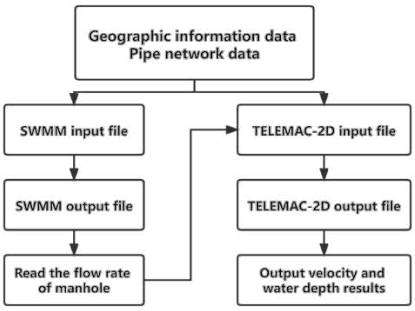

Figure 8. Schematic diagram of coupling data flow

8) Coupling by using TELEMAC-2D source term

For coupling the SWMM model and TELEMAC-2D model, the time-dependent drainage flowrate at each junction was computed and set as a source region in the TELEMAC-2D model as shown in Figure 9.

It is difficult to take all water grates into account in the SWMM model, and as a result, the total number of water collecting points in the model was less than that in reality. Therefore, in order to reduce the uneven drainage in space and truly reflect the drainage capacity of the pipe network, we set the sub-catchment area corresponding to each junction as the source region in the TELEMAC-2D model.

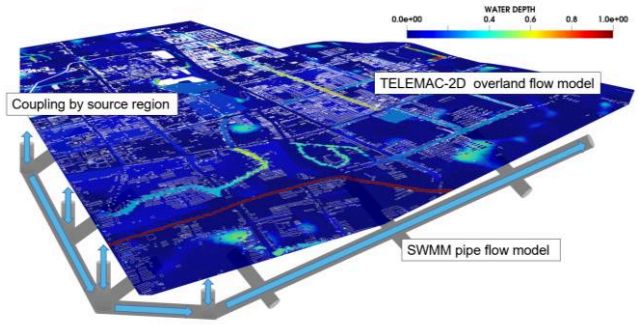

Figure 9. Schematic diagram of TELEMAC-2D coupling with SWMM

9) Definition of drainage flow value

In SWMM, the drainage flowrate at each junction cannot be read directly, so the existing variables need to be used to obtain the flowrate we need.

At time n, considering water conservation in SWMM, the drainage flowrate of each junction is:

$$Q^n_{\text{Source}} = Q^n_{\text{Rain}} + \frac{V^{n-1}_{\text{Pond}} - V^n_{\text{Pond}}}{\Delta t} = Q^n_{\text{Rain}} - \frac{\Delta V^n_{\text{Pond}}}{\Delta t} \quad (9)$$

where, Q_{source} is the drainage flowrate of each junction, Q_{rain} is the runoff flowrate produce by the corresponding subcatchment, ΔV_{pond} is the change of water volume in pond.

As shown in Figure 10 is the schematic diagram of the definition of drainage flowrate of each junction.

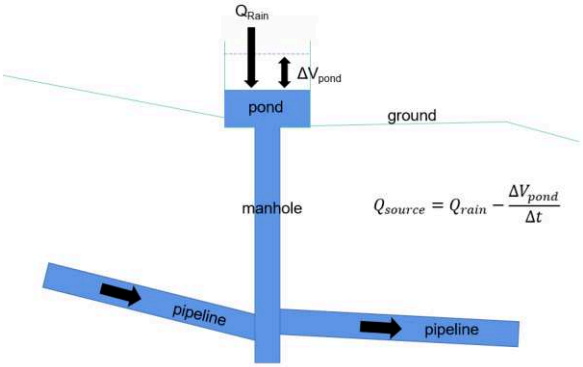

Figure 10. Schematic diagram of the definition of drainage flowrate

VI. RESULTS AND DISCUSSION

A. Typical case verification

The rainfall data for several heavy rains in 2021 and a batch of manually measured water depth data were obtained from the Kaifeng City Bureau of Urban Management. A rainfall with a large total rainfall and the largest amount of measured data last year from 2021.08.28 to 2021.08.29 is selected to verify the model. Figure 11 shows the 3-hour precision hyetograph for this rainfall. The rainfall peaks occurred at the 24th and 39th hour, and the data obtained by manual measurement mainly concentrated on the time period of the second rain peak.

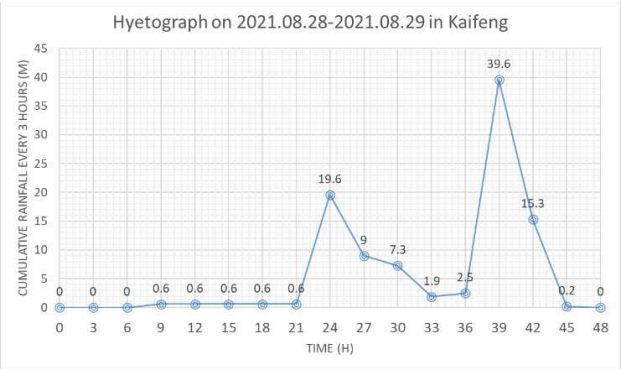

Figure 11. Hyetograph on 2021.08.28-2021.08.29 in Kaifeng

1) Spatial distribution verification

Waterlogging from 2021.08.28 to 2021.08.29 was simulated. The water depth simulation result of TELEMAC-2D is shown in Figure 12. According to the range of water depth, we divided the water depth into three levels as shown in Table IV, among which level 3 is the low risk level and it is only difficult for pedestrians to walk. Level 2 is medium risk level, bicycles and cars are difficult to drive. Level 1 is high risk and it will stop the traffic. The three different levels of danger are shown in light to dark blue.

The locations prone to waterlogging were obtained from Kaifeng City Administration Bureau: red dots indicate positions that have been prone to waterlogging over the years, brown dots indicate underpasses, and yellow-brown squares indicate neighbourhoods prone to waterlogging.

Among the 17 neighbourhoods prone to waterlogging, 5 were at medium risk and 4 were at low risk. All 10 overpasses are at high risk. Among the 27 waterlogging spots, 18 were at low risk, 3 were at medium risk and 6 were at high risk.

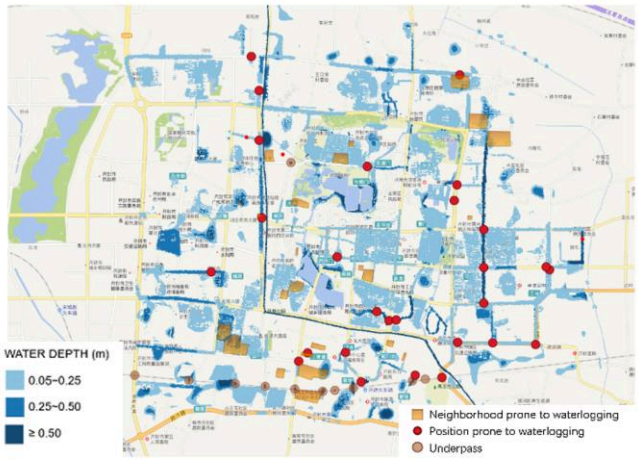

Figure 12. Water depth simulation results of TELEMAC-2D for the waterlogging from 2021.08.28 to 2021.08.29

Table IV Definition of waterloggoing level

Water depth (m)	***0.05~0.25***	***0.25~0. 50***	***≥ 0.50***
Waterlogging level	3	2	1

Comparison of 101 manually measured data with simulation results are shown in Figure 13. The spatial distribution trend of the simulation results is generally consistent with that of the measured data. It shows that the simulation results can reflect the trend of water spatial distribution in reality.

However, we found that 71% of the simulation results were lower compared with the measurement results, which may be caused by two reasons. One reason is that the setting of the CN value is small, which leads to the increase of infiltration rate and the decrease of runoff production, thus resulting in less surface water. Another reason is that after years of use, the drainage capacity of the pipe network system is lower than that of the new one. We can modify the parameters of SWMM in future work, such as the friction coefficient in the pipe, to reduce the drainage capacity of the pipe network.

2) Time distribution verification

We extracted three measurement points and verified the data in terms of time distribution. Figure 14 shows the time-varying water depth curves of Songmenguan Road, 17th middle school and Xihou Road respectively. It can be seen that in terms of time distribution, the simulation results have the same trend as the measured data, but similarly, the simulation results are lower than the measured results.

B. Error analysis and discussion

Based on the deviation between the simulation results and the measured data, we attempt to analyse here the causes of the error, and provide some practical experience for the future use of simulation model for urban waterlogging prevention.

1) Rainfall data

The accuracy of input data has a great impact on the accuracy of results. In order to improve the accuracy of rainfall data, we keep the precision of rainfall input file consistent with the precision of weather forecast. For example, in the waterlogging simulation for the next 24 hours, we use the hourly precipitation data as input. In addition, the more recent the forecast, the more accurate it is, so we feed new rainfall data from the API every three hours to achieve a real-time update of the simulation results.

2) Measurement data

The measurements that we obtained so far were taken manually by different people. Their readings can be off by 5 to 10 centimetres or more. Therefore, in the construction of a twin platform, one should invest in some water level meters and flowmeters, which can obtain more accurate data.

3) Parameters in model

There are many parameters in the model determined according to engineering manuals or relevant literature, such as infiltration rate and friction coefficient. These parameters do not reflect real urban conditions. We expect to calibrate these parameters using data assimilation (the ADAO module of the SALOME platform) after obtaining a sufficient number of measurements from the water level meter and flowmeter.

VII. CONCLUSION AND PERSPECTIVES

In this study, numerical simulations of urban waterlogging in the urban district of Kaifeng City were performed with coupling TELEMAC-2D model and SWMM model. More specifically, the establishment method and simplification principle of overland flow model and pipe network system model, as well as the coupling mode of TELEMAC model and SWMM model are put forward.

For the validation process, a rainfall data from 2021.08.28 to 2021.08.29 is used to validate the model. For the spatial distribution verification, among the 17 neighbourhoods prone to waterlogging, 5 were at medium risk and 4 were at low risk. All 10 overpasses are at high risk. Among the 27 waterlogging spots, 18 were at low risk, 3 were at medium risk and 6 were at high risk. The spatial distribution trend of the simulation results is generally consistent with that of the measured data. It shows that the simulation results can reflect the trend of water spatial distribution in reality. In terms of time distribution validation, the simulation results have the same trend as the measured data. However, 71% of the simulation results were lower compared with the measurement results. In view of this, we propose several reasons for the error of the results, including the error of rainfall data, measurement error, and the error caused by the model parameter settings that cannot reflect the real urban conditions.

In further improving this work, we will keep the precision of rainfall input file consistent with the precision of weather forecast and feed new rainfall data from the API every three hours to achieve a real-time update of simulation results in order to improve the accuracy of rainfall data. In setup of the simulation, we will invest into some water level meters and flowmeters, which can obtain more accurate measurement data. We will calibrate the setting parameters including friction coefficient and CN values by using data assimilation after obtaining a sufficient number of measurements from the water level meter and flowmeters.

ACKNOWLEDGEMENT

We would like to thank the Kaifeng City Administration Bureau for funding this research. Also, we wish to thank EDF R&D for the helpful answers to the questions about the coupling.

REFERENCES

[1] Chuanzheng, L. I. U., & Shuai, H. U. A. N. G. (2022). RESEARCH ON" 7· 20" MOUNTAIN TORRENTS AND GEOLOGICAL DISASTERS IN ZHENGZHOU CITY, HENAN PROVINCE OF CHINA. Journal of Engineering Geology, 30(3), 931-943.

[2] Feng, F. E. N. G., Qianhua, Y. U., Fusheng, L. U. O., Jichao, H. U. O., Yuehua, F. E. N. G., Xiaoying, J. I. N., & Cui, L. I. U. (2022). Urban waterlogging risk assessment of 7.20 heavy rainfall in Kaifeng City. Journal of Water Conservancy and Waterway Engineering, (4), 11-21.

[3] Sina News. The torrential rain in Zhengzhou caused a direct economic loss of 53.2 billion yuan [EB/OL]. (2021-08-02). https://news.sina.cn/kx/2021-08-02/detail-ikqcfncc0496637.d.html.

[4] Bisht, D. S., Chatterjee, C., Kalakoti, S., Upadhyay, P., Sahoo, M., & Panda, A. (2016). Modeling urban floods and drainage using SWMM and MIKE URBAN: a case study. Natural Hazards, 84(2), 749-776.

[5] Guoru, H. U. A. N. G., Haiwan, L. U. O., Wenjie, C. H. E. N., & Jian, P. A. N. (2019). Scenario simulation and risk assessment of urban flood in Donghaochong basin Guangzhou. Advances in water science, 30(5), 643-652.

[6] https://www.earthdata.nasa.gov/sensors/palsar

[7] https://www.openstreetmap.org/

[8] https://www.tianditu.gov.cn/

[9] http://data.cma.cn/

[10] Silveira, A. L. L. D. (2016). Cumulative equations for continuous time Chicago hyetograph method. Rbrh, 21, 646-651.

[11] Rossman, L. A. (2010). Storm water management model user's manual, version 5.0 (p. 276). Cincinnati: National Risk Management Research Laboratory, Office of Research and Development, US Environmental Protection Agency.

[12] Design Standard for Outdoor Drainage [GB 50014-2021] https://www.soujianzhu.cn/NormAndRules/NormContent.aspx?id=470

[13] Poncot, A., Goeury, C., Argaud, J. P., Zaoui, F., Ata, R., & Audouin, Y. (2017). Optimal calibration of TELEMAC-2D models based on a data assimilation algorithm. In Proceedings of the XXIVth TELEMAC-MASCARET User Conference, 17 to 20 October 2017, Graz University of Technology, Austria (pp. 73-80).

[14] Cai, X., & Xu, D. (2022). Simulation and optimization strategy of storm flood safety pattern based on SCS-CN Model. International journal of environmental research and public health, 19(2), 698.

[15] Shrestha, S., Cui, S., Xu, L., Wang, L., Manandhar, B., & Ding, S. (2021). Impact of land use change due to urbanisation on surface runoff using GIS-based SCS–CN method: A case study of Xiamen city, China. Land, 10(8), 839.

[16] Wang, K., Wu, Y., & Fan, Q. (2022). Construction of rainstorm security pattern based on waterlogging prevention and control: A case study on Zhengzhou City. Alexandria Engineering Journal, 61(11), 8911-8918.

[17] Mockus, V. (1964). National engineering handbook. US Soil Conservation Service: Washington, DC, USA, 4.

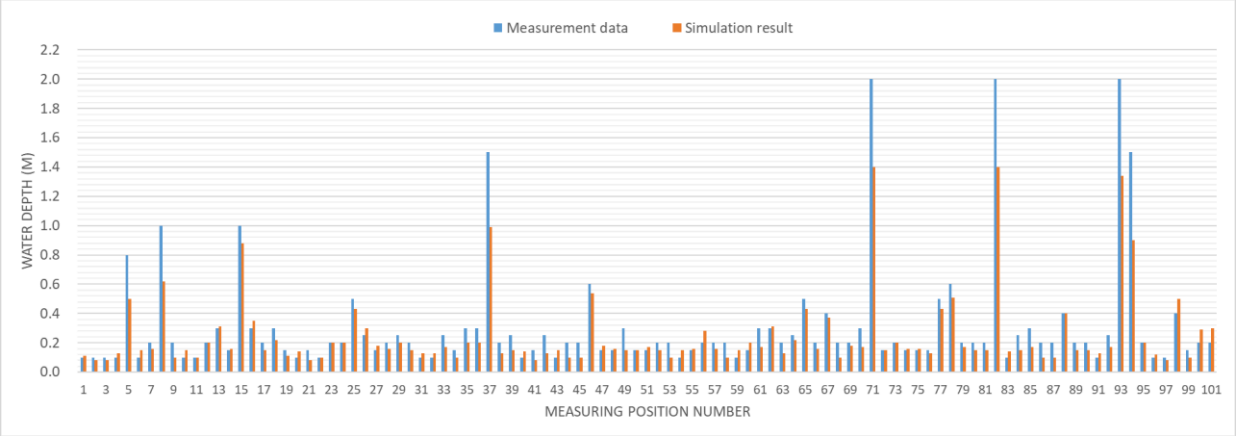

Figure 13. Comparison of 101 manually measured data with simulation results

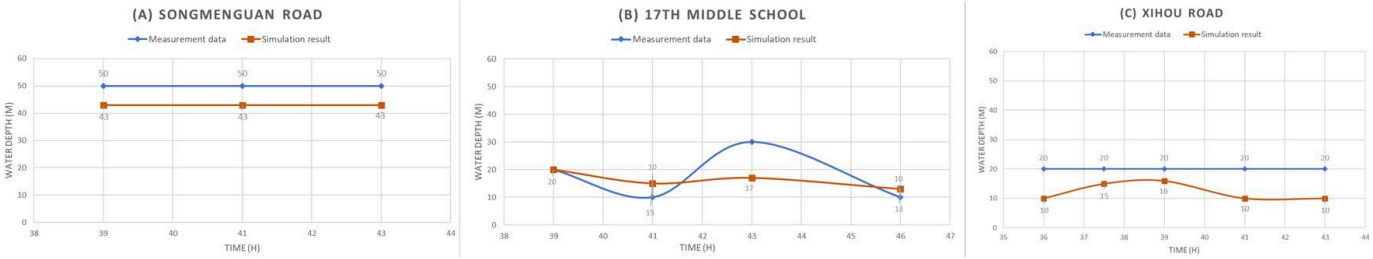

Figure 14. Comparison of 101 manually measured data with simulation results

Idealized modelling of FCA-CRT in European estuaries: an example of the Scheldt estuary

Qilong Bi[1,2] and Joris Vanlede[1]
qilong.bi@mow.vlaanderen.be
[1] Flanders Hydraulics Research, Berchemlei 115, 2140 Antwerp, Belgium
[2] KU Leuven, Department of Civil Engineering, Division of Hydraulics and Geotechnics, Kasteelpark Arenberg 40, 3001 Leuven, Belgium

Abstract – **The concept of combining Flood Control Areas (FCA) and areas with a Controlled Reduced Tide (CRT) to give "Space to the River" is an original idea that has been developed in Belgium. In order to perform knowledge transfer of the FCA-CRT method to other European partners, an idealized modelling approach is proposed as a tool for assessing the applicability for other European estuaries. This study investigated the different topo-bathymetry schematization methods and their impacts to the tidal propagation. Then an idealized model with the implementation of an FCA-CRT is used to explore the influences of its location on the estuarine hydrodynamics and tidal range reduction.**

Keywords: idealized modelling, FCA-CRT, estuary.

I. INTRODUCTION

The concept of combining Flood Control Areas (FCA) and areas with a Controlled Reduced Tide (CRT) to give "Space to the River" is an original idea that has been developed, implemented and monitored in a pilot project in the Scheldt Estuary in Belgium. Through years of development, this nature-based solution has been proved to be an effective approach providing protection against flooding and improving resilience of the estuarine ecosystem under the threat of climate change [1].

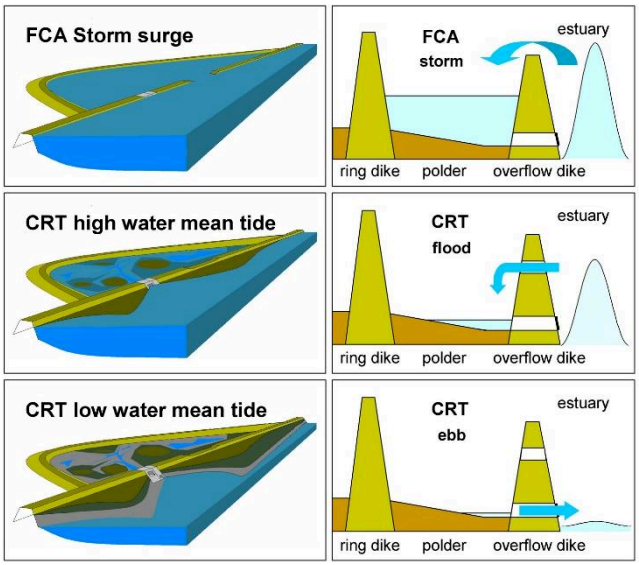

Figure 1. Functioning of a Flood Control Area (FCA) with Controlled Reduced Tide (CRT) at storm surge (upper panels), at high water mean tide (central panels) and at low water mean tide (lower panels) [1].

Figure 1 illustrates the concept of a functional FCA-CRT on the bank of an estuary.

In order to perform knowledge transfer of the FCA-CRT method to other European partners, an idealized modelling approach is proposed as a tool for assessing the applicability for six European estuaries across France, Germany, the Netherlands and the UK. This approach requires schematization of the geometry for each study area, in which the FCA-CRT is modelled as culverts, and only the important physical processes are considered [2].

To investigate the potential effects of FCA-CRT on tidal wave propagation and optimizing its design for each estuary, a large number of simulations have to be carried out in order to exhaust all possible combinations. For each of these simulations, a slightly different mesh with a specific design of the FCA-CRT must be used, which requires a considerable amount of effort in mesh creation, not to mention that the whole process has to be repeated for all six European estuaries. To make this process more efficient, an automated workflow has been developed based on a set of tools and algorithms that can perform topo-bathymetry schematization, mesh generation, simulation execution and post-processing, with given inputs. The process is based on Python scripts and other relevant packages to: (a) process the topo-bathymetric and water level data of each estuary; (b) prepare the necessary information for the Gmsh mesh generator [3]; (c) using the Gmsh API in Python to manipulate the mesh generation according to the desired FCA-CRT design; (d) translate the Gmsh generated mesh file (.msh) into the SELAFIN format mesh (.slf) to be recognized by TELEMAC-2D; (e) create a boundary condition file (.cli) that matches the new mesh; and (f) finally set-up of the schematized model for execution. Another important aim in this study is to use Python and TELAPY to create simulations from a model template and manipulate their inputs, i.e., meshes, steering files, boundary data, etc., to match each individual case to a specific design of FCA-CRT among a large number of combinations, and then submit them to a Linux-based higher performance computer for execution. The post-processing is also integrated in the automated workflow and the effects of FCA-CRT are analyzed.

This paper presents the integrated workflow with an example of the Scheldt estuary.

II. METHODOLOGY

The idealised modelling of an estuarine system usually consists of the following considerations:

- The schematization of the topo-bathymetry.
- The schematization of physical processes.
- The schematization of the measures.

These three aspects are discussed in detail in the following sections.

A. Topo-bathymetry schematization

In nature, the geometry of the estuary could change dramatically, starting much wider in the mouth region and then converging to a much narrower tidal river towards upstream. The bottom of the estuary usually varies in two directions, along the thalweg of the channel (deeper in the estuary mouth and shallower when it reaches further upstream), and across (deeper in the middle of the channel and shallower when it is close to the banks). When deriving the topo-bathymetry for building an idealised model, it is important to choose an appropriate method to perform schematization. In general, this complex natural geometry can be simplified while maintaining important properties like the characteristics of tidal propagation. In the previous study [6], the Scheldt estuary (Figure 2) was schematized as a funnel-shaped single channel from the mouth at Vlissingen to the tidal weir and locks at Ghent. The bottom of the schematized domain was kept constant in the cross-section direction but variable in the horizontal direction following the trend of the measured bathymetry.

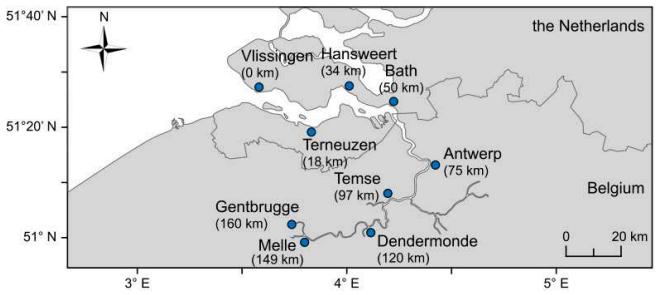

Figure 2. The tidal part of the Scheldt River from Vlissingen to Ghent [6].

Following a similar idea and utilizing the advantage of the TELEMAC-2D modelling framework, a new methodology that could maintain more topo-bathymetric features is proposed for the estuarine domain schematization in this study. To be more specific, the new method allows the presence of intertidal areas next to the main channel, and the shapes of the cross-sections along the estuary are computed by matching the observation-derived wet section areas at mean high water (MHW) and mean low water (MLW). The design of the mesh (distribution of the mesh nodes with spatial dependent size field) is also considered in this procedure.

In the framework of the TIDE project (http://www.tide-project.eu/), the topo-bathymetry and the main water level parameters (MHW and MLW) were collected from several European the estuaries including the Elbe, the Humber, the Scheldt, the Seine, and the Weser based on the previous surveys [4][5]. The topo-bathymetric data of an estuary represents its widths and elevations of the subtidal, intertidal, and supratidal areas located within the dyke lines in the domain.

The following data is reported in [4] and [5] and used in the schematization of the topo-bathymetry in this study:

- Z_{MHW}: mean high water level
- Z_{MLW}: mean low water level
- A_{MWH}: wet section area at mean high water level
- A_{MLW}: wet section area at mean low water level
- W_{MHW}: width at mean high water level
- W_{MLW}: width at mean low water level

1) Shape of the schematized estuary

The first step in the schematization of the topo-bathymetry is the mesh design since it determines the geometric contour or the shape of the schematized estuary. The shape is usually derived from the observed widths at multiple transects along the estuary. In the previous study [4], the estuary widths of the Scheldt were derived from the digital elevation model and the water level parameters.

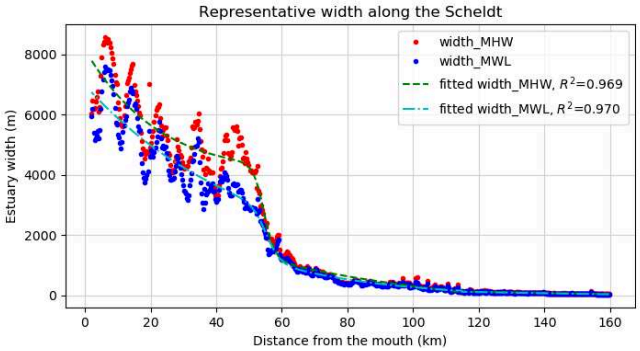

Figure 3. Measured width and fitted curved for the Scheldt Estuary.

Figure 3 shows the observed estuary widths W_{MHW} and W_{MWL} (width at mean water level, which is the average of W_{MHW} and W_{MLW}). Depending on the degree of preservation of topo-bathymetry features, the observed widths can then be fitted with specific functions for having non-smooth or smooth transitions from downstream to upstream. Later these functions are also used for generating the outline for the schematized domain.

2) Mesh generation

The second step involves the design of the mesh. To make the simulation efficient while maintaining enough features in topo-bathymetry, the mesh is designed as follows:

- A fixed number of nodes are evenly placed (with interval of *dx*) in the cross-sectional direction at every transect along the estuary.
- The distance between two transects or cross-sections (*dy*) is proportional to *dx* at the same location.
- The most outward nodes form the outline of the mesh, while the rest are considered as inside nodes

and control the generation of triangular elements within the domain.

The algorithm for generating the mesh outline and the embedded points is illustrated in Figure 4.

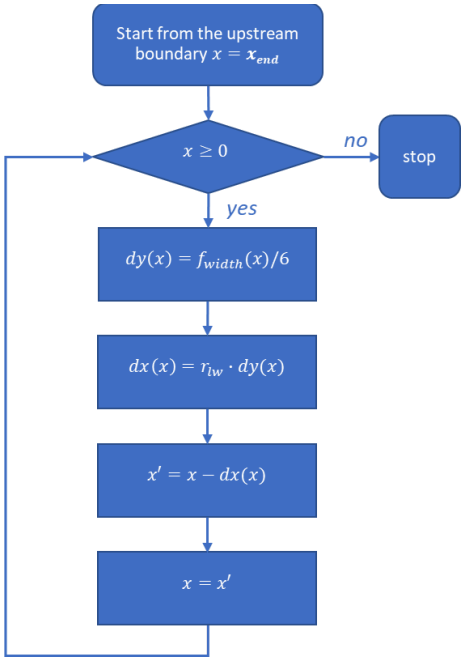

Figure 4. The algorithm for generating mesh nodes for a shcematized estuary (f_{width}(x) is the fitted function for the estuary width).

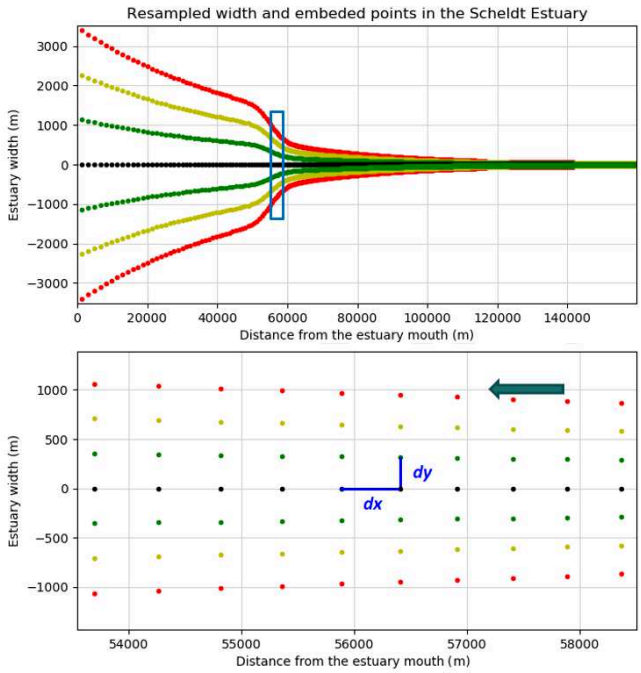

Figure 5. Algorithm generated points for the schematized Scheldt mesh (top: overview of the resampled points, bottom: zoom-in view of the nodes)

The generated outline nodes and inside nodes are shown in Figure 5.

Next, Gmsh is utilized for generating non-uniform triangular elements. The outline and the embedded nodes are arranged in a specific format and the info is passed to the mesh generator via its python API.

Gmsh uses its own file format (.msh, version 4) to store information of a generated mesh following a convention described in the Gmsh reference manual [6]. A python tool was then developed for converting the Gmsh file format into the selafin format (.slf) used by the TELEMAC system. The following mesh data is considered essential and required during the translation between two formats:

- Node number of each mesh node and its coordinates (x, y),
- Definition of each element (connection table with nodes arranged counterclockwise for ensuring positive determinant),
- Node number of the boundary nodes at both open and close boundaries.

The same python tool can also generate the boundary conditions file (.cli) automatically based on the info passed to Gmsh.

3) Resolving the transect profiles

The methodology in [6] assumes the bottom of a schematized estuary is flat in the cross-sectional direction but varies smoothly in the horizontal direction. This is usually not true for real estuaries due to the presence of intertidal areas, which not only affect the tide propagation but also lead to more complex morphological evolutions. Thus, including intertidal area and its potential influence should be considered in the domain schematization.

In the design of the mesh, nodes (including outline and inside nodes) are evenly distributed along each transect. Including intertidal areas will lead to changing elevations at these nodes transect by transect. Hence, a new method is proposed in this study based on the following assumptions:

- Evenly distributed nodes (seven in total) are placed along each transect and the lengths of the transects resemble the observed widths at mean high water W_{MHW}.
- The transect profile is assumed to have platforms next to the main channel representing the intertidal areas.
- The wet cross section areas at Z_{MHW} and Z_{MLW} (A_{MHW} and A_{MLW}, respectively) should correspond to the measured data mentioned in [4].

Figure 6 shows the predefined transect profile with the relevant parameters required for solving the two unknowns, the platform elevation Z_P and the main channel bottom elevation Z_B.

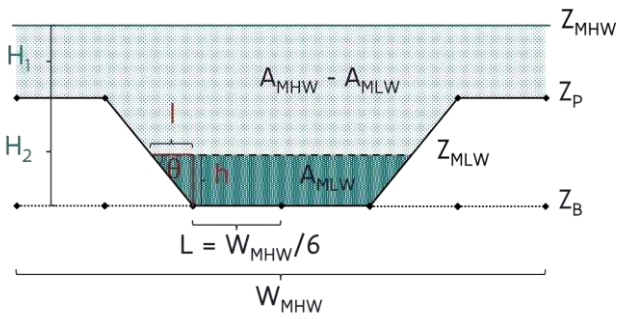

Figure 6. The targeted transect profile for matching the measured wet cross section areas at MHW and MLW

According to the definition of the cross section in Figure 6, the following equations must be satisfied:

$$A_{MHW} = 6L \cdot H_1 + 3L \cdot H_2 \quad (1)$$

$$A_{MLW} = 2L \cdot h + l \cdot h \quad (2)$$

Because

$$Z_{MHW} - Z_B = H_1 + H_2 \quad (3)$$

$$tan\theta = \frac{h}{l} = \frac{H_2}{L} \quad (4)$$

and

$$Z_{MLW} - Z_B = h \quad (5)$$

$$H_1 = Z_{MHW} - Z_P \quad (6)$$

$$H_2 = Z_P - Z_B \quad (7)$$

The eq. (1) and eq. (2) could be rewritten as

$$A_{MHW} = 6L \cdot (Z_{MHW} - Z_P) + 3L \cdot (Z_P - Z_B) \quad (8)$$

$$A_{MLW} = 2L \cdot (Z_{MLW} - Z_B) + \frac{L}{(Z_P - Z_B)} \cdot (Z_{MLW} - Z_B)^2 \quad (9)$$

where, the interval between the evenly spaced nodes along the cross-section L = $W_{MHW}/6$.

Solving the set of eq. (8) and eq. (9) provides the results of the two unknowns Z_P and Z_B that define the profile of the cross section. The python package SymPy for symbolic mathematics is used to solve the set of equations. Note that eq. (6) can be seen as a quadratic equation of Z_B because of the term $(Z_{MLW}-Z_B)^2$, thus solving the equations consequently result in two sets of solutions of H_1, H_2 and Z_B, in one of which it is possible to have $Z_{MLW} < Z_B$. The criterion for selecting the valid solution is that the platform elevation Z_P should fall in between Z_{MHW} and Z_{MLW} at most of the locations, so only one solution remains valid and is used later in the model.

Again, depending on the degree of preservation of topo-bathymetry features, the resolved platform and bottom elevations can be fitted with polynomial functions to smooth out the unwanted local variations. An example is shown in Figure 7.

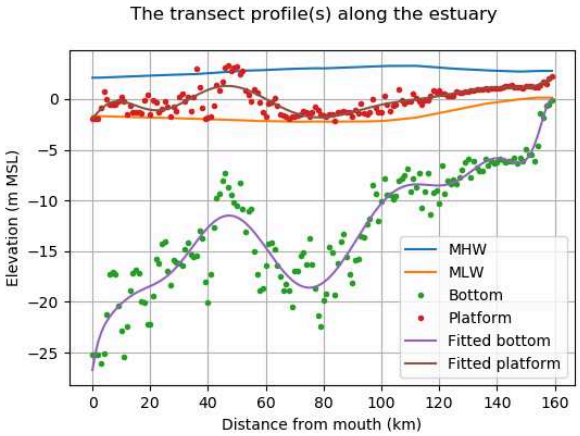

Figure 7. The resolved platform and main channel bottom elevations in the Scheldt estuary with coresponding fiteed polynomial curves.

B. Schematization of the enginerring mitigation (FCA-CRT)

The engineering mitigation considered in this study, i.e., the FCA-CRT, consists of sophisticated hydraulic structures separating the main estuary channel from an adjacent area of land adjacent that can experience flooding during periods of high water. Both the structure and the area of the land must be schematized in an idealised domain. As such, the water volume exchange between the main estuary channel and the FCA-CRT are modelled by culverts in TELEMAC-2D. The following schematization of the FCA-CRT is used in the model (Table I).

Table I Configuration of the culverts linking the main channel and the FCA-CRT

Dimensions of the area	Rectangle, 2500 m by 1200 m	
Mesh size	200 m	
Culverts	12 inlets	Each culvert: length 20m, width 2.6m, height 2.2m
	8 outlets	
Location of the area	Moving along the estuary in each simulation	

To demonstrate the effects on the estuarine hydrodynamics, the FCA-CRT is placed at different locations in different simulations. A python tool is made for generating batches of the models with specified configurations of the FCA-CRT in each one of them. In this case, it is used to shift the location of the FCA-CRT in each simulation, each time 15 km towards upstream starting at 15 km from the mouth area in the first simulation.

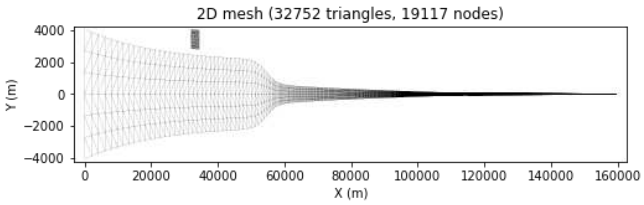

Figure 8. The mesh of the schematized Scheldt estuary with a FCA-CRT

The dimensions of the FCA-CRT and its location relative to the estuary are passed to Gmsh via its API in order to generate a smaller scale separate mesh, and then attached to the main estuary mesh. The boundary conditions file (.cli) is updated as well in order to include the boundary definitions for new area in the original mesh. An example of the estuary mesh (with curve-fitted widths) that has an FCA-CRT can be seen in the example in Figure 8. It is worth mentioning that the storm scenario is not considered in this study, in this case the FCA-CRT allows inflow and outflow via culverts, and there is no overflow from the main channel to the FCA-CRT above the overflow dike. Hence, the FCA-CRT area can be detached from the main mesh, the advantage is that its grid size will not be subjected to the mesh size in the estuary and the dimensions of the FCA-CRT can be defined freely.

C. *Esturine process schematization*

There are many physical processes happening in an estuarine system, e.g. (tidal) wave propagation, transport of suspended matter, salinity mixing, and other relevant ecological processes. In the idealised modelling, depending on the research focus, only the important processes are necessary to be included in the model.

Table II Model configurations

Boundary forcing	Upstream	Constant discharge 60 m^3/s
	Downstream	Tidal constituents (A_{M2} =1.89m, Φ_{M2}=0.0, f_{M2} =1.405e-4, A_{M4}=0.15m, Φ_{M4}=-2.269e-2, f_{M4} =2f_{M2})*
Model parameters	Turbulence model	The Smagorinsky model
	Bottom roughness	Dynamic friction law [8] with ks=0.3m
	Tidal flats	Yes, option 3 with consideration of porosity
	Timestep	10 s
	Duration	20 days

*M2 and M4 are the two major tidal constituents in the Scheldt estuary, and their amplitudes, phases and frequencies are denoted by A, Φ and f respectively. The values are based on [6] with adjustment for matching the tidal amplitude at downstream boundary with the observation.

In this study, the estuarine hydrodynamics is the main focus. The model has two open boundaries, at the downstream boundary (sea boundary), water elevations with two major tidal constituents (M2 and M4 tides) are prescribed, while at the upstream boundary a constant freshwater discharge is imposed. The turbulence (eddy viscosity) is resolved by the Smagorinski model. The overview of the model set-up can be seen in the Table II.

The above model configurations have been applied to all the simulations in this study. The differences in each individual model run are discussed in the next section. Note that considering the Scheldt estuary is well-mixed, the salinity is not included in the models.

III. RESULTS

Two groups of simulations were carried out in this study. The first group aimed to understand the influences of the topo-bathymetry features on the hydrodynamics in a schematized model, while the second group was dedicated to highlighting the effects of the FCA-CRT on the tidal propagation in along the estuary.

A. *Effects of the topo-bathymetry schematization*

The schematization of topo-bathymetry is one of the most important aspects in idealized modelling since the shapes of the estuary will have impacts to the tidal propagation. Different ways of schematization in this sense may result in different hydrodynamics in the domain, which could impact the validity of an idealized model.

In order to gain more insights, three meshes derived from different topo-bathymetry schematization methods are tested in three separate TELEMAC-2D simulations (Table III).

Table III Topo-bathymetry schematization methods used in this study

Method	Transect profile
iFlow method [6] (flat bottom)	Rectangle, curve-fitted width W_{MWL} (see Figure 3), bottom elevation of each transect: $Z_B = \frac{(Z_{MHW} + Z_{MLW})}{2} - \frac{1}{2}\frac{(A_{MHW} + A_{MLW})}{W_{MWL}}$
Proposed method (with tidal flats)	See Figure 6, Z_P and Z_B are solved from eqs. (8) and (9). No curve-fitting to W_{MHW}, Z_P and Z_B.
Proposed method (with tidal flats, smoothed)	See Figure 6, Z_P and Z_B are solved from eqs. (8) and (9). Curve-fitted W_{MHW}, Z_P and Z_B.

The schematized estuarine widths and platform/bottom elevations are shown in Figure 9, and the actual meshes used in the simulations can be seen in Figure 10. The only difference among these model runs is the mesh and the topo-bathymetric info associated with it, the rest of the model configurations are kept the same as in Table II.

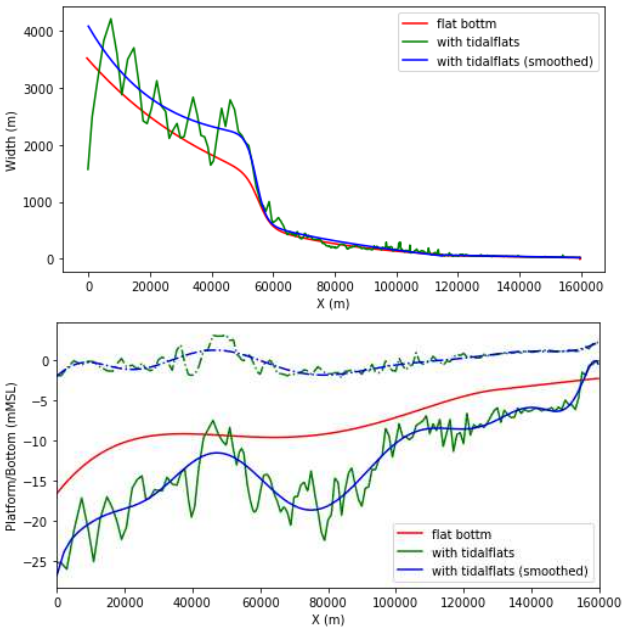

Figure 9. The half of the widths and the platform/bottom elevations of the three meshes (dotted lines: platform elevation, solid lines: bottom elevations)

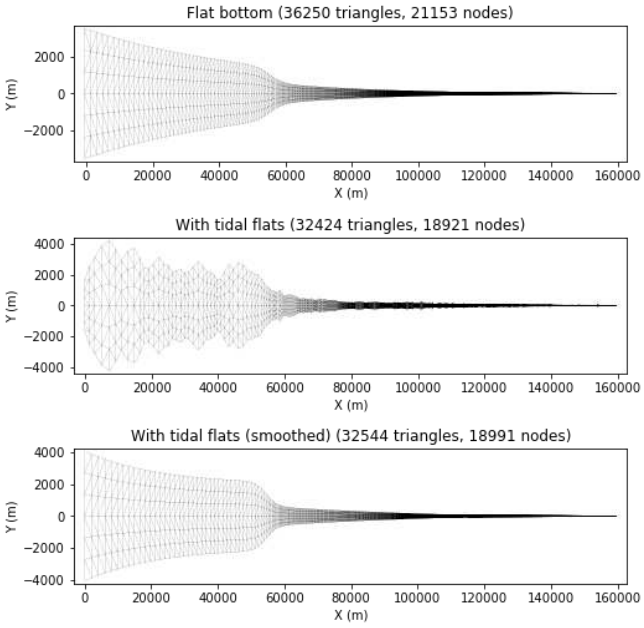

Figure 10. Overview of the meshes used in the simulations

The modelled results are then processed and compared with the observed data provided by [4]. To be more specific, the MHW, the MLW and the tidal range is computed in all the cases and compared with the values derived from the 10-year water level measurements in the Scheldt estuary.

Figure 11 shows that the mesh with tidal flats matches best the observed MLW and tidal range along the estuary, but it underestimates the MHW in the region 0-140 km and overestimates it from 140 km to 160 km. One of the reasons for the relatively poor agreement with the observed MHW especially near the upstream boundary could be due to the imposed constant discharge. In reality, flow can reverse its direction from downstream to upstream during flood around this location. The constant discharge in the model disturbs the flood/ebb transitions in the area, hence causes deviations from the measurements.

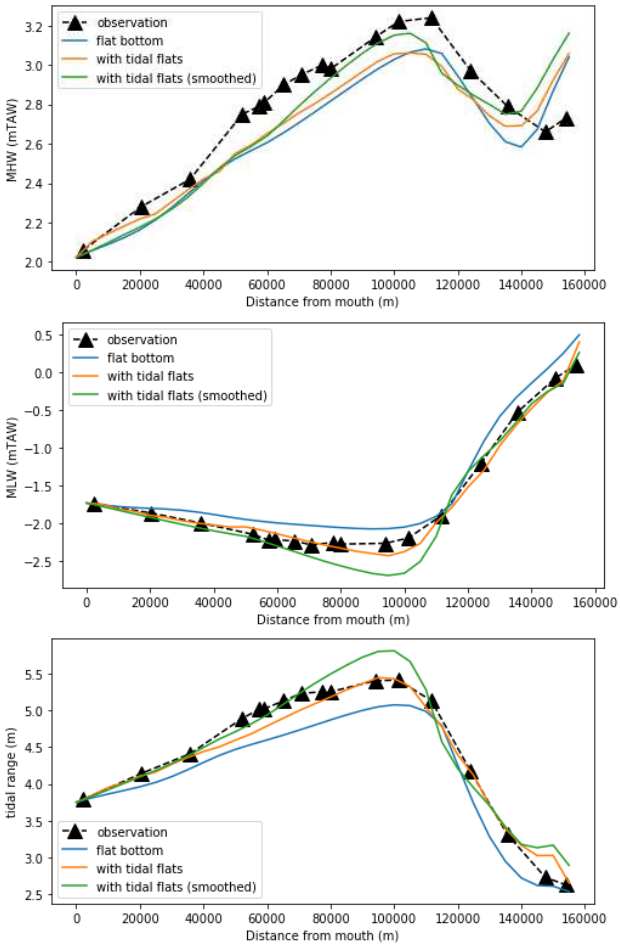

Figure 11. Comparison of MHW, MLW and tidal range

Compared to its non-smoothed version, the smoothed mesh with tidal flats produces similar horizontal patterns but the larger deviations from the observations. In general, it overestimates the tidal range in the region between 60 km and 110 km, which is mainly due to the underestimation of the MLW in the same region. This indicates that the detailed topo-bathymetric features affect the tidal propagation in the estuary and cannot be neglected. It also seems that the local variations in widths and elevations have larger influence in certain region that the other. But it is expected to have less tidal wave attenuation with the smoothed mesh.

The mesh with flat bottom predicts different horizontal patterns in MHW, MLW and tidal range. The peaks in these curves are always further upstream with 10 km shift compared to the observations. This means lack of topo-bathymetric features could lead to different tidal characteristics in the estuary.

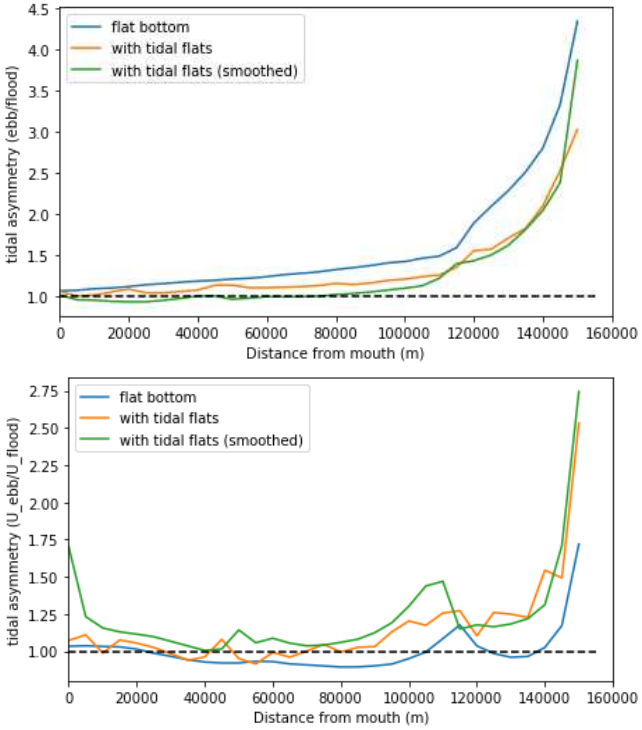

Figure 12. Comparison of tidal asymmetry in the main channel (top: ebb duration/flood duration; bottom: mean ebb velocity/mean flood velocity)

The effects of the topo-bathymetry can be further demonstrated in Figure 12. Two tidal asymmetry indicators were computed, namely the duration asymmetry and velocity asymmetry. The duration asymmetry shows that both meshes with tidal flats result in a less ebb dominant system, meaning that the ebb phase becomes shorter and flood phase longer. Especially with the smoothed version, due to less resistance, the downstream region from 0 km to 60km becomes slightly flood dominant.

The similar trend can also be observed in the velocity asymmetry. The results show that both ebb and flood velocities are increased when using the two meshes with tidal flats and the overall trend is that the system in these two cases become less flood dominant and, in some areas, more ebb dominant. Because the ebb velocity increases even more in the case with smoothed mesh with tidal flats, the system becomes entirely ebb dominant.

B. Effects of the FCA-CRT

The effect of the FCA-CRT on the reduction of tidal range has been assessed with a batch of simulations, in which the location of the FCA-CRT is changed in each run, but the size and the configurations of the culverts are kept the same. All the simulations were done with the smoothed mesh with tidal flats.

Figure 13 shows the tidal range is reduced by the presence of the FCA-CRT near the location where it is implemented. Downstream of it we can also observe a slight increase (compared to the reduction) of the tidal range due to the release of the stored water during ebb. The effect of the reduction is larger in the upstream and becomes smaller towards downstream where the tidal prism greatly increases.

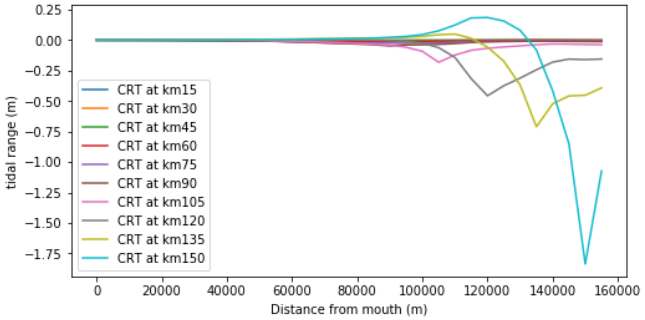

Figure 13. Tidal range differences along the estuary in the scenarios (with FCA-CRT implemetned) compared to the reference (FCA-CRT inactive)

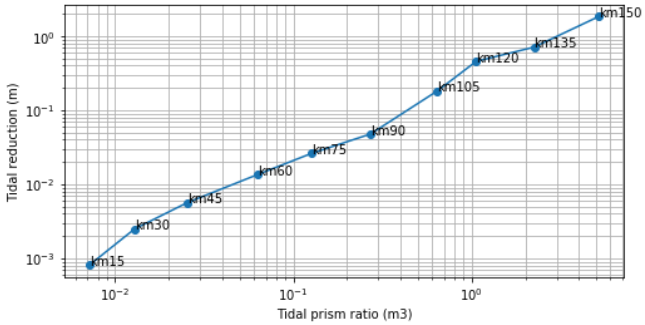

Figure 14. The ratio of the volume passing the transect where the FCA-CRT is implemented in the period between MHW and MLW to the volume entering FCA-CRT in the same period

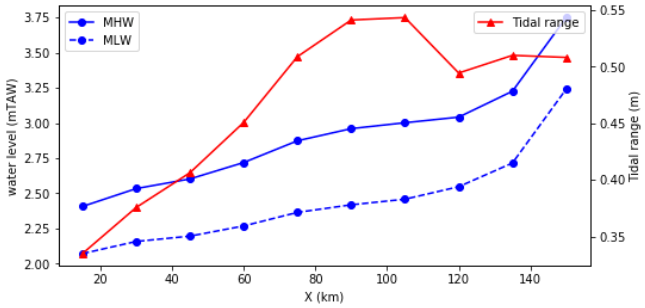

Figure 15. The MHW, MLW and tidal range in the FCA-CRT against the lcoation of the FCA-CRT

Further analysis shows that the reduction of tidal range can be linked to the ratio of tidal prism, which is the ratio of the volume passing the transect where the FCA-CRT is implemented in the period between MHW and MLW to the volume entering FCA-CRT in the same period (Figure 14). The reduction of tidal range increases exponentially, and more volume entering the FCA-CRT after 120 km and further upstream.

Besides the influence in the main channel, the tidal characteristics inside the FCA-CRT was investigated. Figure 15 shows the MHW, the MLW and the tidal range in each scenario case. In general, the water levels increase as the location of the FCA-CRT moves upstream. The highest

tidal range is achieved when placing the FCA-CRT at 105 km and it reduces the tidal range in the main channel by 18.2 cm. In case of requiring less disturbance to the system while maintaining the tidal dynamics in the area, then placing at 90 km will be an optimal option since it only reduces the tidal range by 4.8 cm.

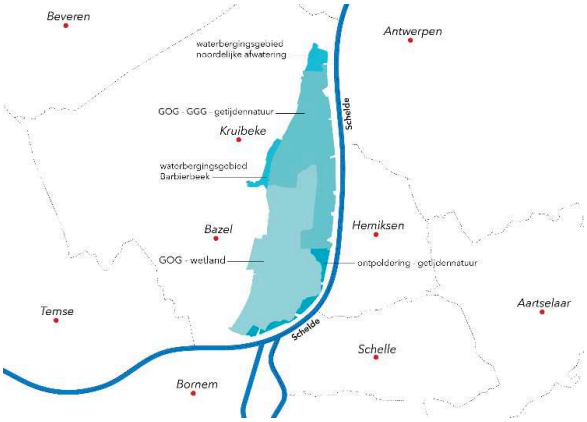

Figure 16. Location of the Bazels FCA-CRT [9].

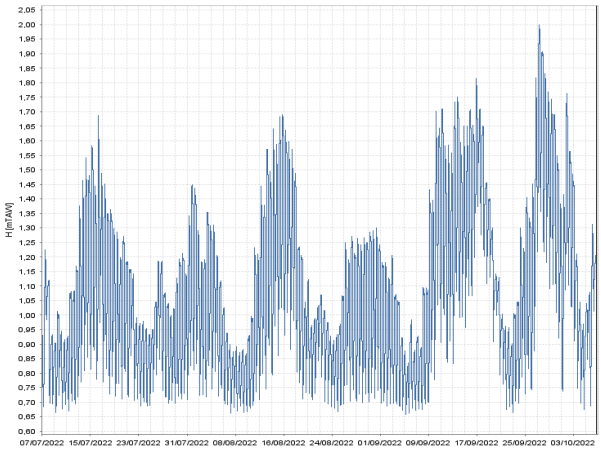

Figure 17. The timeseries of water level in Kruibeke-Bazels FCA-CRT (source: waterinfo.be).

The results are found comparable the pilot projects in the Scheldt estuary. One of the examples is the Kruibeke-Bazels FCA-CRT [9]. The area is situated at 85 km, with 450 ha mud flats and salt marshes now be used as a nature reserve, in which the tidal nature is created via the FCA-CRT concept. The tidal range in the area ranges from 0.5 m to 0.7 m according to the measurements in the past 3 months (6 July – 6 October 2022) (Figure 17).

IV. CONCLUSIONS

An idealized modelling approach is proposed in this study for studying the influence of the FCA-CRT on the estuarine hydrodynamics. As one of the important aspects in the idealized modelling, the schematization of the topo-bathymetry of the estuary was further investigated. The comparison of three difference schematization methods shows that the topo-bathymetry features could impact the tide propagation. More features it can preserve in a schematized domain, higher accuracy it may achieve in an idealised model. The detailed topo-bathymetric variations in the mesh does not only affect the tidal range, but also the tidal asymmetry, and it may lead to different tidal characteristics that deviate from real system.

The second part of this study investigated the influence of a FCA-CRT on the reduction of tidal range by placing it at different locations. The results show that, for a given configurations of the culverts, depending on the ecological and hydrodynamic targets, there always exists an optimal location, where the tidal characteristics in the FCA-CRT is more favourable and it has desired impact to the system. It is worth mentioning that this is only a preliminary study, although it has demonstrated how the methodology can be used to optimize the FCA-CRT design.

ACKNOWLEDGEMENT

This study is supported by the European project LIFE-Sparc (Space for Adapting the River Scheldt to Climate Change).

REFERENCES

[1] Maris, T., Cox, T., Temmerman, S. et al. (2007). Tuning the tide: creating ecological conditions for tidal marsh development in a flood control area. Hydrobiologia 588, 31–43.

[2] Bi, Q., Vanlede, J., Mostaert, F. (2021). LIFE SPARC – action C10: Transfer to other estuaries (Replicability & Transferability): Sub report 1 – Inventory and comparative study. Version 2.0. FHR Reports, 16_072_1. Flanders Hydraulics Research: Antwerp, Belgium

[3] C. Geuzaine and J.-F. Remacle. Gmsh: a three-dimensional finite element mesh generator with built-in pre- and post-processing facilities. International Journal for Numerical Methods in Engineering 79(11), pp. 1309-1331, 2009.

[4] Vandenbruwaene, W.; Plancke, Y.; Verwaest,T.; Mostaert, F. (2013). Interestuarlne comparison: Plydro- geomorphology: Plydro- and geomorphodynamlcs of the TIDE estuaries Scheldt, Elbe, Weser and Plumber. Version 4. WL Rapporten, 770_62b. Flanders Hydraulics Research: Antwerp, Belgium.

[5] Vandenbruwaene, W.; Plancke, Y.; Mostaert, F. (2018). ANPHYECO-Seine – Hydro-geomorphology of the Seine estuary: Interestuarine comparison and historical evolution. Version 4.0. FHR Reports, 14_120_2. Flanders Hydraulics Research: Antwerp.

[6] Dijkstra, Y.M., Schuttelaars, H.M. & Schramkowski, G.P. (2019). Can the Scheldt River Estuary become hyperturbid?. Ocean Dynamics 69, 809–827.

[7] Geuzaine, C. and Remacle, J.-F. (2009). Gmsh: a three-dimensional finite element mesh generator with built-in pre- and post-processing facilities. International Journal for Numerical Methods in Engineering 79(11), pp. 1309-1331.

[8] Bi, Q., & Toorman, E. A. (2015). Mixed-sediment transport modelling in Scheldt estuary with a physics-based bottom friction law. Ocean Dynamics, 65(4), 555-587.

[9] De Vlaamse Waterweg (2022). OMES project: Research on the environment effects of the SIGMA plan and multidisciplinary study on the estuarine environment of the Sea Scheldt. http://www.omes-monitoring.be/en/experiments/.

Wetting and drying improvements in TELEMAC (part 1)

W.Alexander Breugem[1]
abr@imdc.be, Antwerp, Belgium
[1]: IMDC (NV)

Abstract – **This paper addresses wetting and drying using the TELEMAC finite element code in two-dimensional and three-dimensional simulations. Simulations with wetting and drying in TELEMAC can be challenging, especially in situations where the bottom slope is large. Here, high velocity values are regularly encountered, that sometimes can lead to instabilities and crashes of the model and often limit the time step of the simulations, thus increasing the calculation time. In this paper the TELEMAC finite element wetting and drying algorithm is studied. Some alternative methods for the wetting and drying scheme are implemented, which are tested in theoretical test cases as well as in a simplified version of the Scheldt Estuary model.**

Keywords: TELEMAC-2D, TELEMAC-3D, wetting-drying, tidal flats, numerical methods

I. INTRODUCTION

A. Background

In many simulations, the model domain consists of shallow areas, where a part of the time the area becomes dry. Examples of such dry areas include tidal flats, beaches, and riverbanks. The simulation of wetting and drying is numerically and physically challenging. The physical challenge lays in the fact that the shallow water equations, such as they are used in TELEMAC-2D are not valid, as some of the assumptions used in deriving these equations are not satisfied around the transition to dry areas. The numerical challenges in the wetting and drying process are many. The most important of these are:

- Ensuring that negative water depths do not occur.
- The occurrence of spurious pressure gradients on slopes (Figure 1).
- Ensuring correct local and global mass balances (Figure 2).
- The occurrence of shocks at the wet-dry transition. In TELEMAC, this often leads to the occurrence of wiggles in the velocity, with peaks that are unphysically large.
- The occurrence of singularities due to division by the water depth (e.g. in the bed friction term and the horizontal diffusion term).
- Occurrence of instabilities leading to model crashes. In TELEMAC, these typically happen because high velocities occur on (nearly) dry cells.
  Preventing this typically leads to a severe time step criterion and therefore slow calculations. It seems in general, that this problem tends to be more severe close to (steep) slopes in the bathymetry.
- Model crashes due the occurrence of NaN values in the tracers (like temperature or water quality variables) in shallow areas.

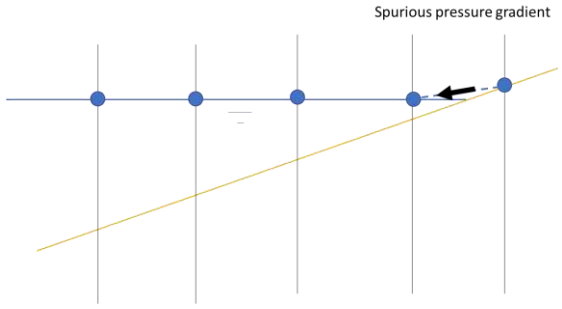

Figure 1. Occurrence of spurious pressure gradients due to wetting drying. Because the water depth is non-negative, the free surface on the dry slope has an incorrect gradient, which drives a spurious flow when left uncorrected.

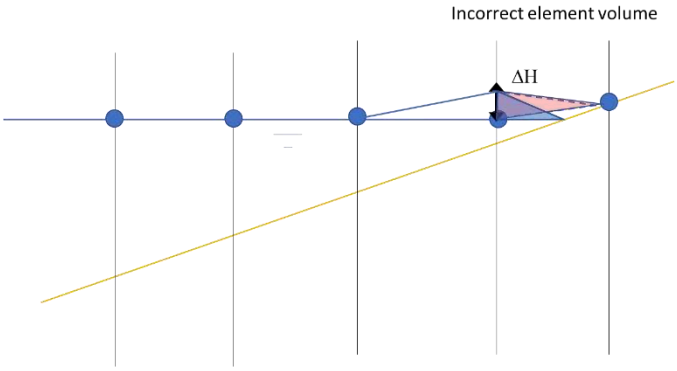

Figure 2. Occurrence of mass balance errors due to wetting drying. The volume that needs to be filled/released on the dry area is larger in the model (red) than it should be in reality (blue), leading to increased flow on the side.

It is interesting to note that the first two problems could disappear in case negative water depths are allowed. This approach is indeed used in the finite element model of Henische et al [1], who apply a very large friction coefficient in areas with negative water depths in order to damp the flow there. Nevertheless, this approach has many limitations, and hence, is not considered in this paper.

B. Objective of the study

The objective of this research is to further improve the wetting and drying algorithm in TELEMAC. In particular, the aim is to make the algorithm more stable, such that larger time steps can be used, and to limit artifacts (wiggles) in the

computed velocity fields, which pose problems for example when sediment transport is considered.

In this paper, the focus is to find solutions that work in TELEMAC-2D and TELEMAC-3D for cases with and without transport of scalars. This means that many numerical options are not considered in the present work, because they are not available in TELEMAC-3D (such as finite volume schemes, the primitive equation option or SUPG on water levels) or because they cannot be used in combination with tracer transport (such as filtering to correct negative depths: TREATMENT OF NEGATIVE DEPTHS = 1). Note that the finite volume method in TELEMAC-2D, while certainly more robust for wetting and drying, has a stringent time step criterium, because it is an explicit scheme, making it rather slow.

These considerations lead us to the choice to inspect the case where the wave equation is used to solve the momentum equations (TREATMENT OF THE LINEAR SYSTEM = 2), in combination with the flux control settings to treat negative depths (TREATEMENT OF NEGATIVE DEPTHS = 2). In the present paper, only simulations are performed using TELEMAC-2D. Improvements in TELEMAC-3D are left to a future paper. Improvements to scalar transport are also not considered in this paper, but these are mentioned in [2].

C. Overview of wetting drying in literature

It is insightful to consider the scientific literature on wetting drying. Most of the work on wetting and drying has been done in finite volume schemes. However, some work has been performed for wetting and drying. An implicit wetting-drying method was presented by Kärmä [3]. In their paper, they change the bathymetric elevation in order to prevent negative depths. The resulting system of equations is non-linear and is therefore solved using a Newton-Raphson solver. Wetting and drying in a finite element simulation for non-hydrostatic simulation is also considered in [4] and [5], whereas the solution of the shallow water using residual distribution schemes is described by [6]. In the latter approach, the scheme is constructed in such way that the water depth cannot become negative. Their approach has some similarities to the negative depth algorithm in TELEMAC, which also uses a residual distribution scheme.

Stelling and Duinmeijer [7], whose approach was later extended to unstructured meshes [8], consider wetting and drying on structured finite difference scheme, and present an implicit scheme for the continuity equation, which still retains a time step limit (only one cell can be flooded per time step), which is needed to make sure the water depth remains positive. Their conclusion is that for correct wetting and drying, an energy balance (obtained using Bernoulli's equation) should be applied on the transition of wet to dry. This shows that the characteristics method used for advection of velocities (such as used in TELEMAC) leads to additional energy dissipation. Hence it is a robust choice, but it may not be suited for all circumstances.

Casulli [9] presented a new finite volume method to take wetting and drying into account. His approach considers the variation in the bathymetry within a cell of the mesh. This has two advantages: the water depth of the volume fluxes is better represented (typically they are deeper, leading to less formation of shock waves), and it solves the volume and pressure gradient problems discussed in section I.A. Because the method uses bathymetry variation within cells, simulations can be performed using coarser meshes while keeping the same accuracy, thus leading to faster calculation times. The method leads to a non-linear system of equations, which is solved using a Newton-Raphson iteration technique that was found to converge rapidly. Unfortunately, it is not straightforward to apply these ideas to the finite element method used in TELEMAC.

D. Overview of wetting drying algorithm in TELEMAC

The algorithm that is used in TELEMAC-2D and TELEMAC-3D to calculate the hydrodynamics is roughly summarized as follows:

1. First, boundary conditions, forcings and source terms (baroclinic pressure gradient, Coriolis force, wave-current interaction etc.) for the hydrodynamic equations are calculated.
2. The changes in the water level and velocities are calculated using the wave equation (subroutines propag.F in TELEMAC-2D and wave_equation.f in TELEMAC-3D). This is a matrix equation, which needs to be solved. The calculation consists of the following sub steps:
   a. Calculation of the vertical flow profile based on vertical diffusion and forces (TELEMAC-3D only).
   b. Calculation of the advection terms (these are explicit).
   c. Calculation of the horizontal diffusion. This is done using an explicit method in TELEMAC-3D, and a somewhat implicit method in TELEMAC-2D[1].
   d. Calculation of the vertical momentum equation to determine the non-hydrostatic pressure component (TELEMAC-3D, non-hydrostatic calculations only).
   e. Calculation of the free surface gradient at time *n*. A correction is applied to eliminate the spurious pressure gradient (Figure 1).
   f. Calculation of an auxiliary velocity, based on source terms, advection and diffusion as well as the surface pressure gradient at step *n* (that does not yet include the effect of changes in the water level).
   g. Solving the wave equation to determine the changes in water levels. At this step a matrix equation is solved.
   h. Applying the changes in water level to determine the water level gradient at time *n*+q, and use this gradient to calculate the final flow velocity.

[1] In TELEMAC-2D the diagonal of the diffusion matrix is applied implicitly, where the off-diagonal terms are applied explicitly. This has the advantage that no extra linear system needs to be solved, while still being stable for large values of DDT/DX^2. Here D is the diffusion coefficient, DT the time step and DX a measure for the mesh size. However, the calculated diffusion term leads to diffusion fluxes that are too low, especially for large values of DDT/DX^2.

3. Determine the volume fluxes of water (subroutine flux_ef_vf.f).
4. Recalculate the water levels using the volume fluxes from step 3 using a residual distribution scheme (subroutine correction_depth_2d.f). This scheme is globally mass conservative, meaning that there is no loss of the mass of water, and at the same time, it prevents the occurrence of negative water depths. The scheme iteratively distributes the water masses that are transported between nodes [10]. In case the algorithm finds that no more water can be redistributed, it stops iterating. Typically, this happens when the flux out of a cell during a time step is larger than the available volume of water (i.e. during drying). A known issue of this scheme is that the results may differ when the number of parallel processes is changed. This issue is not addressed in the present paper.

The advantage of the algorithm used in TELEMAC is that a layer of water (although with a thickness of 0 m) always remains present, thus avoiding instabilities related to including or excluding elements from the calculation. The fact that the algorithm allows the water depth to become zero is also an advantage. In many models, the remaining water layer needs to have a minimum thickness, which leads to problems with the volume balance of water, that can be severe in case large tidal flats are present (e.g. [11]). Finally, the algorithm is implicit, so it should, in theory, not pose any time step criterion.

II. OVERVIEW OF TEST CASES

A. *Introduction*

The tests are performed using the goblinshark branch, which is based on TELEMAC v8p1. However, this branch contains two important changes with respect to wetting and drying:

- The velocities are set to zero at dry areas (defined as $h < 0.01$ cm), as it was found that this prevents many instabilities, thus permitting the use of relativly large time steps.
- Forces in the momentum equation (such as Coriolis force) are set to zero below a threshold depth ($h < 0.10$ m), after finding crashes related to the application of the force in shallow areas when using the NERD scheme for advection of momentum in TELEMAC-3D.

B. *Thacker Fruit bowl*

1) Description of the test

The test case described by Thacker [12] is used as the main test case to test wetting and drying. In this test case, a seiche is calculated in a circular domain, where the bottom has a parabolic variation. Thacker showed that this situation has an analytical solution for cases without any energy dissipation (bottom friction, and viscosity), but including the advection of momentum as well as the Coriolis force.

In this study, a circular domain with a radius of 10,000 m is set up with a mesh size of 100 m. This lead to a mesh with 34,261 nodes (67,787 elements). The bathymetry is chosen such that the water depth in the middle of the basin is equal to 5 m. As an initial condition, the water level from the analytical solution is used for the moment the water level has the most extreme run up to the right (Figure 3). At that moment, the velocities are zero according to the analytical solution, so zero velocities were used as an initial condition.

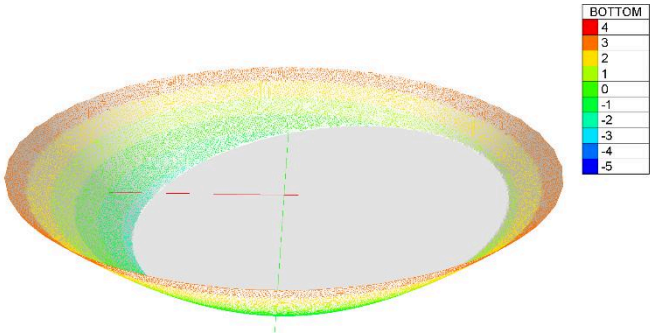

Figure 3. Mesh and bathymetry of the test case, and initial condition of the water level (in grey).

The simulations are performed for a total duration of 12 h, which corresponds to roughly nine oscillation periods. The time step is set to 30 s. The settings for the model were taken as much as possible in accordance to the analytical solution (for the case with a Coriolis coefficient of $f = 0$), with one major exception: bed friction is used applying Nikuradse's law with a friction coefficient of $k = 0.003$ m, which is relatively low. This was done, in order to be able to assess the effect of bed friction, as this is sometimes considered an essential process for the correct numerical simulation of wetting and drying. For advection of momentum, the NERD scheme (14) is used.

In each test case, it is tested that the oscillation period from the simulations corresponds to the value calculated in the analytical solution (80 minutes) and that the mass of water is conserved. Only when differences are found herein, this will be mentioned in the text. Note further that the analytical solution gives a maximum velocity of 0.8 m/s. Any velocity higher than this value is considered a spurious artifact.

2) Results and sensitivity analysis of Thacker fruit bowl

The simulations show that using the finite element method, two problems occur (note that according to the analytical solution, the velocity is expected to be constant in the domain):

- The occurrence of wiggles in the velocity with a rather large magnitude. These occur near the wetting front. (Figure 4 at a distance of -8 km).
- The occurrence of a discontinuity in the velocity, around the drying front (Figure 4 at a distance of +8 km). Apparently, the drying does not occur fast enough in the model, leading to the lagging of the drying front.

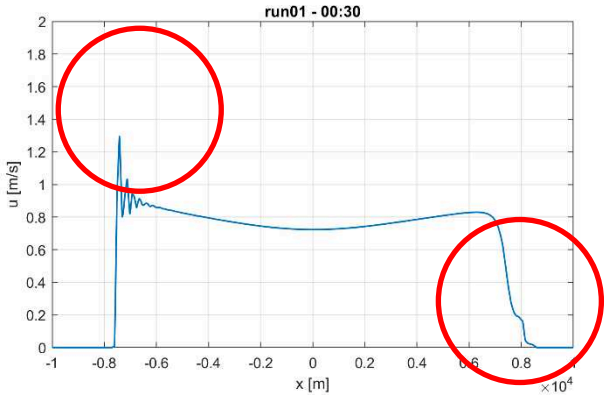

Figure 4. Velocity magnitude after 30 min on a transect through the centre of the basin. The flow at this moment is from right to left.

A sensitivity test is performed, studying a large amount of numerical and physical parameters, in order to understand and to find, whether some numerical parameters can solve the issue. The main conclusions of this sensitivity study are:

- The wiggles are strongly influenced by the time step. Decreasing the time step diminishes the wiggles (but even with a very small time step of 0.5 s, they do not disappear completely. This is in contrast to the finite volume method, which does not show any wiggles. However, the finite volume method is slow (about a factor 10 slower than the base case with a time step of 30 s), due to the fact that it uses a very small time step of approximately 1.5 s.
- Using a high horizontal diffusivity (20 m2/s), diminishes the wiggles. However, it has a strong side effect, namely that the oscillation period changes substantially (with 10% to 88.5 s). Further, there is a stability limit, thus limiting the applicability of this method in case with fine meshes.2
- Some numerical parameters lead to a substantial decrease of the wiggles. The most prominent ones are NUMBER OF SUB-ITERATIONS FOR NON-LINEARITIES = 3, although this leads to a substantially larger calculation time (it increased almost with a factor 3), and FREE SURFACE GRADIENT COMPATIBILITY = 0.
- There is some influence of the advection scheme. Nevertheless, the results using the characteristics method instead of the NERD scheme are rather similar. Other advection schemes have not yet been tested.

C. *Scheldt test case*

1) Description of the test

A field test case is also taken. For this, an extract is made of the upstream branches of IMDC's Scheldt model [13], in order to have a fast model that can easily be run on a single processor. The mesh contains 40,658 nodes (68,230 elements) and contains channel meshes in a large part of the domain (Figure 5). The area contains many narrow branches, often discretised using channel meshes, with small mesh sizes (of the order of 10 to 30 m in the streamwise direction and up to 5 m in the spanwise direction). The bathymetry in many of these branches has rather steep slopes to the side, on which wetting and drying occurs. This makes it a challenging test case for the numerical scheme.

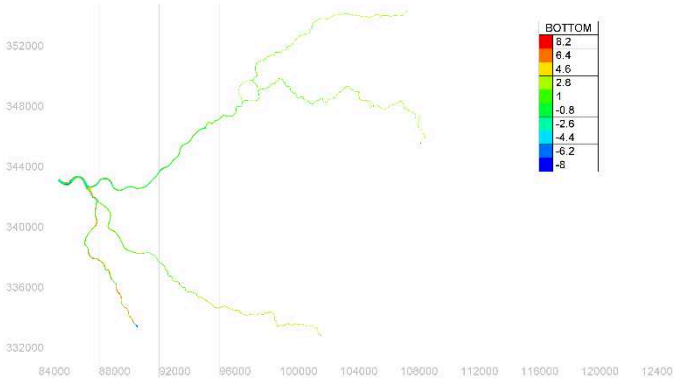

Figure 5. Mesh and bathymetry of the Scheldt test case.

As boundary conditions, measured flow rates are used upstream, whereas a time series of water levels extracted from the full Scheldt model is used at the downstream boundary.

The simulations are performed using TELEMAC-2D with a time step of 30 s. This is a very large time step, but one of the objectives of the test is to increase the time step as much as possible in order to obtain the fastest simulation time. It was found that the fastest simulations on a single processor were obtained using the direct solver (8), whereas simulations using the conjugate gradient method (1) take longer, as more than 500 iterations are needed for the solver to converge. This shows that for very large time steps, the direct solver can be a fast alternative for the iterative solvers (at least in serial mode). This also suggest that for simulations with very large time steps, a speed-up might be obtained using more advanced preconditioning than is currently available in TELEMAC.

2) Results and sensitivity analysis of the Scheldt test case

The model runs even with the large time step. However, relatively high velocities are found (O 10 m/s). These are related to spurious velocities generated on nearly dry areas. A limited sensitivity analysis was performed. It is found that increasing the diffusivity, though showing a tendency to smooth out some shock waves, also rapidly leads to instabilities and model crashes, meaning that setting the diffusion coefficient alone cannot solve drying flooding issues in this case. Moreover, it is found that flow occurred through closed walls (Figure 6). At the location of the closed wall, there are vectors visible with components perpendicular to the wall. Probably, these are generated due to the free surface slope, which is quite steep in that direction. The condition that $\nabla\vec{u}.\vec{n} = 0$ at the closed boundaries, is apparently not fulfilled automatically Therefore, a correction is implemented, which is very similar to the routine airwik2.f in TELEMAC-3D, in which the velocity at the boundary is corrected in order to ensure that $\nabla\vec{u}.\vec{n} = 0$ at the closed boundaries. The results are shown in Figure 7. It is clear that the flow through the boundary is stopped. Further, it appears that the maximum

[2] Indeed increasing the horizontal viscosity in the Scheldt test case let rapidly to instabilities and crashes.

velocities decrease in that case (closer to physical plausible values) and that the flow field is somewhat smoother. Nevertheless, the flow field in Figure 7 clearly has issues, in the sense that there is high flow from the (nearly) dry banks into the river.

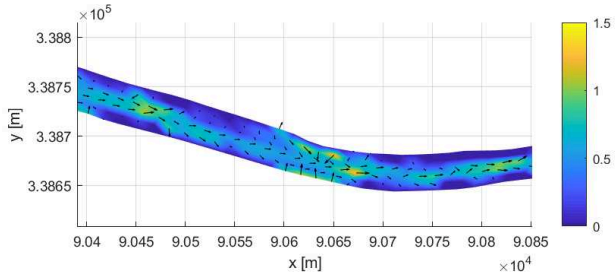

Figure 6. Instantaneous velocity field without boundary correction.

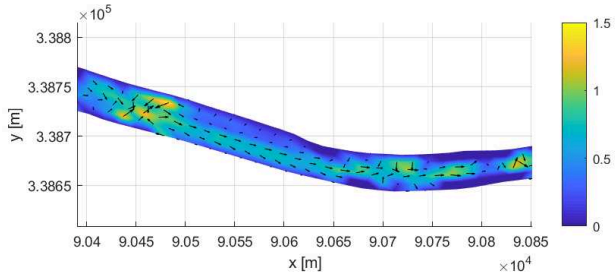

Figure 7. Instantaneous velocity field after correcting the boundary.

III. ALTERNATIVE WETTING DRYING METHODS

A. *Alternative depth for propagation*

From the parameter analysis, it is found that one of the parameters that had an impact on the formation of wiggles was NUMBER OF SUB-ITERATIONS FOR NON-LINEARITIES. This suggests that the wiggles might be mitigated by having a better value of $h_{\{prop\}}$, the water depth that is used in the continuity equation for the calculation of the flux. Indeed, it is remarked [9] that using deeper values for the propagation depth prevents the formation of shocks. However, using sub iterations is slow (roughly three times slower for 3 sub-iterations). Therefore, an alternative method is used here, namely to extrapolate $h_{\{prop\}}$ using the change in the water level at the previous time step Δh^{n-1}:

$$h_{prop} = h^n + \theta_H(h^n - h^{n-1}) = h^n + \theta_H \Delta h^{n-1}$$

Here, θ_H is the implicitation factor for the water depth. The results are shown in Figure 8. As an alternative method, h_{prop} is determined using the characteristics method from the water depth at time n, the results of which are shown in Figure 9 for the Thacker example. This method is inspired by finite volume methods, where the fluxes are often determined at an upwind location for greater stability.

The wiggles clearly decrease in both cases. The decrease is substantially stronger when using extrapolation. The reason may be that flow velocity was used in the characteristics method in order to determine h_{prop}, whereas it might be more physical to use the wave propagation velocity ($\sqrt{ch}$). No negative side effects are found in both cases with respect to mass conservation, change in the oscillation period or calculation time. Note that in both figures, the velocity discontinuity at the drying front does not change substantially, suggesting that the cause of this is unrelated to the calculation of the propagation velocity.

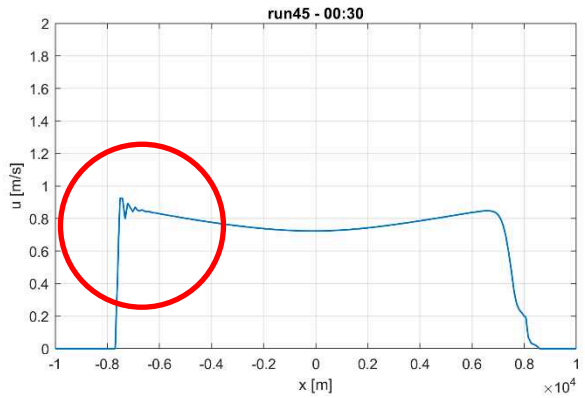

Figure 8. Thacker: Velocity magnitude after 30 min on a transect through the centre of the basin, with $h_{\{prop\}}$ calculated using extrapolation with θ_H=1. The flow at this moment is from right to left.

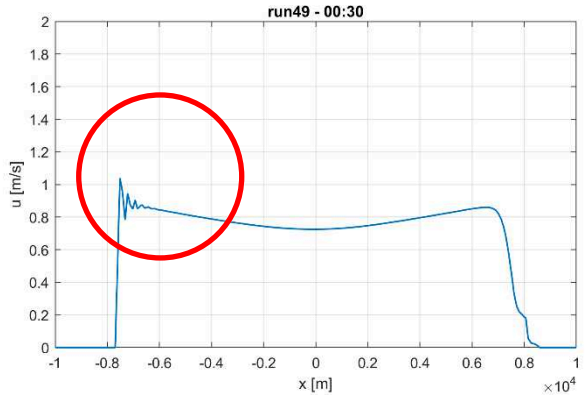

Figure 9. Thacker: Velocity magnitude after 30 min on a transect through the centre of the basin with $h_{\{prop\}}$ calculated using the method of characteristics. The flow at this moment is from right to left.

In the Scheldt test case, clear fronts at wetting areas are not found (temporary dry banks are more important here). Therefore, it is expected that little gain will be obtained from this method. This is to be investigated in future.

B. *Velocity filtering*

As there are clear issues with the velocity field, an attempt has been made to explicitly filter out these wiggles. Thereto a family of filters is implemented, similar as in Wolfram and Fringe [14], where higher order filters are constructed by consecutively applying first order (smoothing) filters. The higher order filters should in principle filter higher frequencies, while not affecting lower frequencies (thus leading to less energy dissipation). Some numeric experiments showed that for the Thacker test case (which has few low frequency components, as the flow is essentially constant in space) the

consecutive application of the first order is most effective, and therefore results of the higher order filter are not presented in this paper. The results are shown in Figure 10 and Figure 11. These figures show that one filter pass already limits the wiggles substantially. Because the water levels are recalculated using a residual distribution scheme that is perfectly conservative, the filter can be applied without affecting the global mass balance. Indeed, in the test, mass is conserved.

Applying more filter steps, leads to a further decrease of the wiggles and also smoothes out the erroneous flow on the right side of the bowl. Interestingly, the smoothing also decreases the wiggles in the free surface to some extent (not shown). However, this method is dangerous, as it can smooth out some flow features that one might be interested in (like eddies behind a bridge pillar). Therefore, it should be applied with care and is certainly not a solution for all cases. More tests are needed to investigate how strong this effect is.

Note that the increase in calculation time was rather limited, even applying the first order filter six times only leads to an increase in calculation time of 5%.

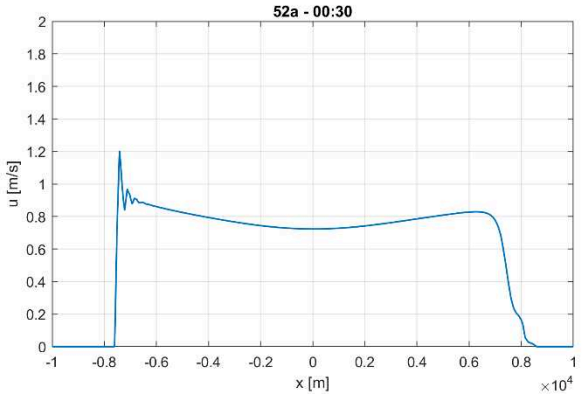

Figure 10. Thacker: Velocity magnitude after 30 min on a transect through the centre of the basin, using one iteration of a first order filter. The flow at this moment is from right to left.

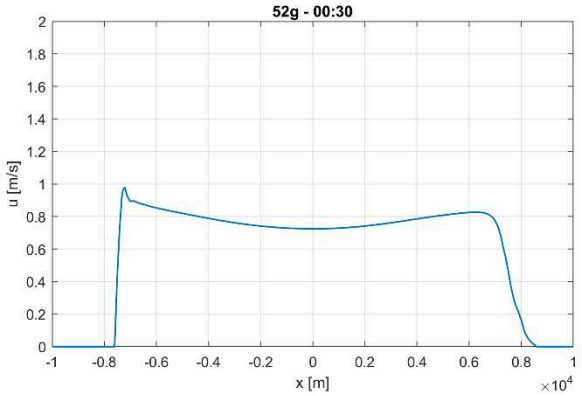

Figure 11. Thacker: Velocity magnitude after 30 min on a transect through the centre of the basin, using six iterations of a first order filter. The flow at this moment is from right to left.

Application of the filtering in the Scheldt test case gives interesting results Figure 12). Due to the use of the filter, all noise in the velocity field has disappeared and the flow is smooth and aligned in the direction of the river branch. However, this leads to a change in the tidal signal in this branch. A comparison with data will need to be performed in a later stage to see whether this is an improvement.

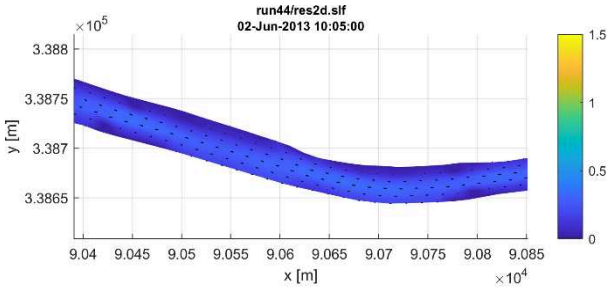

Figure 12. Scheldt: Instantaneous velocity field using five passes of a second order filter.

C. *Alternative pressure gradient calculation*

In the shallow water equations, the free surface gradient drives the flow. With a semi-implicit discretization, this is given by:

$$\frac{u^{n+1}-u^n}{\Delta t} = \theta_u g \nabla \eta^{n+1} + (1-\theta_u) g \nabla \eta^n + \cdots$$

Here, η is the free surface elevation. In TELEMAC, the following expression is applied to write the free surface gradient as function of the change in water depth ΔH:

$$\theta_u \nabla \eta^{n+1} + (1-\theta_u)\nabla \eta^n = \theta_u \nabla(\eta^n + \Delta \mathrm{h}) + (1-\theta_u)\nabla \eta^n = \nabla \eta^n + \theta_u \nabla \Delta \mathrm{h}$$

Then, with the option, OPTION FOR THE TREATMENT OF TIDAL FLATS = 1 or 3, a correction is applied to $\nabla \eta^n$ in order to mitigate the pressure level gradient problem (Figure 1). We have two hypotheses how the wetting drying in TELEMAC-2D could be improved:

1. The correction that is applied to calculate the free surface gradient is not physically correct and may lead to instabilities.
2. The correction for tidal flats is applied only to $\nabla \eta^n$, whereas it should be applied to $\nabla \eta^{n+\theta_H}$, with θ_H the implicitation factor for the water depth. It seems that it is tacitly assumed in TELEMAC that $\Delta \mathrm{h}$ always leads to a free surface profile at time step $n+\theta_H$, which does not have any issues with regard to wetting and drying. However, this may not be the case. This issue is subject to future investigations.

We will first look in more details to the free surface correction in TELEMAC-2D. In TELEMAC-2D, the water levels are corrected (in the routine corrsl.f) comparing the bathymetry with the free surface elevation. When the water level in the node with the highest bed level of an element is too high, it is decreased, whereas in the node with the lowest bed level of the element, it is increased up to the bed level of the node, which has a bed level between the two other nodes of the triangle. The water level in the middle node is left unchanged.

An example of the application of this algorithm is shown in Figure 13, where the free surface elevations before and after the correction are shown for a relatively smooth slope (3:1000) for a constant water depth of 0.1 m and a mesh size of 100 m. This example clearly shows the problems of the algorithm:

1. The free surface gradient is corrected even though it should not be. However, this typically leads to a decrease in the free surface gradient, hence lower velocities and a more stable model.
2. Whether the free surface is corrected depends on water depth and mesh resolution.
3. The correction creates larger free surface gradients in different directions in some elements.
4. For meshes and bathymetries where two nodes in an element have the same bed elevation (like studied here), the resulting corrected free surface depends on randomness/rounding errors in the input.

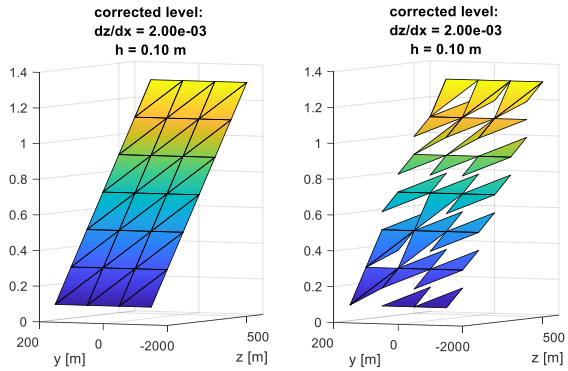

Figure 13. Illustration of the pressure gradient correction algorithm in TELEMAC. On the left, a 3D view of the original water levels is presented for a channel mesh with a constant bed slope and water level slope. On the right the corrected free surface elevation is shown, which is used to calculate the free surface gradient.

Note that the dependence on the resolution is also mentioned by Hervouet [15] (p.123) who states: “In certain cases (large elements along the slope and low water depth), this criterion is false and declares as dry elements that are entirely wet. This limitation should be taken into account while building the mesh. It should be ensured that the difference in level on an element is less than the depth”. This is however a rather stringent criterion, which complicates the mesh making process hugely.

In order to assess the relation between water depth and free surface gradient, the average error in the free surface gradient was determined for a large number of meshes and water depths and summarized in Figure 14. Here, we see that the pressure gradient in the x direction decreases to almost zero for low water depths. Especially for coarse meshes, the water depth at which this happens is quite large. It is also clear that the error in the perpendicular direction can be substantial (i.e. of the same order of the error in the direction of the pressure). This is worrying, because the water level slopes in typical free surface flows are often rather small (of the order of 10-4 for typical lowland rivers as the Danube of the Rhine and even an order of magnitude for tides in coastal seas as the North Sea), which means that in principle, the pressure gradient should be determined rather accurately.

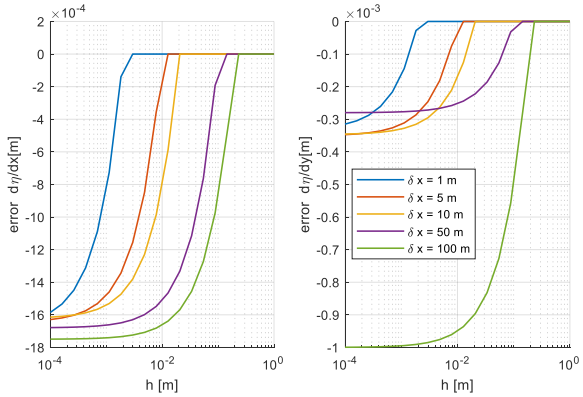

Figure 14. Synthetically determined error in the pressure gradient of TELEMAC’s pressure correction algorithm as function of water depth and mesh resolution for a channel mesh. Left, error in the direction of the free surface gradient. Right: error perpendicular to the direction of the gradient.

An alternative method [6] for the calculation of the pressure gradient is tested here . In this method, the maximum bed elevation in an element is compared to the maximum water level of the wet nodes (using a threshold depth of 1.0 mm), and the water level is decreased for these dry points in order to decrease the gradient. The advantage of this method is that it does not artificially limit slopes when there is a certain water depth (such as happens in original free surface correction method in TELEMAC). The disadvantage of this method is that one has to apply a threshold depth, which specifies when the pressure gradient is modified. Note that this threshold does not have any influence on mass conservation. The results of this simulation are shown in Figure 15.The application of this correction shows limited difference with respect to the wiggles in the wetting front (statistics show it has become slightly worse). However, this equation shows a better velocity profile at the drying front. The reason is that the free surface gradient is not artificially limited, as happens when using the original free surface correction method TELEMAC. This leads to a calmer flow from the shallow areas and a smoother velocity profile.

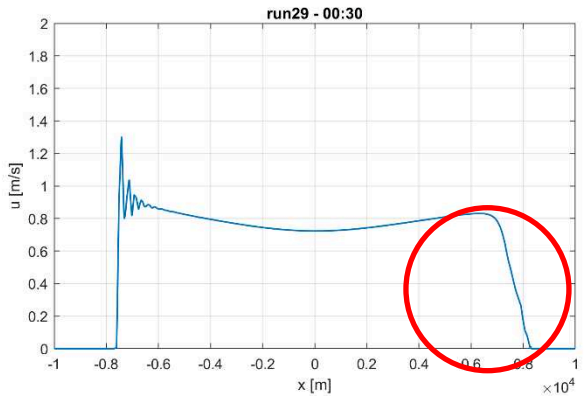

Figure 15. Thacker: Velocity magnitude after 30 min on a transect through the centre of the basin using the modified free surface gradient correction of Ricchiuto and Bollermann [6]. The flow at this moment is from right to left.

Application of the correction in the Scheldt model however, yielded disappointing results. High velocities were generated on the riverbanks, which led to high fluxes from shallow areas into the river. The negative depth algorithm struggled to cope with this. Hence it appears that the algorithm used in TELEMAC has a stabilizing effect by artificially lowering the free surface gradient in shallow areas.

D. Alternative bed friction

Often, additional energy dissipation is used in models to prevent instabilities during wetting drying e.g. [4 and 5], who used increased bed friction and horizontal diffusion in shallow areas. Also in TELEMAC-2D, the bed friction is increased artificially using the maximum of the wave speed, and the flow velocity in the calculation of the bed friction for water depths lower than 0.03 m, (see the routine fricti.f).

Bi and Toorman [16] reason that in shallow areas, the flow becomes laminar, and includes this in the equation for the bed friction, and claims that this improves wetting drying. Based on their work, we propose the following simplified term for the friction drag c_f, which was derived from their equation, neglecting the term containing the molecular viscosity[3]:

$$c_f = \frac{2}{\log\left(11.36\frac{h}{k}\right)} + \left(\frac{0.1k}{h}\right)^2$$

Here h is the water depth and k the Nikuradse roughness length. Basically, the bed friction is increased with an extra term that scales as h^{-2}, so this term increases rapidly for very small water depths. Note that laminar flow on slopes (where the most severe issues with wetting drying occur in TELEMAC) only occurs for very small water depths. For example, Breugem [17] measured a fully turbulent velocity profile in a water depth of only 0.016 m for a smooth bottom with a bed slope of less than 1%.

[3] Some analytical tests were performed in calculating the velocity on a constant slope for a constant water depth with and without this term. It was found that the differences were very small, and only became noticeable for small roughness values (k = 0.003 m) and very small water depth (H = 0.001 m).

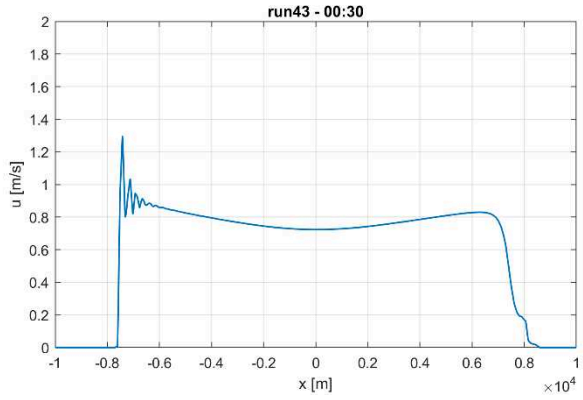

Figure 16. ghacker: Velocity magnitude after 30 min on a transect through the centre of the basin using the modified bed friction according to Bi and Toorman [16]. The flow at this moment is from right to left.

Applying the equation to the Thacker test case (Figure 16), we find extremely limited differences with respect to the occurrence of wiggles as well as with the velocity artifacts in the drying region. This is not very surprising. The increased bed friction only changes the drag coefficient for very low water depths (O (1cm)), whereas the problems in this test occur typically in deeper water depths. Note that in the areas where drying and flooding occur, the change in bed elevation per element is approximately 20 cm, meaning that the increased friction only occurs at areas that are already dry. Given these results it is concluded that the use of increased friction has a limited effect in this considered case, and hence more research to friction parametrisations do not seem the way forward.

Application of this friction law in the Scheldt test case confirmed this. Also in that case, the differences with the base case were very limited.

IV. Discussion

A. On thresholds for the minimum water depth

Often, a threshold for the minimum water depth is used in shallow water models. Also, in TELEMAC, many of these thresholds are found. Examples include THRESHOLD FOR VISCOSITY CORRECTION ON TIDAL FLATS in TELEMAC-3D and THRESHOLD DEPTH FOR WIND in both TELEMAC-2D and TELEMAC-3D. Also, in this paper a threshold depth was used below which no flow occurs (section II.A).

Ideally, one would like to make these thresholds as small as possible. Further, one would like to have a physical base for these thresholds. An obvious lower limit for such a threshold based on physics would be the free molecular path of water, below which the continuum hypothesis, on which the shallow water equations are based, is not valid. However, this gives a minimum value around 2.5 10^{-10} m, which is a value too low to be of practical use.

Another parameter that comes to mind to base the threshold depth on are the roughness length (Nikuradse length scale k)[4]. For situations with $h < k$, the flow is through the roughness

[4] I am indebted to Uwe Merkel for this suggestion.

elements rather than over it. Hence, in this situation, the flow would be largely blocked.

A third possibility is to use the sub grid variation in the bathymetry. A water depth that is lower than this variation is likely to be blocked by these flow features.

B. *Pressure gradient correction*

The pressure gradient correction used in TELEMAC was shown to underestimate the pressure gradient on slopes for coarse resolutions. This resolution dependence is a clear disadvantage of the method and should be taken into account when making meshes. The underestimations lead to a slowdown of the wetting on slopes as well as erroneous pressure gradients (even with wrong directions). An alternative pressure gradient correction algorithm was shown to solve this issue. However, in field cases with steep slopes in the bathymetry, it appeared that the algorithm in TELEMAC is rather stable (more so than the alternative one). The algorithms that were used here are relatively basic, but were not able to solve all problems, therefore, a more advanced algorithm seems necessary. This is the subject of further research.

C. *Negative depth algorithm*

The NERD scheme that is used in TELEMAC to make sure the water depths remain positive is a residual distribution scheme [10; see also section I.C]. First the volume of water F_{ij} is calculated that needs to be distributed between nodes by:

$$F_{ij} = \Delta T \int \vec{u}.h_{prop} \nabla \psi_i d\omega$$

Here, ψ is the basis function, and ΔT is the time step. Then this mass is iteratively distributed from upstream and downstream nodes along an edge. The iteration is stopped when either all the volumes to redistribute has become zero, or when the volumes to redistribute do not change anymore. In this case the fluxes are considered unphysical. Some simulations were performed (both in the Thacker basin and in the Scheldt test case) to find the locations where the fluxes did not converge to zero, and it was found that this happened normally in areas where drying occurs. This means that the non-physical fluxes happen when the flux calculated from the water depth and velocity from wave equation, is too large. In other words, there is not enough water available at these locations. Ideally, one would decrease the flow velocity in these areas in such a way that the flux decreases to a point where no fluxes remain in the redistribution method. However, it is not very obvious how this could be implemented. Instead, another option is to correct the velocities and water depth calculated using the wave equation in such a way that the available volume of water is taken into account. In order to do so, a type of iterative method seems necessary.

D. *Iteration for non-linearities*

The wetting drying process is an inherently non-linear process. Therefore, for the ultimate wetting drying method, it is needed to solve a non-linear system of equations, using an iterative solution method. Different non-linearities should be taken into account. Xia and Jiang [18] argue that at a wetting-drying front, there needs to be an equilibrium between bed friction and pressure gradient, which can only be obtained correctly if the friction term (*FRIC*) is discretised fully implicitly:

$$FRIC = \frac{c_d |u^{n+1}| u^{n+1}}{h^n},$$

whereas in most flow models (including TELEMAC), this term is linearised:

$$FRIC = \frac{c_d |u^{n}| u^{n+1}}{h^n}$$

Further, the importance of a correct representation of $h_{\{prop\}}$ (section III.A) also leads to a non-linearity, that should in principle be solved using iterations, even though extrapolation yielded quite good results. Further, the subgrid method [9], which solves the pressure gradient issue as well as the negative depth problem or Kärma's [3] method for correcting the free surface pressure gradient, leads to a system of non-linear equations.

In TELEMAC, iterations for non-linearities are present, but the implemented method has two disadvantages. First, it uses a fixed number of iterations, which sometimes leads to a high accuracy, and sometimes to a rather low one. Further it is rather slow, as the iteration occurs on the full hydrodynamic calculation.

Therefore, a start was made to implement an additional method to treat the non-linearities, where the first non-linearity that was implemented is the one related to the bed friction term. An accuracy threshold is used, in order to make sure the accuracy of the sub-iterations is always the same. This was done in a loop, containing steps 2f to 2h from section I.D, i.e. without recalculating the diffusion matrix and advection of momentum. This method is substantially faster than the original method (the calculation time increased by "only 50%" for a calculation with between 3 and 7 iterations), compared to a three times higher calculation time for 3 iterations in the original method. It is expected that a further speed-up might be obtained by using better precondition of the matrices and using better methods for dealing with the non-linearities (for example a quasi-Newton method). It is the intention to include step by step more non-linear processes and make more processes implicit (also some not related to wetting-drying like an implicit discretization of the Coriolis force, or some boundary conditions). This will be the building block for an ultimate wetting-drying method, which solves both the spurious pressure gradient and the mass balance method, and can be used in combination with the existing treatment of non-linearities, where the existing method functions similar to the outer iteration in a CFD code, and the new iteration method as an inner iteration.

V. CONCLUSION

In this paper, the wetting-drying scheme for the finite element calculations in TELEMAC is analysed using a schematic test case of a seiche in a parabolic basin (Thacker) and a small model of a part of the Scheldt Estuary. It is shown that there are multiple problems related to the wetting-drying process. The first issue is the occurrence of wiggles. It was shown that these can be limited using either explicit filtering or using a better estimate of the depth for propagation. Further, the algorithm that is used for correcting the spurious pressure gradient has a resolution dependency, which can easily lead to an underestimation of the pressure gradient, and hence drying that happens too slowly. Alternative methods can solve this, but may lead to unphysical high velocities on nearly dry areas for steep bed slopes. Thus, a more advanced method for the calculation of the pressure gradient is necessary. It is also shown that alternative friction calculations (taking into account the occurrence of laminar instead of turbulent flow in very shallow areas) do not bring any improvement to the wetting drying modelling in the presented test case. Finally, ideas are presented how further improvements in wetting and drying can be obtained. Apart from that, it is needed to perform more test cases on wetting and drying. Also, the test in the current paper were performed in serial mode. Testing these features in parallel is still needed.

REFERENCES

[1] Heniche, M., Secretan, Y., Boudreau, P., & Leclerc, M. (2000). A two-dimensional finite element drying-wetting shallow water model for rivers and estuaries. Advances in Water Wesources, 23(4), 359-372.

[2] Kyrousi, F. Chu. K,, Breugem, W.A. Decrop, B. & Gillis L.G. (2022) Water Quality modelling of the Southern North sea using TELEMAC-3D coupled with AED2, In preparation.

[3] Kärnä, T., Legat, V., & Deleersnijder, E. (2013). A baroclinic discontinuous Galerkin finite element model for coastal flows. Ocean Modelling, 61, 1-20.

[4] Funke, S. W., Pain, C. C., Kramer, S. C., & Piggott, M. D. (2011). A wetting and drying algorithm with a combined pressure/free-surface formulation for non-hydrostatic models. Advances in Water Wesources, 34(11), 1483-1495.

[5] Candy, A. S. (2017). An implicit wetting and drying approach for non-hydrostatic baroclinic flows in high aspect ratio domains. Advances in Water Resources, 102, 188-205.

[6] Ricchiuto, M., & Bollermann, A. (2009). Stabilized residual distribution for shallow water simulations. Journal of Computational Physics, 228(4), 1071-1115.

[7] Stelling, G. S., & Duinmeijer, S. P. A. (2003). A staggered conservative scheme for every Froude number in rapidly varied shallow water flows. International Journal for Numerical Methods in Fluids, 43(12), 1329-1354.

[8] Kramer, S. C., & Stelling, G. S. (2008). A conservative unstructured scheme for rapidly varied flows. International Journal for Numerical Methods in Fluids, 58(2), 183-212.

[9] Casulli, V. (2009). A high-resolution wetting and drying algorithm for free-surface hydrodynamics. International Journal for Numerical Methods in Fluids, 60(4), 391-408.

[10] Hervouet, J. M., Pavan, S., & Ricchiuto, M. (2017). Residual distribution advection schemes in Telemac RESEARCH REPORT N° 9087 August 2017 Project-Team CARDAMOM

[11] Balzano, A. (1998). Evaluation of methods for numerical simulation of wetting and drying in shallow water flow models. Coastal Engineering, 34(1-2), 83-107.

[12] Thacker, W. C. (1981). Some exact solutions to the nonlinear shallow-water wave equations. Journal of Fluid Mechanics, 107, 499-508.

[13] Wolf, T., Breugem, W. A., Chu, K., Decrop, B., Van Holland, G., Plancke, Y., & Stark, J. (2021). Sediment transport modelling (TELEMAC-3D + GAIA) case study: sand disposals in the Western Scheldt. In Proceedings of the papers submitted to the 2020 TELEMAC-MASCARET User Conference October 2021 (49-57).

[14] Wolfram, P. J., & Fringer, O. B. (2013). Mitigating horizontal divergence “checker-board” oscillations on unstructured triangular C-grids for nonlinear hydrostatic and nonhydrostatic flows. Ocean Modelling, 69, 64-78.

[15] Hervouet, J. M. (2007). Hydrodynamics of free surface flows: modelling with the finite element method. John Wiley & Sons.

[16] Bi, Q., & Toorman, E. A. (2015). Mixed-sediment transport modelling in Scheldt estuary with a physics-based bottom friction law. Ocean Dynamics, 65(4), 555-587.

[17] Breugem, W. A. (2012). Transport of suspended particles in turbulent open channel flows. PhD thesis.

[18] Xia, X., & Liang, Q. (2018). A new efficient implicit scheme for discretising the stiff friction terms in the shallow water equations. Advances in Water Wesources, 117, 87-97.

How a Flow Aligned Mesh Improves TELEMAC Model Results

Sven Smolders
sven.smolders@mow.vlaanderen.be, Antwerp, Belgium
Flanders Hydraulics Research, dept. of Mobility and Public Works, Flemish Government

Abstract –**In an unstructured 2D mesh the quality can be checked by means of checking the aspect ratio of the individual triangles or even the edge growth ratio. This paper wants to show how the orientation of the triangles can also affect the model results. An estimation of the longitudinal and lateral numerical diffusion is given explaining why flow alignment can be beneficial in reducing the numerical diffusion. This is demonstrated for the advection of a tracer with the rotating cone example.**

The paper also shows an example of a 3D hydrodynamic model of the Scheldt estuary. A comparison is made between a good quality mesh and a flow aligned mesh for the same model domain. All variables are kept equal. The influence on tidal propagation is shown. The effect on the bottom friction coefficient is shown and the potential effect on a coupled sediment transport model is discussed.

The flow aligned mesh reduces the amount of lateral numerical diffusion, it reduces the artificial loss of tidal energy along the estuary, and it improves the calibration result by getting more realistic bottom friction coefficients.

Keywords: Flow aligned mesh, numerical diffusion, advection scheme, rotating cone.

I. INTRODUCTION

At Flanders Hydraulics Research, several Scheldt Estuary models exist in different software packages ranging from a 1D DHI Mike11 model [1], over a TELEMAC-2D model [2], to a TELEMAC-3D model [3] and a Delft3D Simona model [4]. All these models were calibrated using a varying Manning bottom friction coefficient. Water levels measured at different tide gauges were compared with modeled water levels. The spatial varying bottom friction coefficient between each two tide gauges is used to calibrate the water levels in these models. If a modeled water level is higher than the measured value, the bottom friction coefficient is increased and vice versa. In this way the bottom friction coefficient is used as the one parameter to correct for all physical (e.g. bad representation of bathymetry by the mesh or a too simplistic turbulence model) and non-physical (e.g. diffusive advection scheme) errors in the model.

All the forementioned models use a Manning coefficient for the bottom friction and all models were calibrated according to the same method (spatially varying bottom friction coefficient) described above. When calibrating the TELEMAC models it was noticed that, in the upstream part of the estuary, very low Manning coefficients were necessary to correct the water levels. Lowering the Manning coefficient even more was no longer helping to correct the water levels properly. When the Manning coefficients of the four models were compared to each other, see Figure 1, it can be seen that both the 1D Mike 11 model as the Delft3D model have much higher Manning coefficients upstream the estuary.

The same problem was reported in [5] where a TELEMAC-2D model of a tributary of the Weser estuary was presented. Lowering the bottom friction coefficient could not further improve modeled water levels either. Numerical diffusion generated by the advection schemes was pointed out as the problem.

For the TELEMAC-3D Scheldt estuary model the non-physical Manning bottom friction coefficients and the generated numerical diffusion resulted also in problems in the coupled sediment model. A different (physical realistic) bottom friction coefficient needed to be programmed in the code. The very diffusive upstream part of the estuary also did not solve well the cohesive sediment transport. It is known that numerical diffusion decreases, and solver accuracy increases, with a higher resolution mesh and better quality of the triangles used, i.e. triangles must be as equilateral as possible. This was however already the case for this detailed TELEMAC-3D Scheldt estuary model [3].

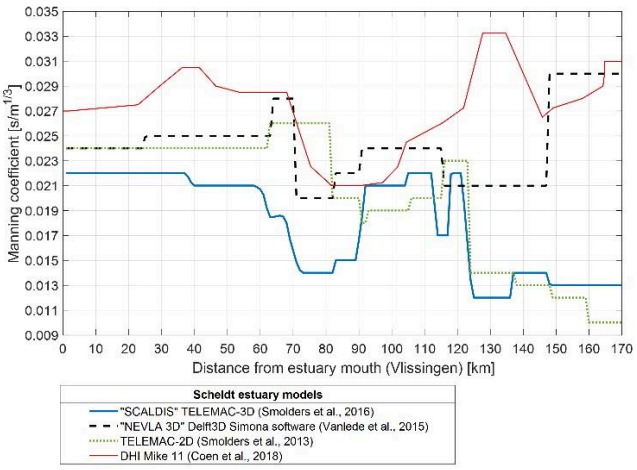

Figure 1. Manning bottom roughness coefficient along the Scheldt estuary for different kind of models

This paper wants to show that besides the mesh quality in terms of triangle shape, proper alignment of the triangles to flow direction or structures can have a large impact on the quality of the model results. the effect of mesh quality, i.e. proper mesh alignment to be precise, on the results of a TELEMAC simulation.

First some general information about grid diffusion and mesh alignment is given. Next the effect of a better flow aligned mesh is demonstrated with an example of tracer advection with a rotating cone. This simple example shows the effect of mesh alignment on numerical diffusion caused by

different advection schemes. Finally, the results of a new flow aligned mesh for the TELEMAC-3D Scheldt estuary model are shown. The Manning bottom friction coefficients before and after mesh alignment will be shown.

II. GRID DIFFUSION AND MESH ALIGNMENT

In [6], an analytical derivation and estimation of grid diffusion is given for a 2D finite element model of the Francisco Bay estuary. The authors start from the modified equation analysis normally applied on finite difference grids [7] and a 1-D, first-order, forward-in-time, backward-in-space scalar advection scheme. The difficulty for applying this on an unstructured grid is that half of the elements have one inflow face and two outflow faces (type B element in Figure 2), and the other half have two inflow faces and one outflow face (type A element in Figure 2). In this paper only the outcome of the derivation in [6] is given in the form of an expression for the longitudinal numerical diffusion coefficient (along the x-axis), K^x (1), the lateral diffusion coefficient (along the y-axis), K^y (2), and the cross-diffusion coefficient, K^{xy} (3). Some assumptions were made: the scalar values are cell averages and are located at the circumcentre of each element. The mesh consists only of equilateral triangles and the angle, θ, gives the orientation of the grid relative to the x-axis (Figure 2). The free-stream velocity U is taken parallel to the x-axis and the edge length of an element is denoted by l (Figure 2). The cross term only gives information about the orientation of diffusion whereas the magnitude of the numerical diffusion depends only on K^x and K^y.

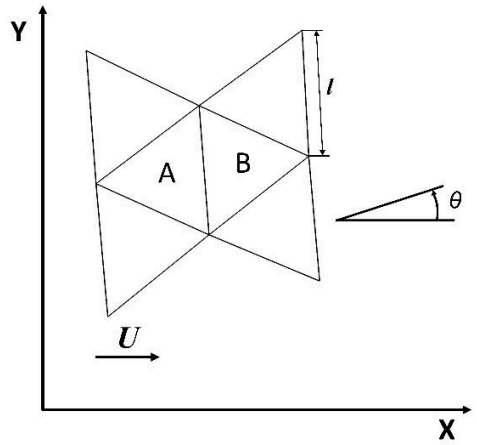

Figure 2. Schematic representation of a mesh with equilateral triangles in a cartesian coordinate system with an overall flow velocity U along the X-axis and θ the angle between a triangle's edge and the X-axis (after [6]).

In a flow aligned mesh (Figure 3) the lateral numerical diffusion equals to zero for $\theta = 0$ (2), because of the averaging over two consecutive type A and type B elements. Any diffusive spreading is geometrically limited to a single width triangle strip as the flow aligned faces have zero flux.

$$K^x = \left[\frac{2\sqrt{3}}{3}\left(cos^2\theta \cos\left(\theta+\frac{\pi}{6}\right) + sin\theta\, cos^2\left(\theta-\frac{\pi}{3}\right)\right) - \frac{\sqrt{3}}{4\sin\left(\theta+\frac{\pi}{3}\right)}\right]\frac{Ul}{2} - \frac{U^2\Delta t}{2} \quad (1)$$

$$K^y = \frac{\sin(3\theta)}{4\sqrt{3}}Ul \quad (2)$$

$$K^{xy} = \left[\frac{2}{\sqrt{3}}sin\theta \sin\left(\theta-\frac{\pi}{6}\right)\sin\left(\theta-\frac{\pi}{3}\right)\right]Ul \quad (3)$$

For a flow aligned grid, when $\theta = 0$, the longitudinal numerical diffusion simplifies to

$$K^x = \frac{Ul}{4} - \frac{U^2\Delta t}{2} \quad (4)$$

Equations (1-3) quantify how much the orientation of the mesh elements affects numerical diffusion and show that elements aligned with the velocity field have no lateral numerical diffusion. This shows that for models where sections of the flow have a dominant direction, it is worthwhile to create a flow aligned section of mesh. In these sections triangles do not even need to be equilateral. Because of the no-flux faces, triangles can be stretched in the dominant flow direction without too much consequences for the quality of the results.

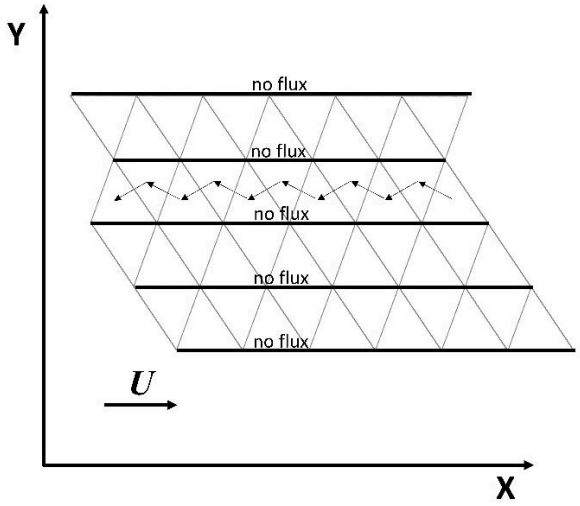

Figure 3. Schematic flow aligned mesh showing no lateral diffusion because of the zero-flux faces. The arrows show the flux for each individual element evaluated for each element's upwind neighbour (after [6]).

III. ROTATING CONE

A. test case for advection of tracer

The rotating cone test case is described in the TELEMAC validation document in 2D in [8] and 3D in [9]. It shows the effect of the different finite element advection schemes on the passive scalar transport. This test case shows the advection of a tracer in a square basin with a flat frictionless bottom and closed boundaries. The dimensions are 20 x 20 m and the mesh is a regular grid where all squares were cut in half (see left panel in Figure 4). The mesh contains 441 nodes and 800 elements. The water depth is constant in time and equal to 2 m. The rotating velocity field is also constant in time and free of divergence. The angular velocity is set to 1 rad.s^{-1} which gives a rotation period of T=2π (6.28 s). The centre of the mesh is the centre of the rotation (x_0=10 m and y_0= 10 m). The initial value for the tracer is given by a Gaussian function off-centered 5 m to the right of (x_0, y_0) representing a cone. The tracer diffusivity is set to zero. In both [8] as [9] are 1D solutions along a slice plane (x, y), y=10 m after a half and a full rotation given to

show which advection schemes preserve the tracer cone the best. In [8] is also shown how an increase in mesh resolution decreases the error propagating on the mesh in the results, i.e. a higher resolution results in less numerical diffusion. The increased resolution demanded in some cases also for a decrease in time step to keep a stable Courant criterium (5) close to unity.

$$C = \frac{u*\Delta t}{\Delta x} \leq C_{max} \quad (5)$$

where C represents the dimensionless Courant number, u is the magnitude of the flow velocity, Δt is the time step, Δx is the mesh resolution, and C_{max} depends on the solver method (where for an explicit solver this value should be close to 1 for stability).

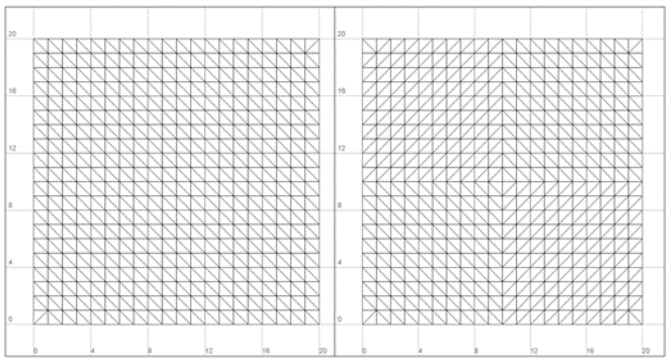

Figure 4. Rotating cone mesh original (left) and simple change for better flow alignement (right)

B. *simple change in mesh to make it more flow aligned*

In the upper left and lower right quadrant of the mesh, the longest edge of the triangles was rotated 90 degrees, resulting in the mesh given in Figure 4 on the right. This makes the mesh more flow aligned with the rotating velocity field. Note that this mesh is still very coarse and that this mesh needs refinement for proper flow alignment. But the current simple intervention in the mesh will show how tracer advection is impacted and will show the potential for further decrease in numerical diffusion.

C. *Difference in advection of tracers*

Like in [8] and [9] the 1D solution along a slice plane (x, y), y=10 m after a half (Figure 5) and a full rotation (Figure 6) are given here with the results for the original mesh in dashed lines (including the analytical solution) and the results for the adjusted and more flow aligned mesh in full line. To keep both figures uncluttered only the results of advection schemes Weak characteristics (blue), NERD (green) and LIPS (yellow) are shown.

Even though the mesh in the example is coarse and the changes made to make it more flow aligned were minimal, the results clearly show a decrease in the numerical diffusion generated by the different advection schemes. For the Weak Characteristic scheme the results are not that different, but this scheme already performs well and generates the least amount of numerical diffusion of all schemes.

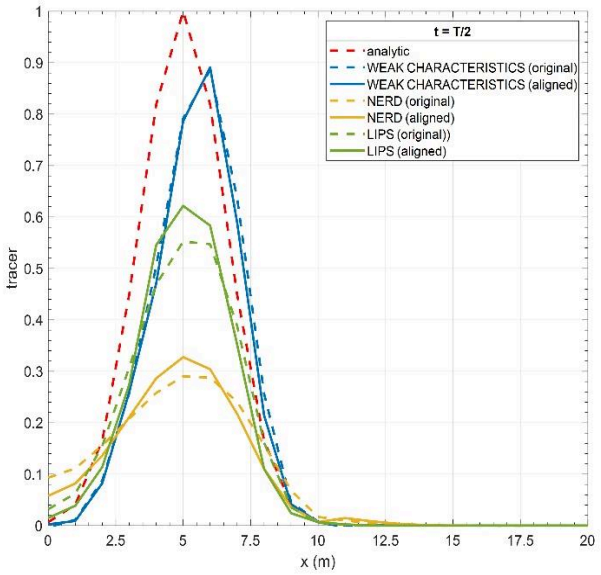

Figure 5. Rotating cone results after a half rotation (t = T/2) for original mesh (dashed lines) and the flow aligned mesh (solid lines) for the Weak Characteristics (blue), NERD (green) and LIPS (yellow) advection schemes. The analytical solution is given in dashed red line.

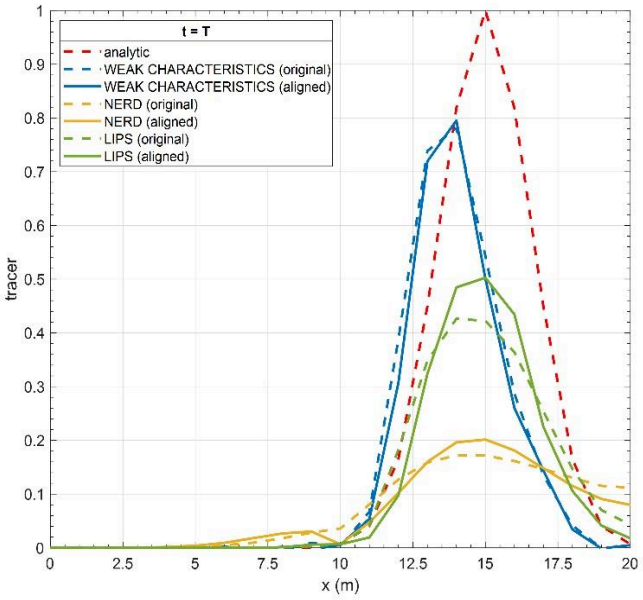

Figure 6. Rotating cone results after one rotation (t = T) for original mesh (dashed lines) and the flow aligned mesh (solid lines) for the Weak Characteristics (blue), NERD (green) and LIPS (yellow) advection schemes. The analytical solution is given in dashed red line.

IV. SCHELDT ESTUARY APPLICATION

A. Flow aligned mesh

For the TELEMAC-3D Scheldt estuary model a new mesh was made using flow lines and a channel mesher to create a mesh that is more flow aligned. Even for the downstream part, which has multiple channels over its width, the mesh was flow aligned inside these channels. In the upstream parts, characterised by a single channel, the channel mesher was used to create more flow aligned structured unstructured mesh. In some parts where the flow direction was really unidirectional, the triangles were even stretched in the flow direction.

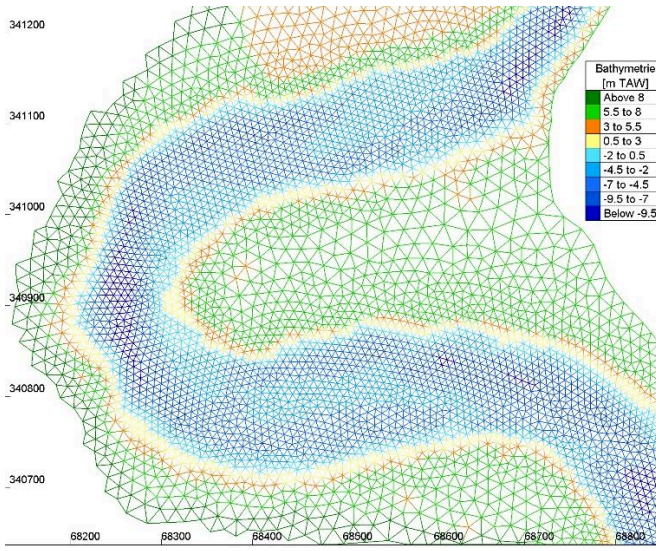

Figure 7. Detail of the mesh at the sharpest bend in the upstream part (km 143-146) of the Scheldt estuary in the original TELEMAC-3D model mesh.

A detail of the original mesh is shown in Figure 7. It shows that the original mesh already contained sufficient mesh resolution to well represent the bathymetry. It also shows that most of the triangles meet the mesh quality standard of being as much equilateral as possible. Figure 8 shows the same location but in the flow aligned mesh. The Blue Kenue Channel mesher was used here and triangles were stretched a little in the longitudinal direction. Although the mesh resolution in this section is coarser for the flow aligned mesh, the overall node count for both meshes was in the same order of around 290000 nodes in 2D.

B. Results

For both simulations all parameters were kept as in the original model [3]and only the mesh changed. So both simulation were performed with the spatially varying bottom friction coefficients of the original calibrated TELEMAC-3D Scheldt estuary model [3]. Figure 9 shows the maximum water level along the estuary for an average tide. From the mouth to upstream the difference in water level keeps increasing along the estuary showing higher water levels for the simulation with the flow aligned mesh.

In a second step the model with the flow aligned mesh was calibrated so that water levels would coincide with the original model. The Manning bottom friction coefficient was used and varied spatially like the original model. The result is shown in Figure 10. The Manning bottom friction coefficient in the flow aligned mesh version is higher than in the original version. In the upstream part the flow aligned version can keep the Manning coefficient at a decent physical level showing a significant reduction in numerical diffusion of the tidal energy in this upper part.

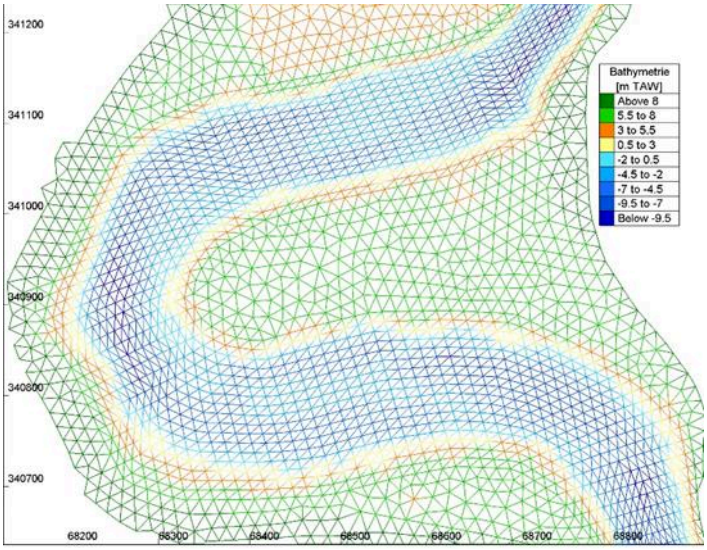

Figure 8. Detail of the mesh at the sharpest bend in the upstream part (km 143-146) of the Scheldt estuary in the flow aligned mesh version of the TELEMAC-3D model

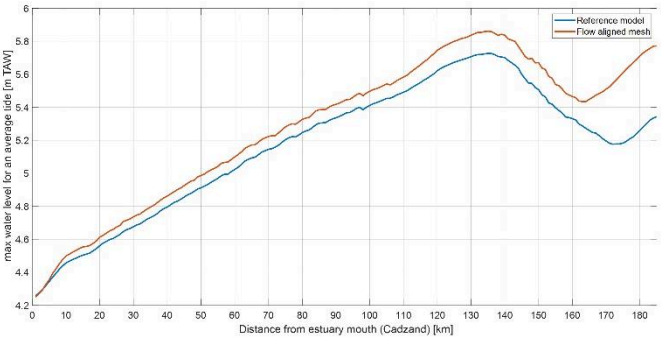

Figure 9. Maximum water level comparison along the Scheldt estuary model results for the original TELEMAC-3D Scheldt estuary model and the new flow aligned mesh. Both simulations used the original calibrated spatially varying bottom friction coefficients.

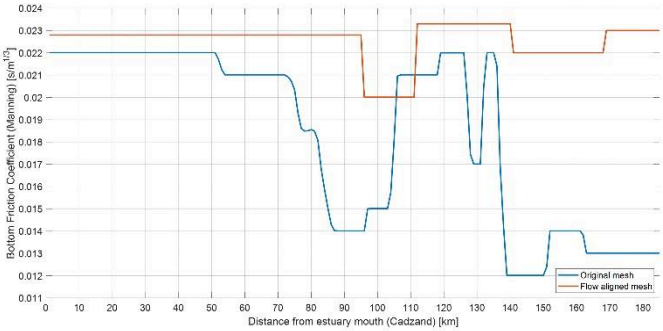

Figure 10. Manning bottom roughness coefficient for the original TELEMAC-3D model (blue line) and for the flow aligned mesh version (orange line)

C. *discussion*

A high quality and good designed structured unstructured mesh can possess faces which are either tangent or normal to the flow field. Construction of flow aligned meshes require more work and a better understanding of the model domain. Higher accuracy and less numerical dissipation can be achieved. Flow alignment of the mesh in region with a dominant flow direction allows for more effective application of solvers in the flux computations, leading to a reduction in discretisation error. The mesh locally mimics the attributes of a structured grid and provides high quality numerical solutions due to the alignment of the element interfaces.

Energy is dissipated by three mechanisms: turbulence, bottom friction and numerical diffusion. In this example by flow aligning the mesh the numerical diffusion was decreased (which probably also affected turbulent dispersion) and therefore the Manning bottom friction coefficient could be increased to reach again physical meaningful values.

D. *Coupled cohesive sediment transport model*

When coupling a sediment transport model, the quality of the hydrodynamic model determines the maximum quality of the sediment transport model. By applying the flow aligned mesh and retrieving again realistic Manning coefficient values for the upstream part of the estuary, the coupled sediment model can use them directly from the hydrodynamic simulation.

One of the problems in the (cohesive) sediment transport model [10] is the large amount of sediments that ended up on the tidal flats, especially in the upstream part of the estuary. The increase in Manning coefficient and the better representation of the tidal velocities in the flow aligned model will increase the local bed shear stress and resuspend more sediment than before.

Furthermore, according to [11] the longitudinal diffusion coefficient K^x is inversely proportional to the lateral one K^y (6).

$$K^x \sim \frac{U^2 h^2}{K^y} \quad (6)$$

with h the water depth. With K^y smaller or close to zero implies an inefficient lateral mixing which tends to increase the effect of differential advection which in turn will improve sediment transport.

Further testing is needed to see if the above-mentioned improvements really improve the sediment transport model.

V. CONCLUSION

In the CFD world mesh alignment to flow features is well known and part of the quality concept of the mesh. In the world of TELEMAC hydrodynamics it is less known and it is hoped that this paper demonstrates the potential for model result improvement for model domains that have dominant one-directional flow fields. It is certainly suited for estuarine applications and especially in the upstream parts where bottom friction is already a dominant tidal energy dissipator. No need to add artificial energy dissipation to the equation.

ACKNOWLEDGEMENT

I would like to thank Kai Chu from IMDC and my colleague Qilong Bi for some interesting discussions on this topic and helping me reach a next step in the quality of our TELEMAC models.

REFERENCES

[1] Coen, L.; Deschamps, M.; Vanderkimpen, P.; Mostaert, F. (2018). Mike11 model Zeeschelde en tijgebonden zijrivieren: Beschrijving versie 2015. Versie 4.0. WL Rapporten, 14_106_6. Waterbouwkundig Laboratorium: Antwerpen.

[2] Smolders, S., Meire, P., Temmerman, S., Cozzoli, F., Ides, S., & Plancke, Y. M. (2013). A 2Dh hydrodynamic model of the Scheldt estuary in 1955 to assess the ecological past of the estuary. In XXth TELEMAC-MASCARET. User Conference 2013 (pp. 137-143).

[3] Smolders, S.; Maximova, T.; Vanlede, J.; Plancke, Y.; Verwaest, T.; Mostaert, F. (2016). Integraal plan Bovenzeeschelde: Subreport 1. SCALDIS: a 3D Hydrodynamic model for the Scheldt Estuary. WL Rapporten, 13_131. Flanders Hydraulics Research: Antwerp

[4] Vanlede, J.; Delecluyse, K.; Primo, B.; Verheyen, B.; Leyssen, G.; Plancke, Y.; Verwaest, T.; Mostaert, F. (2015). Verbetering randvoorwaardenmodel: Subreport 7 - Calibration of NEVLA 3D. Version 4.0. WL Rapporten, 00_018. Flanders Hydraulics Research & IMDC: Antwerp, Belgium.

[5] Malcherek, A. (2000). Application of TELEMAC-2D in a narrow estuarine tributary. Hydrological processes, 14(13), 2293-2300.

[6] Holleman, R., Fringer, O., & Stacey, M. (2013). Numerical diffusion for flow-aligned unstructured grids with application to estuarine modeling. International Journal for Numerical Methods in Fluids, 72(11), 1117-1145.

[7] Warming R, Hyett B. The modified equation approach to the stability and accuracy analysis of finite-difference methods. Journal of Computational Physics 1974; 14(2):159–179.

[8] TELEMAC-2D Validation Manual Version v8p3, chapter 13 Advection of tracers with a rotating cone. December 6, 2021.

[9] TELEMAC-3D Validation Manual Version v8p3, chapter 14 Advection of tracers with a rotating cone. December 6, 2021.

[10] Smolders, S.; Bi, Q.; Vanlede, J.; De Maerschalck, B.; Plancke, Y.; Mostaert, F. (2020). Integraal plan Boven-Zeeschelde: Sub report 6 – Scaldis Mud: a Mud Transport model for the Scheldt Estuary. Version 4.0. FHR Reports, 13_131_6. Flanders Hydraulics Research: Antwerp.

[11] Fischer HB, List EJ, Koh RC, Imberger J, Brooks NH. Mixing in Inland and Coastal Waters. Academic Press, Inc.: New York, 1979.

Overview and lessons learned from performing tailings dam breach modelling with TELEMAC-2D

Pierre-Louis Ligier[1], Non Okumura[1], Carin Alderman[2]

pierre-louis.ligier@sweco.se, Stockholm, Sweden
[1] Power Generation and Dams, Sweco, Stockholm (Sweden)
[2] Boliden Mines, Boliden (Sweden)

Abstract **– Following the dramatic recent tailings dam failures that occurred during the last decade, significant advances have been performed in the fields of tailings dam breach assessments and runout modelling. Numerous research projects and guidelines (e.g., Canadian Dam Association guidelines on Tailings Dam Breach Analysis, International Council on Mining and Minerals' Global Industry Standard on Tailings Management) paved the way for an updated framework to tackle the challenges related with the safety and the identification of potential consequences in case of a failure event.**

In parallel, similar advances have been made amongst several hydrodynamic modelling packages in order to model runout of high-concentrated flows that are governed by non-Newtonian rheological behaviour. This article aims at giving an overview of the lessons learned from performing runout modelling using the non-Newtonian rheological models recently implemented in the two-dimensional depth-averaged TELEMAC-2D code.

The article is based on tailings dam breach assessments performed for the Tailings Storage Facility (TSF) of Garpenberg in Sweden, a mine owned by Boliden. More precisely, focus is put on detailing modelling procedures and relevant features of TELEMAC-2D that can be used in order to model different steps such as *i)* breach opening and outflow hydrograph estimation, *ii)* flood wave modelling, *iii)* transition between non-Newtonian and Newtonian behaviors depending on mixing between tailings and downstream water bodies, and *iv)* hazard assessment and mapping. Finally, the article summarizes the current advantages and shortcomings of the non-Newtonian rheological models implemented in TELEMAC-2D and presents a list of possible improvements.

Keywords: tailings, dam breach analysis, runout modelling, non-Newtonian, TELEMAC-2D.

I. INTRODUCTION

Significant advances have been observed in the field of tailings dam breach assessments and runout modelling in the last few years, both within research projects and guidelines but also the availability of hydrodynamic modelling software modelling flows that are governed by non-Newtonian rheological behavior. This article is based on a case study where a Tailings Dam Breach Analysis (TDBA) was performed for the Tailings Storage Facility (TSF) at Garpenberg in Sweden, a mine owned by Boliden. An overview of the lessons learned from the case study, relevant features available in the TELEMAC-2D that can be used, details in the modelling procedures that are of importance for runout modelling for a TDBA, as well as advantages, shortcomings, limitations, and possible improvements are presented from an engineering perspective.

II. CASE STUDY

A. Garpenberg Mine

A case study was conducted for Boliden's TSF at Garpenberg in Hedemora, Dalarna County, Sweden (see Figure 1). Garpenberg is a complex ore mine carrying mainly zinc, copper, and lead. While mining in the area has historic evidence that dates back to 300 BC, the recent mining operations as well as the construction of the TSF started in the 1960's. The embankment dams have been raised using the upstream method (in which each subsequent dam raising stage is created by building an embankment founded partly on underlying tailings, towards the reservoir), but the design has been revised and will transition to a centerline raise over the original dam crest during the coming three years. The dams are mainly founded on till but there is some evidence that peat remains in parts of the low-lying areas. An aerial view of the TSF is depicted in Figure 1. There are seven dam sections around the TSF (A, C, D, E, E2, I and I2).

The goal of the tailings dam breach and runout analysis was to understand the potential consequences of a breach at six different dams surrounding the TSF as a part of the permit application. The six different breach locations around the TSF considered are illustrated in Figure 2 (section I2 is not included as consequences from failure have already been studied in an earlier project).

The area surrounding the TSF consists of several large lakes with small rivers connecting these lakes, and houses located along the rivers and lakes. This area is not densely populated, but there are local industries that lie in a proximity of the TSF, and thus the risks due to a dam breach are not negligible.

B. Framework

The tailings dam breach and runout analysis were conducted in accordance with the Swedish dam safety guidelines (GruvRIDAS and Svenska Kraftnät, the National Grid regulator), the Canadian dam safety guidelines (provided by CDA) as well as the Global Industry Standard for Tailings Management (GISTM). These latter guidelines define a framework to determine the failure classification of the tailings facility by assessing the downstream conditions

and selecting the classification corresponding to the highest consequence classification for each category. The consequence classes are determined by the incremental losses for five categories of consequences: 1) Potential population at risk, 2) Potential loss of life, 3) Environment, 4) Health, social and cultural, and 5) Infrastructure and economics [1] [2] [3].

Figure 1. Garpenberg mine. Top: Location of the mine in Sweden. Bottom: Aerial view of the TSF. Source: Lantmäteriet ©.

C. Dam breach parameters used

1) Failure mode

The dam breach location has been chosen at the largest dam height or at the location expected to lead to the largest consequences in terms of outflow volume. The credible failure mode considered for the six dam sections corresponds to a stability and/or foundation failure, which then leads to the development of a breach, followed by the liquefaction of the tailings in the TSF. This failure mode corresponds to the highest expected consequences triggered by a geotechnically plausible scenario. The breaching process considered is illustrated in Figure 3.

The breach geometry has been defined based on analysis of historical events and guidelines, and a breach ratio (width-height ratio) of 5 has been used in the case study. This ratio corresponds to a conservative but reasonable hypothesis based on the analysis of historical failures of both tailings dams [4] and rockfill embankment dams [5] in order to take into account the large rockfill volume on the downstream face.

2) Outflow volumes and hydrological scenario

Outflow volumes can be characterized by an estimated erosion cone developing in the TSF. Based on the authors' experience, this method is well suited for TSF with liquefiable tailings and a limited supernatant pond as is the case for Garpenberg. Comparisons with other estimation methods were made and confirmed that the outflow volume based on an estimated erosion cone provided the most conservative assumption. The erosion cone slope can be considered to be lying in a range from 2 to 5 degrees, resulting in a large difference in potential

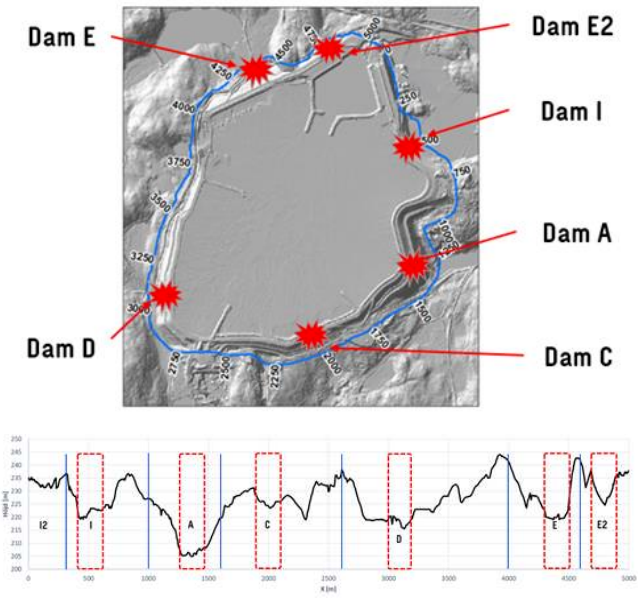

Figure 2. Garpenberg case study. Top: Location of six breach locations considered. Bottom: Location of six breach locations with respect to downstream terrain levels. The blue vertical lines materialize the limit between each of the dam sections.

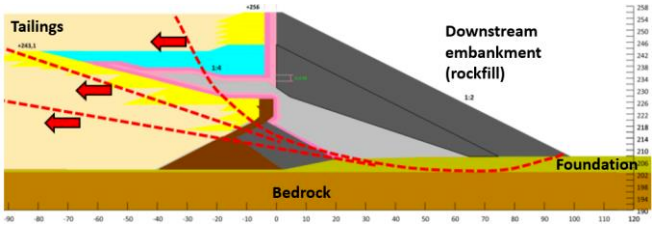

Figure 3. Garpenberg case study. Illustration of credible failure mode considered in the TDBA.

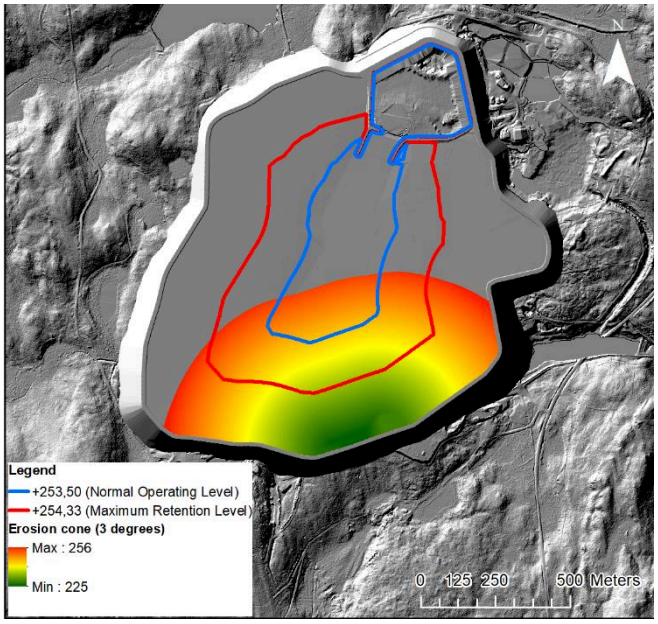

Figure 4. Garpenberg case study. Erosion cone for dam C (slope of 3 degrees, outflow volume of 5.3 Mm^3). Blue and red lines illustrate the supernatant pond extents for the normal operating level and maximum retention level (design flood), respectively.

outflow volumes. In this case study, a range of 3 to 5 degrees were considered based on the analysis of the tailings residual shear strengths at all dam locations and at different depths.

This resulted in outflow volumes ranging from 1.3 Mm^3 to 19.6 Mm^3 depending on the dam section, breach height, breach width and slope angle. The erosion cone for Dam C with a 3 degree slope is illustrated in Figure 4.

To define the hydrological scenarios, the outflow volumes are compared with the volume of water in the TSF for both a normal flow condition (i.e., Sunny day scenario) and a high flow condition (i.e., Flood-induced scenario). The additional volume of water during a high flow condition is small compared to the amount of outflow volume due to liquefaction (max. approx. 9%), and the incremental consequences are expected to be similar for the two hydrological scenarios. Thus, the runout analysis has only been conducted for normal flow conditions.

3) Rheological properties

The non-Newtonian properties of liquefied tailings have been modelled using the Bingham rheological model. This model is well suited for homogeneous suspensions of fine particles, particularly mudflows, and is commonly accepted for modelling flowing tailings [6]. The equation of the Bingham model reads:

$$\begin{cases} \dot{\gamma} = 0 & if \quad \tau_0 \leq \tau_y \\ \tau_0 = \tau_y + \mu\dot{\gamma} & if \quad \tau_0 > \tau_y \end{cases} \quad (1)$$

with τ_0 the non-Newtonian shear stress [Pa], τ_y the fluid yield stress [Pa], μ the fluid dynamic viscosity [Pa·s] and $\dot{\gamma}$ the shear rate [s^{-1}] that is function of the flow characteristics. For more details about the implementation in TELEMAC-2D, readers may refer to [7]. In addition to the yield stress and dynamic viscosity, the fluid bulk density ρ [kg/m^3] is another parameter defining the fluid rheology.

For the Garpenberg case, the Bingham model was used in combination with the "pseudo-biphasic model" in order to take mixing effects with downstream water bodies into account (see more information about this model in Section III). When using the "pseudo-biphasic model", the yield stress, dynamic viscosity, and the fluid bulk density are expressed according to the volumetric sediment concentration C_V [-]:

$$\tau_y = a10^{bC_V} \quad (2)$$

$$\mu = c10^{dC_V} \quad (3)$$

$$\rho = \rho_W + (\rho_S - \rho_W)C_V \quad (4)$$

with ρ_W the water density [kg/m^3], ρ_S the sediment specific density [kg/m^3], a, b, c and d coefficients [-] related to the rheology of the material.

Based on available geotechnical investigations, the tailings stored within the TSF can be assumed to have an in-situ bulk density of ρ = 2040 kg/m^3 and a corresponding volumetric sediment concentration of C_V = 0.52. The specific density is ρ_S = 3000 kg/m^3. Based on available rheological tests and experience from analysis of other historical events, two values for both the yield stress (50-750 Pa) and the dynamic viscosity (0.5-50 Pa·s) have been chosen to perform a sensitivity analysis. A summary of the rheological parameters is given in Table I.

Table I . Garpenberg case. Rheological parameters used in the TDBA.

Parameter	Value
τ_y	50-750 Pa
μ	0.5-50 Pa·s
ρ	2040 kg/m^3
C_V	0.52
ρ_S	3000 kg/m^3
a	0.00345915-0.05188732
c	0.00003459-0.00345915
b and d	8.0*

* A value of 8.0 is considered as a good approximation to model the exponential relationship between τ_y , μ and C_V [8].

4) Sensitivity analysis

A sensitivity analysis has been performed in order to assess the influence of the following dam breach parameters on the runout and consequences:

- Outflow volume (slope of erosion cone 3 and 5 degrees).
- Breaching duration (0.5 hour and 1 or 2 hours depending on breach height).
- Rheological properties:
  - Low scenario (τ_y = 50 Pa, μ = 0.5 Pa·s).
  - High scenario (τ_y = 750 Pa, μ = 50 Pa·s).

III. Performing tailings runout analysis with TELEMAC-2D: overview and lessons learned

This section presents an overview of the modelling features available in TELEMAC-2D to perform a TDBA and describes the lessons learned from the case study. The section is articulated around the classical workflow used in TDBA, from the release of outflow volume, flood wave modelling in downstream areas to hazard mapping and assessment. Results are presented for the dam section E2 only as it is not possible to cover all the dam sections considered in this article. Dam breach assumptions (failure mode, erosion cone slope, breach ratio, breaching duration and rheological properties) are similar for all dam sections.

A. Breach opening and outflow hydrograph estimation

The most important steps in a TDBA is the estimation of the total outflow volume for the failure mode and the breach development time. These two parameters can then be used to estimate the outflow hydrograph. For a dam failure involving liquefied tailings, the estimation of these parameters is a difficult task and is often associated with very large uncertainties. The outflow volume is commonly only a fraction of the total stored volume, and the outflow process is not driven by a pure rheological process but is the result of complex geotechnical processes. This topic is growing with some methods and tools starting to become available to increase the level of detail for breach modelling [9] [10]. However, these methods are still difficult to implement in common engineering practice.

The current methodology commonly used in TDBA to estimate outflow volume and breaching time is based on available documentation from historical events and/or from empirical approaches often used in dam breach modelling. To assess the range of uncertainty in the final results linked to the uncertainties in estimating the outflow volume and breaching time, a sensitivity analysis can be performed by modelling several combinations of plausible parameter values.

For the Garpenberg case, outflow volumes have been estimated by assuming that the failure leads to the formation on an erosion cone within the TSF defined by the breach width and by a slope linked to the residual shear strength of the tailings (see Figure 4). The outflow process can then be modelled directly within TELEMAC-2D by incorporating the erosion cone into the mesh, assigning an initial tailings level within the cone as an initial condition and using a breach structure with time-dependent opening that controls the outflow process according to the predefined breach development time. The breach opening was modelled using the "widening" option, which allows the reproduction of the expected opening phenomena reasonably well (for non-instantaneous failures). The outflow is then governed mainly by the rate of opening of the breach and by the resistive forces (tailings' non-Newtonian rheology and bottom friction). An illustration of the outflow through the breach is presented in Figure 5.

Although this method is a simplification of a very complex process and has some limitations (see Section IV), it can be used to generate outflow hydrographs in a rather simple and systematic way, which is well suited for performing sensitivity analyses. An example of a generated outflow hydrograph is presented on Figure 6. This hydrograph from dam section E2 corresponds to a total outflow volume of 3.0 Mm^3 of tailings and water released (3-degree erosion cone slope), breach maximal height and final width of 27 and 135 m (breach ratio of 5), respectively, low rheological properties and for a breach development time of 0.5 hour.

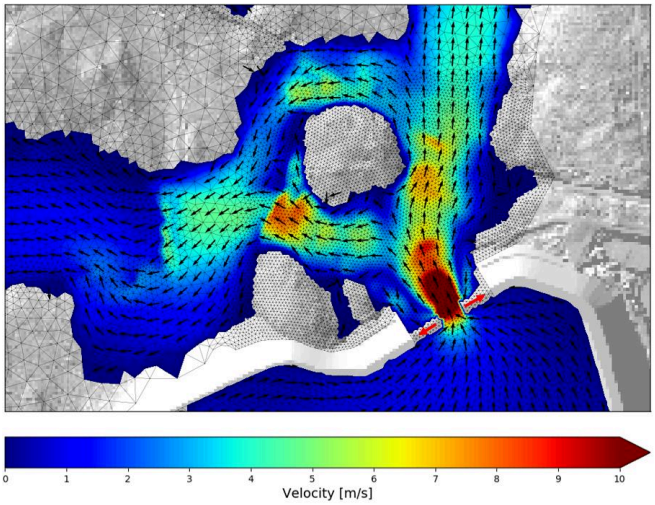

Figure 5. Outflow from dam section E2. Velocity field 20 minutes after breaching start. The breach widening modelled is depicted with the two red arrows.

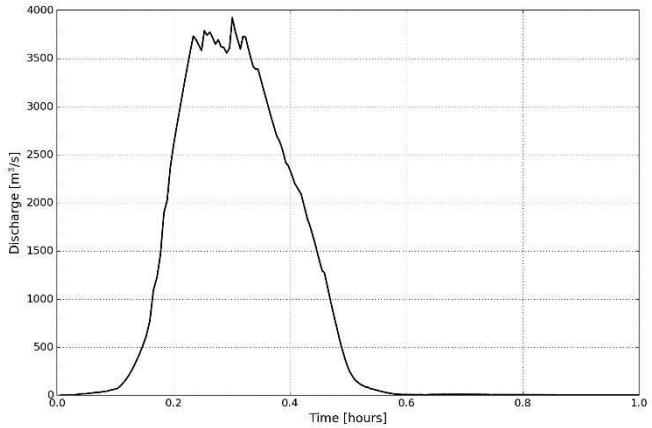

Figure 6. Outflow hydrograph from dam section E2.

The spikes that can be observed around the peak are linked to the breach widening process during the simulation. With the "widening" breach option available in TELEMAC-2D, the nodes located on each side of the opening breach are instantaneously lowered from crest to bottom during one time step, hence triggering a rapid discontinuity of the breach geometry which generates a corresponding increase in the outflow discharge. The outflow discharge then diminishes or stabilizes until the next nodes are lowered, and so on. Similar observations have been made for other dam sections and dam breach scenarios. This "artefact", that can be seen as a defect, is not problematic in the sense that outflow volume remains entirely correct and might even be closer to a real breaching process than a steady breach opening. It is however possible to limit or smooth this effect by lowering the mesh size in the breach region, but at the cost of smaller time-steps due to the satisfaction of the Courant number criterion used in the Finite Volume (FV) kernel. The spikes of the outflow hydrograph disappear however quickly due to flow attenuation of the flood wave.

B. Flood wave modelling

Flood wave modelling is a rather standard step, even with non-Newtonian rheological models. However, an interesting point to mention is the possibility to model cascade failures of downstream dams, embankments or levees using the dam breach module of TELEMAC-2D. As hydrodynamic modelling performed as part of a TDBA usually implies a large number of scenarios due to the need to perform sensitivity analyses, the possibility of modelling cascade failures directly within the simulation is a great advantage and avoids model simplifications (for example, aggregating outflow volumes from the TSF and the clarification pond located near downstream into a unique hypothetical failure event) as well as saving time (less interpretation).

C. Mixing between tailings and downstream water bodies

In most cases, the tailings released from the tailings dam failure that reach the downstream river system and/or lakes will contribute to dilute the sediment concentration by a certain amount. The rheological properties of non-Newtonian fluids are extremely sensitive to the actual sediment concentration. A small dilution ratio can lead to a significant reduction of the yield stress and dynamic viscosity. It is common that the volumetric sediment concentration C_V for tailings within TSFs lie in the range 0.5 to 0.6. The limit between Newtonian and non-Newtonian behavior can be considered to lie around 0.2-0.3 [1] [6] which means that the non-Newtonian behavior of the released tailings can be expected to be negligible once the flood wave is diluted by a factor of approximately 2.

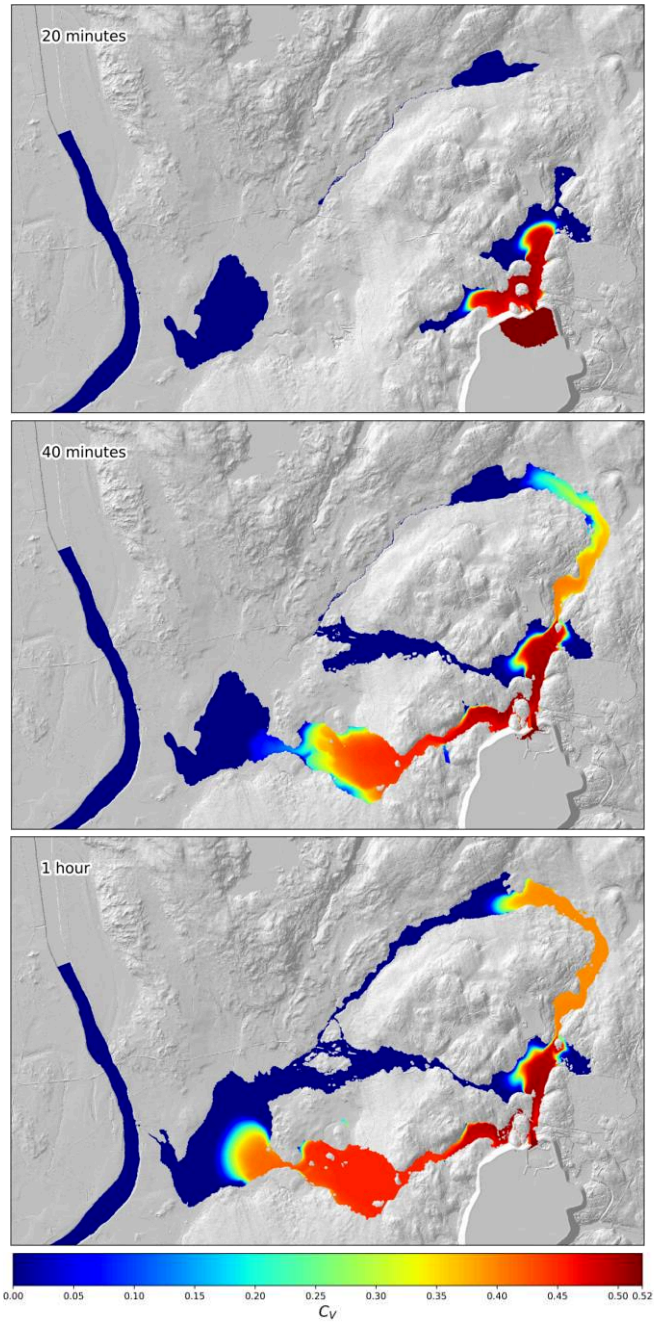

Figure 7. Evolution of volumetric sediment concentration C_V downstream of dam section E2 at different times after breaching start.

The "pseudo-biphasic model" available in TELEMAC-2D can be used to model the mixing between Newtonian and

non-Newtonian fluids. The principle of the model is described in [7]. A passive tracer is used to represent the volumetric sediment concentration C_V and can be assigned either as an initial condition (to distinguish between tailings within the TSF and rivers or lakes, the latter corresponding to $C_V = 0$) or boundary conditions (commonly to model a river inflow with $C_V = 0$ or an outflow hydrograph with $C_V \neq 0$). The fluid rheological properties (bulk density, yield stress and dynamic viscosity) are then computed as a function of C_V using (2) to (4).

Figure 7 presents the evolution of the volumetric sediment concentration C_V downstream of dam section E2 at different times. It can be observed that the local C_V values are varying significantly between the different flow paths depending on dilution in downstream lakes and rivers. For example, the western flow path is characterized by high C_V values and hence high rheological properties whereas those parameters in the northern flow paths are highly influenced by the dilution effects (lower C_V values and hence lower rheological properties).

This model can also be used to take into account the release of both tailings and water during the breaching process. An example from the Garpenberg case study is the release of the water volume corresponding to the supernatant pond using sources located at the edge of the erosion cone with a prescribed tracer value of $C_V = 0$. This is of course a simplification which implies several assumptions (discretization of the supernatant pond by using point sources with assumed outflow hydrograph) but can be acceptable if the water volume is only a minor part of the total outflow volume.

D. Hazard assessment and mapping

The hazard assessments are conducted based on the results from the model and available guidelines for human safety due to floods. The criterion for human safety is often based on the product of flow depth (D) and velocity (V), called the DV product [m^2/s].

Much of the DV criteria available in the different guidelines are mostly provided for water hazards and not for mudflow. For mudflow, the density of the fluid is greater than that of clear water, and therefore a lower threshold of the DV product is assumed to be more adequate for use in the assessment of hazards for loss of life or population at risk [11]. In the case where there is mixing of water and sand, due to a lake or a river downstream of the dam, the C_V value is used to define which threshold DV values are used in which area, i.e., large DV threshold values directly downstream of the dam with little to no mixing of the outflow material, and lower DV threshold values further downstream of the dam after mixing where the outflow material has a similar rheological characteristics as water.

A detailed analysis of the flood wave can give information on flood characteristics over time, especially the type of fluid and its density during the flooding process. Examples are provided in Figure 8 and Figure 9, for two locations along the flow paths affected by a failure at dam section E2 (northern and western flow paths, respectively). The figures show the maximum DV values observed at locations where buildings are affected as well as time series showing evolutions of flow depth, DV, C_V and fluid density. It can be seen that,for the northern location (Figure 8), flooding is initiated by the water from the lakes located downstream of dam section E2, which has negligible sediment concentration. It is only after approximatively one hour that the tailings, mixed with water, reach this location, but the flood peak has already passed. Hence, the flood hazard can be assessed with standard guidelines. For the western location (Figure 9), the tailings concentration in the flood wave is quickly increasing shortly after flooding start as there is only a small lake located downstream of dam section E2 along this flow path. The fluid density reaches approximatively 1900 kg/m^3 10 minutes after flood peak. Hence, fluid density can affect the flood hazard assessment for this location.

IV. CURRENT LIMITATIONS AND POSSIBLE IMPROVEMENTS

A. Outflow hydrograph

As described in Section III, TELEMAC-2D can be used to model the outflow of liquefied tailings from a breach. As earlier mentioned, it should be clear that this can only lead to a very simplified outflow process as the breaching and subsequent material release usually combines geotechnical, rheological and hydraulic processes. For critical cases, it is advised to perform a detailed breach analysis involving state-of-art methods and experts. The Material Point Method (MPM) can be cited as a promising modelling technique to tackle such problems as detailed in [9] and in the Report of the Expert Panel from the Brumadinho failure in Brazil that occurred in 2019 [12]. Another example of dam breach model for tailings dams is the EMBREA-MUD model developed by HR Wallingford [10] [13].

Modelling outflow of liquefied tailings using non-Newtonian rheological models such as the Bingham model should be done with care. In such a simulation, the fluid is characterized by its constant nominal rheological properties (unless if using the “pseudo-biphasic model” to account for mixing with water) corresponding to a liquefied, flowable material, even during the breaching process. This is of course a conservative simplification since the whole outflow volume does not liquefy instantaneously nor have identical properties across the whole mobilized volume. When modelling a very rapid breaching process such as the Brumadinho failure (breaching time was in a range of seconds) [12], modelling the instantaneous release of tailings with constant rheological properties is very likely to overestimate the outflow process and peak discharge. This has been observed in simulations of the Brumadinho failure when comparing results from TELEMAC-2D and MIKE21 with the estimated outflow hydrograph using the EMBREA-MUD breach model. It has also been observed that simulations in which the triggering time for liquefaction was defined depending on time and position within the reservoir gave results in good agreement with the EMBREA-MUD outflow hydrograph [7].

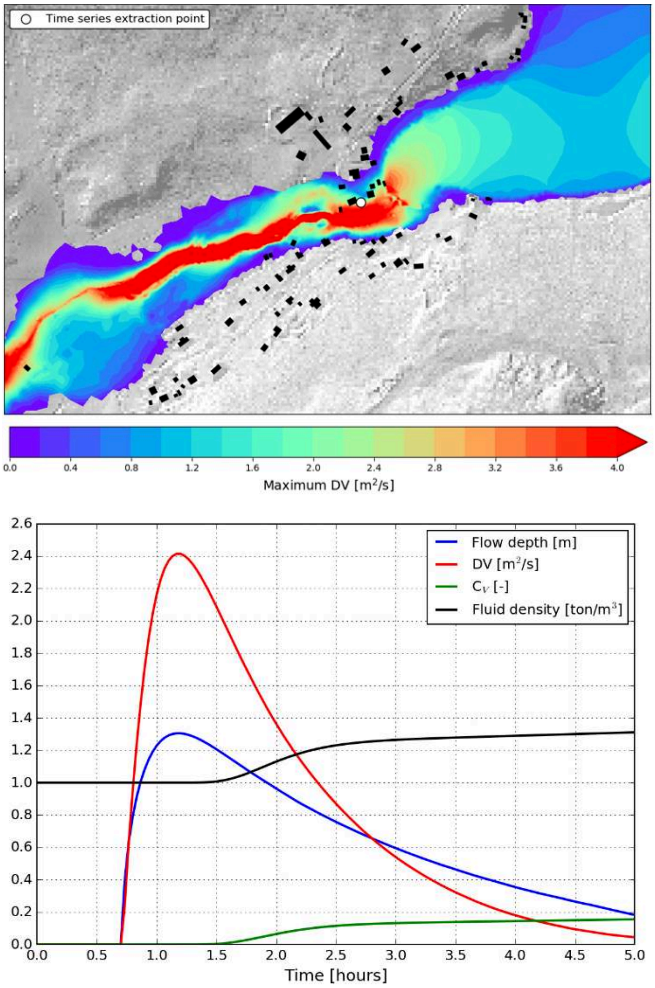

Figure 8. Dam section E2, hazard assessment in northern flow path. Top: maximum DV values. Bottom: time series at location marked in top image.

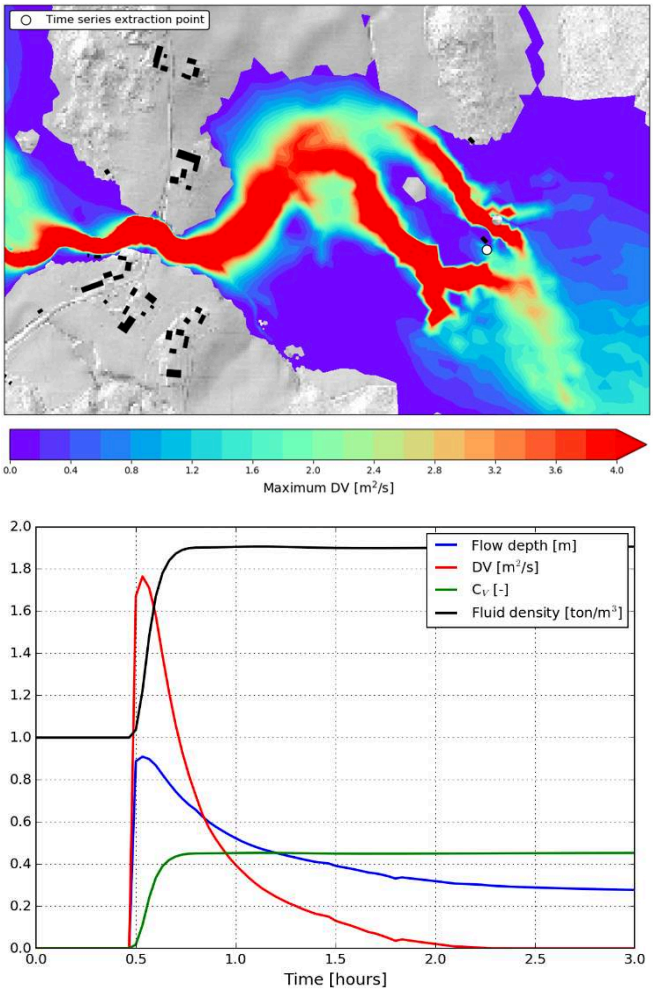

Figure 9. Dam section E2, hazard assessment in western flow path. Top: maximum DV values. Bottom: time series at location marked in top image.

The simplification mentioned above is not limited to instantaneous failures. Estimation of outflow hydrographs for breaching times in the range of 0.5 h or more can become tricky as the tailings flowability characterized by the nominal rheological properties can lead to a faster release than the pre-defined breaching time. This behavior could be observed in the Garpenberg case study. In such a case, using a fictive breaching time longer than the theoretical one can be a way to ensure that the outflow process duration is compatible with the dam breach assumptions to be considered.

B. Numerical diffusion

As it has been observed in the validation cases used to test the non-Newtonian models implemented in TELEMAC-2D [7], one limitation lies in numerical diffusion leading to the spreading of the wave front. This numerical diffusion is linked to the semi-implicit treatment of the non-Newtonian source terms which, on the other hand, ensures the numerical stability of the solution even in regions with strong gradients (e.g., wave front). The numerical diffusion can lead to a loss of accuracy especially in regions where the non-Newtonian stresses are dominant. The numerical diffusion considers mainly the flow depth whereas velocity components do not depict the same trend. Application cases show that this effect can become important when using large cell sizes and/or high values for the rheological parameters (yield stress and dynamic viscosity). It is therefore important that the user verifies the model behaviour beforehand and assesses whether this effect is expected to influence the results in a significant manner or not.

When important, this numerical diffusion is characterized by a wave front that does not stop and similarly, a slow drawdown in regions where deposition is expected. The

effect can be considered as conservative with respect to the maximum flood extents due to the risk of overestimating the front wave propagation. On the other hand, tailings deposition can become hard to predict. Hazard assessment, which is commonly based on the so-called DV product (see Section III), is not affected since the velocity components are treated in a correct manner (i.e., very small velocities once the pseudo equilibrium state is reached). The user should therefore assess the model performance, especially for coarse meshes and with strong non-Newtonian behavior without dilution with downstream water bodies. As this limitation can be important in some cases, it would therefore be beneficial to address this by improving the algorithm's performance.

C. Mixing between tailings and downstream water bodies

When using the "pseudo-biphasic model" available in TELEMAC-2D, the mixing between the different fluid mixtures defined by different values of C_V is governed by the advection and diffusion of the passive tracer representing C_V. The main limitation of this method is that diffusion at the interface between two fluids, and therefore mixing, is overestimated. The "pseudo-bipahsic model" should therefore be seen as a simplified way to account for mixing effects. As mixing and hence dilution are overestimated, the use of this model leads to conservative results since the extra dilution causes a reduction of the rheological properties. However, from an engineering and TDBA perspective, the advantage provided by this model (to model dilution and the subsequent reduction of the rheological parameters) outweighs its disadvantages.

D. Not accounting for sediment transport processes

The non-Newtonian rheological models implemented in TELEMAC-2D treat the fluid mixture as a continuous medium, unlike sediment transport models in which some sediment processes occurring in classical river or coastal flows are considered (erosion, deposition, settling velocity etc.). Consequently, non-Newtonian rheological models used in 2D hydrodynamic models are not aimed at being used in combination with sediment transport models. It is therefore difficult to account for morphological changes linked to erosion processes when performing a tailings runout analysis with non-Newtonian rheological models. Whereas it is generally accepted to overlook erosion processes during a dam break analysis, a clear limitation of the non-Newtonian rheological models used in depth-averaged hydrodynamic models is the impossibility to account for deposition in lakes. When a flood wave of liquefied tailings reaches a lake, the main part of the sediments will deposit at the bottom whereas the outflow from the lake will consist primarily of water that has a lower density. With TELEMAC-2D and with the "pseudo-biphasic model", the stratification process is going to be simplified by assuming a depth-averaged mixing and no deposition, which generally tends to overestimate the tailings outflow. However, the impact on flood wave characteristics should remain limited if the volumetric sediment concentration C_V of the tailings outflow is below 0.3 (e.g., Newtonian behavior).

V. CONCLUSIONS

This article gives an overview on how TELEMAC-2D can be used, in combination with non-Newtonian rheological models, to perform a runout analysis as part of a TDBA. TELEMAC-2D offers several interesting modelling capabilities (dam breach module, "pseudo-biphasic" non-Newtonian model) making it possible to model complex phenomena associated with failures in TSFs and the subsequent release of liquefied tailings. On the other hand, several limitations that can be of importance are presented and detailed. Specifically, the reduction of the numerical diffusion observed in certain cases would be a welcome improvement to the code.

ACKNOWLEDGEMENT

The authors would like to thank Sweco colleagues Aymane Hassan, Francesca Polato and Julius Fritzell for their work during the Garpenberg TDBA project.

REFERENCES

[1] Canadian Dam Association (CDA), Technical Bulletin. Tailings Dam Breach Analysis, 2021. ISBN 978-1-989760-02-4.

[2] Svenska kraftnät (SvK), Guidelines for Dam Safety (Swedish title: Dammsäkerhet Tillämpliga regleverk, vägledningar och stöd), 2022-03-01.

[3] International Council on Mining and Metals (ICMM), Global Industry Standard on Tailings Management (GISTM), August 2020.

[4] Rana, N-M. *et al*, Catastrophic mass flows resulting from tailings impoundment failures, Engineering Geology, Volume 292, 2021.

[5] Wahl, T., Prediction of Embankment Dam Breach Parameters, Dam Safety Office, Water Resources Research Laboratories, July 1998

[6] Julien, P-Y., Erosion and sedimentation, 2nd edition, Cambridge University Press, 2010.

[7] Ligier, P-L., Implementation of non-Newtonian rheological models in TELEMAC-2D, Online Proceedings of the 2020 TELEMAC-MASCARET User Conference, Published by International Marine & Dredging Consultants (IMDC), October 2020.

[8] Oboni, F., Oboni, C., Tailings dam management for the twenty-first century. What mining companies need to know and do to thrive in our complex world, Springer International Publishing, 2020.

[9] Llano-Serna, M., Williams, D., Ruest, M., Analysis of Tailings Dam-Break and Run-Out, Conference Talings 2017, 4th International Seminar on Tailings Management, July 2017.

[10] Petkovšek, G. *et al*, A Two-Fluid Simulation of Tailings Dam Breaching, Mine Water and the Environment, 27 October 2020.

[11] Lee, JiHo, Oak, SueYeun, and Jun, HwanDon, The Study of the Critical Depth and Critical Velocity of Casualites on Mud Flow. J. Korean Soc. Hazard Mitig. Vol. 16, No. 2, pp. 399-405, April 2016.

[12] Robertson, P. K., et al., Report of the Expert Panel on the Technical Causes of the Failure of Feijão Dam I, 2019.

[13] Lumbroso, D., et al., Modelling the Brumadinho tailings dam failure, the subsequent loss of life and how it could have been reduced, Preprint version dated 2020-06-04, Natural Hazards and Earth System Sciences, 2020.

3D modelling of upwelling around a headland

Mcilvenny[1], J., Williamson[1], B. J., Macdowall[1], C., Gleizon[1], P., O'Hara Murray, R.[2],

Jason.mcilvenny@uhi.ac.uk

[1]: Environmental Research Institute, North Highland College, University of the Highlands and Islands, United Kingdom

[2]: Marine Scotland Science, Scotland, UK

Abstract – **Using in situ field measurements and hydrodynamic modelling, this study investigated tidal features around a promontory headland on the United Kingdom mainland. Two acoustic instruments were bottom mounted over a period of 15 weeks and x-band radar data was collected periodically.**

Data showed complex hydrodynamics with an upwelling feature present producing vertical water velocities of up to 0.219 m/s. In association with the upwelling, a prominent surface feature was visible in x-band radar data which developed throughout the tidal cycle.

Data from the instruments was used to calibrate a hydrodynamic model developed using the TELEMAC modelling suite. Models of sufficient complexity are required to resolve fine-scale hydrodynamics associated with such features. Previous 3D models of this region have used 10 equal spaced vertical layers; however, it was found such a model is insufficient to model the vertical upwelling produced by this feature or its development throughout the tidal cycle.

By experiment, it was found 32 vertical layers with a non-equidistant layer spacing produced an upwelling feature similar to what is seen in the ADCP data and x-band data. Upwelling features such as this are important for foraging animals and headlands are also becoming a focus for renewable energy developments.

***Keywords*:** Headland, tidal stream, seabird, modelling

I. INTRODUCTION

The hydrodynamics of a large promontory headland in fast tidal currents are explored with in situ measurements and ground-truthed modelling. The objectives are firstly to calibrate the model to field data and secondly to characterise the hydrodynamics of a fast-moving tidal stream around a promontory headland. In particular, the aim is to understand upwelling observed in the field to better model complex hydrodynamics seen in areas of fast tidal stream, which are of importance to marine megafauna and increasingly of interest for marine renewable energy extraction.

Previously modelling of flow around headlands has aimed to understand the local consequences of sediment depositions, trapping of pollutants, nutrients and marine species distributions ([2],[17],[18],[19],[20],[21]). Such studies have shown eddies cause concentration of nutrients and modifications of the currents. Eddies move across a headland system, causing fluctuations in current speed and direction and a change in the energy density [20]. An increase in density of marine animal foraging has been found around headlands [21]. Upwelling is associated with headlands suggesting that the upwelling of nutrient-rich bottom waters supports life at the ocean's surface [22].

II. METHODS

A. Study site

The Pentland Firth is located between the north mainland of Scotland and the Orkney Islands (Figure 1). The firth is associated with strong tidal flows exceeding 4 m/s in places ([14]; [15]). Plots available in supplementary material show the distribution of currents during flood and ebb tide in the Pentland Firth and M2 amplitude and phase around northern Scotland. Dunnet Head is a promontory which extends approximately 4 km from the mainland into the Pentland Firth. Water velocities around the headland average 1 m/s with a maximum of 2.6 m/s (instrument data from this study). The seabed around the headland rapidly descends to depths of greater than 70 m.

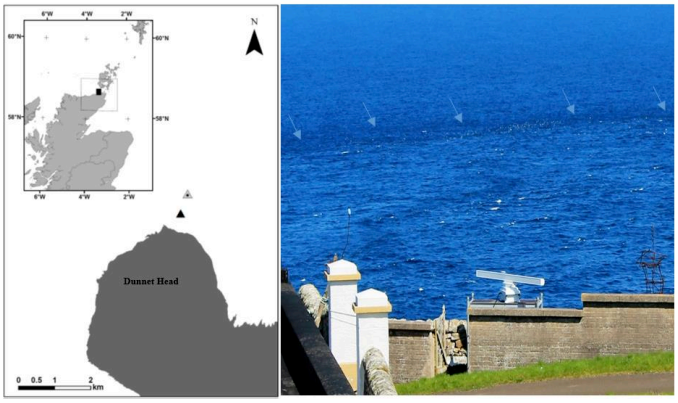

Figure 1. Map showing the location of the study area and model extent (insert) and location of ADCP (black triangle) and AWAC (grey triangle) instruments. Birds assembling along a linear surface feature (arrows) during flood tide. Photo taken from Dunnet Head lighthouse (58.67123◦ N, 3.37623◦ W).

B. Field Data

An ADCP (Acoustic Doppler Current Profiler) and a AWAC (Acoustic Wave and Current) were deployed of the tip of the headland for a period of 109 days between February and May 2018. The ADCP position was approximately 700 m north of the headland (58.67675◦ N, 3.36714◦ W) at 75 m depth. The AWAC was deployed further north, approximately 1.5 km to the north of Dunnet Head (58.68142◦ N, 3.36449◦ W) at approximately 89 m depth. The ADCP was programmed to record 10-min averages from an ensemble of 50 pings at a ping interval of 12 s. A total of 20 vertical bins were sampled, with a bin size of 4 m and a blanking distance of 1.76 m. The AWAC was programmed for 60 pings over a 10-min average with 44 bins, a bin size of 2 m and a 3 m blanking distance.

Post processing of the AWAC data was performed in Nortek STORM software with the removal of near surface bins (Bins 34–44). The AWAC was intermittently recording waves. In addition, a Nortek SeaDarQ X-Band radar system was deployed periodically at Dunnet Head overlooking the two instrument sites.

C. Model

The three-dimensional model was run using TELEMAC-3D (release version V8P0) using the non-hydrostatic version solving the Reynolds Averaged Navier-Stokes (RANS) equations in three directions. The model used the standard k-epsilon turbulence model in the horizontal and vertical directions and solved using the conjugate gradient solver for the linear systems. The N-Scheme for tidal flats was chosen as the advection scheme for the velocities and k-epsilon, The Nikurasde friction law was used (1.265). The TPXO tidal database for the European shelf was used for the tidal constituents.

The 3-D model used the fine-scale horizontal grid tested with the 2-D model using 50 m grid spacing in the proximity of Dunnet Head and 200 m spacing in the Pentland Firth channel with 2000 m spacing elsewhere and 500 m at the open-water boundaries. The time-step for the 3-D model was 5 s with 5-min interval model outputs. The 3-D model used differing vertical resolutions by altering the number of layers and spacing between layers. Increasing the number of layers results in greater accuracy; however, this increases computational time. In the TELEMAC-3D module options for defining equi-distant spacing or non-equidistant spacing are controlled by the mesh transformation keyword and by defining levels in the USER_MESH_TRANSF subroutine.

Table I y+ mesh spacing for differing free stream velocities

Free stream velocity (m/s)	Wall spacing for y+ = 30 (m)	Wall spacing for y+ = 100 (m)	Wall spacing for y+ = 300 (m)
1	1.23	4.1	12.3
2	0.64	2.15	6.4
2.6	0.5	1.69	5
3	0.44	1.48	4.4

Models were run with 10, 16, and 32 layers with the number of layers chosen by using a value of 10 layers from earlier research ([23]; [24]; [25]; [26]) and from calculated y+ values (Table I). The y+ value is a non-dimensional distance to describe the required resolution of a mesh near bottom for a particular flow pattern. Values of $30 < y+ < 300$ have been suggested for the log law region to select the mesh spacing on the bottom ([27]). The log law, or law of the wall, states that the average velocity of a turbulent flow at a point is proportional to the logarithm of the distance from that point to the "wall", or the boundary of the fluid region ([28]). Boundary conditions on the bottom in TELEMAC-3D are, by default, an impermeable slip boundary; however, this can be changed to a no-slip condition provided the vertical mesh is refined at the bottom. This choice is valid if representing turbulence effects due to the bottom, with bottom vertical resolution refined enough to model no-slip conditions. To investigate the effect of bottom boundary conditions on the 3-D model, three model runs were undertaken for distribution layers over the vertical for 10, 16 and 32-layer models with (a) equidistant layer spacing with log law boundary conditions, (b) non-equidistant layer spacing with a refined bottom using both log law and (c) no-slip boundary conditions. The first layer position was calculated using y+ = 30 for the non-equidistant cases.

III. RESULTS

A. Field Data

Periods of high vertical velocity (w) are present during flood tides lasting between 1.5 and 3 h and are associated with the periods of high velocity error. ADCP vertical velocities reached a minimum of 0.206 m/s (downward) and maximum of 0.223 m/s (upward) with the dataset having a mean of the absolute values of 0.45 m/s and standard deviation of 0.028 m/s. The largest magnitude of vertical velocity occurs in Bin 7 of the ADCP data which equates to a mean depth of 46.7 m of a total mean water depth of 76.74 m with a tidal range of 5.08 m; however, vertical velocities > 0.50 m/s occur through all bins (Supplementary material). The data suggest there are periods of complex negative and positive vertical velocities during each flood tide (Figure 2). Similar vertical velocity spikes are seen in the AWAC data but have lower maximum and minimum velocities due to the AWAC position being further north of the headland. Frequency analysis of the AWAC vertical velocity shows a primary spike occurring at 0.4e-5 Hz or approximately 6 h using 15687 10-min samples. The ADCP data show a primary spike occurring at a frequency of 0.2e-5 Hz or approximately 12 h, and a secondary spike at a lower power occurring at approximately 6 h associated with the M2 and M4 tidal harmonics. Vertical velocity spikes exhibit a lag between the ADCP and AWAC data sets. Cross-correlation between the ADCP vertical velocity and AWAC showed 1.5 h in lag. This suggests a similar phenomenon affects the AWAC data later in the tidal phase than the ADCP. Increased periods of ADCP error velocity are associated with the same tidal phase, but error velocity is not strongly correlated with the vertical velocity increases, with a correlation coefficient of 0.14 with zero cross-correlation lag.

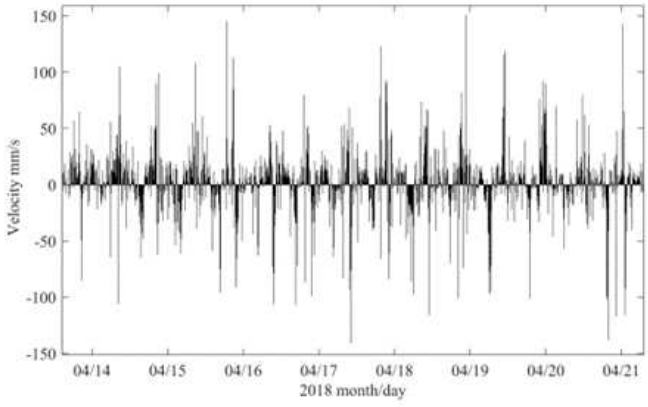

Figure 2. Bin 7 vertical velocities show velocity spikes of > 100 mm/s.

B. 3-D model

To address the complex hydrodynamics, a 3-D model was implemented to explore whether vertical velocities present in the ADCP data could be reproduced. Due to computational restrictions, a time period of increased vertical velocity activity was identified in the ADCP data for which 3-D model runs were undertaken. The 3-D model had an improved relationship with the field data, with a horizontal velocity RMSE of 0.22 for the AWAC position and 0.43 for the ADCP position with a 32-layer model using non-equidistant vertical layer spacing. The error between the model and the data is attributed to the lack of detail in the model in comparison with real variables (bathymetry, coastline shape, bottom type). The bathymetry used in the model is 1 arc second in resolution. However, the primary purpose of the 3-D model was to try to replicate the upwelling features and headland eddies.

Snapshots of the evolution of the vertical water velocity (w) were extracted from the 3-D model chosen to be presented here based on the ADCP data. (Figure 3).

1. Low water + 4 hours; 20/02/18 22:00. Initial formation of eddy during flood tide phase. Phase of negative vertical velocity indicated in ADCP data
2. Low water + 5 hours; 20/02/18 23:30; Mid flood tide
3. Low water + 6.5 hours; 21/02/18 01:00; Point at which maximum vertical velocities recorded in ADCP data. Towards end of flood tide phase.

These 3-time snapshots are extracted from each of the 10-layer, 16-layer and 32-layer models.

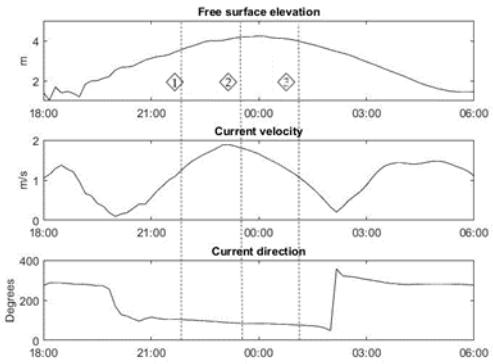

Figure 3. Free surface elevation (m) from 2-D model output, depth averaged current velocity (m/s) and depth averaged current direction (degrees) for from 20/02/18 to 21/02/18 showing time periods chosen (black diamonds, labels for dashed lines) for model snapshot outputs indicated by dashed lines.

10-layer Results

Snapshots from the 10-layer 3-D model for the three time phases (Figure 4) show increased vertical velocities at mid-depth are generated in the early stages of flood tide up to 0.12 m/s which dissipate early in the tidal cycle.

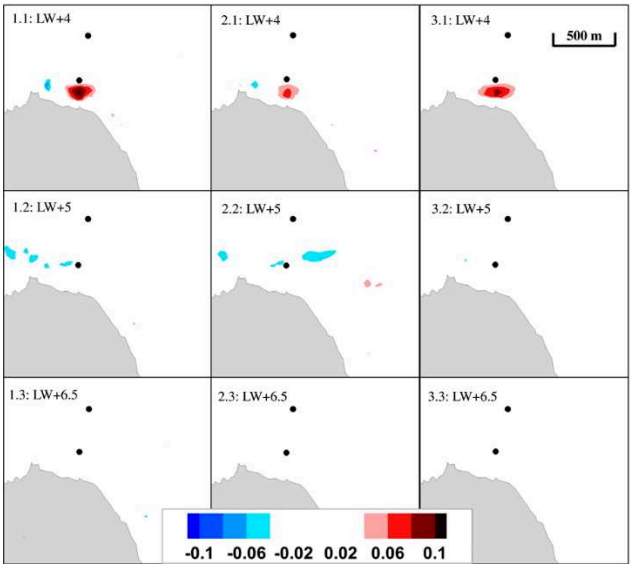

Figure 4. Vertical velocity (m/s) for model with 10 vertical layers, Time = Low water +4 h (x.1), +5 h (x.2) & +6.5 h (x.3) for plan slice at 37 m depth of (w) velocity for 3-D model with (1.x) equidistant vertical layers and log of the wall bottom boundary conditions. (2.x) non-equidistant vertical layers with log law boundary conditions with a first layer at height y+ = 30. (3.x) Non-equidistant layers with no-slip bottom conditions with first layer at y+ = 30. Black circles denote ADCP position (south) and AWAC position (north).

16-layer results

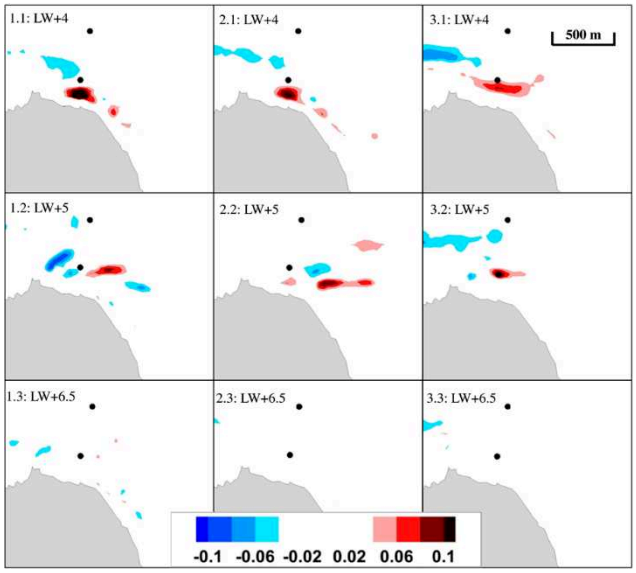

Figure 5. Vertical velocity (m/s) for model with 16 vertical layers, Time = Low water +4 h (x.1), +5 h (x.2) & +6.5 h (x.3) for plan slice at 37 m depth of (w) velocity for 3-D model with (1.x) equidistant vertical layers and log of the wall bottom boundary conditions. (2.x) non-equidistant vertical layers with log law boundary conditions with a first layer at height y+ = 30. (3.x) Non-equidistant layers with no-slip bottom conditions with first layer at y+ = 30. Black circles denote ADCP position (south) and AWAC position (north).

Results using 16 layers show extended evolution of the vertical velocities to low water + 5 hours and dissipation during low water + 6.5 hours. (Figure 5).

32-layer results

Model outputs using 32 layers show continued evolution of the region of increased vertical velocities through low water + 6.5 hours with most development in 2.3 (Figure 6). The vertical velocity reaches similar values as velocities present in the ADCP data during the same time interval (0.13 mm/s).

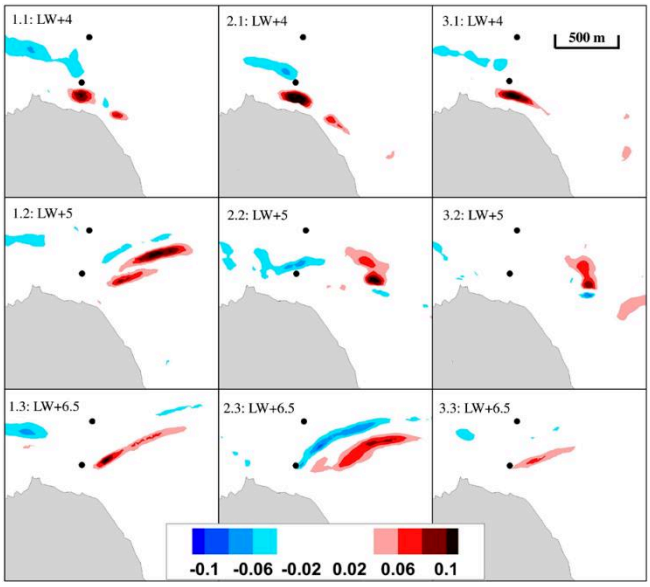

Figure 6. Vertical velocity (m/s) for model with 16 vertical layers, Time = Low water +4 h (x.1), +5 h (x.2) & +6.5 h (x.3) for plan slice at 37 m depth of (w) velocity for 3-D model with (1.x) equidistant vertical layers and log of the wall bottom boundary conditions. (2.x) non-equidistant vertical layers with log law boundary conditions with a first layer at height y+ = 30. (3.x) Non-equidistant layers with no-slip bottom conditions with first layer at y+ = 30. Black circles denote ADCP position (south) and AWAC position (north).

IV. Discussion

A linear surface feature is observed around a promontory headland which has been associated with observations of seabird foraging behaviour. Data from bottom-mounted instruments near this feature showed vertical velocity fluctuations modulated with tidal phase.

2-D and 3-D modelling was undertaken to replicate and understand the development of the features, in particular, the vertical velocity fluctuations seen in the ADCP data. Similar vertical upwelling was produced in a Telemac 3D model using 32 horizontal layers.

A. Field Data

The spikes of increased velocities in the instrument data and lag between the datasets is explained by the change of position of the tidal streak throughout the tidal phase, as the feature develops close to the headland and then moves offshore. For example, ADCP data show high vertical velocities are present at 01:00 on 21/02/2018 (low water + 6 hours). Later, the same spike in vertical velocities is seen in the AWAC data, with a lag of approximately 1.5 hours (low water + 7.5 hours). Vertical velocities of up to 0.219 m/s are recorded by the ADCP data for one 10-minute period. Mid-column velocities are used by other authors when reporting maximum vertical velocity from models ([29]; [30]).

Model results towards the end of flood tide (Low water + 6.5 h) closely resemble the timing of the spikes seen in the ADCP and AWAC data, where at approximately 02:30 on 21/02/18, increased vertical velocities are present in the AWAC data when the model indicated the movement of the area of increased vertical velocities outwards from the headland to the position of the AWAC (Figure 5). The frequency analysis between spikes in vertical velocity for the ADCP and AWAC are different; this is due to the instrument's position in relation to the ebb and tidal flood flow patterns and their relative positions to the headland tip upwelling and downwelling features.

Vertical velocity due to this type of secondary flow has been shown around other headlands. Vertical velocities of 8 mm/s around Cape Saunders, Otago, citing that upwelling caused the water column to be replaced by deeper waters in one tidal cycle [31]. Vertical velocities of 15 mm/s were measured around Rattray Island, Australia [30]. At Dunnet head, upwelling is stronger with the ADCP recording vertical speeds up to 0.223 m/s with a depth of 76.74 m, with the water column replacing itself every 5 minutes and 44 seconds under maximum upwelling conditions.

Strong secondary flow due to flow curvature around the tip of headlands and islands causes strong upwelling in the vicinity which can extend far downstream, where circulation normal to the main flow, the onshore flow near the bottom is drawn upwards and replaces the offshore transverse flow near the surface [30]. They found downwelling occurs with the reverse mechanism on the upstream side of the island and is highly localised and weaker than the upwelling. Here downwelling and upwelling are seen in the ADCP and AWAC data associated with the linear surface feature. This is also seen in the Telemac 3D results and likely a result of headland shape, bathymetry and strength of the tidal flow.

Four mechanisms for vertical motion were identified in previous research [30]; (a) where deficit in volume is larger near the surface than near the bottom, by continuity bottom water comes to surface to replace surface water, causing upwelling; (b) the opposite to this causing downwelling; (c) onshore flow similar to converging flow causing downwelling; (d) curved flows where there is a balance between centripetal acceleration based on the depth averaged velocity and the positive pressure gradient due to the tilting of the sea surface. This causes inward convergence of the bottom water which flows upwards within the water column. They state eddy and

tip upwelling can be encountered with varying magnitudes depending on the radius of curvature, flow intensity and surface pressure gradient. In the case of a study site at Rattray Island, bathymetry and topography of the island lead to the observed upwelling and downwelling present [30]. At Dunnet Head, flood water has a larger curve around the headland due to the flow approaching the Pentland Firth from the west. During ebb tide the flow is deflected prior to reaching Dunnet head by small islands in the firth to the east, causing less curvature. This may partially explain weaker upwelling and downwelling seen in the data during ebb tide; however, another cause of the weaker upwelling and downwelling during ebb tide is the instruments positions in relation to downstream upwelling and downwelling, whereby the instruments are in favourable positions to detect flood tide upwelling and downwelling. The depth, sharp bathymetric slope, flow curvature around Dunnet Head and high tidal current velocity provide the mechanisms for the strong vertical velocities seen in the data.

B. 3D model results

The 32-layer model using a refined bottom mesh with a first vertical layer at y+ = 30 and log law bottom boundary conditions produced results which resemble field data. Other model scenarios showed dissipation of this feature much earlier in the flood tide phase. Whilst the 32-layer, 50-m horizontal resolution, model may be improved upon, it was adequate to represent the field data and could be run on a desktop computer for short model runs of several days. Turbulent features probably have an impact the RANS equations do not accurately reproduce, in part due to the mesh resolution and the difference between horizontal and vertical mesh sizes. No-slip condition results with 32 layers and a refined bottom vertical mesh do not reproduce timings of vertical velocity as seen in field results. The model may not have enough vertical resolution for accurate no-slip conditions, and to do so would greatly increase computational requirements. The 32-layer model with log law bottom boundary conditions has better agreement with the data than an equidistant layer model, where a first layer position of y+ = 30 is a good solution for this flow with the k-epsilon turbulent closure model.

The 32-layer 3-D model produced a 300 m wide 2 km zone of upwelling and 100 m width 1.5 km zone of downwelling on the lee side of headland during flood tide with acceptable computational time, with similar characteristics observed in opportunistic X-band radar field data.

3-D modelling using 10 or 16 layers did not reproduce the extent of vertical velocities present in the instrument data. 3-D modelling using 32 layers and a refined bottom was sufficient to model the timing of the vertical velocity seen in the data but does not reproduce the magnitude of the velocities. However, 3-D modelling indicates the eddy system during flood tide is associated with a tidally induced linear upwelling/downwelling feature which provides explanation for the vertical velocity spikes in instrument field data and potentially explains observed seabird foraging behaviour in the vicinity of the streak feature.

Previous modelling in the Pentland Firth has used a range of vertical resolutions from 10 equidistant layers ([23]; [33]) to 20 layers ([32]). Previous research in the area used the Delft3-D-Flow model using the hydrostatic pressure assumption and 10 equidistant layers for sensitivity analysis of turbulent closure models [32]. In areas of complex hydrodynamics such as Dunnet Head, careful selection of horizontal layers and thickness of horizontal layers is required to model complex vertical movements.

V. CONCLUSIONS

Dunnet Head is an extreme example of upwelling and downwelling associated with strong tidal flow and secondary flow due to flow curvature causing a noticeable surface feature. Vertical velocities of greater than 200 mm/s have been recorded by field instruments.

Initial observations (boat-based and cliff-based) indicate the study site is a preferred feeding location targeted by seabirds, with birds congregating and actively foraging along the surface expression of the tidal streak. As Dunnet Head is a nesting site for many seabirds, the tidal front may act as an important local feeding area affording the seabirds minimum energy to forage in the vicinity of the nesting site. Attraction of seabirds to the feature is likely a result of the hydrodynamic processes affecting prey, either concentrating them or making them more easily available near the surface and may be directly attributable to the vertical currents and turbulence associated with this feature.

The modelling work reproduces upwelling observed in the field and recorded by field instruments; however, models of sufficient complexity are required to resolve fine-scale hydrodynamics which are associated with such features, which is of importance to tidal stream renewable energy developments in these environments, as well as understanding foraging activity of marine top predators. Models using 32 vertical layers were sufficient to reproduce patterns of vertical velocities seen in field data. This study highlights that some areas, in particular headlands, may not be suitable for tidal energy developments due to the nature of the complex hydrodynamics due to secondary flow features, and potentially their importance for foraging megafauna.

Further work is proposed to investigate the role hydrodynamics plays regarding prey availability and the predictable presence and behaviour of foraging marine wildlife. Measuring velocities using a 5-beam ADCP combined with an echo sounder will allow investigation of the role turbulence and vertical currents play in biophysical associations of predators with hydrodynamic features, and changes to prey aggregation, disorientation and availability. Further surveys are planned to include vantage-point surveys for seabirds and marine mammals at Dunnet Head lighthouse and aerial surveys using a small unmanned aerial vehicle for combined biophysical data collection.

ACKNOWLEDGEMENTS

This work is published in more detail at: J. McIlvenny, B.J. Williamson, C. MacDowall, P. Gleizon, R. O'Hara Murray (2021). Modelling hydrodynamics of fast tidal stream around a promontory headland. Estuarine, Coastal and Shelf Science. http://doi.org/10.1016/j.ecss.2021.107474

REFERENCES

[14] Goddijn-Murphy, L., Woolf, D.K., Easton, M.C., 2013. Current patterns in the inner sound (Pentland Firth) from underway ADCP data. J. Atmos. Ocean. Technol. 30, 96–111. https://doi.org/10.1175/JTECH-D-11-00223.1

[15] Neill, S.P., Vögler, A., Goward-Brown, A.J., Baston, S., Lewis, M.J., Gillibrand, P.A., Waldman, S., Woolf, D.K., 2017. The wave and tidal resource of Scotland. Renew. Energy 114, 3–17. https://doi.org/10.1016/j.renene.2017.03.027

[16] Signell, R.P. & Geyer, W.R. 1991. Transient eddy formation around headlands. J. Geophys. Res. Ocean. 96, 2561–2575. https://doi.org/10.1029/90jc02029J

[17] Davies, P.A., Dakin, J.M. & Falconer, R.A. 1995. Eddy formation behind a coastal headland. J. Coast. Res. 11, 154–167.

[18] Bastos, A., Collins, M. & Kenyon, N. 2003. Water and sediment movement around a coastal headland: Portland Bill, southern UK, in: Ocean Dynamics. 53, 309–321. https://doi.org/10.1007/s10236-003-0031-1

[19] McCabe, R.M., MacCready, P. & Pawlak, G. 2006. Form drag due to flow separation at a headland. J. Phys. Oceanogr. 36, 2136–2152. https://doi.org/10.1175/JPO2966.1

[20] Lin, J., Lin, B., Sun, J. & Chen, Y. 2017. Numerical model simulation of island-headland induced eddies in a site for tidal current energy extraction. Renew. Energy 101, 204–213. https://doi.org/10.1016/j.renene.2016.08.055

[21] Waggitt, J.J., Cazenave, P.W., Torres, R., Williamson, B.J. & Scott, B.E. 2016. Predictable hydrodynamic conditions explain temporal variations in the density of benthic foraging seabirds in a tidal stream environment. ICES J. Mar. Sci. 73, 2677–2686. https://doi.org/10.1093/icesjms/fsw100

[22] Russell, P. & Vennell, R. 2017. High-resolution observations of secondary circulation and tidally synchronized upwelling around a coastal headland, J. Geophys. Res. Oceans, 122, 890–913, doi:10.1002/2016JC012117.

[23] Rahman, A., Venugopal, V., 2015. Inter-comparison of 3D tidal flow models applied to Orkney islands and pentland firth. In: 11th European Wave and Tidal Energy Conference (EWTEC).

[24] Chatzirodou, A., Karunarathna, H. & Reeve, D.E. 2017. Modelling 3D hydrodynamics governing island-associated sandbanks in a proposed tidal stream energy site. Appl. Ocean Res. 66, 79–94. https://doi.org/10.1016/j.apor.2017.04.008

[25] Stansby, P., Chini, N. & Lloyd, P. 2016. Oscillatory flows around a headland by 3D modelling with hydrostatic pressure and implicit bed shear stress comparing with experiment and depth-averaged modelling. Coast. Eng. 116, 1–14. https://doi.org/10.1016/j.coastaleng.2016.05.008

[26] Waldman, S., Bastón, S., Nemalidinne, R., Chatzirodou, A., Venugopal, V. & Side, J. 2017. Implementation of tidal turbines in MIKE 3 and Delft3D models of Pentland Firth & Orkney Waters. Ocean Coast. Manag. 147, 21–36. https://doi.org/10.1016/j.ocecoaman.2017.04.015

[27] Salim, S.M. & Cheah, S.C., 2009. Wall y+ Strategy for Dealing with Wall-bounded Turbulent Flows, in: International Multi Conference of Engineers and Computer Scientists, IMECS 2009, Hong Kong.

[28] Chanson, H., 2009. Applied Hydrodynamics: an Introduction to Ideal and Real Fluid Flows. CRC Press. https://doi.org/10.1201/b11464.

[29] Alaee, M.J., Ivey, G. & Pattiaratchi, C. 2004. Secondary circulation induced by flow curvature and Coriolis effects around headlands and islands. Ocean Dyn. 54, 27–38. https://doi.org/10.1007/s10236-003-0058-3

[30] White, L., Wolanski, E., 2008. Flow separation and vertical motions in a tidal flow interacting with a shallow-water island. Estuarine, Coastal and Shelf Science 77, 457-466.

[31] Russell, P. & Vennell, R. 2009. Observations of secondary flow and upwelling at Cape Saunders, Otago Peninsula. Proceedings Australasian Coasts and Ports conference, Wellington Sept 2009.

[32] Baston, S., Harris, R.E., Woolf, D.K., Hiley, R.A. & Side, J.C. 2013. Sensitivity Analysis of the Turbulence Closure Models in the Assessment of Tidal Energy Resource in Orkney. EWTEC 2013 Proc. https://doi.org/10.13140/2.1.3033.3762

[33] O'Hara Murray, R. & Gallego, A. 2017. A modelling study of the tidal stream resource of the Pentland Firth, Scotland. Renew. Energy 102, 326–340. https://doi.org/10.1016/j.renene.2016.10.053

Development of a hydrodynamic model for a subtropical reservoir: Salto Grande, Uruguay

R. Rodríguez[1], S. Delgado[1], M. Fossati[1], P. Santoro[1]

psantoro@fing.edu.uy, Montevideo, Uruguay
[1] Universidad de la República, Montevideo, Uruguay.

Abstract – **The objective of this work is to characterize the hydrodynamics and transport time scales of the main hydroelectric generation reservoir in Uruguay based on a numerical modelling approach. The work is based on the analysis of numerical results from a hydrodynamic model implemented for the Salto Grande reservoir, using the TELEMAC-MASCARET Modelling System (TMS).**

A 2D depth-averaged approach is followed. The model is calibrated and validated using data of surface elevation at several stations along the river-reservoir system. The obtained results show good agreement with the measured data, representing satisfactorily the main features of the Salto Grande dynamics.

A simulation with realistic forcings during several years allows us to analyse the circulation in the river-reservoir system, and the estimation of the transport time scales based on numerical experiments with a passive tracer. The effect of the wind forcing is also analysed.

Keywords: reservoir, circulation, transport time scales.

I. INTRODUCTION

Hydropower reservoirs are semi-lentic water bodies that, in addition to power generation, have other uses e.g., water supply, fishing and recreation. Typically, the increase in the water residence time combined with the increasing process of anthropical eutrophication favours the occurrence of phytoplanktonic blooms. These events have negative consequences on the ecosystem (affecting both its physical-chemical properties and the biota) and interfere with human activities. This work aims to contribute to a better management of the hydropower reservoirs water quality by developing numerical tools that help to understand the system dynamics and allow to predict its future behaviour.

II. STUDY AREA

The Salto Grande Hydroelectric Complex (CHSG) is located on the Uruguay River (31°16'28.7"S, 57°56'21.0"W, kilometer 342.6), upstream from the cities of Concordia (Argentina) and Salto (Uruguay), see Figure 1. The Uruguay River basin up to the CHSG covers an area of approximately 244,000 km^2. The immediate basin is located between the city of Paso de los Libres and the Salto Grande dam and covers an approximate area of 47,200 km^2. The Salto Grande reservoir is an artificial lake with multiple purposes, including energy production, drinking water and recreational activities. It is a reservoir with a dendritic morphology, composed of a single main entrance, the Uruguay River (mean flow rate of 4,400m^3/s), and multiple lateral tributaries, of which the most relevant in terms of flow contributions are the Arapey River (mean flow rate of 65 m^3/s) and the Mocoreta River (mean flow rate of 43 m^3/s). Table I shows the main characteristics of the reservoir [1]. In the last three decades, multiple scientific works have addressed the phenomenon of phytoplankton blooms in the Salto Grande reservoir, giving an account of the water quality problems in this water body [2][3][4][5][6].

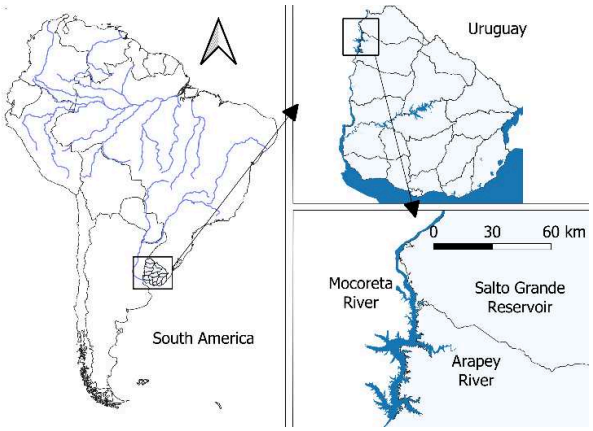

Figure 1. Location of the study area, Salto Grande reservoir.

Table I Main characteristics of Salto Grande reservoir.

Nominal water level (m)	35
Area (km^2)	783
Perimeter (km)	1,190
Volume (hm^3)	5,500
Reservoir length (km)	140
Mean width (km)	5.4
Maximal width (km)	9

III. METHODOLOGY

A. *Numerical model implementation*

The numerical model TELEMAC (www.opentelemac.org) is used, in particular its two-dimensional hydrodynamic module TELEMAC-2D [7]. It solves the depth-averaged free-surface flow equations (Saint-Venant equations), using the finite element method on unstructured grids of triangular elements.

1) Mesh and bathymetry

The computational domain is shown in Figure 2. It includes the Salto Grande reservoir and several kilometers of its main tributary (Uruguay River) up to Paso de los Libres (PL) where boundary conditions are imposed. Some islands in the reservoir were included as land area. The mesh consists of approximately 28,000 nodes and 49,500 elements with dimensions varying from 250 m up to 125 m in refined zones. The bathymetry is provided by the Joint Technical Commission of Salto Grande (CTM-SG), for the area between the dam and Paso de la Cruz (PC in Figure 2). Between PC and PL there is not available bathymetric information, so a linear profile was assumed. The slope is computed based on the available bathymetric information in the last part of the river up to PC.

There is a relatively dense bathymetry (more than 115,000 points in an area of 684 km^2), obtained from more than 400 transversal profiles separated between 500 and 1,000 meters (with spatial resolution of approximately 10 meters), and longitudinal profiles for the main channel and the main tributaries. The bathymetry data is provided by CTM-SG validated to the year 2019 and covers the reservoir region from the dam to approximately 10 kilometres upstream of Monte Caseros (MC in Figure 2).

Several interpolation methods are tested to generate the model bathymetry. The deterministic methods implemented in ArcGIS are used. Although good results are obtained locally (e.g., with Radial Basis Functions), when observing the results globally (i.e.: interpolation between cross-sectional profiles) discontinuities are observed that deviated from what is expected at a natural margin of a river channel. Adding this qualitative criterion, the best results are obtained using the inverse of the distance squared considering the closest 4 points located in different quadrants. Between MC and PL a bottom slope of 1.68x10^{-4} is imposed, value computed from the slope of the last fluvial region with available data.

2) Boundary conditions

The open boundaries of the domain correspond to the dam (output flow) and all the reservoir tributaries (input flows). There are both measured and unmeasured flows in the reservoir. The measured flows are supplied by CTM-SG at Paso de los Libres (PL), Paso de la Cruz (PC), Arapey grande (AG), Arapey chico (AC) and Dam (DA) stations (see locations in Figure 2). On the other hand, there are unmeasured inflows corresponding to the following tributaries: Itapebí Grande (IG), Itapebí Chico (IC), Mocoreta (MO), Mandisovi Chico (MCh), Mandisovi Grande (MG) and Gualeguaycito (G); see Figure 2. The CTM-SG also provided a theoretical total hydrological inflow to the reservoir, computed from a mass balance. The unmeasured flows were computed by distributing the difference between the theoretical total hydrological contribution flow and the sum of the measured inflow flows, proportional to the basin area of each tributary.

At the free surface the effect of the wind was considered. Wind data was obtained from the ECMWF ERA5 reanalysis product [8].

The model is then forced by inflows and outflows as well as the surface wind stress. The boundary conditions in the open boundaries are the free surface elevation and flow discharged at the Dam, using a Thompson boundary condition [9], and flow rates (measured or estimated) in the other open boundaries.

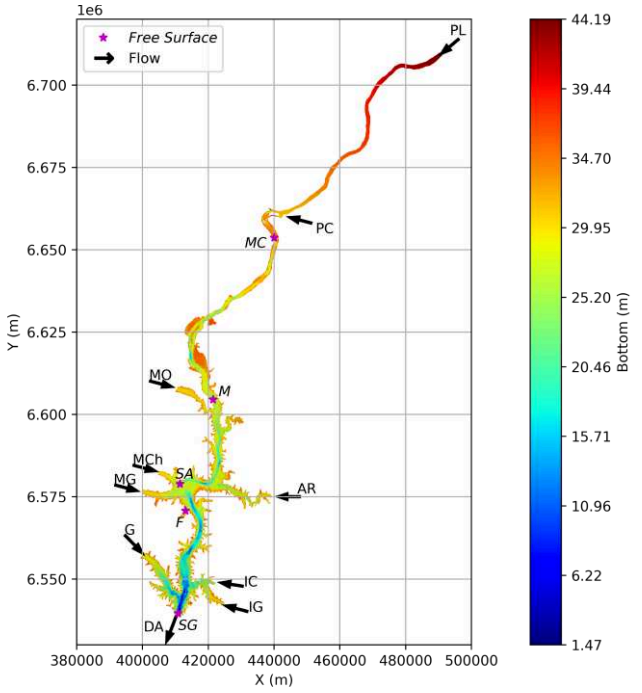

Figure 2. Simulation domain, mesh and bathymetry. Open boundary conditions are indicated as well.

3) Model calibration and verification

There are six free surface elevation gauge stations: Monte Caseros (MC), Mocoreta (MO), Federación (F), Santa Ana (SA), Salto Grande (SG) and Dam (DA). Unfortunately, there is not available water velocity data for model calibration.

The model is then calibrated based on the free surface elevation data. The bottom friction and wind drag coefficients are selected as calibration parameters.

The calibration period is 2019/01/10 until 2020/04/30 (15 months approx., period called window 2). The calibration parameters include the Manning roughness coefficient (n) for which the values 0.020, 0.024, 0.025, 0.026 and 0.030 s/m$^{1/3}$ are tested. On the other hand, the following values are considered for the COEFFICIENT OF WIND INFLUENCE: 1.0x10^{-6}, 1.25x10^{-6}, 1.5x10^{-6}, and 2.0x10^{-6}. The mean absolute error (MAE), root mean square error (RMSE), and BIAS are used to assess the model performance. The model is then validated for the free surface elevation at the MC, M, SA, F, and SG stations, for two time windows: from 2018/2/28 to 2018/7/20 (approx. 5 months, period called window 1), and from 2020/5/27 to 2020/10/21 (approx. 5 months, period called window 3).

The time step used for these simulations is 5 s. The Smagorinsky formulation is used for turbulence closure with a base value of eddy diffusivity of 1x10^{-6} m^2/s and tracer diffusivity of 1 m^2/s.

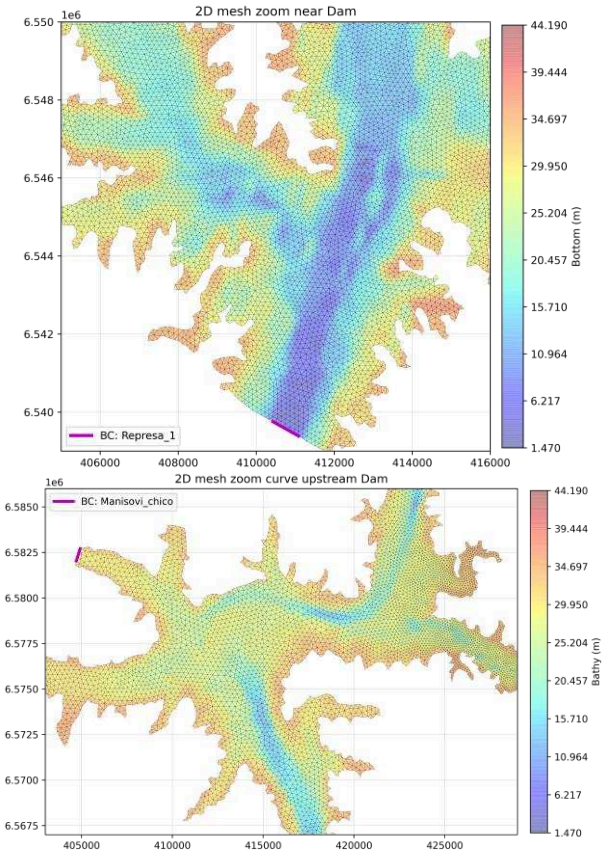

Figure 3. Detail of the simulation mesh and bathymetry in the lower (upper panel) and middle (lower panel) reaches of the reservoir.

B. *Hydrodynamic characterization*

In order to characterize the reservoir hydrodynamic the mean, 10 and 90 percentile maps are computed based on the model results for the simulated period (2017/02-2020/10). The water flux through the entrance of the Gualeguaycito arm is also calculated (see Figure 2). Finally, the influence of the wind on these results is analysed.

To estimate the transport time scales in this work we propose to adapt two local parameters: the exponential flushing time (flushing time - t_{FT}) and the flushing lag time (flushing lag - t_{FL}). They come from an Eulerian methodology which calculation method is adopted from [10]. Initially, a concentration $C_0 = 1$ of a passive tracer is imposed within the domain and a concentration value $C^* = 0$ is assigned to the water flow entering through open boundaries. The time taken for the concentration to reach a threshold value C_1 (arbitrarily set as 95% of C_0) is called flushing lag time and is considered to be the beginning of an exponential decrease in concentration at the observed domain point. The t_{FT} is defined as the "local e-flushing time" and corresponds to the time taken from t_{FL} for the concentration of the passive tracer to reach a value of 1/e^C_0. Both parameters are called local as they are computed for each node of the mesh.

Considering the underlying hypothesis of this methodology it is better suited to analyse steady scenarios. Three scenarios without wind are tested for this work, combining different surface elevations and incoming flowrates at PL: 1) (scenario e3) low level at the dam (percentile 10: SG=32.96 m) and high flowrates (percentile 90: DA=11,586 m^3/s; IG=57 m^3/s; IC=31 m^3/s; AR=469 m^3/s; PC=1,112 m^3/s; PL=9,528 m^3/s; MO=274 m^3/s; MCh=36 m^3/s; MG=46 m^3/s; G=33 m^3/s); 2) (scenario e6) average surface elevation (mean value: SG=34.31 m) and average flowrates (mean value: DA=5,389 m^3/s; IG=25 m^3/s; IC=15 m^3/s; AR=224 m^3/s; PC=395 m^3/s; PL=4,563 m^3/s; MO=113 m^3/s; MCh=17 m^3/s; MG=21 m^3/s; G=16 m^3/s); 3) (scenario e11) high surface elevation (percentile 90: SG=35.32 m) and high flowrates (percentile 90).

Then the wind influence is tested by simulating eight scenarios with average free surface elevation and incoming flowrates, and a constant wind of 10 m/s blowing from eight different cardinal directions.

IV. RESULTS AND DISCUSSION

A. *Model calibration and verification*

The simulated free surface elevation is not very sensitive to the Manning roughness coefficient for the stations located at the lower part of the reservoir (SG, F, and SA), showing variations in the RMSE and MAE of the order from millimetre to centimetre. On the other hand, stations M and MC, which show a transitional and fluvial behaviour respectively, present a greater sensitivity with RMSE and MAE variations of centimetres to decimetre. Regarding the wind drag coefficient, the model presented little sensitivity for all stations in the calibration period, with variations between simulations of the order of a millimetre.

Figure 4 shows qualitatively the results obtained for station F and MC with n = 0.025 $s/m^{1/3}$ and $C_D = 1.0x10^{-6}$ for the calibration period, together with the measured inflows. Table II presents quantitatively the results of the evaluation of the predictions for the calibration and validation periods. The model reproduces reasonably well the water surface elevation at both stations which have different behaviours.

Table II Model performance statistics at stations F and MC for the calibration (Window 2) and validation periods (Windows 1 and 3).

Station *F*	**Window 1**	**Window 2**	**Window 3**
RMSE (m)	0.110	0.138	0.122
MAE (m)	0.101	0.127	0.118
BIAS (m)	-0.099	-0.108	-0.118
Station *MC*	**Window 1**	**Window 2**	**Window 3**
RMSE (m)	0.149	0.223	0.290
MAE (m)	0.116	0.175	0.263
BIAS (m)	0.039	-0.007	0.254

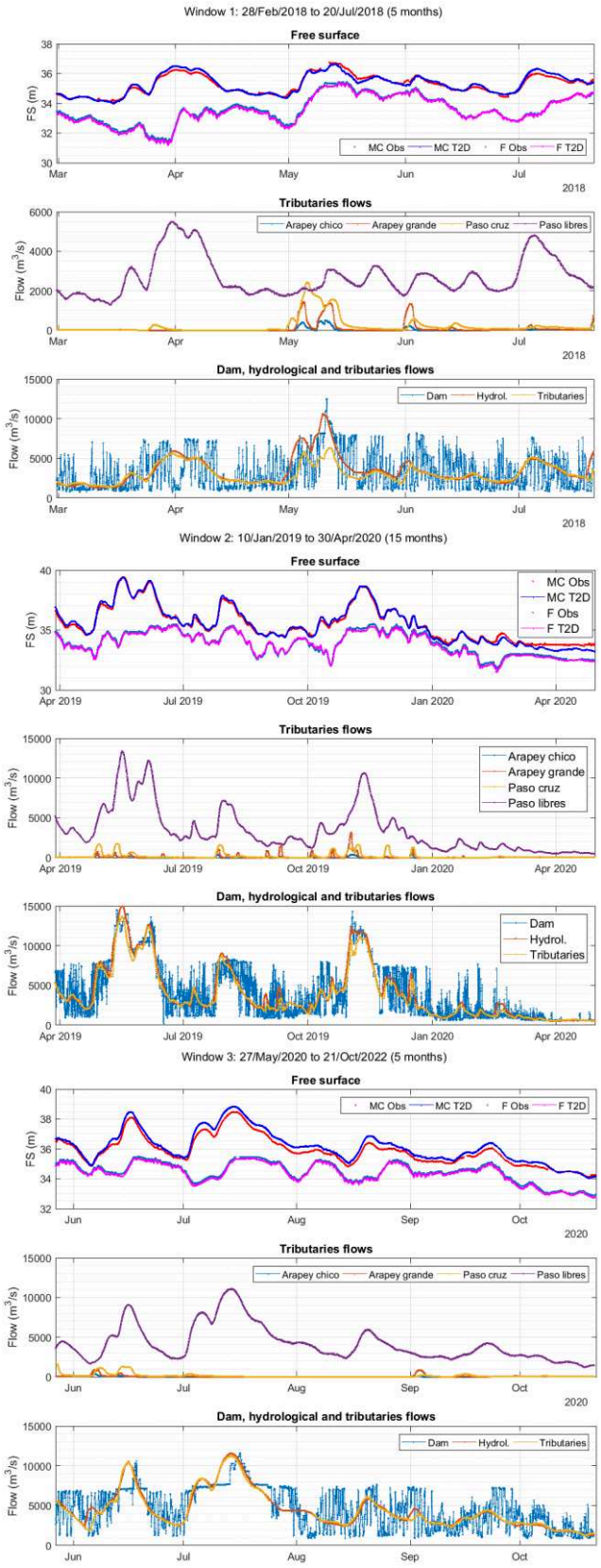

Figure 4. Observed (Obs) and simulated free surface elevations (T2D) for station F and MC (see Figure 1), and measured inflows. Calibration (Window 2) and validation periods (Windows 1 and 3) are shown.

B. *Water circulation*

The mean velocity field (Figure 5) for the simulated period shows a clear difference between the central zone and the reservoir arms, as expected. The mean intensities in the central zone show values around 10 cm/s, while in the arms are one order of magnitude lower. At the Gualeguaycito arm (Figure 5 upper panel) it is interesting to note the circulation patterns showing higher intensities near the coast. This is usually related to the wind effect on the shallower areas and have been reported in other study cases like [11].

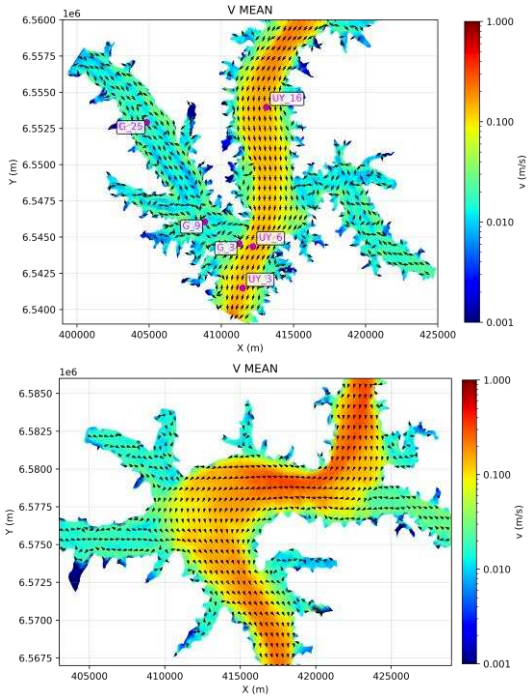

Figure 5. Mean velocity field for the period 2017/02-2020/10 at the lower and middle reaches of the reservoir.

Figures 6 and 7 show the 90 and 10 percentile maps for the simulated period at the lower reservoir reach, while Figure 8 shows a boxplot of the intensity time series at the stations indicated in Figure 5. At the central zone the effect of the flood events is more noticeable showing currents intensities close to 1 m/s.

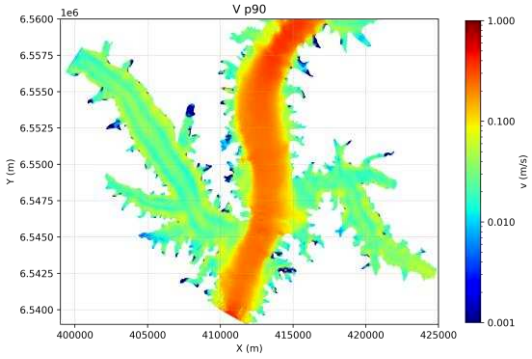

Figure 6. Percentile 90 of current intensities for the simulated period 2017/02-2020/10.

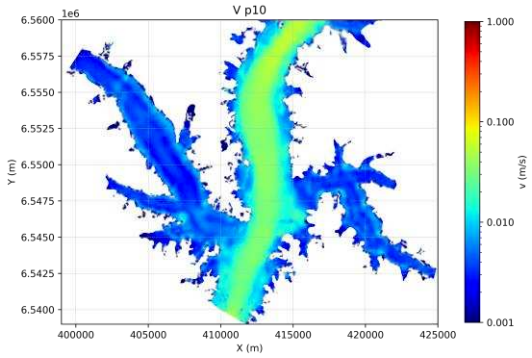

Figure 7. Percentile 10 of current intensities for the simulated period 2017/02-2020/10.

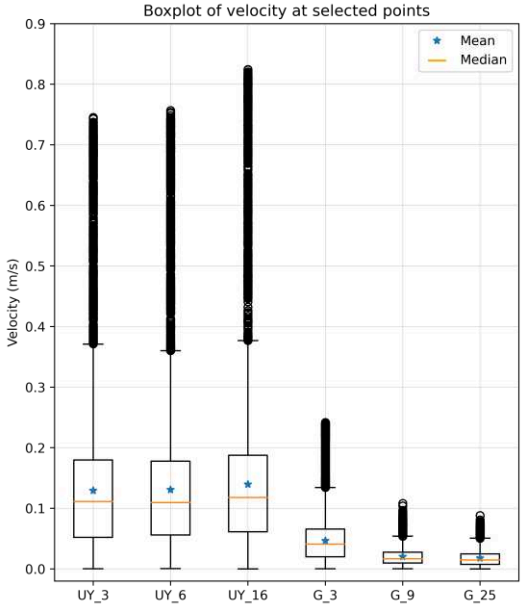

Figure 8. Boxplot of current intensities at several stations at the reservoir lower reach (see Figure 5).

The influence of the wind forcing is relevant specially in the reservoir arms. Figure 9 shows the mean velocity field obtained without including the wind forcing and the difference with the mean current field with wind (presented in Figure 5). As expected the differences are noticeable in shallower areas; specially the Gualeguaycito arm shows a significant change in its circulation patterns and intensities.

C. *Transport time scales*

Figure 10 shows an example of the tracer concentration evolution in the three scenarios without wind at one station located in the central zone (UY_6, see Figure 5) and another in the Gualeguaycito arm (G_25). The thresholds for the flushing lag and local flushing time are indicated as well. It can be seen that the exponential decay assumption underlying the methodology is reasonable in these steady scenarios.

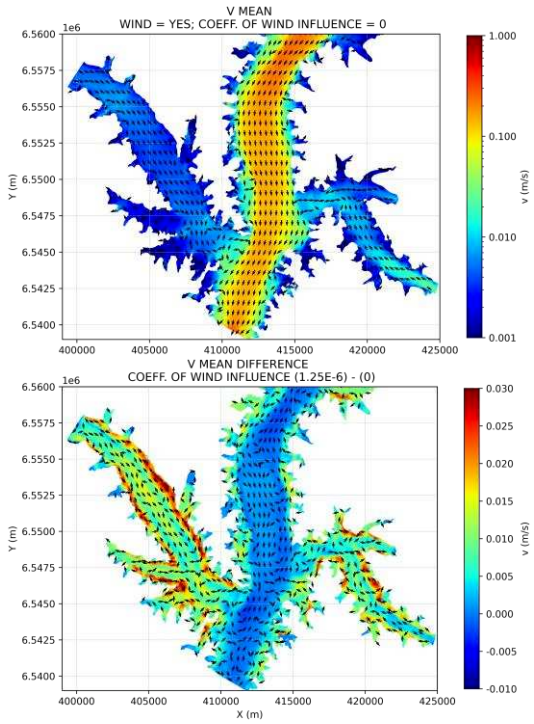

Figure 9. Mean velocity field without wind forcing (upper panel) and its difference with the mean velocity field shown in Figure 5 (lower panel).

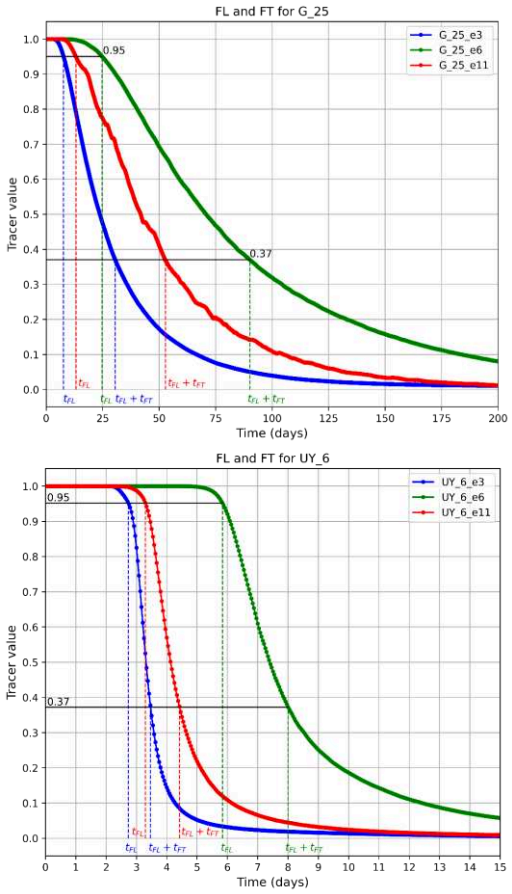

Figure 10. Example of tracer concentration evolution at stations G_25 and UY_6 for the scenarios e3, e6 and e11.

Figures 11 and 12 show the flushing lag and local flushing time maps for the three scenarios without wind forcing and different combinations of water level and inflow rates. The flushing lag results, which give an idea of the arrival time, show lower values in the central zone where the advection is dominant, as well as in the arms close to the open boundaries with imposed inflows. As expected, higher inflow rates and lower water level tends to decrease the flushing time and vice versa. For the mean scenario the flushing time in the central zone is in the order of a few days, while in the Gualeguaycito arm for example can be up to two months.

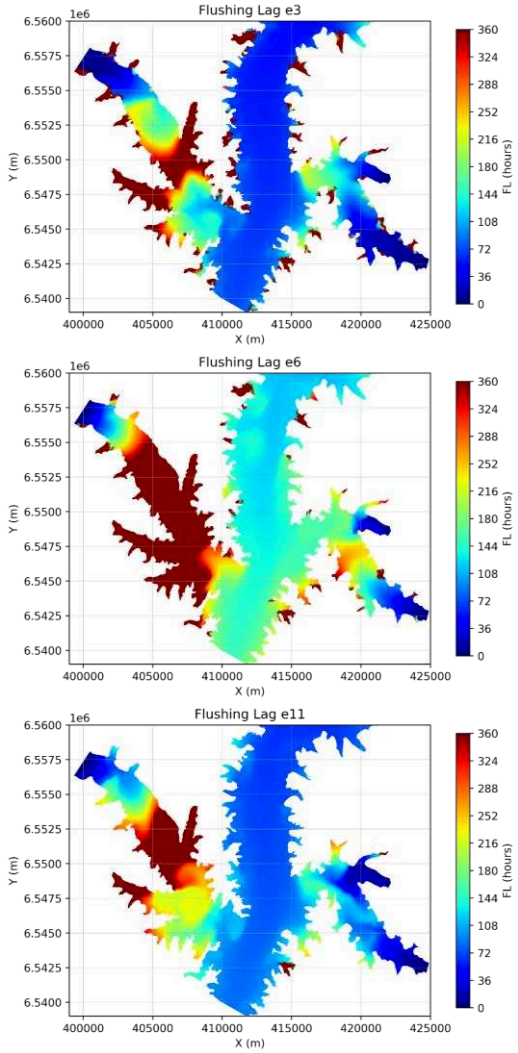

Figure 11. Maps of flushing lag (FL) for the scenarios with low water level and high inflow (e3); mean water level and inflow rate (e6); and high water level and inflow rates (e11).

Figures 13 and 14 show the flushing lag and local flushing time maps for the scenarios with different wind directions. Only four directions are shown (SW, SE, NE, and NW). As it was seen previously in the mean velocity fields, the wind forcing is relevant in the reservoir arms, while the central zone does not show significant changes.

The flushing lag maps clearly show how the fluvial inflow is advected towards the wind direction in the Gualeguaycito arm. When the wind blows cross to the arm (SW and NE directions) the flow is concentrated on the south and north coast respectively. Wind blowing along the arm and towards the reservoir tends to enhance the advection (NW wind) and the opposite when it blows towards the coast (SE wind).

The flushing time maps (Figure 14) shows that wind directions along the arm direction tend to increase the water exchange with the central zone leading to lower transport time scales. On the other hand winds blowing with transversal direction to the arm show much higher transport time scales and an enhanced shear flow at the arm entrance.

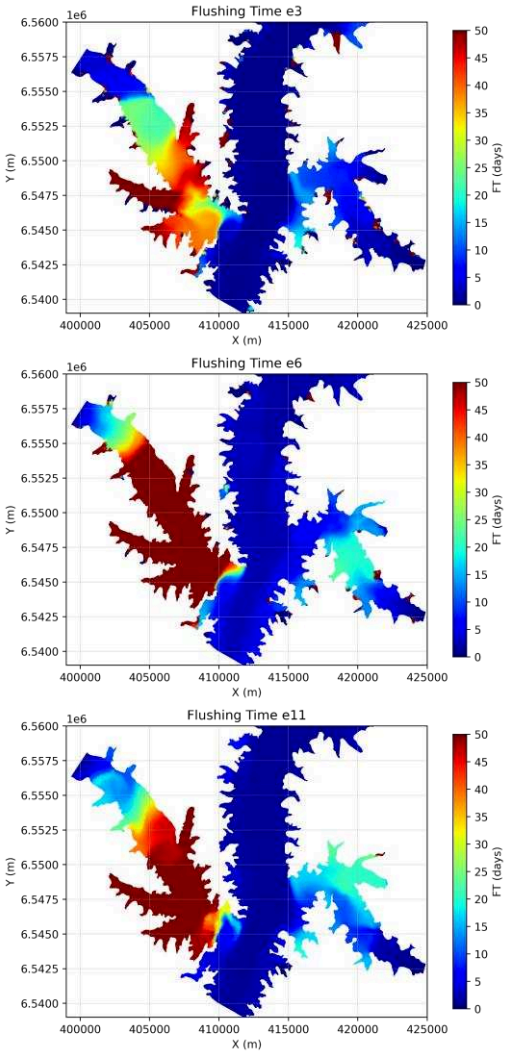

Figure 12. Maps of flushing time (FT) for the scenarios with low water level and high inflow (e3); mean water level and inflow rate (e6); and high water level and inflow rates (e11).

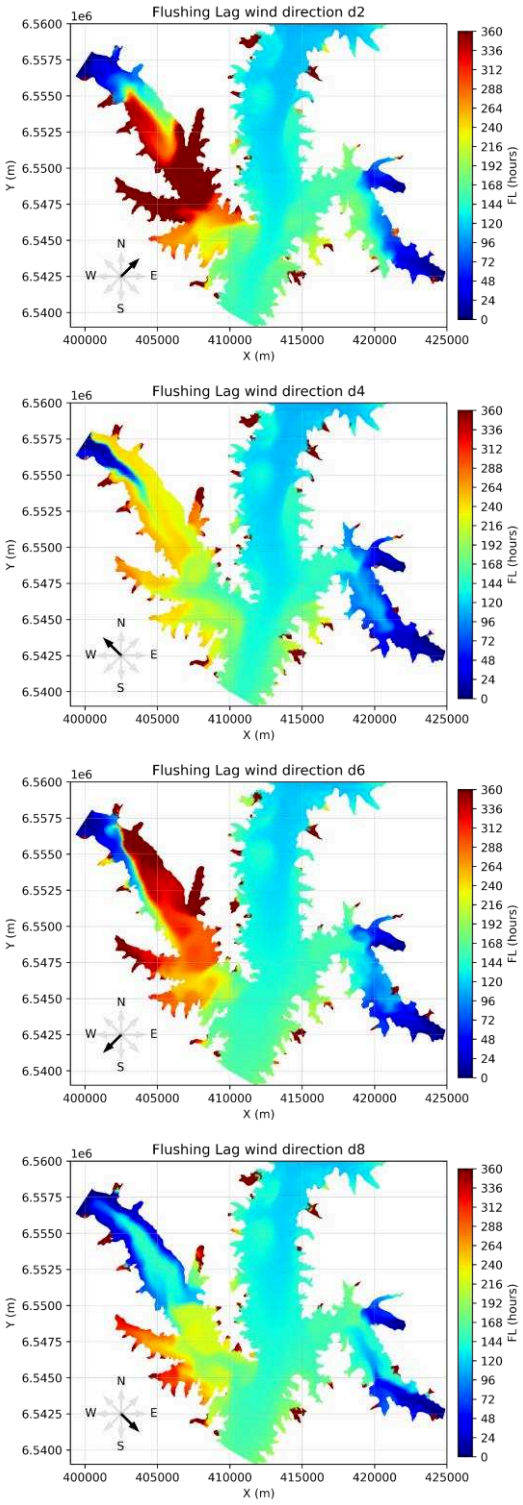

Figure 13. Maps of flushing lag (FL) for the scenarios with mean level and inflow and four different wind directions.

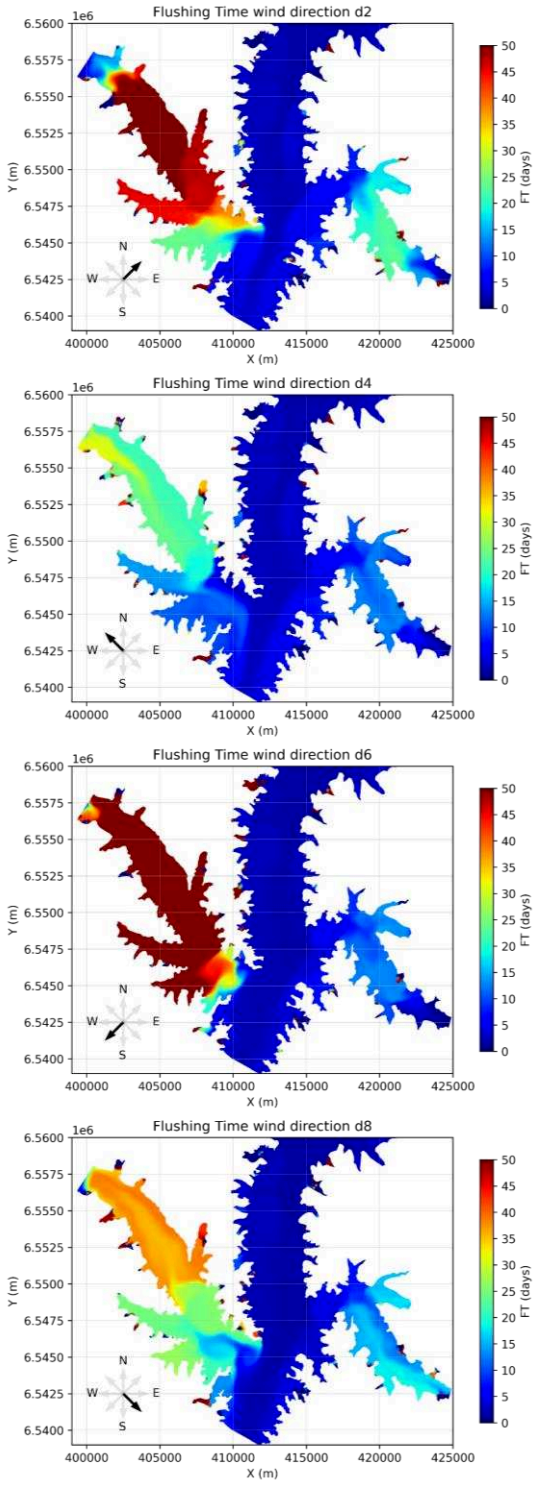

Figure 14. Maps of local e-flushing time (FT) for the scenarios with mean level and inflow and four different wind directions.

V. CONCLUSIONS AND FUTURE WORK

In this work a depth averaged hydrodynamic model is implemented for the Salto Grande hydropower reservoir. The model is able to reproduce adequately the water surface elevation behaviour in different zones of the reservoir with fluvial and transitional regimes.

The circulation in the reservoir is analysed based on the results of a 4 years simulation with realistic forcing. The velocity fields show a clear difference between the reservoir central zone and arms. The wind influence is assessed through numerical experiments and shows to be relevant on the arms circulation.

Numerical experiments with a passive tracer allow us to analyse the transport time scales in the reservoir under idealized steady scenarios. The results show lower transport time scales in the central zone where the advection is dominant. In the reservoir arms the wind again showed to be relevant, and its direction in relation to the arm axis shown may enhance or decrease the transport time scales. This is relevant considering that these arms are the most promised in terms of water quality problems.

Ongoing studies include the evaluation of other techniques to estimate the transport time scales with the numerical model (lagrangian approaches, non-steady scenarios), and a better characterization of the circulation patterns using other methods like empirical orthogonal functions.

ACKNOWLEDGEMENT

This work has been carried out within the framework of the ANII-FMV 2019 research project “Numerical tools to support water quality management in hydropower reservoirs”.

The authors would like to thank the scientific committee, which improved the earlier version of this article.

REFERENCES

[1] CTM-SG, 2018. Memoria Anual de Gestión. https://www.saltogrande.org/memoria_gestion/Memoria_Gestion_2018.pdf

[2] L.E. Berón, (1990). Features of the limnological behavior of Salto Grande’s reservoir (Argentina-Uruguay). Ecological Modelling, 52, 87-102.

[3] R. Quirós, and L. Luchini (2005). Características Limnológicas del Embalse de Salto Grande, III: Fitoplancton y su Relación con Parámetros Ambientales. Natura Neotropicalis, 1(13), 49-66.

[4] I. O’Farrell, F. Bordet, and G. Chaparro (2012). Bloom forming cyanobacterial complexes cooccurring in a subtropical large reservoir: validation of dominant eco-strategies. Hydrobiologia 698 (1), 175-190.

[5] F. Bordet, MS. Fontanarrosa, I. O’Farrell, (2017). Influence of light and mixing regime on bloom-forming phytoplankton in a subtropical reservoir. River Research and Applications, 33 (8), 1315-1326.

[6] A. Drozd, P. de Tezanos Pinto, V. Cañal Fernández, M. Bazzalo, F. Bordet, and G. Ibáñez (2019). Hyperspectral remote sensing monitoring of cyanobacteria blooms in a large South American reservoir: high- and medium-spatial resolution satellite algorithm simulation. Marine and Freshwater Research, 71, 593-605.

[7] J.-M. Hervouet (2007). Hydrodynamics of Free Surface Flows: Modelling with the finite element method. John Wiley & Sons, Ltd.

[8] H. Hersbach, et al. (2020). The ERA5 global reanalysis. Q J R Meteorol Soc. 146, 1999– 2049. https://doi.org/10.1002/qj.3803

[9] J.-M. Hervouet, C. Denis and E. David (2011). Revisiting the Thompson boundary conditions. Proceedings of the XVIIIth Telemac & Mascaret User Club 2011, 142-147.

[10] A. Jouon, P. Douillet, S. Ouillon, and P. Fraunié (2006). Calculations of hydrodynamic time parameters in a semi-opened coastal zone using a 3D hydrodynamic model. Continental Shelf Research, 26, 1395-1415.

[11] O. Boutron, O. Bertrand, A. Fiandrino, P. Höhener, A. Sandoz, Y. Chérain, E. Coulet, and P. Chauvelon, (2015). An unstructured numerical model to study wind-driven circulation patterns in a managed coastal mediterranean wetland: The Vaccarès lagoon system. Water (Switzerland), 7 (11), 5986-6016. https://doi.org/10.3390/w7115986

Optimizing inlet channels of small hydropower plants with TELEMAC-3D

Florian Ronzani[1], Matthieu Gonzales de Linares[1], Pierre Nunes[2], Aurélie Jouve[2], Pierre Balayn[2]

florian.ronzani@arteliagroup.com, Echirolles, France
[1]ARTELIA, 6 rue de Lorraine, 38130 Echirolles, France
[2]CNR, 2 rue André Bonin, 69004 Lyon, France

Abstract – **The work presented here details how TELEMAC-3D was used for a preliminary assessment of the dimensions and shapes of the inlet channels of two projects of small hydropower plants equipped with fish passes that will be added to existing hydropower facilities on the Rhône River. In both cases, the extent of the numerical model comprises both the inlet channel of the plant (width of about ten meters) and the stretch of river (width of about two-hundred meters, longitudinal extent of a few kilometres) on which it will be built. Results of ADCP surveys (cross profiles of flow velocity) and water level measurements in the river were used to calibrate the models.**

For one of the cases, results of a physical scale model were also available to enable validation of the numerical model on measured flow patterns and velocities around and inside the inlet channel. A sensitivity analysis to the parameters of the model (both physical and numerical) was also undertaken. The model was then used to screen the best configurations that will be further studied and optimized with physical scale models

Keywords: TELEMAC-3D, hydropower, physical modelling, scale modelling, ADCP.

I. INTRODUCTION

Adding capacity to existing hydraulic works has a huge potential worldwide for additional energy generation with minimal social and environmental impact [1]. In France, CNR, the hydropower and navigation operator of the Rhône River, is in the process of adding small power plants (SPP) to existing hydropower schemes. These SPP are / will be fed by the environmental flows discharged into the reaches bypassed by the inlet channels of the main hydropower plants. As part of these projects, fish passes for upstream migration and structures for downstream migration are also constructed.

The hydraulic integration of additional capacity to an existing hydraulic works can be problematic from a hydraulic point of view since the original facilities was generally not design to accommodate it. Civil engineering constraints can thus make it difficult to implement smoothly the new structure (e.g. avoiding steep change of direction between the inlet channel and the main flow direction). As a consequence, flow upstream of the additional plant can be non-homogenous, which can affect efficiency and generate vibrations which can lead to turbine damages.

Physical modelling has long been the tool of choice to check the hydraulic design of an inlet channel. In the example presented here, the fact that it is necessary to study the interaction between a relatively large river and a small inlet channel poses a problem of trade-off between the scale and the extent of the model. In contrast, the extent of a hydraulic numerical model is not constrained by the size of the building where it is set. Still, this dual scale (large river / small inlet channel) can also be problematic in terms of model resolution and size, and thus computation cost. TELEMAC-3D, having a proven record in the modelling of large-scale environmental flows, is well adapted for such configurations.

The work presented here describes the setup, calibration and use of two TELEMAC-3D models that were developped to optimize the dimensions and shapes of the inlet channels of two projects of SPP that will be added to existing hydropower facilities on the river Rhône.

II. MODEL DESCRIPTION

A. Cases studied

Two projects of SPP are studied by CNR for adding capacity to the Donzère and Caderousse hydropower facilities. In the case of Donzère, the entrance of the SPP inlet channel will be set immediately upstream Donzère dam, which regulates flows entering the bypassed "Vieux-Rhône" of Donzère (with release of the SPP flow immediately downstream Donzère Dam). In the case of Caderousse the entrance of the SPP inlet channel will be set on the bank of the inlet channel of Caderousse power plant (with release of the SPP flow in the bypassed "Vieux-Rhône" of Caderousse).

B. Mesh and extent

In the two cases presented here, the extent of the numerical models comprises both the inlet channel of the SPP (width of about ten meters) and the stretch of river (width of about two-hundred meters). This enables an adequate simulation of the approach flow upstream of the inlet channel of the SPP.

Extent and bathymetry (based on multibeam bathymetric surveys from CNR) of both models are presented in the figures below.

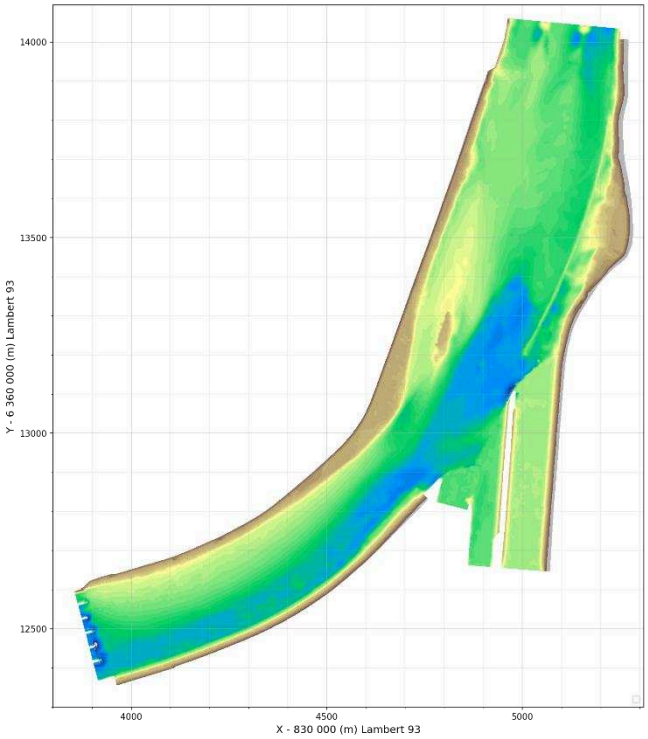

Figure 1. Bathymetry of Donzère model without SPP

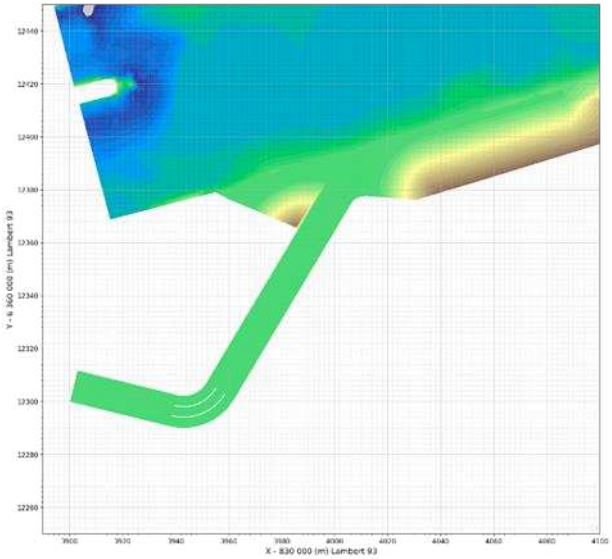

Figure 2. Bathymetry of Donzère model with SPP – local view

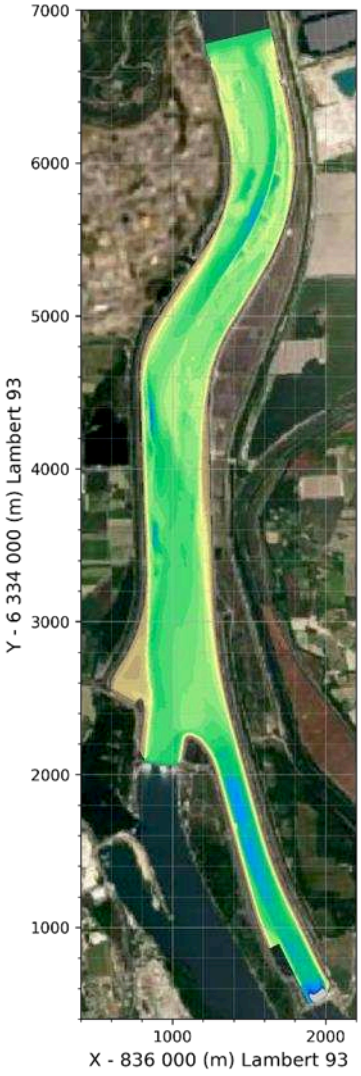

Figure 3. Bathymetry of Caderousse model without SPP

Mesh sizes are similar between the two models, with the following characteristic mesh sizes:

- 5-10 m for the larger sizes
- 1-2 m in section near of the SPP
- 0.2 m in the inlet

The number of nodes is about 140 000 for both Donzère and Caderousse models.

C. Boundary conditions

The models are run with constant imposed discharges:

- positive discharge for the upstream boundaries on the Rhône River,
- negative discharge for the SPP and one of the downstream structures,
- A constant water level is imposed at the other downstream boundary.

D. *Numerical and physical parameters*

The LIPS scheme is used for advection of velocities, in order to minimize numerical diffusion and still be compatible with “tidal flats”. The k-epsilon turbulence model is used. Advection equations for k and epsilon are also solved with the LIPS scheme.

III. MODEL CALIBRATION

A. *Calibration on water levels*

For moderate discharges, water level lines in the reaches are very flat and calibration of the model is thus not very informative. For high discharges, water level lines in the case of Caderousse match very well with simulated water level line, with a roughness length coefficient of 0.01 m.

B. *Calibration on ADCP surveys*

ADCP surveys were available in both cases, which enabled validation of the model results compared to flow measurements on the Rhône River in the vicinity of the entrance of the inlet channel of the SPP.

Measurements and simulations upstream Donzère dam are compared in terms of cross profiles of vertically averaged absolute velocity in Figure 4.

The shape of the simulated velocity cross-profiles matches well the surveyed velocity profile. The average difference between computed and measured is about -0.1 m/s, probably indicating that sediment deposits on the bed were higher at the date of the ADCP survey (2021) than at the dates of the bathymetric surveys available for setting up the model. The tests with two different bathymetries indicate the impact of morphological evolution on velocity profiles.

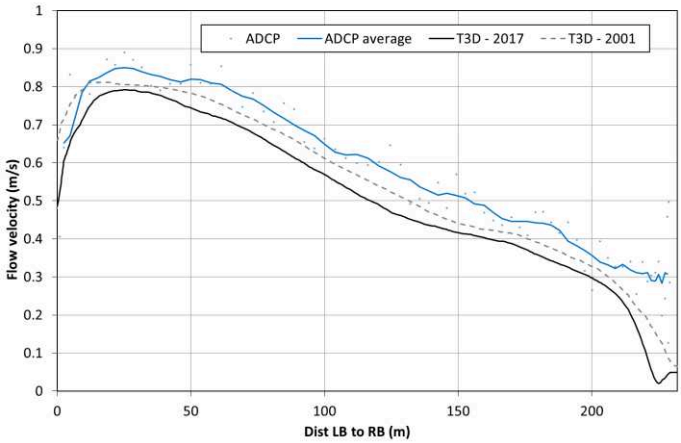

Figure 4. Comparison of T3D results with ADCP survey

C. *Calibration on hydraulic scale model results*

The results of a hydraulic scale model of a previous SPP project at Donzère are available. These results consist in both drawings of surface streamlines, and flow velocities measurements at different cross-profiles of the SPP inlet channel. Although the shape of the computed cross profiles of velocities were in general coherent with the measurements, quantitative calibration was not fully satisfactory. This might as well be an issue with inaccuracies on the physical model (on flow discharge and/or velocity measurement) than an issue with the numerical model itself. Sensitivity tests involving modifications of the turbulence model and of the (horizontal and vertical) mesh resolution had a very limited impact on the model results.

Qualitative calibration on general flow pattern (based on surface streamlines from the scale model) was much more satisfactory. In particular, as shown in Figure 5, TELEMAC-3D was able to capture the recirculation along the bank upstream the entrance of the inlet channel.

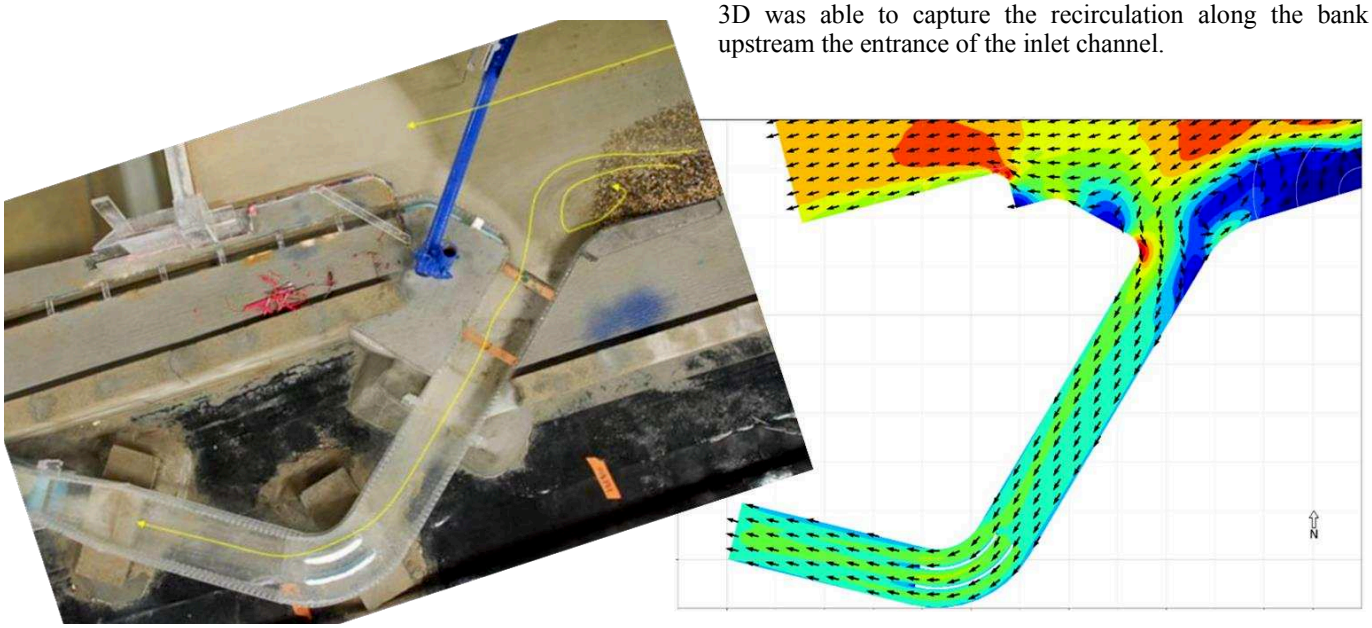

Figure 5. Comparison of T3D results with ADCP survey

IV. MAIN RESULTS AND DISCUSSION

A. Model results

In order to compare and rank different configurations for the inlet channels of the SPP, the outputs of the model have to clearly identify the general pattern of the flow and, allow to quantify the head losses as well as the homogeneity of the flow. Different examples of such outputs (maps of flow velocities in Figure 6, hydraulic head profile in Figure 7) are presented below. Note that the hydraulic head profiles are extracted along streamlines.

These outputs have been produced using the Python post-processing tools of the openTELEMAC system.

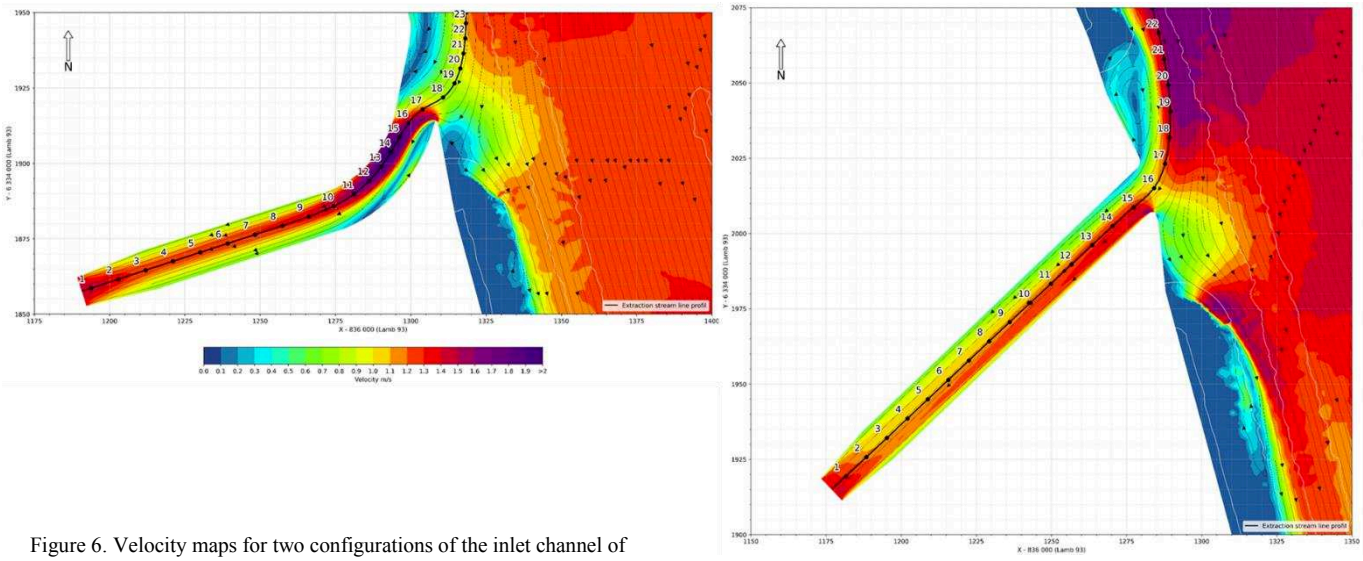

Figure 6. Velocity maps for two configurations of the inlet channel of Caderousse SPP

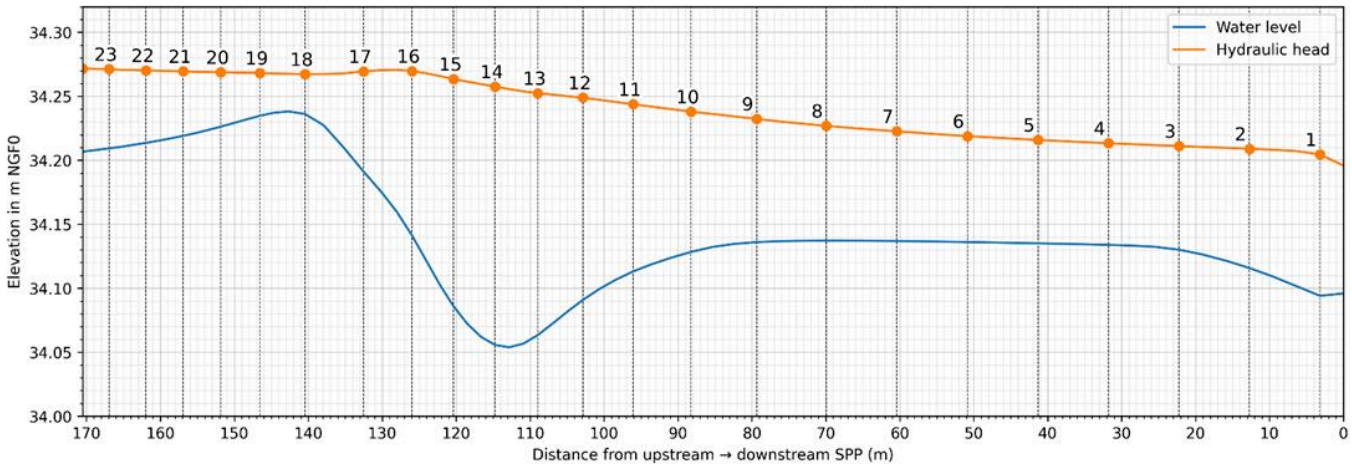

Figure 7. Water level and head profile along a streamline in the inlet channel of one the configurations studied for Caderousse SPP

B. *Optimizing the SPP projects*

An iterative process between numerical modellers and hydraulic engineers, involving hydraulic computations for different geometries of the inlet channel and different operating conditions of the power plant, enabled to reach in each case a geometry satisfying both hydraulic and civil engineering criterions.

In the case of Donzère SPP, the comparison between the different configurations tested enabled to improve the shape of the entrance of the inlet channel. The configuration with the least head losses and flow inhomogeneities at the entrance for the most frequent hydraulic conditions in the main channel was retained. Once the shape of the canal has been designed thanks to numerical modelling, a local scale model allowed to check the absence of periodic flow oscillation, to optimize some civil work features, and to study a floating barrier to prevent debris.

In the case of Caderousse SPP, two very different configurations of inlet channels (with different locations and angles with main channel, see Figure 6) were tested for an initial assessment, with the goal of choosing one of the configurations for further tests on a physical scale model.

In both cases, the numerical model was thus used to narrow the options down for further tests on the physical scale model, which is more costly to build and run than the numerical model.

The numerical model was then used to visualise or extract variables for other purposes (riprap stability, fish pass, debris management) as a tool to aid decision.

C. *Discussion*

For a hydraulic structure such as a SPP, a TELEMAC-3D numerical model appears as a key element of a more general hybrid-model, also involving a 1D pre-design tool and a scale physical model. It helps to distinguish different design options in a very cost-effective way. It also highlights relevant variables to focus on in different parts of the structure. Thus, more expensive tools can be used effectively to confirm and optimize fine details.

After a final step of recalibration on the observations of the physical model, it is also a very powerful tool to answer design adjustment questions during the construction phase.

V. CONCLUSION

This work shows how TELEMAC-3D (with the post-processing tools of the openTELEMAC system) can be used to study the hydraulics in the inlet channels of hydro-power plants. With high resolution bathymetric input data, relevant numerical schemes, and well adapted physical parameters, the model calibration turned out to be straightforward (i.e. the results were immediately satisfactory). This raises the question (we do not suggest a definitive answer yet!) of the necessity of systematically performing a velocity survey to calibrate the numerical model before using it.

Given the financial stakes of both optimizing civil engineering costs and minimizing loss of efficiency of the power plants, hydraulic scale models were used in both cases to confirm and refine the results of the numerical model, and to address debris issues still out-of-reach of practical numerical modelling.

REFERENCES

[1] Kayla Garrett et al., “Global hydropower expansion without building new dams”, 2021, Environ. Res. Lett. 16 114029

Hydrodynamic modelling as a first step to assess marine dune dynamics: influence of waves

Noémie Durand [1,3], Pablo Tassi [2,3], Olivier Blanpain [1], Alice Lefebvre [4]
noemie.durand@france-energies-marines.org, Chatou, France

[1] France Energies Marines, 525 Av. Alexis de Rochon, 29280 Plouzané, France.
[2] EDF Recherche & Développement, 6 Quai Watier, 78400 Chatou, France.
[3] Laboratoire d'Hydraulique Saint-Venant, 6 Quai Watier, 78400 Chatou, France.
[4] MARUM, University of Bremen, Leobener Str. 8, 28359 Bremen, Germany.

Abstract – **Tides, winds, and waves shape the seabed of shallow shelf seas. In sandy, energetic environments, marine dunes can develop. The size and mobility of these bed forms warrant some interest, for example related to the interactions with offshore wind farms. Yet, the morphology and dynamics of dunes are still poorly understood in open marine environments.**

A fully coupled, Reynolds-Averaged Navier-Stokes three-dimensional coastal area model is being developed for an application on the North Sea French coast (Dunkirk).

Keywords: Marine dunes, Sediment transport, Hydrodynamics, Waves, Model calibration, TOMAWAC.

I. INTRODUCTION

Marine dunes are large, flow-transverse bed forms with height of 1 m to 5 m and wavelength of the order of hundreds of metres [1]. They develop almost exclusively on sandy seabeds, in settings where bedload is the predominant mechanism of sediment transport. They are very dynamic: growing, evolving and migrating, at rates of up to tens of metres per year.

Marine dunes are widely present in shallow shelf seas, like the North Sea, where they interact with human activities. The interaction of these large-scale morphodynamic structures with offshore wind farm (OWF) elements is of particular interest. At the end of 2020, there were about 5400 offshore wind turbines, installed or under construction, in European waters alone [2].

One such wind farm project is planned offshore of Dunkirk, on the northern coast of France, close to the Belgium border. Marine dunes of all sizes coexist there with sand banks (Figure 1). A large data set has been collected in the last few years for fundamental research and in support of the OWF project. Recurrent bathymetric surveys indicate average dune migration rates of the order of 30 metres per year towards the North-East.

A numerical model is being developed that aims to reproduce the evolution of the dune field through time scales of 1 month to 5 years. Because the combined influence of currents and waves mobilise the sediments on the seabed, adequately understanding and predicting the prevailing hydrodynamic and wave conditions is a prerequisite to a correct prediction of sediment transport patterns and the dynamics of marine dunes. This paper focuses on the development and validation of a wave model based on TOMAWAC [3] against field data. The development and validation of the companion flow model is the subject of [4] and is only briefly referred to here.

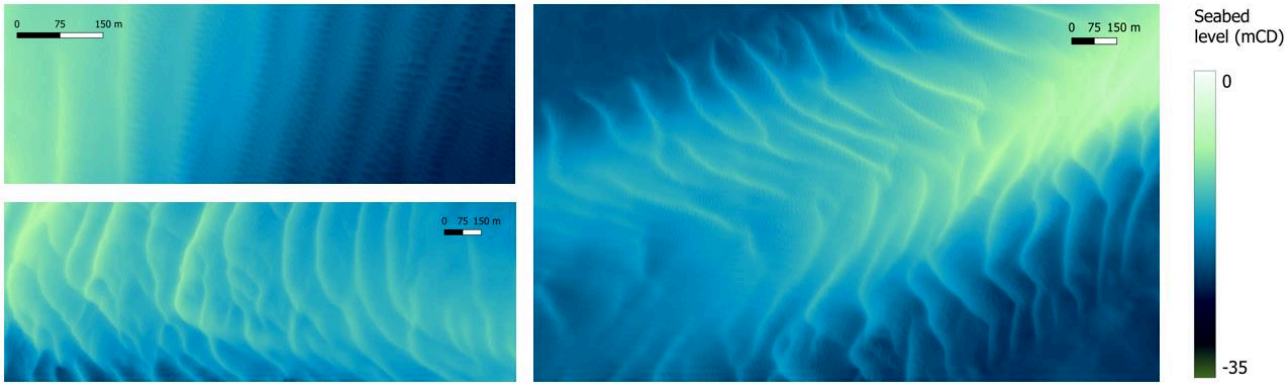

Figure 1. Example of marine dune fields, observed offshore of Dunkirk (Source of the data: Eoliennes en Mer de Dunkerque (EMD))

II. CONTRIBUTION OF WAVES TO SEDIMENT TRANSPORT IN THE STUDY AREA

Water particles in a wave follow an orbital motion, which diameter corresponds to the wave height near the surface. Closer to the seabed, in intermediate and shallow water, this motion induces oscillatory currents, whose strength depends on water depth, wave height and period. Although these currents do not generate net sediment transport, they are susceptible to mobilise the sediment particles. The sediment grains are then available to be transported, for example by the tidal currents.

Owing to the location and depth of the study area, it is anticipated that wave effects reach the seabed during storm events. One of the first steps was, therefore, to check this assumption, to determine whether the modelling should include wave contributions.

The grain bed shear-stresses τ_0 induced by currents and waves were estimated separately, from observations available at a location within the proposed wind farm, in ca. 16 m water depth, between May 2021 and February 2022 (Source of the data: EMD). The shear-stresses generated by currents alone were computed from the water density $\rho = 1027$ kg/m^3, the depth-averaged current speed U, and the drag coefficient C_D assuming a power law velocity profile [5]:

$$(\tau_0)_{currents} = \rho\, C_D\, U^2. \quad (1)$$

Those generated by waves alone were computed using an approximation that gives the root-mean-square orbital velocity for a JONSWAP spectrum U_{rms} [6], and the wave friction factor f_w defined in [5]:

$$(\tau_0)_{waves} = \rho\, f_w\, U_{rms}^2. \quad (2)$$

These calculations are simplifying but deemed adequate as a first approximation to assess the role of waves in the sediment transport, in comparison to currents. The results of this analysis are presented in Figures 2 and 3 for a 4-day period in June and in February, respectively. For completeness, the threshold of motion is indicated on these figures as a dashed black line. It was computed for a well sorted sediment with median grain diameter $d_{50} = 345$ µm, which is representative of the average granulometry in the study area.

The quarter-diurnal variations in tide-induced bed shear-stress are apparent in Figures 2 and 3 (as are the variations through the spring-neap cycle – not shown). In the absence of wind, the magnitude of the peak shear-stress associated with maximum neap currents is of the order of 0.4 N/m^2; 0.8 N/m^2 for spring currents. It can reach 1.5 N/m^2 during stormy periods.

Semidiurnal variations in the wave-induced bed shear-stress are also evident in Figures 2 and 3 in response to the tidal modulations (water level fluctuations and Doppler shifting). In comparison, wave-induced bed shear-stresses are negligible in the summer period (Figure 2), barely reaching 0.1 N/m^2. They are, however, comparable in magnitude to the current-induced bed shear-stresses during the winter period (Figure 3), even at this relatively deep location, with a peak value of 1.3 N/m^2. When considered in relation to the critical shear-stress for onset of movement, it is clear that sediment grains are likely to be mobilised by waves during these times.

It is noteworthy that current reversal does not occur at high / low water in the study area, but is delayed by two to three hours, meaning that low water nearly coincides with peak ebb currents (trending South-West). This is also when wave-induced bed shear-stresses peak. It is, therefore, expected that the additional friction generated by the waves will have an important dynamic and morphogenic effect and it seems essential to take waves into account in the modelling as a result.

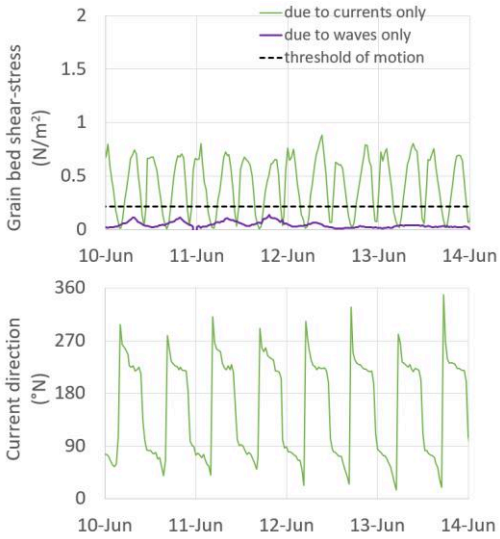

Figure 2. Grain bed shear-stresses estimated from EMD current and wave data observed in the summer of 2021

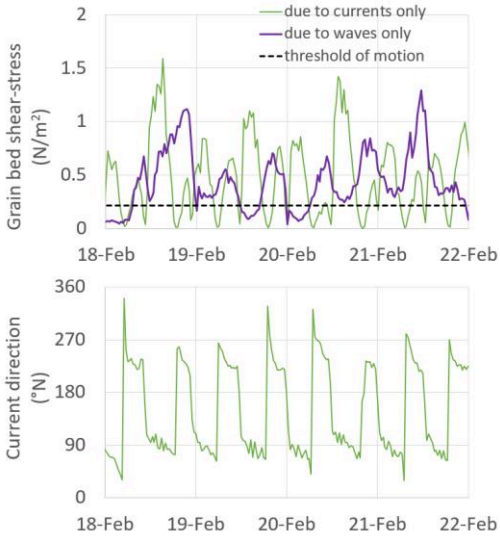

Figure 3. Grain bed shear-stresses estimated from EMD current and wave data observed in the winter of 2022

III. DUNKIRK APPROACHES WAVE MODEL SETUP

The open TELEMAC system is applied to Dunkirk and its approaches to investigate the dynamics of marine dunes in a shallow shelf sea environment. To that effect, hydrodynamic, wave and morphodynamic models are being set up, independently calibrated and validated, then internally coupled. The following presents the setup of the TOMAWAC wave model. The development and validation of the companion flow model is the subject of [4].

A. Model extent and mesh resolution

The model extends for approximately 80 km along the coast, from the port of Calais in the West to Ostend in Belgium in the East. Its offshore extent varies between 15 km in the Dover Strait and 75 km in the East. The model full extent is shown in colour in Figure 4 superimposed on HOMOMIM bathymetry [7] (grey shades) and OpenTopoMap [8] data.

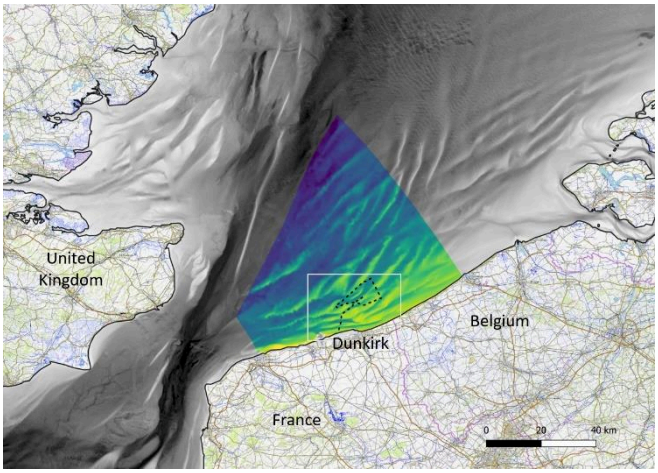

Figure 4. Location map showing the full model extent (in colour) and the proposed offshore wind farm footprint (dashed line)
(Source of the background data: [7] and [8])

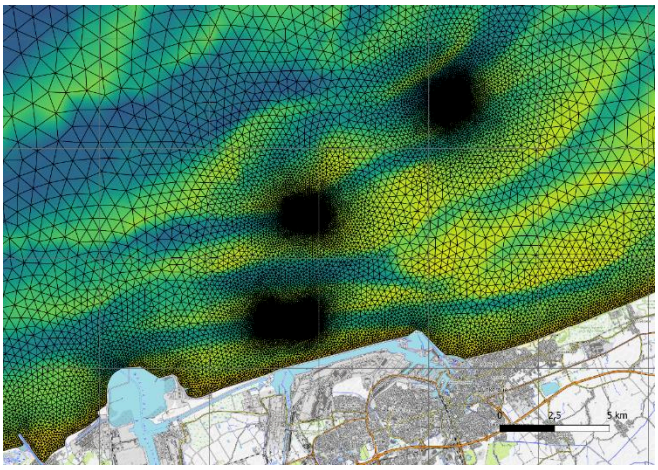

Figure 5. Close-up view of the mesh resolution around Dunkirk, showing increased resolution (10 m) in the three bathymetry tiles
(Source of the background data: [8])

Given the extent of the model area, a triangular finite element mesh with spatially varying resolution was used. The size of the elements varied gradually from 1400 m away from the area of interest down to 100 m at the shoreline. A finer resolution of ca. 10 m was used to represent the three tiles where recurrent bathymetric surveys had been conducted and where we aim to reproduce the evolution of the dune field. This element size is deemed adequate for the purposes of calibration and validation of the hydrodynamic and wave models; further mesh refinements may be necessary for the morphodynamic modelling.

Overall, the model area comprises approximately 60 k nodes and 117 k elements. A close-up view of the variable mesh resolution is shown in Figure 5 for the area identified by a white rectangle in Figure 4.

B. Seabed map

Digital elevation models of the seabed throughout the model area are being constructed that are relevant to different time periods. This is done by combining a range of data sources, where superior data take precedence over data of lesser quality / resolution. Best judgement is being used to integrate data pertaining to different time periods as seamlessly as possible in this highly dynamic environment.

A preliminary seabed map was, however, used for the simulations presented in this paper, which is based solely on the HOMONIM data set [7] as a first approximation. This seabed map is illustrated in Figure 4.

C. Wave forcing

TOMAWAC is driven by wave conditions imposed along the open boundaries. In this study offshore wave data obtained from two different sources were compared: integrated sea states from the ECMWF ERA5 reanalysis data set, and spectral sea states from the ANEMOC-3 hindcast database.

ERA5 ([9] and [10]) is a climate reanalysis data set, generated using Copernicus Climate Change Service (C3S) information. The name refers to the fifth major global reanalysis produced by the European Centre for Medium-Range Weather Forecasts (ECMWF). It provides high quality medium-resolution estimates of atmospheric and surface wave parameters, with a horizontal resolution of 0.25° and 0.50° respectively. Data are archived hourly and were obtained at point 2.0°E 51.7°N.

ANEMOC-3 ([11] and [12]) is the third revision of the ANEMOC database originally developed by EDF R&D and Cerema to hindcast sea states around the French coast (ANEMOC stands for Atlas Numérique d'Etats de Mer Océanique et Côtier). The database covers the Atlantic, the English Channel and North Sea French coast, down to 0.01° horizontal resolution. ANEMOC-3 is developed based on the TOMAWAC 3rd generation wave model [3], where tidal effects are accounted for through water level and current maps predicted using a TELEMAC-2D hydrodynamic model of the same area. The ANEMOC-3 database has recently been updated and extended to include 2021 [12].

Time-varying wave spectra were obtained at 56 locations along the open boundaries of the wave model. The spectra are discretised with 32 frequencies and 36 directions. The use

of spectral data is preferred over integrated sea states, in that it reduces the loss of information at the interface between the hindcast database and our local wave model.

The suitability of these two data sources was assessed by comparing them to wave measurements available at Westhinder from a directional wave rider buoy located at 2°26'08" E 51°22'51" N (Source of the data: VLIZ). The buoy was deployed in January 1997 in approximately 23 m water depth. The recorded parameters include wave height, average wave period, and direction of the swell and wind-sea components. The wave climate is depicted in Figure 6 as a wave rose.

At Westhinder buoy, waves are predominantly from the West-South-West, with some significant events from the North-West through to the North-East. 56% of the waves are under 1 m. The highest wave on record is 5.7 m from the South-West; the second highest 5.6 m from the North-West.

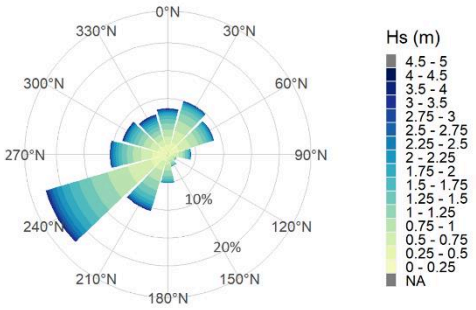

Figure 6. Wave climate at Westhinder buoy (Source of the data: VLIZ)

Wave heights extracted from the ANEMOC-3 database at Westhinder buoy for 2021 were compared to those observed during the same period. Considering a whole year removes any seasonal bias. The result of the comparison on a direct time for time basis is shown as a scatter plot in Figure 7. ANEMOC-3 appears to under-estimate wave heights above 1.5 m at Westhinder, by approximately 7%. The same analysis was performed for mean wave period. It indicated that mean periods were under-predicted by 0.5 s on average. This agreement was deemed satisfactory enough that no correction was applied to the ANEMOC-3 wave spectra in the first instance, before they were used as input to the wave model.

The resolution of the ERA5 data set (approximately 35 km East-West by 56 km North-South for ocean wave data) did not allow a similar comparison to be drawn. The wave heights and periods recorded at Westhinder buoy were bounded by the heights and periods extracted from ERA5 data points on either side of the buoy. Still, the use of ERA5 integrated sea states was carried through in the simulations, as a sensitivity to offshore boundary conditions.

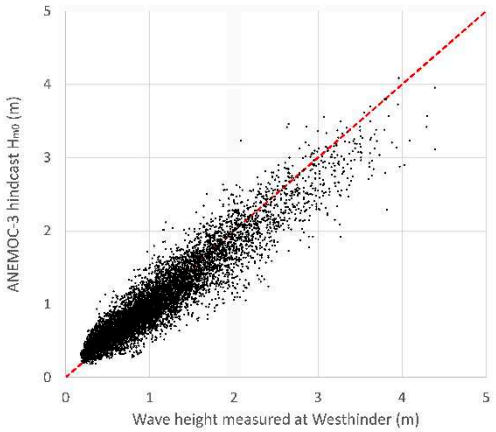

Figure 7. ANEMOC-3 hindcast wave data compared to wave measurements at Westhinder buoy for 2021

D. Meteorological forcing

In addition to wave forcing at the open boundaries, TOMAWAC is also driven by wind forcing processes, which account for local wave generation due to winds. Two sources of offshore wind data were considered and compared to in-situ observations: the ERA5 reanalysis data set, and the AROME database.

AROME [13] is an operational forecast from Météo-France, designed specifically to improve the short-term forecasting of dangerous phenomena such as heavy rains, violent storms, fog or urban heat pockets. The initial model conditions are derived from assimilation of radar network data (precipitation and Doppler winds), with an hourly frequency. The model predictions are available up to 42 hours ahead, at a high resolution of 0.025°. Data are archived hourly and were obtained from the 30-hour forecast over the whole model area such that spatially varying, as well as temporally varying, wind fields could be applied.

Long-term wind measurements are available at Westhinder from an instrumented pile located at 2°26’16" E 51°23’18" N (Source of the data: VLIZ). Water level, wind and pressure data are recorded since January 1997. The wind climate is presented in Figure 8. Winds come largely from the South-West and the Channel.

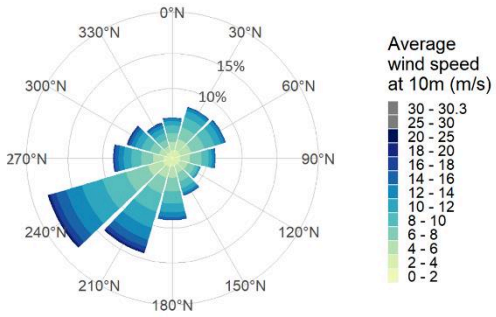

Figure 8. Wind climate at Westhinder pile (Source of the data: VLIZ)

Both sources of offshore wind were compared against these open sea observations for 2021. The AROME winds

agree more closely with the measurements (as shown in Figure 9) than the ERA5 hindcast winds did, and so it was decided to use AROME in our application.

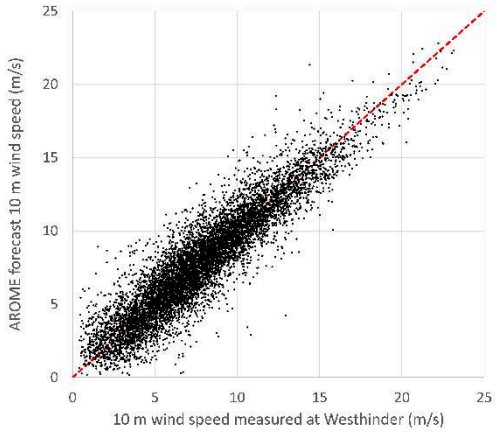

Figure 9. AROME forecast wind data compared to open sea wind measurements at Westhinder pile for 2021

Local wave generation due to winds is accounted for in the model using the WAM cycle 3 formulation, and linear wave growth as in Cavaleri and Malanotte-Rizzoli (1981).

E. Tidal forcing

In shallow shelf seas, tidal effects also play a role on wave propagation and transformation. The currents cause refraction of the waves, Doppler shifting, and in some cases (strong opposing currents) blocking of the waves. In simple environments, opposing currents are expected to steepen the waves, enhancing their height and reducing their wavelength, whilst following currents would dampen wave heights and increase wavelengths.

These effects were considered in the wave model by way of spatially and temporally varying maps of water levels and currents, obtained from a calibrated hydrodynamic TELEMAC model of the same area. This model is described in some detail in [4]. It is driven by harmonic constituents (34) extracted from the FES2014 database [14] produced by Noveltis, Legos and CLS.

The wave model results were found to be quite sensitive to the choice of formulation used to account for the tidal modulations. 'DISSIPATION BY STRONG CURRENT' = 0 seemed to exaggerate the effect of the currents on wave periods and directions. Reasonable results were had when a dissipative term was added as in Van der Westhuysen (2012) (option 2), provided that the dissipation coefficient was tuned. The best results were obtained when the spectra were limited using a Phillips (1977) shape (option 1).

IV. PRELIMINARY CALIBRATION

A. Wave data sources

Wave data were collected in recent years in the study area for fundamental research and in support of the Dunkirk OWF project (Sites 1 to 7 in Figure 10). A range of integrated wave parameters, of which significant wave height H_{m0}, mean wave period T_{m02}, peak wave period T_p, and mean direction, are available:

- in September 2016 at Sites 1 and 2 (Source of the data: SHOM),
- between October 2020 and April 2021 at Site 6 (Source of the data: EMD),
- between May 2021 and February 2022 at Site 7 (Source of the data: EMD).

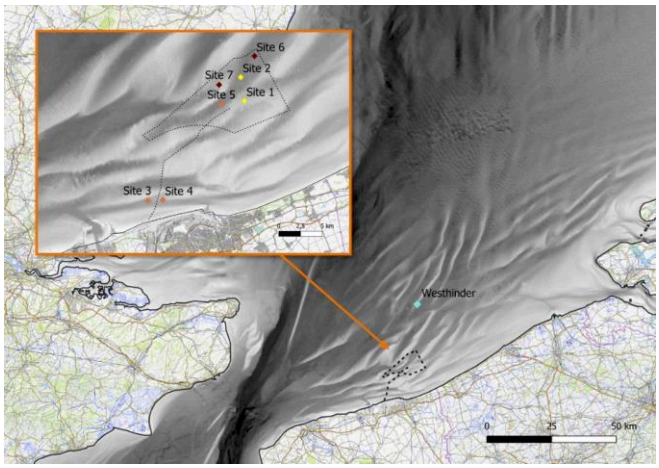

Figure 10. Map showing the location of wave observations in relation to the OWF footprint (Source of the background data: [7] and [8])

Wave data collected at Sites 3 to 5 for approximately 40 days in the Spring of 2021 (Source of the data: FEM) were obtained in raw format and have not been analysed to date.

Wave height and average wave period (taken to be significant wave height $H_{1/3}$ and zero-crossing wave period T_z) are recorded at Westhinder buoy (Figure 10) since 1997 at 30-minute intervals, with relatively minor interruptions in the records. These observed data, albeit further from our area of interest, were also used to assess the performance of the wave model in transforming the offshore waves to the study area.

B. Model comparisons with in-situ data

Given the location of the study area, it is important that the wave model be able to predict accurately the tidal modulations (i.e., the increase or reduction in wave height and period, as well as the change in direction, caused by the current conditions) throughout the tidal cycle. If it can be shown that the model results agree with the in-situ measurements, then it gives confidence in the wave predictions for normal and extreme events.

Two energetic periods were simulated, one in the Autumn of 2016 and the other in the Spring of 2021, for which model predictions were compared to the mooring data presented earlier in the OWF area and at Westhinder buoy. It is reminded that, at this preliminary stage, the most recent bathymetric data have not been incorporated in the current version of the wave model and the model seabed map is a closer representation of the 2016 conditions than it is of the 2021 conditions. As such closer agreement can be expected against data observed in 2016.

The comparisons shown in Figures 11 and 12 are favourable in terms of significant wave height, mean wave period and mean wave direction (all of which have an impact on sediment transport). There seems to be a tendency to under-predict the storm waves during the first period (Figure 11). The tidal effects are apparent in these figures, in particular Doppler shifting and refraction by the currents, and are reasonably well reproduced by the wave model. Some differences are observed. They could be attributed to deficiencies in the offshore wave data, the wave model, inaccuracies in the measured values, or possibly a combination of the three.

To quantify these differences between predictions and measurements, Root Mean Square Errors (RMSE) were computed. The results of this analysis are summarised in Table I for the entire simulation period. Values in brackets were computed based on storm events only. It is expected that agreement at Westhinder could be further improved should the mesh be more finely resolved there (the mesh size is currently of the order of 1 km).

Table I Performance of the wave model against observed data

	RMSE on H_{m0}	**RMSE on T_{m02}**	**RMSE on mean direction**
	September 1 to October 10, 2016		
Site 1	0.13 m (0.20 m)	0.5 s (0.6 s)	39° (15°)
Site 2	0.15 m (0.18 m)	0.4 s (0.4 s)	55° (30°)
Westhinder	0.18 m (0.22 m)	0.6 s (0.5 s)	--
	May 15 to May 30, 2021		
Site 7	0.20 m (0.18 m)	0.5 s (0.5 s)	20° (9°)
Westhinder	0.22 m (0.29 m)	0.5 s (0.5 s)	--

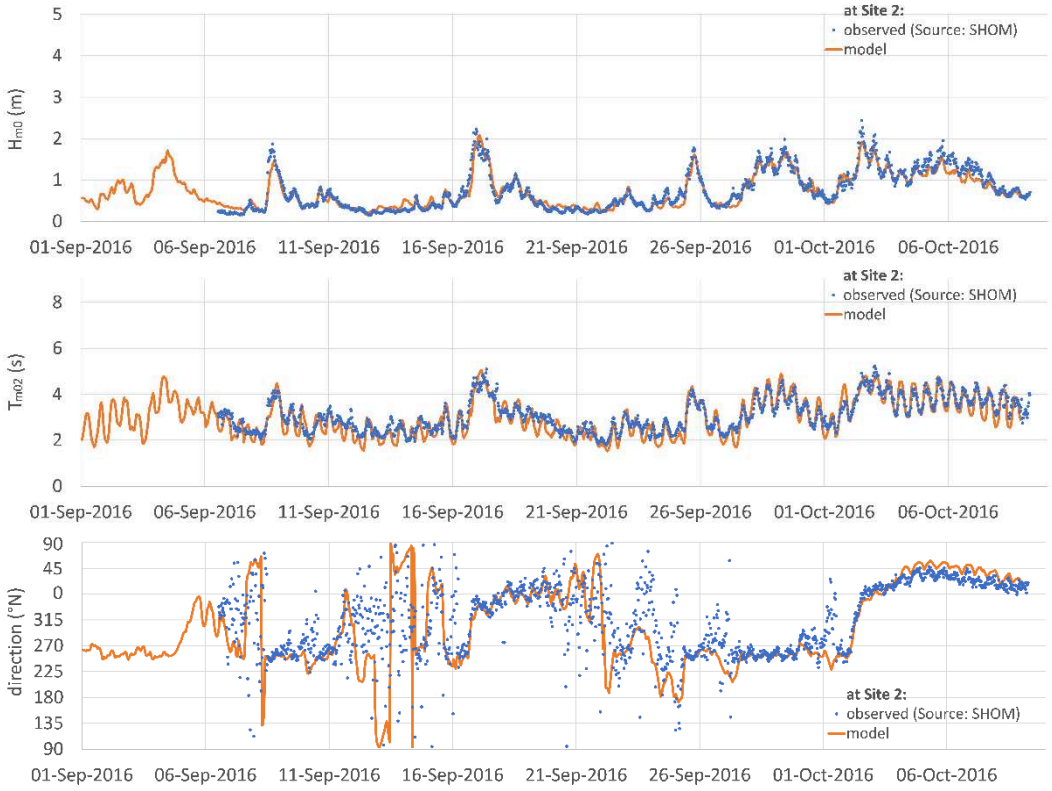

Figure 11. Comparison of model predictions against observed significant wave height H_{m0} (top), mean wave period T_{m02} (centre), and mean wave direction (bottom) at Site 2 between September 1 and October 10, 2016

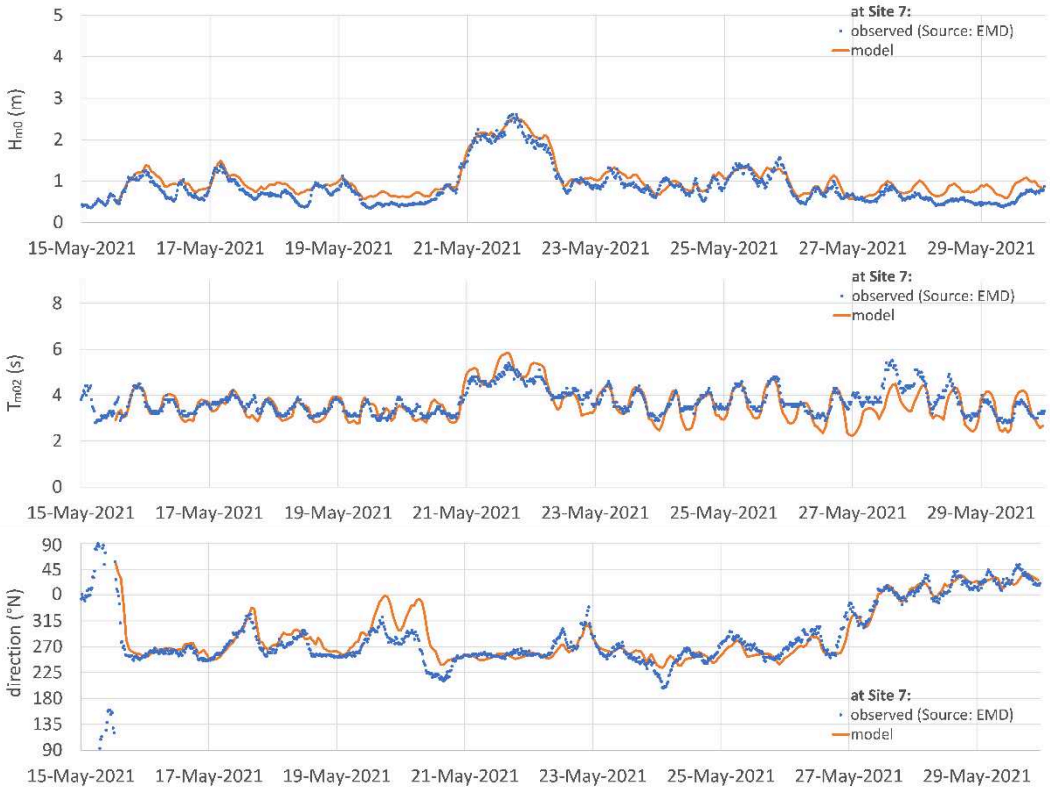

Figure 12. Comparison of model predictions against observed significant wave height H_{m0} (top), mean wave period T_{m02} (centre), and mean wave direction (bottom) at Site 7 between May 15 and May 30, 2021

It is noteworthy that, despite the relatively coarse resolution of the ERA5 data set, which meant that spatially uniform wave boundary conditions had to be applied (conditional to wave incidence), the transformation of the waves as they travel in shallow waters to the moorings was well modelled. Comparable agreement with measurements was obtained with that approach. The use of ANEMOC-3 spectral input is expected to be superior when mixed seas prevail, where the direction of the background swell and that of the winds do not coincide, or when remnants of old storm events are still present. Few such events were, however, initially observed.

With the current model configuration, it takes just over 1.5 hours to simulate one day on one compute node (two Intel® Xeon® Platinum 8260 24-core 2.40 GHz processors = 48 cores). The run times were marginally shorter when uniform boundary conditions were applied from integrated sea states.

V. Conclusion and Future Work

It has been shown that waves are expected to play a role in sediment transport in the study area. Further analysis would indicate to which extent. Given the large computational times of the wave model, there may be a need to optimize the exchange of information between the hydrodynamic, wave and sediment transport models for the morphodynamic simulations. For example, it could be appropriate to relax the coupling period of the wave model when wave activity is not expected to contribute much to sediment transport (to be determined).

Overall, the comparisons presented in this paper indicate that the wave model provides a good prediction of wave conditions in the study area under a range of tidal currents and offshore wave and wind conditions. Importantly the ability of the model to simulate tidal modulations has been demonstrated. This is expected to be critical moving forward to morphodynamic simulations.

Next, the sediment transport and bed evolution processes will be modelled by means of a 3-way coupling between the TELEMAC-3D, TOMAWAC and GAIA modules. Once satisfactory agreement is reached against observed in-situ bathymetry survey data, this comprehensive coastal area model will be used as a research tool to better understand marine dune dynamics in the Dunkirk area and their interactions with OWF elements.

Acknowledgements

This work was initiated by France Energies Marines, with support from the French government, under the “Investissements d’Avenir” programme managed by the French National Research Agency ANR. The authors would like to thank the partners of the MODULLES project for providing site-specific data and giving permission to publish this work.

REFERENCES

[1] G. M. Ashley, “Classification of large-scale subaqueous bedforms: A new look at an old problem”. Journal of Sedimentary Petrology, Vol. 60, No. 1, 1990, pp 160-172. https://doi.org/10.2110/jsr.60.160

[2] The Crown Estate, “Offshore wind operational report 2020”. Technical report, 2020

[3] M. Benoit, F. Marcos, F. Becq, “Development of a third generation shallow-water wave model with unstructured spatial meshing”. In Proc. 25th Int. Conf. on Coastal Eng. (ICCE’1996), 2-6 September 1996, Orlando, pp 465-478. https://doi.org/10.9753/icce.v25.%25p

[4] N. Durand, P. Tassi, O. Blanpain, A. Lefebvre, “Towards numerical modelling of marine dunes in a shallow shelf sea”. In Actes des XVIIèmes Journées Nationales Génie Côtier-Génie Civil, Chatou, France, 2022. in press

[5] R. Soulsby, “Dynamics of marine sands”. Thomas Telford Publishing, 1997. https://doi.org/10.1680/doms.25844

[6] R. Soulsby, “Simplified calculation of wave orbital velocities”. HR Wallingford Technical Report TR 155, 2006

[7] SHOM, MNT bathymétrique de façade atlantique (projet HOMONIM). 2015. http://dx.doi.org/10.17183/MNT_ATL100m_ HOMONIM_WGS84

[8] https://opentopomap.org/

[9] H. Hersbach and D. Dee, “ERA5 reanalysis is in production”. ECMWF Newsletter Number 147 - Spring 2016. Published in April 2016

[10] ERA5, https://doi.org/10.24381/cds.adbb2d47

[11] C. Raoult, A. Joly, M. Andreevsky, and A. Joly-Laugel, “ANEMOC-3: Improving the ANEMOC-2 Sea state database by adding tide effects”. In Actes des 16èmes Journées de l’Hydrodynamique, 27-29 Novembre 2018, Marseille, France

[12] M. Teles, M. Weiss and M. Benoit, “Assessment of the ANEMOC-3 sea state hindcast database for modelling a series of energetic winter storms along the French coast”. In Actes des XVIIèmes Journées Nationales Génie Côtier-Génie Civil, Chatou, France, 2022. in press

[13] F. Boutier, “Arome, avenir de la prévision régionale”. La Météorologie, No. 58, 2007, pp 12-20. https://doi.org/10.4267/2042/18203

[14] FES2014, https://www.aviso.altimetry.fr/

Improved Modelling of hydraulic works including run-of-the-river dam in TELEMAC

Paul Bataille[1], Luc Duron[2], Fabien Leblanc[2], François-Xavier Cierco[2]

paul.bataille@ecl18.ec-lyon.fr, Lyon, France
[1]: École Centrale de Lyon (ECL)
[2]: Compagnie Nationale du Rhône (CNR), Engineering Department

Abstract - **In their vicinity, hydraulic works can lead to fast and multiple transitions from subcritical to supercritical flow regimes. Therefore, modelling weirs or gates or run-of-the-river dams by meshing their 3D geometry makes computations particularly responsive to the flow instabilities and therefore to unsatisfactory simulations. A classical technique to overcome that difficulty consists in the use of specific laws inspired from 1D modelling such as relationships between the flow rate, Q, and the dynamic head, H, estimated upstream and downstream the hydraulic works. Such modelling was often proven to be more relevant than geometrical modelling.**

To correctly implement such laws in TELEMAC (2D and 3D), we represented the hydraulic work as a hole in the mesh. This hole is delimited by a polygon with two opposed boundaries where flow rate boundary conditions are imposed. The imposed flow rate is computed at time step n from the specific laws thanks to the hydraulics conjugate variables read in two control sections located upstream and downstream the hydraulic works at time step n-1. Additionally, we implemented guidelines about control section location, bed geometry, flow regime determination and relaxation to avoid most of instabilities during computation.

This implementation of the structures as hole in the mesh allowed us to add in a second time an option which takes into account the PID controller that regulates flow passing into the Dam in normal time. The outflow is made dependent on a set point at a precise location. This addition makes possible to model the behaviour of the structures in any flow condition.

Finally, we tested this implementation on Donzère-Mondragon reach, which contains four hydraulic works: the local dam ensuring the water level regulation and three keeping dams made to prevent high water level in the power plant channel. Those four dams operate at different time, depending on the flow. We simulated the 1,500-year flood (as an unsteady flow) to test our model.

I. INTRODUCTION

1D simulations are commonly used to model floods in complex hydraulics developments such as those operated on the Rhône River. Nevertheless, as a consequence of advances made in computation and topography's data, 2D and 3D models are increasingly becoming a standard. In this article we deal with the modelling of hydraulic structures in 2D and 3D studies.

For 2D or 3D computations, hydraulics works such as weir or dams (when they are open), need to mesh hydraulic works much more precisely to account for the transient nature of the hydraulic work. As a result, this type of modelling is very costly in term of computational time. Moreover, it makes the opening and closing of gates more complicated.

The solution proposed in this paper is to model each hydraulic work as a hole in the mesh. For each of these holes, we add two opposed boundaries in which flow rate is prescribed by laws depending on hydraulics variables. We created additional module for TELEMAC based on previous work [1] and applied it on 2D model of Donzère-Mondragon Reservoir (DM). The development integrates specific works to protect the 17 km long channel to a power plant. The DM Reservoir was chosen for its complexity which enables to test the robustness of the code. In a first approach we implemented the weir laws and modelled the dams as weir which is relevant for particularly high discharges when dams are fully open. In this case inflow and outflow are computed from water level and velocity. In a second approach we added a regulation system which models normal operations, including adaptative opening and closing of the dam gates. In this case, total flow leaving the reservoir is controlled by the water level at a specific location upstream. The total flow is shared between the dam and a hydropower plant depending on their characteristics (a regulation law is defined for each reach).

This article presents firstly theoretical support used to implement subroutines, then we present the Donzère-Mondragon Reservoir and the associated model. Thirdly we detail the subroutines implemented and finally we present the results and limits of the method.

II. THEORETICAL SUPPORT

A. Integrate 1D hydraulic laws in 2D/3D

The main hypothesis of this study is to consider that flow over hydraulic works can be described by 1D laws. Therefore, we implemented dedicated 1D laws to model works, and we computed average quantities over cross-sections to estimate equivalent hydraulic 1-D variables such as the water level or the discharge. Another solution would be to use directly 2D or 3D variables and to represent hydraulic work node to node with weir laws, but this does not allow the work to be considered as a whole and thus to integrate hydraulic controls.

B. Notations

We defined then the necessary 1-D hydraulics variables used to compute flowrates. We obtain them by computing

integration of 2D or 3D ones over a determined cross section. The physical quantities are considered in three sections: an upstream control section (am), a downstream control section (av), and the hydraulic work section (s). The elevation of weir crest is denoted by Zseuil and the top of gates is denoted by Zsup.

We note:

- Zam = water level elevation in the upstream control section.
- Zs = water level elevation at the hydraulic work.
- Zav = water level elevation in the downstream section.
- Zr = water level at at the regulation section
- Zc = water level set point

Each quantity defined afterwards is considered at the various places with the suffixes (am, av, s, c, r). Q is the water flow over the weir. V is the average velocity of the flow in any specified cross-section denoted by S. S can be different of the hydraulic work section s. In every section S, we have V = Q/S. For every section S, the water depth is computed relatively to the weir crest:

$$y = Z - Z_{seuil}$$

And dynamic head above weir crest:

$$H = y + \frac{V^2}{2g}$$

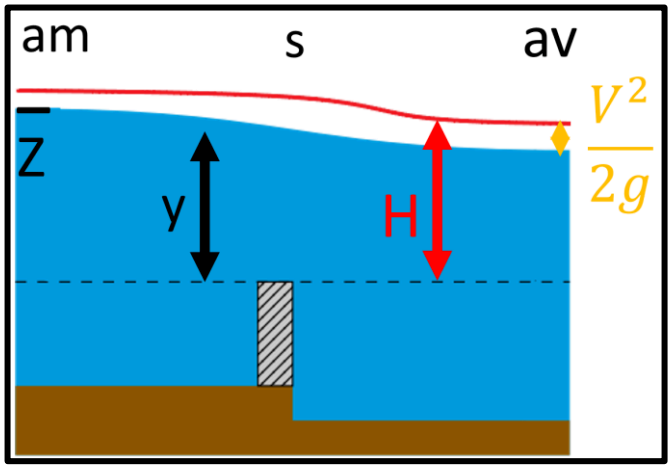

Figure 1. Notation diagram for a weir

C. Weirs and gates laws

The weir laws available in the literature can mainly be classified in 2 categories either if the discharge is computed from i/ the water level, Zam and Zav or ii/ the specific energy Ham and Hav. Here, we chose to consider the specific energy upstream [2] even the increased risk of computation instabilities. These equations derive from energy conservation [3]. In supercritical conditions, weir laws are written:

$$Q = C_{seuil} \times L_{seuil} \sqrt{2g} \frac{2}{3\sqrt{3}} (H_{am})^{\frac{3}{2}}$$

With C_{seuil} the weir conveyance coefficient and L_{seuil} the weir width. Then in subcritical conditions:

$$Q = C_{seuil} \times L_{seuil} \times y_{av} \sqrt{2g} \sqrt{H_{am} - y_{av}}$$

Supercritical condition's gate law is:

$$Q = C_{seuil} \times L_{seuil} \sqrt{2g} \frac{2}{3\sqrt{3}} (Z_{sup} - Z_{seuil}) \sqrt{H_{am} - (Z_{sup} - Z_{seuil})}$$

And subcritical gate law:

$$Q = C_{seuil} \times L_{seuil} \times (Z_{sup} - Z_{seuil}) \sqrt{2g} \sqrt{H_{am} - y_{av}}$$

D. PID Regulation

The PID is an automatism (with three corrector terms: proportional, integral and derivative) designed to set the water level Zr to a set point Zc at a specific location named the regulation section (PR) by adjusting the total flow out of the system. We have thus Q = f(Zr – Zc). The function f is the sum of a proportional and an integral corrector which provides a correction of the measured deviation Zr - Zc. A derivative term is added to anticipate future disturbances.

III. STUDY CASE

A. Donzère-Mondragon Reservoir

Donzère-Mondragon Reservoir is the second oldest CNR reservoir, located near Bollène in the south of France. All the reservoirs on the Rhône River but one are operated by CNR following the same pattern. The site includes a reservoir, contained by with dikes, a diversion channel also contained within dikes and closed by a hydropower plant (here the power plant of Bollène - USB). Finally, the water level in the reservoir is controlled by a dam, here the Donzère run-of-the river Dam (BGRT), equipped with mobile gates.

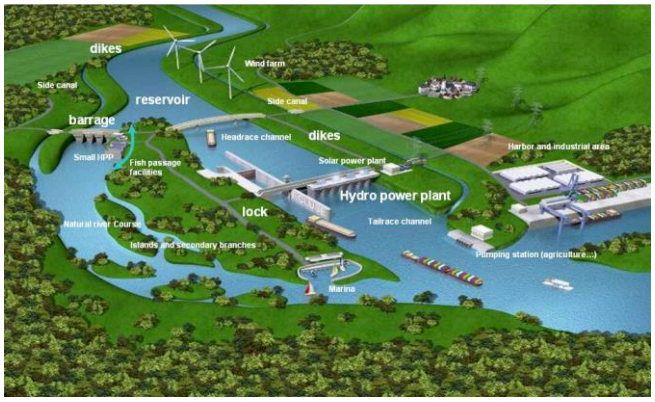

Figure 2. Typical CNR reservoir

Donzère-Mondragon has a 17 km long headrace channel, which is unusually long. Therefore, to protect dikes around channel, dedicated hydraulic structures are disposed at the entrance of the headrace channel, namely three keeping gates. These keeping gates are open in normal circumstances and must be closed gradually during floods. On the left bank, the old navigable gate (APN) consists in two 45 m wide gates and was the initial passage for boats. In the middle the new

navigable gate (NPN) consists in a 60 m wide gate. Those two works are completely closed during floods. On right bank, the hydropower barrage (BGU) was designed to control water level in headrace channel during flood.

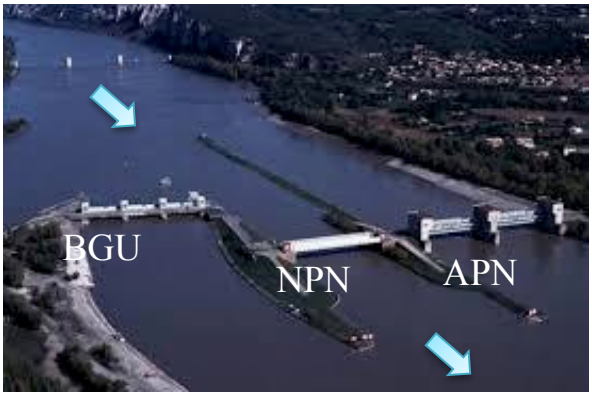

Figure 3. Keeping structures

B. *Operating rules*

To take in account hydroelectricity production, navigation and overflow prevention in headrace channel, operating rules are defined.

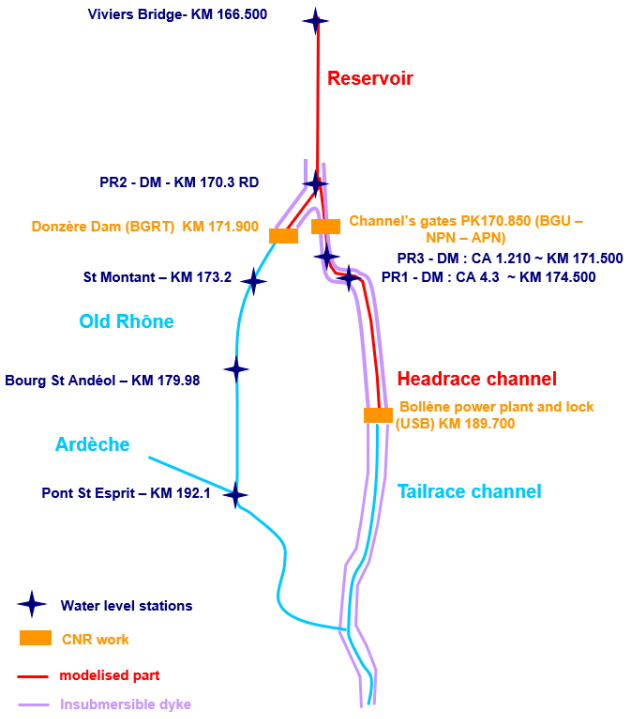

Figure 4. Donzère reach

The PID gives a prescribed flow depending on the difference between the water level at PR, Zr, and the target level, Zc. Flow regulating rules also give the distribution of the total flow between the dam and the power plant. There are three PR in Donzère. This allows us to know the reaction time of the reservoir to a manoeuvre of the dam according to the incoming flow at Viviers.

C. *Mesh and model*

The reach of the model extends from Viviers bridge to downstream the dam, and upstream the power plant. The mesh elements size varies from 10 m close to the hydraulic works, as instabilities may occur, to 90 m in the flood plain. The mesh is composed of about 45 000 elements and 23 000 nodes. The time step is 1s.

D. *Boundary conditions*

Flows at Viviers and upstream of the power plant are prescribed as well as a rating curve downstream the dam. When flow control is considered, the flow through the power plant is managed by subroutines reproducing the PID regulating rules. In this situation we prescribe only two conditions: flow in Viviers and calibration curve downstream the dam.

E. *Model parameters*

The aim of the study is to develop and validate the implementation of hydraulic work laws. Therefore, we primarily focus on the computation robustness rather than on the result precision disregarding the response to the model internal parameters. As a result, in this first approach of the work, we chose a uniform Strickler coefficient equals to 40 $m^{1/3}/s$ everywhere. The turbulence model is constant viscosity with an overall viscosity coefficient equals to 0.05 m^2/s.

IV. TELEMAC IMPLEMENTATION

A. *TELEMAC-2D*

1) Description

We represent the hydraulic works as a rectangular hole surrounded by four boundary segments. The two boundaries perpendicular to the flow have boundary conditions (usptream and downstream the hydraulic work) with prescribed flow (respectively Qam and Qav). Lateral boundaries have solid conditions.

On both sides of each hydraulic work, we define 2 control sections in the mesh (i.e. outside the hole): one upstream and the other downstream to retrieve water level and flow velocity data so as to compute respectively Ham and Hav. Additional specific sections were also defined, e.g., the regulation section, PR, to provide inlet variables (namely, the water level) to the PID flow control. Distance between the hydraulic work and the control sections was carefully chosen to reduce potential oscillations in both discharge and water level. For each work, we indicated the conveyance coefficient, Cseuil, the weir crest elevation, Zseuil, the boundaries and the corresponding control sections (see Figure 4). For the gates, we added the opening rate and the top altitude, Zsup.

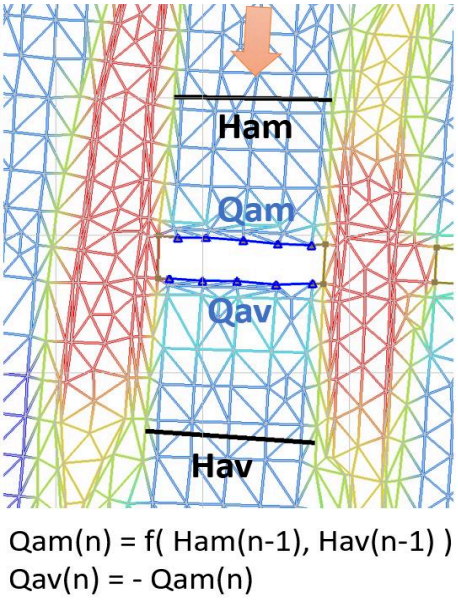

Figure 5. Representation of a work in a mesh dedicated to TELEMAC

2) Theoretical principle

Subroutines are added to TELEMAC to compute flow rate going through the hydraulic works. Computation is done according to the equations detailed in part IIC and the flow rate is updated between each time step. Three main choices are available: weir (or full open dam), gate and regulating work. Weir and gate options solve equations presented in part II C. Since flow rate is computed for step time n with n-1 hydraulics data, our solution can result in instabilities that would not exist with a non-explicit scheme.

3) Regulation detail

Weir and gate options therefore compute a flow resulting from energy conservation laws on a specific structure. This makes possible to model the structures punctually where it is needed. On the other hand, the aim of the 'regulation' option is to model the global operation of a CNR reservoir [4]. That's why, the flow calculated by this option is the total flow crossing both the dam and the plant. The distribution between the two works is computed in a second step. We need then specific laws, which give the active PR., and the target water level, Zc, for every incoming flow at Viviers and the power plant maximum flow,

For the computing part: in a first time, a PID automate derive the total flow from Zr-Zc. Then, the repartition between dam and plant is made depending on instructions. Finally, the flow rate imposed at the dam is the maximum flow rate taken among the PID flow rate and the flow rate obtained by weir laws to consider the case when dam is fully open.

4) Subroutines

We programmed subroutines for the version v8p2 of the TELEMAC system, using the USER_Q and FLUSEC subroutines to interact with TELEMAC during computation. Additionally, specifics parts of flow computation were implemented in a new module called OUVRAGES.

The flowchart in Figure 5 summarises the call sequence for the update of the imposed flow.

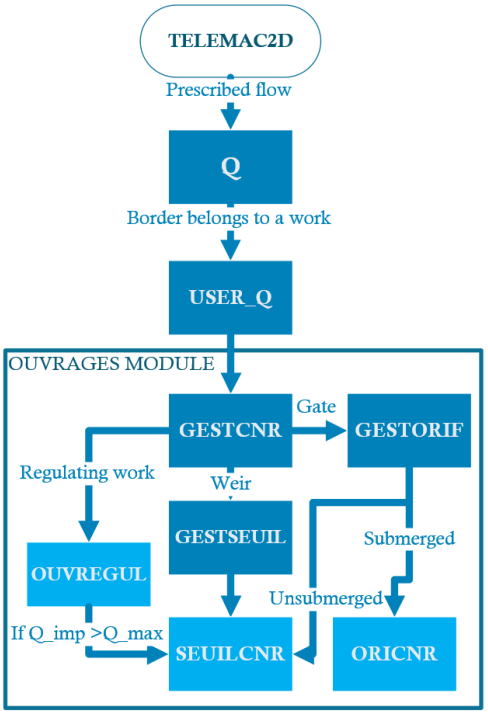

Figure 6. Flow chart

At every time step, USER_Q checks if considered boundary is from a work. If so, module OUVRAGES is called and determines the dedicated flow option (weir, gate or regulation). Then OUVRAGES subroutines call FLUSEC to get the necessary hydraulics variables and compute the prescribed flow, which is finally returned to USER_Q.

B. TELEMAC-3D

Implementation is the same in TELEMAC-3D because it computes also 2D variables which allowed us to keep the same way of computing 1D variables. Some hydraulics variables and subroutines changed of name.

The main difficulty came from the non-implementation of control section in TELEMAC-3D. Therefore, we added this option, starting from 2D subroutine.

V. SIMULATIONS

Results given here are qualitative and will be studied more precisely later. Here the main objective is to check that the procedure works properly.

A. Full open dams

In order to test weir and gate laws, a first simulation is run considering Donzère Dam and headrace channel's gates fully open. The Donzère Dam (BGRT) is modelled as a weir, and the keeping structures (BGU, APN, NPN) are always modelled as gates. In a first approach, the model is

initialized with a defined water level receiving an increasing incoming flow at Viviers to reach the initial discharge of the Q1500 flood hydrogram. This first initialization, although not representing any reality, allowed us to test the limits and instabilities of our model and subroutines. The first tests did not converge and created many oscillations. It resulted that several conditions are necessary to ensure a stable computation. First, the bathymetry must not have any irregularities immediately upstream of the structure so as not to risk drying out the mesh of the upstream boundary. Second, as mentioned above, the control sections must be close to the structure. The recommended distance between the boundary section and the control section should be bigger than one mesh element. Otherwise the computation is not possible. Nevertheless, it is difficult to find the right location. There is also a risk of a wrong evaluation of the upstream and downstream flow conditions (water level and averaged velocity) with tidal flats for example. Moreover, control sections must carefully remain in the minor bed. Finally, a relaxation coefficient is introduced to filter out small frequency disturbances that can generate numerical instabilities on the weir. Despite all this, instabilities can occur during rapid changes of the flow regime and small discharges as seen on Figure 6. To avoid these, it will be necessary to establish a steady state flow over the weir.

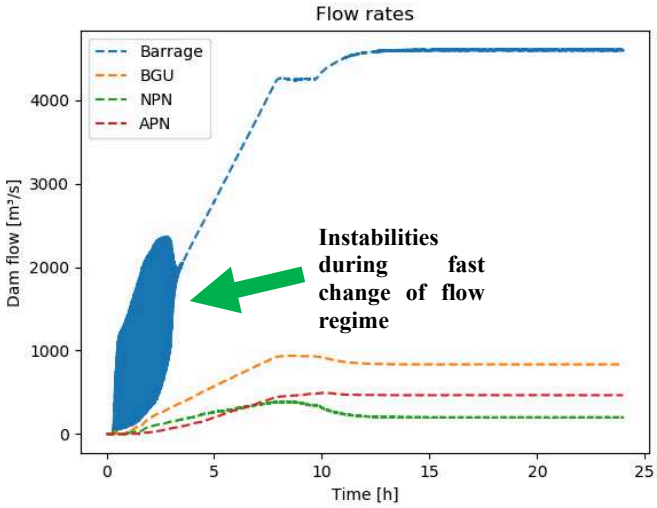

Figure 7. Flow rates into works and level error at PR during reference states

B. *Reference states*

Then regulation options were tested by simulating a succession of steady states flows over a large discharge range covering theoretical flood situations and regulatory scenarios. In those cases, the dam and powerplant (BGRT + USB) are modelled as a single regulating structure, and the keeping structures as gates. The inflow in Viviers ranges from 0 to 8000 m^3/s.

This simulation allows to visualize a realistic behaviour of the structure at every point of interest (e.g. the dam, etc…) for all of the possible configurations (low water level, normal flow, flood) and to investigate the transitory situations such as dam opening, change of PR, change of flow regime, change of plant discharge, etc.

To appreciate the results, we look at the error Zr-Zc at PR which must be kept in a given range. For out-of-range values of Zr – Zc, we focus on the necessary time it takes to the PID regulation to return to the envelope. During a PR change, we observed an error Zr-Zc = 20 cm which took around 8 hours to return into the given range. This error during PR transition can be explained by the rough model calibration and regulation rules. An improvement could be imagined to smooth the change of PR by an arithmetic mean. Finally, to avoid initialization problems (the PID flow rate depends on the previous time step), we decided to impose the input flow rate as the total outflow at first time step.

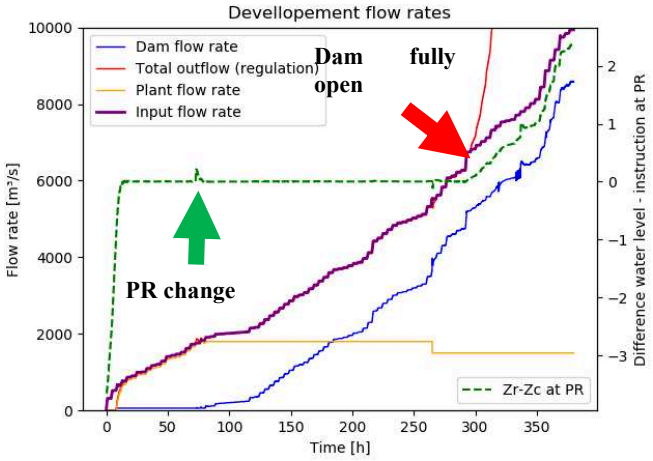

Figure 8. Flow rates into works and level error at PR during reference states

C. *Q1500*

Then the Q1500 flood is simulated in order to compare our results with a 1D model including PID regulation of the Donzère dam. The Donzère dam (BGRT) was modelled as a weir, and the keeping structures were always modelled as gates. Gates were closed progressively with the increasing input flow rate. Input flow at Viviers ranged from 6100 m^3/s to 9000 m^3/s and decreased to 6100 m^3/s. Flows through the modelled works were compared with 1D results in Table I. Few differences were observed in keeping works which can be explained by the fact that diffluences are not modelled as precisely in 1D than in 2D.

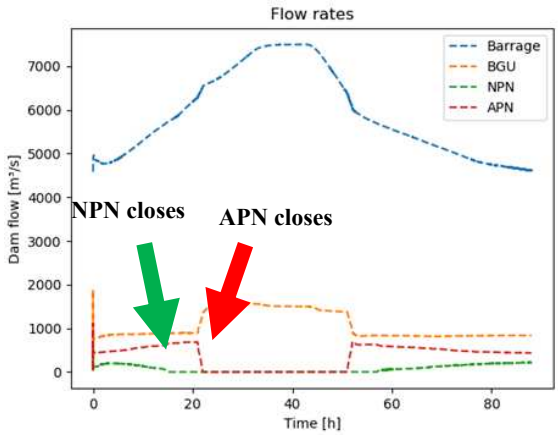

Figure 9. Flow rates through the dam and keeping gates during Q1500

Table I Flow rates at different points and time 1D and 2D results comparison

	2D Initialization flow rate (m^3/s)	**1D Initialization flow rate (m^3/s)**	**2D Flow rate at peak (m^3/s)**	**1D Flow rate at peak (m^3/s)**
BGRT	4615	4595	7490	7394
BGU	834	527	1546	1550
NPN	215	461	0	0
APN	437	512	0	0

D. Hydropower plant trigger

Finally, a hydropower plant trigger is simulated to test the robustness of the PID regulation. In this case, the dam and powerplant dam (BGRT + USB) are modelled as a control structure, and the keeping structures as gates. A hydropower plant trigger is one of the most difficult situations that can occur on a structure. It is a situation where the plant is turbine driven at its maximum flow (here 1850 m3/s). An incident stops it in emergency. The flow passing through the dam is cancelled in a few seconds, creating a large wave that flows up the headrace channel and then the reservoir. The plant can quickly allow to pass part of the flow, but the dam must then take over quickly and efficiently.

We tested the behaviour of our regulation option in this situation. The outflow from the power plant goes from 1800 m^3/s to 0 m^3/s in seven seconds. It then raises back to 855 m^3/s in a few minutes. On Figure 9 a wave of 50cm is observed at the PR. Factually, Zr-Zc reached 50 cm which takes 2h to return into the acceptable range.

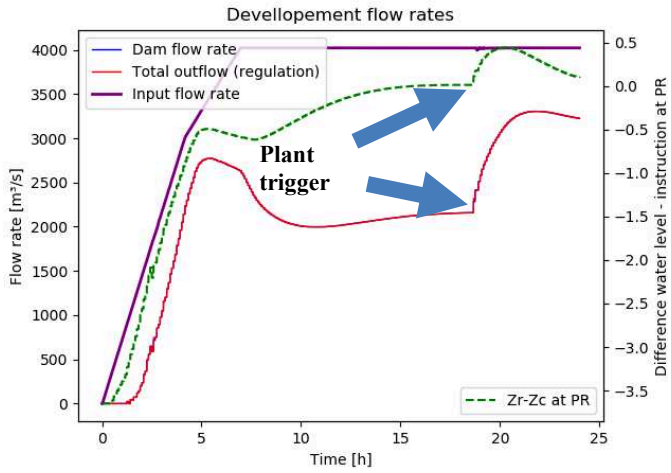

Figure 10. Dam flow rate and level error at PR during plant trigger

VI. CONCLUSION

A hydrodynamic model for hydraulic structures was implemented by FORTRAN subroutines on TELEMAC-2D. These sub-routines allow:

- to model precisely and easily several types of structures, without having to account for their precise geometry in the mesh
- to model the operation of the Rhône structures on a large scale with regulation

The next step is to improve the 3D version, which for the moment has only been made possible and not tested precisely. We could also test this implementation on other structures of CNR, with more complex instructions and thus develop the modularity of the subroutines.

REFERENCES

[1] P. Lang, S. Trossat and J.-P. Bard, “Adaptation of TELEMAC 2D to the regulation of a CNR developement during flood,” 2012.

[2] C. Gemaehling, «Quelques aspects des études des aménagements hydraliques du bas Rhône», La Houille Blanche, 1962.

[3] A. Lancastre, Hydralique générale, Eyrolles, 2015.

[4] CNR, «Régulation hydraulique : algorithme PID, définition et réglage», Unpublished.

Validation of TELEMAC for tsunami inundation modelling in compliance with the NOAA-NTHMP benchmark test cases

Giovanni Cozzuto[1], Thomas Saillour[1], Giorgio Lupoi[1], Giovanni Cuomo[1], Sebastien E. Bourban[2]
gcozzuto@studiosperi.it, tsaillour@studiosperi.it, glupoi@studiosperi.it, gcuomo@studiosperi.it, Palermo, Italy
sebastien.bourban@edf.fr, Paris, France
[1]: Studio Speri Società di Ingegneria S.r.l., Rome, Italy
[2]: EDF R&D LNHE / LHSV, Paris, France

Abstract – **This paper presents initial results from an ongoing validation exercise aimed at validating TELEMAC for tsunami inundation modelling in compliance with the National Oceanic and Atmospheric Administration (NOAA) National Tsunami Hazard Mitigation Program (NTHMP) benchmark test cases.**

Keywords: tsunamis, validation, runup, inundation, TELEMAC-2D, TELEMAC-3D

I. INTRODUCTION

Predicting natural disasters and their likely impact on the natural and built environment is a fundamental step towards the development of better-informed global risk management strategies, contributing to worldwide risk reduction and mitigation. In this context, accurate and effective modelling of tsunamis is not only vital for the safety of coastal communities but contributes to the creation of safer and more resilient world.

The capacity of the TELEMAC solvers to qualitatively model tsunamis has already been proven in previous publications and is further discussed in the twin paper [12] presented for the conference. The purpose of this paper is to present initial results from an ongoing validation exercise aimed at validating TELEMAC for tsunami inundation modelling in compliance with the National Oceanic and Atmospheric Administration (NOAA) National Tsunami Hazard Mitigation Program (NTHMP) benchmark test cases. The initiative was discussed at the last TELEMAC Scientific Committee at the EDF R&D Lab in Chatou, Paris, which confirmed the interest of the TELEMAC users' community as this is expected not only to strengthen the confidence in the usability of TELEMAC for this specific task but is now also a requirement introduced by ASCE 7-16 [11] or the use of any modelling tool in assessing tsunami induced inundation.

II. THE NOAA NTHMP BENCHMARK TEST CASES

Held on March 31st to April 2nd, 2011, at Texas A&M University at Galveston under the auspices of the NTHMP Mapping and Modelling Subcommittee (MMS), the Model Benchmarking workshop participants were tasked with developing and implementing a strategy for the validation of tsunami inundation models.

The workshop report is accessible at [5] and includes a list of NTHMP benchmark tests, which is a further evolution of the set of test cases identified in the OAR-PMEL-135 report [6].

The three categories of reference data used for defining benchmark tests for tsunami numerical model validation and verification are: (a) analytical solutions; (b) laboratory experiments; (c) field measurements.

Accordingly, the proposed benchmark test cases include:

- Analytical benchmarking
  - BP01 - Solitary Wave on a Canonical Beach
  - BP02 - Solitary Wave on a Composite Beach
  - BP03 - Subaerial landslide on simple beach
- Laboratory benchmarking
  - BP04 - Solitary Wave on a Canonical Beach
  - BP05 - Solitary Wave on a Composite Beach
  - BP06 - Solitary wave on a conical island
  - BP07 - Tsunami runup onto a complex three-dimensional beach, Monai Valley
  - BP08 - Tsunami generation and runup due to three-dimensional landslide
- Field benchmarking
  - BP09 - Okushiri Tsunami
  - BP10 - Rat Islands Tsunami

Different acceptability criteria apply to each test, which reflects the complexity of the phenomena being represented as well as the uncertainty in the target values. In this paper we present initial results obtained addressing analytical benchmarking only. A full description of each test case included in the full set can be found in [2], technical information needed to generate test cases and check model results can be found at: https://github.com/rjleveque/nthmp-benchmark-problems.

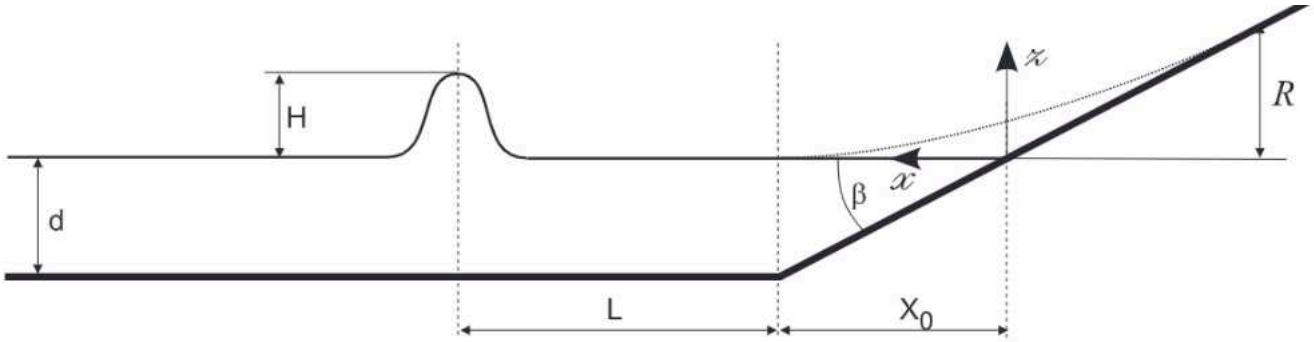

Figure 1. Model setup according to the NOAA NTHMP Benchmark test case "Solitary wave on a slope beach"

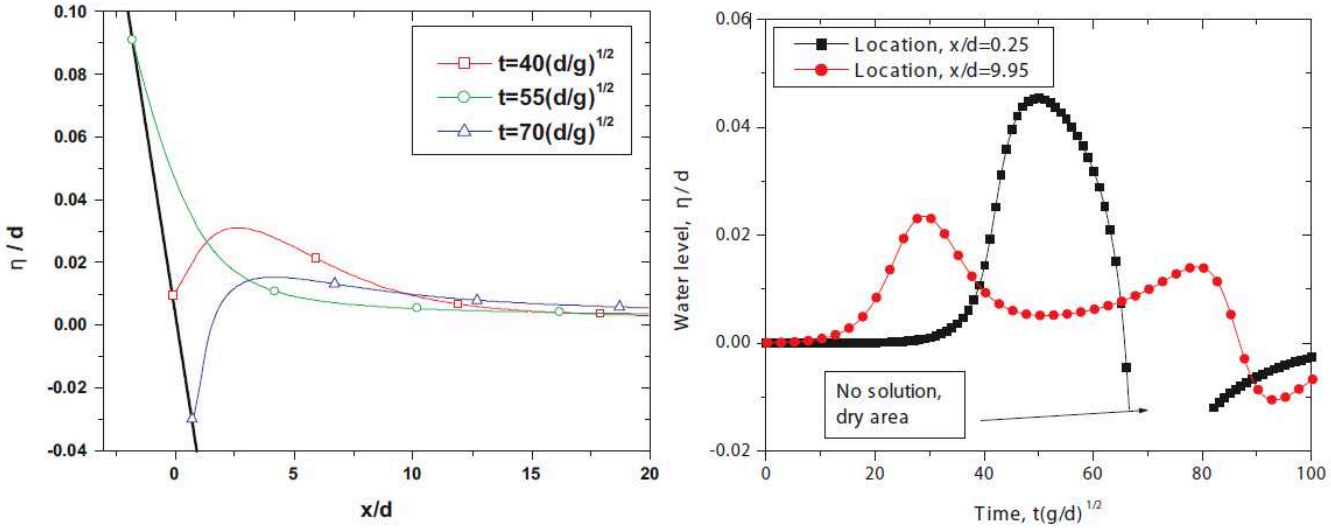

Figure 2. Left: non-dimensional water profile for specific time-steps. Right: non-dimensional water profile at two different probe locations

III. ANALYTICAL BENCHMARKING

A. General overview

The evolution of the tsunami waves from ocean areas to its nearshore targets is modelled in order to calculate tsunami currents, forces, and runup on coastal structures as well as coastal inundation.

For this scope, analytical formulations like the shallow water wave equations are useful for validating numerical models like TELEMAC.

The usefulness of the benchmarking relies on the comparisons of the numerical predictions with analytical solutions for identifying systematic errors, as when using friction factors or dissipative terms to augment the idealized equations of fluids motion.

This document shows only 1+1 (one directional and time) propagation problems.

B. BP01 - Solitary Wave on a Canonical Beach

1) Description of the test case

In this test, the bathymetry consists of a channel of constant depth d, connected to a plane sloping beach of angle β = acot (19.85) = 2.88º. A sketch (with distorted scale) of the canonical beach is displayed in Figure 1. The x coordinate increases monotonically seaward, x = 0 is the initial shore location, and the toe of the beach is located at $x = X_0 = d \cdot \cot(\beta)$.

2) Model setup

The wave of height H is initially centered at $X = X_S$ at t = 0 s. This benchmark test is focused on modeling the runup of an incident non-breaking solitary wave such that H/d = 0.0185, where H/d is the dimensionless wave height.

The initial wave profile η is given by:

$$\eta(x,0) = H\mathrm{sech}^2\left(\gamma(x - X_1)/d\right)$$

The initial water particle velocity u is given by:

$$u(x,0) = -\sqrt{g/d}\,\eta(x,0)$$

3) Results

Results from the model were compared with analytical solution, in terms of:

- water level at specific time-steps,
- water levels at prescribed locations,
- maximum run-up.

For the test to be successfully passed, results from the numerical model must be within 5% of the calculated value from the analytical solution.

NTHMP suggests specific guidelines to validate the numerical model against the analytical solution. For accomplishing this benchmark, TELEMAC3D water level results need to be compared at different timesteps:

- $t = 40\cdot(d/g)^{1/2}$,
- $t = 55\cdot(d/g)^{1/2}$,
- $t = 70\cdot(d/g)^{1/2}$.

Further comparisons should be computed to present water level dynamics at different locations during both the propagation and the reflection phases:

- x/d = 0.25,
- x/d = 9.95.

Computation of the maximum runup, according to the formulation provided by Synolakis (1986, 1987, 2017), must be provided for comparison with the maximum runup modelled with TELEMAC-3D.

Water levels at specific timesteps are compared with the analytical solution in Figure 3. The model appears to be able to represent well the evolution of the relevant process in space, both within the wet and dry regions.

Water levels at specific locations are compared with the analytical solution in Figure 4. The model appears to be able to represent well the evolution of the relevant process in space, both within the wet and dry regions.

Maximum run-up R/d predicted by the model compare well with that calculated according to the analytical solution, respectively equals to 0.073 and 0.089.

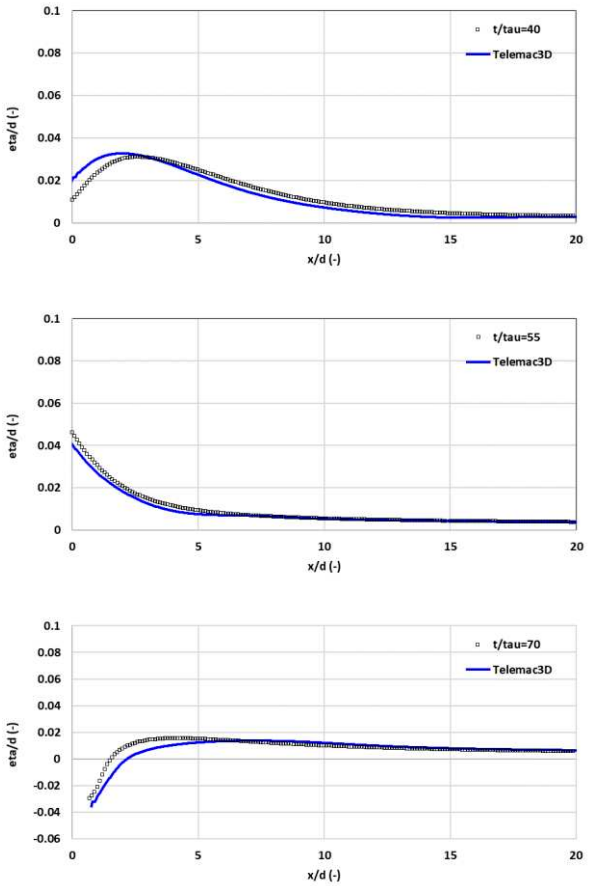

Figure 3. Solitary waves water level horizontal profile at different time-steps: during the propagation phase, the run-up of the wave along the slope and the run-down step

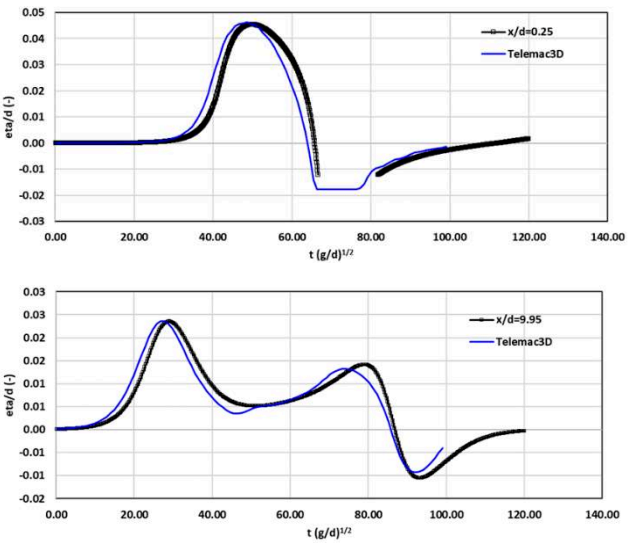

Figure 4. Non-dimensional water profile at two different probe locations

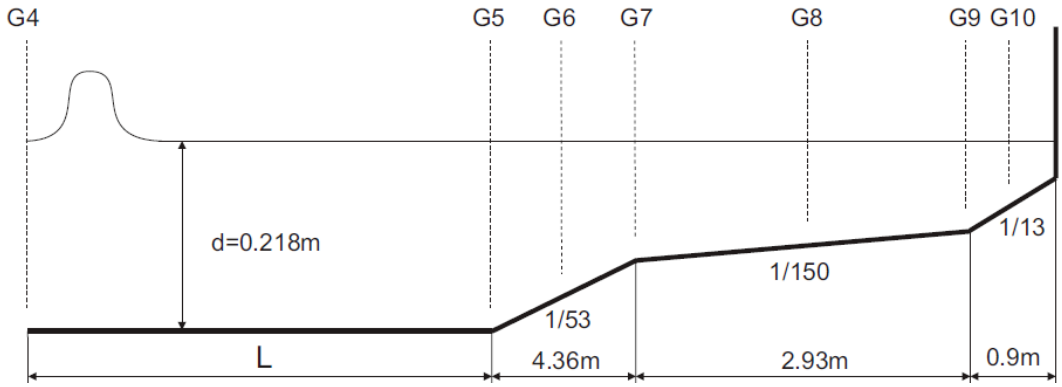

Figure 5. Model setup according to the NOAA NTHMP Benchmark test case "Solitary wave on a composite beach"

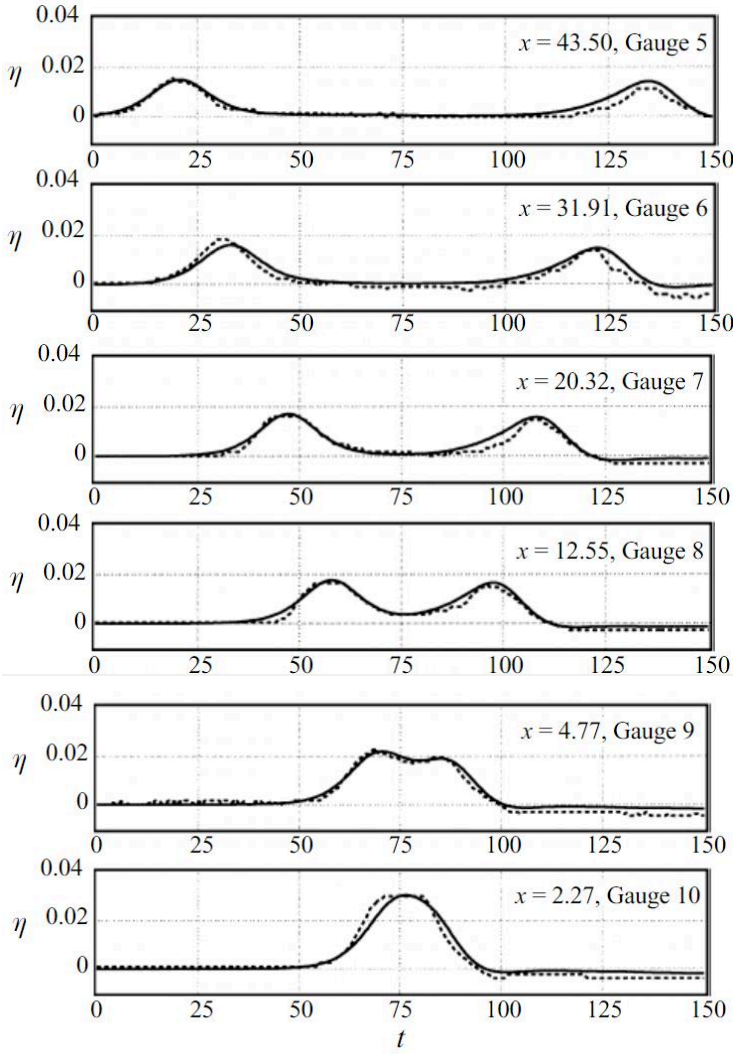

Figure 6. Dimensional water profiles at different probe locations

C. BP02 - Solitary Wave on a Composite Beach

1) Description of the test case

This benchmark has been based on a set of physical model tests performed in a water tank by the U.S. Army Corps of Engineers at the Coastal Engineering Research Center in Vicksburg, Mississippi. The numerical domain represents a composite beach simulating geometrical dimension of the Revere Beach.

Kânoğlu and Synolakis (1998) developed an exact analytical solution to the linear shallow water equations to predict propagation and run-up of an incident solitary wave over the piece-wise linear bathymetry.

This analytical solution was proposed to be used as a benchmark problem by Synolakis et al. (2007).

2) Model setup

The model of the numerical flume presents an initial part having a constant depth and a length which is function of the wavelength. Furthermore, three different slopes follow the constant depth channel equal to 1/53, 1/150 and 1/13, respectively.

Probes are located at different distances from the reflecting wall at the right end of the channel:

- **G10** - 0.43 m distant from the wall,
- **G09** - 0.90 m distant from the wall,
- **G08** - 2.37 m distant from the wall,
- **G07** - 3.83 m distant from the wall,
- **G06** - 6.01 m distant from the wall,
- **G05** - 8.19 m distant from the wall,
- **G04** - 10.59 m distant from the wall.

3) Results

Results from the model were compared with analytical solution, in terms of:

- water levels at probes locations,
- water levels at the wall.

For the test to be successfully passed, results from the numerical model must be within 5% of the calculated value from the analytical solution.

Water levels at probes locations are compared with the analytical solution at location of probes locations in the next figures. The model appears to be able to represent well the evolution of the relevant process in time at the instrumented locations: reflection of the incident wave is qualitatively good represented by TELEMAC-3D.

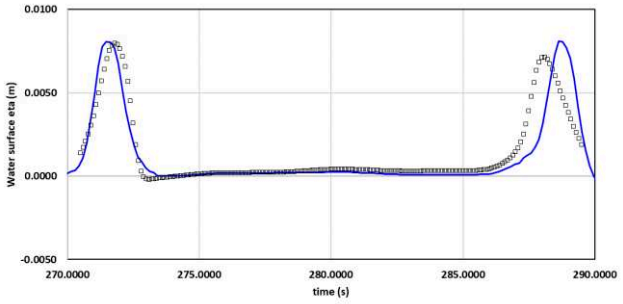

Figure 7. Solitary waves water level horizontal profile at G4 location. Black squared dot lines represent the analytical data. Blue lines are numerical results

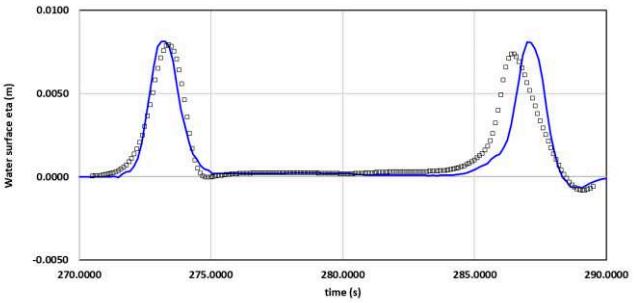

Figure 8. Solitary waves water level horizontal profile at G5 location. Black squared dot lines represent the analytical data. Blue lines are numerical results

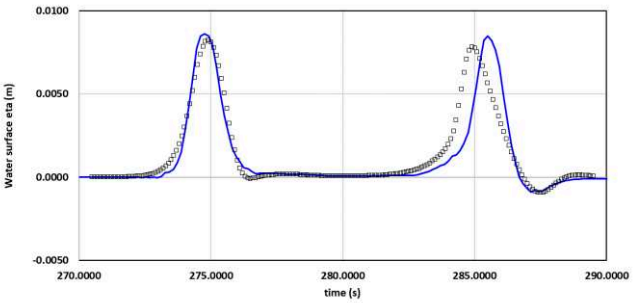

Figure 9. Solitary waves water level horizontal profile at G6 location. Black squared dot lines represent the analytical data. Blue lines are numerical results

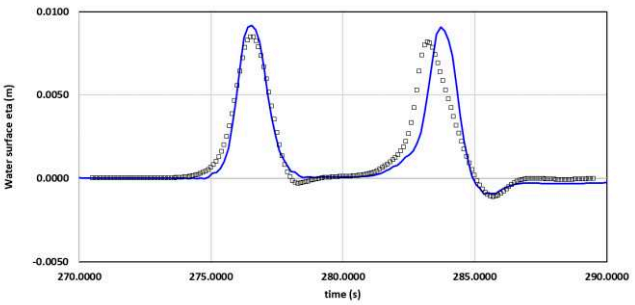

Figure 10. Solitary waves water level horizontal profile at G7 location. Black squared dot lines represent the analytical data. Blue lines are numerical results

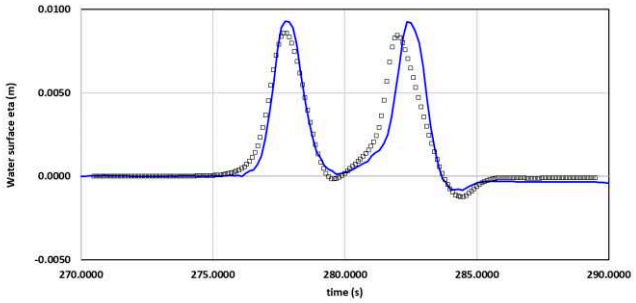

Figure 11. Solitary waves water level horizontal profile at G8 location. Black squared dot lines represent the analytical data. Blue lines are numerical results

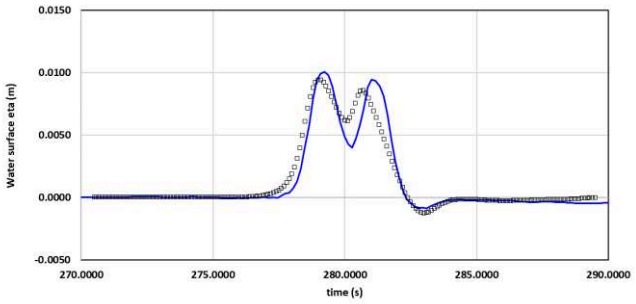

Figure 12. Solitary waves water level horizontal profile at G9 location. Black squared dot lines represent the analytical data. Blue lines are numerical results

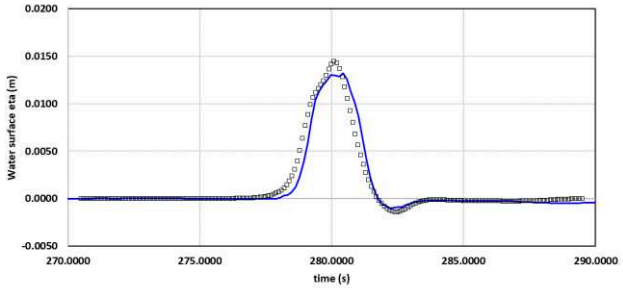

Figure 13. Solitary waves water level horizontal profile at G10 location. Black squared dot lines represent the analytical data. Blue lines are numerical results

IV. LABORATORY BENCHMARKING

A. General overview

Long before the spread availability of numerical codes as well as their increasing reliability and the advancement in computational power of the machines, physical modelling in laboratory at small scale have been used to analyse wave related processes for assessing specific hydraulic performances of the structures and eventually scale results to the prototype.

Nevertheless, nowadays physical models are still used in technical practice to confirm performances of non-standard design configurations, to study specific flow details in the fluid structure interactions and to validate numerical models to be used in the analysis and in the design process of maritime and coastal defences.

For the purpose of validating TELEMAC-3D, the scale differences are not believed to be significantly important. NTHMP reports a significant series of diverse benchmarks of numerical codes developed in the last decade that consistently produced predictions in excellent agreement with measurements from small-scale laboratory experiments. It has been shown that these were able to model geophysical-scale tsunamis well. Furthermore, it has been shown that bottom friction tends to be less important than the inertia of the motion of such long waves like tsunamis.

B. BP04 - SOLITARY WAVE ON A CANONICAL BEACH (Laboratory)

1) Description of the test case

The experiments were conducted in a 31.73 m-long, 60.96 cm-deep, and 39.97 cm-wide flume located at the California Institute of Technology, Pasadena, California wave tank.

The bottom of the tank consisted of painted stainless-steel plates. A ramp was installed at one end of the tank to model the bathymetry of the canonical problem of a constant-depth region adjoining a sloping beach.

Several tests have been carried out (more than 40 experiments) with solitary waves running up the sloping beach (water depths ranging from 6.25 cm to 38.32 cm). The test case problem has been parametrized as follows: 3 parameters can be used to describe the different tests combinations - the offshore depth d; the height of the solitary wave H, and the beach slope β.

2) Model setup

The model of the numerical flume has been setup according to what already presented within the BP01 benchmark (Figure 1): an initial constant depth flume has been setup and the wave height imposed for satisfying the $H/d = 0.0185$ criteria. The wave height has been used as input to parametrize the initial water profile for perturbating the model with.

The beach presents a constant slope ($\cot\beta = 19.85$).

3) Results

Results from the model were compared with laboratory measurements, in terms of:

- water level at specific time-steps,
- maximum run-up.

NTHMP suggests specific guidelines to validate the numerical model against the analytical solution.

For accomplishing this benchmark, TELEMAC3D water level results need to be compared at different timesteps:

- t = 30 s - 40 s - 50 s - 60 s - 70 s.

Numerical results in terms of water profiles are provided in Figure 14 to Figure 18: numerical model (blue lines) is compared with the experiments and a good agreement is achieved.

The maximum run-up was measured during the experiments, and it is reported in non-dimensional form, R/d = 0.077. Run-up result from the numerical modelling is R/d = 0.07.

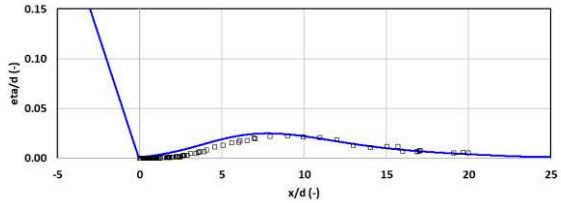

Figure 14. Solitary waves water level horizontal profile at t = 30 s time-step: laboratory measurements (black squared dots) against numerical model results (blue line)

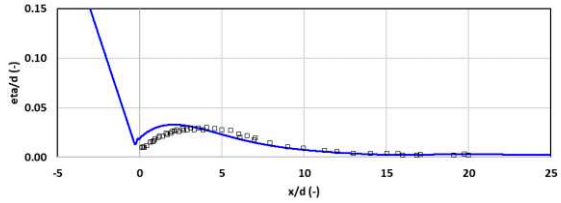

Figure 15. Solitary waves water level horizontal profile at t = 40 s time-step: laboratory measurements (black squared dots) against numerical model results (blue line)

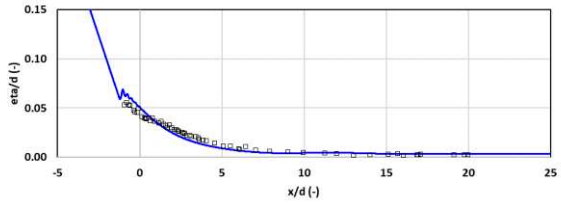

Figure 16. Solitary waves water level horizontal profile at t = 50 s time-step: laboratory measurements (black squared dots) against numerical model results (blue line)

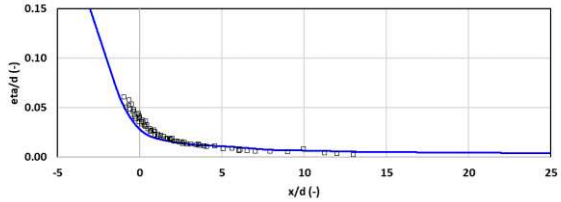

Figure 17. Solitary waves water level horizontal profile at t = 60 s time-step: laboratory measurements (black squared dots) against numerical model results (blue line)

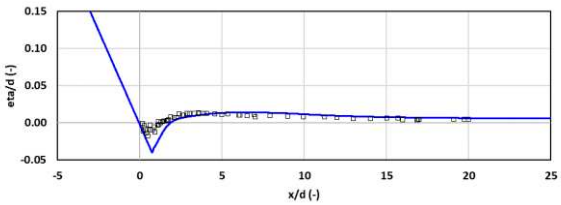

Figure 18. Solitary waves water level horizontal profile at t = 70 s time-step: laboratory measurements (black squared dots) against numerical model results (blue line)

C. BP05 - Solitary Wave On A Composite Beach (Laboratory)

1) Description of the test case

The original laboratory experiments which are presented in the BP05 benchmark were conducted in the Coastal & Hydraulics Laboratory of US Army Corps of Engineers. The set of the original tests to be used as reference are the same ones used for deriving the analytical solution in BP02.

The basin for the experiments was a long narrow flume with reflecting side walls (glass), as shown in Figure 5. The depth variation and all the wave motion occurred strictly in the direction along the flume, and all the measurements were taken on the flume's centreline. Thus a 1D approach seems reasonable to describe the case.

The wavemaker was used to generate solitary waves of the form:

$$\eta(x,0) = d_0 H sech^2(\sqrt{0.75H}x/d_0)$$

The velocities are complemented with corresponding elevation values:

$$v = \eta\sqrt{9.81/(d_0+\eta)}$$

2) Model setup

The model of the numerical flume has been setup according to what already presented within the BP02 benchmark (Figure 5): an initial constant depth of 0.218 m has been adopted as well as three different slopes equal to 1/53, 1/150 and 1/13, respectively. The wave height must satisfy the criteria H/d = 0.30 and it has been used as input to parametrize the initial water profile for perturbating the model with.

3) Results

Results from the model were compared with the laboratory data measurements, in terms of:

- water levels at probes locations,
- run-up at the wall.

The comparison of the water profiles at specific gauges are shown in Figure 19 to Figure 24: the images present the measurements (black squared dots) against the numerical results in TELEMAC-3D (blue lines) and a good agreement is achieved.

The maximum run-up was measured during the experiments, and it is reported in both dimensional and non-dimensional forms, R = 0.45 m and R/d = 2.10 respectively.

Run-up results from the numerical modelling are: R = 0.15 m and R/d = 0.69 respectively. This specific benchmark needs more investigations in order to get better agreement with the physical modelling measurements.

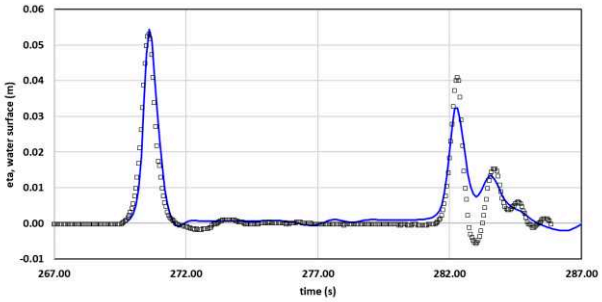

Figure 19. Solitary waves water level horizontal profile at G05 location. Black squared dot lines represent the laboratory data. Blue lines represent numerical results

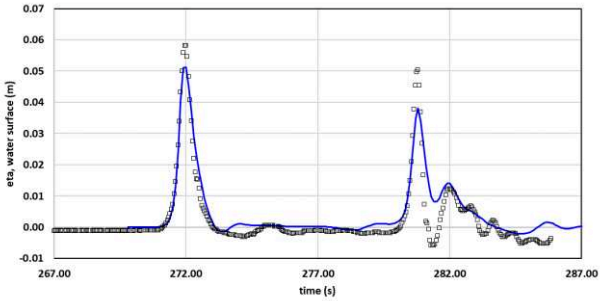

Figure 20. Solitary waves water level horizontal profile at G06 location. Black squared dot lines represent the laboratory data. Blue lines represent numerical results

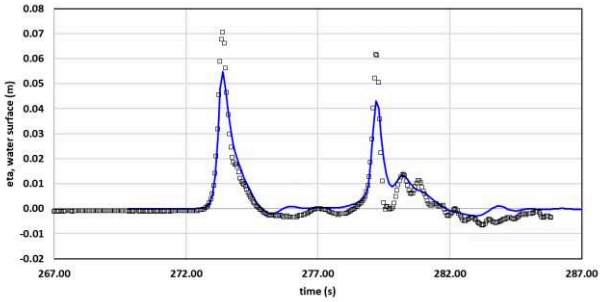

Figure 21. Solitary waves water level horizontal profile at G07 location. Black squared dot lines represent the laboratory data. Blue lines represent numerical results

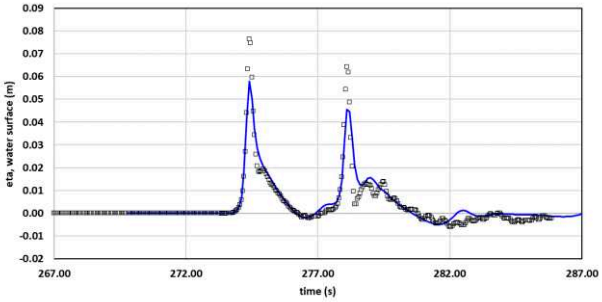

Figure 22. Solitary waves water level horizontal profile at G08 location. Black squared dot lines represent the laboratory data. Blue lines represent numerical results

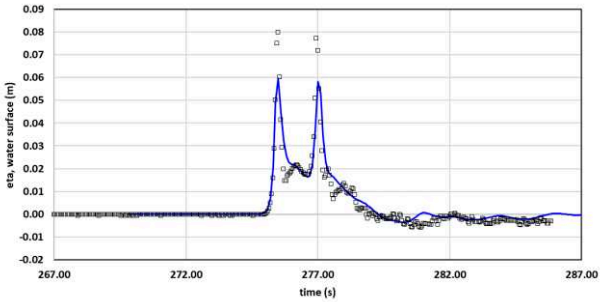

Figure 23. Solitary waves water level horizontal profile at G09 location. Black squared dot lines represent the laboratory data. Blue lines represent numerical results

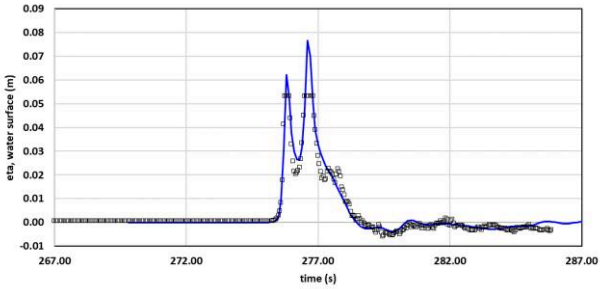

Figure 24. Solitary waves water level horizontal profile at G10 location. Black squared dot lines represent the laboratory data. Blue lines represent numerical results

FURTHER WORK

Work is ongoing to progress testing of TELEMAC with the whole set of benchmark tests. More investigations are needed to obtain better agreement with the reference results.

ACKNOWLEDGEMENT

This research is being carried out as part of the SmartWave Project, funded by Regione Sicilia within the POR2014/20 EU framework. Authors wish to acknowledge the contributions of F. Ligorio, J. Le Goff, G. Gatto.

REFERENCES

[1] Kânoğlu, U. (1998): The runup of long waves around piecewise linear bathymetries. Ph.D. Thesis, University of Southern California, Los Angeles, California, 90089- 2531, 273 pp.

[2] Kânoğlu, U. (2004): Nonlinear evolution and runup–rundown of long waves over a sloping beach. J. Fluid Mech., 513, 363–372.

[3] Kânoğlu, U., and C.E. Synolakis (1998): Long wave runup on piecewise linear topographies. J. Fluid Mech., 374, 1–28.

[4] Kânoğlu, U., and C. Synolakis (2006): Initial value problem solution of nonlinear shallow water-wave equations. Phys. Rev. Lett., 97, 148,501–148,504, doi: 10.1103/PhysRevLett.97.148501.

[5] National Tsunami Hazard Mitigation Program. (2012): "Proceedings and results of the 2011 NTHMP Model Benchmarking Workshop." NOAA Special Report, Boulder, CO, U.S. Department of Commerce/NOAA/NTHMP. https://nws.weather.gov/nthmp/documents/nthmpWorkshopProcMerged.pdf,

[6] Synolakis, C., E. Bernard, V. Titov, U. Kânoğlu, and F. González, NOAA Technical Memorandum OAR PMEL-135, Standards, Criteria, and Procedures for NOAA Evaluation of Tsunami Numerical Models, (2007): (as later modified by the National Tsunami Hazard Mitigation Program), 60 pp. , Pacific Marine Environmental Laboratory, 7600 Sand Point Way NE, Seattle, WA.

[7] Synolakis, C.E. (1986): The Runup of Long Waves. Ph.D. Thesis, California Institute of Technology, Pasadena, California, 91125, 228 pp.

[8] Synolakis, C.E. (1987): The runup of solitary waves. J. Fluid Mech., 185, 523–545.

[9] Synolakis, C.E., and J.E. Skjelbreia (1993): Evolution of maximum amplitude of solitary waves on plane beaches. J. Waterw. Port Coast. Ocean Eng., 119 (3) 323–342.

[10] Synolakis, C.E., and E.N. Bernard (2006): Tsunami science before and after Boxing Day 2004. Phil. Trans. R. Soc. A, 364(1845), doi: 10.1098/rsta.2006.1824, 2231–2265.

[11] American Society of Civil Engineers, Structural Engineering Institute (2016): Minimum Design Loads for Buildings and Other Structures, ASCE/SEI 7-16

[12] T. Saillour, G. Cozzuto, G. Lupoi, G. Cuomo and S.E. Bourban, Modeling historical global tsunamis with TELEMAC, TUC 2022, unpublished.

Gironde flood reference 2020

Patrick Chassé[1], Rémy Gasset[2], Sabine Cavellec[1], Didier Felts[2], Alain Baus[2]
patrick.chasse@cerema.fr, Compiegne, France
[1] Cerema Risques Eau Mer
[2] Cerema Sud-Ouest

Abstract – **This document presents the work carried out by Cerema risks, water, sea, and South-West Cerema) to update the Gironde flood reference system (RIG).**

Keywords: River, estuaries, maritime, coastal flood processes.

I. INTRODUCTION

The Gironde flood reference 2020 is integrated in the flood prevention actions program (PAPI) supported by the SMIDDEST [5] and the French Ministry of Environment. Within this ministry, the Cerema contributes to "improvement of knowledge and awareness of flood risk", in particular with the:

- creation of a data base on estuary knowledge, risks and a cartographic tool
- improvement of the RIG[6] project to make predictions more realistic based on:
  a) actualisation of the bathymetry
  b) modelling of islands and integration in the model
  c) actualization of the model with new structuring elements of the territory
  d) modeling of the overflow events of 1999 (calibration) and 2010 (Xynthia)

Historically, the RIG project started in 2007 with two models:

- a large-scale model (RIG phase 1)
- a model with 5 zones of fine mesh details (RIG phase 2) for a more precise definition of hydraulics in urban areas

The work presented here is about improving the modeling of the Gironde Estuary on the basis of TELEMAC-2D, so to define the new reference, the so-called RIG2020.

II. 2D MODEL UPDATE OF THE GIRONDE ESTUARY

First, Cerema integrated all new data: bathymetry, topography, estuary islands, hydraulic structures, containment systems, high water marks, future overflow events. Structural modifications were used to take into account new issues that emerged after 2009 (embankment footprints, climatic variables, adaptation and quality of the environments, etc.). The update of the 2D model was particularly focussed on:

- Representation of the main flood phenomena and dynamics
- Accurate representation of water levels in minor bed for extreme events
- Correct representation of overflows and flooded areas in flood plain
- Determination of flood zone envelopes and associated water heights

The extent of the RIG2020 model and the boundaries conditions are presented on the Figure 1 hereunder:

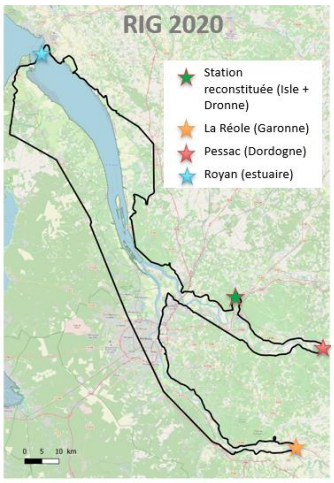

Figure 1. Limits of the model RIG2020

The model has been gradually improved to reach a version deemed satisfactory, here referred to revision v17. This revision has 3 232 466 nodes (while the v13 revision had 266 107 nodes). It integrates:

- Urban areas and representation of street blocks (increasing the number of nodes)
- Additional dyke surveys
- Bridges / embankments of hydraulic works on the Dordogne River
- Improvement of the topography of islands
- Consideration of all hydraulic structures larger than 1 m

For illustration purpose, the Figure 2 below shows an example of city blocks included in the mesh of the RIG2020 model. The Figure 3 shows an example of refinement of the mesh around bridge piers, to increase the details of their

5 Syndicat Mixte pour le Développement Durable de l'Estuaire de la Gironde
6 Gironde Flood Reference

representation in the model. The Figure 4 shows a map of all hydraulic structures taken into account in the model.

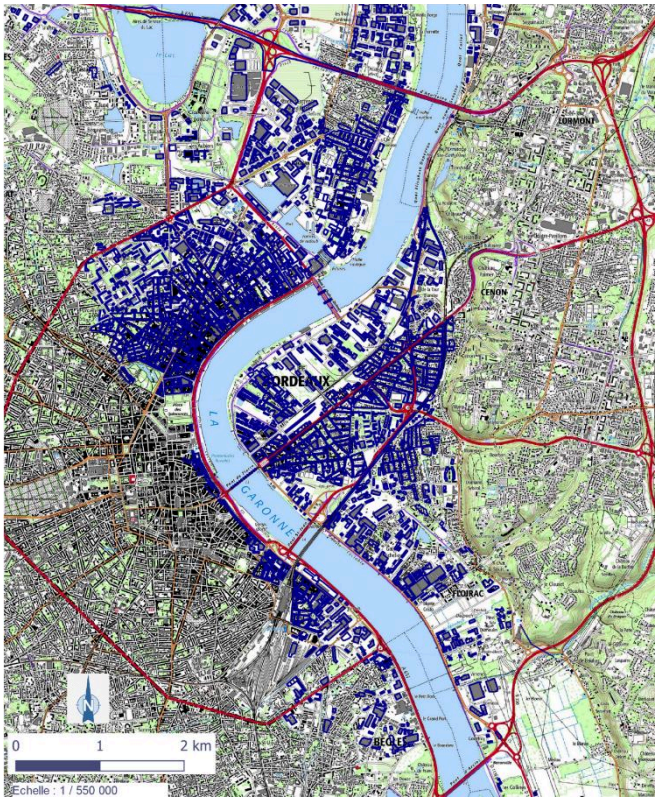

Figure 2. Integration of urban areas

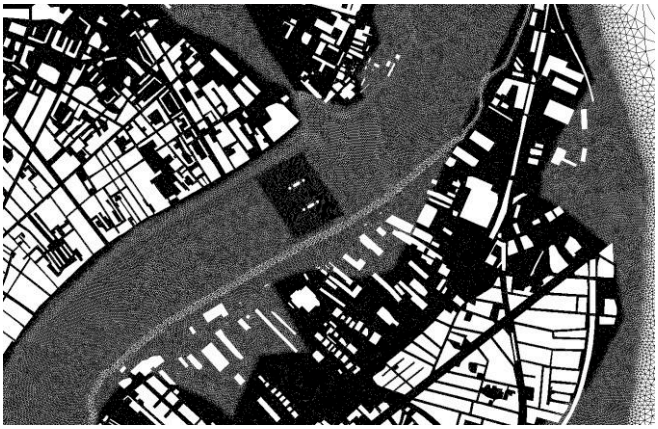

Figure 3. Integration of new bridges

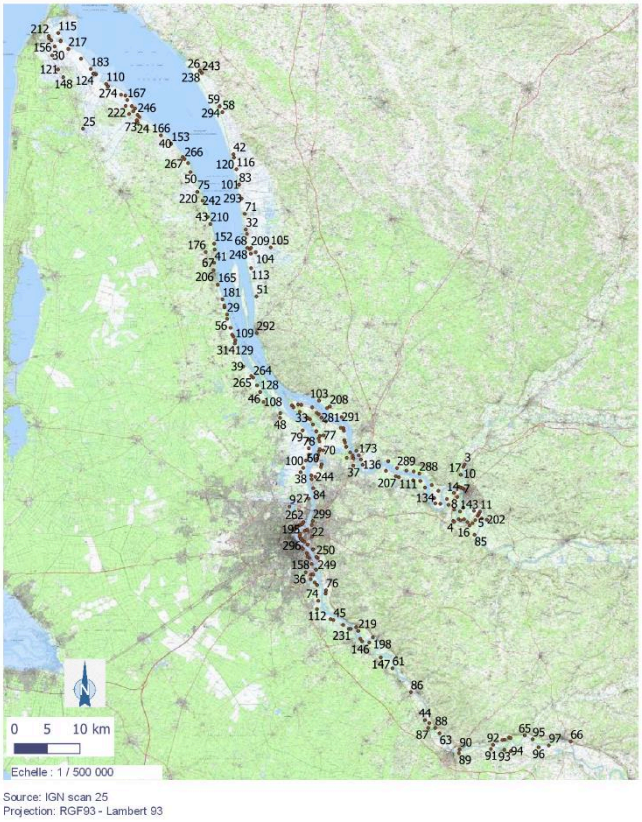

Figure 4. 314 hydraulic structures taken into account

III. CALIBRATION OF THE MODEL

The calibration of the model has been carried out on the basis of the December 1999 flood event. Roughness have been fixed by land occupation with the help of the database Corine Land Cover.

The time-histories of the boundary conditions are presented on the Figure 5 hereunder, with discharges upstream and water level downstream.

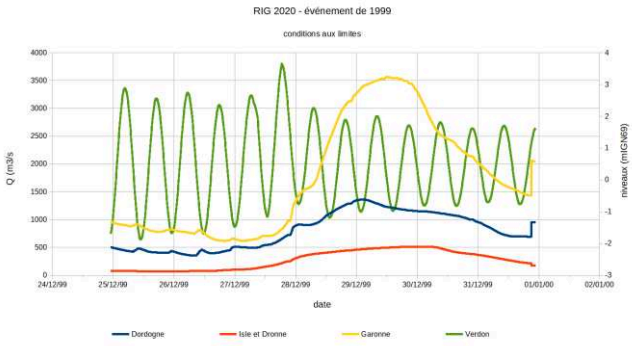

Figure 5. Boundaries conditions for 1999 flood event

Wind conditions have also been taken into account in the model as an average between stations operated by Meteo-France at Royan and at Mérignac.

It was recorded that dyke breaches occurred during the event, causing a significant impact on various estuary stakeholders. While the details of the dynamic of these dyke breaches remain unclear an estimated total of 19 breaches were simulated with the following assumptions, the location of which are shown in Figure 6:

- instantaneous opening,
- start of breach when a certain level in the estuary is reached,
- break on the vertical.

Figure 6. Location of the breaches during 1999 event

The Figure 7 hereunder presents some results of the calibration at various tide gauges in the estuary.

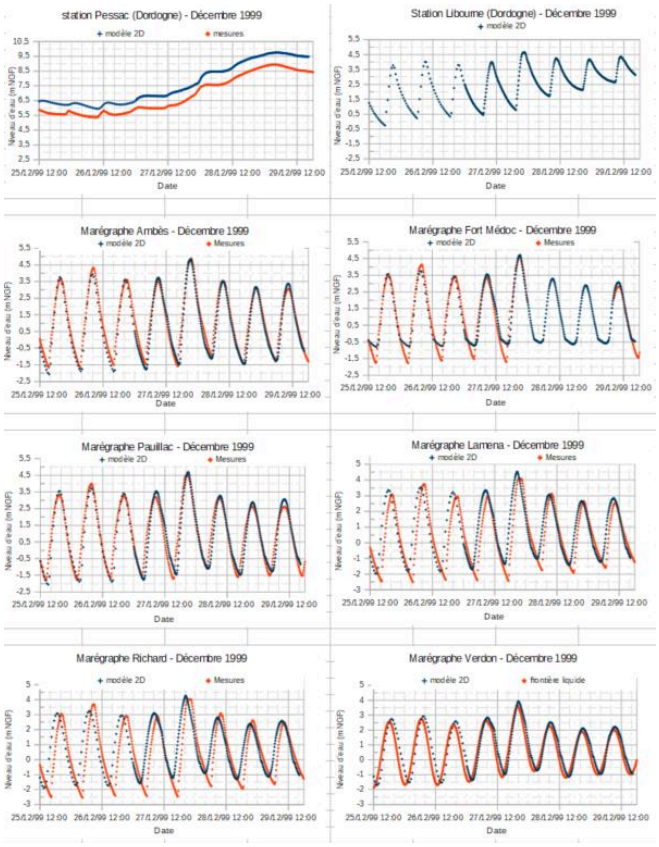

Figure 7. Some results for 1999 calibration at tide gauges

The results are quite good at the flood but overestimated at low tide. The results of the model are also compared to the flood marks. The Figure 8 hereunder presents the comparison between flood mars and calculation. The NASH-Sutcliffe number is 0.8, that is quite good.

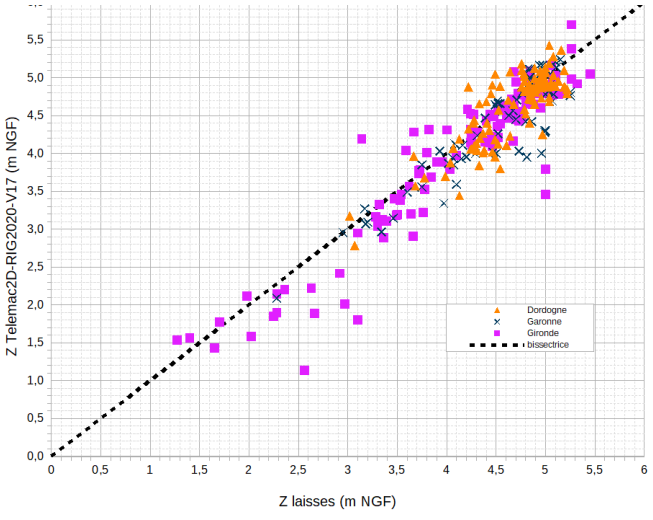

Figure 8. Comparison between flood marks and calculation

IV. VERIFICATION ON XYNTHIA EVENT

The boundaries conditions are Verdon tide gauge and Garonne, Dordogne and Isle flows. The average wind between Royan and Mérignac is taken into account.

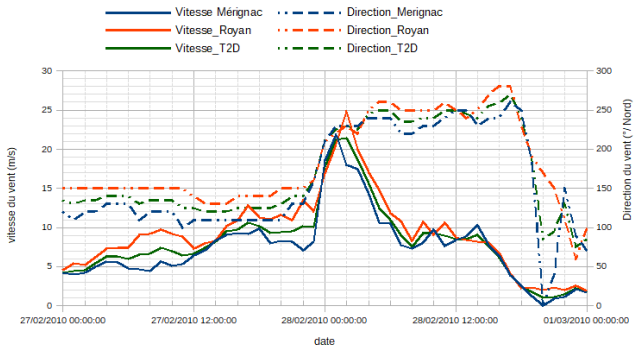

Figure 9. Conditions of the wind's Xynthia

Modelling of the Xynthia event includes 8 breaches, with the same assumptions as for 1999.

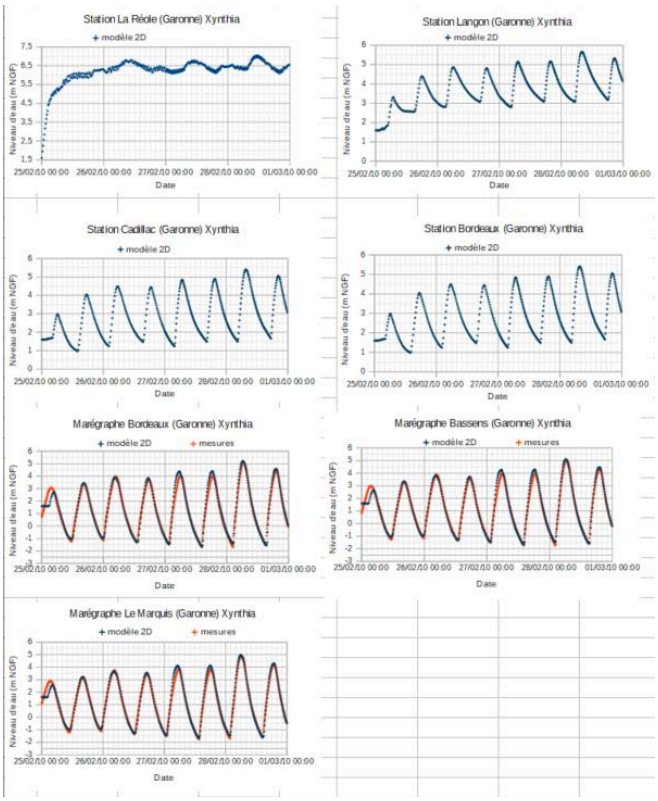

Figure 10. Comparison of measures and calculations at some tide gauges in the estuary for Xynthia

The comparison between flood marks and calculations is presented on the Figure 11 hereunder. The NASH-Sutcliffe number is 0.85, that is satisfactory.

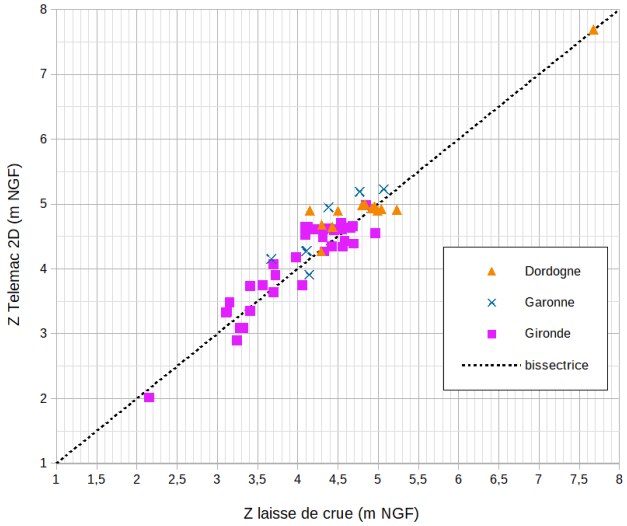

Figure 11. Comparison of flood marks with calculations

V. COMPARISON OF FLOODED AREAS

We compared the flooded areas computed from revision v17 of the RIG2020 model with those computed with the RIG phase 1 and phase 2 and those observed during feedback.

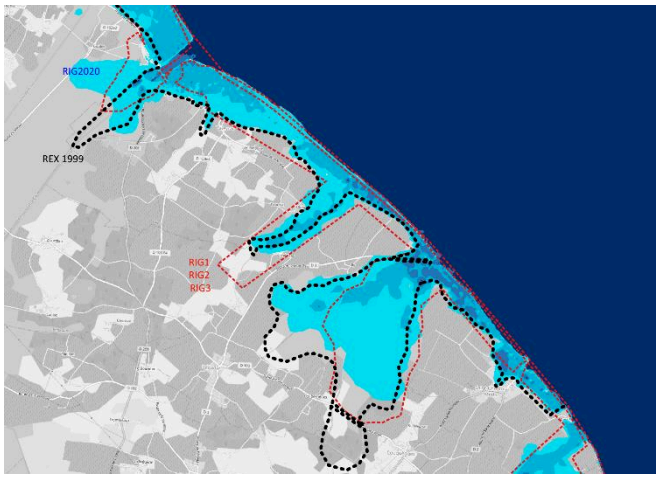

Figure 12. Comparison of flooded areas

The results are quite good at different locations.

VI. V18 REVISION AND LINDNER METHOD

Lindner's method originally developed to represent obstacles due to vegetation is adapted to represent obstacles due to buildings. Buildings are no longer represented explicitly as islands, but urban areas are defined using polygons to which Lindner parameters are assigned (average diameter of obstacles and average distances between obstacles).

The main advantage is that the mesh is less constrained and no longer requires as many nodes as the explicit method.

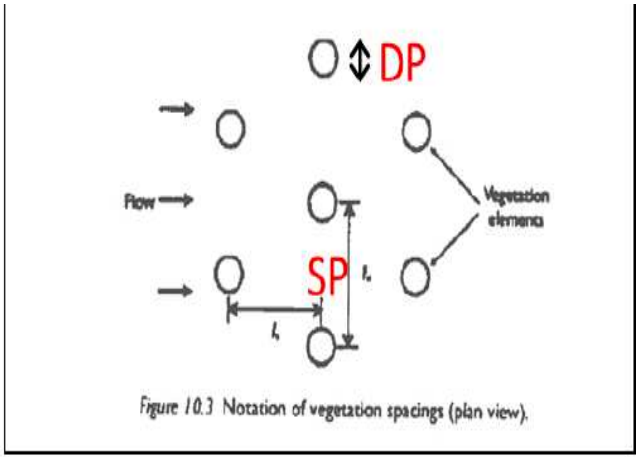

Figure 13. Lindner's method

The comparison of the two models v17 and v18 on the floods of 1999 and Xynthia gives the following results presented in table 1 below.

Table I Comparison between v17 et v18 version

	1999		Xynthia	
Model	**V17**	**V18**	**V17**	**V18**
Mean	-12,0 cm	8,2 cm	11,1 cm	16,9 cm
Medium difference	22,7 cm	28,9 cm	21,5 cm	27,2 cm
NASH-Sutcliffe	0,80	0,75	0,87	0,63

The results with the revision v18 are not as good as with v17, but remain acceptable.

The Lindner method also has several advantages:

- The mesh is lightened because the urban areas are not finely meshed
- Calculation times are reduced
- The size of the result files is reduced

VII. CONCLUSION

In the case of the RIG2020 model, the results obtained between a fine grid of urbanization and a less fine grid with the Lindner method are quite close.

A time saving is also appreciated on the calculation of the mesh with BlueKenue on the mesh of a new urbanization zone.

Meshing of new areas of development projects easier with the Lindner method.

VIII. OUTLOOK

Provide communities, B&E and/or contracting authorities with an updated and reliable model to assess the impact of any development in minor or major rivers and at the interfaces.

Have a follow-up over time of the physical changes made and the cumulative impacts.

Provide research actors with a shared tool to plan / evaluate / contextualize future issues and problems (adaptation to climate change, shoreline erosion, vulnerability and resilience of issues, etc.)

ACKNOWLEDGEMENT

We thank all the actors of the project and especially SMIDDEST, DDTM17 and DDTM33, DREAL NA, etc.

REFERENCES

[1] TELEMAC user manual

[2] SOGREAH - Development of a reference system for protection against flooding on the Gironde estuary.

Developing tropical cyclone simulation in Oman

C.P.C Beraud[1], D.M. Kelly[2] / DKAF Coastal[2]
[1] claire.beraud@cefas.co.uk, [2] dkafcoastal@gmail.com
[1] Centre for Fisheries and Aquaculture Science, Pakefield Road, Lowestoft, NR33 OHT, UK
[2] Beccles, NR34 9UD, Suffolk, UK

Abstract – **Tropical Cyclone (Hurricanes and Typhoons) intensity has increased in recent years, in response to warming sea temperatures. There is therefore the need to predict the cyclone-induced inundation and is paramount to protect local population and limit the cyclone-related risk. The category-5 cyclone Gonu is the strongest observed cyclone in the Arabian Sea and hit Oman in June 2007, causing 49 deaths. The JTWC Automated Tropical Cyclone Forecasting database provides simulated winds speeds and atmospheric pressure and has been validated against observations such as satellite where available. In order to predict the water inundation levels due to the tropical storms the path and strength of the cyclone need to be included in a marine model that simulates waves and sea level response.**

We have developed a methodology to incorporate spatially and temporally varying winds and pressure into a coupled TELEMAC2D-TOMAWAC system. This model has been applied to simulate the Gonu tropical cyclone event with calibration of the simulated waves by comparing with observations.

Furthermore, results are presented of "what if" scenarios, whereby the track of Gonu-like events is shifted further south to assess the potential impact of a similar event on other parts of Oman.

Different model configurations enable the breaking-down of the different cyclone components: the effect of local depression and wind are presented. Uncertainties on the simulation of wind- and wave-induced flooding are discussed and will be further developed in future work with the Omani meteorological institute providing additional observation data that would help us in the calibrating and validating process of the model.

Keywords: Oman, cyclone simulation, tropical cyclone Gonu, coupled TELEMAC2d-TOMAWAC

I. INTRODUCTION

Tropical cyclones are extremely powerful and harmful natural events. One such event was Gonu, a category 5 (maximal) tropical cyclone, which sits among the top 10 costliest known North Indian Ocean cyclones; according to the Oman News Agency Gonu took 49 lives in the country and costed around $4.2 billion (2007 USD) in Oman. Gonu (see Figure 1, bottom) developed in the eastern Arabian Sea from the 1st of June 2007 and made landfall at the most easterly tip of Oman near Ras al-Hadd. It then moved in a northward direction into the Gulf of Oman and made a second landfall in Iran that dissipated its energy. Gonu characteristics were an eye diameter reaching 40 miles (64km), a wind maximum velocity up to 145 miles per hour (65 m/s) and heavy precipitations up to 934 mm at Aljabl alasfer near Muscat (Figure 1). Gonu travelled around 10 degrees in both latitude and longitude throughout the Arabian Sea and impacted the following countries: Oman, Iran, United Arab Emirates and Pakistan.

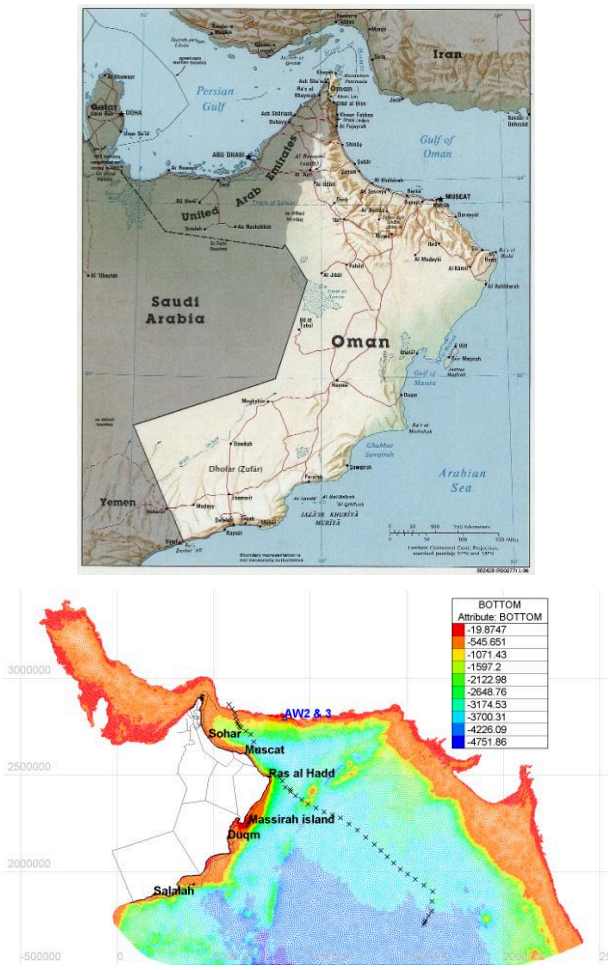

Figure 1. bottom: model bathymetric mesh with Gonu track downloaded from JTWC indicated with crosses, the principal cities/villages and islands are noted. The AWAC (Acoustic Doppler Wave & Current Profiler) stations AW2 and AW3 are in Iran and indicated in blue; x- and y- axis are in metre projection UTM40N. top: overview of Oman topography (CIA 1996 map) with coordinates in latitude-longitude.

Along the Gulf of Oman, several tide gauges failed and could not record any observation of Gonu passing. In order to have further information on this event over Oman [1] established a protocol to collect high water marks and present them in [2] together with the development of an ADCIRC

flood model. High water marks can be elevations of water marks on trees, buildings or debris found and results from the addition of the following two hurricane-induced inundation components: storm surge and storm waves. Reference [3] also reported a high-water mark of 5m at Ras al-Hadd. Gonu maximum observed wind has been reported in Oman: wind at Ras al-Hadd was 46 m/s on the 05/06/2007 in the evening and was 20 m/s near Muscat on the 06/06/2007 13:00:00.

Time-series of wind and wave information during the cyclone Gonu event have been measured at the stations AW2 and 3 (Figure 1, bottom) within and in the vicinity of Chahbahar bay, Iran; further information on the deployed stations can be found in [4] and [5] and observation time-series have been discussed in [5] and [6]. Time-series data at AW3 have been extracted from [10].

In Oman, mountains are present in the northern and southern part of the country (Figure 1, top), and 80% of the population lives in low-lying areas [7] where development of refinery, fish and shrimp farms, desalination plants and real estate development is planned. Aware of the damage that can induce an event such as a Gonu-like cyclone, the Omani government wants to better understand the inundation dynamics and investigate potential cyclone impact if landing hit one of those areas in development.

II. MODEL SETUP

A. *Site location and model domain*

The numerical mesh covers the Oman and Persian gulfs. Cell size ranges from 40m to 12km and totalled ~200,000 cells in number. The refined areas are located on the eastern side of Oman (Figure 1, bottom). The bathymetry stems from GEBCO (General Bathymetric Chart of the Oceans), ETOPO1 (1 arc-minute topography, open source) and local EOMAP (commercial) data sources, which all have been standardized by analysing LAT predictions.

Development to update the Maximum Envelope Of Water every time-step and amend the drag coefficient depending on the wind strength has been done in TELEMAC-suite version v8p1; as the latest version did not allow the use of different meshed in TELEMAC and TOMAWAC, the same mesh was employed to run the coupled TELEMAC-2D and TOMAWAC models. TELEMAC-2D reproduced the surge induced by the depression (inverse barometer) and the wind stresses, TOMAWAC predicted the generation of waves due to the winds. Almost the full history of Gonu was simulated (i.e. from 2nd to 8th June 2006, with cyclone beyond the TELEMAC domain on the 1st June). TELEMAC and TOMAWAC run with a time-step of 10 and 450 seconds, respectively, making TOMAWAC be coupled at every 45th to TELEMAC to limit the running time.

B. *Creation and use of wind and pressure parametric forcing files*

This work builds on developments by D. Kelly at the National Hurricane Centre (NHC) in Miami. An automatic tool has been developed that generates cyclone wind and pressure fields using the following cyclone information: the cyclone track positions (in latitude and longitude) and its intensity defined with both the maximum wind speed (and radius if available) and the storm central pressure. Such information can be downloaded from the Joint Typhoon Warning Center (JTWC, https://www.metoc.navy.mil/jtwc/jtwc.html?best-tracks) for most of the past cyclones and [8] provides a description of the cyclone data compilation and formatting. It is important to note that those tracks are the best available for now, however some data may be improved [10]. It is hoped that track data may be completed or may vary in the future. The tool uses formulations from wind model of Holland ([9]); this stand-alone binary tool can be run in either Linux or Windows and creates a Selafin forcing file.

For this work the tool has been run using JTWC-downloaded information on the super cyclonic storm Gonu and data have been refined in time using linear interpolation. The created atmospheric forcing file is read by the TELEMAC and the TOMAWAC models through the keyword BINARY ATMOSPHERIC DATA FILES. The fortran subroutine PROSOU.f has been amended and is called in the models steering files to adequately include the wind and pressure parametric fields.

III. MODEL CALIBRATION AND VALIDATION

Calibration process consisted in checking the wind fields generated from the JTWC-downloaded information. Once we were satisfied with the physics of the atmospheric forcing, wave generation has also been calibrated to reproduce wave time-series as measured at AW2, Chahbahar bay, Iran. The validation process was carried out by comparing the reported and simulated inundation lands and water levels. This modelled inundation will only be induced by wind stresses, pressure depression, and wave radiation forces. The lack of precipitation forcing, and of wave run-up process is discussed in the next sections.

A. *Calibration*

Just before Gonu landing, observations reported a wind strength of 20m/s at Muscat and 46 m/s at Ras al-Hadd. For those two locations, wind magnitude simulated differs by 7.5 and 22%, respectively (Table I). This mismatch may be due to the linear interpolation of data in the Gonu track and it is also probable that the landing induced some changes in wind dynamics that are not included in the [9]'s model.

To generate waves, the TOMAWAC parameters have been calibrated; the following parameters gave the best predictions: The wind generation followed Janssen's model (WAM cycle 4) associated with a standard value of wind generation coefficient (1.2) have been used. A linear wave growth has been chosen. Wind drag coefficient has been calculated using the Garratt (1977) [13] linear form, a formulation recommended for hurricane wind and used in the NHC Sea, Lake, and Overland Surges from Hurricane (SLOSH) model and the ADvanced CIRCulation (ADCIRC) model.

Table I : Wind strength in m/s measured and TELEMAC predictions during the Gonu event

Date	**06/06/2007 13:00:00**	**05/06/2007 evening**
Location	Near Muscat	at Ras al-Hadd
Model	18.5	36.0
Obs.	20 m/s	46 m/s
Relative error	7.5%	22%

Wave energy was dissipated by white-capping, bottom friction and depth-induced breaking. As waves propagate both in very deep water over the Gulf and in shallow water in coastal areas, non-linear transfer between frequencies (quadruplet interactions) was activated together with the triad interactions. A wave growth limiter was used to limit numerical instabilities; waves were not generated in water shallower than 0.4m. In Figure 2 the wave model reproduces the dynamics in wave growth but under-estimates the final wave height. This lack of wave energy (smaller wave height) agrees with the wind under-prediction.

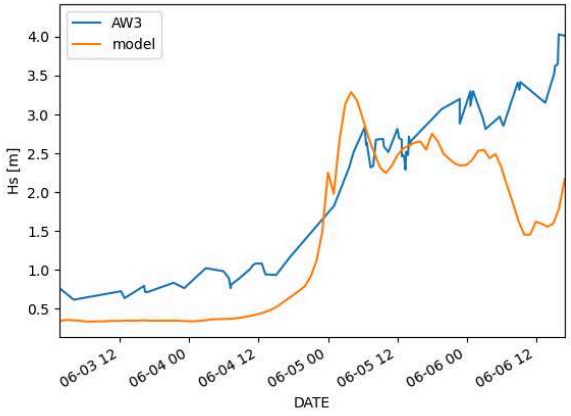

Figure 2. Evolution of wave height measured at station AW3 (extracted from [10]) and modelled during the Gonu event at the station AW3 location (see Figure 1)

B. Validation

The high-water mark (the elevation of the water level above the Mean Sea Level) was measured at Ras-al-Hadd on the 5th of June 2007 as 5 meters. In the model the wind and pressure-induced inundation levels are predicted to 0.8m in ebbing water topped up by 5 to 6 meters wave heights at the coast. The addition of the latter two components slightly exceeds the measured level.As reported in [1] land has been inundated during the Gonu cyclone event. The high-water marks reported in [2] have been plotted in Figure 3along with the prediction of maximum water levels and maximum wave heights from the model. We see that all inundated areas (at coloured diamonds locations) have been predicted to be under water, although there is a mismatch between the predicted and reported inundation levels. Inundation seems more important closer to the eastern tip of Oman, where wave heights are predicted to be large (more than 5m) and close to the shoreline. Wave runup effect is missing in the model and may explain the difference in inundation levels there. In the vicinity of Muscat high amount of rain has been reported ([11]) that are not reproduced in the model and may explain the differences between reported and predicted water levels.

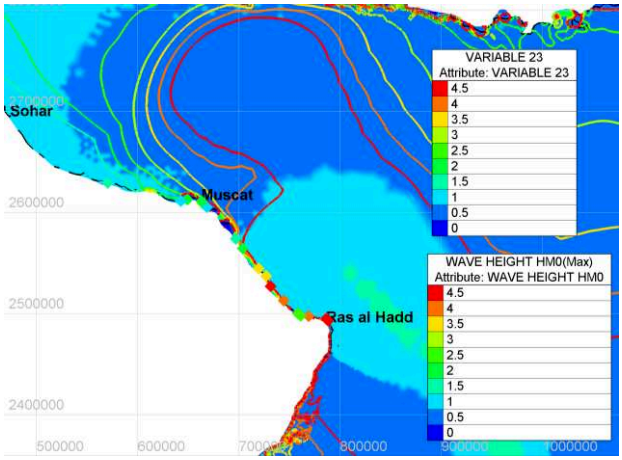

Figure 3. Modelled Maximum Elevation Of Water (m) predictions are indicated with the background colours, the maximum wave heights (m) are showed with the contour lines and the diamonds colour represents the reported high-water marks (m) from [2]

IV. GONU SIMULATION PREDICTION DETAILS

A. *Inundation at Ras al-Hadd*

The observed inundation extent at Ras al-Hadd was well reproduced in the model thanks to a well refined mesh at the coastal tip. The strong cyclone wind was pushing the water toward the lowest land at Ras-al-Hadd (Figure 3).

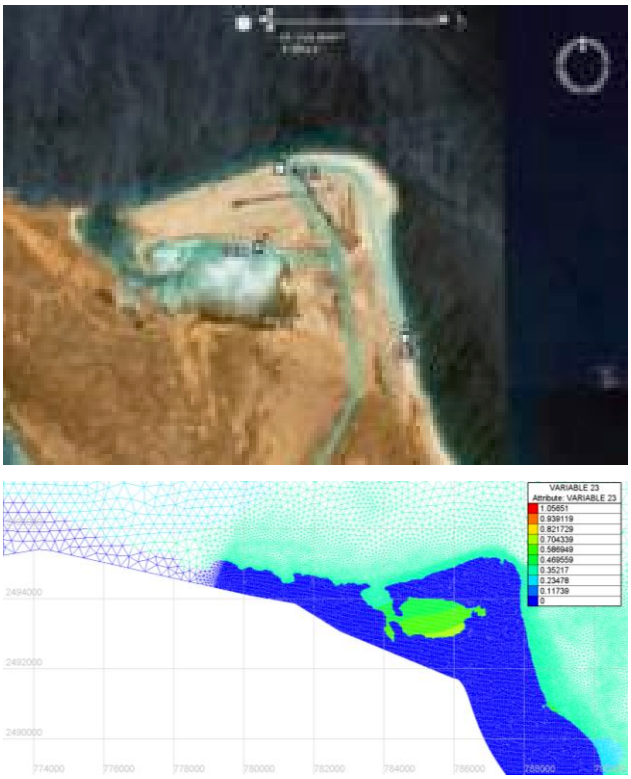

Figure 4. Inundated area near Ras al-Hadd (top, extracted from [2]) and simulated (bottom) MEOW at the end of the Gonu event

B. *Maximum predicted waves and water level*

The TOMAWAC simulated maximum wave height over the Gonu event agrees with the wave results from [10] using the WAVAD model (Figure 5). No calibration parameters are available within the WAVAD model and the wind model used was based on the parametric representation of [9].

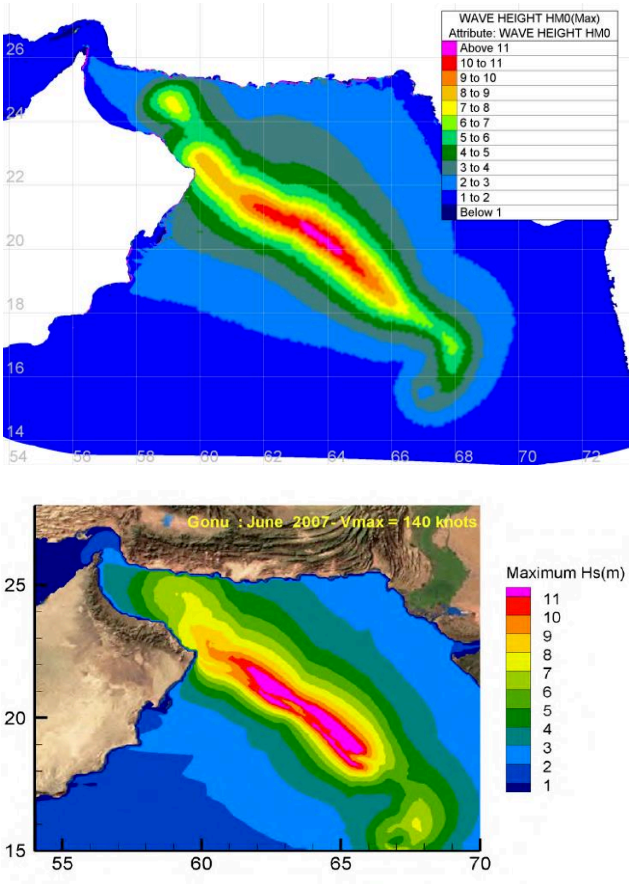

Figure 5. Max. Significant Wave height over duration of the cyclone. The scale runs from 1m (blue) to 11m (purple) for TOMAWAC predictions (top) and WMO-WAVAD predictions extracted from [10] (bottom)

V. REALISTIC STORM-LIKE-GONU WITH A MORE SOUTHERN LANDFALL

In this simulation we discarded the tide as we wanted to focus on the cyclone effect and look at the different cyclone components to better understand the storm dynamics before and when the cyclone land-fell in a low-lying coast of Oman.

A. *Simulation of alternative trajectories*

The initial Gonu track position has been moved by four degrees southward and the new cyclone trajectory landfalls at the Massirah island. Although it is probable that such a cyclone moving over shallow waters will be impacted by the seabed, it is very difficult to determine how the cyclone trajectory and strength may change near and after this landfall and it has been decided to not amend the strength in cyclone characteristics (maximum velocity, diameter, and lowest pressure).

B. *Cyclone components*

Impact along the track can be clearly seen in Figure 6 with the Maximum Elevation Of Water (MEOW) along the track of the cyclone.

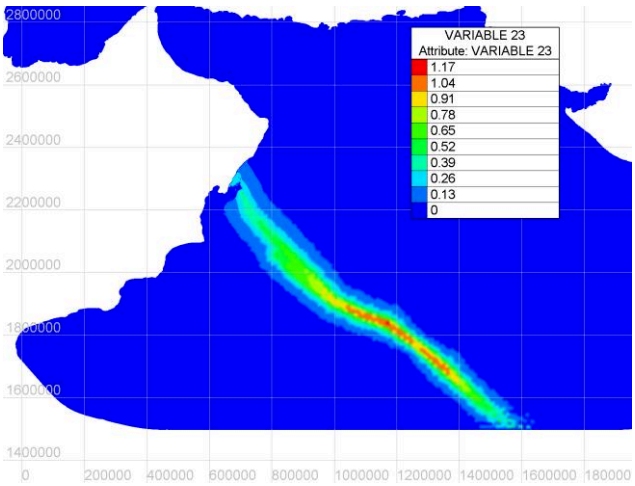

Figure 6. Predicted Maximum Elevation of Water (MEOW in m) over the simulation.

The wind and pressure effects on the maximum water elevation level can be seen in Figure 7. When the model is forced with the wind field only, the inundation happens next to the shoreline where the wind blows toward the south, and the water is pushed against the shore and piles up there; with both wind and pressure being forced, both coastal areas and along the storm track areas are subjected to a rise of water level, with the former being mainly driven by a wind-effect and the later by a pressure effect.

VI. RESULTS AND DISCUSSION

Although the model wind predictions reproduce the spinning dynamics of the wind field, some uncertainties in wind magnitude remain noticeably in vicinity of landfall. Underestimation in wind strength causes an underestimation in wave height predictions, although the overall maximum wave height is comparable to other validated model outputs. We hope that in the future the JTWC dataset will be improved with more accurate wind field when approaching the landfall.

The lack of wave run-up and rainfall can explain some mismatches between predicted and simulated levels of inundation. We assume the wave runup to be large when the cyclone is moving parallel and close to the northern Omani coast. It would be interesting to convert wave spectral predictions from TOMAWAC into wave time-series in water surface using the WAFO module in Python, similarly to what [12] did. The model is also missing the inundation triggered by extreme rainfall and flushing along valleys that has been reported [11], and further model development will focus on reproducing the inland and coastal inundation due to riverine flooding.

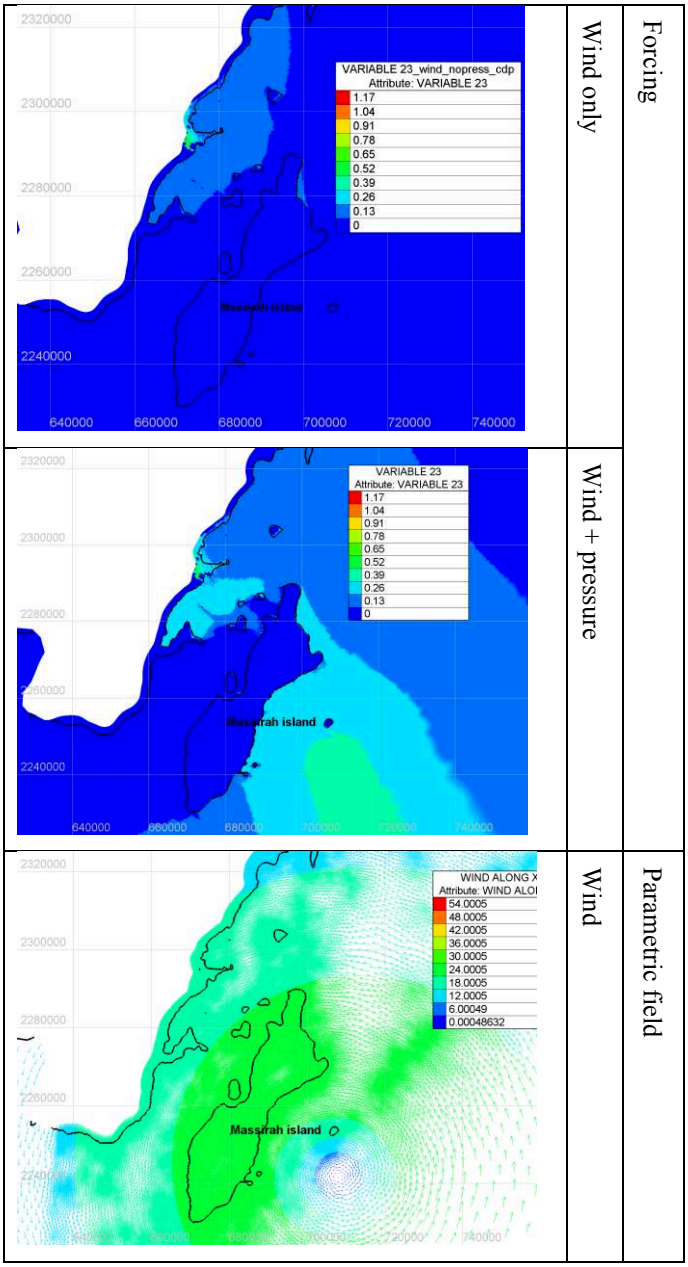

Figure 7. Prediction of the Maximum Elevation Of Water and wind field on the 6th June 2007,16:00 under the impact of the wind only or the impact from the wind and atmospheric pressure. The solid black line depicts the MSL contour line or shoreline.

VII. CONCLUSION

Tropical cyclones are extreme moving events that can become a real threat when approaching the coast by bringing high winds and inducing inundation. This inundation is due to the combined effect of inverse barometer, wind setup, wave setup and runup and rainfall superimposed on the tide. Here we introduce a tool to create cyclone forcing fields for TELEMAC and TOMAWAC that enables the run of a past or synthetic cyclone. The tool proves to be useful to investigate and separate the inundation factors.

REFERENCES

[1] Fritz, H.M., C. Blount, R. Sokoloski, J. Singleton, A. Fuggle, B.G. McAdoo, A. Moore, C. Grass, B. Tate (2007). Hurricane Katrina Storm Surge Distribution and Field Observations on the Mississippi Barrier Islands, Estuarine, Coastal and Shelf Sciences, 74(1-2):12-20, doi:10.1016/j.ecss.2007.03.015.

[2] Fritz, Hermann & Blount, Christopher & Albusaidi, Fawzi & Al-Harthy, Ahmed. (2010). Cyclone Gonu Storm Surge in the Gulf of Oman. 10.1007/978-90-481-3109-9_30.

[3] Fritz, Hermann & Naderi Beni, Abdolmajid. (2015). Comparison between the 2007 Cyclone Gonu Storm Surge and the 2004 Indian Ocean Tsunami in Oman and Hormozgan, Iran. Fifth International Conference on Estuaries and Coasts (ICEC2015), November 2-4, 2015, Muscat, Oman.

[4] Hassannezhad, M., Soltanpour, M., & Haghighi, S. (2011). 2D Hydrodynamic Modeling and Measurements of Chabahar Bay. Journal of Coastal Research, 1043–1047.

[5] Allahdadi, Mohammad Nabi, Chaichitehrani, Nazanin, Jose, Felix, Nasrollahi, Ali, Afshar, Ami, Allahyar, Mohammadreza (2018) Cyclone-generated Storm Surge in the Northern Gulf of Oman: A Field Data Analysis during Cyclone Gonu, American Journal of Fluid Dynamics, Vol. 8 No. 1, 2018, pp. 10-18. doi: 10.5923/j.ajfd.20180801.02.

[6] Soltanpour M, Dibajnia M. Field Measurements and 3D Numerical Modeling of Hydrodynamics in Chabahar Bay, Iran. ijmt. 2015; 3 :49-60 URL: http://ijmt.ir/article-1-226-en.html

[7] Al-Buloshi A, Al-Hatrushi S, Charabi Y (2014) GIS-based Framework for the Simulation of the Impacts of Sea Level Rise and Coastal Flooding on Oman. J Earth Sci Clim Change 5: 238. doi:10.4172/2157-7617.1000238

[8] Knapp, K.R., Kruk, M.C., Levinson, D.H., Gibney, E.J., 2009. Archive compiles new resource for global tropical cyclone research. EOS 90, 46.

[9] Holland, G. (1980). "An Analytic Model of the Wind and Pressure Profiles in Hurricanes". Monthly Weather Review. Volume 108. 1212-1218.

[10] Dibajnia, M., Soltanpour, M., Scott, D. (2009) An assessment of climate change impact on cyclone frequency and design wave height in the oman sea. In 1st WMO international conference on tropical cyclones and climate change (WWRP 2010 – 2), Muscat, Sultanate of Oman, 8 – 11 March 2009, Edited by: Salim Al-Hatrushi and Yassine Charabi Department of Geography Sultan Qaboos University, Muscat, Sultanate of Oman

[11] National Center of Meteorology and Seismology of United Arab Emirates, Abu Dhabi (2007) Gonu, the tropical storm.

[12] Hajivalie, Fatemeh & Arabzadeh, Ahmad. (2017). A 3D Numerical Study of Cyclone Gonu Waves Impact on Ramin Port. International Journal of Coastal and Offshore Engineering. 1. 33-41. 10.18869/acadpub.ijcoe.1.1.33.

[13] Garrat J.R. (1977) Review of drag coefficient over oceans and continents. Monthly Weather Review, American Meteorological Society

Forecasting tropical cyclone surge

Stephen Grey[1], Kate Day[1], Michael Turnbull[1]
s.grey@hrwallingford.com, Wallingford, UK
[1]: HR Wallingford Ltd, Howbery Park, Wallingford, OX10 8BA, UK

Abstract – **Tropical cyclones, with strong winds and low central pressure, can produce very large coastal surges and have led to the most devastating flooding in history. For example, in Bangladesh, flooding from cyclones in 1970 and 1991 has been estimated to have cost the lives of over 300,000 and 150,000 people respectively. While forecasting of cyclones and emergency management have improved dramatically, flooding from cyclone surge still represents one of the most serious global natural hazards and a considerable challenge for humanitarian organisations.**

In 2020, Cyclone Amphan was forecast to make landfall on the border of Bangladesh and India and the UK Foreign, Commonwealth and Development Office (FCDO) approached HR Wallingford to provide a forecast of the potential cyclone surge. Following that event, the FCDO commissioned a pilot study to develop the forecasting of flooding globally, including surge modelling, response of rivers to rainfall, modelling of flooding from both fluvial and coastal sources and analysis of the impact on local population and infrastructure. The aim of the forecast is to provide advance warning of the location, extent and severity of flooding and impact on population in order to aid the coordination of humanitarian relief. The service is provided by a partnership of ECMWF, the Universities of Reading and Bristol, Fathom and HR Wallingford.

As part of this service, a surge forecast system was developed using TELEMAC-2D forced by cyclonic wind and atmospheric pressure fields. The development of the system had to overcome a number of challenges:

- **The TELEMAC-2D models have to be large enough to cover all areas of interest to the FCDO and humanitarian agencies and at risk of flooding from cyclone surge;**
- **The models must adequately resolve the wind and pressure fields of cyclones and coastal bathymetry and topography;**
- **The models must include tide as it is the combination of both tide and surge that determines the elevation of the water and hence the extent and severity of flooding;**
- **The models must run quickly. The goal is to provide a bulletin within one working day and the target for the surge model runtime is less than one hour.**

The surge modelling system includes a number of regional TELEMAC-2D models covering areas of the world vulnerable to cyclone surge flooding and of interest to the FCDO. The regional models include tide and atmospheric forcing. Cyclone tracks are downloaded from relevant meteorological agencies responsible for forecasting tropical cyclones. Within the modelling system, these are converted into wind and pressure fields to force the model. Model results are extracted along the coastline for input into an inundation model and population exposure analysis. The combined results showing areas forecast to be affected by flooding and the impact on the local population and infrastructure are summarised in a concise bulletin for the FCDO. The bulletin is then circulated to local and international aid organisations including the UN OCHA and International Federation of Red Cross and Red Crescent.

Since the start of the pilot study in October 2020, the team have responded to tropical cyclones affecting Central America, Mozambique, Madagascar and the Philippines.

Keywords: Hydrodynamic modelling; surge; flooding; tropical cyclones; forecasting.

I. INTRODUCTION

Tropical cyclones, with strong winds, low central pressure and intense rainfall can produce extensive and severe inundation whether from fluvial flooding, pluvial flooding or coastal surge. Flooding from tropical cyclones is one of the most serious global natural hazards and is a large risk to life, infrastructure, agriculture, food supply and shelter. One severe tropical cyclone can affect a very large area and population.

The humanitarian response to tropical cyclone flooding is challenging, often involving getting supplies of food and emergency shelter to remote areas and contending with damaged infrastructure and lines of communication. In addition, aid is required rapidly. Advance warning of a disaster can, therefore, be extremely useful in the planning and carrying out of humanitarian relief.

A. Background

In 2019 during the approach of Cyclone Idai to Mozambique, Malawi and Zimbabwe, a number of organisations were brought together to provide advance warning of fluvial flooding, and the impact on population, to the UK Department for International Development (DfID) to assist the coordination of humanitarian relief. These institutions (ECMWF, the Universities of Reading and Bristol and Fathom) produced warnings for fluvial flooding a month later during Cyclone Kenneth which affected a similar area of southeast Africa [1].

In 2020, as Cyclone Amphan approached northeast India and Bangladesh, HR Wallingford was approached by DfID as the flooding risk was from coastal surge. Using a model adapted from previous studies in the northern Bay of Bengal, a forecast for coastal surge was provided showing flooding was likely in eastern West Bengal and southeast Bangladesh.

Following these events where forecasts were provided on an ad hoc basis, the Foreign Commonwealth and Development Office (FCDO, formed by the merger of DfID with the Foreign and Commonwealth Office) brought the organizations together to develop a formal process to provide

advance warning for fluvial and coastal flooding from tropical cyclones as part of an ongoing service.

Since 2020, ECMWF, the Universities of Reading (UoR) and Bristol (UoB), Fathom and HR Wallingford (HRW) have developed a Flood Early Warning (FEW) advice service for potential severe flooding events from tropical cyclones including fluvial and coastal flooding.

This paper describes the use of TELEMAC-2D to provide forecasts of tropical cyclone surge as part of the flood forecasting system. Section II provides a brief overview of the whole flood forecast process. Section III describes the application of TELEMAC-2D and the challenges encountered in setting up a capability to model surge over wide areas of the globe. Section IV shows some results from two years of forecasting and Section V provides conclusions from the development and delivery of surge forecasts and discussion on further work.

II. THE FLOOD FORECAST PROCESS

The Flood Early Warning service is designed to provide a rapid response to a request from FCDO for advice in advance of a tropical cyclone making landfall and crossing vulnerable areas.

There are a number of stages to the FEW process. Some of the fluvial and coastal flood modelling and analysis is carried out in parallel. The main stages, also summarised in Figure 1, are as follows:

1) The FEW process is triggered by the FCDO following daily advice from the UK Met Office about global extreme weather,
2) The FCDO meets with the partner organisations (online) to decide on the appropriate response. The options are:
   a. Activate the FEW process,
   b. Pause, monitor and re-assess situation, with the option to issue a short (one paragraph) summary of the situation,
   c. Stop the process.
3) Following a decision to proceed, fluvial and surge flood modelling are carried out in parallel,
   a. Fluvial forecasting is carried out by ECMWF, UoR, UoB and Fathom,
   b. Surge modelling is carried out by HRW with predicted water levels passed to Fathom for inundation modelling,
4) Exposure analysis is carried out by UoB and Fathom to assess the impact on local populations and infrastructure,
5) The results of the forecasts and analysis are compiled in a bulletin delivered to the FCDO. The bulletin contains a one page summary followed by more detailed information and is designed to provide advice for the coordination of humanitarian relief.

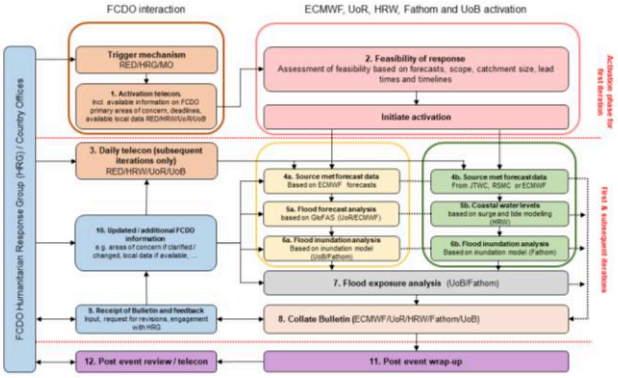

Figure 1. Flowchart showing the Standard Operating Procedures for the Flood Early Warning system following a trigger and activation

The above process is designed to be carried out over the duration of one working day. FCDO have shared the bulletin with organisations within the affected countries and international organisations such as the United Nations Office for the Coordination of Humanitarian Affairs (UN OCHA) and the International Federation of Red Cross and Red Crescent (IFRC).

The process may start up to five days in advance of cyclone landfall and may be repeated a number of times before and during the passage of the cyclone. After each event, the forecasts, advice and process are reviewed and compared with observations, reports from on-the-ground and feedback from FCDO.

III. MODELLING TROPICAL CYCLONE SURGE WITH TELEMAC-2D

TELEMAC-2D has been shown to be capable of simulating tropical cyclone surge [2] and has been used extensively either to hindcast surge caused by historical cyclones or synthetic cyclones to examine surge risk at a location or along a potentially vulnerable coastline [2]. Using TELEMAC-2D to forecast surge in advance of landfall throws up a range of technical and practical challenges.

A. Challenges

There are a number of factors that influence the arrangement and running of the TELEMAC-2D models in order to provide a good quality forecast of surge within the time scale and constraints of the FEW system.

- Models have to be large enough to cover all areas that are at risk of flooding from cyclone surge and of interest to the FCDO;
- Models must adequately resolve the wind and pressure fields of cyclones, coastal bathymetry and topography;
- Models must include tide as it is the combination of both tide and surge that determines the elevation of the water and hence the extent and severity of flooding;
- Models must run quickly. The target for the surge model runtime is less than one hour to fit in with the FEW schedule (Section II).

The cyclone modelling procedure and the basis of the models used in for FEW have been based on experience gained in projects where it has been necessary to model cyclones, for example to estimate extreme conditions for design of coastal and offshore infrastructure.

B. Meteorological forecast sources

The World Meteorological Organisation (WMO) recognises six Regional Specialised Meteorological Centres (RSMC) and four Tropical Cyclone Warning Centres (TCWC) as responsible for issuing tropical cyclone warnings within designated areas. In addition, the Joint Typhoon Warning Center (JTWC), based in Honolulu, issues warnings for the western Pacific, southern Pacific and Indian Ocean. The European Centre for Medium-Range Weather Forecasts (ECMWF) also provides global cyclone forecasts.

In order to have consistent forecasts and methods the surge forecasting system has initially been set up to run with forecasts from JTWC and the National Hurricane Center (NHC) in Miami. Both are US agencies and provide the same information in the warnings. In addition, and following the Flood Early Warning response provided for Cyclone Eloise, warnings produced by RSMC La Réunion have been included for southwest Indian Ocean cyclones and the Indian Meteorological Department (IMD) for the northern Indian Ocean.

The averaging period for which wind speeds are quoted is not consistent across the agencies. The US agencies, JTWC and NHC, use a 1-minute average wind speed as their maximum sustained wind speed convention. Most other agencies quote a 10-minute average wind speed. For modelling purposes, the 10-minute averaging period is more appropriate, so all wind speeds are converted to that standard following WMO guidance [3].

The agencies provide forecasts in the form of warning bulletins, an example of which is shown in Figure 2 from JTWC. Warning bulletins provide a forecast path of the cyclone at 12 or 24 hour intervals together with the maximum wind speed (V_{max}). Also provided by JTWC, NHC and RSMC La Réunion are the radii at which standard wind speeds are expected. These data are used to create time-evolving 2D fields of atmospheric pressure (at sea level) and wind (10m above sea level (ASL)) which are then used to drive the surge model.

```
WTXS32 PGTW 220900
MSGID/GENADMIN/JOINT TYPHOON WRNCEN PEARL HARBOR HI//
SUBJ/TROPICAL CYCLONE 12S (ELOISE) WARNING NR 011//
RMKS/
1. TROPICAL CYCLONE 12S (ELOISE) WARNING NR 011
   03 ACTIVE TROPICAL CYCLONES IN SOUTHIO
   MAX SUSTAINED WINDS BASED ON ONE-MINUTE AVERAGE
   WIND RADII VALID OVER OPEN WATER ONLY
    ---
   WARNING POSITION:
   220600Z --- NEAR 18.8S 38.0E
     MOVEMENT PAST SIX HOURS - 255 DEGREES AT 15 KTS
     POSITION ACCURATE TO WITHIN 020 NM
     POSITION BASED ON CENTER LOCATED BY SATELLITE
   PRESENT WIND DISTRIBUTION:
   MAX SUSTAINED WINDS - 065 KT, GUSTS 080 KT
   WIND RADII VALID OVER OPEN WATER ONLY
   RADIUS OF 064 KT WINDS - 025 NM NORTHEAST QUADRANT
                            025 NM SOUTHEAST QUADRANT
                            025 NM SOUTHWEST QUADRANT
                            025 NM NORTHWEST QUADRANT
   RADIUS OF 050 KT WINDS - 040 NM NORTHEAST QUADRANT
                            040 NM SOUTHEAST QUADRANT
                            040 NM SOUTHWEST QUADRANT
                            040 NM NORTHWEST QUADRANT
   RADIUS OF 034 KT WINDS - 110 NM NORTHEAST QUADRANT
                            100 NM SOUTHEAST QUADRANT
                            090 NM SOUTHWEST QUADRANT
                            110 NM NORTHWEST QUADRANT
   REPEAT POSIT: 18.8S 38.0E
```

Figure 2. Example of a warning bulletin from JTWC

C. Cyclone wind and pressure fields

1) Wind and pressure profile

For each tropical cyclone selected for modelling, time-evolving wind fields are set up based on the information included in the track data. At each model time step, a cyclonic wind field is set up based on the Holland parametric profile model [1][5][7].

The Holland model describes a profile of wind speed radially from the centre of the cyclone. Here, as the warning bulletins list maximum wind speed much more often than central pressure, we have followed [5][7] where the radial wind speed profile at 10 mASL is defined relative to the reported maximum wind speed (rather than central pressure), skipping the need to convert from gradient-level to 10 mASL wind speeds.

The cyclonic wind speed at radius r from the centre of the cyclone is:

$$V_{cyc}(r) = V_{max}\left\{\left(\frac{R_{max}}{r}\right)^{B} e^{\left[1-\left(\frac{R_{max}}{r}\right)^{B}\right]}\right\}^{1/2} \quad (1)$$

where V_{max} is the maximum wind speed, R_{max} is the radius of maximum wind and B is a shape parameter which describes the rate of decay of the wind speed beyond the radius of maximum wind.

The cyclonic wind direction is applied tangentially with an inflow angle, β, dependent on radius from the centre [8]:

$$\begin{aligned} \beta &= 10\frac{r}{R_{max}} && r < R_{max} \\ \beta &= 75\frac{r}{R_{max}} - 65 && R_{max} \le r < 1.2R_{max} \\ \beta &= 10 && 1.2R_{max} \le r \end{aligned} \quad (2)$$

Added to the cyclonic wind is the velocity of forward motion of the whole cyclone [8]:

$$V_{tot}(r) = V_{cyc}(r) + \frac{V_{fm}}{2}\{1 + \cos(\theta_{fm} - \theta_{cyc})\}\frac{V_{cyc}(r)}{V_{max}} \quad (3)$$

where V_{fm} is the velocity of forward motion and $\theta_{fm} - \theta_{cyc}$ is the difference between the direction of the cyclone motion and the direction of the cyclonic wind at the location under consideration. Hence, on the side of the cyclone where the cyclonic wind and the forward motion are in the same direction, wind speeds are higher than on the opposite side. The contribution from the forward motion velocity also decreases as the cyclonic wind speed decreases so that at the outer limits of the cyclone, there is no residual wind speed.

The sea level atmospheric pressure field is also based on the Holland model [1] and is assumed to be circularly symmetric. Pressure increases from the minimum at the centre of the cyclone and at radius r is defined by:

$$p(r) = p_c + (p_a - p_c)e^{-\left(\frac{R_{max}}{r}\right)^B} \quad (4)$$

where p_c is the cyclone central pressure and p_a is the ambient atmospheric pressure outside the cyclone.

2) Estimating R_{max} and B

The parameters used in the Holland wind field model, R_{max} and B, are estimated by fitting a Holland profile, with R_{max} and B as free parameters, to the V_{max} and the radii of wind speeds quoted in the warnings (Figure 2). An example is shown in Figure 3.

The fitting procedure is first carried out for the quadrant where the cyclonic wind and forward motion are in the same direction which is where the winds are strongest and, for a simple case of a cyclone making landfall on a long coastline, is the quadrant where winds are blowing onshore. This determines B and R_{max} for the forward quadrant. R_{max} is assumed to be constant for all quadrants but B is varied by fitting Holland profiles to the other quadrant wind speeds. Hence the wind field has some 2-dimensional structure. An example is shown in 0.

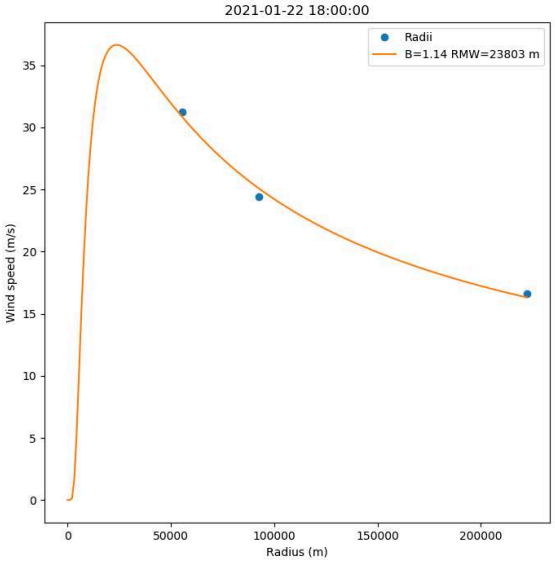

Figure 3. Example of fitting a Holland profile to radii specified in a JTWC warning bulletin

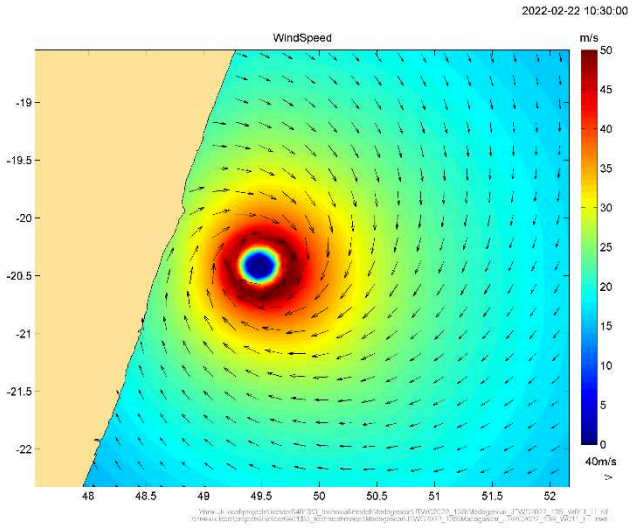

Figure 11 An example wind field from Cyclone Emnati as it approached the east coast of Madagascar in February 2022.

IV. RESULTS AND DEVELOPMENTS

At the time of writing, seven forecast responses have been provided to the FCDO which are listed in Table I. Development of the process has progressed as the forecasts have been run. Cyclone Amphan occurred before the formal start to the project and Hurricane Amphan very soon afterwards. Each response was an opportunity to learn and the modelling methods were developed. A sample of these cyclones, and the modelling process, are described below and used to illustrate the development of the system and how the challenges (listed in Section III.III.A) have been addressed.

Table I Tropical cyclones for which a TELEMAC2D model was run and a forecast provided to the FCDO

Cyclone name	Date	Affected countries
Cyclone Amphan	May 2020	India, Bangladesh
Hurricane Iota	November 2020	Nicaragua
Cyclone Eloise	January 2021	Mozambique
Typhoon Rai	December 2021	Philippines
Cyclone Batsirai	February 2022	Madagascar
Cyclone Emnati	February 2022	Madagascar
Cyclone Gombe	March 2022	Mozambique

A. *Cyclone Amphan*

The response for Cyclone Amphan was carried out hurriedly using an existing model of the northern Bay of Bengal. The TELEMAC-2D model of the Bay of Bengal was extended over the low lying land around the area of landfall. Automated systems had not been created and much of the preparation, such as interpretation of the warning advisory from the IMD, had to be done manually. The model was run with a constant tidal water level of +1.7 mMSL, equivalent to MHWS at the forecast location of landfall.

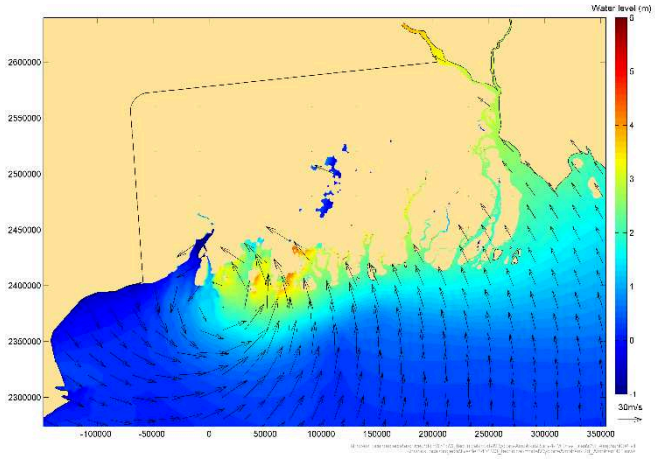

Figure 4. Water level as Cyclone Amphan made landfall close to the border of India and Bangladesh.

Figure 4 shows the predicted water level (relative to MSL) close to the time of landfall. While this was a very rushed response and some short cuts and approximations had to be made to achieve results in the time available, it was a valuable experience and a number of lessons were learnt :

- The model predicted flooding over an extensive area and, while quantitative data were not available to validate the predictions, the approximate location of inundation was consistent with anecdotal reports;
- The model did not include time-varying tide so predicted maximum water level could have been too high by up to 3 m depending on the time of peak surge relative to tidal phase;
- The response demonstrated the feasibility of forecasting cyclone-generated surge rapidly;
- For an effective operational service, the event showed the necessity for a well-organised system and models with as much automation as possible to ensure a fast delivery.

B. *Hurricane Iota*

Hurricane Iota developed in the Caribbean Sea and headed towards the east coast of Nicaragua. No existing local model was available at the time so it was decided to use the The Earth TELEMAC-2D model [9]. The global model works on a regular triangular mesh and the version relevant to cyclone forecasting has a grid spacing of approximately 16 km. There are finer resolution versions but these are computationally too expensive to run, at present, in a responsive forecast system.

The Earth TELEMAC-2D model bathymetry and coastline is based on GEBCO bathymetry data [10]. The Earth model has the advantage that it covers everywhere so can be deployed for any cyclone. However, there are disadvantages owing to the coarse mesh and generic nature of the model.

The model was used to predict surge for Hurricane Iota which made landfall on the Nicaraguan coast in November 2020 and this test illustrated both the benefits and drawbacks of the global model. The tidal range on the Caribbean coast of Nicaragua is very small so the model was run with a constant tidal level of mean sea level (MSL).

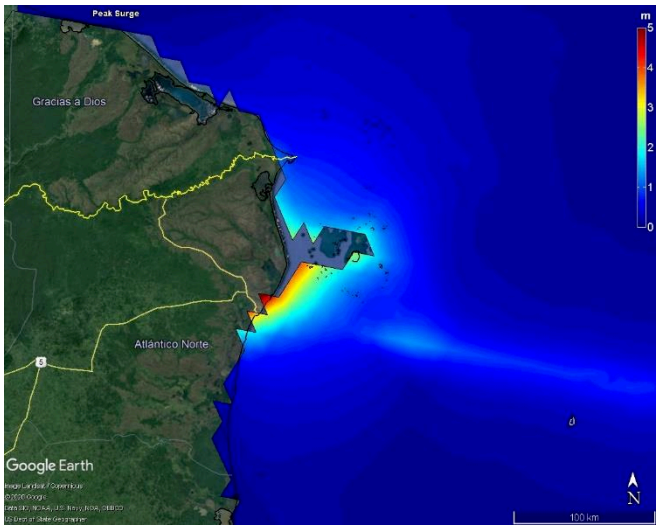

Figure 5. Hurricane Iota peak surge predicted by The Earth by TELEMAC.

Figure 5 shows the peak surge predicted by the Earth by TELEMAC model superimposed on Google Earth image. The effect of the coarse, regular grid can be seen in the artefacts in the model coastline, which joins node to node, creating the jagged line, compared to the smoother natural coastline. In addition to artificial triangular bays, the model has interpreted the offshore islands as a peninsular connected to the mainland.

- The Earth model is useful for identifying the locations at risk of large surge and potential coastal inundation in

locations where no regional high resolution surge model is available,

- The coarse resolution, regular mesh and bathymetric errors lead to unrealistic coastlines which affects the accuracy of predicted surge,
- The Earth at present does not represent tide well enough to be included in a model run and would require a longer spin-up period.

C. *Cyclone Eloise*

Following Hurricane Iota, and with the northern hemisphere cyclone season coming to a close, the focus moved to the southern hemisphere, with Mozambique identified as a country vulnerable to cyclones and coastal flooding. A regional model was set up covering the Mozambique channel and the full coast of Mozambique (Figure 6).

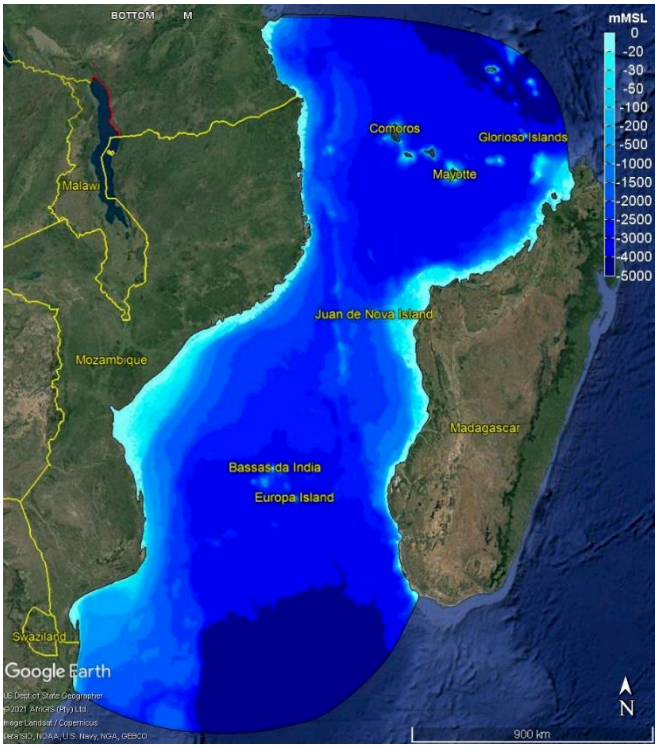

Figure 6. The TELEMAC-2D model area and bathymetry of the Mozambique Channel

The Mozambique Channel mesh spacing varies from 10 km in the open ocean to 1 km close to the shore. The flexible mesh allows the model boundary to follow the coastline. The model was extended to include coastal land up to approximately 10 mAMSL. Tide is imposed from the global tide model TPXO [11][12] along the offshore boundary of the regional model. The model was calibrated and represents the tidal water level variation well compared to Admiralty tide tables at ports around the coastline.

Cyclone Eloise made landfall on the coast of Mozambique just south of the city of Beira on 23/01/2021. The cyclone surge was forecast using cyclone warning bulletins from RSMC La Réunion and JTWC. Cyclone-generated surge was forecast from 21/01/2021.

The regional surge model was run with tide and atmospheric forcing based on the cyclone track forecasts from RSMC La Réunion and JTWC. The predicted high water mark, which includes both surge and tide, based on RSMC La Réunion warning bulletin No. 27 released at 0600 UTC 22/01/2021 is shown in Figure 7. The model is able to resolve the coastal features – such as the Rio Pùngué estuary next to Beira and the Baia de Sofala – where the water level is highest owing to constriction of waters driven into the inlets by the wind.

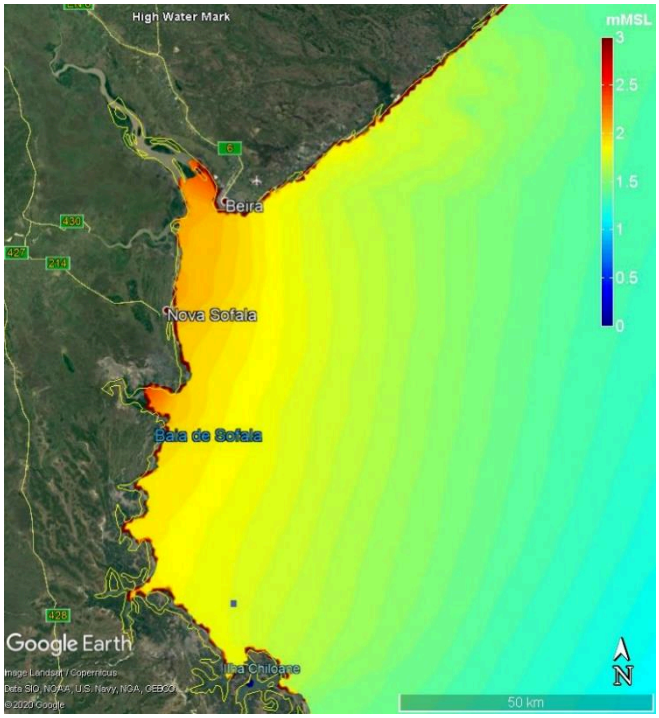

Figure 7. Maximum water level during Cyclone Eloise predicted by the Mozambique Channel TELEMAC-2D model

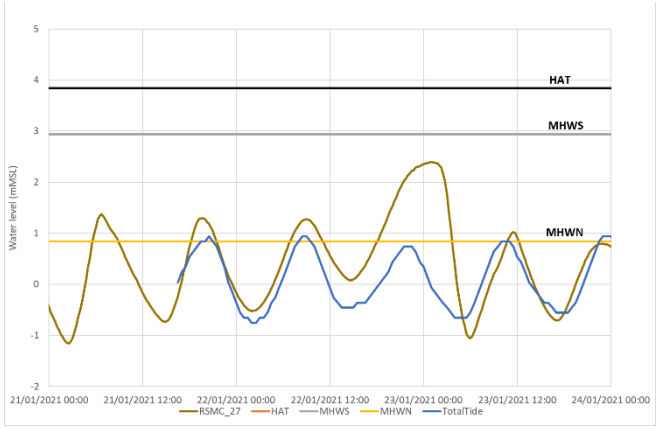

Figure 8. Time series of forecast water levels at Beira during Cyclone Eloise. Also shown are the tidal planes from Admiralty Tide Tables (horizontal lines) and a tide-only prediction from TotalTide.

The TELEMAC-2D runs resulted in time varying water levels which include tide and surge (Figure 8). Cyclone Eloise coincided with neap tides so, while the residual surge exceeded 2 m, the maximum water level was predicted to be lower than MHWS and so no widespread coastal flooding was expected. This appears to have been confirmed by anecdotal reports from the area.

- The model run was successful and included both atmospheric driven surge and time-varying tide.
- The model run-time was approximately 30 minutes on 36 cores of an HPC,
- The exercise demonstrated the advantage of a dedicated regional model.

D. Typhoon Rai

Typhoon Rai, known in the Philippines as Typhoon Odette, was a strong Typhoon that passed over the Philippines in December 2021. The storm underwent rapid intensification as it approached the Philippines and the JTWC estimated sustained wind speeds (1-minute average) of 140 kt before landfall.

A TELEMAC-2D model of the Philippines was available from previous projects but needed to be adapted to the purpose of predicting surge around the coast. The resolution was refined to approximately 1 km around all the Philippines coastline and the boundary and offshore resolution were optimised to maintain stability but with a practical run-time.

The complex topography and bathymetry of the Philippines make the representation of tides with a 2D hydrodynamic model particularly challenging. In addition to the complex coastlines with many islands and straits and a wide range of water depths, the western Pacific Ocean waters are stratified with a shallow mixed layer of typically less than 100m, and a steep thermocline below. The consequence is that currents, including those due to tide, are often baroclinic, and hence there are limitations to the use of a 2D model.

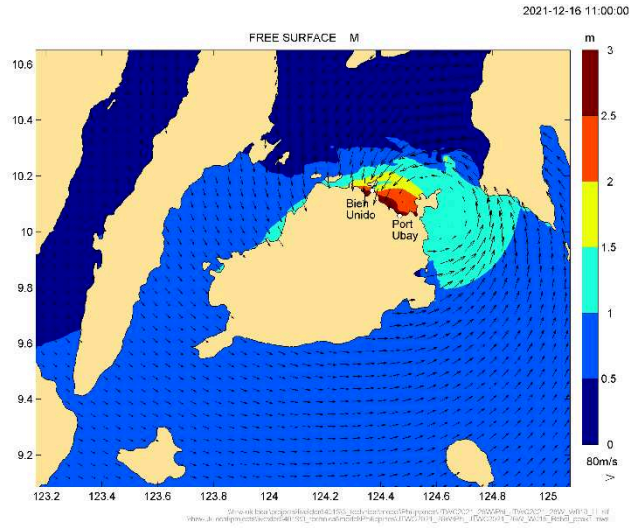

Figure 9. Predicted water level (relative to MSL) as Typhoon Rai passed the island of Bohol

The model was run with tide and no atmospheric forcing for a two-week spring-neap cycle in December 2021. Water levels were extracted at standard and secondary ports around the archipelago and compared with water levels based on harmonic analysis. TELEMAC-2D performs well at sites along the Pacific and South China Sea coasts but in some internal ports has a tendency to overpredict the range of the spring tide. This discrepancy may be because of the inability of a 2D model to represent baroclinic effects, as described above. Further tests to improve the model are ongoing but for now, overprediction of the tide will be compensated after the modelling stage with adjustments to the final water level predictions.

Some lessons from the exercise are:

- There are circumstances where 3D processes, which cannot be simulated by a 2D model, may make a significant contribution to the water level. This is likely to affect tide more than surge and may need compensation during in post-processing.
- In the case of islands, onshore winds may occur from any direction and therefore it is important to replicate the 2-dimensional structure of the wind field. The method, described in Section III.C, had been implemented before the Typhoon Rai. It is not possible, with this approach, to include the effects of island orography on wind fields which would a require a high-resolution atmospheric model.
- As the islands in the Philippines are of a similar scale to that of a cyclone, the predicted surge is very sensitive to the forecast track. TELEMAC-2D simulations using tracks forecast at different times and by different agencies produced noticeably different predicted surge although tracks varied by only tens of kilometres. This highlights a limitation of a deterministic approach and that a probabilistic approach should be considered.

V. CONCLUSIONS AND FURTHER WORK

A system to forecast tropical cyclone surge has been set up, is able to respond quickly when a cyclone is approaching and is a potential threat to a coastline and vulnerable population. TELEMAC-2D run times are typically 0.5 to 1 hours on 36 cores of a Linux HPC and, together with coastal inundation modelling, fluvial flood modelling and population exposure analysis, allow a warning bulletin to be provided to the FCDO within one working day. Forecasts have been provided with up to five days lead time with updates before and during landfall.

Warning bulletins have been shared with local government and non-governmental organisations, UN OCHA and IFRC and have allowed a head start to the humanitarian relief process.

A system has been developed to automatically download and process cyclone track warnings from meteorological agencies and create the steering files and atmospheric inputs required to run a surge forecast. Regional models have now been set up, calibrated and tested for:

- Bay of Bengal,
- Mozambique Channel,
- Philippines,
- Madagascar east coast,
- Caribbean Sea.

Validation data are very difficult to obtain in these areas of interest – there are very rarely tide gauge measurements available during the cyclones. Anecdotal reports have been generally consistent with predictions but it is often difficult to differentiate damage due to surge from other sources such as wind, fluvial and pluvial flooding. TELEMAC-2D has previously been validated for predicting cyclone surge in Australia [2], Bangladesh and The Bahamas. As more events are responded to, data may become available to assess the performance of the forecasting.

In terms of the location of cyclone surge, the largest source of uncertainty is the atmospheric forecast. As demonstrated by the Typhoon Rai tests, where the coastline is complex and detailed, a small change in cyclone track can lead to large differences in both the location and severity of the surge. This highlights a limitation of a deterministic approach.

ECMWF currently run a deterministic cyclone forecast on a high resolution model and ensemble model runs on a lower resolution model. The forecast tracks are publicly available and allow for the possibility of ensemble modelling of cyclone surge and the use of a probabilistic approach. There are practical implications for running 50 ensemble runs as well as the deterministic and the handling and processing of the resultant data. There will also be a need to consider the presentation of the results and how to effectively convey the predictions in a way that is comprehensible and useful to the recipients of the Flood Early Warning bulletins. A research project to investigate a probabilistic to surge and coastal flood forecasting is being discussed with the FCDO.

ACKNOWLEDGEMENTS

There are many people who have assisted with the development of the cyclone surge forecasting system and the individual forecasts. We would like to thank Rebecca Emerton, Calum Baugh and Christel Prudhomme of ECMWF, Justin Heming and Helen Ticehurst of the UK Met Office, Rich Heap and Emma Holden-Maillard of DAI and James Savage of Fathom. In HR Wallingford we have been assisted by Juliette Parisi, John Baugh, Olivia Bentley, Pedro Godinho, Alberto Riera, Paulo Martinho, Alan Cooper and several others.

REFERENCES

[1] R. Emerton, H. Cloke, A. Ficchi, L. Hawker, S. de Wit, L. Speight, C. Prudhomme, P. Rundell, R. West, J. Neal, J. Cuna, S. Harrigan, H. Titley, L. Magnusson, F. Pappenberger, N. Klingaman, E. Stephens, "Emergency flood bulletins for Cyclones Idai and Kenneth: A critical evaluation of the use of global flood forecasts for international humanitarian preparedness and response." International Journal of Disaster Risk Reduction, Vol. 50, pp. 101811, 2020.

[2] A. J. Cooper, M. Turnbull, S. M. Grey, and K. Day, "Tropical Cyclone Modelling with TELEMAC-2D", Proceedings of the XXth TELEMAC-MASCARET User Conference, Karlsruhe, pp.43-45, 2013

[3] S. M. Grey and Y. Liu, "A probabilistic approach to tropical cyclone modelling" International Conference on Offshore Mechanics and Arctic Engineering (Vol. 58851, p. V07BT06A009). American Society of Mechanical Engineers, 2019.

[4] B. A. Harper, J. D. Kepert and J.D. Ginger, "Guidelines for converting between various wind averaging periods in tropical cyclone conditions." WMO, Geneva, Switzerland, 2010.

[5] G. J. Holland, "An analytic model of the wind and pressure profiles in hurricanes", Monthly Weather Review, 108, 1212-1218, 1980.

[6] G. J. Holland, "A revised hurricane pressure–wind model" Monthly Weather Review, 136, pp.3432-3445, 2008.

[7] G. J. Holland, J. I. Belanger, and A. Fritz. "A revised model for radial profiles of hurricane winds." Monthly Weather Review, 138, pp.4393-4401, 2010.

[8] J. D. McConochie, T. A. Hardy, and L. B. Mason, "Modelling tropical cyclone over-water wind and pressure fields." Ocean engineering, 31(14-15), pp.1757-1782, 2004.

[9] S. Bourban, M Turnbull, A. J. Cooper, "The Earth by TELEMAC" Proceedings of the XXIVth TELEMAC-MASCARET User Conference, Graz, Austria, pp1-8, 2017.

[10] GEBCO Compilation Group, "*GEBCO 2020 Grid"* doi:10.5285/a29c5465-b138-234d-e053-6c86abc040b9, 2020.

[11] G.D. Egbert, A.F. Bennett, and M.G. Foreman, "TOPEX/POSEIDON tides estimated using a global inverse model". Journal of Geophysical Research: Oceans, 99(C12), pp.24821-24852, 1994.

[12] G.D. Egbert, and S.Y. Erofeeva, "Efficient inverse modeling of barotropic ocean tides." Journal of Atmospheric and Oceanic technology, 19(2), pp.183-204., 2002.

Modelling historical global tsunamis with TELEMAC

Thomas Saillour[1], Giovanni Cozzuto[1] , Giorgio Lupoi[1], Giovanni Cuomo[1], Sebastien E. Bourban[2]
tsaillour@studiosperi.it, gcozzuto@studiosperi.it, gcuomo@studiosperi.it, Palermo, Italy
sebastien.bourban@edf.fr, Paris, France
[1]: Studio Speri Società di Ingegneria S.r.l., Rome, Italy
[2]: EDF R&D LNHE / LHSV, Paris, France

Abstract – **This paper presents the results of a highly resolved metocean model of the world oceans and its application to the modelling of a selection among the most energetic transoceanic tsunamis, with particular emphasis on the Tōhoku tsunami. Thanks to its adaptive resolution and new features implemented in the source code, the model is able to better represent the complexity of the seismic source and predict the tsunami wave characteristics around the globe. After a short introduction and discussion of the possible representation of the tsunami source terms, the paper illustrates initial results and the accuracy of the model and introduces possible ways of improving the model performances, which includes modelling simultaneously the evolution of different physical processes (tides, surges, tsunamis) thanks to the versatility of the TELEMAC solver suite [2][1].**

Keywords: global, tsunamis, validation, TELEMAC-2D

I. INTRODUCTION

Predicting natural disasters and their likely impact on the natural and built environment is a fundamental step towards the development of better informed global risk management strategies, contributing to worldwide risk reduction and mitigation. In this context, accurate and effective modelling of tsunamis is not only vital for the safety of coastal communities, but contributes to the creation of safer and more resilient world.

The capacity of the TELEMAC solver to qualitatively model tsunamis at a global scale has already been proven in previous publications [4][7]. The purpose of this paper is to illustrate the implementation of state-of-art generation techniques and quantitatively compare the modelled tsunami waves heights with the DART buoys system.

Traditionally, seismically generated tsunamis modelling is initiated using the Okada model to translate earthquakes parameters (that can be inferred using, for example, joint earthquake source inversion techniques [3]), onto initial instantaneous deformation of sea bottom and/or ocean surface. Having the most accurate source possible contributes to improving the ability of any model to accurately represent the dynamics of the tsunami. With this in mind, we add new features in the source code of TELEMAC-2D, features that will be described further down the article. All the modelling described in this paper has been done using TELEMAC-2D.

The goal of this of the paper is trifold: (1) prove that TELEMAC can accurately predict Tsunami wave propagations, (2) demonstrate that tsunamis can be run at a global scale along with other processes – for instance tides – and (3) identify the weaknesses of the solver in order to propose the next axis of development for tsunami applications. The ultimate achievement being: bringing the solver to a sufficient level of accuracy to reliably provide tsunami alerts or risk assessments for national entities and communities.

II. TSUNAMIS

A succinct literature review has been undertaken in order to identify the most relevant tsunamis for this study. In total, more than 2700 events are registered on the NGDC/WDS Global Historical Tsunami Database [5].

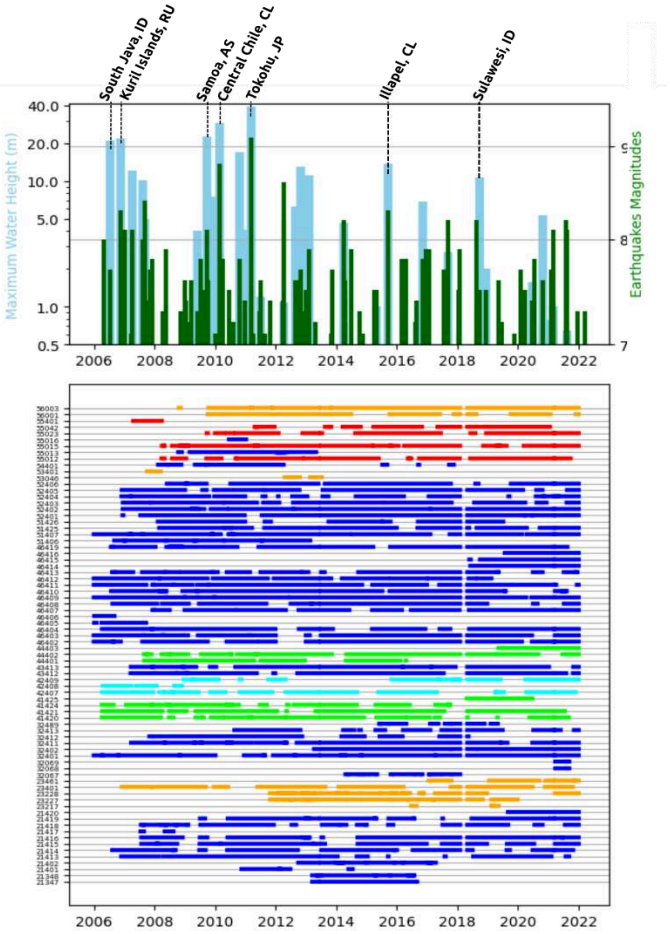

Figure 1. Top: tsunami runups in blue and earthquakes magnitudes in green. Bottom: superposition of the events with the DART system activity. Blue, green, orange, cyan and red colors indicate DART buoys in Pacific, Atlantic, Indian, Carribbean and Tasman sectors.

Figure 1 compiles all the highest observed runups and matched their timeline with the DART buoys activity in every ocean. The following criteria have been defined in order to refine the selection over the whole database: (1) the event has happened after the launch of the DART program in 2006, (2) the event had a runup higher than 10m and (3) the earthquake that generated the tsunami had a magnitude higher than 7.0 on the Richter scale. For every event matching the previously defined criteria (a dozen), the signal in the hours following the tsunami has been undertaken for each active buoy.

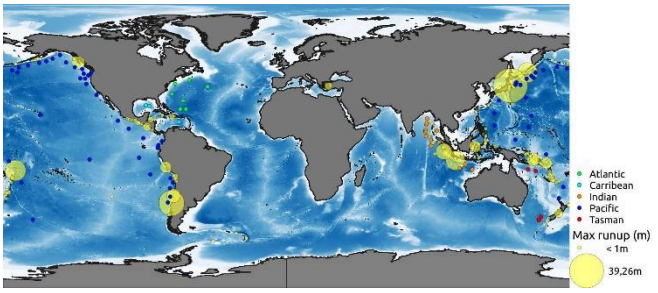

Figure 2. Tsunami runups since 2006 in yellow. Blue, green, orange, cyan and red circles indicate DART buoys in Pacific, Atlantic, Indian, Carribbean and Tasman sectors as referenced in Figure 1.

Figure 1 shows the repartition of the DART buoys around the world and the distribution of tsunami events since 2006, represented by their associated maximum runup. Among all events, only four of them had data recorded by more than ten DART buoys. Global tidal records can also be found [6], but the scope of this paper is to compare the deep water wave heights before investigating runup levels at tidal stations.

As the selection shrunk to the four events detailed in Table I, four global models have been setup. However, to illustrate the capacity of TELEMAC to quantitatively predict tsunamis (and also for the sake of the length of this paper), the results of only one study case will be fully detailed; the event with the biggest number of observations i.e. the Tōhoku tsunami in February 2011. The three other case studies will have their preparation and meshing detailed as a demonstration of the ability to model tsunamis at a global scale.

Table I Tsunami events and number of active DART buoys

Event	Time (UTC)	Magnitude	Number of buoys records
Tōhoku Japan	2011-03-11 05:46:24	9.1	28
Central Chile	2010-02-27 06:34:23	8.8	23
Illapel, Chile	2015-09-16 22:54:32	8.3	24
Samoa	2009-09-29 17:48:10	8.1	16

III. MESHING THE WORLD OCEANS

Since the scope of the model is to be able to account for the tsunami wave heights at a global scale, only global databases have been used for the setup of the model. The General Bathymetric Chart of the Oceans, developed by the International Hydrographic Organization (IHO) and the Intergovernmental Oceanographic Commission (IOC), provides gridded bathymetry data which covers lands and oceans around the whole globe with a resolution of ~ 0.004° (~ 450m). As mentioned in [4], unstructured grid generated for the study needs to resolve multiphysics metocean processes at different scales. Thus, the triangle mesh has an adaptive resolution, and an optimised procedure has been developed to size the mesh elements to effectively resolve the features of the bathymetry and the coastlines.

A tailored mesh has been created for each event, by enhancing its resolution in the vicinity of the source, in order to better model the initial conditions according to the sub-fault models, but also to better model the wave heights at the first location of impact of the tsunami. For all meshes, a common global mesh with a target resolution of 10km at the coastlines has been associated with a higher grade mesh with a resolution from 2km up to 450m close to the shores where the tsunami hit the coastlines first. The highest resolution is in fact limited by the input data (i.e. the resolution of the GEBCO bathymetry i.e. 450m).

Using a better defined bathymetry would have permitted a higher and better resolution of the final mesh, however evaluating the tsunami surge and inundations on the coastlines is not the scope of this paper… yet (see chapter VII: Perspectives). The number of nodes and elements of each unstructured mesh is specified in Table II.

Table II Tsunami events and number of active DART buoys

Event	Number of elements	Number of triangles
Tōhoku Japan	1 359 682	695 042
Central Chile	1 328 456	680 911
Illapel, Chile		
Samoa	1 054 588	543 345

Although there were four events selected, two of them happened in Chile. This is the reason why only *three* different meshes have been generated. For the Chilean configuration, the refinement in the resolution has been done so that both of the events (from 2010 or 2015) could be modelled using the same and only grid, represented in the centre inset of Figure 3.

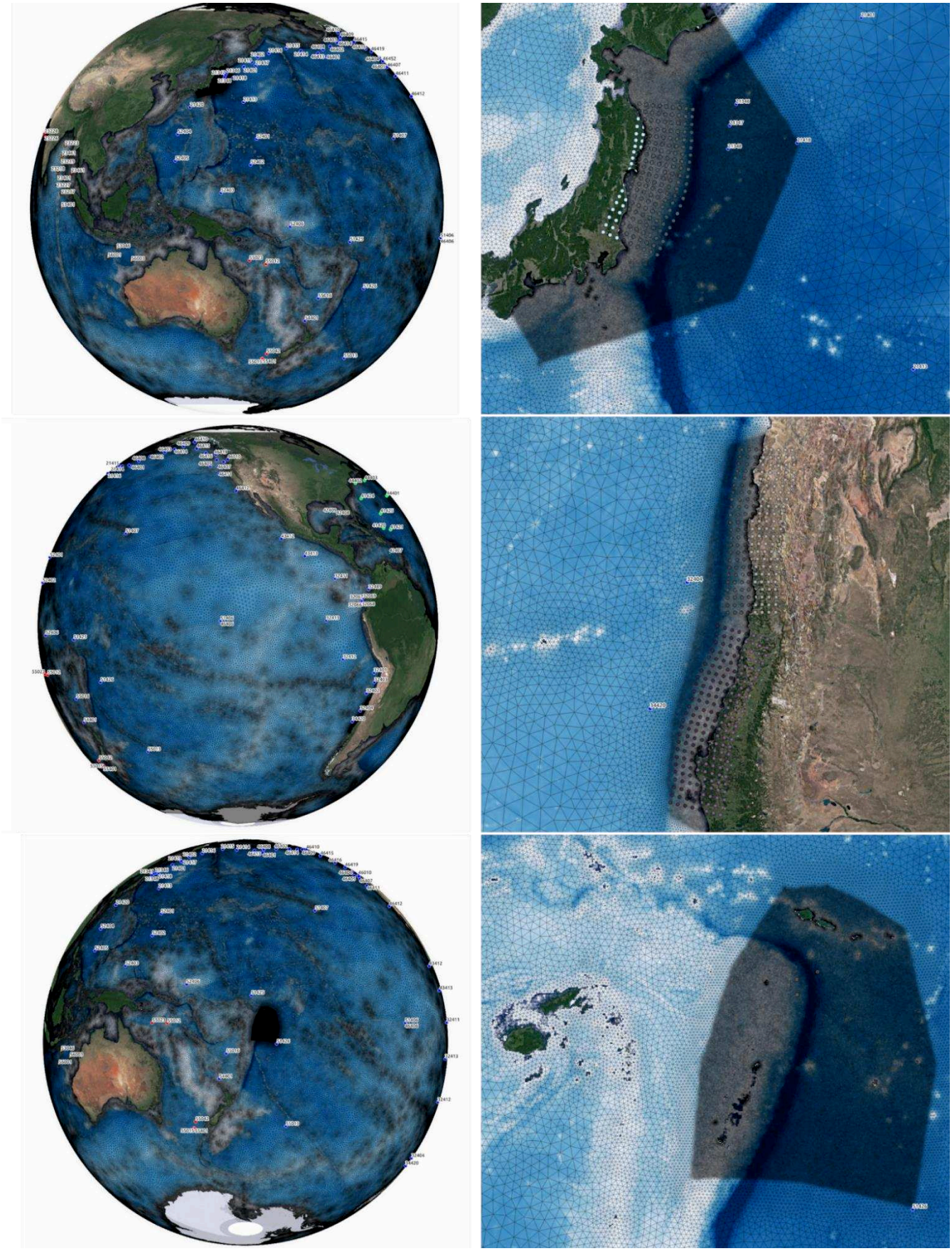

Figure 3. Unstructured grids for four events: Tōhoku 2011 (top insets), Chile 2010 and 2015 (centre) and Samoa 2009 (bottom insets). The fault models have been indicated with the points laying under the mesh

IV. MODELLING TSUNAMIS IN TELEMAC-2D

A. *The Okada model*

The Okada model [8] is widely used in earth and ocean science for specifying the deformations induced by seismic events. The Okada generator has been implemented since version v7p2 of the TELEMAC system in 2012 [7]. The seabed deformation is characterized by its focal depth D, its fault length L and width W, its dislocation (or slip) u, its strike direction d, its dip angle δ, its slip angle (or rake) ϕ, its epicentre coordinates (lat_E, lon_E) and the size E of the ellipse of influence of the tsunami. Tsunamis are enabled in TELEMAC-2D (and TELEMAC-3D) by the following keywords:

✓ OPTION FOR TSUNAMI GENERATION**; and**

✓ PHYSICAL CHARACTERISTICS OF THE TSUNAMI

A single fault model will then induce the following vertical bottom displacement ζ along x and y:

$$\zeta(x,y) = O(x,y,D,W,L,\delta,d,\phi,u,lat_E,lon_E,E) \quad (1)$$

with O being the Okada solution, (x,y) the latitude and longitude of a point in the model, and the ten input parameters for the Okada model, in the order they were defined above.

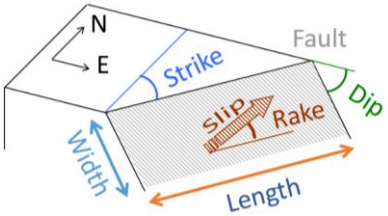

Figure 4. Tsunami characterisation and parameters used in Okada's solution

The Okada model generator implemented in TELEMAC only allows the generation of single faults source events and imposes the deformation ζ as an initial state condition at the beginning of the model. To obtain results comparable with the other software used in the literature [9][10][11], it was needed to add multi-source events but also enabling the *active* deformation of seafloor.

B. *Multi-faults tsunami sources*

Implementing multiple sources is rather simple, as is consists in defining the local deformation of the bottom displacement from each contribution of the finite fault model[12]. If the fault plane is discretised in N_x sub-faults along strike and N_y sub-faults along the dip angle, we define the final deformation of the earth surface as follows:

$$\zeta(x,y) = \sum_{i=1}^{Nx \times Ny} O(x,y,D_i,W_i,L_i,\delta_i,d_i,\phi_i,u_i,lat_i,lon_i,E_i) \quad (2)$$

If there are overlaps between the sub-faults, all the contributions from the co-seismic parameters of each fault are summed together. The following figure shows the difference between a single fault model and three different multi-faults models for the Tōhoku 2011 tsunami.

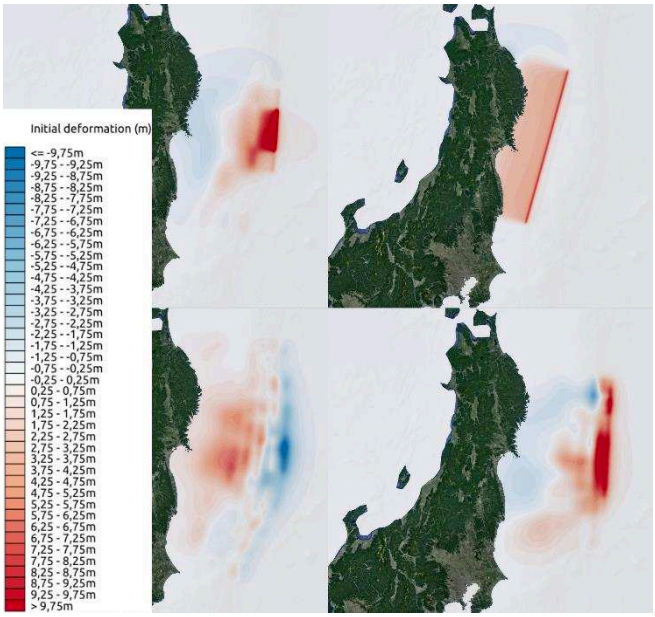

Figure 5. Representations of the initial condition for three different multifaults and one single fault models for the Tōhoku tsunami in 2011; Fuji 2011[13] with 40 sub-faults (top left), Ravi 2013[14] with one single fault (top right), Romano 2012[15] with 189 sub-faults (bottom left) and Yamasaki 2018[16] with 240 faults (bottom right).

A comparison between the signals generated by the different tsunami sources has been done for the closest active buoy to the tsunami source (DART 21418) and is represented in the next Figure 6. The single fault source from Ravi 2013 [14] will then be ignored for the Tōhoku case study as not fit enough to describe properly the bottom deformation for the initial state of the simulation.

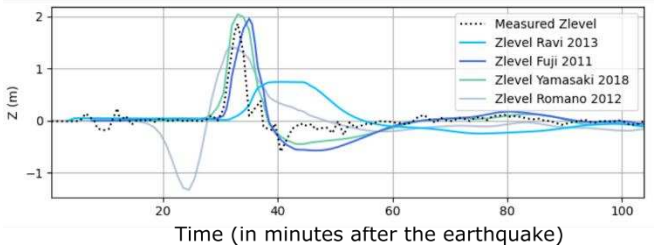

Figure 6. Signals measured and modeled at the closest active buoy to the earthquake epicenter (DART 21418).

C. *Passive and active tsunami generation*

The Okada generator routine uses Okada's solution as initial condition for the free surface, while all velocities are set to zero. We will follow the example of Mitsotakis[17], who defines this as the *passive* generation of a tsunami. The equations of the free surface at t = 0 are as follows:

$$\eta(x, y, 0) = \zeta(x , y) \; ; \; \mathbf{u}(x, y, 0) = 0 \quad (3)$$

with ζ(x , y) defined in equation (2)

The *active* generation is achieved by specifying zero initial conditions for both the free surface and the velocities and assuming that the bottom is changing over time. We define the sub-faults activation times t_i in order to trigger the

sub-faults ruptures in a desynchronized way. The bottom motion depends on the rising time t_r of the fault rupture. The deformation of the seabed is expressed as follows:

$$h(x,y,t) = D(x,y) + \sum_{i=1}^{N_x \times N_y} \mathcal{H} \cdot T \cdot O_i(x,y,\dots) \qquad (4)$$

where $\mathcal{H} = \mathcal{H}(t - t_i, t_r)$ is the Heaviside step function, and $T = T(t - t_i, t_r)$ is the trigonometric scenario of the bottom motion (Dutykh 2013[12]).

Although the literature cited above [12][17] refers to applications based on the use of numerical models solving the Boussinesq equations, the active generation – that is applying a dynamically changing seabed condition – is also valid for modelling using TELEMAC, as it adds velocities to the seabed deformation and thus generates bigger tsunami waves. The total time of the sea floor deformation (or rising time t_r) will impact the speed of the bathymetric motion and hence the amplitude of the tsunami wave.

The Figure 7 shows the influence of the rising time value on the amplitude of the modelled free surface. We also tried an instantaneous deformation of the seabed as it is used in some of the publications cited in this paper [13].

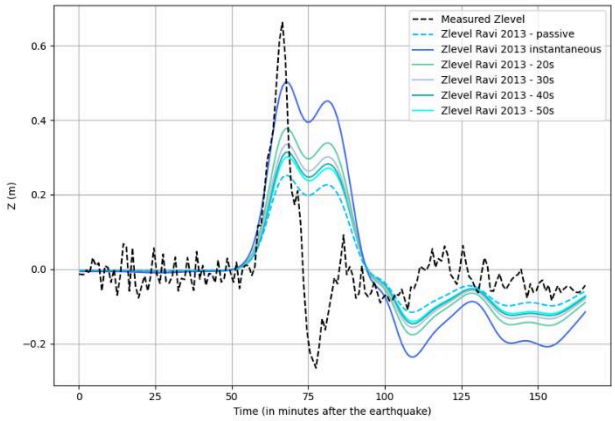

Figure 7. Influence of the rising time on the amplitude of the tsunami. Comparison done for the single fault description of the Tōhoku earthquake at one of the nearest active buoys (DART 21401).

We have introduced two new parameters (t_i and t_r) that we use for the generation of tsunamis. Each subfault is now characterized by 12 parameters: t_i, t_r, D_i, W_i, L_i, δ_i, d_i, ϕ_i, u_i, lat_i, lon_i and E_i which are the discretized parameters defined in (1) preceded by the activation time t_i and the rising time t_r of each subfault.

V. VALIDATION OF THE RESULTS

A. *Tōhoku 2011*

For the 2011 Tōhoku earthquake of 2011, three different multi-faults models have been considered and are detailed in the Table III. All the detailed information about the faults models is open source and available under the section "Supplementary Information" for all publications. (Or directly in a table of the publication for Fuji 2011). An *active* generation has been implemented for all three faults models. In the cited publications, Yamasaki 2018 [16] uses 32 seconds rising times t_r for the high resolution fault model (with 240 subfaults) with different initial activation times t_i, with a whole faulting time of 150 seconds, Fuji 2011[13] assumes a instantaneous deformation and Romano 2012[15] does not mention it. Following an iterative procedure of calibration, we finally also assumed an instantaneous deformation for all models.

Table III Source fault models used for tsunami generation in TELEMAC

Fault model	Number of faults	Size of the subfaults
Romano 2012 [15]	189	25km x 25km
Yamasaki 2018[a] [16]	240	20km x 20km
Fuji 2011 [13]	40	50km x 50km

a. Here we use the "Initial model P-MOD2. i.e. the 240 subfaults high resolution model. The authors also provide a downsampled and calibrated version of the model (TMOD model: 60 subfaults of 40km×40km). Both models gave us really similar results.

The source fault model propagation in Figure 8 corresponds to the Yamasaki 2018 configuration. Only the active DART buoys that recorded a tsunami signal are displayed on the map with their identification number.

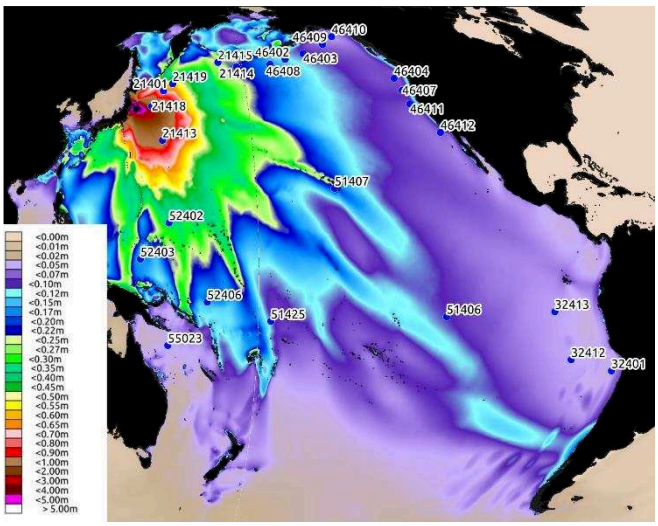

Figure 8. Maximum water level recorded in the Pacific after the event. Only active buoys are presented on the map.

The comparison between the results of the TELEMAC-2D models (using the 3 different faults configurations) are presented in the Table IV and in the Figure 9. Out of the 28 buoys that recorded a tsunami signal, 24 DART buoys were kept for the comparison in the following figures. In fact, for some buoys we couldn't filter out properly the tide constituents in the signal, due to too much noise or missing patches in the data signal.

The signal has been upsampled and "detided" using a simple low-pass filter. The upsampling was necessary because of the difference in frequency acquisition between DART's normal sampling time (15 min) and their Tsunami Response Mode sampling (15 seconds).

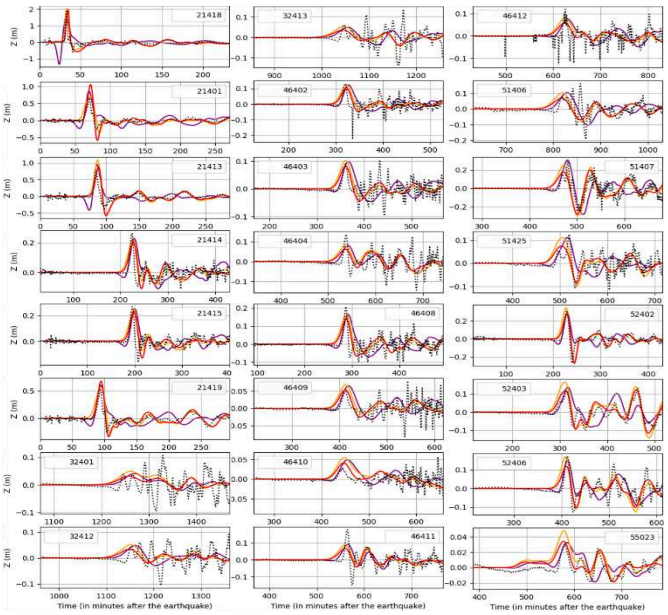

Figure 9. Comparison between the modeled free surface for all configurations (Fuji 2011 in red, Yamasaki 2018 in yellow and Romano 2012 in purple) and the measured free surface (dashed black line).

Table IV Comparison between the different model configuration and the measures at the DART buoys locations.

DART Buoy No	Distance (km)	a (m) measured	a (m) modelled using source by Fuji (2011)		a (m) modelled using source by Romano (2012)		a (m) modelled using source by Yamasaki (2018)	
21401	961	0,66	1,05	58%	**0,70**	5%	0,86	29%
21413	1190	0,77	**0,88**	15%	1,09	42%	0,96	25%
21414	3063	0,26	0,20	-23%	0,23	-14%	**0,23**	-13%
21415	2655	0,27	0,23	-15%	0,25	-8%	**0,25**	-6%
21418	507	1,87	**1,96**	5%	2,05	10%	1,42	-24%
21419	1279	0,54	0,68	27%	**0,56**	4%	0,61	13%
32401	16023	0,11	0,03	-70%	**0,05**	-54%	0,04	-62%
32412	14762	0,11	0,03	-69%	**0,05**	-53%	0,05	-56%
32413	13430	0,05	0,04	-27%	0,05	8%	**0,05**	0%
46402	4343	0,13	0,10	-21%	**0,13**	-3%	0,12	-6%
46403	4820	0,10	0,08	-21%	**0,10**	-2%	0,10	-5%
46404	6988	0,14	0,06	-54%	**0,08**	-40%	**0,08**	-40%
46407	7221	0,20	0,07	-66%	0,09	-57%	**0,09**	-55%
46408	3930	0,21	0,14	-33%	**0,17**	-21%	**0,16**	-21%
46409	5334	0,08	0,05	-32%	**0,07**	-13%	0,07	-17%
46410	5578	0,06	0,04	-31%	**0,05**	-9%	0,05	-19%
46411	7467	0,18	0,07	-63%	0,09	-51%	0,09	-49%
46412	8380	0,12	0,06	-51%	**0,08**	-33%	0,08	-37\%
51406	10768	0,16	0,07	-57%	0,10	-37%	**0,10**	-36%
51407	6142	0,30	0,20	-32%	0,25	-15%	**0,31**	4%
51425	6761	0,13	0,07	-40%	**0,11**	-11%	0,11	-10%
52402	3100	0,31	0,28	-11%	0,34	10%	**0,29**	-8%
52403	3784	0,13	0,12	-8%	0,17	25%	**0,14**	3%
52406	5320	0,17	0,12	-31%	**0,17**	-1%	0,15	-12%
55023	5961	0,03	0,03	14%	0,05	60%	**0,03**	9%

a. Comparison of the modelled and measured tsunami heights, as shown on Figure 9. In the column Distance, nuances of blue show the most distant DART buoys. For the comparisons, Green shows the best agreements and red the worst.

B. Discussion

1) Difference between the sources

The model results compare differently (Table IV) depending on the wave form used to initiate the model (Table III), and depending on the location of the buoy used for comparison.

Romano 2012 has an overestimated rundown prior to the first crest for the set of buoys nearest to the epicentre (DART 21418, DART 21401 and DART 21413) but the same rundown becomes appropriate in the Alaskan-Aleutian Islands sector (DART 46402, DART 46403 and DART 46408) or in Hawaii (DART 51407).

The Fuji 2011 configuration has the right crests in the vicinity of the tsunami but the rundown after the first wave is too important in the vicinity (DART 21401 and DART 21413, which are location between 900 km and 1100 km of the epicentre) of the tsunami and then becomes too weak in the far field.

The Yamasaki 2018 configuration has the best match overall and also is the one having the most accurate estimation for the waves/perturbations happening after the first tsunami hit.

2) Limitation of the use of TELEMAC-2D

Although the results of the three different fault models are slightly different, another immediate deduction is that there is better match between the model and the observation in the vicinity of the tsunami.

The further away from the tsunami source, the worse the model appears to match with measurements. The DART buoys offshore from the Californian coast (46404 and 46411) or from the Chilean coast (32401, 32412 and 32413) illustrate well the problem. The modelled incident waves have a longer wavelength than the ones measured (at least twice as long).

The increasing deviation we observe along the travelled distance is most likely due to the non-dispersive equations used to propagate the tsunami waves using TELEMAC-2D as we used the wave equation (default since v8p2).

Whilst this could be overcame using TELEMAC-3D the authors felt that the community would have benefitted from the present work which explores the use of TELEMAC-2D for modelling of some of the largest global tsunamis and identifies strengths and limitations of the use of this model for this purpose. The authors nevertheless intend to move onto the use of TELEMAC-3D as it represents the most obvious next step for the on-going development of the larger project of modelling the world oceans. Since the beginning, our approach has been that of increasing the level of complexity of the modelling gradually at every step of the project.

C. Other case studies

Whilst this paper presents only the results obtained modelling the most documented event, further information can be gathered from the next set of figures showing the max

tsunami-induced water elevation generated by the events enumerated in Table I.

1) Central Chile 2010

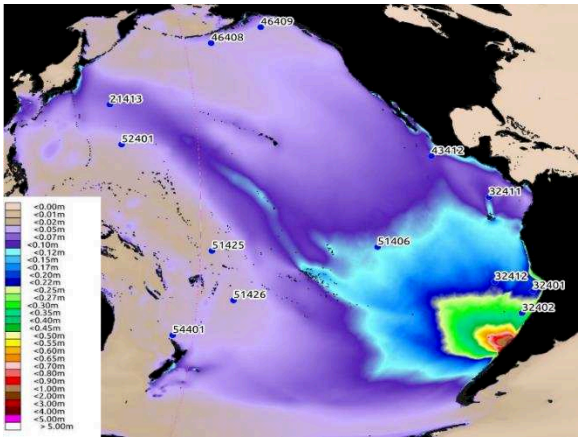

Figure 10. Maximum water level in the Pacific after the Chilean tsunami of 2010. Only the active buoys during the event are presented on the map.

2) Illapel, Chile 2015

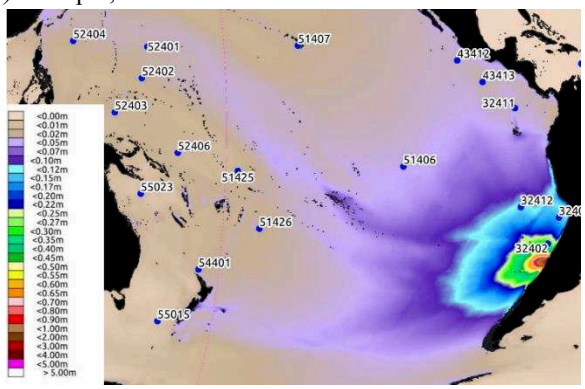

Figure 11. Maximum water level in the Pacific after the Chilean tsunami of 2015. Only the active buoys durting the event are presented on the map.

3) Samoa, 2009

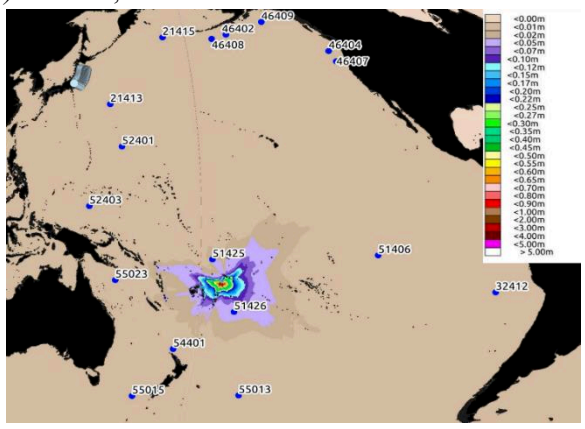

Figure 12. Maximum water level in the Pacific after the tsunami of Samoa in 2009. Only the active buoys during the event are presented on the map.

VI. RUNNING TIDES AND TSUNAMIS

The modification of the source code for the implementation of the active generation of tsunamis in TELEMAC-2D has permitted to add a temporal dimension for the triggering of the tsunami (thanks to the parameters t_i or initial activation time of the rupture fault). The following figure will just show – as a proof of concept – that multiple process can be handled in TELEMAC-2D i.e. tides and tsunamis simultaneously.

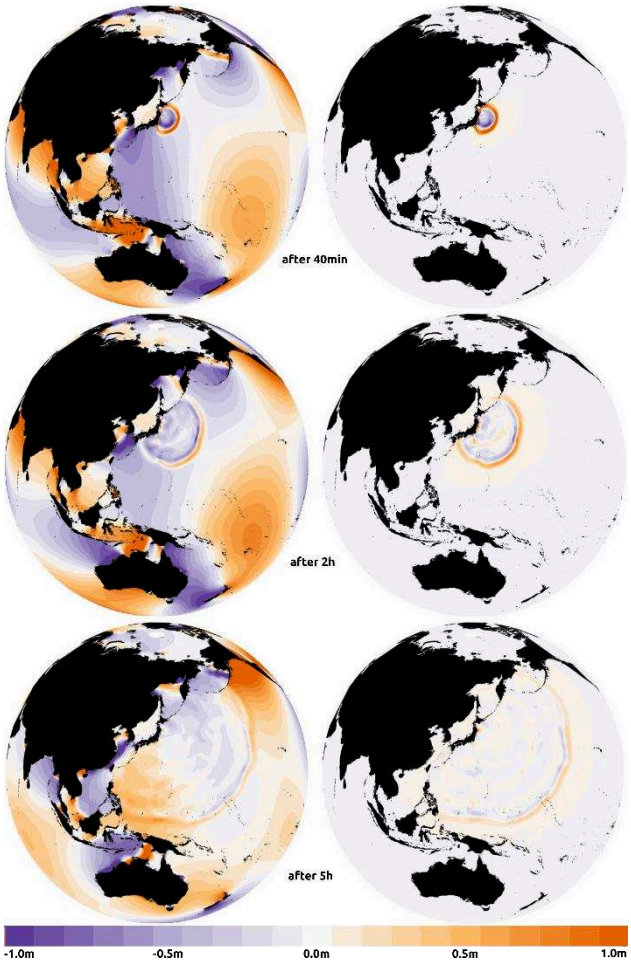

Figure 13. Snapshot comparison between the results with (insets on the left) and without (insets on the right) TIDE GENERATING FORCE. 40min (top), 2 hours (center) and 5 hours (bottom) after the earthquake

VII. PERSPECTIVES

A. TELEMAC-3D

As mentioned previously in the discussion of the results from the modelling, TELEMAC-3D is the next logical step for tsunami applications. In fact, a non-hydrostatic option is available in the code to solve equations that include the dynamic pressure allowing the resolution of the shorter wavelengths [18]. This feature will avoid having too much dispersion of tsunami waves in order to have a better estimation at the far-field locations. TELEMAC-3D will also enable a better representation of runups.

B. Runups

The three dimensionality that brings TELEMAC-3D will enhance the modelling of runups over complex coastlines. The non-hydrostatic option (mentioned in the last paragraph) will model with more accuracy tsunami surges over the shallower parts of the seabed, like trenches or steep slopes. Depending on the resolution of the bathymetric data, the estimation of surges and the modelling of inundations at the coastlines will also be possible.

The twin paper presented for this conference [19] will develop more on the on-going developments related to tsunamis runup using TELEMAC-3D.

ACKNOWLEDGEMENT

This research is being carried out as part of the SmartWave Project, funded by Regione Sicilia within the POR2014/20 EU framework. Authors wish to acknowledge the contributions of F. Oliva, A. De Prisco, S. Leo, D. D'Elia, F. Simonelli.

REFERENCES

[1] J.C. Galland, N. Goutal, J.M. Hervouet, “TELEMAC: A new numerical model for solving shallow water equations”, Advances in Water Resources, 1991, Volume 14, I. 3.

[2] J.M. Hervouet, R. Ata, User manual of open software TELEMAC-2D, Report, EDF-R&D, 2017, http://www.opentelemac.org/, ISBN:9780470035580.

[3] J. Weston, A.M.G. Ferreira, G. J. Funning, Joint earthquake source inversions using seismo-geodesy and 3-D earth models, Geophysical Journal International, Volume 198, Issue 2, August, 2014, Pages 671–696, https://doi.org/10.1093/gji/ggu110

[4] T. Saillour, G. Cozzuto, F. Ligorio, G. Lupoi, S.E. Bourban, Modeling the world oceans with TELEMAC. In: A.W. Breugem, L. Frederickx, T. Koutrouveli, K. Chu, R. Kulkarni, B. Decrop, Proceedings of the papers submitted to the 2020 TELEMAC-MASCARET User Conference October 2021. Antwerp: International Marine and Dredging Consultants (IMDC), 2021, S. 86-91.

[5] National Geophysical Data Center / World Data Service: NCEI/WDS Global Historical Tsunami Database. NOAA National Centers for Environmental Information. doi:10.7289/V5PN93H7 [01/09/2022]

[6] Flanders Marine Institute (VLIZ); Intergovernmental Oceanographic Commission (IOC): Sea level station monitoring facility, 2022. Accessed at https://www.ioc-sealevelmonitoring.org on 2022-09-01 at VLIZ. DOI: 10.14284/482

[7] S.E. Bourban, M.S. Turnbull, A.J. Cooper, The Earth by TELEMAC. In: C. Dorfmann, G. Zenz, Proceedings of the XXIVth TELEMAC-MASCARET User Conference, 17 to 20 October 2017, Graz University of Technology, Austria. Graz: Graz University of Technology. 2017, S. 1-8.

[8] Y. Okada, Internal deformation due to shear and tensile fault in a half space. Bulletin of the Seismological Society of America. 92, 1992, 1018-1040.

[9] Y. Yamazaki, K. F. Cheung, Z. Kowalik, T. Lay, G. Pawlak, NEOWAVE. In Proceedings and Results of the NTHMP Model Benchmarking Workshop, 2012, pp. 239–302. Galveston, TX: NOAA Special Report.

[10] G. Davies, F. Romano, S. Lorito, Global dissipation models for simulating tsunamis at far-field coasts up to 60 hours post-earthquake, multi-site tests in Australia, Front. Earth Sci ., 2020, 8 , 497.

[11] NTHMP. Technical Report. Proceedings and results of the 2011 NTHMP model benchmarking workshop. National Tsunami Hazard Mitigation Program, NOAA Special Report, 2012.

[12] D. Dutykh, D. Mitsotakis, X. Gardeil and F. Dias, On the use of finite fault solution for tsunami generation problems. Theoretical and Computational Fluid Dynamics, Springer Verlag, 2013, 27 (1), pp.177-199. 10.1007/s00162-011-0252-8. hal-00509384v3

[13] Y. Fujii and K. Satake, Slip Distribution and Seismic Moment of the 2010 and 1960 Chilean Earthquakes Inferred from Tsunami Waveforms and Coastal Geodetic Data, 2013, Pure Appl. Geophys. 170, 1493–1509.

[14] P.K. Ravi, Computer Simulation of 2011 East Japan. Earthquake and Tsunami. UTRIP-2013. 10th June - 19th July, 2013. https://www.s.u-tokyo.ac.jp/en/utrip/archive/2013/pdf/07RaviPrabhatKumar.pdf

[15] F. Romano et al. Clues from joint inversion of tsunami and geodetic data of the 2011 Tohoku-oki earthquake, 2012, Sci Rep 2, 385.

[16] Y. Yamazaki, K.F. Cheung and T. Lay, A Self-Consistent Fault Slip Model for the 2011 Tohoku Earthquake and Tsunami. J. Geophys. Res. Solid Earth 123, 1435–1458, 2018.

[17] D. Mitsotakis, Boussinesq systems in two space dimensions over a variable bottom for the generation and propagation of Tsunami waves. Mathematics and Computers in Simulation, 2009, 80(4):860–73.7

[18] A. Cooper, G. Cuomo, S.E. Bourban, Testing TELEMAC-2D suitability for tsunami propagation from source to near shore. In: S.E. Bourban, N. Durand, J.M. Hervouet, Proceedings of the XIXth TELEMAC-MASCARET User Conference 2012, 18 to 19 October 2012, St Hugh's College, Oxford. Oxfordshire: HR Wallingford. S. 89-92

[19] G. Cozzuto, T. Saillour and G. Lupoi, Tsunamis induced run-up benchmarking with Telemac3D, unpublished.

Modelling runoff for extreme rainfall events on large catchments using TELEMAC-2D

Jean-Paul Travert[1], Florent Taccone[1], Vito Bacchi[1]
jean-paul.travert@edf.fr, Chatou, France
[1]: National Laboratory for Hydraulics and Environment, EDF R&D, Chatou, France

Abstract – **The increase in frequency of intense rainfall events throughout the world brings new challenges that necessitate mitigation measures. Some conceptual hydrological models are already used to estimate discharge at outlet of catchments linked to 2D hydrodynamic model to simulate the downstream floods. However, with the increase of computation capacities, it may be possible to use physically based hydraulic models to simulate runoff directly on large catchments. This paper presents a preliminary application of runoff modelling on large catchments using TELEMAC-2D. The goal is to set up a complete methodology for simulating runoff on large scales. First, a convergence study on catchments of different sizes is done to test the model mesh resolution and has shown that the mesh resolution for these specific applications should be at least 25 m. Second, for catchments larger than 50 0000 km², it is possible to decompose them in sub-catchments and chain the simulations from upstream to downstream to address issues such as simulation time or preparation of data on too large scales. Third, initial investigations have underlined a high sensitivity to the water infiltration parameters particularly towards the end of the simulations when different rainfall events are considered over a long period of time. Even though initial results are encouraging, further investigations are recommended to better characterise infiltration and roughness coefficients at this scale, based on a wider variety of rainfall events and catchments.**

Keywords: floods, runoff, large catchments, SWE, infiltration

I. INTRODUCTION

Extreme floods have become more frequent and severe in the recent years exacerbated by climate change. There are numerous recent examples of major floods such as the July 2021 catastrophic flooding events in Germany [1] and in China [2], or the floods of the streets of Agen in France in September 2021 [3]. These extreme events caused human casualties, high economical costs and damages in sensitive areas. To design appropriate mitigation measures, especially under increasing urbanization and decreasing infiltration rates, numerical models are proactive tools widely used.

Conceptual rainfall-discharge models are often used to evaluate the discharge at the outlets of defined catchments during rainfall events. However, a physically based model, that geographically maps the geometry and the physical properties of a watershed, could be more efficient, because it allows using spatialized water depths and velocities data in the catchment with a better accuracy than the conceptual rainfall-discharge models. Some rainfall-discharge models using the Shallow Water Equations (SWE) in 2D, have already been used successfully for extreme events on rather small catchments up to 100 km² [4][5][6].

These models have been tested on small catchments, but there is still a need to test the capacity and the relevance of numerical models as TELEMAC-2D (www.opentelemac.org) to respond to these issues on larger scales. In this context, the main objective of this work is to explore a numerical strategy to simulate runoff on a large catchment with a good accuracy both for discharges and water depths and evaluate the computation cost, necessary for practical applications.

In this paper, the study area and the available data of the chosen event and catchment are presented. Then, a mesh convergence is carried out to check that the models on larger catchment than the literature remain valid. Finally, based on the mesh convergence, a model built by splitting the larger catchment into sub-catchments is presented along with its calibration for the infiltration and bottom friction laws. The results are compared with hydrometric stations within the catchments.

II. STUDY AREA AND DATA

A. Rain event

During the night of the 8th to the 9th of September 2021, extreme rain precipitations have fallen over the South-West of France. More than 130 mm of precipitations were registered over Agen in only a few hours (an absolute record for its hydrometric station), over 50 mm of rainfall on most of the Garonne catchment and even higher amounts locally during the night, as shown in Figure 1.

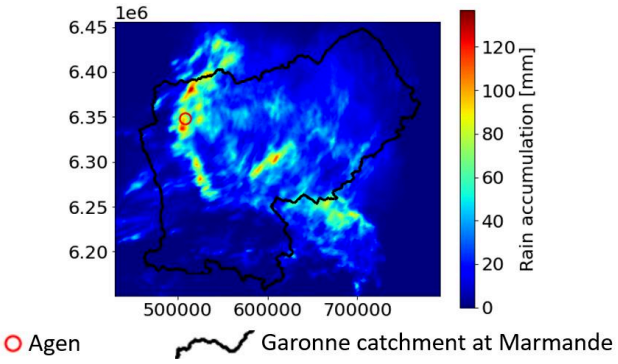

Figure 1. Rain accumulation during the night of the 8th of September.

There were also two other significant events in the following days that will be considered in the model. These rain events happened over the region from the 9th of September at 3

pm to the 10th of September at 5 am and between the 14th of September at 3 pm to the 16th at 2 am.

B. Study area

The study area is the region of Agen and its topographic catchment. Considering that there is no validated data at the hydrometric station of Agen, the outlet of the catchment is placed 50 km downstream of Agen at Marmande where there is a hydrometric station with validated data. The catchment's area can be visualized in Figure 2 (in blue). The area of the catchment (hereafter referred as Garonne catchment) is more than 50 000 km². A smaller sub-catchment (hereafter referred as Hers catchment) is considered, for a purely numerical viewpoint to compare results of the large and small models and to have preliminary results on a smaller scale. This catchment is represented in orange in Figure 2 and is about 786 km².

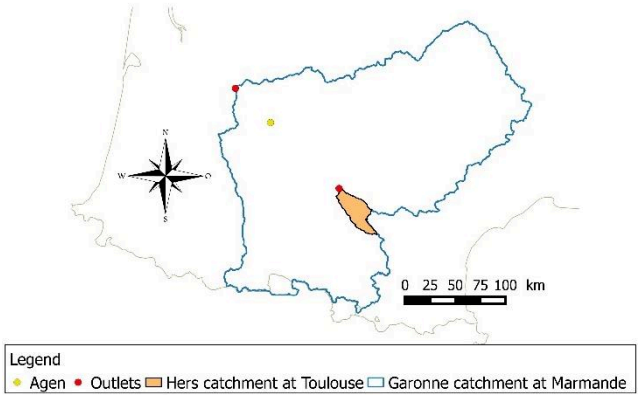

Figure 2. Delineation of the catchments of interest.

C. Data

Most of the data used are open-source data.

Waterways' discharge and water depths are recorded by hydrometric stations that are freely available on a national database (hydro.eaufrance.fr). Within the Garonne catchment, more than thirty hydrometric stations have available data to compare with the results of the model. For instance, in Figure 3 is presented the discharge at the Marmande hydrometric station for the period of 10 days following the start of rainfall. This record is used for the model calibration.

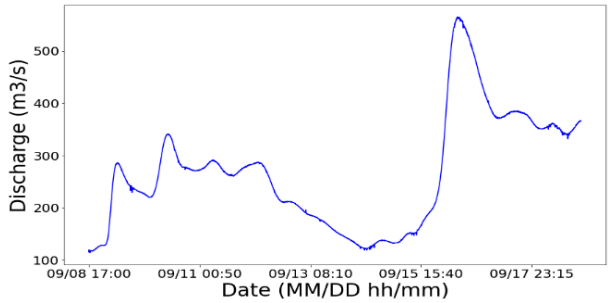

Figure 3. Observed discharge at the hydrometric station of Marmande.

The topography of the numerical model, which is a key parameter when it comes to runoff with SWE, is extracted from the Digital Elevation Map (DEM) of France, at 1 m resolution, measured by Laser Imaging Detection And Ranging (LIDAR), and produced by the National Institute of Geographic and Forest Information (www.ign.fr). The land use is extracted from the Corine Land Cover (CLC) 2018 product provided by the Copernicus Mission, at a resolution of several decametres, and the soil hydrological groups from the Food and Agriculture Organization at a resolution of 250 m. Rainfall data can be extracted from radar products provided by "Météo France", at 1 km resolution every 5 minutes. These data are given in a raster form with the accumulative rainfall over the last 5 minutes for each image. The three events of rain (see section II.A) have been bought from "Météo France". With each image an additional raster is provided to describe the quality of the measurements. On the whole dataset, there are more than 110 000 points of measurements.

III. MATERIAL AND METHOD

The different simulations are performed using the two dimensional (2D) hydrodynamic module (TELEMAC-2D v8p3r1) which solve free-surface flows in the two horizontal dimensions.

A. Overland flow simulation

TELEMAC-2D solves the 2D Shallow Water Equations [7], that are derived from the Navier-Stokes equations, averaged over the vertical with hydrostatic pressure assumption [8].

These equations write, in their conservative form:

$$\begin{cases} \frac{\partial h}{\partial t} + \frac{\partial hu}{\partial x} + \frac{\partial hv}{\partial y} = max(0, R - I) \\ \frac{\partial hu}{\partial t} + \frac{\partial \left(hu^2 + \frac{gh^2}{2}\right)}{\partial x} + \frac{\partial huv}{\partial y} = gh\left(-\frac{\partial z}{\partial x} - S_{fx}\right) \\ \frac{\partial hv}{\partial t} + \frac{\partial huv}{\partial x} + \frac{\partial \left(hv^2 + \frac{gh^2}{2}\right)}{\partial y} = gh\left(-\frac{\partial z}{\partial y} - S_{fy}\right) \end{cases} \quad (1)$$

where h $[m]$ is the water depth, t $[s]$ the time, u $[m \cdot s^{-1}]$ the flow velocity in the x-direction, v $[m \cdot s^{-1}]$ the flow velocity in the y-direction, R $[m \cdot s^{-1}]$ the rain intensity, I $[m \cdot s^{-1}]$ the infiltration rate given by an infiltration model (see section III.D), g $[m \cdot s^{-2}]$ the gravity constant, z [m] the bottom elevation, and S_{fx} $[-]$ and S_{fy} $[-]$ the friction slope in the x- and y-directions.

B. Numerical resolution

An unstructured triangular mesh is used to discretize the domain in space. These type of meshes enable a better adaptation to complex topography of a watershed especially for the river system.

To solve the SWE (1), TELEMAC-2D provides either finite element or finite volume schemes; the work presented here will be based on the finite volume scheme, for which a control volume C_i around each node P_i is constructed as shown in blue in Figure 4. The control volume passes through the centre of gravity for each adjacent node [9].

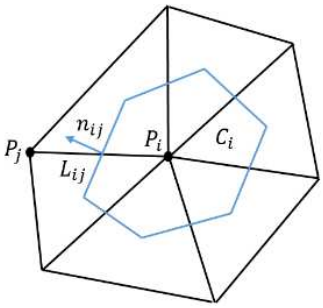

Figure 4. Representation of a control volume for unstructured 2D-meshes.

The SWE (1) are solved with a finite volume scheme. The scheme writes:

$$U_i^{t+1} = U_i^t - \sum_{j \in V_i} \left(\frac{\Delta t}{\Delta x_{ij}} F_{ij}^t + \frac{\Delta t}{\Delta x_{ij}} S_{ij}^t\right), \qquad (2)$$

where $U_i^t = (h_i^t, h_i^t u_i^t, h_i^t v_i^t)$ the state variables at time t at the node P_i, V_i all the nodes surroundings P_i, Δt the time step, $\Delta x_{ij} = \frac{C_i}{L_{ij}}$ with C_i the area of the control volume constructed around the node P_i and L_{ij} the length of the interface between the control volumes C_i and C_j, F_{ij}^t the numerical flux at the interface between C_i and C_j along the normal vector n_{ij} and $S_{ij}^t = \left(R_i - I_i, s_{ijx}^t, s_{ijy}^t\right)$ the source terms of mass and of momentum along x- and y-directions.

The SWE are solved with the equation (2) and the interface fluxes F_{ij}^t are calculated with the Kinetic method [10].

The main difficulty of this method is the representation of the source terms s_{ijx}^t and s_{ijy}^t with regards to the positivity of the water depth, the hydrostatic equilibrium and the management of the dry/wet interfaces for steep slopes. For some combinations of slope, mesh, and water depth, there could be some numerical instabilities generating negative water depths or not preserving the steady state depending on the discretization of these source terms.

To overcome this problem, a hydrostatic reconstruction is used in TELEMAC-2D. The discretization proposed by Chen and Noelle [11] writes:

$$\begin{cases} z_{ij} = min\left(max\left(z_i, z_j\right), min\left(h_i + z_i, h_j + z_j\right)\right) \\ h_{ij} = min\left(h_i + z_i - z_{ij}, h_i\right) \\ S_{ij} = \frac{g}{2}\left(h_i + h_j\right)\left(z_i - z_{ij}\right) n_{ij} L_{ij} \end{cases}, \qquad (3)$$

where S_{ij} represents the slope source term discretization.

C. Friction term

Two friction models have been tested to develop the methodology. At first, the Manning-Strickler law for bottom friction [12] is tested, that writes:

$$V = K_s \cdot R_h^{\frac{2}{3}} \cdot S_f^{\frac{1}{2}}, \qquad (4)$$

where K_s $[m^{\frac{1}{3}} \cdot s^{-1}]$ represents the Strickler coefficient, R_h $[m]$ the hydraulic radius, S_f $[\frac{m}{m}]$ the friction slope and V $[m \cdot s^{-1}]$ the mean velocity of the cross section.

The Strickler coefficients are derived from the characteristics of the catchments using CLC data with land use and related Strickler coefficients from the literature as defined in Table I.

Table I Strickler Coefficients with regards to the land use.

Overall nature of the surface	**Strickler coefficient ($m^{\frac{1}{3}}/s$)**
Waterbodies	35
Fields and meadows without crops	20
Cultivated fields with low vegetation	15 to 20
Cultivated fields with high vegetation	10 to 15
Shrubland and undergrowth areas	8 to 12
Areas of low urbanisation (town)	8 to 10
Highly urbanised areas (agglomeration)	5 to 8

The second model that was used in the catchment application is the friction term defined by Lawrence [13] to spatialize the friction term according to a constant size of roughness k_s $[m]$. This law is physically based and asserts that friction coefficient varies depending on a ratio of inundation $\Lambda = \frac{h}{k_s}$ $[-]$. When the water depth is low compared to the size of the roughness on the soil, the coefficient of friction is then high and inversely as illustrated in Figure 5. When the water accumulates in the hydraulic network the friction is then less important.

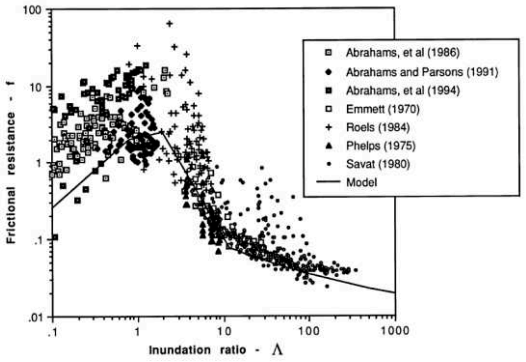

Figure 5. Frictional resistance in function of the inundated ratio [13].

The bottom friction law writes:

$$S_f = \frac{f}{8g} \frac{u|u|}{h}, \qquad (5)$$

with

$$f = \begin{cases} \left(\frac{1}{1{,}64 + 0{,}803\, ln(\Lambda)}\right)^2 \text{ if } \Lambda \geq 10 \\ \frac{10}{\Lambda^2} \text{ else if } 1 \leq \Lambda \leq 10 \\ \frac{8}{\pi} \cdot C_D \cdot min\left(\frac{\pi}{4}, \Lambda\right) \text{ otherwise} \end{cases}, \qquad (6)$$

where S_f $[-]$ is the friction slope, f $[-]$ the Darcy-Weisbach coefficient and C_D $[-]$ the coefficient of drag force of the rough particles fixed to 1 in [13] for roughly spherical particles even if it can vary with the shape of the particles.

It should be noted that this model is not yet included in the TELEMAC-2D official sources and has been added by the authors via specific development.

D. Infiltration model

The model Soil Conservation Service Curve Number (SCS-CN) [14] is a widely used model that is implemented in TELEMAC-2D [15]. This model estimates the net rainfall based on the rough rainfall and a spatially variable coefficient called the Curve Number (CN) that depend on the land use and the soil hydrologic group. For the higher CN, the potential of storage of the soil is lower and there is more runoff. With this model, it is considered that until a certain amount of infiltrated water (called initial abstraction) there is no runoff. Then, a part of the rain is infiltrated, and the other part runs off.

The equations of the model are listed below:

$$\begin{cases} P_e = \frac{(P-Ia)^2}{P+Ia+S} \; if \; P > I_a, \\ Pe = 0 \; otherwise \end{cases} \quad (7)$$

where $P\,[m]$ the rough rainfall, $P_e\,[m]$ the runoff, $S\,[m]$ the potential of storage of the soil and $I_a\,[m]$ the initial abstraction,

with $$S = (\frac{25.4}{CN} - \frac{254}{1000}). \quad (8)$$

The Figure 6 illustrates the principle of this infiltration model.

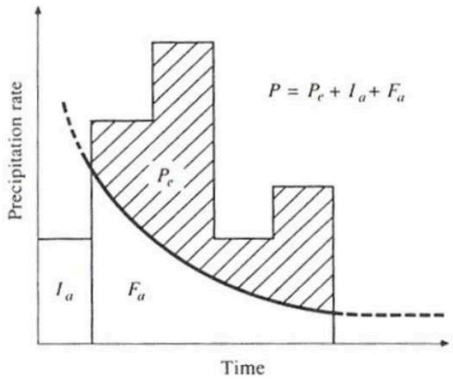

Figure 6. Scheme of principle of SCS-CN [16] .

This 0D model is simple, based on empirical data, and has the advantage of having only one variable CN to calibrate which represents the runoff properties at a node within the unstructured mesh mapping the watershed.

The usual $CN(II)$ values are determined for an initial abstraction of $Ia = 0.2S$ and normal antecedent moisture conditions. For dry ($CN(I)$ lowest runoff potential) or wet ($CN(III$) highest runoff potential) antecedent moistures conditions the CN values can be converted with the following equations [13]:

$$\begin{cases} CN(I) = \frac{4.2 \cdot CN(II)}{10 - 0.058 \cdot CN(II)} \\ CN(III) = \frac{23 \cdot CN(II)}{10 + 0.13 \cdot CN(II)} \end{cases}. \quad (8)$$

And when it is considered $Ia = 0.05S$, then the $CN(II)$ values are changed [17] to:

$$CN(II)_{I_a=0.05S} = \frac{100}{1.879 \cdot \left(\frac{100}{CN(II)} - 1\right)^{1.15} + 1}. \quad (9)$$

It should be noted that in the official sources of TELEMAC-2D numerical model, the routine was not adapted for rain varying in space and has been modified to include this feature.

For the interested reader, the authors also implemented and tested on basic cases the Green-Ampt [18] and Horton [19] models for infiltration with the same design as SCS-CN implementation [15]. These models will be available in the next version of TELEMAC-2D, but they have not been tested on real applications yet, such as the one described in this paper on large catchment.

E. Spatially variable rain

In the real case application, the rain is set spatially in time and space. In the TELEMAC-2D official sources it is already possible to include rain varying in space or in time, but not both simultaneously. In this study, we adapt the wind subroutine to read through a formatted file including the spatially variable rain. It is based on the example "wind_txy" from the official sources of TELEMAC-2D with the wind varying in time and space. In Figure 7 is described the structure of the formatted file for rain spatialization.

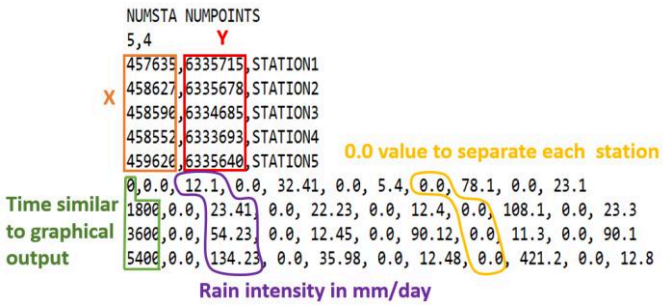

Figure 7. Example of formatted file for varying rainfall in time and space.

The number of stations and measurements should be provided, along with the coordinates of each station. For practical purposes, and to keep the same format as the "wind_txy" example, the time step for graphical output is set the same as for the measurements and the rain intensity is given in mm/day separated by a null value for each station. After reading the formatted file, the interpolation on the mesh is achieved using inverse distance weighting (IDW) method.

IV. MODELS

A two-step approach is presented in this paper. First, a mesh convergence is carried out based on the TELEMAC-2D models covering the whole catchments (Hers and Garonne). Then, the Garonne catchment is split into sub-catchments and results are compared against observations.

Both approaches, described hereafter in sub-section IV.A and IV.B, share similarities. The same numerical schemes described in III.A and III.B are used, and the meshes are both unstructured triangular constructed with BlueKenue (https://nrc.canada.ca). All the simulations are performed on

two of the best High-Performance-Computers (HPC) of EDF R&D.

A. Mesh convergence

1) Geometry

The first goal is to test the sensitivity of the model to the mesh size. A first 100 m resolution mesh was created for the Hers catchment and 800 m for the larger Garonne catchment. Then each triangle was divided by four resulting in resolution divided by two each time. Table II describes the meshes with their respective number of nodes.

Table II Specifications of the different meshes.

Catchment	Resolution [m]	Number of nodes
Hers	100	84 792
Hers	50	337 562
Hers	25	1 347 039
Hers	12.5	5 381 741
Hers	6.25	21 514 137
Garonne	800	84 916
Garonne	400	337 942
Garonne	200	1 348 327
Garonne	100	5 386 429
Garonne	50	21 531 961
Garonne	25	86 100 337

2) Boundary and initial conditions

As for the boundary conditions, a free surface elevation was set up downstream of the domains.

The hydrographic network has not been initialized.

3) Simulation duration

The total simulated time is 111 hours for the smaller catchment and up to 23 days for the larger one to be sure to simulate on larger scales than the time of concentration (time needed for water to flow from the most remote point in a watershed to the watershed outlet).

4) Friction term

For all simulations carried out for the mesh convergence, the Manning-Strickler bottom friction law was used on the Hers and on the Garonne catchments. Figure 8 shows the spatial variation of the Strickler coefficients on the two catchments.

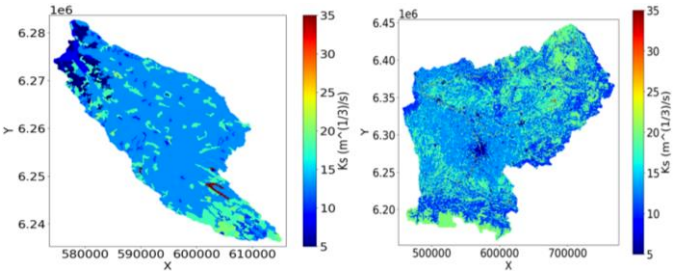

Figure 8. Spatially distributed Strickler friction coefficients (K_S) according to the catchment land-use and land-cover characteristics.

5) Rain inputs

For all simulations carried out for mesh convergence, the input was a constant rain over the domain of one hour with a precipitation rate of 50 mm/h.

B. Sub-catchments splitting application

1) Geometry and splitting of the catchment

The whole catchment is delineated into smaller sub-catchments, as shown in Figure 9.

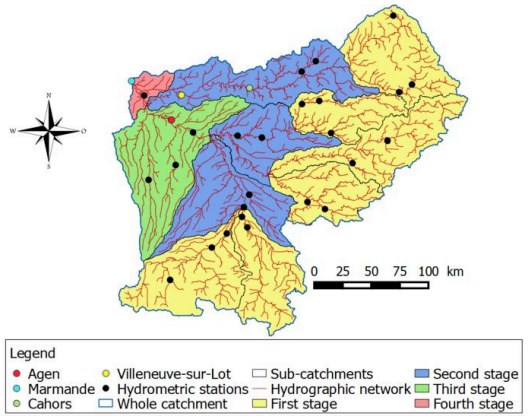

Figure 9. Decomposition of the domain into sub-catchments and hydrometric stations in the catchment.

The Garonne catchment of 50 558 km² has been divided in 11 smaller sub-catchments from 848 km² to 7225 km² from a filled DEM of 100 m resolution by computing the flow directions and the raster of flow accumulation (the functions "r.fill.dir", "r.watershed" and "r.water.outlet" from QGIS 2.6.1 (www.qgis.org) are used). A mesh with a resolution of 25 m (based on the results of the mesh convergence in section V.A) was created on each sub-catchments constrained by the hydrographic network from 1 461 977 to 12 446 175 nodes in their meshes. On each catchment a 25 m resolution DEM is used to extract the elevations and the hydrographic network.

2) Boundary and initial conditions

As for the mesh convergence approach, for each sub-catchment, a free surface elevation was set up downstream. For the catchments in the second to fourth stages in Figure 9, a prescribed discharge is set up upstream, considering the base discharge of the river at the hydrometric stations and the discharge at the outlet of the precedent stages.

The hydrographic network has been initialized in the sub-catchments by retrieving the base discharge before the rainfall event for filling the main river in the catchment, and then the computation restarts from this initial state. An important comment is that the bathymetric data are missing (for rivers the DEM represents the water surface and not the riverbed), and it could have a significant impact in terms of river flow.

3) Chaining of the simulations

The simulations are launched on HPC in parallel from the upstream of the catchment to the downstream by retrieving the discharge at the outlet of the upstream sub-catchments and using the discharge as boundary condition at the inlet of the downstream sub-catchments (as described in section IV.B.2).

The computational process is fully automated from upstream, to downstream with python scripts to create the discharge varying files (for the upstream boundary condition) and linux-bash scripts to chain the TELEMAC-2D simulations and python scripts.

4) Simulation duration

The simulation duration is 10 days on each sub-catchments which is larger than the concentration time of the whole Garonne catchment.

5) Friction term

The chosen bottom friction law is Lawrence. The Manning-Strickler seemed inadequate during initial testing as the CLC is not suited to determine the Strickler parameter within the rivers channel. The CLC map is designed for the flood plains where the roughness coefficients are not calibrated. For instance, in Figure 10, it is shown that along the black line representing the hydrographic network the Strickler coefficient is often too low with this approach.

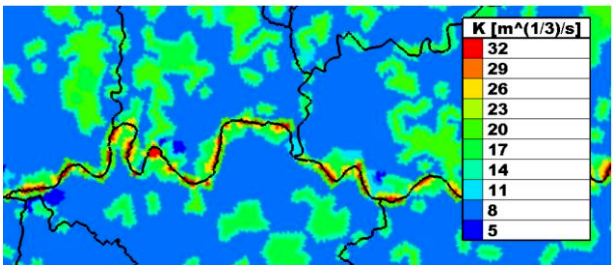

Figure 10. Strickler coefficients within one of the sub-catchments.

Furthermore, the Manning-Strickler law is well-defined for uniform and gradually varying flow but not for runoff with shallow water depths.

6) Rain inputs

The rain is set variable in time and space as explained in section III.E and extracted from the "Météo France" radar data. Only the three events described in section II.A are considered. During the periods between these events, the rainfall is not significant, and the results should not be affected by the lack of data. Indeed, the low rainfall rates between the events would get mostly infiltrated. For the formatted files, extracting all the stations on the whole watershed is not very efficient, and it can be gained three to four hours of simulation by sub-catchment by pre-treating the data and by considering only the stations within each sub-catchment.

V. RESULTS

A. Mesh convergence

In Figure 11 is presented the convergence study with the resolution of the mesh varying between 100 m and 25 m and representing the discharge at the outlet of the Hers catchment for a constant uniform rain of 50 mm/h.

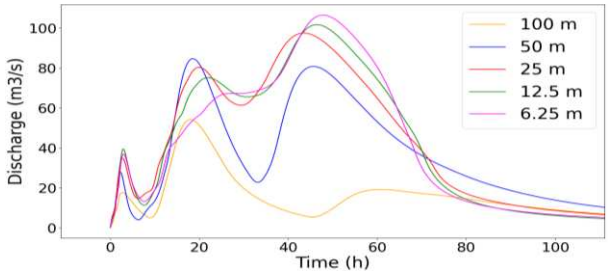

Figure 11. Mesh convergence: discharge at the outlet of Hers catchment.

It appears that the difference of discharge at the outlet between the different meshes is getting closer and is acceptable for a mesh resolution of 25 m. In Table III, the CPU times and the duration of the simulations are given.

Table III Simulation time for the hers catchment.

Resolution [m]	Number of processors	User time [h]	CPU time [days]	Simulated time [h]
100	96	0.03	0.1	111.1
50	96	0.27	1.1	111.1
25	96	3.00	12.0	111.1
12.5	288	8.76	105.1	111.1
6.25	1 056	31.95	1 405.8	111.1

For the 25 m resolution, the simulation time is also reasonable compared to the smaller resolutions, so it appears to be a good compromise between precision and simulation time.

In parallel, some other tests have been carried out to improve the convergence and to try to limit the computational cost. Figure 12 shows a comparison between methods of interpolation of the DEM on the mesh.

It has been tested for the nearest neighbour method (NNM) as well as for the IDW method.

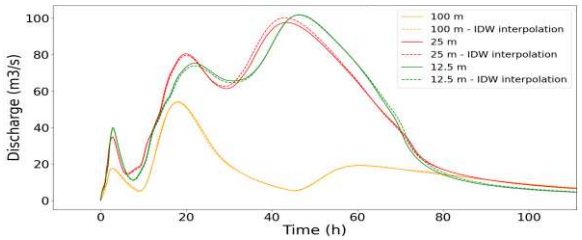

Figure 12. Mesh convergence: difference between NNM and IDW for topography interpolation.

The duration of simulation for both cases is similar, it only changes the time of pre-treatment to create the mesh with IDW that is several hours longer. Using IDW method does not change drastically the results for the discharge at the outlet. Then, it will be chosen to keep with the NNM for the rest of the paper and demonstration.

Another interesting test was to constrain the mesh by forcing the nodes to be placed along the hydrographic network which can be extracted from the DEM. It enables the water to follow the low elevation points and the flows converge in the river network. In Figure 13 are presented the difference

between simulations on different resolution meshes with or without constraint lines.

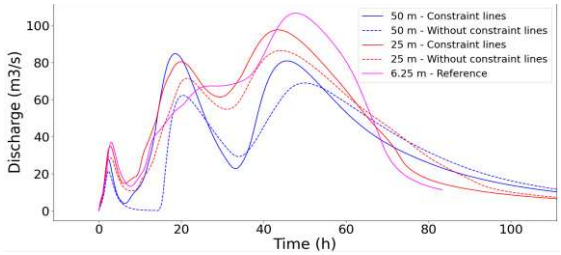

Figure 13. Mesh convergence: discharge at the outlet with and without constraint lines in the meshes.

With constraint lines, the results are closer to the 6.25 m resolution mesh, which is considered as a reference. The simulation time is around 25% longer, as some of the meshed triangles are smaller with the constraint lines, and thus the time step is smaller to preserve the desired Courant number (0.9). It is considered that the difference is worth waiting for a longer simulation because the gain in precision is important.

All these recommendations and first conclusions have been used for the simulations on the larger catchment of the Garonne River at Marmande. The same methodology is used with the same numerical schemes and parameters. In Figure 14 is represented the discharge at the outlet of the catchment for resolution from 800 m to 25 m for a constant rain of 50 mm/h.

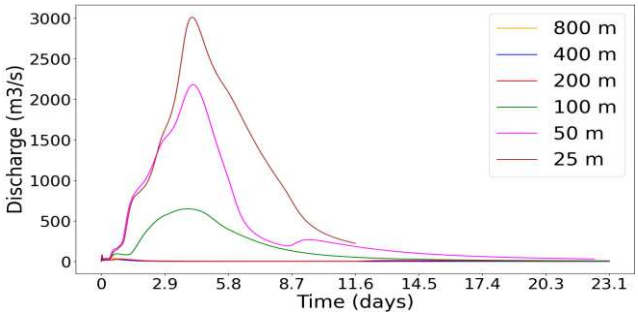

Figure 14. Mesh convergence: discharge at the outlet of Garonne catchment.

These resolutions were used to have similar number of nodes in the mesh as for Hers catchment. For a 25 m resolution mesh the numerical limits are reached, and it is not reasonable to push the convergence further on the large catchment. In Figure 14 there is no convergence before 25 m. Thus, it appears that the use of 25 m resolution mesh (at least) is required for the larger catchment to model the appropriate discharge at the outlet. It could be suggested that if the discharge is sufficiently captured for a resolution of 25 m on the Hers catchment, it can be so for the Garonne catchment, given that both have similar physical and geographical properties and typologies. In Table IV, the simulation times and the CPU times are given.

Table IV Simulation time for the Garonne catchment.

Resolution [m]	Number of processors	User time [h]	CPU time [days]	Simulated time [days]
800	96	/	/	23.1
400	96	/	/	23.1
200	768	0.36	11.7	23.1
100	1152	2.96	142.0	23.1
50	1152	40	1920	23.1
25	2880	55.63	5 575.9	11.6

The user and CPU time is very consequent to achieve the simulation on such a large scale to simulate more than 10 days of physical time even by trying to optimize the use of processors with 20 000 mesh nodes by processor.

The following points can be noted:

- A mesh with a resolution of 25 m is required (at least) to obtain the correct order of magnitude of the discharge at the outlet for the chosen catchments. A finer mesh is too computationally demanding.
- Directly simulating runoff over a catchment of 50 558 km² has proven to be difficult for the chosen catchments because of the long simulation time.
- It is important to extract the hydrographic network with sufficient accuracy and use it to constrain the mesh.

To overcome these challenging points, splitting the whole catchment into smaller sub-catchments is recommended in any case.

B. Sub-catchments splitting application

This approach allows extracting the data and the hydrographic network more easily while using less processors simultaneously. More importantly it becomes less computational costly and more efficient to calibrate the sub-catchments with the hydrometric stations within the catchments. The different hydrometric stations are represented by filled points in Figure 9.

At the time of the redaction of this article, the calibration of the model was not finalized, but preliminary results can already be extracted. The main calibration parameters are the size of the roughness of the soil k_s and the CN for the infiltration model. The CN has been spatialized over the domain as described in section III.D, as can be seen in Figure 15.

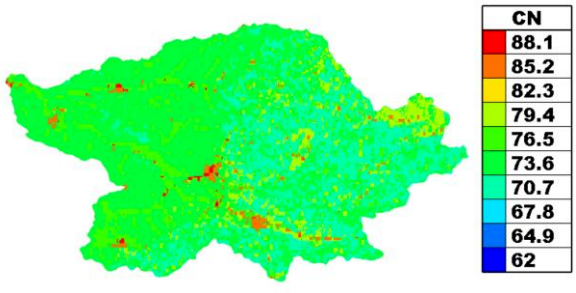

Figure 15. Example of spatialization of CN over one sub-catchment.

For the calibration of the CN parameter, it is proceeded mainly by playing with the antecedent moisture conditions and the initial abstraction ratios ($Ia = 0.2S$ or $Ia = 0.05S$) that are available in the sources of TELEMAC-2D. Some tests of CN sensitivity include variations of the CN values on the whole domain uniformly.

Previous results suggest that the first events of rain are difficult to represent with too much infiltration whatever the chosen parameters of CN or k_s. For the last rainfall event, the runoff following this event is too important on every simulation compared with observed values at the hydrometric stations (Figure 16), because the infiltration rate is getting smaller after the first events of rainfall. In Figure 16, this phenomena at Marmande and at Villeneuve-sur-Lot (Figure 9) within the watershed can be observed.

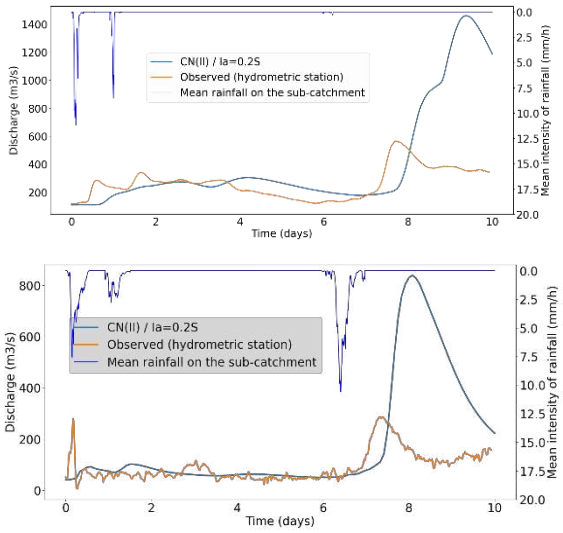

Figure 16. Examples of simulations results for the discharge at Marmande (top) and Villeneuve-sur-Lot (bottom).

Results at Marmande are chosen here because located at the outlet of the entire catchment. At Villeneuve-sur-Lot and Cahors (plotted in Figure 17), they are within an intermediate sub-catchment, therefore showing the dynamic within the global catchment at different places.

For using the SCS-CN model with different events of rain in the simulation, since there was no rainfall for four days between the second and the third event, the water infiltrated stored should decrease. The cumulated storage of infiltration could be partially decreased or totally erased, so the infiltration rate can become higher when there is no rainfall during a certain amount of time before a new rainfall event.

In Figure 17, the discharge is compared with different trials of calibration representing the discharge at Villeneuve-Sur-Lot and Cahors where there are hydrometric stations (Figure 9) in one of the sub-catchments.

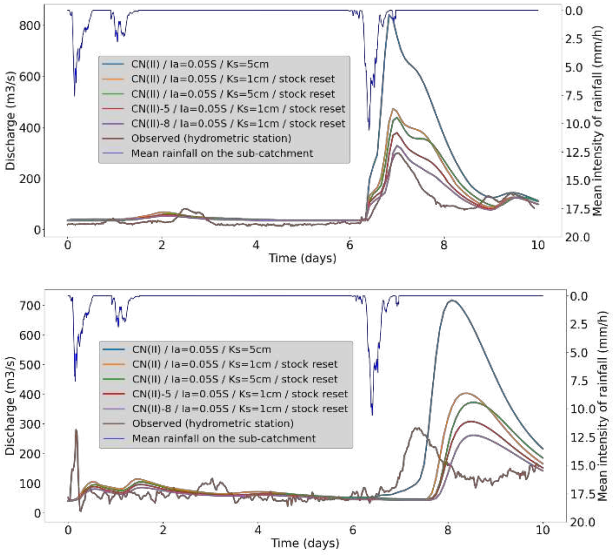

Figure 17. Discharge at Cahors (top) and Villeneuve-sur-Lot (bottom) with different infiltration configurations.

It can be seen, that in a first approach, by taking in a rough way the SCS-CN model the discharge for the second peak is too high (blue plots in Figure 17). So, it has been considered to reset the storage of infiltration in the soil with a null value after the second event of rainfall. And by adjusting the CN and k_s values the good order of magnitude for the discharge can be grasped for the second peak. Depending on the hydrometric stations there are still an important time deviation that must be investigated, with probably some changes needed in the bottom friction law.

The river network is not well represented, because there are no bathymetric data and associated roughness. It is one of the problems that probably explains the time lag that can be observed for some stations. Add a notion of humidity index to use SCS-CN model for following rainfall events as explored in [20] could be promising while playing with the different options and probably adjusting the CN spatialized values as it has been done in the simulation for the red and purple plots by subtracting 5 or 8 to every CN value on the whole domain. The sensitivity to the CN value is a key factor in the calibration that can make it difficult to achieve.

VI. CONCLUSION AND PERSPECTIVES

This paper has presented an introduction and some guidelines to modelling runoff on a large catchment. From the mesh convergence and sub-catchments splitting some key results could be underlined.

First, the mesh convergence has shown that the mesh resolution should be at least 25 m for the chosen catchments to obtain the correct order of magnitude for the discharge at the outlet of the catchment.

For a mesh resolution of that size, the simulation time for large catchment application is very high (on thousands of processors), and it could be complicated to calibrate the model.

It has also been underlined that at this resolution of 25 m with the available DEM data, choosing NNM gives similar

results as IDW method for the interpolation of the elevations on the mesh. For practical purposes the NNM method is recommended.

Using the hydrographic network to constrain the mesh is also recommended. Indeed, the simulation time might be a little longer, but the discharge at the outlet is significantly closer to the reference discharge. However, directly extracting the hydrographic network on catchments of 50 000 km² can be difficult with Geographic Information System software.

The CLC map is adapted for flood plains but not for the channel of rivers. In addition, the Manning-Strickler law may not be suitable for shallow water depths in the case of rainfall. So, the model of friction of Lawrence which is physically based seems more adequate to use with the size of the roughness of the soil that needs calibration.

In view of these challenges, the second approach presented in this paper seems more suited for runoff modelling on large catchments. Indeed, splitting the whole catchment in sub-catchments and chaining the simulations enable the user to prepare the necessary data for the construction of the model more easily. And more importantly, the calibration is easier with the possibility to calibrate each sub-catchments with its own parameters with less computation time and needed processors.

The first results of the calibration with this second approach, have shown that there is a high sensitivity to the calibration parameters (CN and k_s). In addition, the correct order of magnitude on the discharge comparing with observed data cannot be grasped with a naive application of the SCS-CN model. When they are several consecutive rainfall events, the infiltration rate only decreases and cannot go up again. The SCS-CN model is more adapted for a single event of rain. However, it has been presented, that more closer results could be found by decreasing the infiltrated storage in the SCS-CN formula, when there is no significant rainfall for a long period.

Looking ahead, the calibration of the model is not complete, and some modifications in the SCS-CN model of infiltration should be explored, such as considering the humidity index of the soil which can decrease after a certain amount of time without abundant rainfall. Besides, the SCS-CN method may not be the best fit to model runoff on large catchments: new implemented model for infiltration (Horton and Green-Ampt) should be tested as they could be more adapted to the situation. Having said that, the approach could be applied to other large catchments and other rainfall events to validate or not the chosen models. A significant improvement factor is the bathymetry of the rivers (at least the main ones) which is not considered. More data on the bathymetry are needed or it could be explored bathymetric reconstruction with the discharges and the topography.

ACKNOWLEDGEMENT

This research was supported by EDF R&D through the funding of a 6-month internship on the hydraulic modelling of extreme events on large catchments.

REFERENCES

[1] F. Kreienkam, SY. Philip, JS. Tradowsky, SF. Kew, P. Lorenz, J. Arrighi et al., “Rapid attribution of heavy rainfall events leading to the severe flooding in Western Europe during July 2021”, World Weather Attribution, 2021

[2] J. Sun, S. Fu, H. Wang, Y. Zhang, Y. Chen, Y. Wang, H. Tuang, and R. Ma, “Primary characteristics of the extreme heavy rainfall event over Henan in July 2021”, Atmospheric Science Letters, 2022

[3] Météo-Paris, “Bilan des orages et inondations du 8 septembre 2021 dans le sud-ouest, notamment à Agen“, https://www.meteo-paris.com/actualites/bilan-des-orages-inondations-du-8-septembre-2021-dans-le-sud-ouest-notamment-a-agen

[4] F. Taccone, A. Germain, O. Delestre, and N. Goutal, “A new criterion for the evaluation of the velocity field for rainfall-runoff modelling using a shallow-water model”, Advances in Water Resources, 2020, vol. 140, article 103581

[5] P. Brigode, F. Bourgin, R. Yassine, O. Delestre, and P. Lagrée, “Are hydrologic-hydraulic coupling approaches able to reproduce Alex flash-flood dynamics and impacts on southeastern French headwaters?”, SimHydro2021, 2021

[6] R. Yassine, M. Lastes, A. Argence, A. Gandouin, C. Imperatrice, P. Michel, R. Zhang, P. Brigode, O. Delestre, and F. Taccone “Simulation of the Alex storm flash-flood in the Vésubie catchment (south eastern France) using TELEMAC-2D Hydraulic Code”, SymHydro 2021, 2021

[7] A. B. de Saint Venant, « Théorie du mouvement non permanent des eaux, avec application aux crues des rivières et à l’introduction des marées dans leur lit », Rapport technique, Académie des sciences, 1871

[8] J. F. Gerbeau, and B. Perthame, « Derivation of viscous saint venant system for laminar shallow water; numerical validation”, Discrete and Continuous Dynamical Systems, 2001, vol. 1, pp. 89-102

[9] E. Audusse, and M. O. Bristeau, « A well-balanced positivity « second order » scheme for shallow water flows on unstructured meshes”, Journal of Computanional Physics, 2005, vol. 206, no 1, pp. 311-333

[10] E. Audusse, M. O. Bristeau, and B. Perthame, « Kinetic schemes for saint-venant equations with source terms on unstructured grids”, Thèse de doctorat, INRIA, 2000

[11] G. Chen, and S. Noelle, “A new hydrostatic reconstruction scheme based on subcell reconstructions”, SIAM Journal on Numerical Analysis, 2017, vol. 55(2), pp. 758-784

[12] R. Manning, “On the flow of water in open channels and pipes”, Transactions of the Institution of Civil Engineers or Ireland, 1891, vol. 20, pp. 161-207

[13] D.S.L Lawrence “Macroscale roughness and frictional resistance in overland flow”, Earth Surface Processes and Landforms, 1997, vol.22, no 4, pp. 365-382

[14] V. Mockus, National Engineering Handbook, chapter Estimation of Direct Runoff from Storm Rainfall, United States Department of Agriculture, 1972

[15] P.L Ligier, “Implementation of a rainfall-unoff model in TELEMAC-2D”, Proceedings of the XXIIIrd TELEMAC-MASCARET User Conference 2016, 2016, pp. 13-19

[16] U.S. Department of Agriculture, National Resources Conservation Service, National Engineering Handbook, Part 630 Hydrology, Chapter 9 Hydrologic soil-cover complexes, 2004

[17] M. Huang, J. Gallichand, Z. Wang, and M. Goulet, “A modification of the Soil Conservation Service curve number method for steep slopes in the Loess Plateau of China”, Hydrological,2006, vol. 20, pp. 579-589

[18] W. H. Green, and G. A. Ampt, “Studies on soil physics”, The Journal of Agricultural Science, 1911, vol. 4, pp. 1-17

[19] R. E. Horton, “The role of infiltration in the hydrological cycle”, American Geophysical Union, 1933, pp. 446-460

[20] C. Delcourt, F. Taccone, and O. Delestre, “Determination of initial soil moisture for a small highly erodible mountain basin with TELEMAC”, Proceedings of the papers submitted to the TELEMAC-MASCARET User Conference 2021, 2021, pp. 116-122

Flash flood simulations in a steep catchment using Telemac2D - hydrodynamic rainfall-runoff model

Nitesh Godara, Oddbjørn Bruland, Knut Alfredsen
nitesh.godara@ntnu.no, Trondheim, Norway
Department of Civil and Environmental Engineering, Norwegian University of science and Technology Trondheim, Norway

Abstract – **The frequency of extreme events is increasing as the consequences of climate change. According to the World Meteorological Organization (WMO, 2021), floods are the third largest hazard in terms of human losses (58 700 deaths) and second largest in terms of economic losses (US$115 billion). The extreme events are likely to increase in the future years because of the changing climate. Flash flood events also have large environmental and economic damage potential. Flash floods triggered by rain-on-snow events in small and steep catchments can lead to snow avalanches, landslides, debris flow, sedimentation and erosion of the riverbanks and bed. Hence, the analysis of such events is very important in terms of potential damage assessment and preparedness for such extreme events.**

In the present work, Telemac2D is used for flash flood calculations in a small and steep snow-covered Norwegian catchment using rain-on-grid technique. Telemac2D is originally a hydrodynamic model but has an option to include rainfall-runoff module making it a hydrodynamic rainfall-runoff model (HDRRM). Use of single model for both hydrological and hydraulic calculations save time for calibration and offline coupling of two different models. Also, it is possible to calculate high velocities, sheer stresses, water depths and extract flow hydrograph at any point in the catchment unlike a traditional hydrological approach where the flow hydrograph is generated usually only at the outlet of the catchment. At the moment, the hydrological module present in Telemac2D uses curve number method for hydrological calculations. The current study evaluates the model for flash floods calculation in small and steep catchments and suggests further improvements. Spatially distributed precipitation with hourly resolution was used.

The results show that this model can be used satisfactorily for short term events with peak flows but for longer events, the results indicate a need for time-varying curve number. Alternatively, implementation of another hydrological method can be done which includes time-varying infiltration abstractions and store the infiltrated water as subsurface flow which can further contribute to the recession part of the hydrograph. Furthermore, the study explores the benefits and limitations through a comprehensive description of model construction, calibration, and sensitivity analysis.

Keywords: Flash flood, Small and Steep catchments, rainfall-runoff modelling, rain-on-grid, Telemac2D.

TELEMAC as a hydrodynamic rainfall-runoff model: New extension using the Green-Ampt-infiltration

Karl Broich, Thomas Obermaier, Lucas Alcamo, Markus Disse
karl.broich@tum.de, Munich, Germany
Chair of Hydrology and River Basin Management Munich, Technical University of Munich TUM, Munich, Germany

Abstract – **Within the cooperation project HiOS (2017-2021) TELEMAC-2D had been intensively used as a Hydrodynamic Rainfall-Runoff Model (HDRRM) using the SCS-CN-method for the calculation of the effective rainfall. This TELEMAC-2D model proved to be an efficient and versatile tool for the simulation of flash floods. Nevertheless, the accumulated run-off was frequently overestimated. The reason for this could be the inability of the SCS-CN-method to represent re-infiltration. Therefore, a new extension considering the physically based Green-Ampt-infiltration was implemented. The methodology and the results of the testing are given. The plausibility of the new extension was validated using a case study area nearby Bayreuth in Bavaria (Studio-project, 2021 ongoing).**

Keywords: rainfall-runoff, infiltration, re-infiltration, ponding time, non-uniform rainfall.

I. INTRODUCTION

Rainfall-Runoff modelling is an essential part of flood hazard analysis. Most of the time, the analysis is carried out combining separately hydrological and hydrodynamic models. For catchment sizes <100km² small scale models hydrodynamic rainfall-runoff models are a promising alternative melting two models into one.

During the cooperation project HiOS more than 40 Bavarian catchments and municipalities were analysed using HDRRM. Simulated results were compared to measured data for each catchment. Even without calibration, the simulation met peak of discharge and evolution with time comparatively well.

Frequently the total volume in terms of accumulated runoff was overestimated. A typical result for the simulated accumulated discharges at the catchment outlet compared to the measured accumulated discharge and the accumulated precipitation is given in **Erreur ! Source du renvoi i ntrouvable.**.

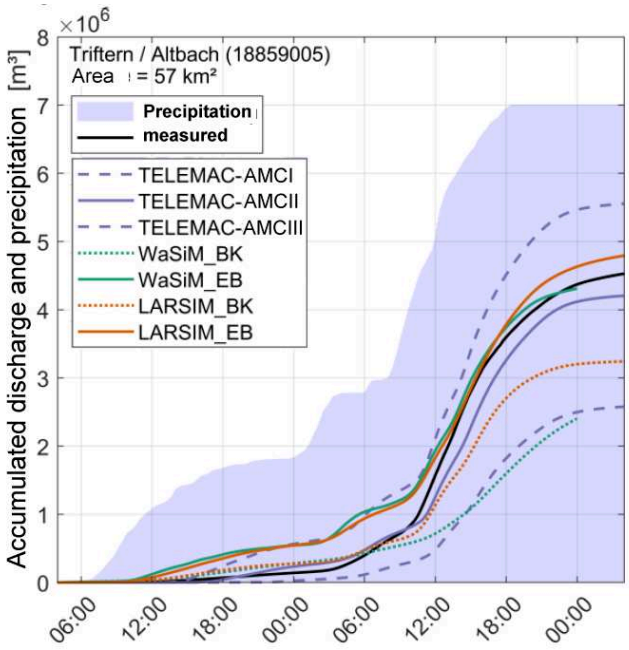

Figure 1. Accumulated discharges and precipitation [m³] for case study Triftern (HiOS-project) for TELEMAC-2D and other hydrological models

For this case, the antecedent moisture content class III is valid (AMCIII = wet conditions). The dynamic of the graph is represented sufficiently, but too much water is kept in the simulation model. It is assumed that the conceptual approach of the SCS-CN-method does not represent the infiltration process adequately. This method defines infiltration as a portion of the precipitation. Therefore, using SCS-CN-method implies zero infiltration, if there is zero rainfall. This is obviously not realistic, because re-infiltration can continue after the rain provided surface water is present.

The Green-Ampt-infiltration is physically based and has non-zero infiltration in wetted regions even if there is no rainfall. The influence of the Green-Ampt-approach applied to HDRRM is analysed hereafter.

II. IMPLEMENTATION

The Green-Ampt-Infiltration is implemented in parallel to the existing SCS-CN-method. Thus, either Green-Ampt-infiltration or SCS-CN-method can be chosen.

A. SCS-CN-method

The Ligier-implementation [3] enhanced by the possibility to accomplish for spatial variable rainfall also called non-uniform rainfall has been already described [5]. The subroutines *prosou* and *run_scs_cn* were modified and the subroutines *radarmap* (reading of rainfall radar data) and *rfasp* (NNB-mapping of rainfall radar data) added.

B. Green-Ampt-method

The Green-Ampt method is similar to Darcy's law. It calculates the infiltration rate f [L³/(s L)] using the following relation:

$$f(t) = K_{sat}\left[1 + \frac{|\psi_f|\,(\theta s - \theta i)}{F}\right] \quad t > tp \qquad (1)$$

$$f(t) = P \quad t \le tp$$

where K_{sat} [L/T] is the saturated hydraulic conductivity, ψ_f [L] the suction head at the wetting front, θ_s [-] is the volumetric moisture content near saturation, θ_i [-] the initial volumetric moisture content and F [L] the cumulative infiltrated water.

According to equation (1), the model yields an implicit equation for the estimation of the infiltration rate. However, the infiltration rate at a certain time can only be obtained by using iterative computation techniques. Over time, several authors developed explicit approximations to overcome this problem. Here, the explicit formulation of Serrano [2] is used and implemented in subroutine *infiltration_ga*.

III. TESTING

The testing of the implementation consists of two parts. During the first part (A) of the implementation the Serrano-approximation is checked against the exact solution of the Green-Ampt-equation (1). For this test, the Serrano-approach is extracted and executed separately. In the second part (B), the plausibility of the enhanced TELEMAC-2D is checked using the Ligier-testcase and a test-case area near Bayreuth/Bavaria (STUDIO-project).

The Serrano-approach uses the following decomposition of the cumulative infiltration F.

$$F(t) \approx F_0(t) + a\ln(m_1(t))\left[1 + \frac{m_2(t)}{[1-m_1(t)][1+m_2(t)\ln(m_1(t))]}\right] \qquad (2)$$

for $t > t_p$

using the following relations:

$$F_0(t) = K_{sat}(t - t_p) + F_p$$

$$a = |\psi_f|\,(\theta_s - \theta_i)$$

$$m_1(t) = (F_0(t) + a)/(F_p + a)$$

$$m_2(t) = a/(F_0(t) + a)$$

The comparison of the approximation of Serrano [2] and the exact solution for equation (1) is given in using the Studio-case-study (see next chapter III.B). The resulting ponding time is 76 min. For the simulation time, the differences between the exact solution and the Serrano-approximation are negligibly small.

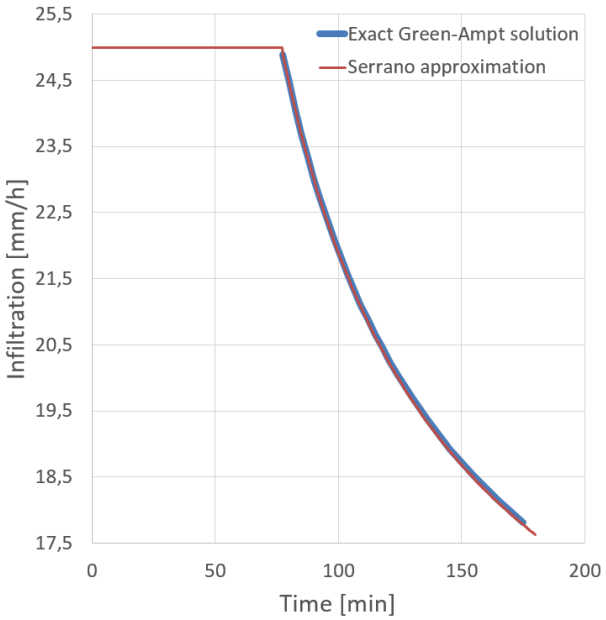

Figure 2. Comparison of exact GA-solution and approximated according to Serrano [2]

A. Testing the implemented GA-method

Global test 1: The simple reservoir-setup by Ligier [3] was used to test the basic requirement: inside a flooded area the infiltration should continue after the rainfall stops. A rainfall intensity p= 100mm/h lasting for one hour was defined. After one hour the rainfall is zero. The water level inside the reservoir decreased after one hour when Green-Ampt was applied. For SCS.CN-method the water level stayed constant.

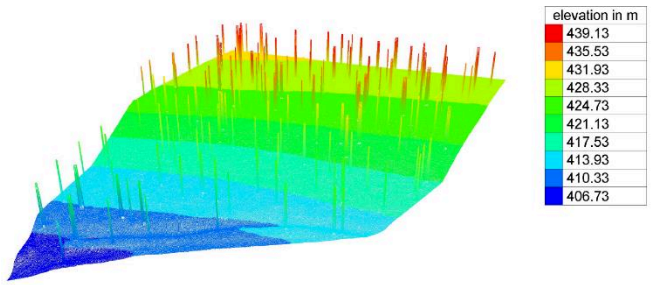

Figure 3. Case study area for Green-Ampt-infiltration, 3d-view (STUDIO-project).

Global test 2: For the domain given in Figure 3 a uniform unstationary rainfall is defined. For this case, the basic requirement is that the infiltration rate is uniform and equal to the rainfall intensity as long as $t<t_p$. For $t>> t_p$ the infiltration rate f [L/T] should converge to the saturated

hydraulic conductivity K_{sat} [L/T]. The rainfall is constant for 2 hours with P=25mm/h and then zero. When the rainfall stops, the infiltration is limited to the water availability and becomes water depth dependent. The saturated hydraulic conductivity is $K_{sat.}$= 3.03 10^{-6} m/s = 10.905 mm/h. The pressure head at the wetting front is $\psi_{f.}$= 0.1524m. The volumetric moisture content θ_s near saturation is practically equal to the soil porosity n = θ_s = 0,5050. The initial water content is θ_i = 0,2335. The total simulation time is 3 hours. The simulation result for these assumptions is given in Figure 4.

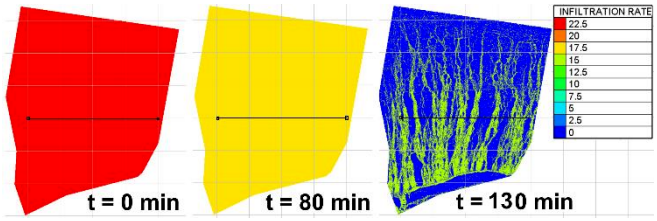

Figure 4. Infiltration rates [mm/h} at different time levels (STUDIO-project) for TELEMAC-2D with Green-Ampt-infiltration.

After the ponding time t > t_p=76min. the infiltration rate decreases. When the rainfall stops after 2 hours, infiltration is limited to areas with flow concentration.

IV. CONCLUSION

The first results demonstrate the general suitability of the Green-Ampt approach and proofs the correctness of the implementation. Next step is the calibration and validation of the approach. Further enhancements with un-ponded, infiltration and unsteady rainfall might improve the quality of the results.

ACKNOWLEDGEMENT

The cooperation project “Hinweiskarte Oberflächenabfluss und Sturzflut” (Indicator Map for Surface Runoff and Flash Floods) abbreviated HiOS, analyses surface runoff and flash floods in various aspects. HiOS started in 2017 and lasted until 2021. It consisted of three teams working on GIS, hydrologic and hydrodynamic modelling. Technical University of Munich TUM, Ludwig-Maximilians-Universität LMU and the Leibniz-Supercomputing Centre LRZ are partners in this project. HiOS was funded by the Bavarian State Ministry of the Environment and Consumer Protection (StMUV) and supervised by the Bavarian Environment Agency.

The project STUDIO investigates nature-based solution against consequences of droughts in a forest area nearby Bayreuth/Bavaria. STUDIO is funded and supervised by the Bavarian Environment Agency.

REFERENCES

[1] W. H. Green and GA Ampt, “Studies on Soil Phyics”, The Journal of Agricultural Science 4.1, 1911, pp. 1–24.

[2] S. E. Serrano, “Improved decomposition solution to Green and Ampt equation”, Journal of Hydrologic Engineering, 8.3, 2003, pp. 158-160.

[3] SCS, “National engineering handbook”, Section 4: Hydrology, Soil Conservation Service SCS, USDA, Washington, D.C., 2004.

[4] P.-L. Ligier, “Implementation of a rainfall-runoff model in TELEMAC-2D”, Proc. of the XXIIIrd TELEMAC_MASCARET User Conference, 11.-13. October 2016, Paris, France.

[5] K. Broich, T. Pflugbeil, M. Disse, “Using TELEMAC-2D for Hydrodynamic Modeling of Rainfall-Runoff”, Proc. of the XXVIth TELEMAC_MASCARET User Conference, 16.-17. October 2019, Toulouse, France.

[6] for increasing the drought resilience of forests using hydrodynamic rainfall-runoff modeling”; Masterthesis, Technical University of Munich, 12th September 2022.

An intercomparison of flow around a 3D wall-mounted cylinder using TELEMAC-3D and OpenFOAM

M. Renaud[1], M. Gonzales De Linares[2], T. Oudart[2], O. Bertrand[2], C. Bonamy[1], J. Chauchat[1]

matthias.renaud@grenoble-inp.org, Grenoble, France
[1]Univ. Grenoble Alpes, CNRS, Grenoble INP, LEGI, 38000 Grenoble, France
[2]ARTELIA, 6 rue de Lorraine, 38130 Echirolles, France

***Abstract* – This work presents the comparison between results of two different simulation codes, TELEMAC-3D and OpenFOAM, on a well-documented test-case of the flow around a cylinder (Roulund *et al.*, 2005). Both codes are based on the Navier-Stokes equations but rely on different numerical methods, turbulence models and types of mesh. For TELEMAC-3D, a k-ε turbulence model is used, while for OpenFOAM, a k-ω SST turbulence model is used. Both codes are able to predict the main characteristics of the flow, such as vortex shedding in the wake of the cylinder and the presence of a horseshoe vortex upstream of the pile. However, the dynamics of the eddies downstream of the pile are different, TELEMAC-3D predicting smaller vertical movements and vortices than OpenFOAM. The characteristics of the flow, such as flow velocity profiles or bed shear stress are used to evaluate the numerical results. The pros and cons of each software are highlighted and discussed.**

Keywords: TELEMAC-3D, OpenFOAM, hydrodynamics, vortex, turbulence

I. INTRODUCTION

Scouring around hydraulic structures is a phenomenon of great importance for the safety of structures. Understanding and predicting scour is therefore a major challenge for engineering in order to design structures and, if necessary, protections limiting the risks of failure to an acceptable level.

This work focuses on the modelling of the flow hydrodynamics around an obstacle, the first step in the development of a morphodynamic solver. For this purpose, two CFD (Computational Fluid Dynamics) software packages, TELEMAC-MASCARET and OpenFOAM, both based on the RANS equations, are used to simulate the flow around a vertical cylinder. An academic configuration that has been widely studied and for which laboratory measurements are available [1] is used, allowing to assess the quality of the results.

When a vertical cylinder is set in a steady current, the impact of the flow on the cylinder creates a pressure gradient upstream of it, leading to a downflow along the pile. As the downflow reaches the bed, it generates a recirculation cell called the horseshoe vortex which evolves on both sides of the cylinder. As the flow pass around the cylinder, it accelerates before decelerating at the cylinder leading to a static pressure drop and thus to an adverse pressure gradient. Except for really small pile Reynolds number $Re_D = UD/\nu$, the adverse pressure gradient leads to a flow separation along the cylinder which generate vortices in the wake of the cylinder. Different flow regimes exist depending on the value of Re_D. For $5 < Re_D < 40$, a pair of symmetric vortices attached to the cylinder exist in the wake. When Re_D further increases, the wake becomes unstable, and vortices are alternatively shed on both sides of the cylinder [2].

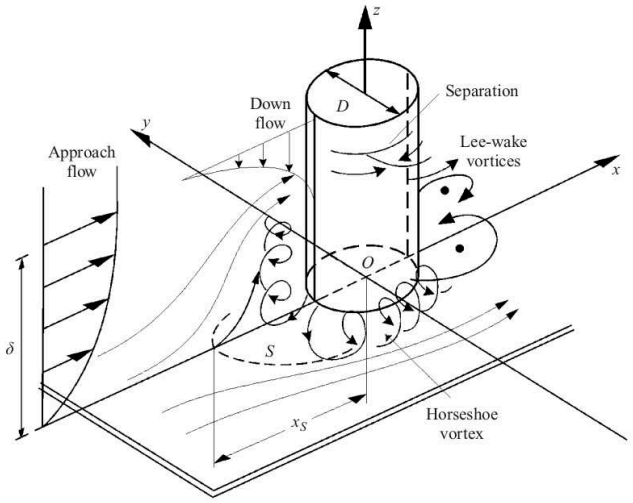

Figure 1. Scheme of the flow around a cylinder. From Roulund et al. [1].

II. GOVERNING EQUATIONS

The incompressible Reynolds averaged Navier-Stokes equations (RANS) are solved in both solvers using two-equations turbulence model. Two different models are used in this study, the standard k−ϵ model from Launder and Sharma [3] is used in TELEMAC-3D and the k − ω SST model from Menter [4] is used in OpenFOAM. In the k−ϵ model, the eddy viscosity is defined as $\nu_t = C_\mu k^2/\epsilon$ where k is the turbulent kinetic energy and ϵ is the dissipation rate of turbulent kinetic energy. The spatio-temporal evolution of k and ϵ are obtained as the solution of two transport equations. This model is known to give good results in free shear flows at high Reynolds numbers but is not very accurate in the near wall region or in presence of adverse pressure gradient. These discrepancies have motivated the development of the k − ω SST model (not

available at this time in TELEMAC). It consists in a blending of the k − ω turbulence model [5] in the near wall regions and of the k − ϵ model in the outer regions. The k − ω SST model uses a blending function to switch from the behaviour of a k − ϵ to the one of a k − ω depending on the distance to the nearest wall.

Apart from the turbulence models themselves, one of the major differences between TELEMAC-3D and OpenFOAM resides in the wall treatment and boundary conditions. In TELEMAC-3D, the assumption of a local equilibrium between the production and dissipation of turbulent kinetic energy is made. Boundary conditions for k and ϵ are described in the TELEMAC-3D theory guide (2021) and reads:

$$k = \frac{u_*^2}{\sqrt{C_\mu}} \quad ; \quad \epsilon = \frac{u_*^3}{\kappa\delta}$$

where u∗ is the friction velocity, κ ≈ 0.41 is the von Karman constant, $C_\mu = 0.09$ is an empirical constant and δ is equal to 1/2 of the local mesh size measured along the normal direction to the wall. The boundary conditions for both k and ϵ require the knowledge of the friction velocity u∗ at the wall. In the smooth case, u∗ and y+ are computed using the Reichard law:

$$\frac{u}{u_*} = \frac{1}{\kappa}\ln(1+\kappa z^+) + 7.8\left(1 - e^{-z^+/11}\right) - \frac{z^+}{11}e^{-0.33z^+},$$

which requires an iterative procedure as $z^+ = u_* z/\upsilon$ depends on u_*.

In OpenFOAM, all velocity components are set to 0 at the wall. Boundary conditions for k are set as suggested by [6], k = 0 in presence of a smooth wall. For ω the omegaWallFunction of OpenFOAM is used, the value of ω in the first cell next to the wall depends on the distance of the cell center to the wall, in wall unit z^+. The value is a blending between the viscous solution ω_{vis} and the log-law solution ω_{log}:

$$\omega_{vis} = \frac{6\upsilon}{\beta_1 z^2} \quad ; \quad \omega_{log} = \frac{\sqrt{k}}{C_\mu \kappa z},$$

where $\beta_1 = 0.075$ is an empirical constant. The turbulence viscosity υ_t is then computed as a function of k and ω.

The friction velocity is then computed using the velocity field gradient and the turbulent viscosity.

$$\tau_b = \rho(\upsilon + \upsilon_t)\frac{\partial u}{\partial n} \quad ; \quad u_* = \sqrt{\frac{\tau_b}{\rho}},$$

∂u/∂n being the derivative of the wall tangent velocity component with respect to the normal coordinate to the wall. A precise knowledge of the velocity field near the walls is needed to accurately compute the wall shear stress and the bed friction velocity.

III. SIMULATIONS

A. *Straight flume*

Before proceeding to the numerical study of the flow around a cylinder, the capabilities of TELEMAC-3D (with k − ϵ turbulence model) and the OpenFOAM solver (with k − ω SST turbulence model) to simulate a unidirectional flow over a fixed wall are studied. The objective is to verify and discuss the capabilities of the two solvers to reproduce the physics of the flow in a channel based on experimental profiles but also to identify their sensitivities to the vertical mesh resolution, especially near the wall (cf. Table below). Results by Roulund et al [1], and Fuhrman et al. [6] are used as references. The vertical profiles of the velocity field in the direction of flow and the turbulent kinetic energy k are extracted from the different simulations and compared with the experiment. As the flow characteristics (water head, flow velocity) are different in the configuration used by Fuhrman et al. [6], the results are scaled to allow for comparison.

Table I Characteristics of the different meshes used. "geometric transformation" indicates the reason rg of the geometric sequence defining the vertical distribution of the vertical cells/nodes composing the mesh. "distance to wall" indicates for openFOAM the distance between the center of the first cell in contact with the wall and the wall. For TELEMAC-3D it is one-tenth of the local mesh fineness at the wall (distance between two neighboring nodes), which is the variable δ defined previously

	OpenFOAM	TELEMAC-3D
mesh 1		
Number of planes	120	30
Geometric transformation	1,043	1,1
Distance to wall	0,1 mm	0,36 mm
mesh 2		
Number of planes	60	30
Geometric transformation	1,06	1
Distance to wall	1 mm	1,8 mm
mesh 3		
Number of planes	30	15
Geometric transformation	1	1
Distance to wall	9 mm	4 mm

The OpenFOAM results in terms of vertical velocity profiles, turbulent kinetic energy k, and Reynolds shear stress are shown in Figures 1. The results are made dimensionless in order to enable the comparison with the experimental results of Fuhrman et al [6]. The velocity profile is not much affected by the mesh resolution. In contrast, the mesh resolution has more influence on the profile of k especially near the bottom where a cusp appears. The value of k increases when approaching the bottom before decreasing abruptly near the wall. The maximum reached by k is systematically underestimated by the k - ω SST model. In particular, it can be seen in the case of mesh 1 and 2 that the curvature of the profile of k around the maximum value is less steep than what is observed experimentally. This difference with experiments was also observed by Fuhrman *et al.* [6] with the use of a standard k - ω turbulence model. It is observed that mesh 3 is not fine enough near the wall, resulting in an abrupt peak in k on the vertical profile. The first cell near the wall must be inside the viscous sublayer to satisfactorily describe the peak in turbulent kinetic energy k.

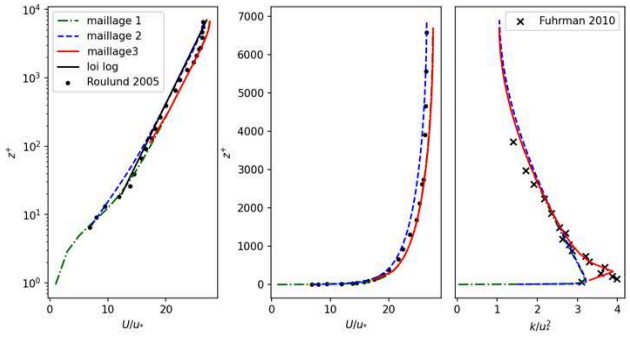

Figure 2. Vertical profiles of U and k predicted by openFOAM for the smooth channel obtained with the 3 meshes. Experimental data from Roulund et al (2005) (•) and Fuhrman et al. (2010) (x).

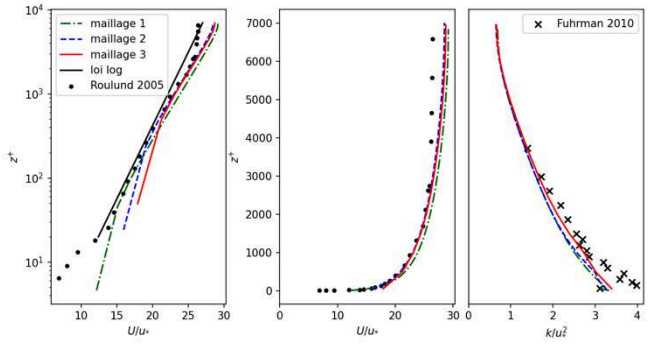

Figure 3. Vertical profiles of U and k predicted by TELEMAC-3D for the smooth channel obtained with the 3 meshes. Experimental data from Roulund et al (2005) (•) and Fuhrman et al. (2010) (x).

The results obtained by TELEMAC-3D (figure 2) are only slightly affected by the vertical resolution of the mesh. It is found that there is no cusp on the k-profile regardless of the mesh refinement near the wall. This is explained by the wall treatment implemented in TELEMAC-3D described previously. In TELEMAC-3D, it is considered that at the wall, a local equilibrium is established between the production and dissipation of turbulent kinetic energy. Moreover, the local velocity profile is considered to be linear in the direction normal to the wall. This equilibrium between production and dissipation corresponds to the maximum of k near the wall observed experimentally and numerically. As seen previously, TELEMAC-3D considers that the nodes of the mesh located on the wall are in fact at a distance δ from the wall depending on the local mesh refinement. It is therefore at this distance δ from the wall that the maximum turbulent kinetic energy k is located. Thus, the TELEMAC-3D wall laws always consider that the maximum of k is located at the first node at the wall, and thus cannot capture the decrease of k toward the wall.

The results of TELEMAC-3D seem to be robust and little affected by the mesh resolution, allowing the use of a coarser mesh compared with openFOAM. This property allows TELEMAC-3D to study phenomena at large scales, which corresponds to its usage in engineering. This software is indeed primarily used to simulate phenomena at the scale of a river reach or a stretch of coast. On the one hand, the wall laws used by TELEMAC-3D does not allow to accurately describe the flow in the near wall region, even with extreme mesh refinement. On the other hand, OpenFOAM requires a very fine mesh near the wall to correctly describe the boundary layer flow. Another result not shown in the different figures is the value of the friction velocity. Once again, TELEMAC-3D provides robust results that are not much affected by the mesh resolution. OpenFOAM clearly underestimates the bottom shear stress when coarse mesh is used. In conclusion, OpenFOAM requires a fine mesh near the wall to correctly model the physics of the boundary layer while TELEMAC-3D is more robust to the mesh but is unable to correctly capture the details of the flow near the wall.

B. Flow around a cylinder

The configuration of the experiments conducted at the Technical University of Denmark (TUK) by Roulund et al. [1] without sediment transport is used as benchmark. The smooth bottom case is considered herein, and the cylinder surface is smooth as well.

The computational domain consists of a vertical cylinder of diameter D = 53.6 cm located in a rectangular parallelepipedic domain (see figure 3). The upstream length is 10D, the downstream length is 20D and the domain width is 12D. The different parameters of the problem are summarized in Table II.

Table II Simulation parameters for the smooth case corresponding to the Roulund et al. experiments.

paramètres	fond lisse
vitesse débitante amont U (cm/s)	32,6
diamètre du cylindre D (cm)	53,6
hauteur d'eau H (cm)	53,6
nombre de Reynolds lié au cylindre $R_{e_D} = UD/\nu$	$1,8 \times 10^5$
nombre de Froude $F_r = U\sqrt{gH}$	0,14
vitesse de frottement expérimentale u_* (cm/s)	1,3 - 1,5
longueur de rugosité équivalente de Nikuradse k_n (cm)	-

At the surface, a symmetry condition is used in OpenFOAM, which is equivalent to applying a rigid lid at the surface. The free surface is therefore not considered in OpenFOAM. In reality, the water surface near the cylinder shows variations. Upstream of the cylinder, the water height increases due to the overpressure generated by the obstacle, on the sides of the cylinder, the flow accelerates and the water surface drops locally before returning to an undisturbed level downstream. The free surface effects are more important as the Froude number, $F_r = U/\sqrt{gh}$, increases. In the present case, the Froude number remains relatively small (Fr = 0.14), and it is argued in the work of Roulund et al. [1] and Baykal et al. [7] that free surface effects remain negligible for Fr < O(0.2). This justifies the rigid lid assumption in OpenFOAM. TELEMAC-3D solves the flow and the free surface, the results obtained on this configuration show a maximum variation of the free surface height around the cylinder of 1.3 cm or about 2% of the water depth. This small variation of the free surface level near the cylinder supports the choice of a rigid lid approximation in OpenFOAM. The boundary conditions at the entrance and exit of the domain are different between OpenFOAM and TELEMAC-3D and are described below.

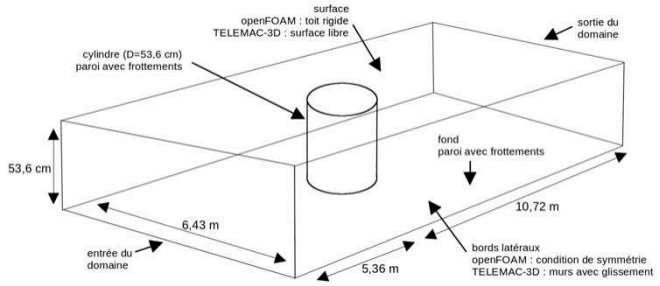

Figure 4. Sketch of the with dimensions and boundary conditions.

In OpenFOAM, vertical profiles of U, k and ω are imposed at the inlet over the width of the domain. These profiles are derived from a 1D simulation with the same turbulence model and wall-normal mesh. At the downstream end, the gradients of the different quantities are set to zero except for the dynamic pressure for which a Dirichlet condition p = 0 is applied.

In TELEMAC-3D, a discharge is imposed at the inlet and the water level is imposed downstream. The downstream level is constant over time and is set to h=53.6 cm.

For each solver, two different meshes are used: a first one, relatively coarse and a second one finer. The characteristics of the meshes are summarized in the table below.

Table III Characteristics of the meshes tested.

	OpenFOAM	TELEMAC-3D
mesh 1		
number of nodes/cells	$4{,}9 \times 10^5$	$5{,}8 \times 10^5$
number of planes	25	25
geometric transformation	1	1
distance to cylinder wall	5 mm	2 mm
distance to bed wall	1,07 cm	2,2 mm
mesh 2		
number of nodes/cells	$5{,}18 \times 10^5$	$1{,}47 \times 10^6$
number of planes	35	30
geometric transformation	1,0995	1,08
distance to cylinder wall	0,5 mm	0,5 mm
distance to bed wall	2 mm	0,5 mm

Both solvers are able to qualitatively reproduce the major hydrodynamic structures characterizing the flow around a vertical cylinder. The representation of iso-volumes of Q criterion (see **Erreur ! Source du renvoi introuvable.**) allows t o visualize this. The Q criterion is a criterion classically used to represent vorticies coherent structures present in the flow. For both solvers, a horseshoe vortex is present at the upstream end of the cylinder and rolls up around the cylinder. The vortex shedding phenomenon is also reproduced by both solvers. In the case of TELEMAC-3D, it is observed that the vortices downstream of the cylinder have a more homogeneous vertical structure than those predicted by OpenFOAM.

The mean velocity profiles in the plane of symmetry and at different elevations are shown in figure 5 for the coarse mesh and in figure 6 for the fine mesh. The numerical results are compared with measurements from Roulund et al. [1] for assessment. The RANS model used solves the mean flow and models the turbulence. However, in this case, the RANS model is used to study a flow with varying properties, especially via the phenomenon of vortex releases. This is often referred to as a URANS model (for Unsteady RANS). In this section, we discuss the time average of the flow solved by the RANS equations.

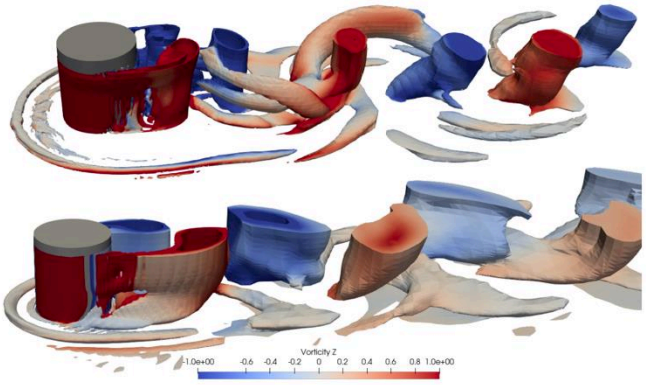

Figure 5. Visualization of coherent flow structures by representing isocontours of Q criterion. The color scale represents the values of the vertical component of the vorticity. Seen from above, the red vortices rotate clockwise and counter-clockwise for the blue vortices.

In the case of the coarse mesh (mesh 1), the horseshoe vortex is not observable on the velocity profiles predicted by OpenFOAM (see figure 5). The signature of this vortex results in negative u component of the velocity field upstream of the cylinder near the bottom, as observed on the TELEMAC-3D profiles. By refining the mesh near the bottom, the horseshoe vortex appears in the OpenFOAM simulations as shown in figure 6. On the contrary, when the mesh is refined with TELEMAC-3D the results are worst, the recirculation cell associated with the horseshoe vortex becomes too large. At the downstream side of the cylinder close to the free surface, the experimental results show the existence of a positive u value before becoming negative further away from the cylinder. Neither OpenFOAM nor TELEMAC-3D succeed in capturing this behaviour quantitatively. Again, TELEMAC-3D results are worst when the mesh is refined. Another observation is the small variation with z of the TELEMAC-3D velocity field downstream of the cylinder. The velocity profiles have indeed almost the same shape at all elevations. OpenFOAM results show more variations of the flow as a function of z, consistently with experimental results. Also, OpenFOAM results improve downstream of the cylinder when the mesh is refined while the TELEMAC-3D results are getting worst.

To conclude, OpenFOAM needs a fine mesh near the walls to reproduce the flow characteristics in a satisfactory manner, and in particular the horseshoe vortex. The flow downstream of the cylinder predicted by OpenFOAM is close to the experimental results and the horseshoe vortex is present. The TELEMAC-3D results are getting worst when refining the mesh. The horseshoe vortex whose size corresponds to the experiment with mesh 1, becomes two to three times larger with mesh 2. Moreover, the mean fields at the downstream side of the cylinder are very different from the experiments.

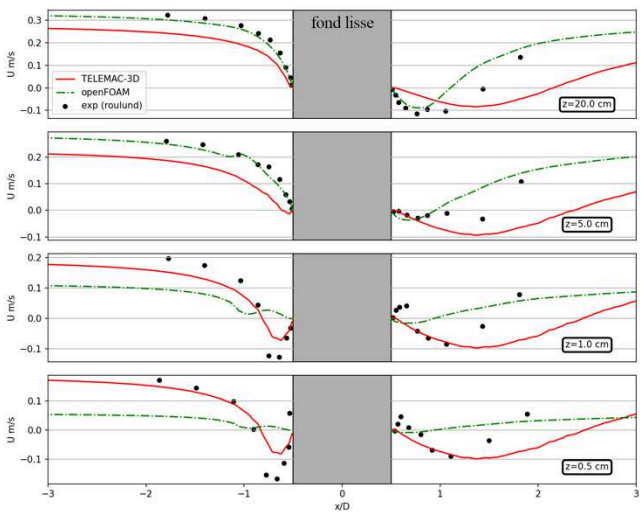

Figure 6. Mean horizontal component u of the velocity field visualized in the plane of symmetry at different elevation z above the bed predicted by openFOAM (green dash-dotted lines) and TELEMAC-3D (red solid lines) compared with experimental results from Roulund et al. (2005). The mesh used corresponds to mesh 1.

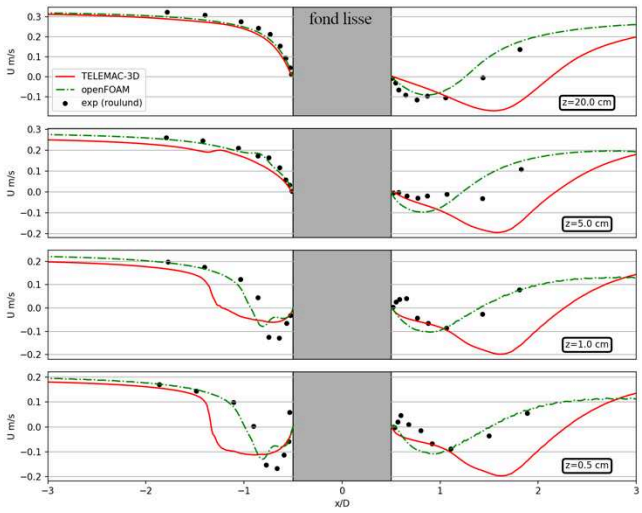

Figure 7. Mean horizontal component u of the velocity field visualized in the plane of symmetry at different elevation z above the bed predicted by openFOAM (green dash-dotted lines) and TELEMAC-3D (red solid lines) compared with experimental results from Roulund et al. (2005). The mesh used corresponds to mesh 2.

The end goal being the computation of scouring, the prediction of bed shear stress patterns is of outmost importance. Figure 7 shows the bed shear stress amplification profile in the plane of symmetry upstream of the cylinder.

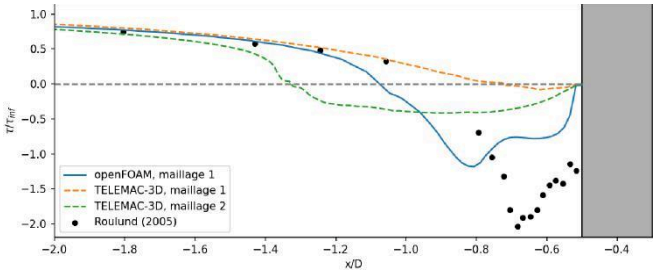

Figure 8. Amplification of the bed stress τ0/τ∞ along the symmetry plane upstream of the cylinder compared with Roulund et al. [7] hot film measurements.

Both TELEMAC-3D and OpenFOAM underestimate the bed shear stress associated with the horseshoe vortex. This was also observed in the numerical results presented by Roulund et al. [1] and Nagel et al. [8], using RANS models. TELEMAC-3D results show that for mesh 1, although the signature of the horseshoe vortex is well present on the velocity field (see figure 5), it is almost totally absent on the upstream stress profile (figure 7), for which the stress becomes very slightly negative but on a very restricted area almost in contact with the cylinder wall. For mesh 2, the horseshoe vortex is too large compared to what is observed by Roulund et al. [1], and the bed shear stress associated with the vortex is also underestimated. OpenFOAM results with mesh 2 predicts qualitatively the shape of the bed shear stress profile even though the maximum negative value is underestimated. This discrepancy is probably due to the fact that the bed shear stress is computed from a parametrization based on the velocity in the first cell near the wall in TELEMAC-3D while the true definition is used in OpenFOAM. This is a problematic finding because the horseshoe vortex is the main contributor to scouring around the cylinder. If the prediction of the bed shear stress associated with the horseshoe vortex is not accurate, it is likely that the sediment transport fluxes and the subsequent morphological evolution will not be accurate as well.

IV. CONCLUSION

The numerical study of scour requires first an accurate model for the flow around the obstacles. The work presented here enables to evaluate the capabilities of two software to simulate the flow around a wall-mounted cylinder, acting as a bridge pier at a reduced scale.

In a first step, an undisturbed flow is simulated and the results are compared with experiments for different meshes. The results show a low sensitivity to the mesh resolution for TELEMAC-3D. This is due to the wall laws which allow more robust results at the expense of an inability to reproduce the physics of the flow near the walls. On the other hand, OpenFOAM results are very sensitive to the mesh resolution and a fine mesh near the walls is needed to obtain satisfactory results.

Neither of the two softwares provides fully satisfactory results for the flow around a cylinder. The stress generated by the horseshoe vortex is systematically underestimated or even absent if a coarse mesh is used. OpenFOAM, with a sufficiently fine mesh near the walls, provide satisfactory results that are close to the experiments, and other studies from

the literature have shown that further refinement of the mesh allows to obtain even better results [8]. With TELEMAC-3D using $k-\epsilon$ model, flow patterns are coherent qualitatively, but not satisfactory quantitatively with both mesh configurations. Bed shears stresses are also further from the measurements than OpenFOAM. These results suggest the following areas of improvement in order to make TELEMAC-3D with k-epsilon model more reliable for scouring applications: optimization of the mesh (e.g. based on a dimensionless wall distance criterion), and modification of the computation of the bed shear stress.

REFERENCES

[1] Andreas Roulund, B. Mutlu Sumer, Jørgen Fredsøe, and Jess Michelsen. Numerical and experimental investigation of flow and scour around a circular pile. J Fluid Mech., 534 : 351–401, 2005

[2] B. Mutlu Sumer and Jergen Fredsøe. Hydrodynamics around cylindrical structures. World Scientific Publishing, 2006.

[3] B.E. Launder and B.I. Sharma. Application of the energy-dissipation model of turbulence to the calculation of flow near a spinning disc. Letters in Heat and Mass Transfer, 1974.

[4] F. R. Menter, M. Kuntz, and R. Langtry. Ten years of industrial experience with the sst turbulence model. Technical report, Software Development Department, ANSYS, 83714 Otterfing, Germany, 2003.

[5] David C. Wilcox. Turbulence Modelling for CFD. DCW Industries, 2006.

[6] David R. Fuhrman, Martin Dixen, and Niels Gjøl Jacobsen. Physically-consistent wall boundary conditions for the $k-\omega$ turbulence model. J. Hydraul. Res., 48(6):793–800, 2010.

[7] C. Baykal, B.M. Sumer, D.R. Fuhrman, N.G. Jacobsen, and J. Fredsøe. Numerical investigation of flow and scour around a vertical circular cylinder. *Phil. Trans.*, 373, 2014.

[8] Tim Nagel, Julien Chauchat, Cyrille Bonamy, Xiaofeng Liu c, Zhen Cheng, and Tian-Jian Hsu. Three-dimensional scour simulations with a two-phase flow model. *Adv. Water Resour.*, 2020.

3D hydrosedimentary models of the Loire Estuary using TELEMAC-3D-TOMAWAC and GAIA

Guillaume Isserty[1], Régis Walther[1], Olivier Bertrand[1]
guillaume.isserty@arteliagroup.com
[1]: ARTELIA, 6 rue de Lorraine, 38130 Echirolles, France

Abstract – **Supervised by the Loire Estuary Public Interest Group (GIPLE), 3D hydrosedimentary models were built and calibrated to provide answers at the scale of estuary, for several physical processes: hydrodynamics conditions, mud dynamics, water quality, dumping and dredging processes. These models take full advantage of the GAIA module in TELEMAC, and shows its ability to provide good results of complex processes at a large scale. This paper presents the building and calibration steps for 2 of the models developed: the global hydrosedimentary model, and the local dumping model. Water quality, and dredging processes modelling in still an ongoing work.**

Keywords: estuaries, sediment processes, maritime, sandy-mud mixtures, salinity.

I. INTRODUCTION

The Loire estuary is one of the three major French estuaries. It is a macro-tidal estuary with a mean spring tidal range of about 5 m allowing the tide to propagate up to Ancenis, 90 km upstream from the mouth (Saint-Nazaire). The water quality of the estuary is considered as relatively bad with a large maximum turbidity due to significant developments over the two last centuries including a deep-water port development downstream in the Saint-Nazaire area with an outer navigation channel down to -12.5m Chart Datum and the creation of a unique inner navigation channel at -5m CD up to the city of Nantes located 55 km upstream from Saint-Nazaire. Large scale hydrosedimentary modelling can be a great decision making tool for any stakeholder in such estuary, whether it is to properly manage the cities drinking water supply, to assess the filling rate of navigation channels… To that extent, several 3D numerical models were built under the supervision of the Loire Estuary Public Interest Group (GIPLE) using TELEMAC3D coupled with GAIA and TOMAWAC. These models provide an update of the existing ones on the estuary, which were set up in 2012. It will take full advantage of the GAIA module which was not available at that time. The global model was calibrated for each of the main processes that occur in the estuary. A more local and specific model for sediment dumping was also developed. A third model is still being developed in which we model the dredging processes of the estuary, along with dumpings and dispersion of sediments.

II. GLOBAL HYDROSEDIMENTARY MODEL

The goal of the global hydrosedimentary model is to solve global scale hydrodynamics and sedimentary processes inside the estuary. Water levels, salinity and sediment transport are at stake and the hydrosedimentary model will be the basis for the other models. All the different processes modelled may impact one on each other. It was thus decided to calibrate the model in a "step-by-step" way, adding processes one after another, starting with simple hydrodynamics, and ending with fully coupled hydrosedimentary model, including wave effects.

A. *Extent, bathymetry and mesh*

The global hydrosedimentary model extends from a marine boundary more than 100 km from the coast to the upstream boundary located roughly 100 km upstream inside the estuary. The marine boundary is located far enough away to limit the suspended sediment concentration exit from the model. The upstream boundary is located above the tide effects upward limit.

The model bed elevations are based on several bathymetric sources. They were aggregated carefully to avoid gaps or jumps at the connections. Inside the estuary, the bathymetry available has fine resolution (around 1 meter). Outside, bathymetry from HOMONIM project is used (50 meters resolution).

Final mesh has 50,000 2D nodes, and 12 vertical planes, leading to roughly 650,000 3D nodes. The vertical planes are a mix between fixed elevation planes and sigma planes. If the water levels are low, the vertical mesh is made of only sigma planes. This will allow good representation of stratification phenomena, whatever the hydrodynamics conditions. Global scale model bathymetry is shown in Figure 1.

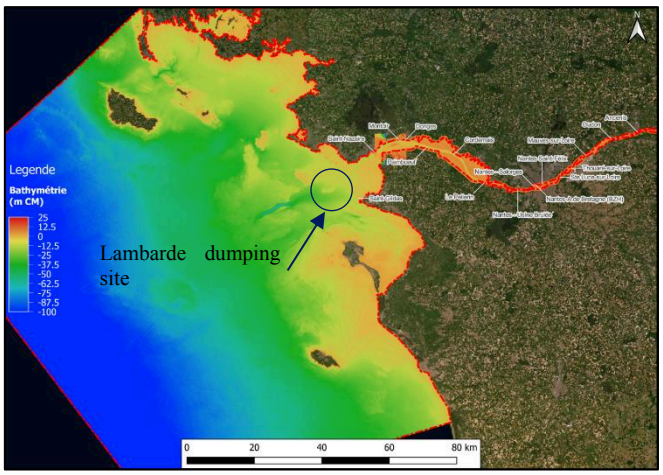

Figure 1. Global scale model bathymetry

B. Hydrodynamics

At first, only hydrodynamics is modelled and calibrated.

1) Stakes and goals

The modelled area is subject to semi-diurnal tide. The upstream border location was set up to be the tide influence limit. Regarding river flows, Loire has the highest contribution by far. Two of its tributaries are also present in the Nantes city area.

During floods, the flow can reach around 6,000 m^3/s, while in extreme low-waters it can decrease down to 60 m^3/s. Mean annual flow is around 800 m^3/s.

Competition between tide and river flow has to be well modelled to ensure proper results regarding salinity, SSC or water quality.

2) Numerical implementation

a) Tide and river flow forcing

At the downstream maritime boundary, astronomical tide is reconstructed from 32 waves extracted from FES2012 model [5]. At the upstream boundary, the combined Loire and Evre discharges are imposed. Inside the model, two of the Loire tributaries river rates discharges are imposed in source points.

b) Meteorological forcing

Pressure effects are taken into account thanks to temporal variation of the mean sea level at the maritime boundary. Wind temporal and spatial variation are imposed on the whole model. Data is extracted from the HOMERE database. Inside the estuary, wind intensity is lowered, up to a certain point where it is set to zero. From this point, the shading by buildings or vegetation is too pronounced to account for wind effects.

c) Friction coefficient

Friction coefficient is variable in space, and time, as a function of the upstream flowrate. A Nikuradse friction coefficient is used. Fluid mud plays an important role for the friction inside the estuary and is therefore taken into account.

Depending of the flowrate, the fluid mud is located rather upstream or downstream in the estuary. Lateral and longitudinal limits need to be calibrated. The Nikuradse friction coefficient is lowered to 0.00087 m for the fluid mud parts. This value comes from lab experiments that were made on Loire muds [2].

d) Calibration methodology

Six different periods are chosen for calibration. They are each representative of a particular flowrate. During these periods, we mainly focus on a 24 hours period during which flowrate is quite constant, and we calibrate bottom friction coefficient and fluid mud position to match the measured water-levels all along the estuary.

Calibration validity is controlled thanks to root mean square error, mean error and standard deviation, along with three other time percentage parameters which are presented in the Table I.

Table I – Definition of CF, POF, COF

CF(X)	Percentage of errors inside [-X;X]
POF(X)	Percentage of errors over X
NOF(X)	Percentage of errors below -X

The calibration is considered good if CF(X) is above 90% during the 24 hours period, with X set to 0.2 meters. Results are also compared on the whole period (2 weeks) to ensure that they have the same quality. The calibration results in a set of friction coefficient and mud positions for each of the 6 flowrates. For the simulations these values are interpolated linearly for every flowrate.

This method is finally validated on three long-term periods of three months each, representative of different hydrodynamic conditions.

3) Results and discussion

a) Friction coefficient map

Friction coefficient and mud positions are calibrated (see II.B.2)c)).Table II summarizes mud positions (indicated in kilometric point (KP) from the estuary mouth) as a function of flowrate.

Table II – Mud position as a function of upstream flowrate

Flowrate (m^3/s)	**125**	**200**	**400**	**850**	**2500**	**4000**
Downstream limit (KP[7])	17.6	13	10	2	-5	-5
Upstream limit (KP)	65	50	35	22	13	11

A total of 15 gauge stations are used for this calibration phase. The resulted friction coefficients are shown in Figure 2. Friction values are summarized at every gauge stations available. In addition, the Downstream Limit (DL) and Upstream Limit (UL) of fluid mud are added.

[7] Kilometric Point from Saint-Nazaire harbour

Nom	Flowrate / KP (km)	4000 m³/s	2500 m³/s	850 m³/s	400 m³/s	200 m³/s	125 m³/s
Downstream limit of navigation channel	-15	0.002	0.002	0.002	0.002	0.002	0.002
DL(4000)/DL(2500)	-5	0.00087	0.00087				
Saint-Nazaire	-0.5	0.00087	0.00087	0.05	0.05	0.002	0.002
DL(850)	2	0.00087	0.00087	0.00087			
Montoir	7.9	0.00087	0.00087	0.00087	0.05	0.002	0.002
Donges	9.4	0.00087	0.00087	0.00087	0.002	0.002	0.002
DL(400)	10	0.00087	0.00087	0.00087	0.00087		
UL(4000)	11	0.00087	0.00087	0.00087	0.00087		
UL(2500)/DL(200)	13		0.00087	0.00087	0.00087	0.00087	
Paimboeuf	16.4	0.002	0.05	0.00087	0.00087	0.00087	
DL(125)	17.6			0.00087	0.00087	0.00087	0.00087
UL(850)	22			0.00087	0.00087	0.00087	0.00087
Cordemais	24.7	0.15	0.05	0.15	0.00087	0.00087	0.00087
UL(400)	35				0.00087	0.00087	0.00087
Le Pellerin	37.7	0.15	0.1	0.15	0.05	0.00087	0.00087
Nantes - Usine Brûlée	48.1	0.2	0.2	0.15	0.1	0.00087	0.00087
UL(200)	50					0.00087	0.00087
Nantes -Salorges	53	0.2	0.2	0.2	0.15	0.15	0.00087
Nantes - A. de Bretagne	53.5	0.2	0.2	0.25	0.15	0.2	0.00087
Nantes - Saint Félix	56	0.2	0.2	0.25	0.15	0.25	0.00087
Sainte-Luce	61.8	0.1	0.1	0.15	0.15	0.3	0.00087
UL(125)	65						0.00087
Thouaré	66.5	0.3	0.4	0.4	0.4	0.3	0.3
Mauves	72.3	0.3	0.2	0.1	0.2	0.2	0.3
Oudon	82.1	0.3	0.2	0.1	0.2	0.1	0.1
Ancenis	90.5	0.3	0.5	0.2	0.15	0.1	0.1
Upstream Boundary	100	0.3	0.5	0.2	0.15	0.1	0.1

Figure 2. Final Nikuradse friction coefficients (in m) for the 6 flowrates

b) Calibration and validation results

A good calibration (CF(0.2)>90%) was reached for nearly all retained gauge stations and for every time period. RMSE is nearly always below 0.1m. Figure 3 shows graphical comparison of water levels evolution at a station located rather upstream inside the estuary. The model is particularly able to reproduce correctly the period if river flow influence is greater than tide influence. Scores of the model are summarized for this same station in the scatter plot displayed in Figure 4. Most of the simulated water levels are very close to the measured one. Only for < 10 measurements the deviation is bigger than 0.2 m.

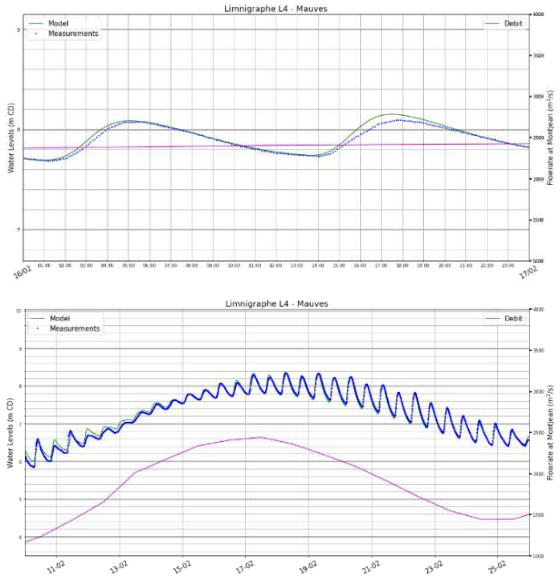

Figure 3. Temporal water levels evolutions for Mauves gauge station. Green line: model results; pink line: flowrate; blue dots: gauge data

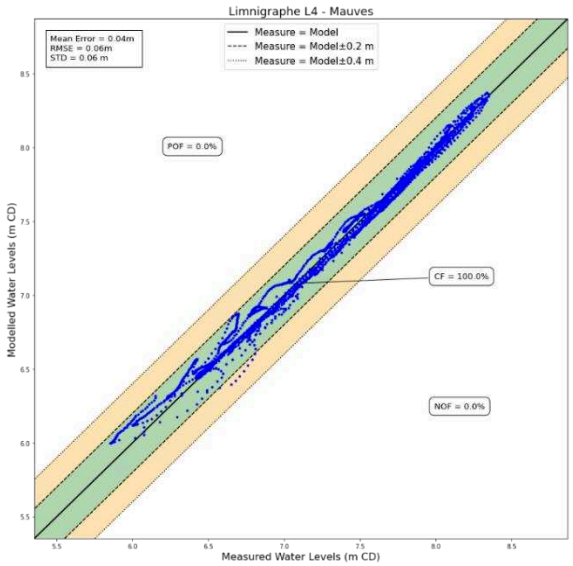

Figure 4. Scatter plot for Mauves gauge station – Calibration period

Validation step was made of three different periods lasting three months each. Hydrodynamics condition were either flood (winter 2021), severe low-waters (summer 2019), or mean conditions (spring 2011). Once again, RMSE was often around 0.1 meters. Comparison can be synthetized in one scatter plot for each gauge station. Figure 5 is an example of a validation result over the 2011 period, at the mouth of the estuary.

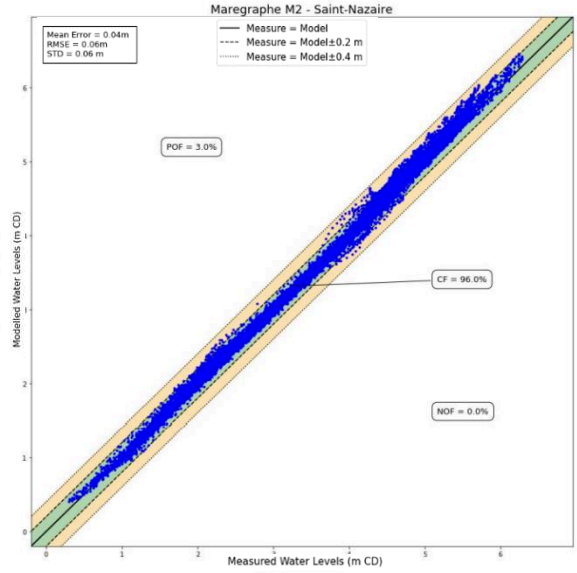

Figure 5. Scatter plot for Saint-Nazaire gauge station – Validation period

C. *Salinity*

1) Stakes and goals

Vertical salinity layering in the downstream part of the estuary can be quite significant, especially on extreme hydrodynamics conditions:

- During flood, a high freshwater surface flow is opposed to bottom saline water flow, leading to high stratification
- During low-waters, tidal force is not high enough to mix the water vertically. A two-layer flow (one saline, the other fresh) thus exists, with very little exchanges between them. Density driven flow occur, and as the river flow is too low, it induces high salinity upwell, from the sea towards inner estuary.

A good representation of vertical turbulent diffusion will be necessary to reproduce such phenomena.

2) Numerical implementation

a) *Vertical turbulence modelling*

The turbulence model used for this study is a modification of the standard mixing-length model [7]. It adds a correction based on the grade of stratification. In the standard mixing-length model, a damping function is used to account for stratification effects. The formulation of this function is based on experimental or in-situ data. The main issue with this model is that the height of the main dissipating scale must be given.

In cases where stratification is high enough, turbulent production in the lower layer is independent from production in the upper layer. The mixing length is thus calculated in an independent way in the two layers. If it is not high enough, standard mixing length in used. Schematic of the modification between the two models is shown in Figure 6.

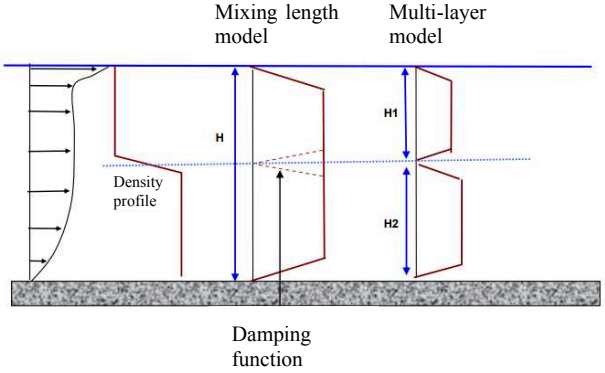

Figure 6. Mixing length and multi-layer vertical turbulence model

The Richardson number is used to consider if stratification is dominant. If the Richardson is above a chosen threshold (typically around 0.2-0.25), stratification dominates, and multi-layer model is used.

The Loire models from 2012 show similar results with this multi-layer model to a k-epsilon model, but with lower computational costs.

b) *Waves action*

In addition to forcing used for the modelling of hydrodynamics, waves parameters have to be computed at each point of the model. The model is forced at its maritime boundary by data from HOMERE database regarding waves: wave height Hm0, peak period Tp, Peak Direction Dp and direction spread Spd.

3) Results and discussion

One of the parameters that can be calibrated is the critical Richardson number, which determines if the two layers are considered independent for turbulent production (and mixing length calculation).

Critical Richardson was finally set up to 0.2. Comparison of the model results to available measures is analysed qualitatively, making sure that the model can correctly reproduce the following phenomena:

- Good representation of stratification period, whether it is low-water (with weak vertical mixing, and weak horizontal spread), low flow (with weak vertical mixing, and little opposition to density driven currents going upward), or flood (with freshwater flow in surface, and saline water entering the estuary in the bottom);
- Good representation of mixing periods whether it is spring tide with a strong vertical mixing, and horizontal spreading or a wind blow inducing a strong vertical mix.

The final choice of parameters was made so that the model reproduces as well as possible the saline upwells. These phenomena will be important to also reproduce cohesive sediment upwells for the final hydrosedimentary model. Figure 7 shows the good representation of salinity evolution during a whole year, including two high flowrate periods.

Blue squares in the figure indicates periods where measurements behave strangely. Discrepancies during these periods are not representative of the model performance.

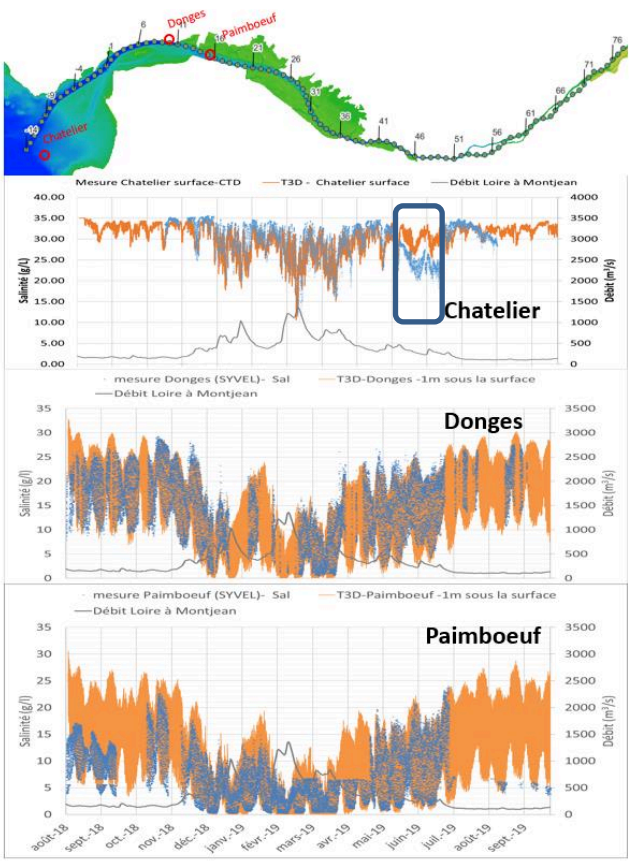

Figure 7. Temporal evolution of salinity – Model (orange) versus measure (blue dots)

D. *Sediment*

1) Stakes and goals

This global scale model is particularly made to reproduce the mud dynamic inside the whole estuary. Parameters that will be of interest are the following ones:

- Suspended matter → temporal and spatial evolution and stratification depending on hydrodynamics conditions
- Fluid mud dynamic → temporal and spatial evolution of the thickness of the different types of fluid mud layers, being:
  - consolidated fluid mud (325 to 375 g/l);
  - Sensu-stricto fluid mud (125 to 300 g/l);
  - Liquid fluid mud (40 to 100 g/l).

2) Physical processes

a) *Settling Velocity*

For the global model, we mainly focus on the mud cap dynamic inside the estuary. Only mud is transported, not sand. The dynamics of this cohesive sediment are determined by solving the transport equation:

$$\frac{\partial c}{\partial t} + u\frac{\partial c}{\partial x} + v\frac{\partial c}{\partial y} + w\frac{\partial c}{\partial z} + \frac{\partial W_s c}{\partial z} = \frac{\partial}{\partial x}\left(\varepsilon_x \frac{\partial c}{\partial x}\right) + \frac{\partial}{\partial y}\left(\varepsilon_y \frac{\partial c}{\partial y}\right) + \frac{\partial}{\partial z}\left(\varepsilon_z \frac{\partial c}{\partial z}\right) \quad (1)$$

The settling velocity W_s is determined using three different field measurement data. A Thorn/Mehta law [8] is matched to this data. Two different behaviours are observed depending on the concentration. At lower concentrations, the law obtained is in the form

$$Ws = k_1 \times C^{m1} \quad (2)$$

At higher concentrations, flocs induce a velocity decrease. The corresponding law is:

$$Ws = Ws_0 \times (1 - k2 \times C)^{m2} \quad (3)$$

In addition, flocculated or unflocculated state of the flow is simply determined by mean velocity and is taken into account by reducing the settling velocity in case of unflocculated flow.

b) *Deposition fluxes*

At the interface between soil and water, deposition and erosion occur, at rates that need to be determined. According to the theory detailed in [1], consolidation starts when concentration is roughly above 40 g/L. Mass transfer between suspended sediments and the first bottom layer thus occur as soon as the concentration is greater than 40 g/L. The deposition flux is calculated as follows

$$F_{dep} = W_s \times C_{bottom} \quad (4)$$

with W_s being the settling velocity at the bottom of the water column.

c) *Mud erosion*

An erosion rate law is established for this study, based on measurements from [2] Sanchez.

d) *Pure sand erosion*

In the case of pure sand, transport is calculated using van Rijn transport 2004 model [3] which is not detailed here.

e) *Mud/sand mixture erosion*

In the case of a mixture of sand and mud, the law used is a function of the fraction of mud. If the mud mass fraction inside a sand/mud mixture is below 0.3, the critical erosion shear stress is higher than the one of pure sand. Mud infiltrates inside holes between sand grains and adds cohesion to the mixture. If the fraction is higher than 0.3, sand grains lose contact between each other, and critical erosion shear stress gets lower. Finally, if the fraction is higher than 0.5, the mixture behaves as pure mud.

f) *Consolidation*

The consolidation model uses different sediment layers (16 for our model), each one having a fixed concentration and critical erosion shear stress. Mass transfer between layers is calculated with a simple transfer function:

$$\frac{dm}{dt} = a \tag{5}$$

a being a coefficient that needs to be calibrated for each layer. In our case, a was determined using [1]. One can found in this paper the solid discharge (Q_c) through a constant concentration (C) layer:

$$Q_c = VC\left[A_2 A_1 \left(\frac{C}{\rho_s}\right)^{A_3} - 1\right] \tag{6}$$

with A1=1.6 m/s, A2=72 and A3 = 0.65 for a Loire mud. This solid discharge corresponds exactly to the mass transfer between two layers and is thus equal to the parameter a in equation (5).

g) Sliding

Without any sliding, sediment tends to settle rapidly in navigation channel banks, and are quite never getting back into suspension, because hydraulic stress is not high enough. In our model, for layers of concentration ranging from 40 to 100 g/l (liquid fluid mud), deposited sediments slide in the direction of the strongest slope, as soon as a critical slope is overpassed. The critical slope chosen in the model corresponds to observations in the Saint-Nazaire port and is equal to 2.5% (1.43°). This sliding process is numerically done within the gaia_maxslope routine, modifying the angle value for the considered bed layers (for the previously described concentrations).

3) Numerical implementation

a) Sediment forcing

Regarding sediment modelling, three different kinds of forcing are used:

- Upstream boundary condition, with a sediment flowrate, reconstructed from available measurement data;
- Bottom boundary condition, with initial composition of the bed layers, based on sediment composition extracted from the EMODnet project [4];
- Initial fluid mud conditions, shown in Figure 8.

Figure 8. Initial fluid mud conditions (mud: green, no mud: blue): liquid fluid mud on the left, stricto-sensus and consolidated fluid mud on the right

b) Bed model using GAIA

The bed model is composed of 16 sediment layers between which mass transfer can occur, along with an additional layer which represents the initial sediment composition (based on the EMODnet project) and which is independent from the other layers (i.e. mass-transfer cannot occur). An active layer is also set up at the top.

The sixteen layers are sand and mud mixtures, of different mud concentration. They can be divided into 3 main groups:

- Consolidated fluid mud: 3 layers with concentration ranging from 325 to 375 g/L;
- Sensu-stricto fluid mud: 9 layers with concentration ranging from 125 to 300 g/L;
- Liquid fluid mud: 4 layers with concentration ranging from 40 to 100 g/L.

Mass transfer between layers is calculated thanks to the consolidation model equations detailed before.

4) Results and discussion

Figure 9 shows the annual dynamic of SSC inside the inner estuary. The mud cap (concentrations below 40 g/L) signal corresponds well to the one observed in situ by the GIPLE [6]. Its length and intensity vary with tide cycles (strong concentration and big length for high-tides, and the opposite for low-tides), and its core moves upward or downward depending on river flow. When river flow is important, mud cap is contained below kilometric point 25, and when it is very low, it can climb up to Mauves (kilometric point 70).

Model is also compared to several SYVEL (a continuous measurement network) gauge stations measurements of the SSC. The three stations presented in Figure 10 show different mud dynamic depending on longitudinal locations.

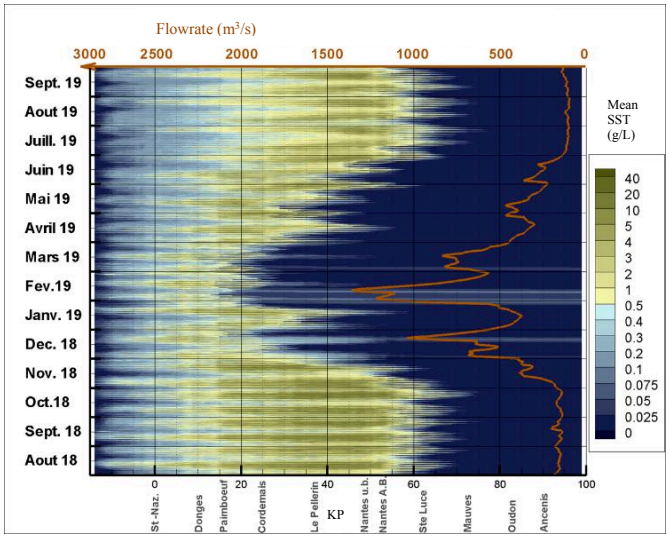

Figure 9. Modelled annual dynamic of SSC

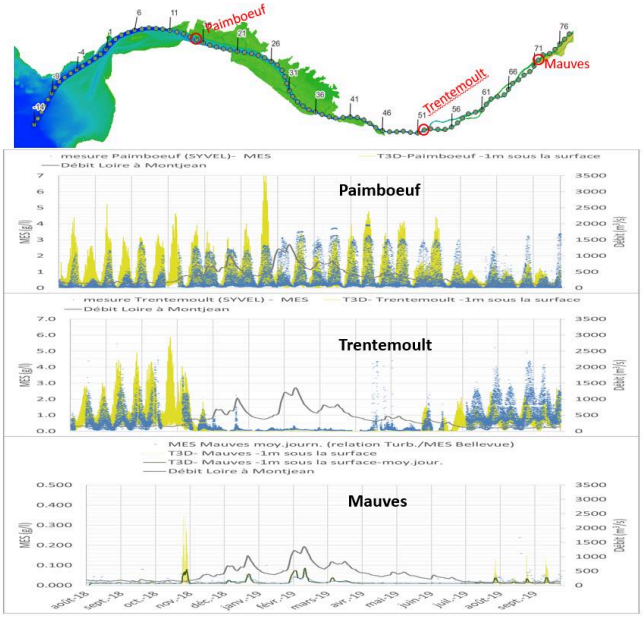

Figure 10. Model results versus SYVEL measurements for SSC

Finally, Figure 11 shows the global fluid mud dynamics. Measurement of fluid mud deposits are regularly performed by the port authority along the navigation channel. The analysis of these data indicates that there is no mud in the channel navigation upstream of the kilometric point 30 for a discharge of 500 m3/s (mean discharge of the ten last days). This phenomenon is reproduced with the numerical model during a one year simulation. We can see on Figure 11 that during flood conditions the mud is located downstream and then moves up to the kilometric point 30 when the discharge of the ten last days is less than 500 m3/s.

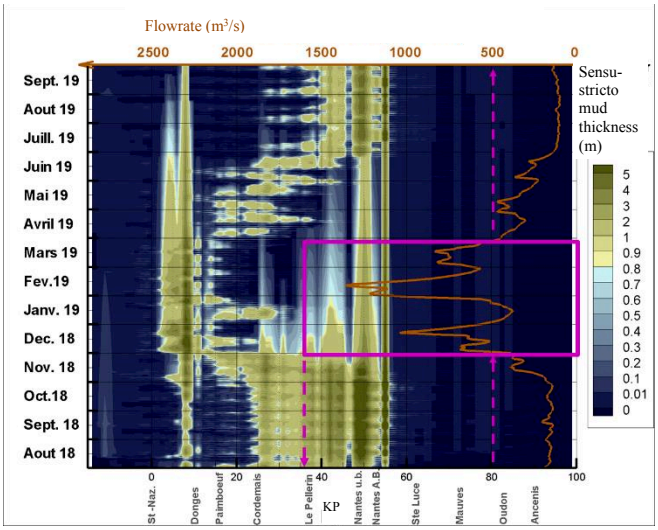

Figure 11. Modelled annual dynamic of fluid mud

III. LOCAL DUMPING MODEL

The port is dredging sediments from the navigation channel and then dumping it at the Lambarde dumping site. Evolution of bottom elevation at the site and assessing the stability rate of the area can help defining dumping scenarios for future operations. The aim of this local model is to represent the bottom evolutions of each dumping sub-zone, and the global sediment volume that consolidates over time, compared to the dumped volume.

A. Model set up

To achieve this goal, a new mesh is created, highly refined around the dumping area. The model boundary nodes correspond exactly to nodes from the global hydrosedimentary model. This allows us to force our local "sub-model" with results from the global model, for the hydrodynamics part. Waves' parameters are still extracted from the HOMERE database. Wind is not taken into account anymore, to reduce computational times, and because levels imposed at the boundary already include wind effects. In addition to the forcing data of the global hydrosedimentary model, dumped sediment mass is taken into account. All the dumping operations are integrated in the model one by one, and with respect to the real chronological order. A map of every dumping "sub-zone" and the time period associated is shown in Figure 12.

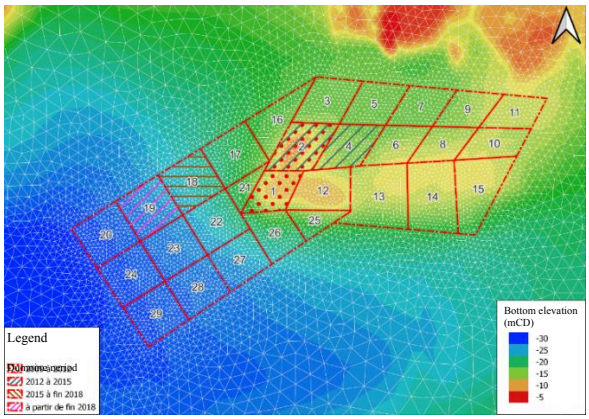

Figure 12. Dumpings sub-zones and time period associated

B. Dumpings modelling

Usually, one would distinct three different phases in the dumping: suspension, bottom deposit, and bottom turbid plume. On this local model, bottom turbid plume is not pre-defined with parameters, but derives from the suspended sediment fall. This gives more realistic results than when you impose the turbid plume with a predefined geometry.

Mass repartition inside the two phases is fixed after calibration at: 100% bed deposit for sand, 60% suspension and 40% bed deposit for mud. The suspended part is injected uniformly thanks to source terms in each of the horizontal plane of the 3D-model. The bed deposit is modelled in a way that it represents the crater geometry that is observed in-situ. In the model, it depends of three parameters, as shown in the Figure 13.

The different radii are used to:

- R1: handle size of inner crater;
- R2: handle size of footprint;
- R3: handle mass repartition inside the geometry

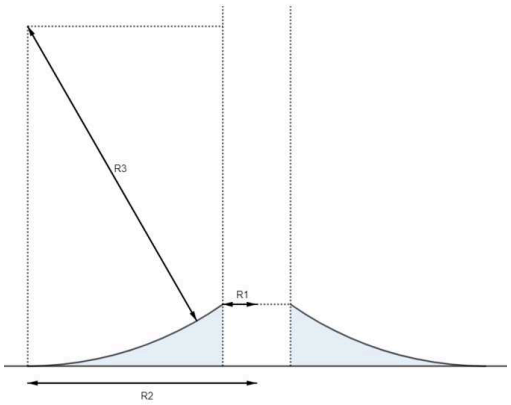

Figure 13. Geometry of ground deposit

The sediment mass that composes this deposit is added into layers of the bed model. The layers are adapted during the calibration phase, to find the best repartition to properly reproduce in-place volume and sub-zone elevations.

C. Results and discussion

The local model of the Lambarde dumping site is calibrated over around 9 years, from September 2011 to May 2020. During this calibration, bed deposit geometry, suspension percentage for mud, layers chosen for bed deposit and critical slope for sliding were adapted to properly reproduce both the temporal evolution of the global volume on the area, and the temporal evolution of mean elevations for every sub-zone. Data for mean elevations and volume is calculated from the different bathymetric set available (around 1 per year). Uncertainty in the calculated volume can thus be quite high, depending on the bathymetry uncertainty (which is never below 0.1 meters in our case).

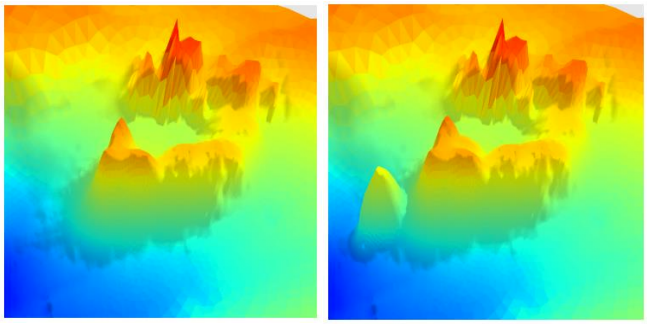

Figure 14. Model bathymetry at the start of the simulation (left) and after 9 years of dumping (right)

The Figure 14 shows a 3D view of the dumping site at the start of the simulation, and after the 9 years of dumping.

The main objective is to reproduce the global evolution of the site, with good correlation between model and measurements as far as volume is concerned. The final results obtained are shown in the Figure 15.

Figure 15. Calibration result for in-place volume – Model in red line, dumped volume in green line and in-place volume data in blue dots

Stability of the site which is the ratio between the deposited volume and the dumped volume, is calculated for different representative dumping periods. Table III summarizes modelled stability rates versus in-situ ones.

Table III – In-situ and modelled stability rates

09/2011 → 09/2019		**09/2011 → 05/2015**	**05/2015 → 06/2018**	**06/2018 → 07/2019**
In-situ	18.7 %	10.5 %	26 %	13.3 %
Modelled	18.4 %	11.4 %	25.4 %	7.6 %

As far as elevations are concerned, a good calibration shows the capability of the model to reproduce the spreading of the deposit, and the erosion flux during period where no dumping is done. Final results for mean elevations are shown in Figure 16.

Figure 16. Calibration results for mean elevations. Model in plain lines and data in dots.

IV. CONCLUSION AND PERSPECTIVES

A global 3D hydrosedimentary model of the Loire estuary has been built up and calibrated with diverse data and on diverse periods. So far, the model shows good capability to represent the large scale dynamics of sediment transport, or fluid mud movement. A local dumping model of the Lambarde site has also been built and calibrated. It reproduces quite well the stability of the dumping site, over

10 years, and also over a sub-zone dumping period. The global model is currently being improved by adding:

- The modelling of dredging processes inside the estuary. The local dumping model will be included inside the global mesh, and refinement will be made on the coastal at the mouth of the estuary, with a goal to reproduce dispersion of sediments after the dumping process. Mass-balance inside the whole estuary will be at stake;
- A water quality module, using WAQTEL.

It should in the end provide answers to a lot of hydraulic related topics that stakeholders can be interested in. The information provided by this model is even more important when facing harsh natural phenomena such as the draught that happened this summer, and to which we should be more and more subject in the future.

ACKNOWLEDGEMENT

Authors acknowledge the GIP Loire Estuaire for funding the study and for all the data provided.

REFERENCES

[1] Sanchez M., Grimigni P et Delanoe Y.,2004. “Distribution des sédiments cohésifs en relation avec la vitesse de la phase solide dans l’estuaire de la Loire , VIII journees Nationales Génie Civil-Génie Côtier, Compiègne 7 et 9 septembre 2007”

[2] Sanchez M., Levacher D.,2008. “Erosion d’une vase de l’estuaire de la Loire sous l’action du courant”, Bull Eng Envir (2008) 67, p597

[3] Van Rijn, L. 2007. Unified View of Sediment Transport by Currents and Waves. Journal of Hydraulic Engineering, ASCE / June 2007

[4] European Marine Observation and Data network: http://www.emodnet-geology.eu/

[5] Carrère L., F. Lyard, M. Cancet, A. Guillot, L. Roblou, FES2012: A new global tidal model taking taking advantage of nearly 20 years of altimetry, *Proceedings of meeting "20 Years of Altimetry"*, Venice 2012

[6] GIPLE, cahier indicateurs numéro 1, fiche L1E2, Avril 2014 : https://www.loire-estuaire.org/accueil/actualites/10_52198/nouvelle_fiche_de_synthese__l1e2___la_dynamique_du_bouchon_vaseux

[7] Walther R, Schaguene J, Hamm L, David E, Coupled 3D modeling of turbidity maximum dynamics in the Loire estuary,, Coastal Engineering Proceedings, 1(33), ICCE 2012– Santander, Spain, 06/2012

[8] Thorn, M. F. C. (1982), Physical processes of siltation in tidal channels, in Hydraulic Modelling in Maritime Engineering: Proceedings of the Conference/Organized by the Institution of Civil Engineers, Held in London on 13 – 14 October 1981, pp. 47 – 55, Thomas Telford, London

Sediment transport modelling in Texas: challenging the conventional knowledge on littoral drift direction

Knaapen, M.A.F.[1], Blanco, B.[1], Lewis, R.[2]
m.knaapen@hrwallingford.com
[1]: HR Wallingford, Wallingford, UK
[2]: HR Wallingford Inc, Houston, Texas, USA

Abstract – **The sediment transport at a regional level along the southern coast of Texas has not yet been analysed in detail. In the existing literature, there is agreement that the net sediment transport direction along the coast of the south of Texas is northward along the coast of the Padre Islands. A numerical model is developed that computes the fully coupled waves, currents and sediment transport in the area using the open TELEMAC modelling system. The results of the model show that our prior understanding of the nearshore littoral processes was incomplete. The combination of stronger ocean currents during high wave events from the north results in a dominant southerly transport along most of the South Texas coast. Only in the northern half of Kenedy County are the residual transport rates to the north. So, where the literature assumes a drift convergence near Kenedy County, the modelling presented here identifies this area as a drift divide.**

Keywords: Sediment transport, coast, littoral drift.

I. INTRODUCTION

The work presented here describes the sediment transport modelling of the Texas coast to inform the Texas General land Office (GLO) on the best approaches to their beach management. The GLO is particularly interest in the best locations for both nourishments and borrow areas.

The sediment transport along the southern coast of Texas (USA) has not yet been analysed in detail. The model focusses on the counties of Cameron, Willacy and Kenedy (Figure 1). The remaining part of the Texas coast will be modelled in 2 further models. For a consistent model set-up, all three models and all figures in this paper use the coordinate system UTM Zone 15 North.

In the existing literature, there is agreement that the direction of the net alongshore sediment transport - littoral drift - along the coast of the south of Texas is northward along the coast of the Padre Islands [1][2]. Earlier studies suggest that the net northward drift decreases with distance north and towards a zone of convergence located near 27°N [2][3], as shown by the grey arrows in Figure 1. However, the location of the convergence point, which would be a great location to extract sediment for any nourishments, is understood to move up and down the coast seasonally such that northerly directed transport may extend to Port Aransas.

More detailed analysis by [1] reports a sediment budget around South Padre Island and Brazos Santiago Pass, while [4] provides rates of sediment lost from the seaward faces of the barrier islands into the lagoon behind by overwash and aeolian processes. Both confirm the northward direction of the littoral drift along the southern part of the Texas coast.

These studies assumed that the longshore sediment transport is caused by waves and wave driven currents only. This paper describes a numerical study modelling the sediment transport due to the combination of waves, wave driven currents and the ocean currents in the Gulf of Mexico. The model results challenge the conventional knowledge in the literature.

II. MODELLING APPROACH

A. General approach

A numerical model that computes the sediment transport pathways in the area using the openTELEMAC- modelling system is set-up [5]. In the model, modules TELEMAC-2D, TOMAWAC and SISYPHE are fully coupled to simulate the two-dimensional, depth-averaged flow field, waves and sediment transport, respectively - as well as the interactions between them. The computational domain covers a surface of approximately XXX × XXX250 × 90 km^2. The model is run for each month in 2018 in 12, preceded by a 2-day spin-up period for each 1-month simulation. Numerical results are then combined to compute the annual sediment transport pathways and bed level changes.

B. Bathymetry

Bathymetric and topographic data were supplied along with the ADCIRC grid provided by the USACE to 10 m water depth. Beyond the 10 m depth contour, the bathymetric data supplied with the USACE grid was supplemented with the 2019 General Bathymetric Chart of the Oceans [7] bathymetric data, to extend the bathymetric data to the offshore boundary. The spatial resolution of the ADCIRC grid bathymetric data is in the same range as the TELEMAC grid with edge lengths between approximately 15 m and 1.5km. The spatial resolution of the GEBCO bathymetric dataset is approximately 500 m near the coast and 3 km around the 50 m depth contour. Both bathymetry data sets are relative to MSL, which is 0.27 m above MLLW at Brazos Santiago Pass and 0.28 m at Bob Hall Pier.

C. General Parameter settings

The model parameters (Table I) used were almost identical to the settings used for a similar study for Poole and Christchurch Bay in the United Kingdom [8][9], which also modelled non-cohesive sediment transport using the Soulsby-van Rijn formulation [10]. Model verification in that study showed a very good validation against measured values of water level, velocities, wave characteristics and suspended sediment transport rates at 9 locations over a double spring-neap cycle.

Modifications in the model set up compared to that previous study - other than the boundary and wind forcing conditions - are the wind growth calculations, which are now based on Yan [11] and 3 calibration parameters: wind velocity correction for the waves, bed friction for the currents and the grain size for the sediment transport.

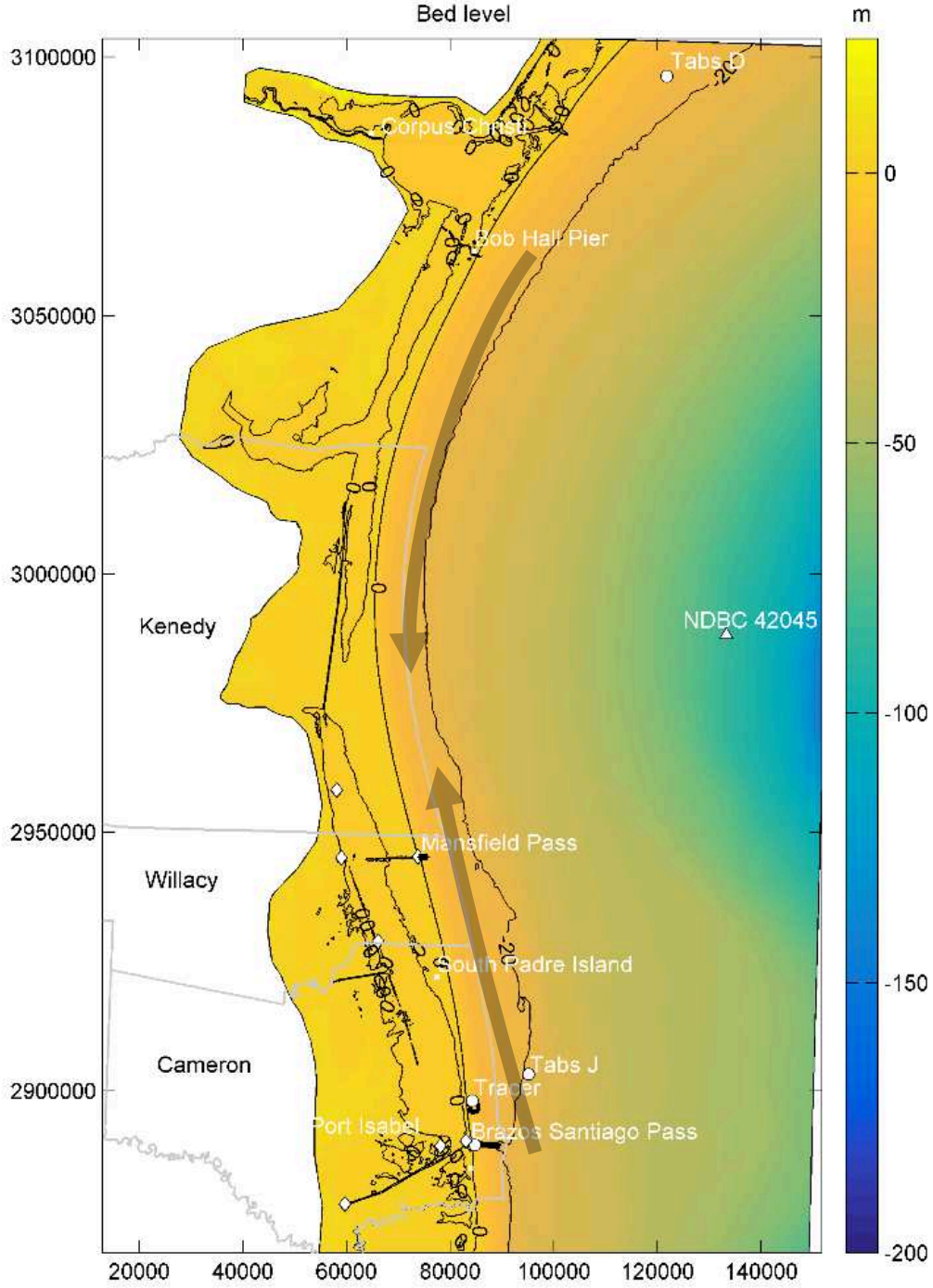

Figure 1. Computational domain and bed levels (colours and contours). TheThe assumed sediment transport directions according to **Erreur ! Source du renvoi introuvable.** are indicated with arrows..

Table I Key parameter setting

Parameter	Setting
Turbulence model	Smagorinsky
Friction law	Nikuradse, variable friction factor
Coriolis acceleration	6.485e-5 m/s
Wind model	Yan
Wave breaking dissipation	Battjes and Janssen
Bottom dissipation	Hasselman, (0.038 m^2/s)
Suspended transport	Soulsby-van Rijn
Bedload transport	Soulsby-van Rijn

The bed composition is taken from a collection of sources [2][12][13], mostly grain size classifications, with few actual diameters. These classifications are translated into 6 spatially varying model sediment fractions. Where no data is available, the fractions are extrapolated using a single fraction for the deep water, nearshore areas, and the Laguna Madre. Figure 2 shows the mean diameter from these sediment fractions.

III. CALIBRATION AND VALIDATION

The model was calibrated against measured data for January 2018 and validated against data from September 2018.

A. Calibration parameters

The calibration of the model only included the setting of 1 parameter for each of the model components. The wave model required a 20% increase of the measured wind speed, for speeds over 20 m/s, with a linear ramp up from 10 m/s to 20 m/s. This is applied as a correction on the energy transfer from the wind to the wave model for higher wind speeds.

The bed roughness in the model (Figure 3) is spatially varying based on the different sediment characteristics of the seabed. There are 5 areas defined. The silty bed of predominantly the deeper Gulf of Mexico, the sandy bed predominantly nearshore, the inlets and two parts of the Laguna Madre with distinctly different bed composition as used by [2].

B. Model quality currents and waves

The model skill quantifies the ability of the hydrodynamic models to reproduce the variations in the measured values of waves and currents, is defined following the methodology proposed by [14]. This method compares the square of the prediction error with the square of the variation in the modelled and measured data. A perfect fit will have a value of 1, predicting a constant value equal to the mean of the measured data will have a value of 0. A model is adequate with values between 0.55 and 0.65; sufficient between 0.65 and 0.75; good between 0.75 and 0.85; and very good above 0.85.

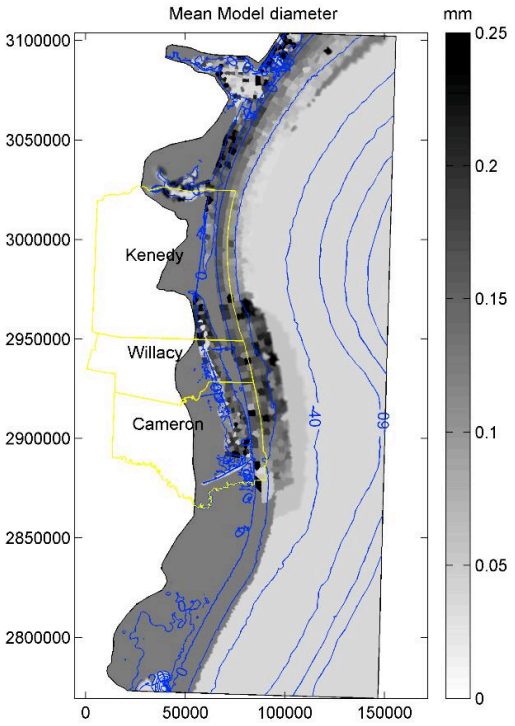

Figure 2. Mean diameter of the model grain sizes

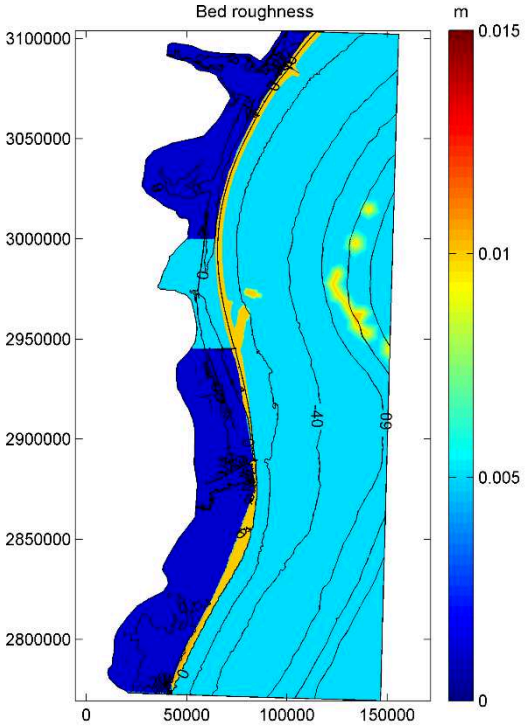

Figure 3. Bed roughness

The model quality, following this classification was very similar in both the calibration (Table II) and validation month (Table III).

The water level predictions qualify as very good for all location. The waves predictions classify as very good for heights and good for directions. The flow velocity predictions were good to very good in the inlets and nearshore areas, but sufficient in the offshore areas, reflecting the uncertainty in wind forcing and the modelling of wind driven currents.

Figure 4 shows the comparison between the predicted currents and those measured by Figlus et al. in their tracer study [15] during November 2018. It shows that the currents are well reproduced both when the tides dominate and when ocean currents increase the current velocities above 0.5 m/s.

Table II Calibration quality

Variable	**Quality**			
	Location		***RMSE***	***Skill***
Water level (m)	Aransas Pass	I	0.10	0.92
	Bob Hall Pier	C	0.10	0.93
	South Padre Island	I	0.11	0.86
	Port Isabel	L	0.10	0.90
Velocity (m/s)	Port Isabel	L	0.16	0.79
	Laguna Madre	L	0.07	0.77
	Brazos Santiago Pass	I	0.20	0.83
	Tabs Buoy J	O	0.13	0.77
	Tabs Buoy D	I	0.14	0.58
Wave height (m)	NDBC 42045	I	0.23	0.92
	South Padre Island	I	0.21	0.89

L=Laguna; I=Inlet; C=Coast ;O=Ocean.

Table III Validation quality

Variable	**Quality**			
	Location		***RMSE***	***Skill***
Water level (m)	Aransas Pass	I	0.29	0.93
	Bob Hall Pier	C	0.29	0.93
	South Padre Island	I	0.27	0.89
	Port Isabel	L	0.28	0.94
Velocity (m/s)	Tabs Buoy J	O	0.06	0.66
	Tabs Buoy D	O	0.14	0.55
Wave height (m)	NDBC 42045	O	0.28	0.85
	Figlius, Nov. [15]	C	0.14	0.95
Velocity (m/s)	Figlius Sep. [15]	C	0.06	0.60
	Figlius Nov. [15]	C	0.11	0.89

L=Laguna; I=Inlet; C=Coast ;O=Ocean.

Figure 5 shows equally good results for the wave height predictions during that month, even if the peak of one of the high wave events is underpredicted. Interestingly, that is the period where the flow predictions have the largest error in Figure 4. In general there seems to be a correlation between errors in the currents and the waves indicating the importance of the wave current interactions.

The first two weeks there is an offset in the wave direction, but that might well be related to the ADCP measurements, after the bed-mounted frame moved at the end of October. The ADCP measurements of direction are very noisy, which is a measurement error rather than highly varying wave directions.

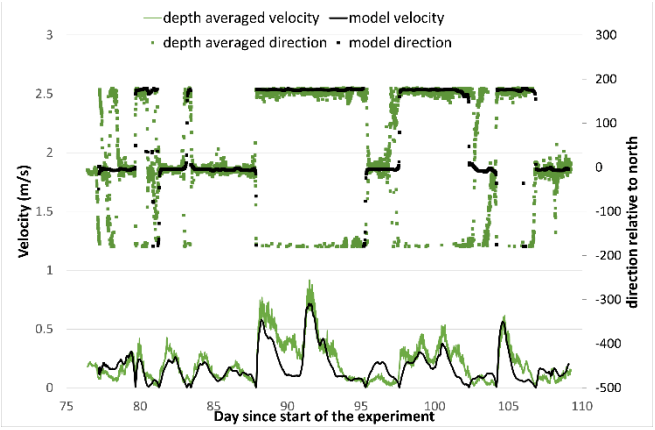

Figure 4. Comparison of measured and modelled currents (velocity and direction) at the Tracer Study site for November 2018

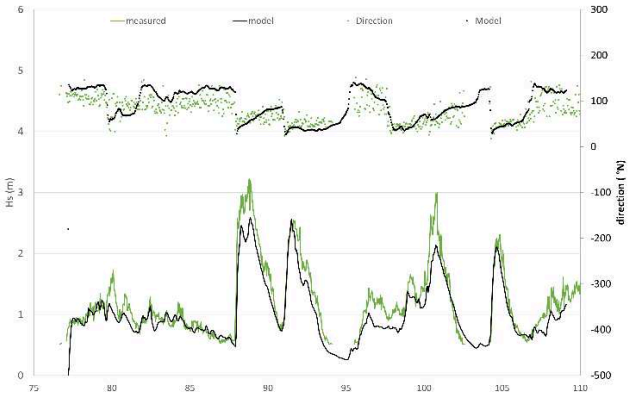

Figure 5. Comparison of measured and modelled waves (significative height and direction) at the Tracer Study site for November 2018

Most importantly for littoral drift calculations, the wave direction during the high wave events is predicted accurately.

C. Model quality sediment transport

No direct measurements were available for the sediment transport rates. However, the quality of the sediment transport predictions can be assessed by the predicted sedimentation into the two navigation channels within the region: Brazos-Santiago Pass and Mansfield Pass (see Figure 1 for location).

Comparisons were done over a few months as well as for the annually averaged sedimentation rates. For Brazos Santiago Pass measured bed level changes between July and November 2018 were available. For Mansfield Pass, bed level changes were measured between March and September 2018.

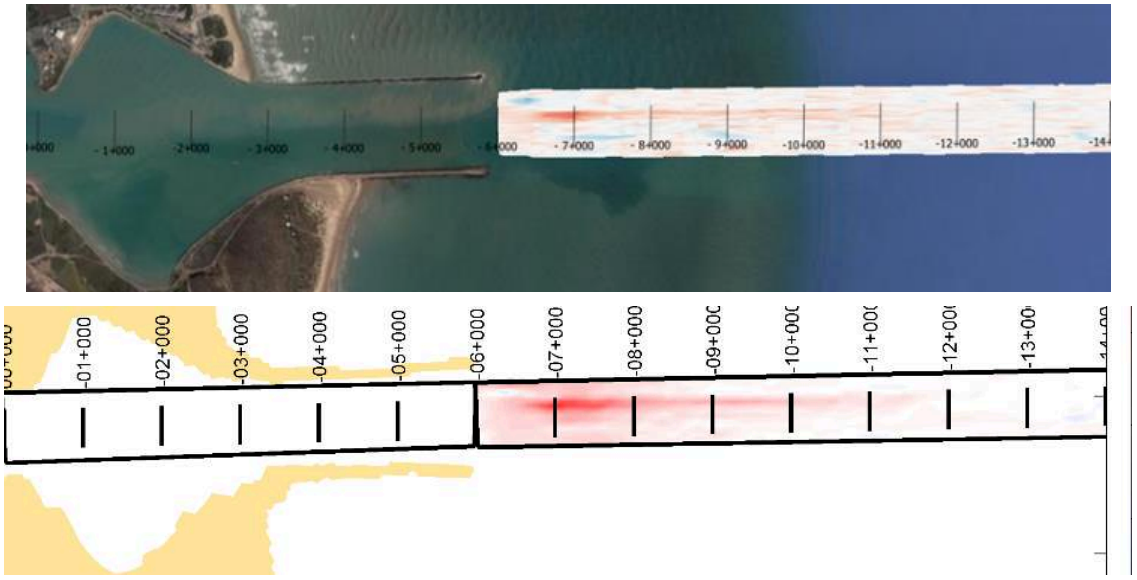

Figure 6. Observed (top) and predicted (bottom) bed level changes for the outer channel of Brazos Santiago Pass. The numbers indicate the distance in yards from the inshore end of the pass.

The model predicts satisfactorily the sedimentation patterns and volumes for the Outer Bar Channel in Brazos Santiago Pass, see Figure 6 and Table IV.

In addition, the predicted annual infill is compared with the long-term observed infill rates in Table V, for both the area between the jetties and the area outside of the jetties. Mansfield Pass has not been dredged in recent years, allowing for the comparison with the bed level changes measured by the USACE between 2015 and 2020. As Brazos Santiago Pass is regularly dredged, such a comparison was not possible. Instead, the annual averaged maintenance dredging volumes [5] are used taken over a period of about 3 decades.

All predicted sedimentation rates match well with the observed annual sedimentation. The errors for Brazos Santiago Pass are less than 10% of the observed sedimentation. The errors for Mansfield Pass are slightly larger at about 50% of the measured sedimentation. However, the measured sedimentation rates are very low and the measurement period relatively short at 5 years. Therefore, there is more uncertainty related to measurement errors and annual variations in the sedimentation rates.

IV. RESULTING SEDIMENT TRANSPORT PATHWAYS

A. Continental shelf

On the continental shelf, the annual cumulative sediment pathways in the area show a consistent trend over the domain of fine sediment transport towards the south (Figure 7), a trend that is completely driven by the ocean currents (tide and geostrophic).

B. Littoral drift

Close to the shoreline, the annual residual sand transport - littoral drift - pathways are consistently directed to the north, driven by the dominant direction of the wave driven currents (inset in Figure 7). This agrees with the work of previous authors who have studied nearshore sediment transport processes in the region [1][2][3]. There is a small gradient in the magnitude of this northward residual sediment transport, with the northward drift increasing towards the south.

However, in slightly deeper water, roughly between the -5m and the -10m contour, the residual sand transport is directed to the south (see inset in Figure 7). This transport is driven by the combination of storm waves and the ocean currents. The intensity of the southward directed annual transport increases to the south. Figure 8 shows the north south component of the yearly averaged transport. The residual transport rates off the coast of Kenedy County are lower than that off the coast of Willacy County, which in turn are lower than the transport rates off the coast of Cameron County. Off the coast from the Rio Grande to Brazos Santiago Pass and going into Mexico the residual transport is stronger than elsewhere in the study area.

Table IV Short term sedimention rates

Channel	Measured infill	Model infill
	m^3/y	m^3/y
Brazos Santiago jetties	62,000	58,000
Brazos Santiago outer	78,000	73,000
Mansfield jetties	-45,000	-22,000

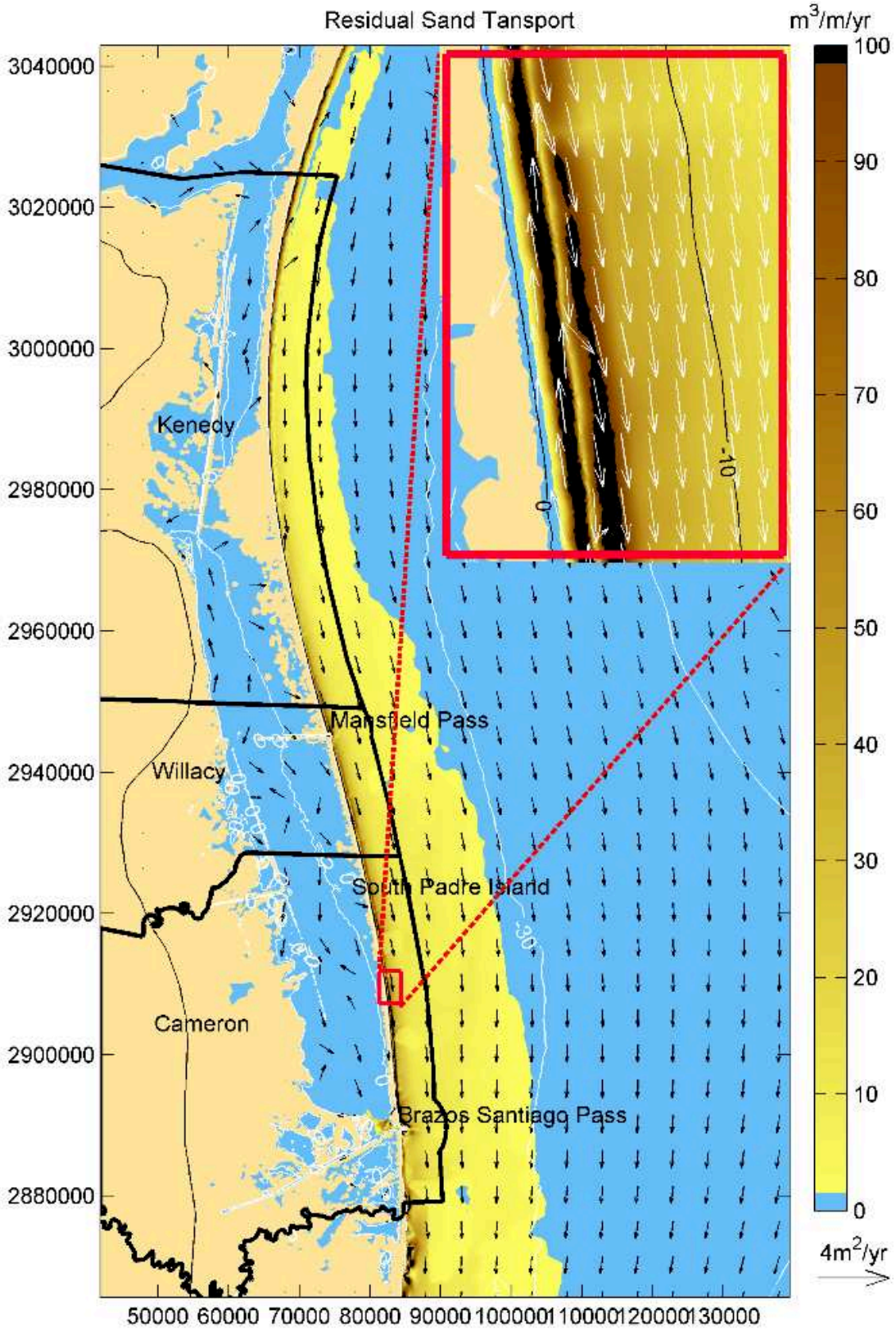

Figure 7. Resulting yearly averaged sediment transport along the South Texas coast

Table V Annual sedimention rates

Channel	Measured infill	Model infill
	m^3/y	m^3/y
Brazos Santiago jetties	157,000	154,000
Brazos Santiago outer	132,000	124,000
Mansfield jetties	27,000	41,000
Mansfield outer	2,000	0

The combination of northward directed transport close to the shoreline, which increases to the south, and a southward directed transport in deeper water, which increases to the south results in a drift divide somewhere in the middle of Kenedy County. North of this area, the littoral drift integrated over a period of one year and over a profile perpendicular to the coast is directed to the north. South of this area the littoral drift integrated over the profile and the year is to the south. The precise location of the drift divide is difficult to determine and will vary from one year to another, because of variable forcing such as storms and hurricanes.

V. COASTAL MANAGEMENT IMPLICATIONS

Findings of this study might have some important implications for coastal management decisions. The design of beach nourishments should be done with care. Material placed on the beach will gradually move north, but shoreface nourishments will gradually move south.

Dredged material from the Brazos Santiago channel that is dumped into the placement sites immediately north of the channel will soon return to the channel. It should either be disposed on the southern side, or closer to the shore. The design of breakwaters should bear in mind that the length of them will influence the direction of the sediment bypassing.

VI. CONCLUSIONS

A fully coupled model of waves, currents and sediment transport has been set up to compute the sand transport fluxes and pathways for the South Texas coast. The model has been calibrated against measured waves, currents and water levels and the sediment transport model has been verified against measured channel infill. In all cases the comparisons were good which indicates that the model performs well along the open coast. The predicted channel infill rates match well with observed bed level changes in 2018 and with the long-term dredging records presented in [2].

Comparisons have also been made against predictions of littoral drift rates using well-established coastal sediment transport models and recently published rates of shoreline change in the area. Conventional wisdom is that littoral drift is directed northwards. However, when the combined influence of both waves and currents are considered, the modes of sediment transport and respective pathways are more complex than reported by previous authors.

The combination of stronger ocean currents during the high wave events from the north results in a dominant southerly transport along most of the South Texas coast. Only in the northern half of Kenedy County are the residual transport rates to the north.

ACKNOWLEDGEMENT

The authors thank the Texas General Land Office for funding this project and their assistance in the data collection; the USACE for the provision of the bathymetry from their ADCIRC model of the Texas waters and Freese & Nichols Inc. for their project management and feedback.

REFERENCES

[1] Shiner Moseley and Associates, inc. "Isla Blanca Park beach nourishment with beneficial use of dredged material project, South Padre Island, Texas," CEPRA Work Order No. 1209-05-002, Final Report, August 2005.

[2] D.B. King, M.A. Bryant, R. Styles, T.C Lackey, E. Smith and R. Visperas. "Brazos Santiago Inlet, Texas shoaling study," USCAE ERDC/CHL TR-18-2, 2018.

[3] J.H. McGowen, L.E. Garner, and B.H. Wilkinson. "The Gulf shoreline of Texas: Processes, characteristics, and factors in use," Geol. Cir. 77-3, Bureau of Economic Geology, University of Texas, 27 pp. 1977.

[4] R.A. Morton, G.H. Ward and W.A. White. "Rates of sediment supply and sea-level rise in a large coastal lagoon," Marine Geology, vol. 167, pp. 261-284, 2000.

[5] C. Villaret, J-M. Hervouet, R. Kopmann, A. Davies, U. Merkel. "Morphodynamic modeling using the Telemac finite-element system," Computers & Geosciences, vol. 53, DOI: 10.1016/j.cageo.2011.10.004, 2013.

[6] U.S. Geological Survey, "National water information system data," USGS Water Data for the Nation, accessed on April 21, 2021. https://help.waterdata.usgs.gov/faq/automated-retrievals, 2016.

[7] GEBCO Compilation Group, "General bathymetric chart of the oceans", GEBCO 2019 Grid, doi:10.5285/836f016a-33be-6ddc-e053-6c86abc0788e, 2019.

[8] M.A.F. Knaapen, "Sediment modelling for Poole and Christchurch Bay," Proc. TELEMAC-MASCARET User Conference, Toulouse 2019.

[9] R. **Lewis**, J. Sutherland, M.A.F. Knaapen and J.D. Simm, "Regional sediment transport study in Poole and Christchurch Bays, UK," Proc. ASBPA 2019 National Coastal Conference, 2019.

[10] R.J. Soulsby, "Dynamics of Marine Sands", Thomas Telford, London, 1997.

[11] L. Yan "An improved wind input source term for third generation ocean wave modelling," Rep. No. 87-8, Royal Dutch Meteor. Inst., 1987.

[12] BOEM. "Marine Mineral Information System (MMIS), "Bureau of Ocean Energy Management and University of Texas Institute for Geophysics. 2019.

[13] TCSG, Texas Coastal Sediments Geodatabase. http://cgis.glo.texas.gov/txsed/index.html, 2019.

[14] C.J. Willmott, "On the validation of models," Physical Geography, 184-194, 1981

[15] J. Figlus, Y-K. Song, C.K. Maglio, P.L. Friend, F.L. Engel, D. Schnoeblen and K. Boburka. "Particle tracer analysis for submerged berm placement of dredged material near South Padre Island, Texas, " WEDA Journal of Dredging, vol 19 (1), 2021.

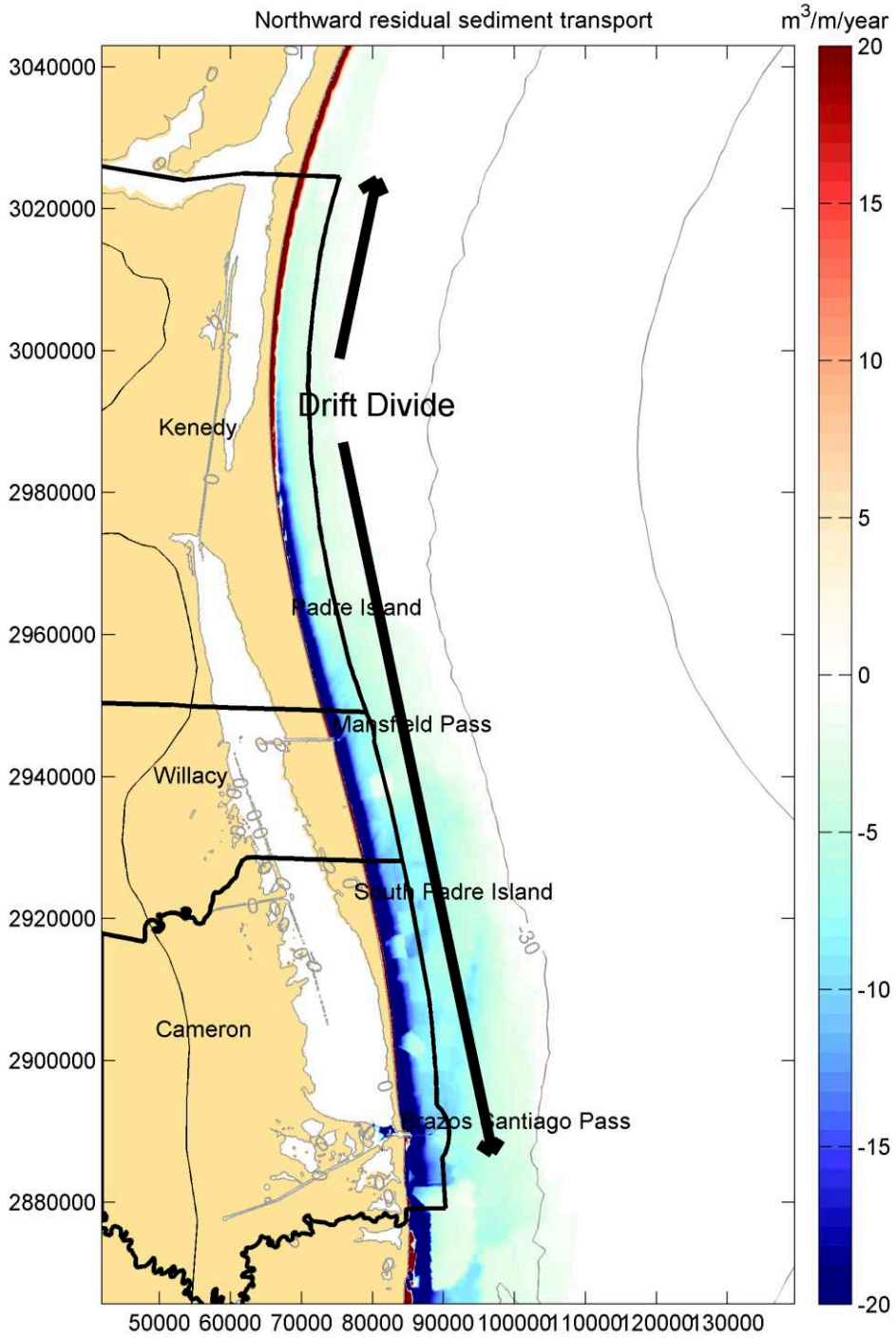

Figure 8. Northward component of the yearly averaged sediment transport along the South Texas coast

Coastal sediment modelling (TELEMAC-2D / TOMAWAC / GAIA): scour in offshore wind farm

Hanyu ZHAN[1], Zijun MAI[1], Tingyu DAI[1], Lu ZHOU[2], Jiesheng MIN[2]
hyzhan@yuansuan.cn, Hangzhou, China
[1]: Zhejiang Yuansuan Technology Co., Ltd., Hangzhou, China
[2]: EDF China, R&D Center, Beijing, China

Abstract **–The radial sand ridges of the southern China Yellow Sea, located in the coastal zone where the interaction between land, sea and human activities is the strongest, is well known as the largest tidal ridges in the world. To evaluate the effects of sediment transports to an offshore wind farm, a fully coupled TELEMAC(2D)-TOMAWAC-GAIA model was thus developed to analyse the associated morpho-dynamics resulting from the influence of currents and waves.**

The process of numerical simulation was divided into two parts. Firstly, a large-scale simulation using TELEMAC-2D + TOMAWAC was performed around the China Yellow Sea and the East China Sea to obtain the boundary-imposed wave spectrum suitable for the offshore area. Secondly, a local scale coupling of TELEMAC-2D + TOMAWAC + GAIA around the radial sand ridges was performed using the wave spectrum obtained from the large-scale simulation. The influence of the pile foundation on the flow conditions was simulated by providing a drag force close to each pile foundation. The fully coupled model demonstrates its ability to simulate the sediment transports and morpho-dynamics evolution of the study area.

Keywords: Sediment transports. Non-cohesive sediment. Coupled model.

I. INTRODUCTION

The South Yellow Sea's radial sand ridge is situated south of the former Yellow River Delta and north of the Yangtze River Delta, in a shallow sea area off the coast of middle Jiangsu with rich offshore wind energy resources. The sand ridge spreads over a huge area and is characterized by a unique fan shape forming the seabed and a clear asymmetrical frame between the north and the south [1] (cf. Figure 1). Due to the interaction between ocean tides, waves and the particular properties of the sediment deposited, the bed features and their displacements are very large, causing considerable trouble to offshore wind power projects.

As a new energy resource, wind power is often regarded as green and pollution-free energy. With the maturity of the basic technology, China's offshore wind power market is gradually expanding. Up to 2021, the cumulative total installed capacity of China's offshore wind power had reached 25.35 GW [2]. During the operation and maintenance of the offshore wind farm, it was found that the pile foundations were affected by important scouring issues.

This article presents a numerical study of flow and sediment transport processes in the study area, based on the 3-way coupling 2D models of TELEMAC-2D, TOMAWAC and GAIA. Firstly, the numerical model and its setup are briefly introduced. Secondly, the model calibration against tidal and wave data is presented. Finally, numerical results are summarized and discussed.

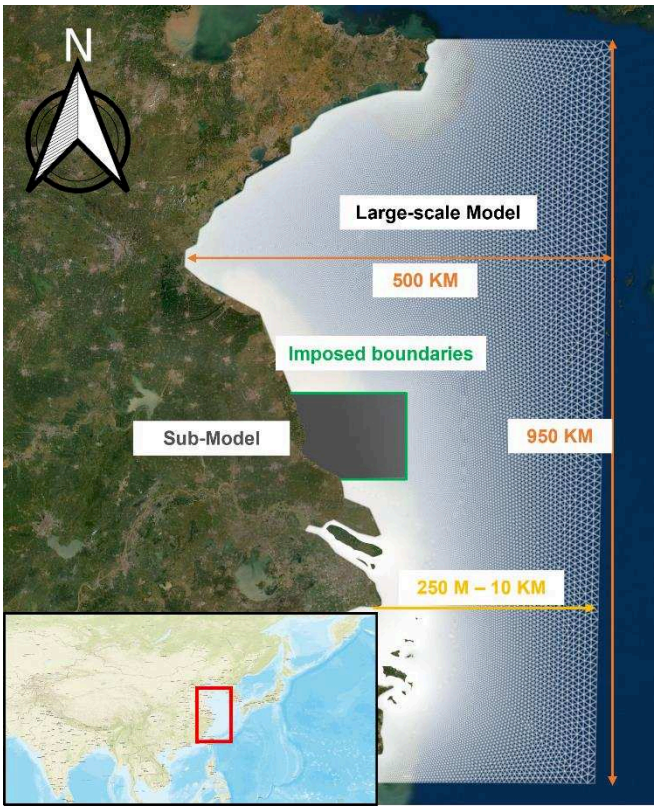

Figure 1. Study area and the nested mesh (mesh 1).

II. NUMERICAL MODEL

Since the area where the wind farm is located is in offshore shoal, to reasonably consider the local wave and hydrodynamic conditions, the model is a nested model of two different scales. By considering the coupling between TELEMAC-2D and TOMAWAC in the large-scale model (cf. Figure 1), the boundary input wave spectrum of the small-scale wave model is computed. In the small-scale model (or sub-model), the Soulsby-Van Rijn formula [3] was used to compute sediment fluxes due to the combined action of waves and tides.

Hereafter, about the general modelling strategy, bathymetric and boundary conditions are briefly introduced.

A. General model

This simulation work handles a total of two meshes which are described below.

To fully account for the influence of waves in the small-scale model (sub-model), the boundaries of the waves in the sub-model are extracted from the large-scale model. The large-scale model (named Mesh 1, cf. Figure 1) contains 96,589 nodes and 189,257 elements, with a resolution varying between 250 m and 10 km, which is sufficient for wave and hydrodynamic studies. The model spans about 950 km from north to south and can reach as far as 500 km offshore and includes the sub-model at its centre.

The study area (sub-model) is also centred on the radial sand ridge in the South Yellow Sea (cf. Figure 2). The boundary of the model is about 120 km away from the coastline, and the north and south spatial span of the model is about 100 km. In this area, the transports of both bedload and suspended sands is considered for prediction of bed evolution using a three-way coupled 2D-model.

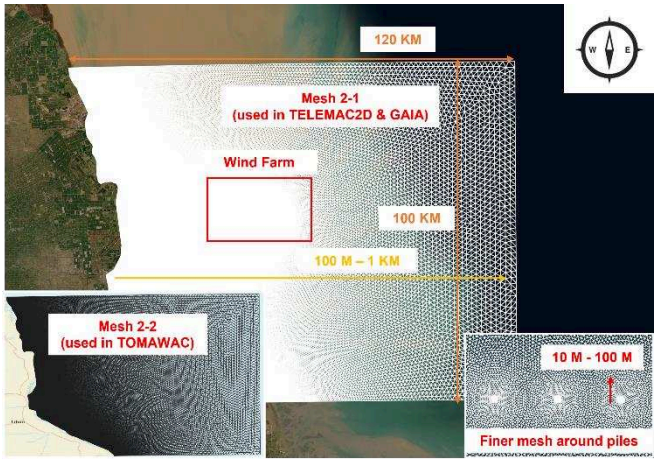

Figure 2. Mesh of sub-model used in TELEMAC-2D&GAIA (mesh 2-1) and used in TOMAWAC (mesh 2-2).

To guarantee the accuracy of the simulation over the radial ridge while being able to reduce its computation time, two meshes with different mesh resolutions are used for TELEMAC-2D and TOMAWAC modules, using the TEL2TOM feature. For TELEMAC-2D, a finer mesh (named Mesh 2-1) is used: it is progressively refined from an element size of 1 km far from the piles to an element size of 100 m close to the shore. The resolution is further adjusted to an element size of 10 m in a square domain of 100 m x 100 m around each pile. The number of elements of this mesh is 330,505 elements, and the number of nodes is 165,803. For TOMAWAC, a progressively refined mesh is adopted (named Mesh 2-2): from an element size of 1.5km far from the shore to a size of 200 m on the shore. The mesh contains 100,370 elements and 50,736 nodes.

Table I Model and corresponding mesh

Mesh Name	**Mesh Properties**		
	TELEMAC Module	***Mesh Size***	***Element***
Mesh 1	TELEMAC-2D/	950 km X 500 km	189 257
Mesh 2-	TELEMAC-2D/GAIA	120 km X 100 km	330 505
Mesh 2-	TOMAWAC	120 km X 100 km	100 370

B. Bathymetry

The bathymetric data in the study area was projected onto the mesh by linear interpolation using data from the General Bathymetric Chart of the Oceans (GEBCO) 2021 dataset [4]. The GEBCO dataset is a global terrain model for ocean and land, providing elevation data, in meters, on a 15 arc-second interval grid. For the large model, the seabed is gradually raised from -124 m offshore to 9 m near shore (cf. Figure 3). However, it is not the same case with the sub-model, bathymetry levels vary between -50 m and 9 m due to the radial sand ridge.

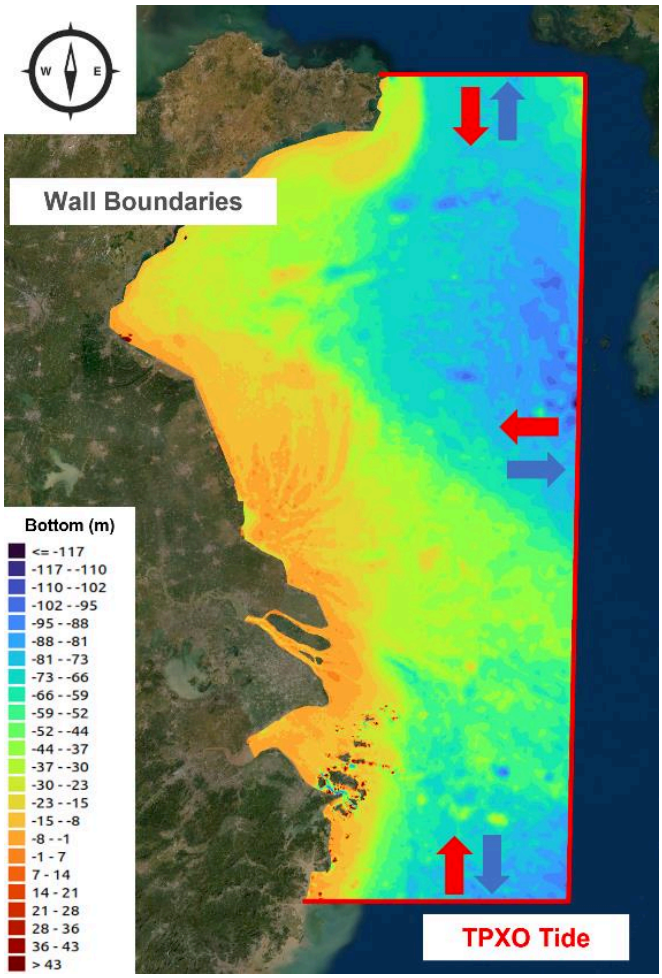

Figure 3. Bathymetry and forcing scheme of large model (TPXO Tide = Oregon State University Tidal Predicition Model).

C. Tidal boundary conditions

In both the large- and local-scale models, the liquid boundary is read from Oregon State University Tidal Prediction Model (TPXO Pacific model). TPXO is a global

model of ocean tides, which best-fits, in a least-squares sense, the Laplace Tidal Equations. The methods used to compute the model are described in details by Egbert et al. 1994 [5] and further by Egbert and Erofeeva, 2002 [6].

The TELEMAC-2D model is then forced by TPXO tidal model (cf. Figs 3 and 4), providing water depth and velocities at the oceanic open boundaries to reproduce local tides in the study zone. To stabilize the hydrodynamic conditions in the early sediment simulations, a stable initial TELEMAC-2D model was computed before starting the coupling step. After testing different boundary types, both water depth (H) and velocity components (U, V) were imposed on liquid boundaries.

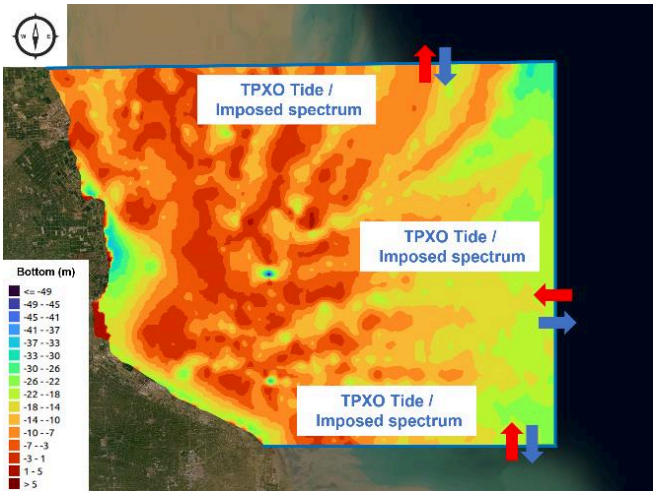

Figure 4. Bathymetry and forcing scheme of sub-model.

D. Wave boundary conditions

In the large-scale model, waves generated by the wind are considered. Dissipation mechanisms such as white-capping, depth-induced wave breaking, dissipation by bottom friction, and nonlinear wave effects between quadruplets are also modelled. Similar mechanisms are considered in the sub-model. The wave spectrum extracted from the large-scale model is imposed at the nested boundaries to better describe surges in the vicinity of the wind farm, cf. Figure 5.

As for the tides-only case, a stable initial condition of both hydrodynamics and waves is computed by considering the combined influence of tides and waves. This result is then used as initial condition for the three-way coupling model to guaranteed stability and convergence of the solution.

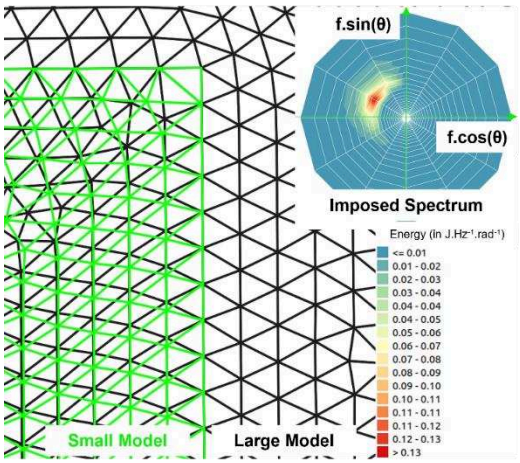

Figure 5. Imposed spectrum and boundary of TOMAWAC model.

E. Atmospheric conditions

The National Oceanic and Atmospheric Administration (NOAA/NCEP CFSv2) hourly reanalysis of wind field data is filled into the model using linear interpolation [7]. The National Centres for Environmental Prediction (NCEP) Climate Forecast System (CFS) is a fully coupled model representing the interaction between the Earth's atmosphere, oceans, land, and sea ice. CFS was developed at the Environmental Modelling Centre (EMC) at NCEP. The operational CFS has been upgraded to version 2 (CFSv2) on March 30, 2011. Wind-generated waves was computed in TOMAWAC using hourly data of 10 m high wind field. With atmospheric pressure data, the influence of wind on hydrodynamic conditions was also computed in TELEMAC-2D.

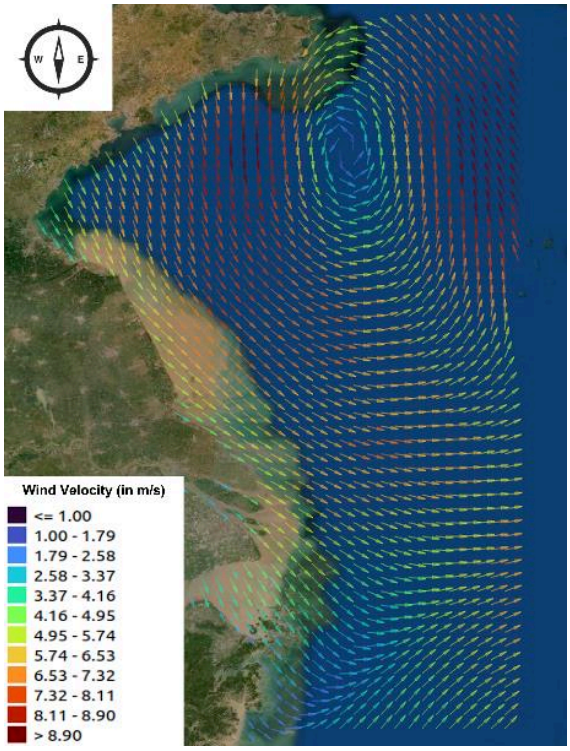

Figure 6. NOAA/NCEP CFSv2 wind data (in July 2020).

F. Bed conditions and others

Based on in-situ measurements, the sediment in the study area is mainly composed of silt with a particle size of about 0.25 mm, a porosity of 0.7, and a density of 1960 g/m^3 under wet conditions. In this work, a single layer of non-cohesive sediment was set in GAIA.

Sediment transport fluxes were computed by the Soulsby−van Rijn formula in the fully coupled model, which accounts for bedload and suspended transport processes. To account for the sediment transport direction, the slope effect is considered in the numerical simulations. Moreover, to accelerate the sediment simulation, a morphological factor equal to 5 was adopted.

To calculate the effect of wind power pile foundations on hydrodynamic conditions, drag force is computed by [8]:

$$F_D = -\frac{1}{2}\pi R^2 \rho C_D U_r |U_r|$$

Table II Acronym list of the drag force formula

Variable Name	Meaning
F_D	Drag force along the central axis of the pile foundation
R	Radius of the pile foundation
ρ	Ocean water density
C_D	Drag coefficient (1.5 was used)
U_r	Vector velocity read in TELEMAC-2D

Due to the wide range of latitude covered by the computational domain, the Coriolis force term is included in the TELEMAC-2D model. Since the seabed properties of wind farms are relatively consistent, a uniform Manning friction coefficient (0.015) is used. In addition, in order to make the computation of sediment stable, the bottom smoothing effect (BOTTOM SMOOTHINGS = 2) is considered in both TELEMAC-2D and TOMAWAC models.

III. CALIBRATION AND VALIDATION

After constructing the model and obtaining preliminary results, the authors investigated methods on how to evaluate its accuracy. This work is reported in this section.

A. Tidal model

Based on the tidal data from the National Marine Data and Information Service of China, the data of astronomical tide level was first calibrated in the hydrodynamic model.

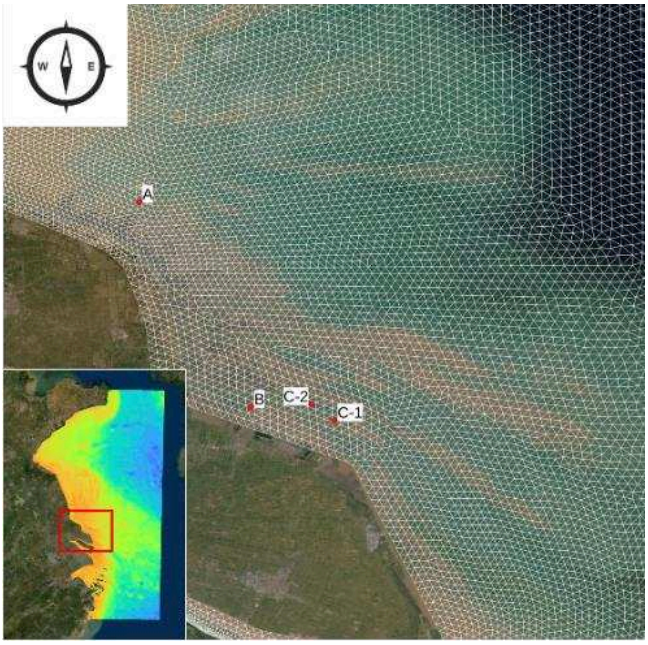

Figure 7. Positions of the stations (A/B station is for tide and C-1/C-2 station is for wave)

The water level data of local station A (cf. Figure 7) was compared with the results of the TELEMAC-2D model (data of July 2020 and data of October 2021). After the calibration of the large model, since the calibration station A is located in the area corresponding to the sub-model, the same parameters as the large-scale model, including the Coriolis force coefficient, tidal range, friction formula and coefficients, were used to compute the sub-model results. As shown in Figs 8 and 9, by comparing the 20 days' astronomical tide data, the water levels in the sub-model are well reproduced by the model with a maximum bias of about 30 cm in station A.

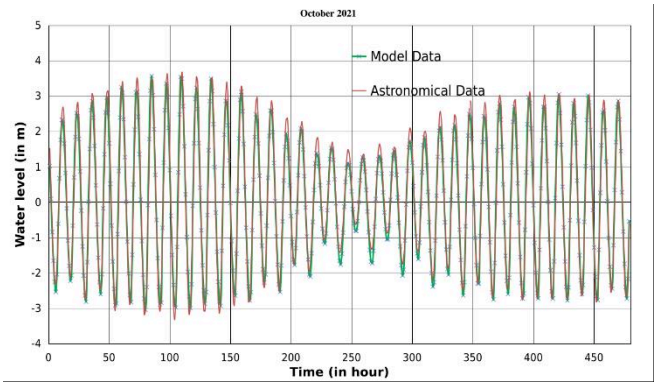

Figure 8. Comparison of water levels modelled and astronomical tide data in staton A in October 2021.

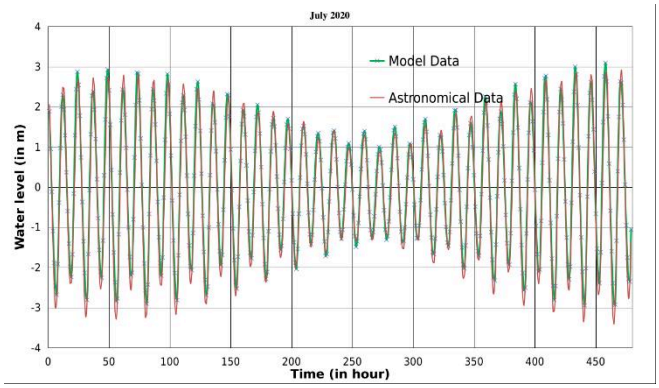

Figure 9. Comparison of water levels modelled and astronomical tide data in staton A in July 2020.

The correlation coefficient R of the comparison data is obtained using the following formula, where x and y represent the astronomical tide data and model data respectively. The correlation coefficient is 0.99 at calibration position A, cf. Figure 7.

$$R = \frac{\sum(x-\bar{x})(y-\bar{y})}{\sqrt{(\sum(x-\bar{x})^2 \sum(y-\bar{y})^2)}}$$

Using the same parameters (friction coefficient, tidal range...), the results of tidal level were also obtained in station B (cf. Figure 10). The overall fitting at B station is not as good as that of A, and its correlation coefficient is about 0.94. The bias mainly exists at low tide level and neap tide. In station A, the change of water level at low tide is better calibrated, while in station B, the change of water level at high tide is better calibrated. The reason was identified to be the precision and smoothness of the bathymetry data. As the authors have not attempted to adjust the bathymetry data, this reason is speculative. This assumption will be further investigated in a future work.

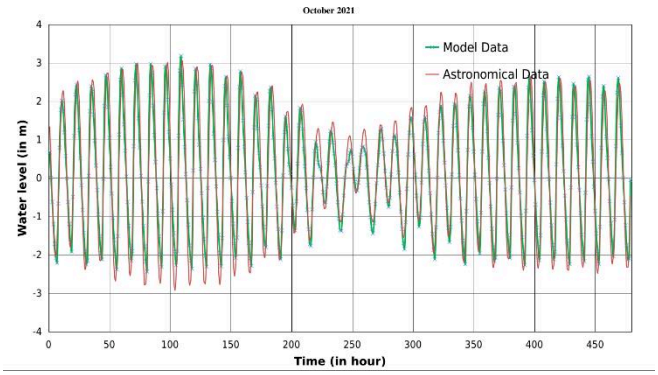

Figure 10. Comparison of water levels modelled and astronomical tide data in station B in October 2021.

B. Wave model

In the TOMAWAC model, the calibration is performed by comparing the significant wave height measured by the offshore buoy and the results. After testing different source terms and dissipation terms to calibrate the results with the measurements at buoy C-1 and C-2, it can be found that the trend and value are basically consistent, as shown in Figs 11 and 12.

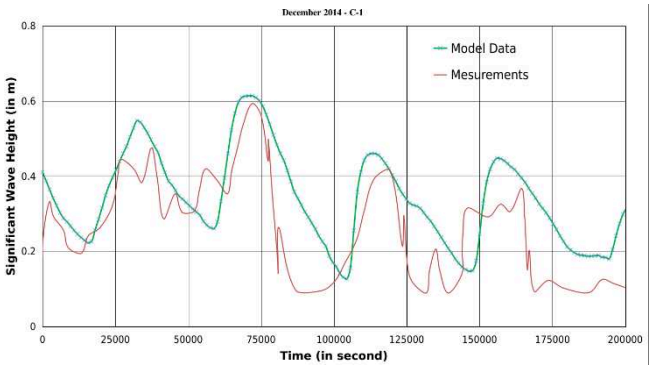

Figure 11. Comparison of significant wave height modelled and measurements in station C-1 in December 2014.

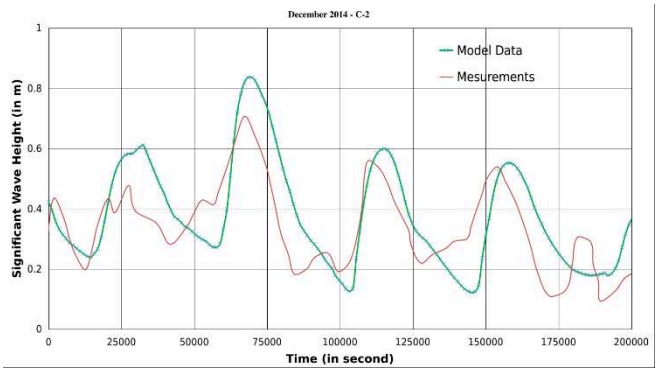

Figure 12. Comparison of significant wave height modelled and measurements in station C-2 in December 2014.

The results of calibration of significant wave height showed that the wave is well reproduced when white capping, nonlinear transfers between quadruplets, bottom friction, current dissipation, and wave breaking are considered. Therefore, in subsequent simulations , the influence of these source terms on waves is taken into account.

IV. RESULTS AND DISCUSSION

On the basis of the position of pile foundations in the wind farm, the drag force is applied by matching mesh nodes within a radius of several meters from the (x,y) coordinates of each pile foundation. To maintain the adopted Courant-Fredrichs-Lewy condition, time steps for both TELEMAC-2D and TOMAWAC sub-models are equal to 1 s and 10 s, respectively. These time-steps guarantee the stability of the solution.

In the study area, the velocity field is influenced by the drag force, with lower velocity magnitude values in the backflow direction (cf. Figure 13). Furthermore, sediment transport is strongly influenced by the combined effects of tides and waves in the dune area and the centre of the flat sandbar. In proximity of the nearshore boundary, the migration of large sediment deposit is also observed.

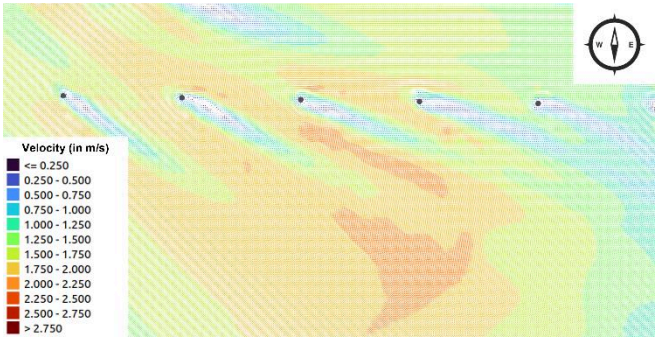

Figure 13. Velocity field near pile foundation after applying drag force

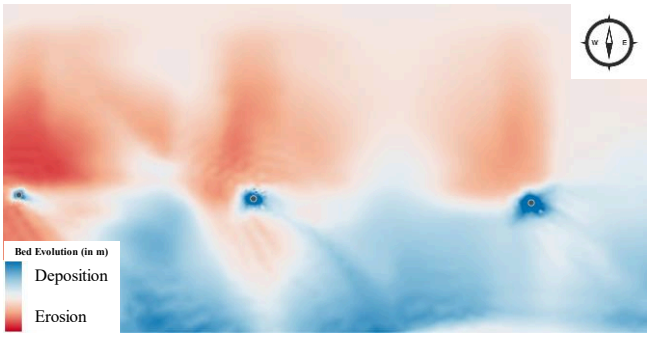

Figure 14. Erosion and deposition in wind farm around the pile foundation, the results indicate that the scour pit will be backfilled during this time.

Morpho-dynamic results show that there are some pile foundations are seriously affected by erosion and deposition. In addition, due to the drag force, in the wind farm there is an obvious tendency to strengthen the scour near some pile foundations, but there exists also scour near pile foundations that have been backfilled, as shown in Figure 14. In some areas next to the wind farm, sediment erosion or deposition is less intense than that on the other side of the wind farm, due to weaker tidal and wave conditions.

V. CONCLUSION

In this study, the three modules TELEMAC-2D-TOMAWAC-GAIA are coupled to to simulate sediment transport processes in an offshore wind farm area. Models of different scales are implemented in order to predict the wave conditions around an offshore windfarm.

By applying the drag force, the influence of the pile foundation on the hydrodynamic conditions and the formation of the scour pit are studied. Based on calibration for tidal and wave conditions, an attempt was made to study the evolution of scouring processes by using reanalysed wind field data. This assesses the coupling of modules TELEMAC-2D, TOMAWAC and GAIA at predicting scouring formation around offshore structures.

In future work, the model will be refined and benchmarked against actual site data to better calibrate it for predicted offshore scouring formation.

ACKNOWLEDGEMENT

The authors would like to thank Pablo TASSI, Thierry FOUQUET, Sebastien BOURBAN from EDF R&D for their technical support on this work.

REFERENCES

[1] Kang, Yanyan, Jinyan He, Bin Wang, Jun Lei, Zihe Wang, and Xianrong Ding. 2022. "Geomorphic Evolution of Radial Sand Ridges in the South Yellow Sea Observed from Satellites" Remote Sensing 14, no. 2: 287. https://doi.org/10.3390/rs14020287

[2] Statistics of China's offshore wind power installed capacity in 2021, wind energy, 2021 年中国海上风电装机统计. 风能, 2022,(08):46-49.

[3] Soulsby R. Dynamics of marine sands. H.R. Wallingford, 1997.

[4] GEBCO Compilation Group (2022) GEBCO_2022 Grid (doi:10.5285/e0f0bb80-ab44-2739-e053-6c86abc0289c)

[5] Egbert, G.D., Bennett, A.F. and Foreman, M.G.G. (1994). TOPEX/POSEIDON tides estimated using a global inverse model. Journal of Geophysical Research 99: doi: 10.1029/94JC01894. issn: 0148-0227.

[6] G. Egbert and S. Erofeeva, "Efficient inverse modeling of barotropic ocean tides," Journal of Atmospheric and Oceanic Technology, 19, 183-204, 2002.

[7] Saha, S., et al. 2011, updated daily. NCEP Climate Forecast System Version 2 (CFSv2) 6-hourly Products. Research Data Archive at the National Center for Atmospheric Research, Computational and Information Systems Laboratory. Accessed dd mmm yyyy.

[8] A. Joly, C.T. Pham, M. Andreewsky, S. Saviot, L. Fillot, Using the DRAGFO subroutine to model Tidal Energy Converters in Telemac-2D, Proceedings of the XXIInd TELEMAC-MASCARET User Conference, STFC Daresbury Laboratory, UK, 13 to 16 October 2015.

Modelling of sediment transport pattern in the estuary of the Piave River

Antonia Menzione[1] , Marco Mancini[1]
antonia.menzione@polimi.it, Milan, Italy
[1]: Department of Civil and Environmental Engineering. Politecnico di Milano

Abstract – **Sediment transport and the related sedimentary and suspension processes play a fundamental role in the dynamics of coastal environments (Holdaway et al., 1999) [1], such as lagoons and estuaries. Furthermore, it is of primary importance to understand and quantify the hydrodynamics driving the processes.**

Historically, the traditional techniques used are based on the acquisition of precise in situ measurements of current velocity, water flow and concentration of suspended solids (SSC). The main limitation of this approach is, therefore, the poor spatial and temporal resolution, which is very often insufficient to describe the variability associated with highly dynamic coastal environments (Gartner, 2004) [2]. Therefore, alternative methodologies are proposed to evaluate the plume of sediments in estuary areas. The results and methods may be helpful in coastal management and understanding the evolution of the entire estuary from the perspective of shoreline change.

Keywords: Sediment transport, Estuary, Coastal areas

I. INTRODUCTION

Over the last decades numerous models for sediment transport prediction have been proposed with application to fluvial transport or littoral transport. However, the morpho-dynamic interactions that occur at the river mouth are still difficult to predict given different concurring phenomena, deriving from both river hydrology and estuarine hydrodynamics. Knowing the magnitude of these phenomena is important to analyse and predict sediment patterns suspension, deposition and potential effects on biological processes. The paper investigates the possibility to use satellite image of suspended sediment patterns at river mouth for the calibration of numerical estuarine hydrodynamic models.

II. CASE STUDY

The present study analyses the sediment transport at the Piave estuary (Italy, Adriatic Sea) (Figure 1).

A. Dataset

In order to qualitatively ascertain the plume of dispersed sediments, the most severe condition was considered. In fact, among the most recent flood events, that of December 2020 was considered. The flood event lasted several days from 5th to 7th December 2020, when the hydrometric level exceeded 1.5m at the hydrometric station of Eraclea (8.6 km from the mouth of the Piave River), peaking on 6th December at 20.00, when the hydrometric level reached 2.92 m.

For this event, a hydraulic analysis on the Piave River was carried out, assessing the flow discharge recorded from water level (https://www.arpa.veneto.it/). On the seaside, the main forcing studied was the tide, also given the geographical configuration of the Adriatic Sea. The tide levels were therefore obtained from the Ispra website (https://www.isprambiente.gov.it/it) from the Ravenna tidal station, the ideal boundary of the basin and boundary condition of the regional model.

B. Methodology

The simulation of the sediment transport patterns in the study area was undertaken using mostly open-source data and tools.

The numerical modelling suite TELEMAC (see details in sub-section C) was selected for the computation of local hydrodynamics and sediment transport. The modelling approach consisted of sequential coupling between the modules TELEMAC-2D [2] and SISYPHE [2]. The circulation module TELEMAC-2D provided the current fields and water levels used to force the morpho-dynamic module SISYPHE for the estimation of suspended sediment and bedload transport.

The estuary of the Piave River is a focal point for the jet currents from the fluvial discharge, sea-water circulation currents and wave-generated currents. The current field resulting from the interaction of these different current sources dictates the local morpho-dynamics both in terms of the dispersion patterns but also the intensity of the sediment mobilization. The computation of the sediment transport in the study area was essentially undertaken following three major phases:

a) Regional hydrodynamic model of the North Adriatic Sea forced by a time-series of water levels (combined tide and storm surge) – using TELEMAC-2D;

b) Local hydrodynamic model of the estuarine area forced by the regional model currents on the offshore boundaries and by the river discharge on the lower stage of the river – using TELEMAC-2D;

c) Morphodynamic model of the estuarine area forced by the local hydrodynamic model and the initial suspended sediment concentration of the upper stage of the river – using SISYPHE.

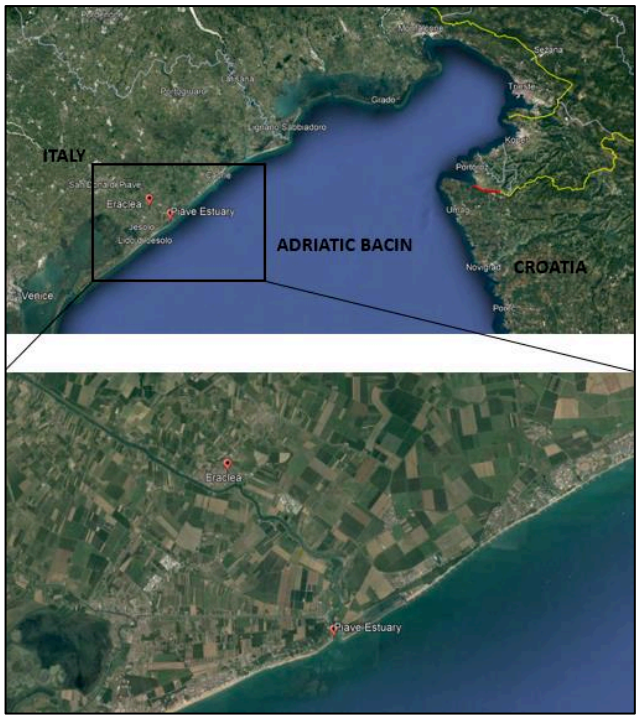

Figure 1. Case study location (Credit: Google Earth)

Although possible, internal coupling of the TELEMAC-2D and SISYPHE modules was not used, meaning that seabed changes induced by the currents have not been considered for the computation of the currents in the successive time-steps. The seabed remains static throughout the hydrodynamic modelling.

The modelling comprised a real-time period of 5 days spanning from the 5th to the 10th of December 2020. The period was selected due to the occurrence of a major flood in the Piave River, peaking at over 1200m^3/s on the 7th of December 2020.

The different simulation phases were intercalated with calibration and validation of the models according to the availability of data. The results for the sediment transport were compared with the sediment plume and sediment concentrations qualitatively estimated using the Remote Sensing technique with images collected by the Sentinel-2 mission (see details in sub-section D).

It is worthy of note that wave-generated currents have not been implemented on the present work although their influential role on estuarine dynamics is recognized.

C. Numerical Model Description

TELEMAC is an open-source modelling system, principally developed by EDF-R&D and a consortium of international organisations, which integrates various modules for the computation of fluvial and coastal processes using finite-elements techniques.

TELEMAC-2D solves the depth-averaged free surface flow based on the Saint-Venant equations. The system is of general application to hydraulic problems as it is able to take into account various phenomena including: propagation of long waves; friction on the bed; Coriolis force; turbulence; supercritical and subcritical flows; tidal flats and flood plains. The module is particularly convenient for cases when coupling with other phenomena is required (e.g. waves) or when difference forcing terms are at play.

The boundary conditions can be set for each individual boundary node as a pair of depth and velocity (or flowrate) conditions, as follows:

d) Depth conditions:
- Open boundary with prescribed depth;
- Open boundary with free depth;
- Closed boundary.

e) Velocity conditions:
- Open boundary with prescribed flowrate;
- Open boundary with prescribed velocity;
- Open boundary with free velocity.

The combination of boundary conditions allows for example, for the simulation of a sea boundary forced by tidal elevations and currents together with a river boundary forced by a stage and a discharge. Furthermore, the model supports the use of a Thompson Boundary Condition which allows the implementation of an over-constrained boundary for which one of the boundary variables (either velocity or water depth) is not known precisely. The feature is particularly useful when simulating tidal currents inside the domain as typically data on tidal elevations are more easily available than tidal currents.

SISYPHE is a sediment transport and bed evolution modelling system that allows for the computation of bedload and suspended load on cohesive and non-cohesive sediment based on various transport relations.

The suspended load is calculated based on the Rouse profile for vertical concentration distribution.

$$C(z) = C_{ref}\left(\frac{(z-h)}{z}\,\frac{a}{(a-h)}\right)^{R}$$

where:

- C_{ref} is the near-bed concentration;
- h is the water column depth;
- z is the reference elevation in relation to the position of the boundary layer that separates the bedload and suspended load;
- a is the reference elevation above the bed elevation;
- R is the rouse number which related the vertical-settling velocity and the friction velocity corresponding to the total bed shear stress.

In the model the two-dimensional sediment transport equation for the depth-averaged suspended load concentration is obtaining by integrating a three-dimensional sediment transport equation over the suspended-load zone.

The near-bed concentration used to determine the suspended-load profile was based on the Zyserman and Fredsoe formula.

The bed-shear stress formula was calculated based on the Manning friction, for consistency with the TELEMAC-2D hydrodynamic model.

SISYPHE allows the user to define an initial concentration of suspended sediments at the boundary which can be used to introduce the fine sediment that is eroded and transported along the upper stages of the river.

D. Remote Sensing Images

Remote sensing is, by definition, the process of detecting and monitoring the physical characteristics of an area by measuring its reflected and emitted radiation at a distance (typically from satellite or aircraft). In the present study, two different datasets were used to obtain satellite images: the widely known satellite Sentinel-2, led by the ESA (https://sentinel.esa.int/web/sentinel/missions/sentinel-2); and the network of commercial satellite imagery Planet [2]. Both allow to obtain aerial images for extreme events. Note that the satellite imagery from Sentinel-2 has a lower temporal frequency than the areal imagery available in the Planet database. Also note that the images do not exactly capture the peak of the event, so in this work the image of reference in the one closest to the peak of the flood event.

III. MODEL IMPLEMENTATION

A. Regional Hydrodynamic Model Setup

A regional hydrodynamic model of the North Adriatic Sea was setup to compute the tidal-driven circulation in the region and inform the sea boundary conditions for the local hydrodynamic model in the proximities of the Piave River estuary. The need for a regional-level model is justified by the limited availability of the source terms related to currents in order to drive the numerical model. The water levels, however, may be obtained from publicly available databases and create an over prescribed model that is solved with the Thompson characteristics method.

The Italian government agency Ispra maintains a network of tide gauges, the RMN (Rete Mareografica Nazionale), that provides surface elevation measurements at many locations along the Italian coast at a time step of 10 minutes.

It is important to note that even tough tidal constituents are known in several stations across the Adriatic, both along the Italian and the Croatian coast, the use of tidal prediction methods to generate the boundary conditions at the boundaries had to be discarded due to the predominance of the storm surge component in the water levels for the period simulated. Generally speaking, the astronomical tidal excursion in the Adriatic Sea is relatively small. The Northern end of the Adriatic Sea, however, is infamous for its exceptional floods (*acqua alta)* that result from a combination of phenomena including the storm surge generated by the South-Eastern winds (Scirocco) and tendency for *seiching* at the main basin and sub-basins.

Given the complexity of simulating all the phenomena that make up the total sea water levels it was instead decided to use as boundary condition the actual total levels measured by the tidal gauge network. Three locations have been selected: Ravena, Trieste and Venezia. The first used as boundary condition and the other two to verify the model accuracy. It is noted that over the five (5) days period of simulation the mean sea level was on average 0.6 m above the overall annual level. Water level measurements on the Croatian coast were not available which hindered the possibility to establish properly the water elevation gradient along the offshore boundary of the model.

The numerical model simulations using TELEMAC-2D were performed in a finite-element triangular flexible mesh created in BlueKenue (Figure 2). The model bathymetry was based on free-source gridded data from GEBCO with a spatial resolution of 15 arc-second. The mesh has 29,767 elements with an edge length ranging from 20 m to 4,000 m.

The numerical model simulated the period between the 5th December and the 10th December 2020 for a total of 172,800 timesteps. The timestep of the input conditions varies every 600s (10min) and the computational timestep is 2.5 s.

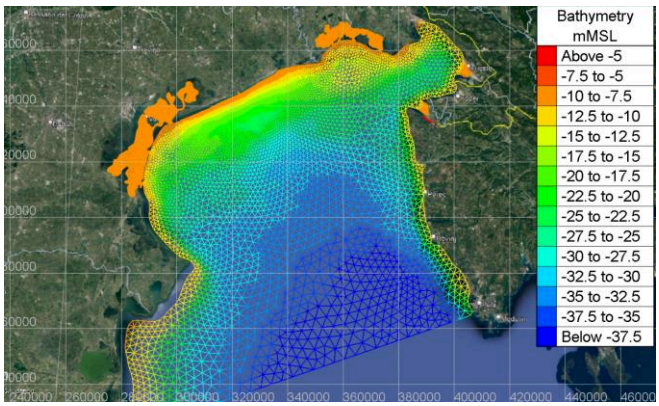

Figure 2. Regional Model mesh and bathymetry.

A. Local Hydrodynamic Model Setup

The local hydrodynamic model of the Piave River estuary and vicinities was setup to compute the interaction of sea currents and river currents. The nested approach was considered necessary due to the high requirements of the estuarine area in terms of spatial and temporal resolution. It is reasonable to assume that the river flow has no impact in the regional hydrodynamics. The same is not true on a local level, particularly in the vicinities of the mouth.

The local model domain was setup with a refined mesh (17,221 elements with edge-length varying between 2 m and 300 m) and bathymetry near the shore and includes the lower stage of the river up to the location of the Eraclea stream gauge used for the forcing of the fluvial discharge in the model.

The Italian agency ARPA provides free-source time series of hydrometric levels at various sections along the Piave River at hourly intervals. The stage-discharge curves are frequently calibrated based on *in situ* measurements and published to the public.

The model was setup with fully defined terms on the sea boundary (water depths and current velocity vector on each node) obtained by the interpolation of the regional model results over the local model boundary (Figure 3). The river boundary was forced with the discharge time-series obtained from ARPA (Figure 4).

The local model simulated the period between the 5th December and the 10th December 2020 for a duration of 432,000 timesteps. The timestep of the river input conditions varies every 3600 s (1 hour) and the computational timestep is 2.5 s.

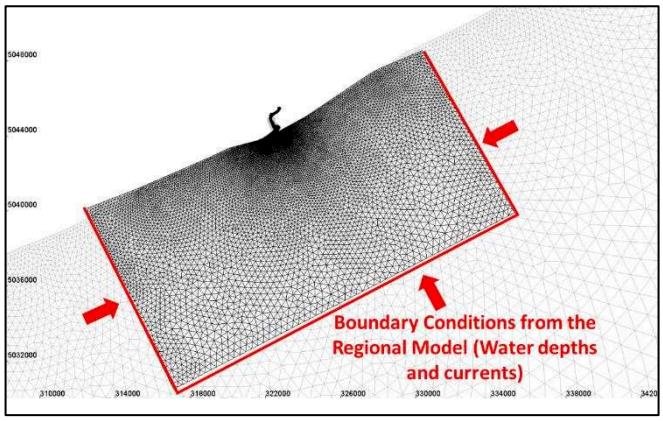

Figure 3. Local hydrodynamic model, sea boundary conditions.

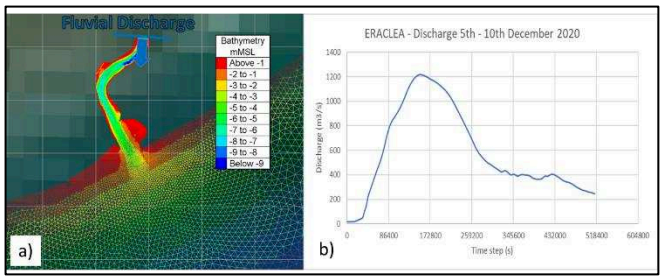

Figure 4. a) Detail of the local hydrodynamic model at the Piave River mouth. b) Discharge curve for the period of simulation.

B. *Sediment Transport Model*

The sediment transport modelling with SISYPHE was performed over the local model domain. The currents field (water depths and currents) calculated in the local hydrodynamic model simulations is used to drive the computation of the sediment transport.

The sediment properties are represented as a non-cohesive non-uniform sand with mean diameter of 0.20 mm based on data obtained from [5]. Critical shear stress for suspension is based on Shields theory. Friction is consistent with the semi-empirical model selected hydrodynamic model.

IV. RESULTS

A. *Validation*

The calibration / validation procedures are fundamental for the accuracy and confidence in numerical models, even more so when the models are chained or coupled and include processes of different origin.

Unfortunately, validation requires comparison of the numerical data with actual measured data which for the majority of the cases requires *in situ* instrumentation and measurements and is, therefore, spatially and/ or temporally limited as well as costly.

A major hinderance to the development of the present study case was the availability of open-source data that could be used for the validation of both the hydrodynamic and the morpho-dynamic models.

Thanks to the network of tide gauges installed along the Italian coast, it was possible to compare the surface elevations time-series produced in the numerical model with the measurements at two tidal stations, Venezia and Trieste, each about 30 km from the project site (Figure 5). The results show a reasonable agreement of the modelled heights and measured heights considering how limited was the input data and the specific phenomena at play during the modelled event (extreme surge elevations were registered over the period).

The magnitude and direction of currents, arguably the most important parameter was, however, not verified due to the unavailability of data.

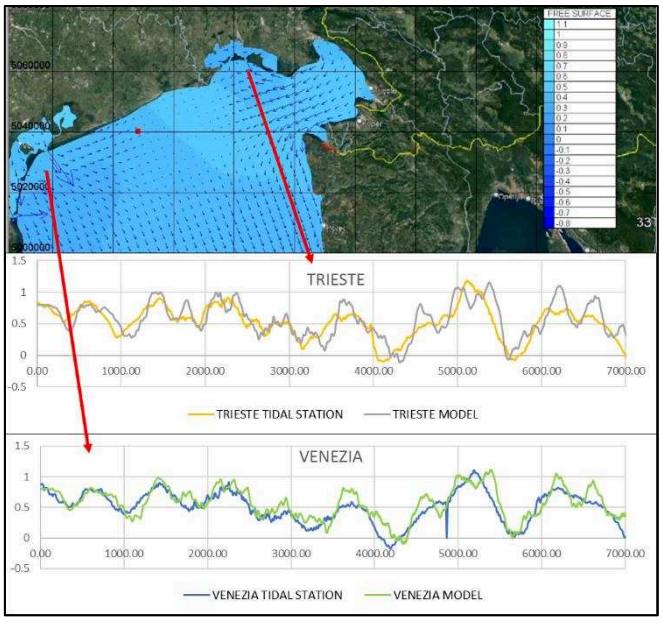

Figure 5. Validation of modelled surface elevations against tide gauge measurements at Venezia and Trieste.

During the validation process it was also noted how important is the quality of the shoreline detail for these types of sea bodies. An initial iteration of the Regional Model with a less detailed shoreline that did not include many of the

most complex morphological features that are characteristic in the Adriatic coast, such as the lagoons and coves, was observed to perform significantly worse in reproducing the evolution of water levels along the domain. These types of water bodies, most notably the larger lagoons such as the one at Venice, appear to act as reservoirs and play a role in regulating the circulation of water in the regional basin. Increasing the detail of the shoreline at the regional scale is time-consuming but fairly inexpensive given the widely available open-source satellite imagery.

In is to expect as well that a better description of the bathymetry near the coast and particularly in the previously mentioned water bodies could provide further improvements on the hydrodynamic model quality. Free-source bathymetric data of higher resolution is, however, scarcer.

The local hydrodynamic model was not validated as it required a dedicated *in situ* campaign at the Piave River estuary. However, the observed evolution of the sediment plume in the river during the events as captured by the Sentinel-2 images allows for a high-level qualitative perception of the model's ability to reproduce the overall current direction.

To validate the dispersion of the sediment plume, the images obtained by remote sensing are compared with the results extracted from the model. This procedure allows to use observed sediment plume as a representation of the estuarine hydrodynamic pattern that may be used as a model calibration target.

Figure 6. Remote sensing image for the flooding event of 7th December, time 10.17 am (Credit: Planet Earth Observation)

B. *Role of the Sea Currents*

The magnitude of the currents generated by the water level variation at sea is observed to be much lower in comparison to the discharge of the river during the flood event. Nonetheless, even in this case it is notorious how the interaction of the river currents with the sea currents affects the propagation of the river discharge "jet". A comparison of the discharge "jet" shape, at the same time-step, with and without the inclusion of sea currents is shown in Figure 7.

Despite their lower magnitude, the sea currents interact with the river discharge currents and are able to divert the flow direction. The resulting jet is reminiscent of the observed sediment transport patters.

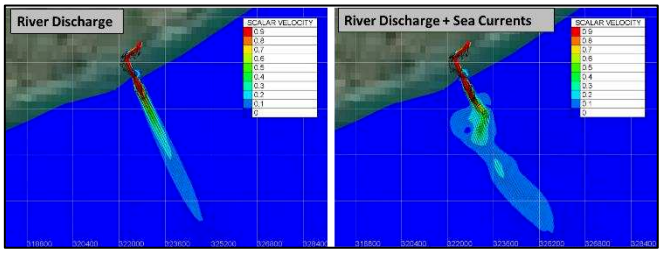

Figure 7. Effect of the sea currents in the discharge jet.

C. *Sediment Plume*

Finally, the SISYPHE results are shown (Figure 8). It is noted that the plume is dispersed in the south-west direction as confirmed by the remote sensing image (Figure 6). It is also highlighted that the extent and shape of the sediment dispersion is generally well reproduced, even if in the north-east part in the model has an arched shape that is not reproduced in the reality. The spatial variation of the concentration magnitude, however, is not measurable using the remote sensing image.

We further note that the implemented bathymetry has a very low spatial resolution especially near to the beaches and the shoreline (dx=450m), which could generate a variation in the shape of the plume.

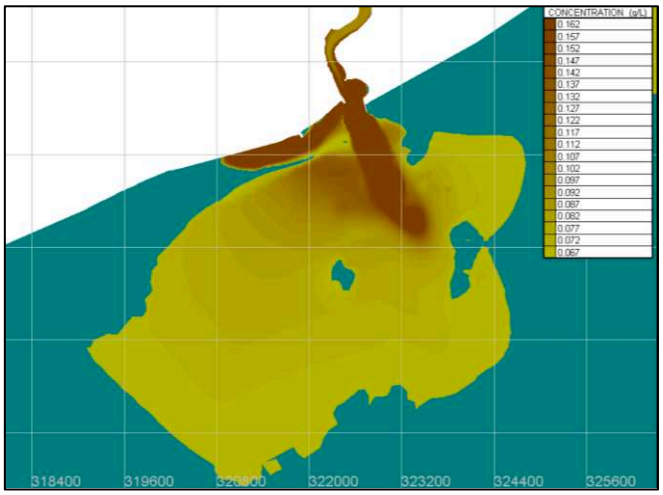

Figure 8. SISYPHE simulation result for the flooding event

V. Conclusions and Future Developments

The present study case aimed at reproducing the morpho dynamics of the flooding event occurred at the Piave River in the period of 5th to 10th December 2020. Numerical modelling of fluvial discharge, water circulation and sediment transport was undertaken using the open-source modelling system TELEMAC, namely the modules TELEMAC-2D and SISYPHE.

The first results show potentiality in the use of satellite images of suspended sediment plume as a calibration target of numerical models.

Acknowledgement

The authors are particularly grateful to Manuel Josè Dias Da Silva for providing us with tidal harmonic constituents and Dr. Mariano Buccino (University of Naples Federico II) for valuable advice. Thanks to Planet's Education and Research Program for giving us access to the satellite images. The work is funded by POR Puglia FESR 2014 - 2020 in the framework of SWIM project (https://por.regione.puglia.it/)

Reference

[1] G. P.Holdaway,P.D.Thorne,D.Flatt,S.E. Jones,D. Prandle. Comparison between ADCP and transmissometer measurements of suspended sediment concentration, March 1999, Pages 421-441.

[2] J.W.Gartner, Estimating suspended solids concentrations from backscatter intensity measured by acoustic Doppler current profiler in San Francisco Bay, California, 2004I.

[3] J.M. Hervouet, Hydrodynamic of free surface flow, finite elements systems, Wiley, 2003.

[4] C. Villaret, SISYPHE 6.0 User Manual, Rapport EDF R&D LNHE HP-P73-2010-01219-FR, 2010.

[5] Planet Team (2017). Planet Application Program Interface: In Space for Life on Earth. San Francisco, CA. https://api.planet.com

[6] Studio e monitoraggio per la definizione degli interventi di difesa dei litorali dall'erosione nella regione veneto – Linee guida. Regione Veneto.

Detailed TELEMAC modelling to evaluate the effectiveness of sediment recycling

Thomas Benson[1,2] and Jeremy Spearman[1]
[2] t.benson@hrwallingford.com
[1] HR Wallingford, Howbery Park, Wallingford, Oxfordshire, OX10 8BA

Abstract – **It is common in many parts of the world, to find large ports and harbours lying adjacent to ecologically important areas of coastal habitat and these ports and harbours have to manage their maintenance dredging in a manner that is sustainable for neighbouring wetlands. Part of this consideration includes considering whether dredged sediment can be used beneficially in and around the wetland areas to improve habitat and functioning.**

This paper considers the use of sediment recycling (also known as non-direct or "strategic" placement) of cohesive sediment in the Stour-Orwell Estuary system in the south east of the UK, which has been in operation since 1998. The paper summarises how monitoring and well-validated morphological models can be used to identify the effectiveness of this type of scheme.

***Keywords*:** sediment recycling, beneficial use, monitoring, morphological modelling, validation.

I. INTRODUCTION

A. Background

It is common in many parts of the world, to find large ports and harbours lying adjacent to ecologically important areas of coastal habitat and these ports and harbours have to manage their maintenance dredging in a manner that is sustainable for neighbouring wetlands. Part of this consideration includes considering whether dredged sediment can be used beneficially in and around the wetland areas to improve habitat and functioning.

Beneficial use of dredged material for habitat creation, also termed "sediment recycling", can take many forms. This paper is specifically concerned with "*sediment recycling*", also known as non-direct or "strategic" placement, of cohesive sediment, arising from ongoing water column recharge in the Stour-Orwell Estuary system in the south east of the UK. This estuary system is the location of the Port of Felixstowe is situated, which is the UK's largest container port. Sediment recycling has been ongoing in this estuary system since 1998, with the objective of mitigating for perceived impacts arising from deepening of the approaches to the port (see Section I.C).

B. The Stour/Orwell Estuary System

The Stour/Orwell system (Figure 1) is meso-tidal (3.6m mean spring tidal range at the estuary mouth). The fluvial input into the system is low (the mean total fluvial discharge into the Stour and Orwell Estuaries is less than 5 m^3/s).

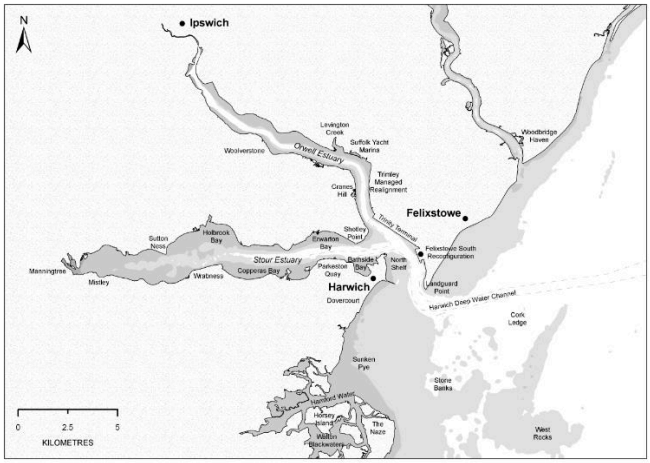

Figure 1. Stour/Orwell Estuary System

With the exception of Harwich Harbour (which is the name given to the confluence of the Stour and Orwell Estuaries, at the estuary mouth) waves inside the estuary system are locally wind-generated. Typical wave heights are 0.2-0.3m in the Stour and 0.1-0.2m in the Orwell [1, 2]. During strong westerly winds, however, waves can rise up to 1 m throughout much of the Stour Estuary [3]. Waves in the Orwell are generally lower because of the reduced fetch lengths. The Stour and Orwell estuaries have extensive muddy flats (and to a lesser extent, saltmarsh) which are protected habitats because they support nationally and internationally important numbers of migratory and wintering bird species.

The Port of Felixstowe is located on the east side of Harwich Harbour. Harwich Haven Authority (HHA) annually undertakes maintenance dredging of 2.4 Mm3 of soft mud. Up until the present day this mud was dredged by trailer suction hopper dredger (TSHD), aided by plough dredging in the berths. This material is disposed around 30 km offshore. The sediment supplied to the estuary is almost all from offshore marine sources [1] and predominantly enters from the near-shore zone north of the entrance along the Suffolk Coast.

C. The sediment recycling strategy

Sediment recycling was instigated within the Stour/Orwell Estuary system as a condition of consent for the 1998/2000 capital deepening of the approach channel to Felixstowe Port from -12.5 mCD to -14.5 mCD [4]. There was a concern that the deepening, trapping of sediment and subsequent offshore disposal, could reduce the supply of sediment to intertidal areas within the estuary system [5]. Sediment recycling of

maintenance material was proposed as a mitigation to any increase in the overall erosion rate of intertidal habitat, the idea being that the release of dredged material into the water column would increase suspended solids, and hence deposition, over intertidal habitat.

The mitigation proposed to offset this risk was sediment recycling. The sediment recycling began in 1998 and has continued to the present day. Over the first decade there were various adjustments as to the method and amount of recycling [1, 6], but after 2008 the annual amount of sediment recycling was set at the level of 50,000 tonnes dry solids per annum, which has remained consistent until today. Sediment recycling can occur in the Stour/Orwell at any time of the year but it is normal for 3 sediment recycling campaigns to be carried out annually. These campaigns typically occur over a 4 or 5 day period with 3 to 5 placement operations on the flood tide only. Placement occurs at each of the three placement sites (Erwarton Bay, Copperas Bay and the Lower Orwell – see Figure 2) in succession.

Placement typically occurs over a period of around 20 minutes with the dredger (hopper capacity: 1,500 m^3) moving landwards at an over-the-ground speed of 2-2.5 m/s. Typically each placement discharges an average of 560-570 tonnes dry solids each over this 20 minute period. The intention is to release the sediment slowly into the water column to enhance the mixing of the placed sediment. This modified mitigation (representing placement of approximately 4% of the maintenance dredging mass/volume) appears to be successful in enhancing intertidal habitat whilst not causing adverse effects on fishery interests. At the time of writing an estimated 2.3 Mtonnes, representing the *in situ* volume of around 4.6 Mm^3, has been recycled.

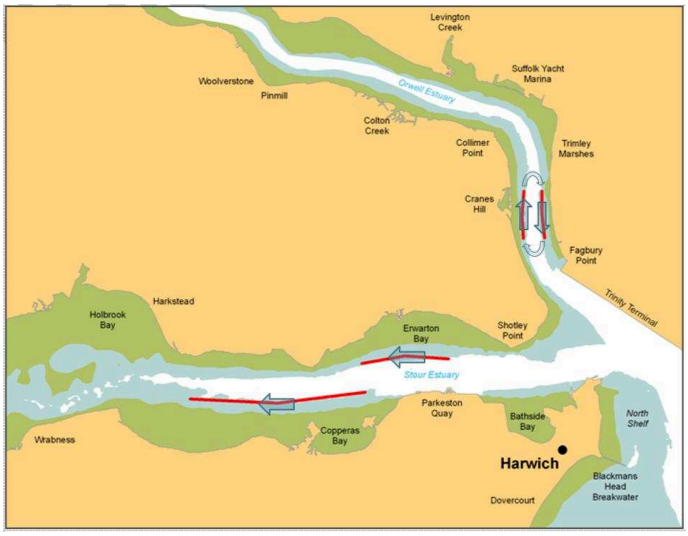

Figure 2. Sediment recycling methodology

II. METHODOLOGY

A. Bathymetric Monitoring

As part of the consent agreement for the 1998-2000 approach channel deepening a package of monitoring tasks was implemented, including subtidal bathymetric surveys over the whole estuary system and LiDAR measurements over the whole of the intertidal areas every 5 years. Surveys of the subtidal (using multibeam) and intertidal bed levels (using flown LiDAR) were undertaken in 2005/6 and 2015/6 by Harwich Haven Authority. These surveys were combined to produce representations of the subtidal tidal and intertidal bathymetry in the Stour and Orwell estuary system for 2005 and 2015. The change in bed levels over the period 2005-2015 (shown below in Figure 3) were used as a basis for calibration of the morphological model.

The results of the bathymetry/LiDAR surveys undertaken in 2005 and 2015 indicate a gain of 2.2 ha/yr of intertidal area in the Stour and a gain of intertidal area in the Orwell of 2.8 ha/yr (at the 0 mCD level). The gain in intertidal area in the Stour is principally the result of net accretion in the upper Stour in Holbrook Bay and west of this on the lower intertidal between the 0 mCD and +1 mCD contours. Erosion principally occurs in the lower Stour in Erwarton Bay, east of Harkstead on the north bank, and in the east of Copperas Bay on the south bank. The main feature in the Orwell Estuary is the loss in the volume of intertidal areas above +1m CD, but again considerable accretion occurs between the 0 mCD and +1 mCD contours.

B. Tidal discharge and sediment flux measurements

Data on water discharge and sediment flux were collected during surveys commissioned by HHA in February 2001 (spring tide conditions), on 21 October 2020 (spring tide conditions) and on 25 October 2020 (neap tide conditions). Profiles of current velocity and acoustic backscatter were collected along transects using a vessel mounted ADCP. Figure shows the location of the ADCP transects used to collect discharge and flux data at regular intervals through a spring tide on in February 2001 and October 2020.

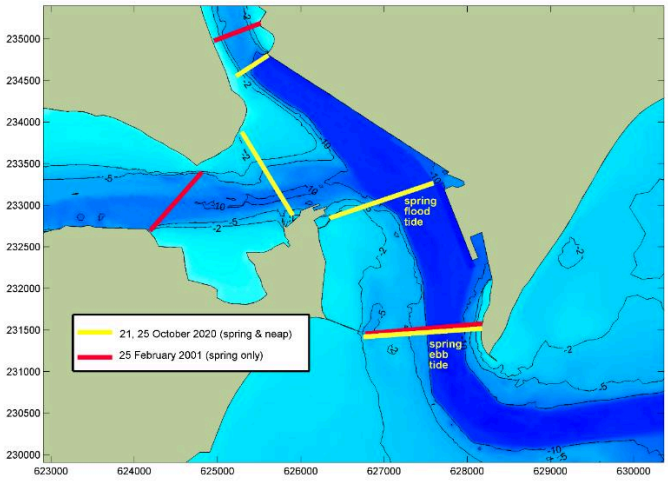

Figure 4. ADCP transect locations for 2001 and 2020 surveys

C. Water level measurements

Water level measurements for validation of the flow component of the sediment transport model were obtained from the Tide Gauge at Harwich and were provided by HHA. In particular, the model was compared against water levels for the 16 February to 2 March 2001 and 12 October to 10 November 2020.

III. MODELLING

A. *Flow model set up*

The TELEMAC-3D code was used as the basis of the morphodynamic model. Figure 5 shows the model domain and mesh used in the present study. The resolution of the mesh is coarsest in the middle of the domain, away from coastal boundaries, with an element size of about 5 km. Resolution within the outer channel was approximately 90 m reducing to 40 m or finer inside the Harbour (Figure 6). Resolution within the Stour and Orwell estuaries was set to approximately 80 m or finer.

The flow model was driven on the boundaries of the model using predicted tides for a spring-neap cycle provided by the UK Admiralty's TotalTide© software. A total of 8 tidal station locations were use, and the levels between each tidal station were linearly interpolated along the length of each of the tidal boundaries. The freshwater flow input to the Stour and Orwell Estuaries is generally very low and so no freshwater runoff was included in the model.

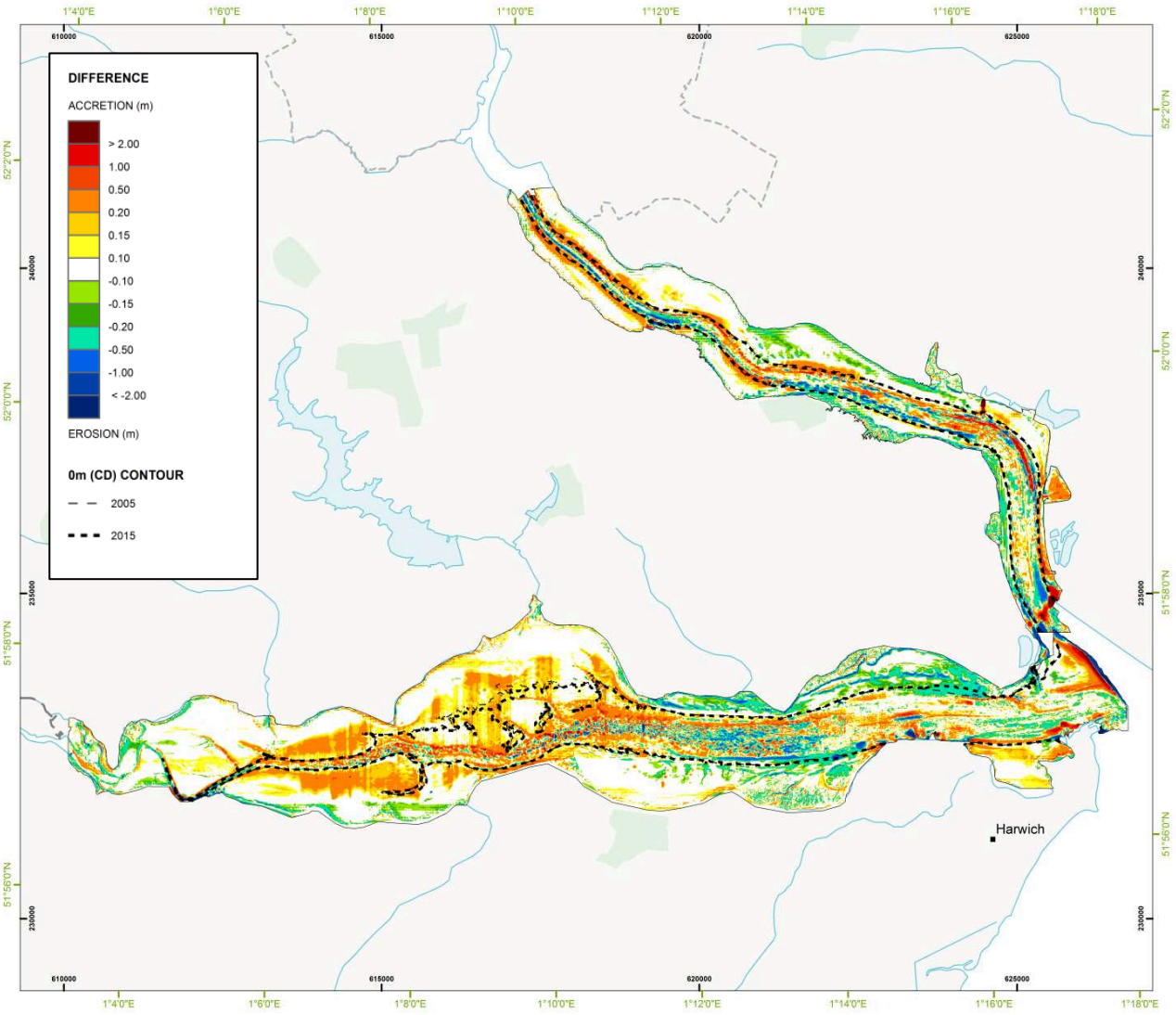

Figure 3. Measured change in bathymetry over the period 2005-2015

B. *Wave model set up*

Instead of TOMAWAC, the wave model SWAN was used to consider the processes of wave generation by local wind conditions and wave transformation owing to the potential for wave reflection from the Port of Felixstowe and Harwich International quays (wave reflection was not represented within the TOMAWAC wave model at the time of the studies). SWAN is a 3rd generation spectral wave model, which simulates the transformation of random directional waves including wave shoaling; wave refraction; depth-induced breaking, bottom friction and whitecapping; Wave growth due to wind; wave reflections from structures or rocky shorelines; and, far-field wave diffraction. The SWAN model has been extensively validated [8, 9, 10] and is widely used for coastal wave modelling.

The SWAN model was configured so that the model mesh was identical to the TELEMAC-3D mesh. The SWAN wave model was driven by application of wave conditions to the offshore boundaries of the model and by a spatially varying wind over the model domain. Wind data were obtained from Met Éireann's MÉRA reanalysis [11, 12] for a point offshore from Felixstowe at 51.9°N 1.328°E. These wind conditions were analysed to derive representative wind conditions (see below) for eight direction sectors. The spatial variability of the wind was modelled using the WAsP model [13].

Offshore wave conditions were derived from the ERA5 global wave hindcast produced by the European Centre for Medium-range Weather Forecasting (ECMWF). Wave conditions were associated with the wind conditions from MÉRA by correlation by direction sector.

The variation in wave direction, size and period was characterised into 8 "representative" waves which represent the "average" wave from each of 8 different directions . "*Average*" here means the wave whose contribution to fine sediment transport is average across the whole range of wave conditions experienced from this direction . These representative waves are sometimes referred to as "morphological" waves and the methodology used to derive the representative wave is described in [14]. The representative or "morphological" waves are presented in Table I. For each wave simulation in the morphological model, the water levels within the SWAN wave model were varied according to the water level predicted by the flow model. This allowed the effects of the reduced fetch and reduced water depth resulting from Low Water, and the resulting reduction in wave action, to be represented within the morphological model.

Figure 5. Model domain and mesh, showing locations of Admiralty tide gauge stations used

Table I Morphological wind and wave conditions

Direction	Wind speed (m/s)	Offshore wave height Hs (m)	Offshore wave period Tp (s)	Wave Direction (°N)	Percent of time (%)
0	7.9	1.50	6.1	8.8	8.4
45	9.1	1.26	5.4	32.5	10.4
90	7.8	1.04	5.2	62.7	8.4
135	8.0	0.90	4.9	112.1	7.2
180	10.2	1.30	4.9	194.0	15.2
225	10.5	1.77	5.7	229.0	22.1
270	9.0	1.70	5.7	270.0	16.4
315	8.4	1.80	6.5	337.0	11.9

The additional bed shear stress due to wave stirring was computed using the method of Soulsby and Smallman [15] and combined with the bed shear stress from tidal currents using the approach of Soulsby and Clarke [16].

C. Sediment transport model set up

The sediment transport model used in this study was the TELEMAC-3D model – i.e. the same model as the flow model. This enables the sediment and flow to be fully coupled and able to influence each other at the time-step level. The change in bed morphology arising from the sediment transport prediction affects the flow (and for high sediment concentrations, the mixing of the sediment throughout the water column) and the resulting changes in flow cause changes in erosion/deposition and in the distribution of sediment through the water column.

Settling of the suspended mud was parameterised using the formula for settling of suspended cohesive sediment developed by Soulsby et al [17]. This formula estimates the median settling velocity of macroflocs and microflocs and the respective weighting of these two components of the spectrum of floc sizes and has been validated against several detailed data sets in different NW European estuaries. The formula is based on the shear stress and suspended sediment concentration and thus gives a spatially and time-varying representation of flocculation of suspended mud particles.

Hindered settling was represented by the formula given in [18] which is based on the equation developed by Richardson and Zaki [19] for fine sediment particles. At high concentrations the density of the suspended mud in suspension starts to become sufficient to cause some stratification of the density of water through the water column. At this point the suspended mud starts to contribute to the (negative) buoyancy effect and introduces damping of the vertical mixing, leading to potential increases in the near-bed concentrations. This mechanism is included in the model using the formulation of Munk & Anderson [20].

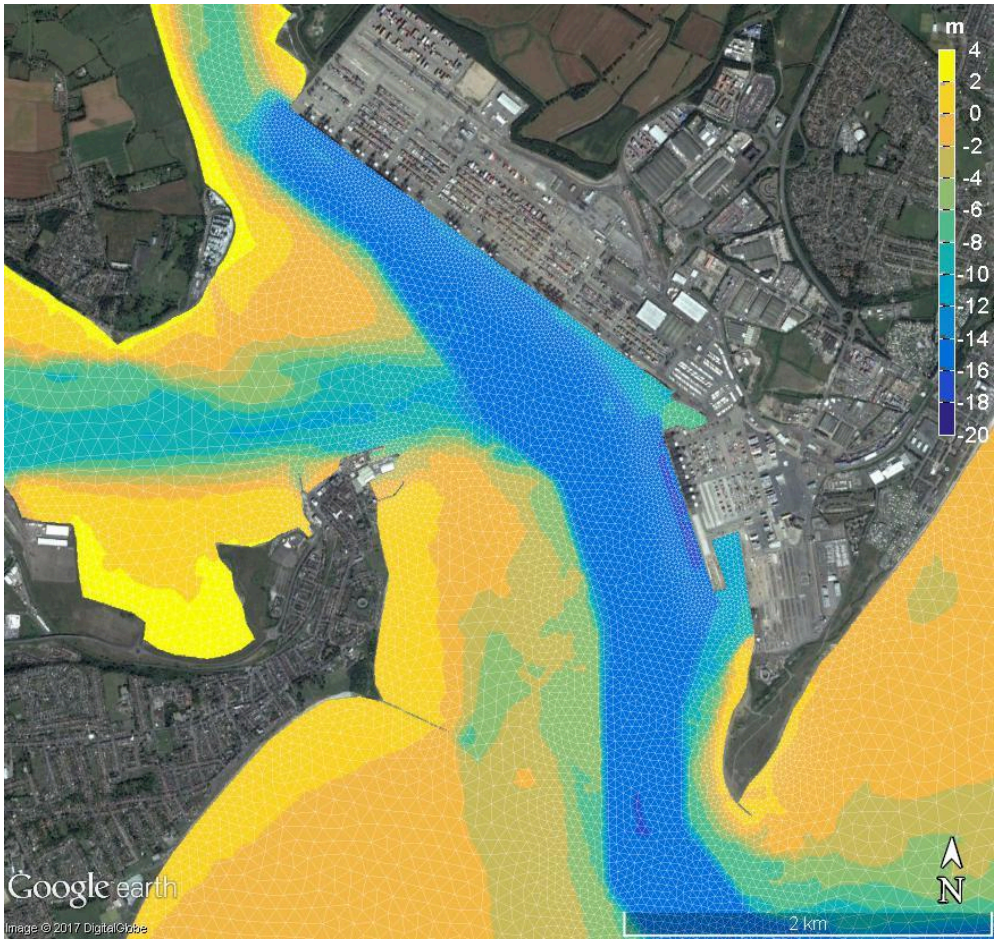

Figure 6. Model geometry and mesh within Harwich Harbour

A two layer bed model was used for modelling the bed exchange processes in the model. In the bed model, the uppermost sediment layer represents mobile material that is readily eroded each tide by the combined action of currents and waves. Net erosion or deposition occurs in the model depending on the balance between the erosion flux from the bed and the deposition flux. Deposition of sediment from the water column is assumed to occur continuously into the top sediment layer at a rate equal to the product of the settling velocity and the near bed suspended concentration.

For the top bed layer, a critical shear stress for erosion of 0.2 N/m^2 was set everywhere. When this threshold is exceeded by the combined effect of waves and currents flows, erosion is initiated and material erodes from the top bed layer at a rate predefined by the erosion rate constant [21] and in this case the constant was calibrated to be 0.001 kg/m^2/s. This value is within the range used by other researchers generally found in the literature (e.g., [18]). The underlying bed layer represented the in situ sediment that has experienced previous consolidation. The critical shear stress for erosion for this layer was parameterised with spatially varied values. The dry density for the lower layer was set to a higher value of 750 kg/m^3 (bulk density of approx. 1470 kg/m^3) representing consolidated cohesive material.

D. Application to the Stour/Orwell model

For this study the sediment transport model was run to reproduce the morphological change in the estuary system over the period 2005-2015, including the effect of the sediment recycling over this period. Over this period (which included larger placements occurring before 2008) placement as assumed to be (on average) about 66,000 TDS/year with about 44,000 placed into the Stour and about 22,000 TDS/year being placed into the Orwell. The simulation presented the moving discharge of sediment into the water column on the flood tide in the lower Stour and lower Orwell as described in Section I.C.

Simulations of sediment transport over a month-long period were undertaken for each of the wave conditions in Table I, and the wave conditions were chosen to be representative of the period 2005-2015 (8 simulations). The modelling was then repeated without sediment recycling (a further 8 simulations). The predicted changes in morphology over the course of these 16 simulations were then combined and weighted to provide the (mean) annual deposition both with sediment recycling (i.e., for 3 campaigns per year) and without any sediment recycling at all.

IV. RESULTS

A. Model prediction of observed intertidal morphological change over the period 2005-2015

The model prediction of bathymetric change is shown in Figure 7. The figure of predicted change matches that of the observed change well in Figure 3. Figure 9 shows a more detailed comparison of intertidal change in different regions of the estuary system (see Figure 8).

The figures show that the model does a good job of reproducing the distribution of intertidal volume changes over the 2005-2015 period. Here we use an objective method of assessing the performance of morphological models [22, 23].

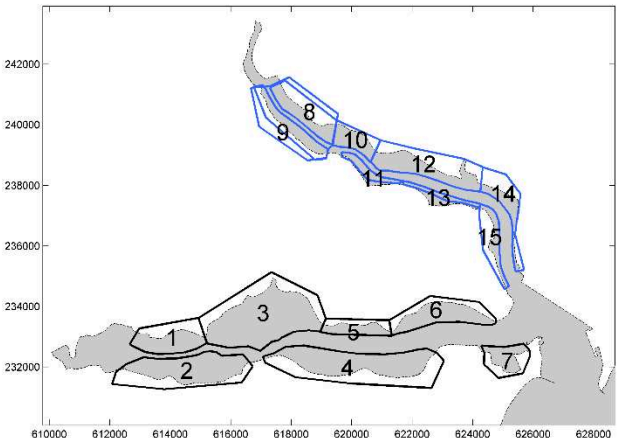

Figure 8. Zones used in comparisons of intertidal erosion/deposition rate throughout the estuary system

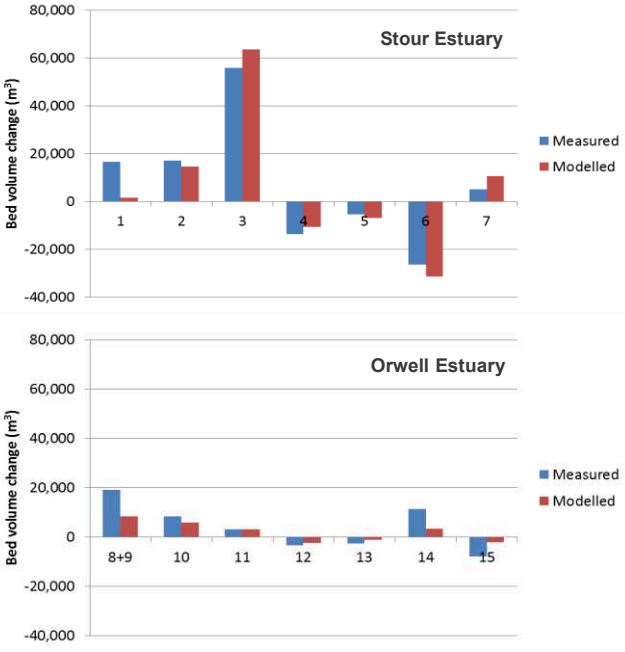

Figure 9. Comparison of the observed and predicted mean annual deposition (+ve) or erosion (-ve) in the (*Top*) Stour and (*Bottom)* Orwell, in each of the zones highlighted in Figure 9

Skill scores are considered to represent a more critical test of a model because they represent measurement of performance in relation to a baseline prediction – which normally in morphodynamic modelling is an assumption of "no change" [22]. Here we use a Briers Skill Score (BSS) based on the mean square error,

$$BSS = 1 - \frac{\langle (Y-X)^2 \rangle}{\langle (B-X)^2 \rangle} \qquad (1)$$

where $\langle (Y-X)^2 \rangle = \frac{1}{N}\sum_{i=1}^{N}(y_i - x_i)^2$; Y is set of is a set of model predictions, $y_1, y_2, \ldots, y_N$, and X is a set of observations, $x_1, x_2, \ldots, x_N$; B is a set of baseline predictions, $b_1, b_2, \ldots, b_N$, with the nth baseline prediction occurring at the same place and time as the nth value of the predictions and observations, Y and X. B represents the hypothesis of no change so $b_1 = b_2 = \ldots = b_N = 0$.

A BSS value of 1 indicates a perfect model. A BSS value of 0 indicates that the model is no better than the null hypothesis of "no change". A negative BSS score that the model performs worse than assuming no change. Sutherland et al [22] defined a classification table enabling broad rating of the performance of a model based upon the BSS score (Table II). A BSS of > 0.5 is considered as excellent. The data presented in Figure 10 results in an BSS of 0.89.

Table II Classification of model performance according to [22] for the BSS based on Mean square error (Equation 1)

	BSS score
Excellent	1.0 – 0.5
Good	0.5 – 0.2
Reasonable/Fair	0.2 – 0.1
Poor	0.1 – 0.0
Bad	< 0.0

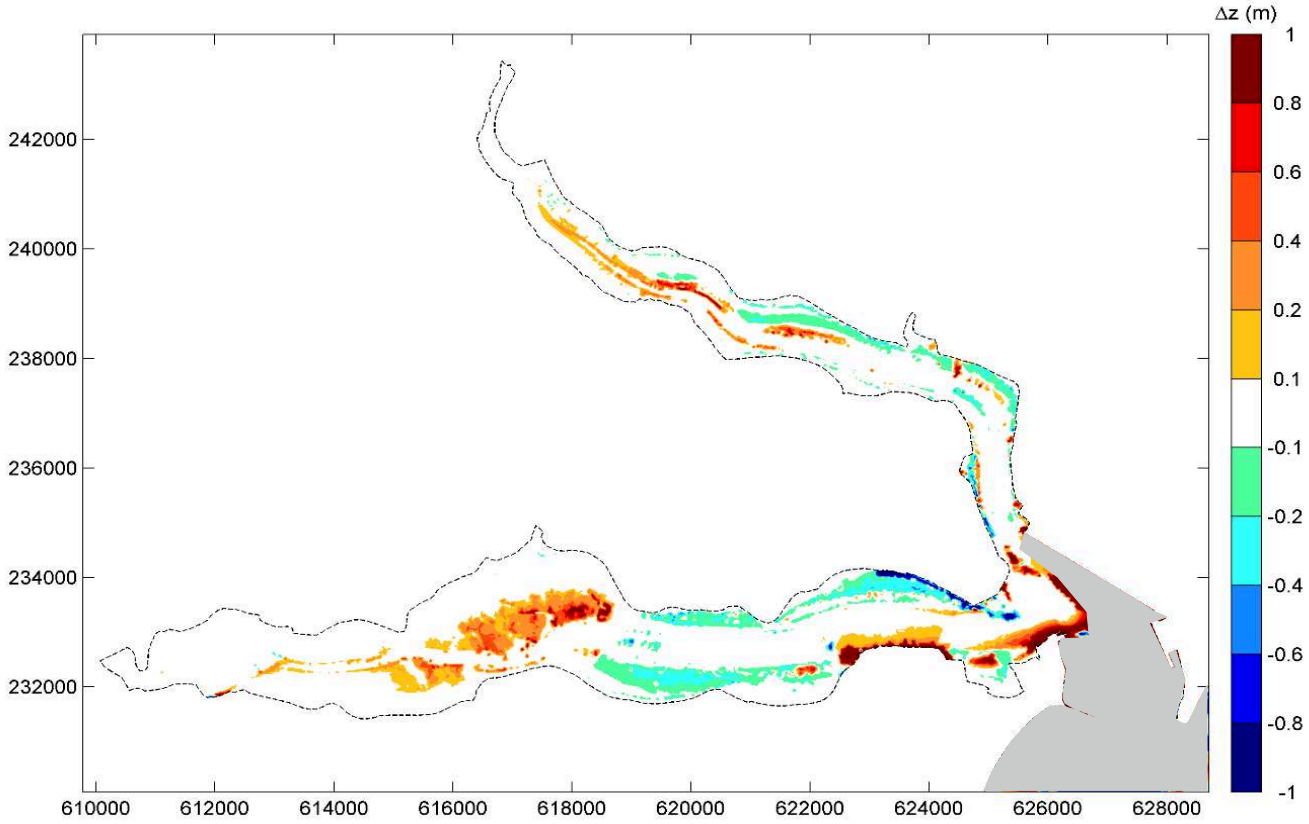

Figure 7. Predicted change in the rate of bed level in the Stour and Orwell 2005-2015

B. Morphological evolution resulting from the sediment recycling

The validated model results shown in Section IV.A allowed the morphodynamic model to be used as a tool to assess the difference in morphodynamic evolution that occurred as a result of the sediment recycling alone over the period 2005-2015.

The assessment of morphological change including the effect of sediment recycling was repeated but now only including the effect of background sediment transport alone. For simplicity from now on, we refer to results in terms of the average annual change (over 2005-2015). The additional annual deposition (or reduced erosion) resulting from the sediment recycling is summarised in Figure 11. The model results indicate the following:

- The main area fed by the sediment recycling is the lower part of the intertidal profile, and the shallow subtidal areas of Holbrook Bay.
- In general deposition is fed to the lower parts of the intertidal in both estuaries.
- Much more intertidal deposition results in the Stour Estuary than the Orwell Estuary. 21% of the recycled sediment settles on the intertidal and shallow subtidal (defined as above -1 mCD) in the estuaries with percentages of 17.5% (Stour) and 3.5% (Orwell).
- In the estuary system as a whole, subtidal deposits (defined as below -1 mCD), representing 8% of the placed material, are distributed roughly equally between the Stour and the Orwell.
- A substantial proportion of the recycled sediment (47%) deposits in the maintained areas of Parkeston Quay and the maintained areas of the approaches and berths to the Port of Felixstowe.

In terms of change in intertidal area Tables III, IV and V summarise the effects (changes in volume and area) of the placement above CD and also above Mean Low Water (MLW). MLW is the level above which the intertidal area is designated as a

Special Protected Area. The figures show that the placement causes an increase of 1.7 ha/yr above CD but results in a smaller increase of 0.8 ha/yr above MLW. The sediment recycling contributes a significant proportion of the year by year increase in intertidal area in the system as a whole.

Table III Predicted annual changes in volume (m3/yr) above the -1 mCD contour in the Stour and Orwell Estuary

	Stour	Orwell	Total
Without placement	6,500	-9,200	-2,700
With placement	28,600	-4,700	23,900

Table IV Predicted annual changes in intertidal area above CD (ha/yr) in the Stour and Orwell Estuary

	Stour	Orwell	Total
Without placement	4.3	0.6	4.9
With placement	5.9	0.7	6.6

Table V Predicted annual changes in intertidal area above MLW (ha/yr) in the Stour and Orwell Estuary

	Stour	Orwell	Total
Without placement	0.0	0.8	0.8
With placement	0.5	1.1	1.6

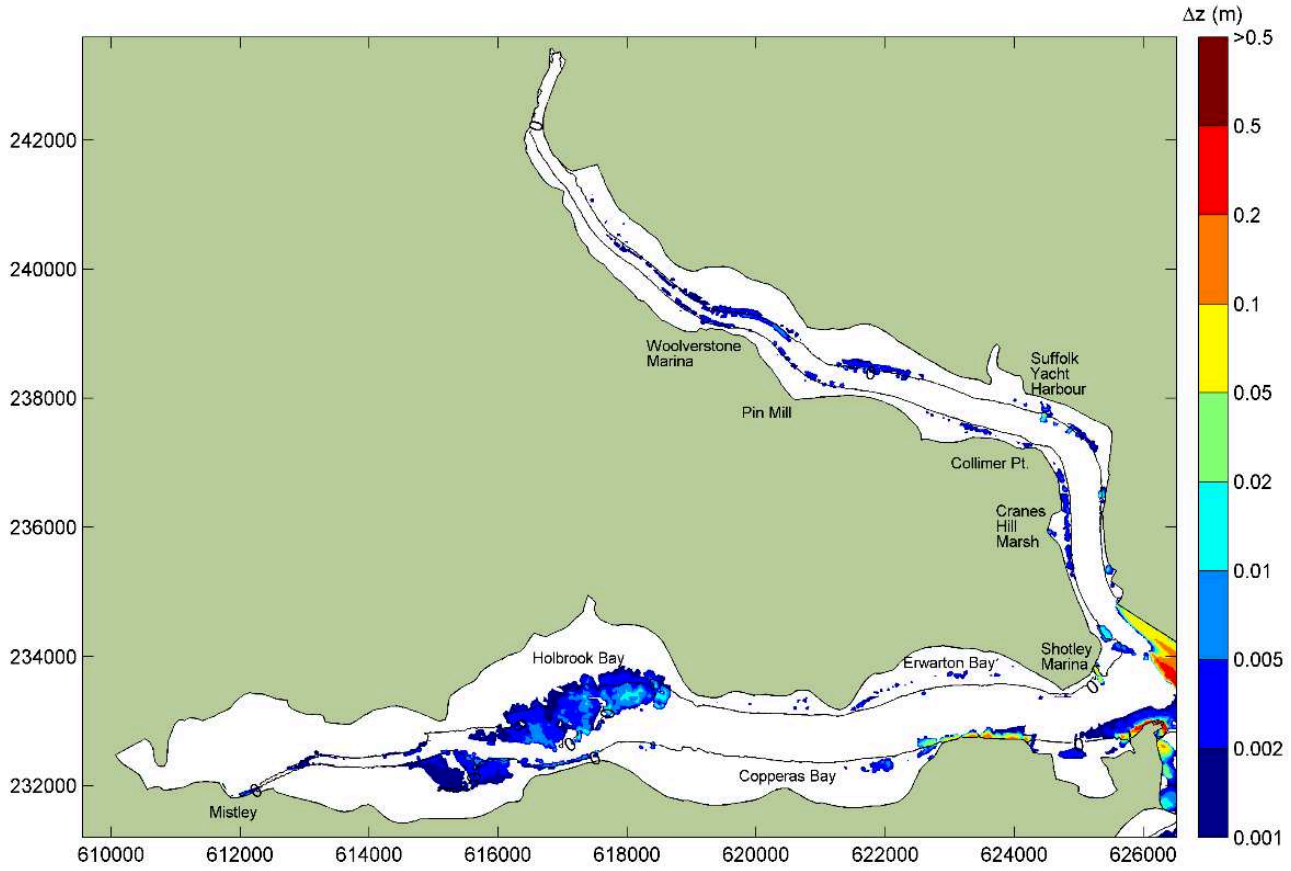

Figure 11. Predicted changes to the annual evolution of the estuary system due to the sediment recycling (the iso-contour shown is the 0 mCD contour)

V. CONCLUSIONS

Sediment recycling has been undertaken in the Stour/Orwell Estuary system since 1998. The use of long term bathymetric and LiDAR surveying, together with detailed and highly-calibrated sediment modelling, has enabled the effectiveness of this sediment recycling to be identified with 21% of the release material permanently depositing on the intertidal and shallow subtidal areas. This result offers clear evidence that sediment recycling approaches of fine sediment can offer substantial benefit. However. whilst effective in stable or more quiescent areas, this sediment recycling does not represent a solution in areas of the estuary system which are eroding more rapidly.

ACKNOWLEDGEMENT

The authors we would like to thank Harwich Haven Authority for their cooperation in the writing of this paper.

REFERENCES

[1] J. Spearman, J. Baugh, N. Feates, M. Dearnaley and D. Eccles, "Small Estuary Big Port - Progress in the management of the Stour-Orwell Estuary system", Estuary Coastal and Shelf Science, 150: 299-311, 2014.

[2] HR Wallingford, Wave prediction studies for Harwich Harbour, HR Wallingford Report EX 3030, June 1994.

[3] HR Wallingford, Bathside Bay Development Studies. Impact of proposed scheme on sediment transport and estuary morphology. HR Wallingford Report EX4426, Supporting Document 1-10, Oct 2001. In: Bathside Bay Container Port Planning Applications, Environmental Statement, Royal Haskoning 2003.

[4] Posford Duvivier Environment and HR Wallingford, Harwich Haven Approach Channel Deepening, Mitigation and Monitoring Package, Report prepared by Posford Duvivier Environment and HR Wallingford for Harwich Haven Authority, July 1998.

[5] HR Wallingford, Harwich Harbour Approach Channel Deepening, Impact of channel deepening on mud transport. HR Wallingford Report EX 3748, February 1998.

[6] HR Wallingford, Review of sediment replacement activities in the Stour and Orwell, HR Wallingford Report EX 5651, Release 4.0, 2007.

[7] N. Booij, R. C. Ris, and L. H. Holthuijsen, "A third-generation wave model for coastal regions, Part I: Model description and validation", J.Geoph.Research, 104, C4, pp7649-7666, 1999.

[8] L. H. Holthuijsen, N. Booij, R. C. Ris, J. H. Andorka Gal, and J. C. M. de Jong, "A verification of the third-generation wave model SWAN along the southern North Sea coast", Proceedings 3rd International Symposium on Ocean Wave Measurement and Analysis, WAVES'97, ASCE, 49-63, 1997.

[9] Bosboom J, Reniers A J H M, Luijendijk A P (2014) On the perception of morphodynamic model skill Coastal Engineering 94:112–125..

[10] R. C. Ris, N. Booij, and L. H. Holthuijsen, "A third-gener,ation wave model for coastal regions, Part II: Verification, J.Geoph.Research", 104, C4, 7667-7681, 1999.

[11] E. Gleeson, E.Whelan, and J. Hanley, "Met Éireann high resolution reanalysis for Ireland", Adv. Sci. Res, 14, pp.49-61, 2017.

[12] E. Whelan, E. Gleeson, and J. Hanley, J., An Evaluation of MÉRA, a High-Resolution Mesoscale Regional Reanalysis. Journal of Applied Meteorology and Climatology, 57(9), pp.2179-2196, 2018.

[13] N.G. Mortensen, L. Landberg, O. Rathmann, H. P. Frank, I. Troen and E. L. Petersen, "Wind atlas analysis and application program (WAsP)", In Wind Energy Department: Scientific and technical progress 1999-2000, 2001.

[14] T. J. Chesher and G. V. Miles, "The concept of a single representative wave", In: R A Falconer, S N Chandler-Wilde and S Q Liu (Eds), Hydraulic Environmental Modelling: Coastal Waters, Ashgate, Brookfield, pp271-380, 1992.

[15] R. L. Soulsby, and Smallman, J.V (1986). A direct method of calculating bottom orbital velocity under waves, HR Wallingford, Report No. SR76.

[16] R. L. Soulsby and S. Clarke, Bed shear-stresses under combined waves and currents on smooth and rough bed, HR Wallingford Report TR137, August 2005.

[17] R. L. Soulsby, A. J. Manning, J. Spearman and R. J. S. Whitehouse Settling velocity and mass settling flux of flocculated estuarine sediments, Marine Geology, 339: 1-12, 2013.

[18] R. Whitehouse, R, Soulsby, W. Roberts and H. Mitchener, Dynamics of estuarine muds, Thomas Telford Publications, London, 2000.

[19] J. F. Richardson, and W. N. Zaki, "Sedimentation and fluidization: Part I" Trans. Instn. Chem. Engrs., 32, 35-53, 1954.

[20] W. H. Munk, and E. R. Anderson, Notes on a theory of the thermocline. J. Marine Res., 7, p. 276, 1948.

[21] E. Parthenaides, "Erosion and deposition of cohesive soils", Journal of the Hydraulic Division, ASCE91, HY1, p.105–139, 1965.

[22] Sutherland J, Peet A H, Soulsby R L (2004) Evaluating the performance of morphological models, Coastal Engineering, 51: 917– 939.

[23] Bosboom J, Reniers A J H M, Luijendijk A P (2014) On the perception of morphodynamic model skill, Coastal Engineering 94:112–125.

Hydro-morphodynamic modelling of the Dijle Valley [Belgium] under land-use/land-cover changes

Sardar Ateeq-Ur-Rehman[1,3], Qilong Bi[2,4], Ward Swinnen[3], Nils Broothaerts[3,5], Gert Verstraeten[3]

sardar.ateeq@anteagroup.be, Berchem, Belgium
[1]: Antea Group, Business Unit Water, Roderveldlaan 1, 2600 Berchem, Belgium
[2]: Flanders Hydraulics Research, Berchemlei 115, 2140 Antwerp, Belgium
[3]: KU Leuven, Division of Geography and Tourism, Department of Earth and Environmental Sciences, Celestijnenlaan 200E, B-3001 Heverlee, Belgium
[4]: KU Leuven, Division of Hydraulics and Geotechnics, Department of Civil Engineering, Kasteelpark Arenberg 40, B-3001 Heverlee, Belgium
[5]: Thomas More University of Applied Sciences, Zandpoortvest 60, B-2800 Mechelen, Belgium

Abstract – **Regular sampling from the graphic printout file is required to couple TELEMAC-2D/SISYPHE outputs as inputs to groundwater, ecological modelling, or preparing flooding maps. It is possible to use constant time step which is computationally costly for long-term simulations using millions of mesh nodes for valleys or rivers. Although variable time steps can significantly reduce the computational cost without violating the stability criterion, they lead to irregular sampling from the graphic printout file and control listing. In addition to that, maximum water levels within sampling time are required to be saved as output for preparing maximum flooding maps. This can be extracted by saving water levels at each time step which can lead to excessively large files.**

Therefore, in the Future Floodplains project, we updated the TELEMAC-2D code for regular sampling from the graphic printout file and control listing using variable time steps. To save maximum water levels within a sampling time, we updated the PRESRES_ and the NOMVAR_ subroutines. To further save computational time from weeks to hours, we used different morphological factors.

Finally, for calculating missing SSC samples for sediment load boundary conditions, we used wavelet transform coupled with artificial neural networks for Belgian rivers.

Keywords: morphological factor, variable time step, hydro-morpho-dynamics, spatiotemporal roughness.

I. INTRODUCTION

The TELEMAC system is an open-source integrated suite of solvers used in hydro-morpho-dynamic simulations. The software package provides an opportunity for users to adapt and modify the source codes for more precise simulations as per their study area requirements. In addition to that, the package is also programmed for parallel processing and can be installed on high-performance computing machines, very easily. Despite the fact of the parallel processing option in TELEMAC-2D, reducing computational cost is still challenging while simulating large computational domains. In particular, when the outputs are required after constant time intervals.

For fast simulations, variable time steps can reduce the computational cost by automatically adjusting time step dt in (1) while keeping CLF between > 0 and ≤ 1.0.

$$\mathrm{CFL} = \frac{\mathrm{u} * \mathrm{dt}}{dx} \qquad (1)$$

However, the graphic printout file and the listing printout (defied output in the below equation) are changed as they use variable time step dt (2). The graphic printout period defined by the user in a steering file remains constant.

$$Output = dt * graphic\ printout\ period \qquad (2)$$

Therefore, (2) leads to irregular sampling (when using variable time step) from the graphic printout files and control listing. To achieve regular sampling (for example after every 24 hours at 00:00:00), we use a constant time step while coupling TELEMAC-2D/SISYPHE output as input in other models. Using a constant time step (dt) requires huge computational cost as dt should be the minimum numbers for the whole computational domain and the whole simulation period for satisfying CFL number criteria [1]. In most cases, simulation time spreads over weeks while simulating millions of mesh nodes for a decadal time scale. However, regular sampling can be achieved using variable time step (dt) by adjusting graphic printout time (2) in NOMVAR_ and the PRERES_ subroutines. Which requires certain updates in the source code of TELEMAC-2D.

To prepare flooding maps, the output of the maximum water level within the sampling time is also required. Saving the water levels at each time step and post-processing the binary result file for extracting maximum water levels can serve the purpose. However, this method can lead to excessively large files of many terabytes (TBs) containing water levels at each mesh node for each time step. Therefore, an extra coding in PRERES_ and NOMVAR_ is required to hold/save the maximum water level at each mesh node within the sampling period.

In addition to that, morphological factors can further reduce the computational cost of decadal-scale simulations containing hundreds of thousands of mesh nodes [2].

In the Future Floodplains project [3], we updated the source code of TELEMAC-2D for saving daily output (at 00:00:00) of maximum water levels using variable time

steps. The maximum water levels were required for groundwater and ecological models for decision support system development. Maximum water levels are also required to prepare maximum flooding maps of different return periods.

II. STUDY AREA

The Future Floodplains project study area includes four river valleys for which we used TELEMAC-2D/SISYPHE for hydro-morpho-dynamic modelling and prepared inputs from for groundwater and ecological models. In this article, we are presenting the results of Dijle Valley (Figure 1) which we replicated for other study areas.

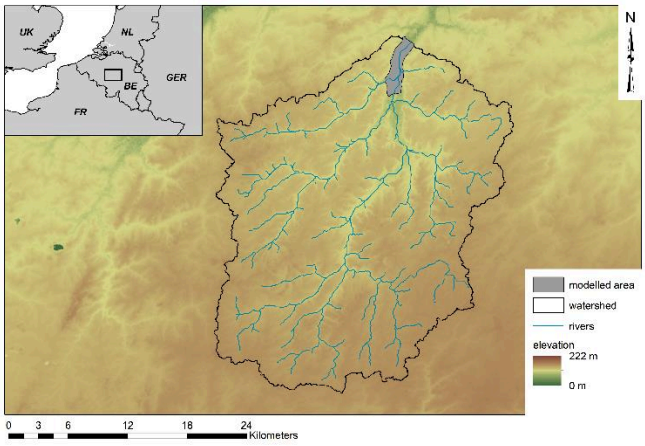

Figure 1. Location of the study area within the Dijle Catchment, upstream of the KU Leuven Heverlee Campus.

The study area within the Dijle Valley has an area of 791 hectares starting from Sint-Joris-Weert (Figure 1), where the Dijle River enters from Wallonia province to Flanders province in Belgium. Till 1990 the river in Flanders was dredged and cleaned regularly for sediment depositions, fallen trees, and bushes. Since 1990, the study area is managed under natural processes, allowing the river to flood and to meander freely, as a strategy to reduce downstream risks of flooding. Until 1990, river deepening and widening were observed in the river thalweg survey (Figure 2), which were driving more groundwater seepage to the river during dry seasons. The river cleaning was also causing lower rainfall retention time in the valley and providing efficient rainwater drainage.

After 1990, more sedimentation in the riverbed was observed (Figure 2) which is allowing more groundwater recharge and flood protection to downstream cities like Leuven. Managing the river under the natural processes allows fallen trees to stay in the river course and beavers to build dams across the drainages (Figure 3) which can be modelled by blocking drainages in TELEMAC-2D. Data availability and more details about the study area are discussed in the following section.

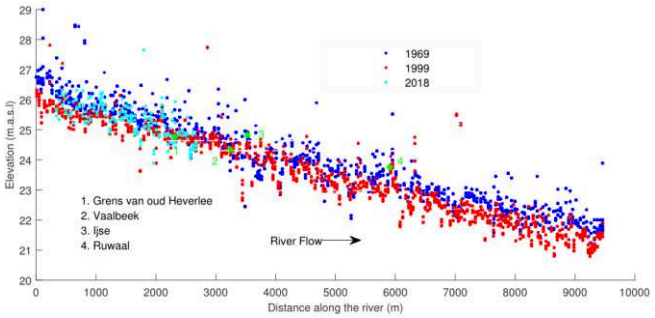

Figure 2. Measured river thalweg data is showing river deepening till 1999 and recovery afterwards. The layout of tributaries can be found in Figure 4.

Figure 3. Dijle River under natural management where (a) fallen trees are not picked up from the river and (b) beavers can block ditches. Photo (a) is the river section upstream of Korbeek Dijle and (b) is a small tributary near Grens van Oud Heverlee blocked by Beaver. For the location, see Figure 1 and Figure 4. (Photos are taken on 18 April 2021 by the first author)

III. MODEL DEVELOPMENT

A. Computational grid

We have the river thalweg cross-sectional survey conducted in 1969, 1999, and 2017 at approximately every 20 m distance along the river. As before 1990 the river was artificially dredged and riverbanks were cleaned up, it was challenging to model the dredging processes and represent river bedforms. Therefore, we used 1999 river cross-sectional surveys to build a non-uniform computational grid for the main Dijle River, its four tributaries, drainage network, and floodplain (Figure 4). By comparing cross-sections extracted from the 2D geometry base map of TELEMAC-2D with measured cross sections, we found a suitable mesh size of 1.0 m for river channels, <0.5 m for tributaries and small drainages, and 10.0 m for the floodplain. As small drainages are a very important part of Dijle River networks, their correct representation in the computation domain is very important to model the processes correctly. For representing river tributaries, and drainage networks in the computational grid, we post-processed (for <0.5 m mesh) the very detailed 1.0 x 1.0 m resolution light detection and ranging (LiDAR) surface elevation survey of the whole Dijle floodplain conducted in 2014 [4]. To represent the floodplain, we used it without any post-processing. The final mesh has 588,551 mesh nodes and 1,174,697 mesh elements.

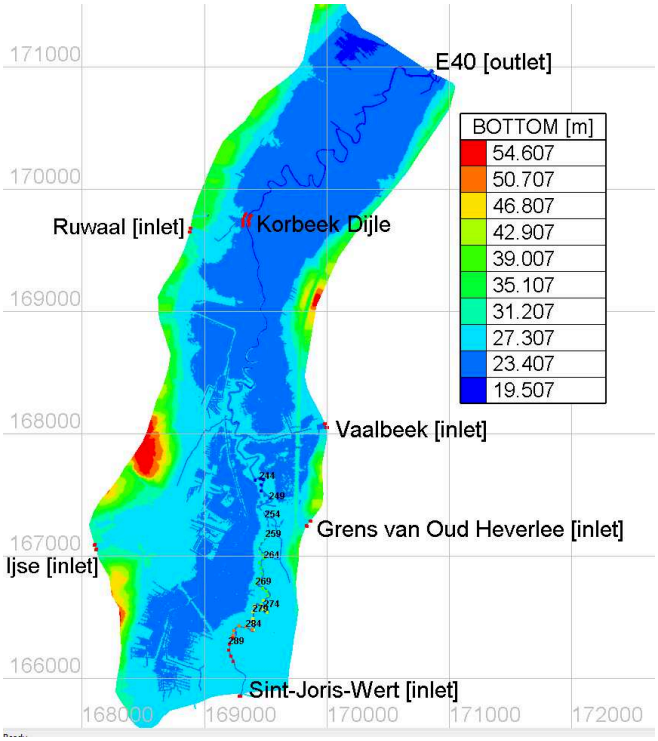

Figure 4. Location of all boundary conditions, four tributaries, and thalweg cross sections (243 till 292, 50 cross sections, see Figure 2) collected in 2017 by KU Leuven for calibration purposes. For the location of the study area, see Figure 1.

B. Initial conditions

We used 'PARTICULAR' initial conditions and provided 1.0 cm positive water depth at the inlet of discharge boundary conditions (Figure 4) by programming it in SUBROUTINE CONDIN.

C. Boundary conditions

We implemented discharges at Saint-Joris-Weert, Grens van Oud Heverlee, Vaalbeek, Ruwaal, and Ijlse as upstream boundary conditions (BC). While water levels were used at downstream boundary conditions at E40 near the KU Leuven Heverlee campus (Figure 4, Figure 5). The daily discharges measured by Flanders Environmental Agency (VMM and can be found at https://www.waterinfo.be/) at Sint-Joris-Weert were used at Sint-Joris-Weert BCs while STREAM model simulated discharges were used as discharge BCs for the tributaries [5]. Water levels measured by VMM at Korbeek Dijle Bridge (KD) were implemented as downstream boundary conditions at E40 by adjusting water levels using (3).

$$WL\_E40 = WL\_KD - 1.40 \quad (3)$$

From 1969 to 1999 negligible bed level changes in the river cross sections were observed at both locations, therefore, (3) stays valid for computing water levels at E40 using measured water levels at KD.

For SISYPHE BCs, we used wavelet transform coupled with artificial neural networks (WA-WNN) and reconstructed SSC (g/l) as upstream BCs, while downstream BC was set as an open boundary with free traces. As measured SSC data was only available between 1998 till 2000 which was collected by [6] at E40, we used it to build the WA-WNN model (Figure 6). The WA-WNN model was used to generate SSC boundary conditions from 1990 to 2020 (Figure 5).

D. New implementation for regular sampling using a variable time step

To have regular sampling, we adjusted LISTING PRINTOUT PERIOD and GRAPHIC PRINTOUT PERIOD in (2) by updating the TELEMAC subroutine:

```
!                    ********************
                     SUBROUTINE TELEMAC2D
!                    ********************
C***********************************************************************
C ATEEQ CHANGES START
      INTEGER AQ_AT,AQ_ATT,AQ_DIFF,AT_DIFF_K,AQ_DUPLICATE
!ATEEQ- EDIT FOR PRENTOUT WITH VARIABLE TIME STEP
      AQ_ATT=(INT(AT)/INT(LISPRD))*INT(LISPRD)
      AQ_AT=INT(AT)
      AQ_DIFF=ABS(AQ_AT-AQ_ATT)
      AT_DIFF_K=INT(DT)!Thresh hold coefficient set by ATEEQ.
      IF(LT.EQ.1)THEN
        AQ_DUPLICATE=AQ_DIFF
      ENDIF
C       IF((AQ_AT.LE.AQ_ATT.AND.AQ_DUPLICATE.NE.AQ_AT.
C     &  AND.LT.GE.PTINIL).OR.LT.EQ.NIT) THEN
      IF((AQ_DIFF.LE.AT_DIFF_K.AND.AQ_DUPLICATE.NE.AQ_ATT.
     &  AND.LT.GE.PTINIL).OR.LT.EQ.NIT) THEN
        ENTET=LISTIN
        AQ_DUPLICATE=AQ_ATT!Avoid many saving/printing when DT<1 AS AQ_DIFF IS INT.
      ELSE
        ENTET=.FALSE.
      ENDIF
!ATEEQ- END EDIT FOR PRENTOUT WITH VARIABLE TIME STEP
C ATEEQ CHANGES END
C***********************************************************************
!
!     CONSTRAINS TELEMAC-2D OUTPUT IN THE LISTING
!
      IF (PRESENT(DOPRINT)) ENTET = ENTET .AND. DOPRINT
!
      IF(ENTET) CALL ENTETE(2,AT,LT)
!
!=======================================================================
!
! BACKUP OF UN, VN, HN, TN, AKN AND EPN (THEY ARE IN FN)
!
! THIS IS NOT DONE WHEN ITERATING FOR THE COUPLING WITH ESTEL-3D
```

Finally, the output was saved by editing the subroutine PRERES_ with the following changes:

```
!                    *************************
                     SUBROUTINE PRERES_TELEMAC2D
!                    *************************
C***********************************************************************
C ATEEQ CHANGES START
      INTEGER AQ_AT,AQ_ATT,AQ_DIFF,AT_DIFF_K,AQ_DUPLICATE1
      INTEGER AQ_DUPLICATE2
      SAVE AT_DIFF_K,AQ_DUPLICATE1
!ATEEQ- EDIT FOR PRENTOUT WITH VARIABLE TIME STEP
        AQ_ATT=(INT(AT)/INT(LISPRD))*INT(LISPRD)!ATEEQ
        AQ_AT=INT(AT)!ATEEQ
        AQ_DIFF=ABS(AQ_AT-AQ_ATT)!ATEEQ
        AT_DIFF_K=INT(DT)!Thresh hold coefficient set by ATEEQ.
        IF(LT.EQ.1)THEN!ATEEQ
          AQ_DUPLICATE1=AQ_DIFF!ATEEQ
        ENDIF!ATEEQ
        IF(AQ_DIFF.LE.AT_DIFF_K.AND.AQ_DUPLICATE1.NE.AQ_ATT.
     &  AND.LT.GE.PTINIG).LEO=.TRUE.!ATEEQ
!SAVE LAST AQ_DIFF
        IF(LEO)THEN!ATEEQ
C         AQ_DUPLICATE2=AQ_DUPLICATE1
          AQ_DUPLICATE1=AQ_ATT!ATEEQ Avoid many saving/printing when DT<1 AS AQ_DIFF IS INT
C         WRITE(LU,*)'AQ_AT',AQ_AT,'AQ_ATT',AQ_ATT,'AQ_DIFF',AQ_DIFF,
C     &  'AT_DIFF_K',AT_DIFF_K,'AQ_DUPLICATE2',AQ_DUPLICATE2,'LT',LT
        ENDIF!ATEEQ
!ATEEQ- END EDIT FOR PRENTOUT WITH VARIABLE TIME STEP
C ATEEQ CHANGES END
C***********************************************************************
C       IF(LT.EQ.LTT.AND.LT.GE.PTINIG).LEO=.TRUE.!ORIGINAL
!       FOR GRAPHICAL OUTPUTS
        IF(LEO)COMPLEO=COMPLEO+1
      ELSE
!       FVM
        GPRDTIME=LEOPRD*DTINI
        LPRDTIME=LISPRD*DTINI
```

E. New implementation sampling of maximum water level

To save maximum water level in all timesteps within output/sampling interval (2), we compared the water levels at each mesh node with its previous values and only kept the maximum values by editing subroutine PRERES_:

```
C*****************************************************************
C ATEEQ CHANGES START
C #if 0
C WATER LEVEL COMES HERE AFTER EACH TIME STEP
C SO APPLY CONDITION OF SAVING MAXIMUM WATER LEVEL HERE
      DO N = 1, NPOIN
        IF (LT.GT.0) THEN
          IF(H%R(N).GT.KK(N))THEN
            KK(N) =H%R(N)
          ENDIF
        ENDIF
      ENDDO
C #endif
C ATEEQ CHANGES END
C*****************************************************************
!-------------------------------------------------------------------------
!
! 1) PART WHICH MUST BE DONE EVEN IF THERE IS NO OUTPUT FOR THIS TIMESTEP
!    BUT ONLY AFTER FIRST TIMESTEP FOR GRAPHIC PRINTOUTS
!
!-------------------------------------------------------------------------
!
      IF(LT.GE.PTINIG) THEN
!
!=======================================================================
! COMPUTES THE MAXIMUM ELEVATION AND ASSOCIATED TIME
!=======================================================================
```

After each output/sampling interval (2), we reset the maximum water levels with the actual values calculated in the respective time step dt.

```
C*****************************************************************
C ATEEQ SAVING MAXIMUM WATER LEVEL- CHANGES STARTS
      IF((LEO.AND.SORLEO(23)).OR.(IMP.AND.SORIMP(23))) THEN
        DO N = 1, NPOIN
          IF (LT.GT.0) THEN
            PRIVE%ADR(1)%P%R(N) =KK(N)
          ENDIF
          IF (LT.GT.0) THEN
            KK(N)=H%R(N)!TO RESET FOR NEXT GRAPHIC PRINTOUT PERIOD
          ENDIF
        ENDDO
      ENDIF
C ATEEQ CHANGES END
C*****************************************************************
!=======================================================================
! CALCUL DE LA SURFACE LIBRE EXACTE
!=======================================================================
```

In subourtine NOMVAR_ we defined the name of maximum water level as H_{max}. More details about general programming can be referred to [1].

F. Morphological factor

Without using any morphological factor (MF), the computational cost to simulate Dijle Valley from 1990 to 2022 was approximately two weeks using 36x7 processors of the Flemish Supercomputers (VSC). To reduce the computational time, we tested different MFs [2] and compare their results with no MF. Using MF=24, our computational time was reduced from two weeks to just a single day at the cost of a slight reduction in modelling accuracy. Comparing bed level changes calculated using MF=24 with no MF, R^2 was approximately at 0.76 [7]. It was at 0.80 using MF=10, however, the computational cost was more than a week.

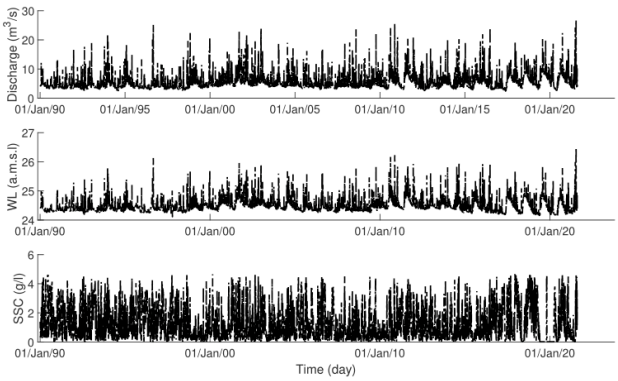

Figure 5. Model boundary conditions upstream and downstream of the study area (Figure 1).

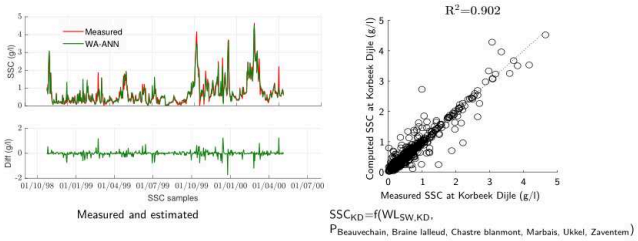

Figure 6. Suspended sediment load boundary conditions were generated using wavelet transform coupled with artificial neural networks [7]. The upstream SSC boundary conditions are a function of 64 days of previous rainfall in the catchment.

IV. RESULTS AND DISCUSSION

Using daily measured water levels at Korbeek Dijle Bridge measured by the Flanders Environment Agency (VMM), we calibrated our hydrodynamic model for the river channel. Using water level measurements collected by Research Institute Nature and Forest (INBO) in the Dijle Valley, we calibrated our hydrodynamic model for the floodplain. To represent different bedforms, we updated the subroutine CORSTR for setting different roughness ranges from 0.028 to 0.05 using Manning's roughness law. We found roughness equal to 0.05 best for the floodplain as it is a natural conserved area which is vegetated. While its value of 0.028 was best for the river channel. After setting the correct roughness, our model has R^2 at 0.74 (Figure 7), NSE at 0.72, RMSE at 9.9 cm, and MAE at 7.8 cm (Table I), compared to the measured data. The simulated water level difference with the measurements in the valleys stays less than 50 cm (Figure 8).

The calibrated TELEMAC-2D model was coupled with SISYPHE for morpho-dynamic calibrations where we updated several morpho-dynamic parameters. The calibrated hydro-morpho-dynamic model has R^2 at 0.70 while comparing its results with the daily measured water level at Korbeek Dijle (Figure 10). The NSE was at 0.67, RMSE at 9.5 cm, and MAE at 8.8 cm (Table I). By comparing our bed level measurements conducted by the Department of Geography, KU Leuven in 2017, we have R^2 at 0.58 (Figure 9), NSE at 0.12, RMSE at 39.8 cm, and MAE at 38.0 cm (Table I). The overall difference between simulated and

measured water levels in the valley stays less than 50 cm (Figure 10, and Figure 11).

A. Hydrodynamic calibration

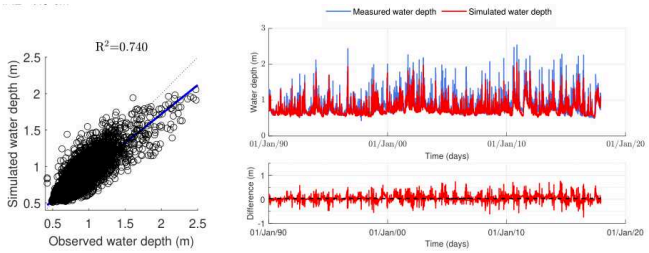

Figure 7. Hydrodynamic calibration at Korbeek Dijle

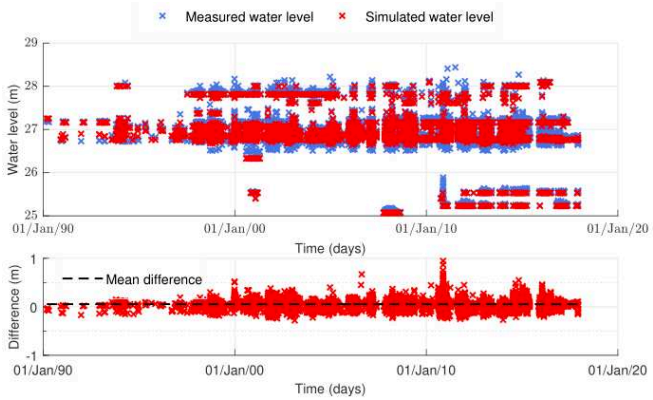

Figure 8. Hydrodynamic calibration for the water levels in the Dijle Valley

B. Hydro-morpho-dynamic calibration

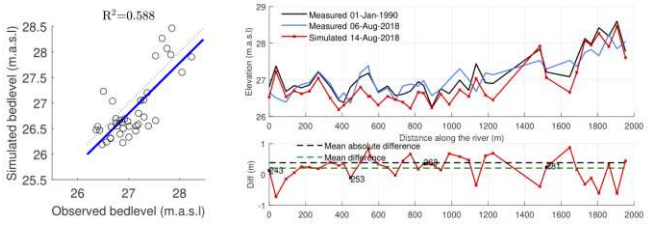

Figure 9. Morpho-dynamic calibration using bed level changes

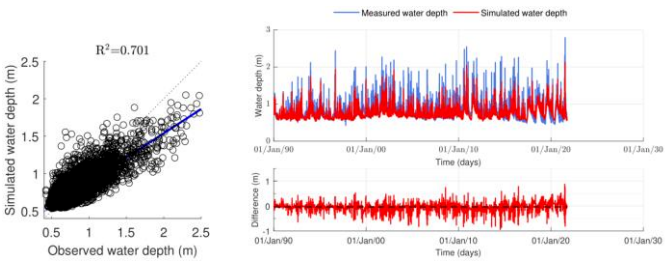

Figure 10. Hydro-morpho-dynamic calibration using water levels at Korbeek Dijle.

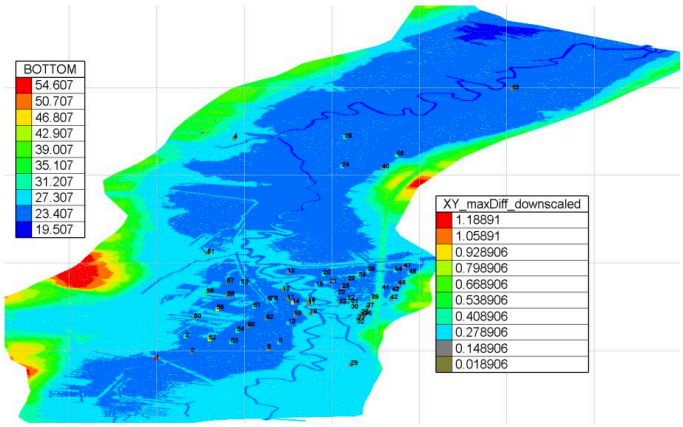

Figure 11. Maximum difference with water level measurements in the Dijle Valley remains less than 50 cm [units in figure are in m].

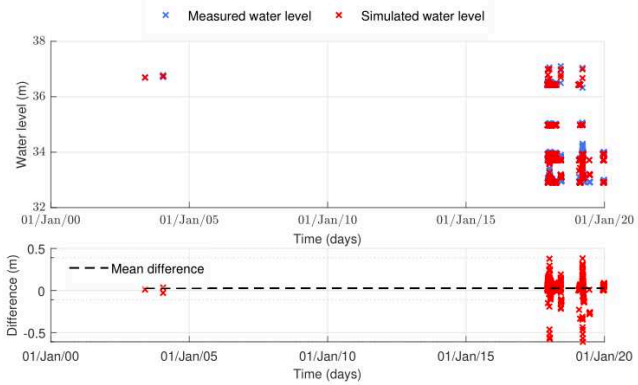

Figure 12. Comparison of water levels in the Dijle Valley in hydro-morpho-dynamic calibration.

Table I Overview of modelling performance in hydrodynamic and hydro-morpho-dynamic calibrations

Variable	R² [-]	NSE [-]	RMSE [cm]	MAE [cm]
Hydrodynamic calibration				
Water levels at Korbeek Dijle	0.74	0.72	9.9	7.8
Hydro-morphodynamic calibration				
Bed level changes	0.58	0.12	39.8	38.0
Water levels at Korbeek Dijle	0.70	0.67	9.5	8.8

C. Flooding maps

Using updated code (section III.E), we saved maximum water levels within a day (at 00:00:00) calculated in each time step (single values at each mesh node). Using the whole outputs (daily sampling from 1990-2022) of maximum water levels, we calculated their maximum values at each mesh node (Figure 13). The method not only saved many terabytes (TBs) of space but also saved post-processing computational costs.

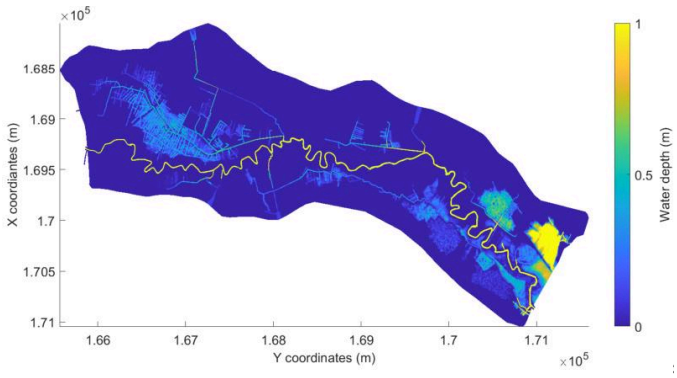

Figure 13. Map of flooding (using updated source code of TELEMAC-2D) that occurred in Dijle Valley on 17 July 2021 has a discharge of 30.7 m³/s. Although the actual discharge of the event was higher, it was not recorded due to the overtopping of water level measuring gauges installed at the Sint-Joris-Weert Bridge and Korbeek Dijle Bridge.

V. CONCLUSION

The TELEMAC-2D modelling environment is a very powerful open-source tool to simulate hydro-morpho-dynamic variables using variable time steps for regular sampling. Therefore, its hydrodynamic outputs can be used as inputs in other modelling tools at desired spatiotemporal resolutions without creating excessively large files. In addition, the computational time of long-term simulations can significantly be reduced using variable time steps, and morphological factors. The model also provides the opportunity to prepare flooding maps by saving maximum water levels within any temporal resolution. The updates in subroutines can be included in the next version which can save the huge computational cost of the machines using TELEMAC-2D all over the world.

ACKNOWLEDGEMENT

This research was partly financed by the Fonds Wetenschappelijk Onderzoek (S003017N - Future Floodplains - Ecosystem Services of Floodplains under socio-ecological changes; and grant no. 1167019N). The computational resources and services used in this work were provided by the VSC (Flemish Supercomputer Center), funded by the Research Foundation - Flanders (FWO) and the Flemish Government.

REFERENCES

[1] R. Ata, "*TELEMAC v7.2 user manual.*" 2007, Chatou, France: Open TELEMAC-MASCARET.

[2] S. Wurms and P.M. Schröder, "*Evaluation of strategies for the acceleration of morphodynamic simulations against the background of waterways maintenance,*" in *River flow 2012 : Proceedings of the international conference on fluvial hydraulics, San Jose, Costa Rica*, R. Murillo Muñoz, Editor. 2012, Taylor & Francis: London.

[3] G. Verstraeten, "*Ecosystems services of floodplains under socio-ecological changes FWO-SBO projects,*" 2016. Available from: https://www.futurefloodplains.be/.

[4] B. Notebaert, G. Verstraeten, G. Govers, and J. Poesen, "*Qualitative and quantitative applications of LiDAR imagery in fluvial geomorphology,*" Earth Surf. Process. Landf., 2009, vol 34(2), pp. 217-231.

[5] S. Ateeq-Ur-Rehman, J. Meylemans, W. Swinnen, N. Broothaerts, and G. Verstraeten, "*Numerical modelling of the effects of change in river channel morphology on flooding frequency in the Dijle valley, Belgium, using TELEMAC-2D modelling system,*" in *Online proceedings of the papers submitted to the 2020 TELEMAC-MASCARET User Conference*, W.A. Breugem, et al., Editors. 2020, International Marine & Dredging Consultants: Antwerp, Belgium. p. 40-45.

[6] A. Steegen, "*Sediment deposition in and export from small agricultural catchments,*" in *PhD thesis, Department of Earth and Environmental Sciences*. 2001, KU Leuven: Leuven.

[7] S. Ateeq-Ur-Rehman, N. Broothaerts, W. Swinnen, and G. Verstraeten, "*Numerical modelling of hydro-morphodynamic channel processes at decadal timescales using optimization methods: an application to the Dijle River, Belgium,*" in *EGU General Assembly 2021*. 2021, EGU: Vienna Austria. p. 1329.

1D numerical modelling of the longitudinal profile evolution of riverbeds and reservoirs: application of COURLIS bedload on a real case

Nicolas Claude[1], Lucie Mesquita[1], Florent Taccone[2], Magali Jodeau[2], Minh-Hoang Le[3], Matthieu Secher[1], Lauréat Tchicou Midou[2], Eric Valette[1]

nicolas-n.claude@edf.fr
[1] EDF CIH La Motte Servolex France
[2] EDF R&D Chatou France
[3]Laboratoire d'Hydraulique Saint-Venant Chatou France

Abstract – **The aim of this work is to reproduce the morphological evolution of a reach of an alpine river: the Buëch river. For that, a 1D modelling with the COURLIS bedload module is used. It allows the representation of bedload sediment transport in the riverbed. However, some limitations of the code were initially highlighted, and it was necessary to implement new features to have results corresponding to the bathymetric measurements.**

These developments, including among others a new transport formula, the possibility to vary longitudinally the size of the sediments, the possibility to represent dredging, are tested and validated and will be integrated in V8P4.

Results obtained with the latest implementations of COURLIS show that the code can satisfactorily reproduce the morphological evolutions observed in the field along the longitudinal profile. The computational times are also acceptable with 3 hours computational time to model a 5-years period. In addition, COURLIS results are close to those obtained with CAVALCADE, a model based on similar assumptions. These preliminary, and encouraging, results show that COURLIS may be used for future operational studies aiming at representing the longitudinal profile evolution of riverbeds and reservoirs on multiannual time scales.

Keywords: COURLIS, longitudinal profile, bed evolution, bedload.

I. INTRODUCTION

Modelling the morphological evolution of riverbeds and reservoirs is invaluable to better identify the control factors of hydro-systems, to predict evolutionary trends of riverbeds and to help define and optimize river management projects.

To meet this need, major developments have been made to improve the one-dimensional sediment transport module COURLIS of the TELEMAC-MASCARET system. For example, recent implementations have been carried out:

- to have a new scheme for energy slope calculation;
- to add new bedload formulas (Lefort formula);
- to simplify sediment supply management on the upstream boundary condition;
- to consider morphological widths in bedload transport rates calculations;
- to allow for a longitudinal evolution of the granulometry;
- to reproduce dredging during simulations.

The aim of this work is to develop a module that can faithfully reproduce the dynamics of suspended load and/or bedload as well as the morphological evolution of riverbeds and reservoirs. The objective is also to build a COURLIS code able to model, within reasonable computational times, bed evolutions at time scales ranging from the period of a flood to a decade.

A new version of COURLIS integrating the latest developments mentioned above has been tested on a reach of the Buëch river in the French Alps composed in its upstream part by a straight and embanked channel and in its downstream part by a reservoir. The objective of this application of the bedload model is to assess and validate its ability to reproduce correctly the spatial and temporal 5-year evolutions of a longitudinal profile observed on a real/operational case. The simulation results are also compared with the 1D hydro-sedimentary code CAVALCADE, which is developed and owned by ARTELIA. CAVALCADE solves the simplified shallow water equations in steady regime coupled to a bedload transport formula and a volume balance and has been used to study the longitudinal profile evolution of numerous (mostly) gravel-bed rivers [1; 2].

The article is organised as follows: the latest developments in the code are presented first, the study site and available data are then described, the parametrization of the COURLIS numerical model is detailed later, and finally, the model results are presented and compared with the measurements and the CAVALCADE simulations.

II. LATEST DEVELOPMENTS

A. New scheme for energy slope calculation

MASCARET supports steady and unsteady flow computations thanks to the three computational kernels: SARAP the steady flow kernel for subcritical, supercritical or mixed flow regimes (finite differences), REZO the unsteady subcritical flow kernel (finite differences),

MASCARET the unsteady trans-critical flow kernel (finite volumes). These three kernels can be used with COURLIS and chosen according to the specificity of the study cases. Different ways to estimate the energy slope can be used in steady simulations. For the steady kernel (SARAP), the equation of the water line discretized between two successive sections 1 (upstream section) and 2 (downstream section) with no singularities originally implemented in MASCARET is given in Equation 1 (below [3]):

$$\frac{Z_2-Z_1}{\Delta x}+\frac{2}{\frac{1}{J_1}+\frac{1}{J_2}}=0, \quad (1)$$

with Z_i the free surface elevation on section i, Δx the distance between two sections, and J_i the energy slope at section i.

A new option is now proposed which can in certain configurations (Soni and Newton test-cases mainly) allow a faster mesh convergence (converged results with coarser meshes). The upstream slope J_1 is no longer taken into account to approximate the energy slope between two successive sections as presented in Equation 2 below:

$$\frac{Z_2-Z_1}{\Delta x}+J_2=0. \quad (2)$$

The option is used through the `<decentrement>true<\decentrement>` command in the MASCARET xcas file. Note that the morphodynamic results obtained with the new option for the Soni and Newton test-cases do not show significant differences with those modelled with the first method.

B. Upstream solid discharge through an equilibrium slope

To meet operational requests, a new option is also added to COURLIS to use an equilibrium slope instead of explicit bedload laws at upstream boundary conditions. The upstream solid discharge is then calculated from the chosen transport law considering a user-defined equilibrium slope and hydraulic variables calculated on the upstream boundary condition. This option is activated with the keyword `UPSTREAM SEDIMENT CONCENTRATION FROM EQUILIBRIUM SLOPE` set to `YES`. The equilibrium slope value is set in the steering file with the keyword `UPSTREAM EQUILIBRIUM SLOPE`.

C. Lefort formula

As "classical" bed load formulas are more adapted to 2D models [4], it has been decided to implement in COURLIS the Lefort formula [5] which is more dedicated to 1D models due to its formalism. The Lefort formula, which is frequently used on gravel bed rivers in French engineering studies, requires the introduction of the adimensional diameter d_m^* which writes:

$$d_m^*=d_m\left(\frac{gR}{\nu^2}\right)^{1/3}, \quad (3)$$

with d_m the actual particles average diameter, g the gravity constant, $R=\frac{\rho_s}{\rho}-1$ the relative density, considering ρ_s is the sediment density and ρ the water density and ν is the water kinematic viscosity.

The transition discharge Q_0 which separates partial bedload from general bedload is chosen such as:

$$\frac{Q_0}{B\sqrt{g(Rd_m)^3}}=C(d_m^*)\left(\frac{d_m}{B}\right)^{1/3}\left(\frac{K}{K_p}\right)^{-1/2}J^{-m_0}, \quad (4)$$

with $C(d_m^*)$ a function to describe the critical Shields stress variation with the mean grain diameter:

$$C(d_m^*)=0.0444\left(1+\frac{15}{1+d_m^*}-1.5exp\left(-\frac{d_m^*}{75}\right)\right), \quad (5)$$

B is the bed width, K the Strickler coefficient, K_p the skin friction coefficient and m_0 is an exponent corresponding to an increase of the shear stress with slope which writes:

$$m_0=1.6+0.06log_{10}(J). \quad (6)$$

The solid discharge is then estimated as:

$$Q_s=1.7QJ^m\frac{R+1}{R^{1.65}}\left[0.5\left(\frac{d_{84}}{d_{50}}+\frac{d_{50}}{d_{16}}\right)\right]^{0.2}C_d\frac{F(Q)}{(R+1)(1-n)}, \quad (7)$$

with n the bed porosity, Q the water discharge, $m=1.8+0.08log_{10}(J)$, d_{84}, d_{50}, d_{16} are respectively the 84th, 50th and 16th percentile of the grain size distribution and C_d is a dune correction coefficient which models the increase in friction due to the development and the transport of dunes. It is set for grain diameters above 0.6 mm. According to [5], it has little influence on the results.

$$C_d=\begin{cases}1-1.4\exp\left(-0.9\left(\frac{K}{K_p}\right)^2\sqrt{\left(\frac{Q}{Q_0}\right)}\right) & \text{if } d_m^*<14 \text{ and } \frac{K}{K_p}<0.63\\ 1 & \text{otherwise}\end{cases}. \quad (8)$$

The discharge function F describes the partial bedload of fine particles and general transport, first bedload and then bedload and suspended load, via the following expression:

$$F(Q)=\begin{cases}0.06C_M\frac{Q}{Q_0} & \text{if } Q<Q_0,\\ \left[6.1\left(1-0.938\left(\frac{Q_0}{Q}\right)^{0.284}\right)^{1.66}\right]^{m_z}\end{cases}, \quad (9)$$

with m_z the add-on exponent for solid discharge during the transition between bedload and suspension:

$$m_z=\begin{cases}1+\frac{0.38}{d_m^{*0.45}}\left(\frac{Q}{B\sqrt{gd_m^3}}\right)^{0.192} & \text{if } Q>3.4Q_0,\\ 1 & \text{otherwise}\end{cases} \quad (10)$$

and C_M reduction factor of transport for partial bedload:

$$C_M = \begin{cases} \frac{1}{200}\left(\frac{Q}{B\sqrt{gJd_m^3}} + 2.5\right) & \text{if} \quad \frac{Q}{B\sqrt{gJd_m^3}} < 200, \\ 1 \quad \text{otherwise} \end{cases} \tag{11}$$

It is important to note that, when the ratio $\frac{K}{K_p}$ is unknown, an alternative is suggested by Lefort and can be activated in COURLIS with the boolean `ROUGHNESS RATIO WITH QSTAR FOR LEFORT`. When set to `TRUE`, the friction coefficient ratio is given by:

$$\frac{K}{K_p} = \begin{cases} 0.75\left(\frac{Q}{200B\sqrt{gJd_m^3}}\right)^{0.23} & \text{if} \quad \frac{Q}{B\sqrt{gJd_m^3}} < 200, \\ 0.75 \quad \text{otherwise} \end{cases} \tag{12}$$

D. Morphological width

It is possible to modify the morphological width B introduced in the Lefort formula by setting the keyword `OPTION OF VARIABLE MORPHO WIDTH` to `TRUE` along with the keyword `FILE FOR GRANULOMETRY AND MORPHO`. The latter should include the width information considered for each profile, and an example is provided in Figure 1. Although originally proposed by Lefort, the option of morphological width is available in COURLIS for all the bedload transport formulas.

```
#Granulometry & Morpho file
#Keyword    BiefName    ProfileName Abscissae   Morpho_width    d50
Profil  Bief_1  1   -3991.99    35.0    0.0320
Profil  Bief_1  2   -3976.99    35.0    0.0320
Profil  Bief_1  3   -3961.99    35.0    0.0320
Profil  Bief_1  4   -3946.99    35.0    0.0320
Profil  Bief_1  5   -3931.99    35.0    0.0320
Profil  Bief_1  6   -3916.99    35.0    0.0320
Profil  Bief_1  7   -3901.98    35.0    0.0320
Profil  Bief_1  8   -3886.98    35.0    0.0320
Profil  Bief_1  9   -3871.98    35.0    0.0320
Profil  Bief_1  10  -3856.98    35.0    0.0320
```

Figure 1. Granulometry and morpho file format.

The morphological width gives the effective width of the erodible area in each profile. In particular, this allows to calculate the solid discharge more precisely in rivers where active channels are less wide than the minor bed.

Note that the morphological width is usually a variable which can be adjusted during calibration procedures.

E. Longitudinal distribution of the grain size

The grain size distribution is considered constant on a cross section. However, it is possible to give each profile a different average sediment size. This option makes possible, for example, to represent numerically the sorting in granulometry upon arrival in a reservoir, and thus to more accurately describe the sediment transport that occurs there. Nevertheless, it is worth noting that the longitudinal distribution of grain size will remain constant during the computation (i.e., sorting processes are not solved).

This option can be activated through the keyword `OPTION FOR VARIABLE GRANULOMETRY = TRUE`, along with the keyword `FILE FOR GRANULOMETRY AND MORPHO`. The file format is shown in Figure 1.

Note that the average sediment grain size on each section is usually defined from field measurements. A calibration of this parameter can be eventually performed where data are missing or uncertain.

F. Dredging

During the calculations, in particular on long time series, it may be necessary to represent the dredgings which were carried out to be able to reproduce the morphological evolutions.

One or more dredgings can be performed using the keyword `NUMBER OF DREDGING`. Then the location of the dredgings should be set with the combination of keywords `ABSCISSAE OF THE BEGINNING OF THE DREDGING` and `ABSCISSAE OF THE END OF THE DREDGING`, giving one value for each dredging. Then, for each dredging, the depth must be set with the keyword `DREDGING DEPTH`. The time, in the simulation, during which dredging is desired must be filled in with the keyword `DREDGING TIME`, giving a value for each dredging. Note that a dredging can be carried out on one or several timesteps as a function of its duration.

III. Study Site and Field Measurements

A well monitored complex site is selected to test the COURLIS bedload module and to show the relevance of the latest developments on real applications.

A. Study site

The study site is located in the southern French Alps, on a 4 km long reach of the Buëch river starting at the Serres bridge and finishing at the Saint Sauveur Dam (Figure 2). The upstream part of the reach corresponds to a straight and embanked channel of approximately 60 m wide with an alternate bar pattern. The riverbed slope varies between 0.004 and 0.006 m/m. The downstream part of the reach is composed of a reservoir. There, the bed width increases significantly to reach between 150 and 250 m. The upstream end of the reservoir has a braided morphology while further downstream the bed shows a sinuous single-channel layout, constrained by lateral bars located near the banks in areas of low bed shear stress. The slope of the bed in the reservoir varies according to its sedimentation level.

Figure 2. Presentation of the study site. The black lines indicate the cross-section locations of the bathymetric surveys. The purple polygon corresponds to the dredged area at the upstream end of the reservoir.

Several small tributaries flow into the Buëch between the Serres bridge and the dam. In terms of water supply, only the Blème river is a significant tributary.

The hydrological regime is pluvio-nival. The mean flow discharge is 16.3 m^3/s. The discharge values associated with 2-year, 5-year and 10-year floods are, respectively, 210, 320 and 390 m^3/s.

Buëch sediments are of two types:

- gravels with a D_m varying between 3 to 6.4 cm and a D_{50} of around 3.4 cm [6];
- fine sediments with a D_{50} of about 6 µm.

The annual gravel supply is estimated between 42,000 and 60,000 m^3/year [6]. The discharge for initial motion of gravels is roughly evaluated at 30 m^3/s. The annual fine sediment volume transported in suspension is assessed at 400,000 t/year.

The upstream end of the reservoir was dredged between 29th August and 4th November 2016 (see location of these works on Figure 2). Approximately 44,000 m^3 of sediments were extracted from the riverbed.

B. Field measurements

The hourly flow discharge of the Buëch ($Q_{Buëch}$) river is directly measured at the Serres bridge (Figure 3). The discharge of the Blème tributary ($Q_{Blème}$) is considered equal to $0.0644 Q_{Buëch}$ (based on the ratio of the two catchment areas).

The elevation of the free surface in the reservoir is measured directly at the dam only during normal operations as well as during the beginning and the end of floods when the gates are opened and closed (Figure 3). During floods, when the gates are totally open and not activated, the elevation of the free surface cannot be measured, so it is calculated from the theoretical valve capacity curves.

Four bathymetric surveys were performed in February 2015, December 2016, June 2019 and July 2020 along 36 cross-sections to observe the morphological evolution of the riverbed (Figure 2 and Figure 3).

IV. MODEL DESCRIPTION

A. Physical and numerical parameters

In both models (COURLIS and CAVALCADE), the Lefort transport law is used with calibrated morphological bed widths. A non-erodible substratum is found between 2,100 and 2,300 m upstream the dam and is modelled by a sediment layer thickness between 5 and 25 cm. Everywhere else, the sediment layer is supposed to be 3 m thick.

The mean diameter of sediment is set at 3.2 cm with a grain size gradient between the upstream end of the reservoir (at the longitudinal abscissae 1,450 m) and the dam from 3.2 to 2 cm respectively.

The dredging carried out in 2016 is numerically represented as a uniform extraction of sediment between 1,450 and 1,750 m upstream the dam.

The steady kernel SARAP of MASCARET is coupled with the COURLIS module with a ratio 1:1. The time step is set at $\Delta t = 10$ s and the Strickler bottom friction coefficient is uniformly chosen as $K = 30$ $m^{1/3}/s$. This value of bottom friction is defined arbitrary and not calibrated due to the lack of recent water surface elevation measurements.

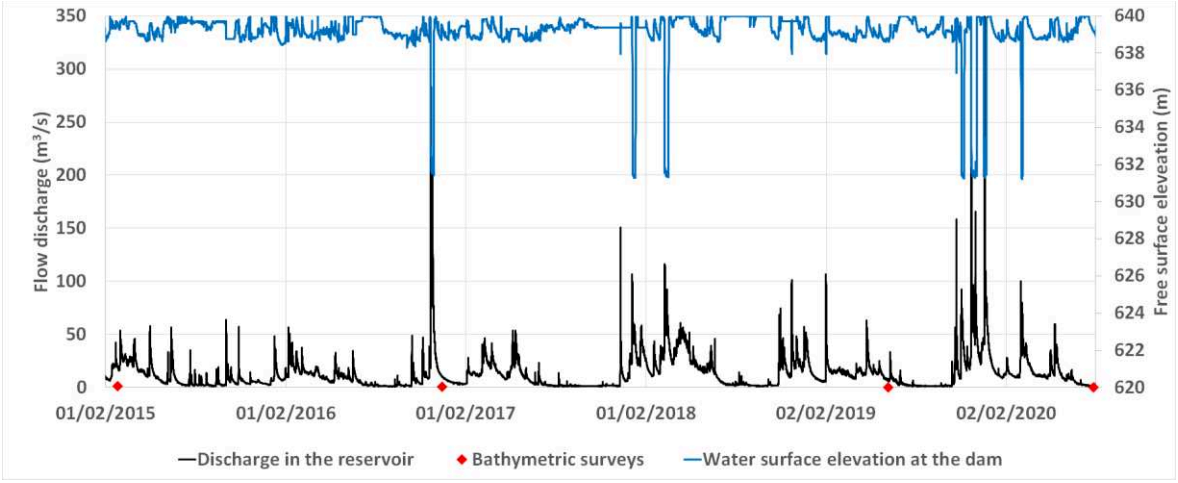

Figure 3. Flow discharge entering the reservoir and water surface elevation at the dam measured between 2015 and 2020. The bathymetric surveys are indicated in red.

B. Boundary conditions

At the Buëch inlet, the discharge is set from the Buëch hydrology measured between 2015 and 2020. Due to numerical difficulties to model low flows in large rectangular sections (see part IV. C), the physical time is cut off when the flow discharge drops below 20 m^3/s. This choice is motivated by an estimated threshold for initial movement of sediment of 30 m^3/s. The confluence with the Blème river at the abscissae 2,445 m is modelled through a liquid-only inflow.

The Buëch solid discharge is set by considering an equilibrium slope of 4.7‰ calibrated in order to reproduce the bed stability observed in the upstream part of the reach during the last years. Blème sediment supply is neglected.

At the dam, free surface levels are adapted from hourly water level measurements and calculations.

C. Initial conditions

The initial bed river is based on 2015 bathymetric measurements. Each cross section has been simplified to a rectangular cross section with a bed width calibrated to reproduce the main trends of erosion and deposition observed between 2015 and 2020. The 3 dam valves are modelled by an additional 36 m x 16 m cross section at the longitudinal abscissae 0 m. The longitudinal space step is chosen iteratively to smooth the Froude number at $\Delta x =$ 15 m which allows to limit the instabilities observed for rougher meshes. Note that the effect of mesh resolution was not investigated during this study.

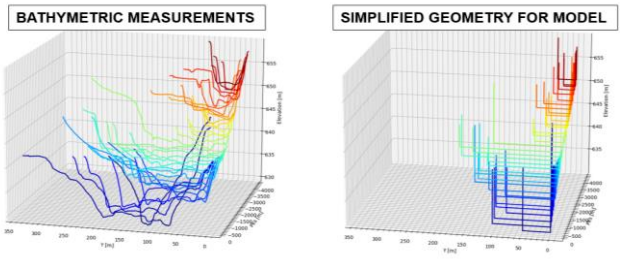

Figure 4. Simplification of riverbed in model.

V. RESULTS

The study starts with the model calibration step. As mentioned before, the first calibration procedure consists in adjusting the upstream sediment supply in order to reproduce the bed stability observed in the upstream part of the reach during the last years. Then, the rectangular cross-section width, the morphological width and the riverbed grain size are successively adapted profile by profile from field measurements (to avoid physical non-consistency) to model correctly the bed evolutions observed between 2015 and 2020. The final parameterization is identical in COURLIS and CAVALCADE models. Complementary simulations named “no options” in the following parts are also performed without the sediment size longitudinal variation, without the dredging, and with a morphological width in the Lefort formula equal to the rectangular cross-section. This allows to observe the influence of these functionalities.

Figure 5 presents the final longitudinal profiles observed and simulated in 2020. Bed evolutions measured and modelled from the initial bed geometry at the time of each bathymetries are shown in Figures 6, 7 and 8. Results demonstrate that the COURLIS calibrated model (with all the new options) can correctly reproduce the main bed evolutions observed between 2015 and 2020 which are characterised by a stability of the upstream part and a persistent erosion of the upstream end of the reservoir after the dredging of 2016. This observation is particularly true for the surveys of 2016 and 2020 for which the Root Mean Square Error (RMSE) reaches, respectively 17.1 cm and 19.3 cm. For these cases, the main difference with the measurements concerns an underestimation of the erosion in the dredging area. For the survey of 2019, the RMSE is higher (63.4 cm). However, this value is mainly due to the non-representation by the model of a large deposition of fine sediments in the reservoir (processes not considered in this current model application). Upstream this bed aggradation, the simulation results are good with centimetric errors on

bed evolutions. Furthermore, the computational times are acceptable with 3 hours computational time to model the 5-years period.

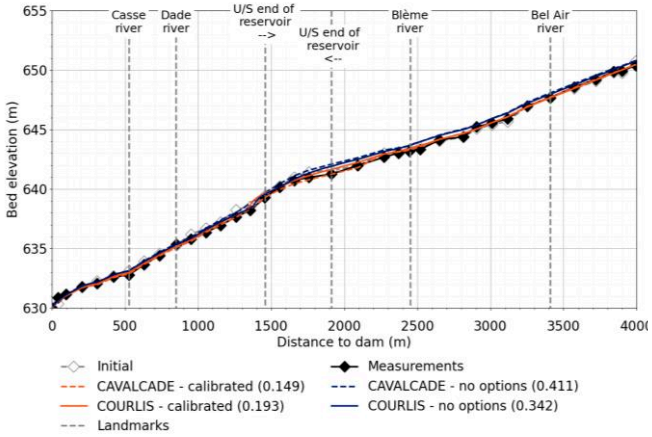

Figure 5. Longitudinal profile of riverbed in July 2020 - comparison between measurements, COURLIS results and CAVALCADE results under the same assumptions. RMSE (m) is computed between each model result and the measurements.

One can see a good agreement between COURLIS and CAVALCADE results (Figure 6, Figure 7 and Figure 8). In particular, the erosion and deposition patterns in the upstream part of the model are very similar, as are the erosions in the downstream part of the reservoir, near the dam. On the other hand, in the upstream end of the reservoir, some differences are observed with erosions clearly more marked for the CAVALCADE results, whereas the COURLIS results show some areas of deposit. Tests will be performed to better understand the origin of these differences. Despite this, the two codes stay relatively close to the measurements with maximum differences of about 20 cm.

Additional simulations are performed to quantify the effect of the grain size gradient, the dredging in 2016 and the use of morphological widths in Lefort formula with both COURLIS and CAVALCADE software. Results without aforementioned options are presented on Figure 5-8 (blue curves). As expected, the riverbed in the upstream end of the reservoir in December 2016 (Figure 6) is higher in simulation than what was measured on the field mainly because of the absence of the dredging carried out the same year. Compared with 2019 and 2020 measurements (Figures 7 and 8), the simulated riverbed shows similar patterns but remains higher all alongside the river because of this additional volume of sediment. Smaller bed widths in Lefort transport formula, using morphological bed widths, also permitted the limitation of the deposition all alongside the Buëch river. Finally, minor refinements of the solutions in the reservoir are done thanks to the implementation of a grain size gradient to approach the particle size distribution actually observed in reservoirs.

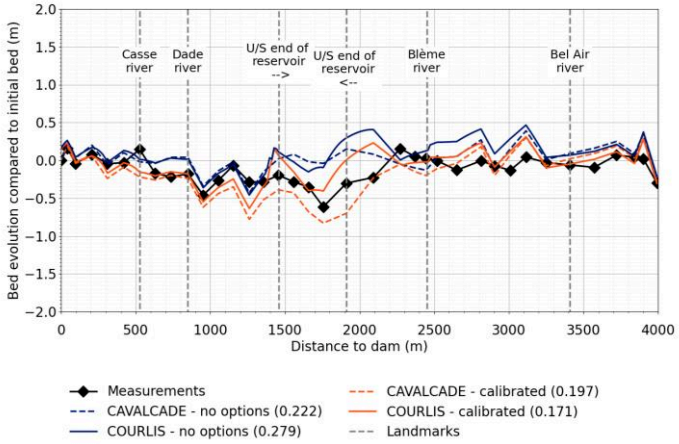

Figure 6. Longitudinal profile of bed evolution between February 2015 and December 2016 - comparison between measurements, COURLIS results and CAVALCADE results under the same assumptions. RMSE (m) is computed between each model result and the measurements.

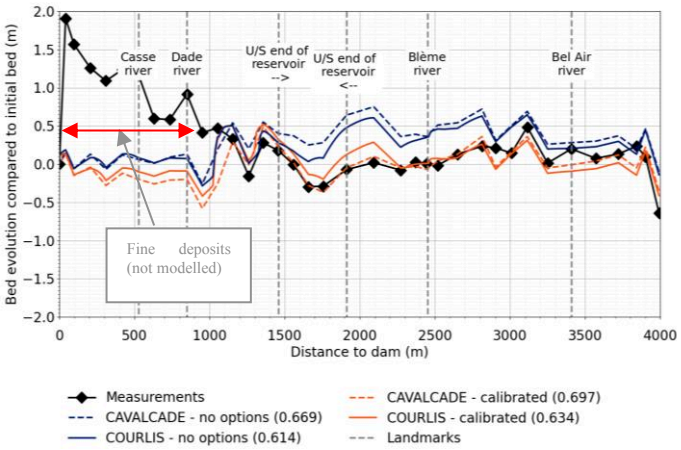

Figure 7. Longitudinal profile of bed evolution between February 2015 and June 2019 - comparison between measurements, COURLIS results and CAVALCADE results under the same assumptions. RMSE (m) is computed between each model result and the measurements.

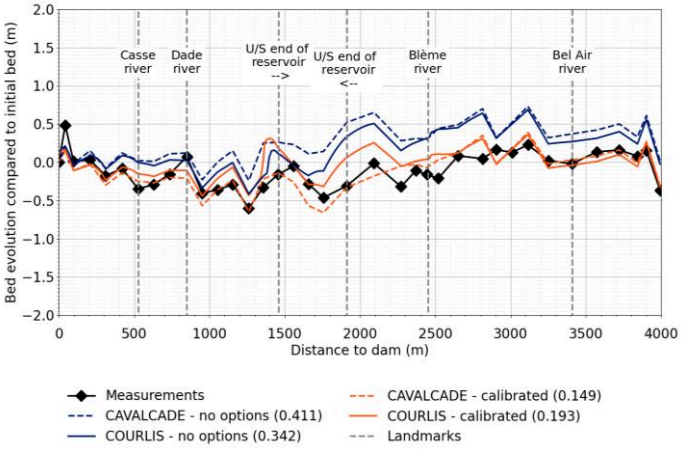

Figure 8. Longitudinal profile of bed evolution between February 2015 and July 2020 - comparison between measurements, COURLIS results and

CAVALCADE results under the same assumptions. RMSE (m) is computed between each model result and the measurements.

VI. CONCLUSION

The aim of this work is to reproduce with COURLIS bedload module the 5-year longitudinal profile evolution of a 4-km long reach of the Buëch river (Southern French Alps). The study site, which is a gravel bed river, includes a reservoir. The model is also compared with CAVALCADE, a similar calculation tool that can predict changes in river morphology due to bedload transport.

Several developments are made to be able to represent more accurately some processes. Indeed, a modification of the numerical resolution of the water level calculation in the kernel SARAP was carried out, as well as a new treatment of the condition at the sedimentary upstream boundary. Moreover, a new bedload transport formula is implemented, with the possibility to introduce the notion of spatialized morphological width along the river reach. The possibility to modify the size of the sediment according to its location along the river has also been added. Finally, a new option has been implemented to represent dredging during simulations. All these new functionalities, which will be integrated in the next version of TELEMAC-MASCARET (V8P4), are used to represent the morphological evolution of the study site.

Simulation results show that the COURLIS and CAVALCADE codes give similar results. This comparison provides a cross-validation of the algorithms implemented in both codes. The addition of new features in the code have greatly improved the results with simulation results that are closer to the observations. COURLIS, and its bedload module, allows to represent, with acceptable computational times, the main trends of the river and reservoir morphodynamics over a long period of time. These preliminary, and encouraging, results show that COURLIS may be used for future operational studies aiming at representing the longitudinal profile evolution of riverbeds and reservoirs on multiannual time scales.

Many features can still be added to the code to take into account other physical processes that can be relevant in some cases. For example, implementing a module of non-uniform grain size to the bedload part of the code would allow to better reproduce bed evolutions in some rivers. To model the behaviour of the river during extreme floods, it would also be interesting to take into account the possibility of having overflows on a major bed while keeping the possibility of having transport by bedload in the minor bed. The possibility of extending the application of COURLIS to a coupling with a multi-bief MASCARET model could also allow a wider spectrum of application for the code. Finally, modelling the transport of bedload and suspended load at the same time in the calculations would offer interesting possibilities to better reproduce the evolution of the bed in some real cases as the one presented in this study for which fine sediment deposition happens in the reservoir.

ACKNOWLEDGEMENT

The authors want to thank ARTELIA for providing the CAVALCADE code and the colleagues of EDF Hydro Med for the transfer of data and their support.

REFERENCES

[1] ARTELIA. Logiciel CAVALCADE Version 5.2.P. Notice technique - v5.3.a (provisoire), 2018.

[2] Andre, A. Loaec, J.-M., Loire, R., Valette, E. Retour d'expérience et modélisations hydrosédimetaires 1D du piège à graviers du Buëch, 2022. Colloque transport sédimentaire : rivières et barrages et réservoirs.

[3] TELEMAC-MASCARET. MASCARET Theory Guide version V8P3, 5 July 2022.

[4] Recking, A., Piton, G., Vazquez-Tarrio, D., Parker, G. Quantifying the morphological print of bedload transport, 2016. Earth Surface Processes and Landforms.

[5] Lefort, P. Morphodynamique fluviale - Approches théorique et expérimentale. Ponts et Chaussées (Presses), 2018. ISBN 978-2-85978-516-1.

[6] Brousse, G. Efficacité des travaux de restauration et résilience des rivières torrentielles altérées. 2020. PhD Thesis of Université de Paris Diderot. pp.334.

Evolution of river cross-sections due to bedload transport: a new model implemented in the 1D sediment module COURLIS

Minh-Hoang Le[1], Lauréat Tchicou Midou[2], Florent Taccone[2], Magali Jodeau[2,1], Nicolas Claude[3], Lucie Mesquita[3], Matthieu Secher[3], Eric Valette[3]

minh-hoang.le@enpc.fr
[1] LHSV - ENPC Chatou France
[2] LNHE - EDF R&D Chatou France
[3] EDF CIH La Motte Servolex France

Abstract – **COURLIS is the 1D sediment transport module of the TELEMAC-MASCARET open-source system. Evolution of riverbeds due to bedload transport is classically modelled by coupling the Shallow-Water equations for hydrodynamic processes (solved in the MASCARET module) and the Exner equation for bedload mechanisms. In such a 1D model, this later equation of sediment mass conservation only describes the time-evolution of bed elevation, precisely the volume of sediments eroded or deposited on riverbeds. Consequently, a bottom level update method is needed to determine how the river cross-section geometries are modified during erosion and deposition processes. A new simple method has been implemented in COURLIS which allows from a simplification of bed geometries to trapezoid profiles, a direct analytic computation of hydraulic variables along vertical discretization on each cross-section. We first introduce the present method for the evolution of cross-sections, the associated vertical discretization functions and the corresponding keywords in the steering file. Next, several test cases on simplified geometries and a real application for the case of the Saint-Sauveur dam on the Buëch River (Southern Alps, France) are provided.**

Keywords: COURLIS, bed evolution, bedload, transverse profile.

I. INTRODUCTION

Modelling sediment transport in rivers is crucial to deal with both environmental and safety issues. Nowadays, although several 2D and 3D CFD codes including sedimentary modules are available for numerical studies, the 1D models are still appropriate for long-time simulations due to their high stability behaviour and low computational cost.

COURLIS has been developed for more than 10 years and has recently been integrated into the open-source TELEMAC-MASCARET system. In particular, the bedload module has received important developments in the last years by EDF CIH, see e.g. [1], which have largely improved the use of COURIS for real applications. In this paper, we present a new development on COURLIS bedload, as part of a recent collaboration between EDF CIH, EDF R&D and LHSV, to predict the time-evolutions of river cross-sections.

The paper is organised as follows. Governing equations and numerical solvers are briefly recalled in section 2. Next, we discuss the planimetry problem associated with these solvers and we detail the proposed solution in section 3. Numerical validation and a real application of the model on a 4-km long reach of the Buëch River is presented in section 5. Conclusion and several further works are also presented.

II. GOVERNING EQUATIONS AND SOLVERS

Let us briefly introduce the main notations and recall the governing equations of the 1D model. Let us consider a river following hydraulic axis x and delimited by the left-bank y_L and the right-bank y_R. The geometry of a river at longitudinal position x is represented by the bottom height function, $b(x,y)$, which describes the riverbed elevation along the river cross-section. We also define

$$Z_b(x) = min(b(x,y)) \quad \text{for} \quad y_L \leq y \leq y_R,$$

i.e. the lowest point of the cross-section. See Fig. 1.

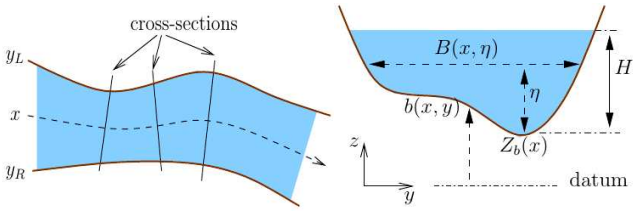

Figure 1: Sketch of river geometry: plan view (left), cross-section (right).

Evolution of the hydraulic state and the riverbed due to bedload transport can be modelled by coupling the section-averaged Shallow-Water equations (1)–(2) and the Exner equation (3) in order to solve the unknown hydro-sedimentary state (A, Q, A_b) whose rigorous definition will be given in the sequel. Omitting lateral inflow, these equations write:

$$(1) \quad \frac{\partial A}{\partial t} + \frac{\partial Q}{\partial x} = 0,$$

$$(2) \quad \frac{\partial Q}{\partial t} + \frac{\partial}{\partial x}\left(\frac{Q^2}{A}\right) + gA\frac{\partial Z_s}{\partial x} = -gAJ,$$

$$(3) \quad \frac{\partial A_b}{\partial t} + \frac{\partial Q_b}{\partial x} = 0,$$

where the wetted area also called hydraulic section, $A(t,x)$, and the flow discharge, $Q(t,x)$, corresponding to the water height $H(t,x)$ are defined by

$$(4) \qquad A(x,H) = \int_0^H B(x,\eta)d\eta\,, \quad Q = UA,$$

in which $B(x,\eta)$ is the width of the cross-section at height η from the bed Z_b, U the section-averaged flow velocity and g the gravity acceleration. We have denoted, for convenience,

$$(5) \qquad Z_s = Z_b + H$$

the free surface water level.

The friction source term, J, is commonly estimated by empirical laws, *e.g.* the Manning-Strickler formula:

$$(6) \qquad J = \frac{U^2}{{K_s}^2 {R_h}^{4/3}}, \quad R_h = \frac{A}{P},$$

in which K_s the Strickler friction coefficient, R_h the hydraulic radius and $P(x,H)$ the wetted perimeter.

Finally, mass conservation equation (3) for sediments describes the evolution of the riverbed during bedload processes, with

$$(7) \qquad A_b = \int_{y_L}^{y_R} b\,dy, \quad Q_s = \underline{q_s}|y_R - y_L|$$

the available volume and the bedload discharge of sediments on the cross-section respectively. The section-averaged sediment flux $\underline{q_s}$ depending on the bed shear stress and is commonly estimated by empirical laws, *e.g.* Meyer-Peter & Muller (1948), Engelund & Hansen (1967), Recking (2011), Lefort (2015) which are currently available in COURLIS.

In the TELEMAC-MASCARET system, a sequential (weak) coupling algorithm is used to solve the system (1)–(3). Providing the state $(A,Q,A_b)^n$ at time t^n, the MASCARET module solves $(A,Q)^{n+1}$ at time t^{n+1} by equations (1)–(2). These updated hydrodynamic states are next used by the COURLIS module to estimate the bedload discharge Q_s and then solves equation (3) to obtain ${A_b}^{n+1}$.

MASCARET provides 3 numerical solvers, also called *kernel* (see [2]):

- **Sarap** considers permanent flows and solves the simplified equations:
  $$(8) \qquad Q = cst, \quad \frac{d}{dx}\left(\frac{U^2}{2g} + Z_s\right) = J;$$
- **Rezo** considers fluvial flows and solves (1)–(2) by a finite difference method;

Transcritic relaxes the fluvial condition by using a finite volume method to solve (1)–(2) under conservative form; hence, it is able to capture discontinuous solutions such as hydraulic jumps. Recall that introducing the section-averaged hydrostatic pressure P_h:

$$(9) \qquad P_h(x,H) = g\int_0^H S(x,\eta)\,d\eta$$

with $S(x,\eta) = \int_0^\eta B(x,z)\,dz$, *i.e.* $A \equiv S(x,H)$.

COURLIS uses a finite volume scheme when solving the Exner equation (see [3]).

III. RIVERBED EVOLUTION AND PLANIMETRY PROBLEM

It's worth remembering that the Exner equation solved in COURLIS does not really describe how the riverbed has been modified due to bedload transport. Indeed, once obtained ${A_b}^{n+1}$ after solving equation (3), the riverbed elevation function b^{n+1} can not solely be determined from relation (7), except for very particular cases, *e.g.* rectangular cross-sections. Therefore, an additional closure is needed in order to fully solve the updated river cross-section profiles.

A simple conceptual closure commonly used in literature [4] has been implemented as the default option in COURLIS. It consists in considering a flat profile at the lowest part of the cross-section for deposition case while imposing, in the opposed case, an uniform erosion height overall the submerged part of the cross-section. This height can be locally weighted by the local water height on the cross-section. See also [3,5] for more detail on the implementation.

Besides, the updated riverbed needs to be systematically planimetered. In other words, one needs to *numerically* rebuild the associated planimetry functions $(B,P,S)^{n+1}(x,\eta)$ which are demanded by MASCARET when solving equations (4), (5), (6) and (9). Unfortunately, this later step is very time consuming. Therefore, an *ad-hoc* threshold condition has been often adopted after which the planimetry calls are only carried out if the thickness of deposition or erosion is higher than 1% the water height.

A. Simple model for cross-section evolution

Let us now present an alternative conceptual closure for the riverbed cross-section evolution, as sketched in Fig. 2 and called *uniform erosion and deposition*. The cross-section profile at any time will be directly deducted from the initial one. This allows to *analytically* rebuild the updated planimetry functions from $(B,P,S)^0(x,\eta)$ given at initial time.

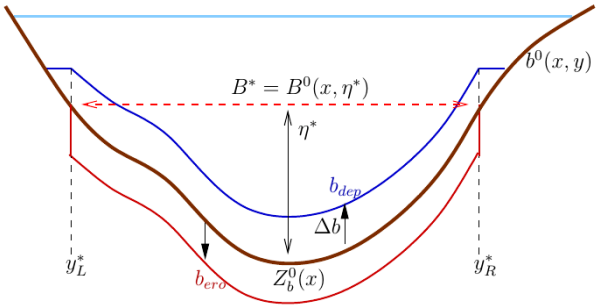

Figure 2: Sketch of the evolution type *uniform erosion and deposition.*

The present model relies on the **width of erosion**, $B^* = B^0(x,\eta^*)$, a user parameter defined for each initial riverbed cross-section function $b^0(x,y)$. The idea behind this approach is that we consider the riverbed evolution only taking place on a part of width B^* of the section; this parameter can be estimated from observation or calibration. So, the associated specific height η^*, the cross-section area $S^* = S^0(x,\eta^*)$ and the positions ${y_L}^*, {y_R}^*$ can be determined

accordingly. Once solved the Exner equation at time t^{n+1}, we compute the *cumulative* volume of transported sediments

(10) $\Delta A_b = \sum_{k=0}^{n} \Delta A_b{}^{k+1}$.

Next, one can deduce an uniform erosion or deposition height, $\Delta b > 0$, with mass conservation for sediments (regarding the initial time).

- Erosion case: $\Delta A_b < 0$, only the part of initial riverbed cross-section lying between ${y_L}^*, {y_R}^*$ (*i.e.* corresponding to the imposed erosion width B^*) is displaced downward a distance Δb. That is

$$\Delta A_b = -B^* \Delta b,$$

$$b_{\text{ero}}^{n+1} = \begin{cases} b^0 - \Delta b & \text{if} \quad y_L^* \le y \le y_R^*, \\ b^0 & \text{otherwise.} \end{cases}$$

- Deposition case: $\Delta A_b > 0$, the cross-section part of the initial riverbed cross-section between ${y_L}^*, {y_R}^*$ is lifted by a distance Δb followed by horizontal junctions at the left and right riverbanks. In other words,

$$\Delta A_b = S^0(x, \eta^* + \Delta b) - S^*,$$

$$b_{\text{dep}}^{n+1} = \begin{cases} b^0 + \Delta b & \text{if} \quad y_L^* \le y \le y_R^*, \\ \max(b^0, \eta^* + \Delta b) & \text{otherwise.} \end{cases}$$

Finally, the resulting planimetry functions are easily obtained. For example, the geometric cross-section $S^{n+1} \equiv S^{n+1}(x, \eta)$ reads

$$S^{n+1} = \begin{cases} S^0(x, \eta) & \text{if} \quad 0 \le \eta \le \eta^*, \\ S^* + (\eta - \eta^*)B^* & \text{if} \quad \eta^* \le \eta \le \eta^* + \Delta b, \\ S^0(x, \eta - \Delta b) + B^* \Delta b & \text{if} \quad \eta \ge \eta^* + \Delta b. \end{cases}$$

$$S^{n+1} = \begin{cases} S^0(x, \eta) & \text{if} \quad 0 \le \eta \le \eta^*, \\ S^0(x, \eta + \Delta b) - \Delta A_b & \text{if} \quad \eta^* \le \eta. \end{cases}$$

for erosion and deposition cases respectively.

This option is activated with the keywords in the steering file of COURLIS:

- `OPTION FOR PROFILE EVOLUTION = 2`
- `FILE FOR THE WIDTH OF EROSION = filename`

B. Construction of trapezoidal cross-section

In order to validate the present model, we are interested here in constructing a trapezoidal type cross-section from a given rectangular one. This specific geometric form allows, in one hand, a simple way to investigate the "key" parameter "width of erosion" and, in the other hand, to find again the available result of rectangular case which is noting that a particular case. Thus, we consider an uniform flow of water height H and discharge Q on a rectangular channel of width L. According to equation (8) and using the Manning-Strickler formula (6), one obtains $Q = K_s A {R_h}^{2/3} \sqrt{I}$ with I the channel slope. Next, we build a (double) trapezoidal cross-section P_1–P_6 as sketched in Fig. 3 with the identical K_s, A, R_h, I in order to have the same flow discharge. Consequently, if the considered flow entrains an erosion or deposition process on the rectangular channel, it does the same for the case of the trapezoidal one, at least for a short enough initial time.

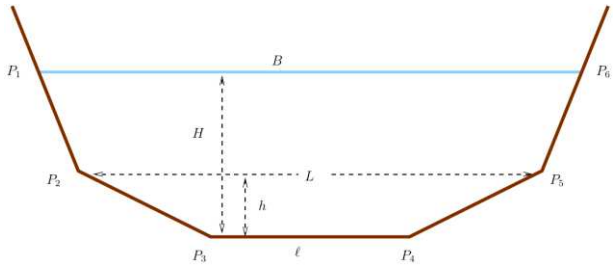

Figure 3: Setting up of the trapezoidal cross-section

In addition, we retain the same water height H while imposing the base $P_2P_5 = L$. So, one can deduce the other bases $P_1P_6 = B, P_3P_4 = l$ providing the height h of the lower trapezoid $P_2P_3P_4P_5$. We introduce the following dimensionless parameters:

(11) $\alpha = \frac{h}{H}, \ \beta = \frac{l}{L}, \ \varepsilon = \frac{H}{L}$.

Preserving the hydraulic section leads to

(12) $\frac{B}{L} = 1 + \frac{\alpha(1-\beta)}{1-\alpha}$.

Next, we substitute equations (11)–(12) into the expression of wetted perimeter and use the change of variable

(13) $x = (1 - \beta)/2\varepsilon$

to obtain the final equation

(14) $\sqrt{(1-\alpha)^2 + \left(\frac{\alpha}{1-\alpha}\right)^2 x^2} + \sqrt{\alpha^2 + x^2} = 1 + x.$

In summary, the trapezoidal cross-section depends only on one variable $\alpha = h/H$ and can be dimensioned as follows. Given a value ε deduced from the rectangular channel and a chosen value of parameter α, we first compute x – solution to equation (14) and obtain β from (13). The dimension of the cross-section is done by equations (11)–(12). In Fig. 4, we plot β as function of α for two values of ε corresponding to the Newton and Soni test cases which will be investigated in the next section. One can see that condition $\beta \ge 0$ leads to only the values $\alpha \ge \alpha_{min}$ can be used for constructing of the cross-sections. Furthermore, it's worth noticing that when α tends to 1, the constructed trapezoidal cross-section becomes the rectangular one.

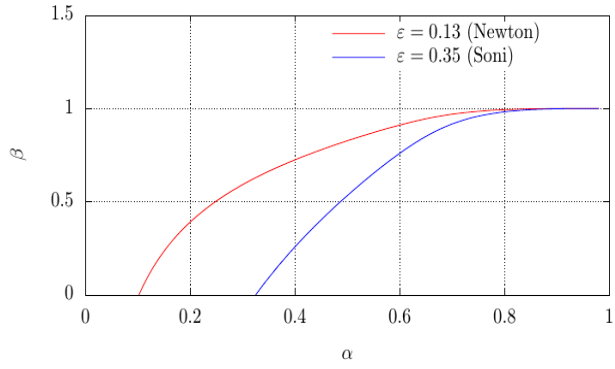

Figure 4: Solving $\beta = l/L$ as function of $\alpha = h/H$ for trapezoidal form

When applying these trapezoidal cross-sections to the proposed option *uniform erosion and deposition,* we impose the width of erosion $B^* = L$, and so the specific height $\eta^* = h$. Examples of the resulting (dimensionless) planimetry function $S^{n+1}(x, \eta)$ are plotted in Fig. 5.

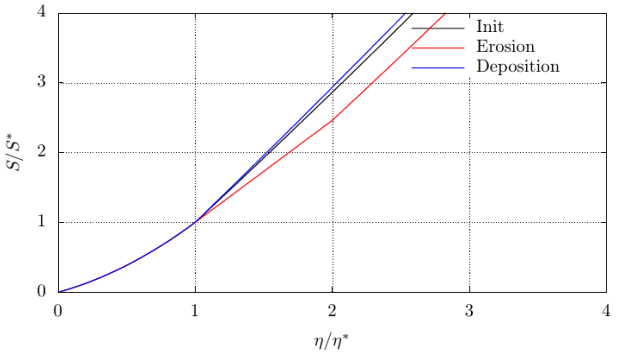

Figure 5: Plot of the change of geometric cross-section area for the Newton case with $\alpha = 0.2, \beta = 0.37, \Delta b/\eta^* = 1$.

IV. TEST CASES

All the test cases presented here are done with the **Sarap** kernel when solving the Shallow-Water equations. Indeed, the involving sediment transport processes in these test cases are very slow compared to the hydrodynamic one. So, the flows can be considered with permanent regime.

A. Erosion: Newton test case on trapezoidal channel

We aim at validating our new closure on cross-section evolution for a simple erosion case. For this purpose, we have re-used and modified the Newton test case which is well documented in COURLIS [5]. Initial setting up consists in a rectangular channel of 9.14 m long, 0.3048 m width and a slope 0.416%. A uniform flow is initially established with water height H = 0.041 m and a mean velocity U = 0.45 m/s. The resulting bed shear stress is higher than its threshold value for sediment motion. Without sediment supply at the upstream boundary, the bed of the channel is eroded during the experiment. The Meyer-Peter & Muller formula for bedload flux is used. More details on the setting can be found in the COURLIS validation document.

We first build a trapezoidal channel from the rectangular one relying on equations established in section III.B. We find the resulting parameter $\varepsilon = 0.13$ corresponding to $\alpha_{min} \simeq 1.2$. So we used increasing values $\alpha = 0.2, 0.4, 0.8$ to make 3 runs with time $T = 1\,\text{h}$. Obtained results on longitudinal profile compared to the case of rectangular cross-section and the observations are plotted on Fig. 6. We see that small values of α lead to important erosion. We find, in particular, that the results of trapezoidal cross-section tend to those of the rectangular one when α tends to 1 (so β tends to 1 which asymptotically becomes the rectangular section).

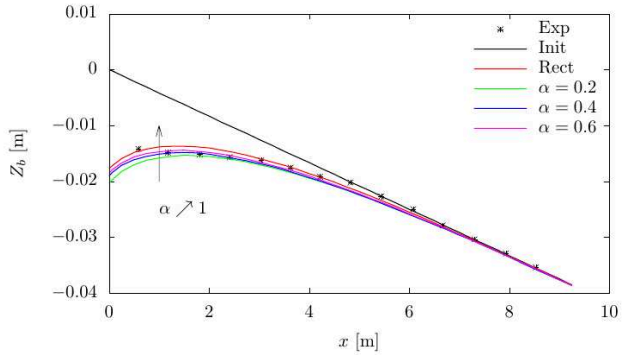

Figure 6: Newton test case – longitudinal profile at T=1h.

Cross-section evolution according to the proposed closure along the channel are also shown on Fig. 7.

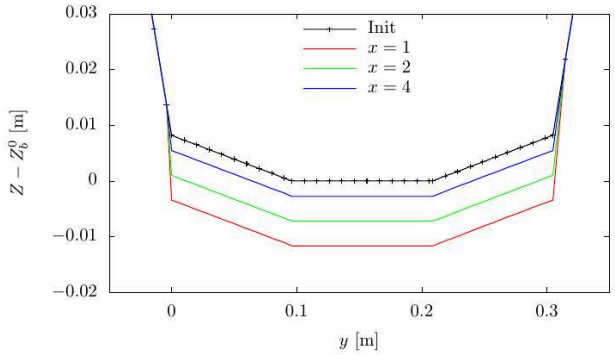

Figure 7: Newton test case with $\alpha = 0.2$: cross-sectional profiles

B. Deposition: Soni test case on trapezoidal channel

This second test case is very similar to the first one but is devoted to investigating the cross-section evolution in a deposition case. The experiment was carried out on a rectangular channel of 30m long, 0.2m width and a slope 0.427%. Initial uniform flow with water height H= 0.072m and velocity U =0.49m/s was imposed. Injected sediment concentration C_b= 4.88 kg/m3 at inlet boundary leads to a progressive deposition along the channel.

The configuration results in a value $\varepsilon = 0.35$ corresponding to $\alpha_{min} \simeq 0.34$ when building trapezoidal cross-sections. So, we set $\alpha = 0.4, 0.6, 0.8$ and made 3 runs with T=1h. The results are plotted on Fig. 8–9. As we can see, evolution of longitudinal profile shares a good agreement with that of rectangular cross-section and compared to the observation. Contrary to the Newton case, large values of α lead to important deposition.

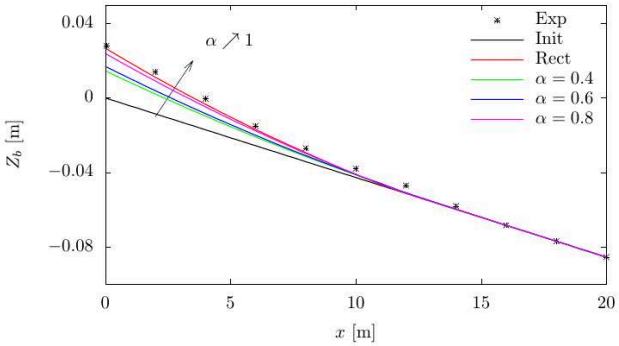

Figure 8: Soni test case: longitudinal profile at T = 1h.

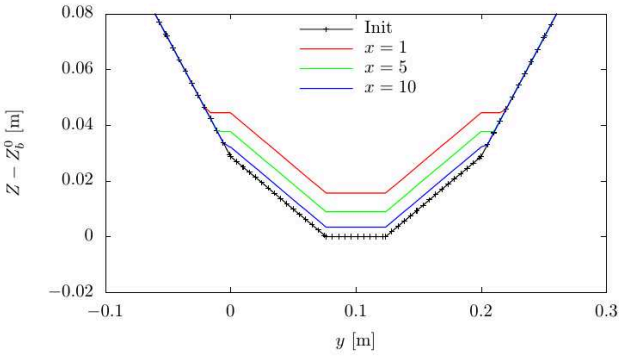

Figure 9: Soni test case with $\alpha = 0.4$ – cross-sectional profiles.

Results from the Newton and Soni tests cases, both on longitudinal and transversal evolution of the channel, show that the proposed model is correctly implemented.

C. Real application: the Buëch river

We now investigate the ability of the proposed model in a real application. The study site is located in the southern French Alps, on a 4 km-long reach of the Buëch river starting at the Serres bridge and finishing at the Saint Sauveur Dam (see Fig. 10). The riverbed slope varies between 0.004 and 0.006 m/m. There exist numerical simulations carried out recently by EDF CIH with the 1D hydro-sedimentary code CAVALCADE and COURLIS. See, e.g. [6] for more details. All these simulations are done with rectangular cross-sections built and calibrated from 36 observed cross-section profiles of the riverbed. For illustration purposes, time-evolution of the riverbed at the 6th cross-section from 2010 and 2016 are plotted on Fig. 11.

Our simulation is built from the last model made with COURLIS, based on an initial riverbed from the 2015 bathymetric measurements and tries to reproduce the spatial and temporal 5-year evolutions of the riverbed. The longitudinal space step is chosen iteratively to smooth the Froude number at $\Delta x = 15$m. Trapezoidal profiles are built from the given geometry constituted of 269 rectangular cross-sections (interpolated from the observed ones). It's worth noting that, contrary to the Newton and Soni test cases, the parameter $\varepsilon = H/L$ resulting by a permanent flow is no longer constant but varies accordingly to the change of water height and channel width from one cross-section to others. Consequently, fixing a value for α will result in different values of β at each of the cross-sections and inversely. Hence, one can investigate the behaviour of the new model by varying both α and β for this real application.

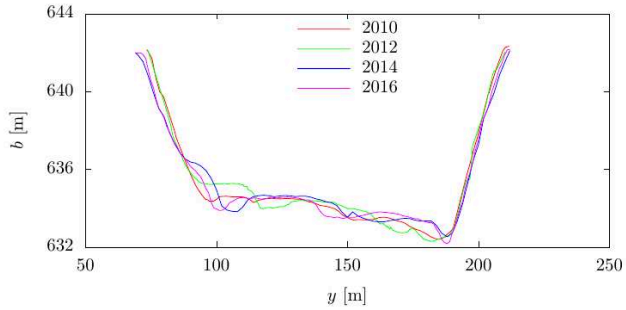

Figure 11. Observed riverbed profile at the cross-section n°6 of Buëch river

Numerical simulations used Lefort formula [7] to estimate sediment flux of gravels with a D_m of 3.2 cm. Performance of the new model with trapezoidal cross-sections regarding to rectangular ones is evaluated by comparing the Root Mean Square Error (RMSE) on the observed longitudinal profiles in 2016, 2019 and 2020. The result is reported in Tab. 1.

Table I RMSE on longitudinal profiles between simulation and observation

	2016	**2019**	**2020**	**Mean**
Rect	0.2868	0.6216	0.3788	**0.4290**
α = 0.4	0.2630	0.6984	0.4593	0.4725
α = 0.6	0.2487	0.6606	0.4396	0.4450
α = 0.8	0.2465	0.6455	0.4259	0.4393
β = 0.2	0.2477	0.6924	0.3324	**0.4241**
β = 0.4	0.2614	0.7205	0.4092	0.4637
β = 0.6	0.2724	0.7307	0.4828	0.4953

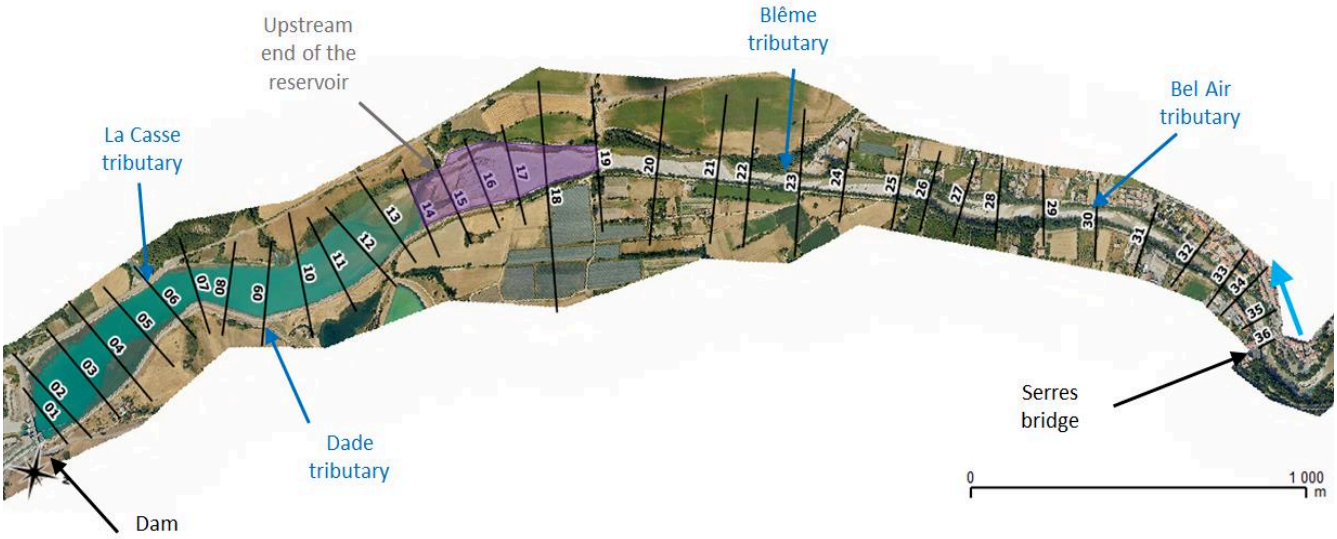

Figure 10: Presentation of the study site. The black lines indicate the cross-section locations of the bathymetric surveys.

One can see that the calibration based on parameter β seems to be more appropriate than α. The best RMSE value 0.4241m corresponds to $\beta = 0.2$ and slightly lower than the case of rectangular cross-sections. Corresponding time-evolution of the longitudinal profiles is plotted on Fig. 12 and Fig. 13.

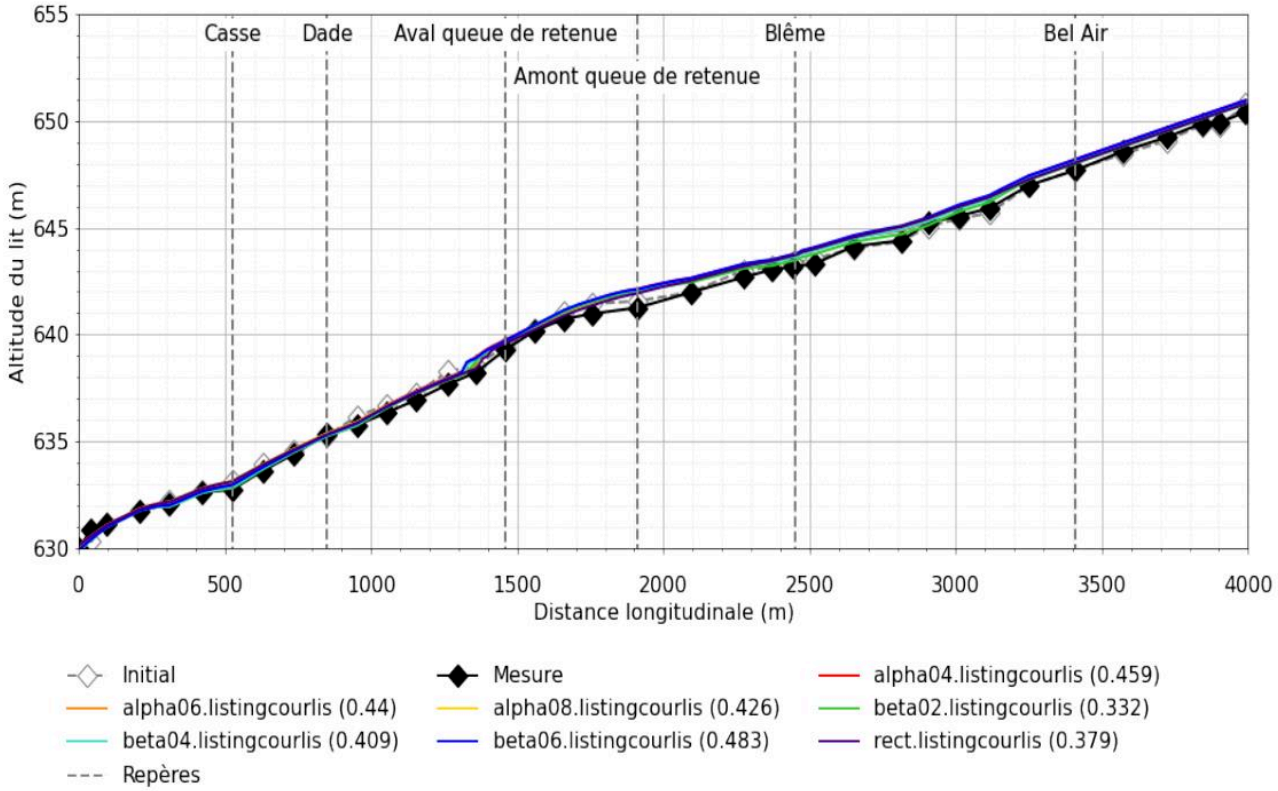

Figure 12: Longitudinal profile of riverbed in July 2020 - comparison between measurements, COURLIS with rectangular cross-sections and with trapezoidal cross-sections.

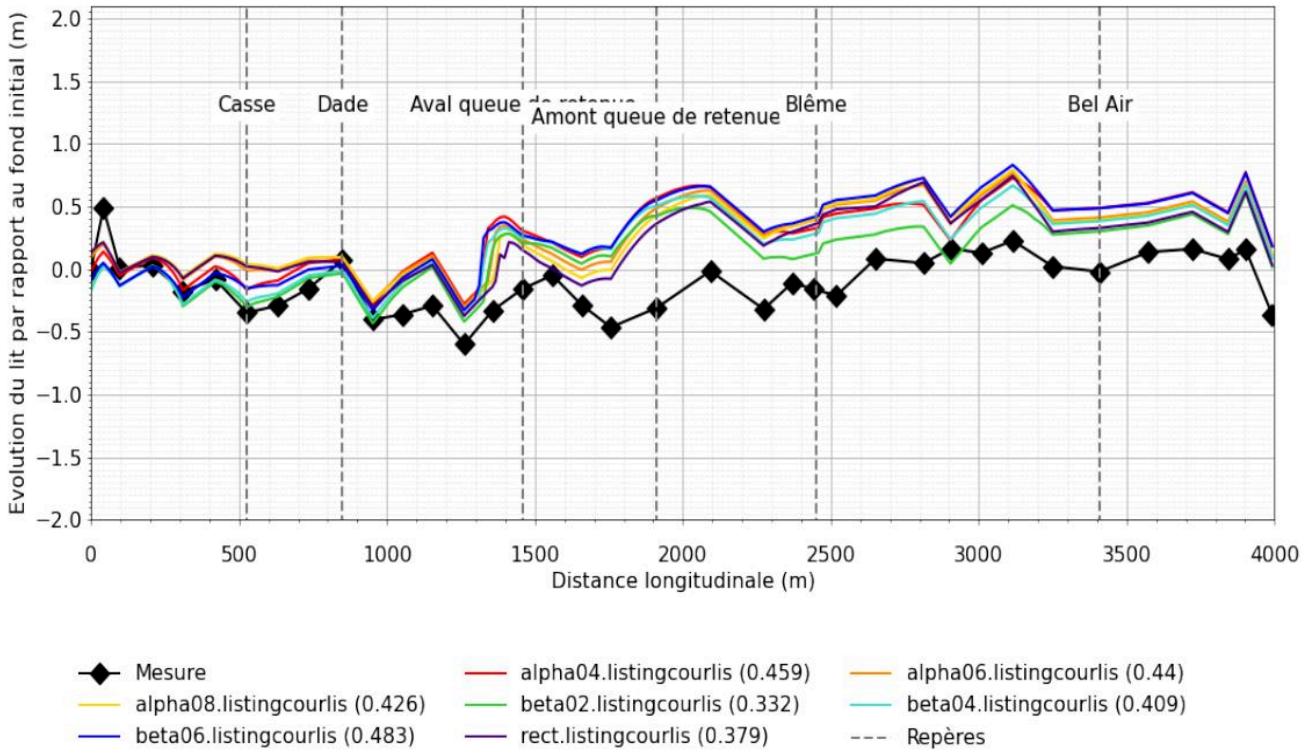

Figure 13: 5-years longitudinal evolution of the riverbed at July 2020

V. CONCLUSION AND FURTHER WORKS.

We have presented a new *conceptual* model, called *uniform erosion and deposition*, for the evolution of riverbed cross-section due to bedload transport. This closure is based on a user-provided input *width of erosion* defined for each cross-section. Planimetry functions can be built analytically from the initial ones. The option has been implemented in COURLIS, validated by two laboratory test cases Newton and Soni, and next applied to the real case of the Buëch River with trapezoidal cross-sections.

Application of the proposed model to the real (measured) geometry of riverbed is interesting and can be done in the following. Furthermore, we are also interested in investigating other *physically based* closures, *e.g.* those derived from the *stable river* theory [8,9] recently proposed in the literature.

ACKNOWLEDGEMENT

The authors want to thank the colleagues of EDF Hydro Mediterranée for the transfer of data and their support.

REFERENCES

[1] Sécher, M., Ung, P., Valette, E., Jodeau, M., & Goutal, N. (2018). COURLIS: a 1D suspension and bedload code. In *E3S Web of Conferences* (Vol. 40, p. 05038). EDP Sciences.

[2] TELEMAC-MASCARET. MASCARET Theory Guide version V8P3, 5 July 2022.

[3] Valette, Eric, et al. "COURLIS: a new sedimentology 1D module for MASCARET." *Proceedings of the XXIVth TELEMAC-MASCARET User Conference, 17 to 20 October 2017, Graz University of Technology, Austria*. 2017.

[4] El kadi Abderrezzak, K., & Paquier, A. (2009). One-dimensional numerical modelling of sediment transport and bed deformation in open channels. *Water Resources Research*, *45*(5).

[5] TELEMAC-MASCARET. COURLIS Validation Manual version V8P3, 5 July 2022.

[6] Claude, N. & al. 1D numerical modelling of the longitudinal profile evolution of riverbeds and reservoirs: application of COURLIS bedload on a real case. Submitted to *Proceedings of the XXVIIIth TELEMAC-MASCARET User Conference, 18 to 19 October 2022.*

[7] Lefort, P. Morphodynamique fluviale - Approches théorique et expérimentale. Ponts et Chaussées (Presses), 2018. ISBN 978-2-85978-516-1.

[8] Seizilles, G., Lajeunesse, E., Devauchelle, O., & Bak, M. (2014). Cross-stream diffusion in bedload transport. *Physics of Fluids*, *26*(1), 013302.

[9] Abramian, A., Devauchelle, O., & Lajeunesse, E. (2020). Laboratory rivers adjust their shape to sediment transport. *Physical Review E*, *102*(5), 053101.

Simulation of embayment lab experiments using TELEMAC-3D/GAIA

Rebekka Kopmann

rebekka.kopmann@baw.de, Karlsruhe, Germany
BAW

Abstract – **One of the focal topics at BAW is the impact of river control structures such as groynes to optimise waterways maintenance strategies e.g. by means of sediment management. Hydro-morphodynamic numerical modelling supports the investigations of sediment management tasks. For inland river projects, sediment transport was usually considered as bedload only. For large-scale and long-term simulations, however, the exchange of suspended sediments between groyne fields and the main channel must be taken into account.**

To investigate the numerical modelling capability of the lateral sediment exchange of non-cohesive material on inland waterways the laboratory experiment of [1] was chosen. Within this experiment the distribution of suspended sediment and its deposits in different configurations of lateral embayment were investigated. Using the two-dimensional approach of TELEMAC-2D/GAIA the numerical model could be calibrated to one discharge configuration but not validated to the other two discharges performed in the laboratory model [2], [3]. Therefore, further investigations were done with a higher resolution 2D model and with a three-dimensional model using TELEMAC-3D/GAIA.

The seiche effect of oscillating water levels found in the measurements could be reproduced by the high resolution 2D model. With the 3D model the centre of the embayment vortex was captured and the simulated deposition patterns could be improved. However, both models fail to reproduce the decrease in deposited material with increasing discharge.

Keywords: suspension, lateral sediment exchange, embayment.

I. INTRODUCTION

For inland river projects at BAW suspended sediment transport becomes more and more important. The requirements of the European Water Framework Directive cause investigations at the floodplains and the interaction between floodplain and main channel (e.g. the Federal program "Blaues Band Deutschland"). Within the BAW internal R&D project "Numerical modelling of lateral sediment exchange" the numerical modelling capability of the lateral sediment exchange of non-cohesive material on inland waterways is investigated. For long-term and large-scale studies the focus in the R&D project is on the lateral sediment exchange between groynes and main channel.

To validate the lateral sediment exchange, a laboratory experiment with lateral embayment was selected [1]. In this experiment the distribution of suspended sediment and its deposits in different configurations of lateral embayment were investigated. The simple geometry, the presence of concentration and deposition measurements and the excellent description of the laboratory experiment seem to be good reasons to use this laboratory model as validation test case.

Using the two-dimensional approach of TELEMAC-2D/GAIA the numerical model could be calibrated to one discharge configuration but not validated to the other two discharges performed in the laboratory model [2], [3]. Especially the decrease in deposited material with increasing discharges could not be reproduced by the 2D model. Three possible causes were determined: the loss of material in the pores of the laboratory model, the embayment pumping effect, also known as seiche effect and a distinct three-dimensional flow in the shear zone between embayment and main channel.

It was assumed that the loss of material in the pores would not disturb the general trend of less deposition with higher discharges. Therefore, the two other possible reasons were followed for the configuration 3.1 of the experiment (see Figure 2).

The laboratory model is described briefly in chapter II. The applied numerical models are characterised in chapter III. In chapter IV the results of the numerical simulations are compared to the measurements with a focus to the deposition of sediment in the embayment areas.

II. EMBAYMENT FLUME EXPERIMENT

A 7.5 m long and 1 m wide flume with a longitudinal slope of 0.1 % were investigated by [1] (see Fig. 1). The experiments were done in a straight flume and four different embayment-length configurations. For this investigation configuration 3.1 was considered only (Fig. 2). In the experiment an artificial sediment of polyurethane corresponding to non-cohesive fine sediments were recirculated and mixed in upstream and downstream tanks. The measured main sediment parameters are a mean grain size of $d_{50} = 0.2$ mm, a density of 1160 g/m^3 and a settling velocity of 0.00276 m/s.

Three different discharges (low flow: 4.8 l/s, medium flow: 8.5 l/s, high flow: 15 l/s) were conducted. The recirculating sediment mass which determines the boundary sediment concentration was found experimentally to the maximum suspended capacity of the flow for each discharge. It follows that no sediment deposited in the main channel.

The boundary conditions of the experiment are summarized in Table I. The concentrations or sediment masses were not measured at the boundaries. At two positions in the main channel orientated at the embayment configuration (see Fig. 1), turbidimeters were installed which monitored the concentrations. The vertical position of the turbidimeters was experimentally chosen to the vertical averaged value of the concentration profile. The averaged values of both measurement points are displayed in Fig. 3 for the reference configuration without embayment (3.0). The decrease in the concentration results from trapped sediments in small gaps between bricks and walls as in this configuration no bed evolution appeared. Furthermore, it was observed that the recirculating sediment procedure did not produce a constant feed but a decreasing, slightly oscillating one. The experiments were finished after 3, 4 and 5 hours when the bottom evolution in the lateral embayment were not measurable anymore. The concentrations reached a quasi-equilibrium concentration state for low, medium and high discharges, respectively (see Fig. 4 for configuration 3.1).

After the experiment the sediment mass trapped in the embayment was collected, dried and weighed. The total sediment mass divided by the total embayment area gives the trapping efficiency which is decreasing with increasing discharges (see Fig. 5).

The water level measurements show oscillations for all embayment configurations. The configuration 3.1 was one of those with the largest oscillations. This phenomenon is induced by a seiche, which occurs in dead zones of a flow (e.g. [4], [5]). Water level fluctuations of 1 – 3 mm were observed [1].

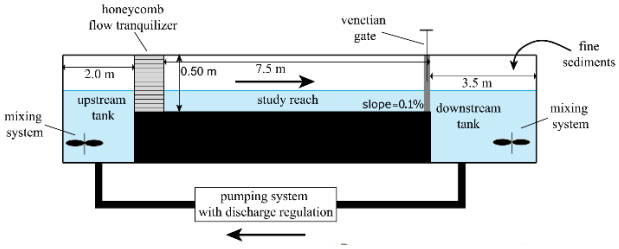

Figure 1: Side view of the set-up of the flume experiment (from [1]).

Table I Boundary conditions of the laboratoy experiment.

Discharge (l/s)	4.8 (low)	8.5 (medium	15 (high)
Water depth (m)	0.035	0.05	0.07
Recirculating sediment mass (kg)	2.75	5.5	8.25
Target sediment concentration (g/l)	0.5	1.0	1.5

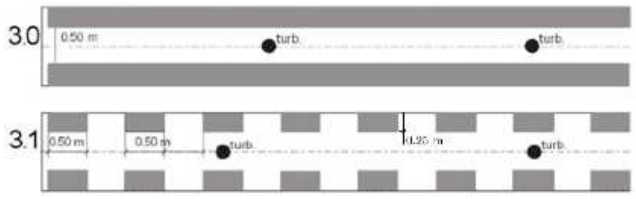

Figure 2: Embayment configuration 3.0 and 3.1 (from [1]).

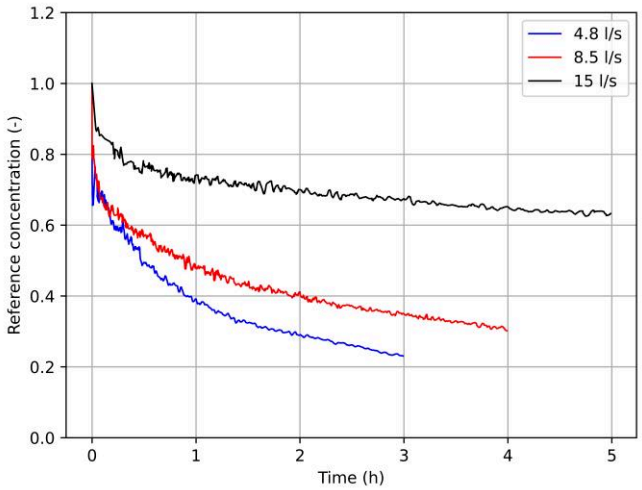

Figure 3: Measured concentrations for the configuration without embayment (3.0) (values are taken from [1]).

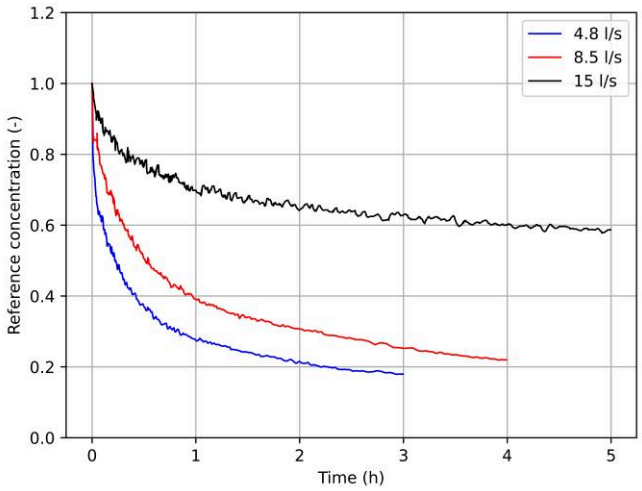

Figure 4: Measured concentration for configuration 3.1 (values are taken from [1]).

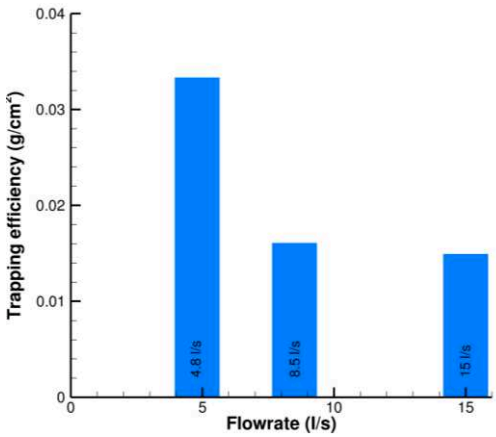

Figure 5: Measured trapping efficiency for configurations 3.1 and all discharges (values are taken from [1]).

III. NUMERICAL SIMULATION OF EMBAYMENT FLUME EXPERIMENT

Based on the numerical modelling of the laboratory experiment presented in [2] and [3] two new models were set up to improve the numerical results: A high resolution two-dimensional model (TELEMAC-2D/GAIA), denoted in the following as "2Dseiches", was used to investigate the influence of seiches to the lateral sediment exchange. A moderate resolution three-dimensional model (TELEMAC-3D/GAIA), denoted in the following as "3Dcoarse", was applied to resolve vertical processes. The "TUC2021" model is described in detail in [2] and is used in this paper for comparison. The new simulations were done for configuration 3.1 only. Table II shows the grid specifications of the different models. For stability reasons the inlet and outlet part without embayment areas are enlarged for the models 2Dseiches and 3Dcoarse.

The boundary conditions for the numerical modelling are summarised in Table III. At the inlet boundary the discharge and at the outlet boundary the water levels were imposed. For the TUC2021 simulations the horizontal velocity distribution at the inlet was set, taken from a previous steady state simulation. This procedure minimises the boundary impact but was not needed for the models 2Dseiches and 3Dcoarse due to the enlarged inlet. For the boundary sediment concentration at the inlet the averaged measurements along the channel (Fig. 4) were used.

Table II Applied models and their grid specifications.

Model name	Number of horizontal nodes	Number of horizontal elements	Number of vertical levels	Avg. horizon. node distance (m)	Avg. vertical node distance (m)	Time step (s)
TUC2021	2167	3872	1	0.05	-	0.05
2Dseiches	115067	224218	1	0.01	-	0.005
3Dcoarse	22838	42282	5	0.03	0.004 – 0.008	0.05

Table III Boundary conditions for the numerical models.

Discharge (l/s)	4.8 (low)	8.5 (medium)	15 (high)
Water depth (m)	0.035	0.05	0.07
Sediment concentration (g/l)	Measured concentration (see Fig. 3)		
Experiment duration (h)	3	4	5

TUC2021 simulations were started with steady state flow and concentration conditions found by a previous computation. No influence of this procedure to the trend of trapping masses with discharge could be found. Therefore, for the other models the initial velocities and concentrations were set to zero.

The roughness coefficients for the bottom (Nikuradse 0.5 mm) and for the lateral walls (Nikuradse 2.1 mm) were taken from the calibration of model TUC2021. For all models k-ε turbulence model was applied.

The sediment parameters were initially taken from TUC2021 but 2Dseiches and 3Dcoarse both consider sediment diffusion:

- Non-cohesive uniform grain size of 0.2 mm, porosity of 40%, density of 1160 g/m^3, settling velocity of 0.00276 m/s
- Meyer-Peter Müller formula with factor 5 for bed load transport, slope effect (deviation: Talmon, magnitude: Soulsby), no secondary currents effect,
- adapted van Rijn reference concentration (20% of Nikuradse friction coefficient and between 1 and 20 % of water depth), including settling lag.

A. Model "2Dseiches"

The aim of the 2Dseiches model was to simulate the seiche effect in order to investigate the influence of the water oscillations on the trapping masses. With the numerical options of the TUC2021 model no seiches were simulated with the finer grid. Starting from the TELEMAC-2D validation example "cavity" the following options produce oscillating water levels:

- High resolution to minimise the numerical diffusion,
- no-slip boundary conditions for the embayments,
- Smagorinsky turbulence model,
- space discretisation with quasi-bubble.

For the space discretisation with quasi-bubble (DISCRETISATION IN SPACE = 12;11) the edge-based matrix storage (MATRIX STORAGE = 3) is required. This is not a default value in GAIA and must be set – otherwise the simulation will fail.

Some simulations were done with higher order schemes using finite volumes and higher resolution. The resulting oscillations are even higher and show more fluctuations laterally to the main flow direction while the finite element approach with quasi-bubble used here shows mainly fluctuations in the flow direction. Unfortunately, the higher order schemes did not run in coupled case with GAIA and were therefore not followed for this investigation.

B. Model "3Dcoarse"

In order to take three-dimensional effects into account the 3Dcoarse model was set up. The TUC2021 model could reproduce the embayment vortex but not completely at the correct position. Furthermore, the deposition areas did not fit very well to the measurements. Even a higher resolution of 1 cm node distances did not enhance these aspects [2].

Different horizontal and vertical resolution were tested. A relatively coarse resolution with 3 cm node distance in the horizontal and five vertical layers were chosen. Finer resolutions needed more computing time and showed some

strange effects if coupled to GAIA which could not be resolved.

Due to instability issues some changes / simplifications for GAIA needed to be done: no bedload transport, no settling lag but equilibrium concentration of van Rijn [6].

IV. Comparison of the numerical results to the measurements

A. Modelling of seiche effect

With the 2Dseiches model the measured water level oscillations could be simulated. In Fig. 6 the simulated free surface with coloured concentrations is visualised at half time of the experiment for all three discharges. In the centre of the left hand forth embayment (see marked probe position) the evolution of the water depth and concentrations over time are presented starting from the half time for 200 s. In [1] only the range of water level fluctuations were mentioned. Thus, the exact value for the experiment and the probe position is unknown. The probe position for the evaluation in Fig. 6 was chosen inside an embayment and with maximal distance to the open boundaries.

The simulated water level fluctuations are very much related to the probe position and vary from about 1 to 7 mm. Typically the oscillations are high in the shear zone and low in the embayment areas. In the main channel higher oscillations can be found in the narrow parts without lateral embayment areas. At the probe position water depth fluctuation of about 1 mm for 4.8 and 15 l/s and 2 mm for 8.5 l/s were found. This fits quite well to the measured 1 to 3 mm.

The concentrations at the probe position show also high frequent oscillations and additional a lower frequent disturbance. The high frequent amplitude increases with increasing discharge. The available concentration measurements are not precise enough for a useful comparison.

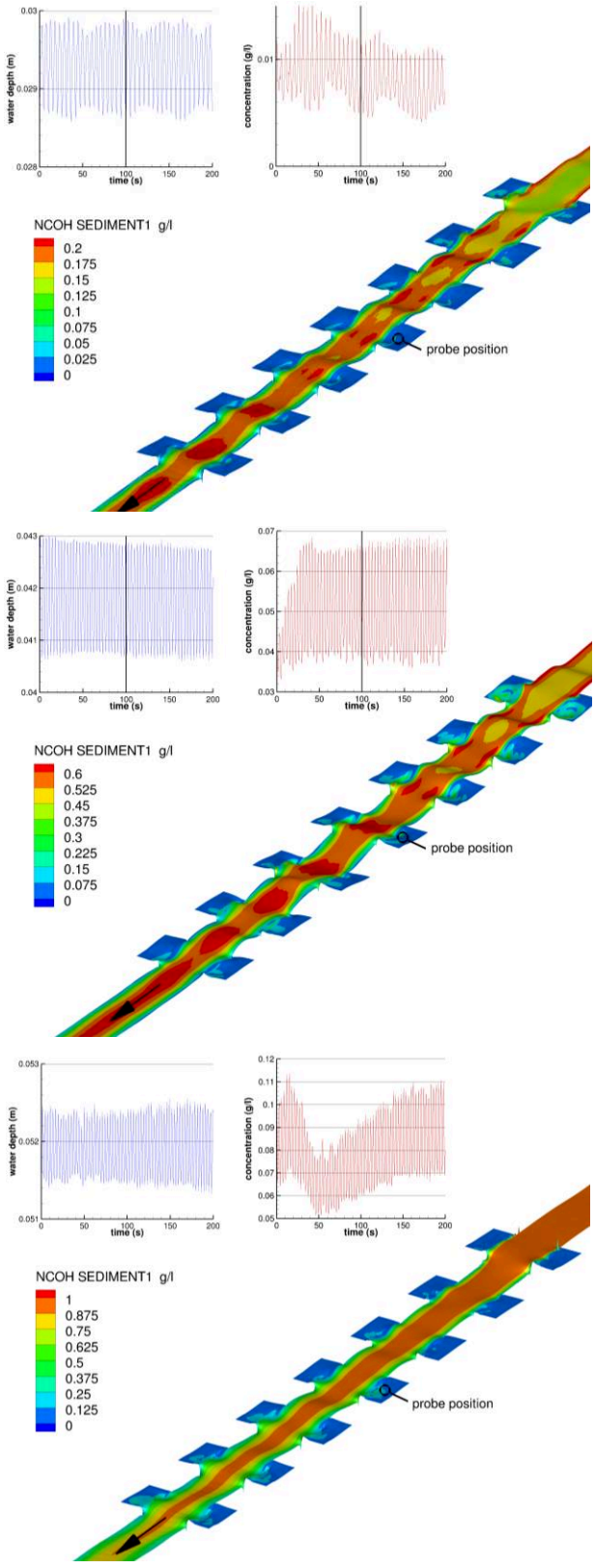

Figure 6: Oscillating water levels and depth averaged concentrations for a discharge of 4.8 l/s (top), 8.5 l/s (middle), 15 l/s (bottom) at half time of the experiment.

B. *Modelling three-dimensional effects*

Fig. 7 shows the simulated embayment vortex for all discharges in comparison to the measurements. Fig. 8 compares the embayment vortex for the TUC2021 model and the 3Dcoarse model for the high discharge. The three-dimensional simulations fit better to the measurements. The centre of the embayment vortex is at the dimensionless length parameter of the embayment x/l ≈ 0.7 for the measurements and the 3Dcoarse model but at x/l ≈ 0.55 for the TUC2021 model.

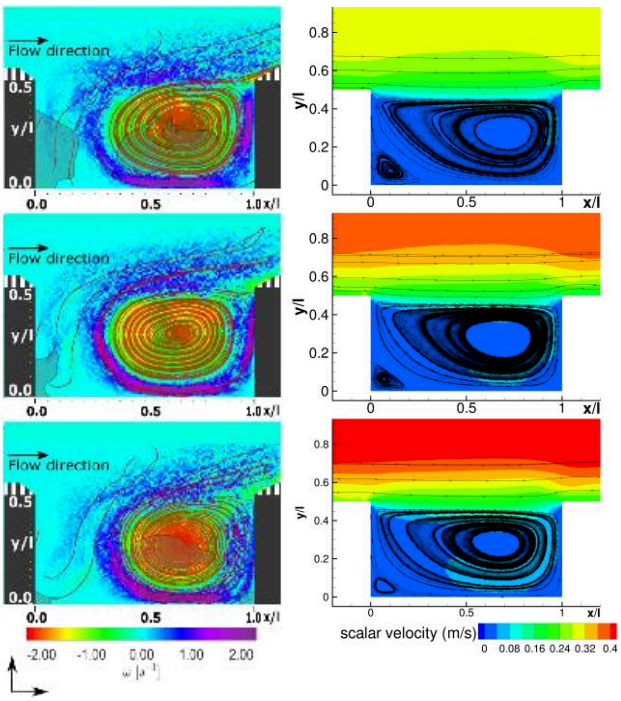

Figure 7: Comparison of measured vorticity and streamlines of the embayment vortex (left, from supplementary online data of [1]) and simulated scalar velocity and streamlines of the embayment vortex (right) for low (top), medium (middle) and high (bottom) discharges.

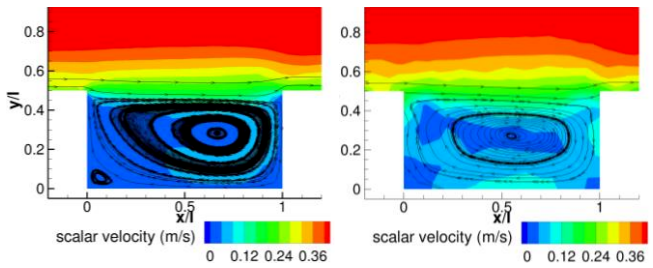

Figure 8: Comparison of simulated scalar velocity and streamlines of the embayment vortex for the 3Dcoarse model (left) and the TUC2021 model (right) for high discharge.

The simulated deposition pattern compared to the measurements is plotted in Fig. 9. As expected with three-dimensional simulation the material was deposited at the centre of the vortex. For the low discharge the lateral exchange seems to be too small to transport the sediment through the shear zone. For this discharge the sediments deposited only along the shear zone. The measurements show for the low and the high discharge the typical deposition pattern in the centre of a vortex. Additionally, in the laboratory experiment deposition occurred mainly at the upstream corner. This effect could not be captured by the 3Dcoarse model although a second vortex was simulated in the upstream corner (see Fig. 8 left).

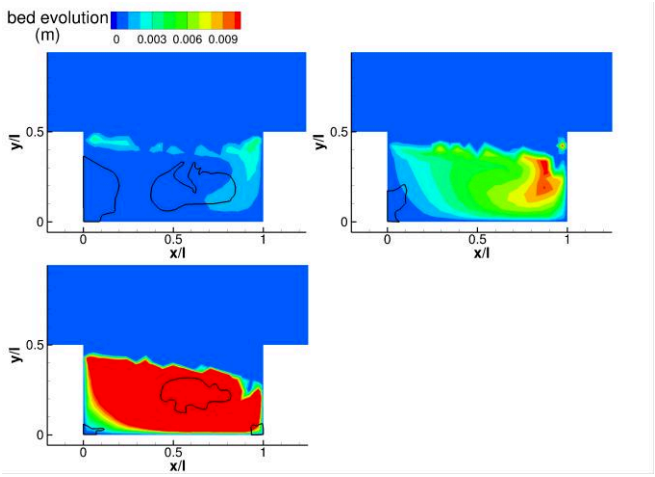

Figure 9: Simulated deposition for the 3Dcoarse model and position of measured deposition (black lines) for all discharges.

C. *Comparison between simulated and measured trapping masses*

The simulated deposited masses in the embayment areas are compared to the measured ones. In the experiment the deposition masses decreased with increasing discharges and increasing inlet concentrations. Fig. 10 presents the trapping efficiency over time for the models TUC2021, 2Dseiches, 3Dcoarse and the final value measured in the lab experiments.

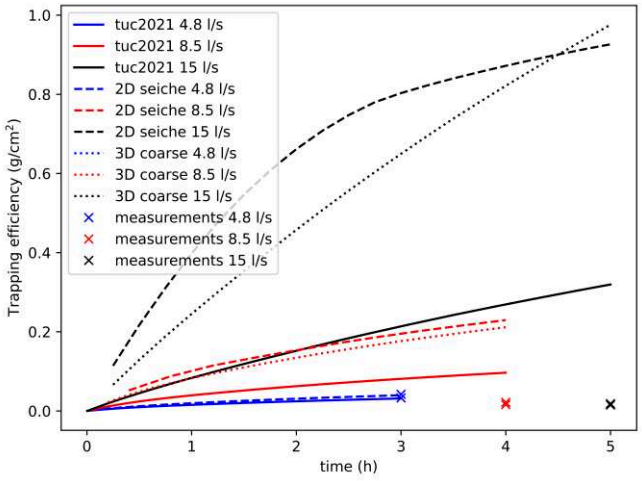

Figure 10: Trapping mass efficiency for the models TUC2021, 2Dseiches, 3Dcoarse and the measurements for all discharges.

For the small discharge the results of all numerical models fit very well to the measurements. But contrary to the measurements all models showed an increasing trend in deposition masses with increasing discharges respectively inlet concentrations. The increase was even higher for the more complex models. Both the seiche effect and the resolution of the vertical dimension leaded to a higher input of concentration into the embayment areas and a subsequent deposition.

The deposition of suspended sediments can be computed from the net sediment flux (E - D) as the result of the sedimentation (D) and erosion (E) processes. In GAIA the Sedimentation is calculated as product of the settling velocity w_s and the available concentration C_{zref} at a certain reference height *zref*. In 2D modelling a Stokes profile is assumed for the vertical distribution of the sediments. In 3D the simulated concentration at the reference height is used. The erosion for non-cohesive material is computed in GAIA as the product of the settling velocity and the equilibrium near-bed concentration C_{eq}, which is determined by an empirical formulation. For this investigation the formula of van Rijn was used which is dependent of sediment parameters, the reference height and the ratio between the Shields parameter and the critical Shields parameter.

$$E - D = w_s (C_{eq} - C_{zref}) \quad (1)$$

With increasing discharge, the inlet concentration in the experiment was increased, which led to higher concentrations in the embayment areas (see Fig. 6). The higher reference concentrations initiated higher sedimentation. It is assumed that the fluctuations also led to higher lateral sediment exchange, which increases the concentration inside the embayment areas, which in turn led to higher sedimentation. This would explain the higher trapping efficiency values for the 2Dseiche model compared to the TUC2021 model.

The 3Dcoarse model computed significantly smaller velocities (see Fig. 8) respective bottom shear stresses than the TUC2021 model (see Fig. 11). This caused smaller erosion which resulted in higher deposition tendencies. Fig. 11 shows the calculated Shields parameter of the TUC2021 and the 3Dcoarse model. GAIA computed a critical Shields parameter of 0.1. Therefore, erosion did not occur at dark blue parts. The 3Dcoarse model calculated much smaller Shields parameter than the 2Dseiche model because of the smaller flow velocities. For the 3Dcoarse model all sediments which were transported to the embayment areas were deposited with time. The linear increase for the trapping efficiency in Fig. 10 shows this.

For calibration purposes, the bottom shear stress was increased due to turbulence using the formulation proposed in [7]. This approach was already used within the TUC2021 model. Furthermore, the critical Shields parameter was reduced from 0.1 to 0.08 (after Soulsby & Whitehouse [8]). Both of these changes reduced the depositions for the higher discharges but did not change the general behaviour.

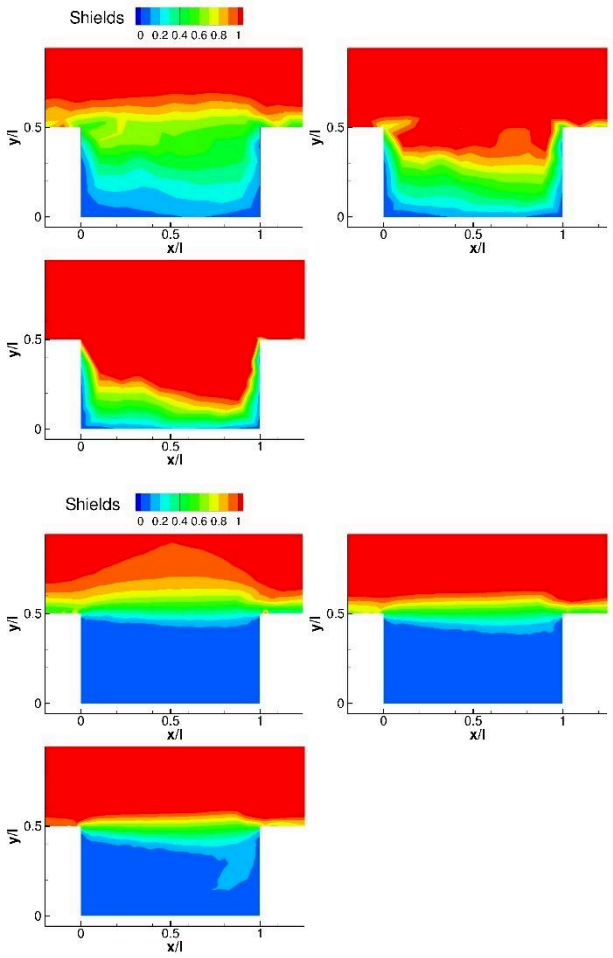

Figure 11: Comparison of simulated Shields parameter for the TUC2021 model (top) and the 3Dcoarse model (bottom) for all discharges.

V. CONCLUSION AND OUTLOOK

With the embayment experiment of [1] the capability of TELEMAC/GAIA to simulate lateral sediment exchange was investigated. Building upon the work of [2], [3] three different numerical models were compared to the experimental results in order to capture the measured decrease in trapped mass in the embayment areas with increasing discharge. Some shortcomings of the low resolution two-dimensional TUC2021 model could be overcome. With a high resolution 2D model (2Dseiches) it was possible to simulate the measured water level fluctuations. A three-dimensional approach (3Dcoarse) could also reproduce the centre of the embayment vortex and computed more reasonable evolution pattern in the vortex centre. But the deposition at the upstream corner of the embayment areas could not be reproduced.

All models considered could reproduce the trapping mass for the low discharge. Unfortunately, the decrease in the trapping mass with increasing discharges could not be simulated by any of them. The results of the new models were even worse probably due to the only rudimentary calibration. With increasing discharge and increasing inlet

concentration more sediment came into the embayment areas. So, the sediment deposition flux increased. For a smaller net sediment deposition, the erosion flux needed to be increased more than the deposition flux. But the bottom shear stresses increased only slightly and could not compensate the increased sediment flux.

It is assumed that the configuration of the laboratory experiment is quite special and probably related to a strong sensitivity of the light artificial material to turbulence. It seems that with higher discharges the sediments transported to the embayment areas did not settle but stay in the water column. In the literature, the effect of vortex trapping [9] is described. Sediment particles can move indefinitely along any circle in a forced vortex. It is unlikely that these special effects play a role in large-scale long-term lateral sediment exchange between main channel and groyne fields. Furthermore, the implemented formulas in GAIA were developed for natural sediments (sand) and produce not necessarily good results for artificial material and their sensitivities to turbulence. Therefore, the laboratory experiment seems not suitable as a validation test case for lateral sediment exchange of river groyne sections. Nevertheless, the investigations showed that even a low resolution 2D model (TUC2021) can be calibrated to catch the lateral sediment exchange.

The transferability to other discharges of emerged groynes could not be proven. Probably the long-term lateral sediment exchange is influenced mainly by the sequences between the flow of emerged and submerged groynes. Further investigations are planned including the validation on the basis of different laboratory experiments. One validation test case will be a new laboratory model with movable bed and bends conducted at BAW. Another could be a laboratory model with groynes [10].

ACKNOWLEDGEMENT

The author thanks Javier Obreque Perez for the fruitful collaboration and his work for this investigation.

REFERENCES

[1] C. Juez, I. Bühlmann, G. Maechler, A. J. Schleiss, & M. J. Franca, Transport of suspended sediments under the influence of bank macro-roughness. Earth Surface Processes and Landforms, 43 (1), 271–284, 2018, https://doi.org/10.1002/esp.4243.

[2] R. Kopmann, J. Perez-Obreque, Simulation of embayment lab experiments with TELEMAC-2D/GAIA. Proceedings of the TELEMAC-MASCARET User Conference October 2021.

[3] J. I. Pérez Obreque, Modelling of lateral sediment exchange using TELEMAC2D/GAIA, Master thesis, Karlsruhe Institute of Technology, 2021

[4] I. Kimura, T. Hosoda, Fundamental properties of flows in open channels with dead zone, Journal of Hydraulic Engineering 123: 98–107, 1997.

[5] Y. Akutina, Experimental investigation of flow structures in a shallow embayment using 3D-PTV. PhD thesis, McGill University, Montreal, 2015.

[6] L.C. van Rijn, Sediment transport - Part II : suspended load. Journal of Hydraulic Division, HY11:1631–1641, 1984.

[7] A. Goll, 3D Numerical Modelling of Dune Formation and Dynamics in Inland Waterways. PhD thesis, Université Paris-Est, École du Pont ParisTech 2017, https://hdl.handle.net/20.500.11970/104213.

[8] R.L. Soulsby, and R. J.S. W Whitehouse. Threshold of sediment motion in coastal environments. In, Proceedings Pacific Coasts and Ports ’97 Conference, 1, 149154. New Zealand: Christchurch, University of Canterbury, 1997

[9] P.F. Tooby, G. L. Wick, and J. D. Isaacs, The motion of a small sphere in a rotating velocity field: A possible mechanism for suspending particles in turbulence, J. Geophys. Res., 82(15), 2096–2100, 1977.

[10] Mohamed F. M. Yossef and Huib J. de Vriend, Sediment Exchange between a River and Its Groyne Fields, Mobile-Bed Experiment, Journal of Hydraulic Engineering, 136(9), 610–625, 2010 https://doi.org/10.1061/(ASCE)HY.1943-7900.0000226.

Water Quality modelling of the Southern North sea using TELEMAC-3D coupled with AED2

Foteini Kyrousi[1], W. Alexander Breugem[1], Kai Chu[1], Lucy G. Gillis[1], Boudewijn Decrop[1]
foteini.kyrousi@imdc.be
[1]International Marine and Dredging Consultants n.v.
Van Immerseelstraat 66, 2018 Antwerp, Belgium,

Abstract – **The increased number of marine works occurring in the North Sea, such as for offshore renewables infrastructure and aquaculture, gave rise to more frequent Environment Impact Studies in the area. Activities with impact on turbidity or light penetration might have secondary impact on water quality and other aquatic parameters such as primary production and nutrient levels.**

To study such phenomena, IMDC has recently started the implementation of water quality simulations in TELEMAC-3D. As a basis, the three-dimensional hydrodynamic model of the Southern North Sea and English Channel has been chosen (KaZNo model). TELEMAC-3D was applied coupled to the AED2 library to determine the nutrient cycle, primary production, and zooplankton grazing. The coupling allows to solve the interactions between hydrodynamics (transport, diffusion) and the aquatic ecodynamics. Assumptions were made for river inflow nutrient conditions. This step resulted, after calibrating a number of parameters, in a satisfactory comparison of modelled and in situ monitored seasonal patterns of Chl-a levels.

Keywords: Water quality; TELEMAC-3D; North Sea, English Channel, AED2

I. INTRODUCTION

Eutrophication and algae blooms has been one of the major environmental issues in the North Sea for decades, enhanced by anthropogenic stressors. More specifically, eutrophication is driven by the continuous increase of nutrient concentration, especially the increased availability of nitrogen and phosphorous. The North Sea is considered a nutrient-enriched coastal zone where nutrient loads primarily arrive by riverine sources (such as rivers Scheldt, Rhine and Seine). High nutrient concentration drives intense phytoplankton blooms with large phytoplankton biomass. Along the continental coast line of the North Sea, dominant phytoplankton are diatoms that are characterised by early spring blooms, followed by an important development of Phaeocystis colonies [1].

Climate change plays an important role on the expansion of biomass production by affecting the temperature of the area. It is expected that the following years the North Sea will become warmer. For this reason, an increasing interest is observed into managing the biochemical pollution observed in the area. Numerical models that allow to predict the aquatic ecodynamics of the system accurately under different meteorological and eutrophication scenarios, are proven to be useful tools for understanding and managing these issues. However, a crucial parameter for the proper use of the numerical models is the availability and accessibility of monitoring data (for calibration and validation). For the moment, available data is limited despite the great deal of scientific research has been carried out in this region [3].

In the framework of an OSPAR initiative six ecosystem models (MIRO&CO-3D BE, ECO_MARS3D FR, ECOHAM4 DE, Delft3D-GEM NL, Cefas GETM-BFM UK, POL POLCOMS-ERSEM UK-POL) have been developed to investigate the influence of the riverine nutrient loads on the North Sea system. In this project, it was concluded that the winter sea nutrient concentration has a high response with the reduction of the riverine nutrient inputs. However no similar behaviour was observed for chlorophyll or net primary production [2]. In addition, it was proven that models could be applied to support the assessment process and predict the future eutrophication status of specific water bodies.

The goal of this paper is to use the aquatic ecodynamics library AED2 coupled to TELEMAC-3D to calculate the temporal evolution of nutrients and chlorophyll-a (chl-a) in the Southern North Sea. The performance of the model was tested against available measurement data in the area of interest. The long-term objective of this work is that the developed model will be used for environment impact assessment studies in the area.

The present text is organised as follow: Initially, the setup of a model of the Southern North Sea is presented in section II and in section III the required changes made to the TELEMAC code are described. Since the water quality variables depend strongly on the water temperature, the calibration of the water temperature is described in detail in section IV. Preliminary results of the water quality model in terms of nutrient and chlorophyll-a concentration for a full year simulation are reported and compared to observations in section V. Finally, the paper ends with some conclusions.

II. MODEL SETUP

The water quality modelling is performed with the in-housed developed TELEMAC-3D model of the Southern North Sea (KaZNo model), coupled with AED2 library see Figure 1.

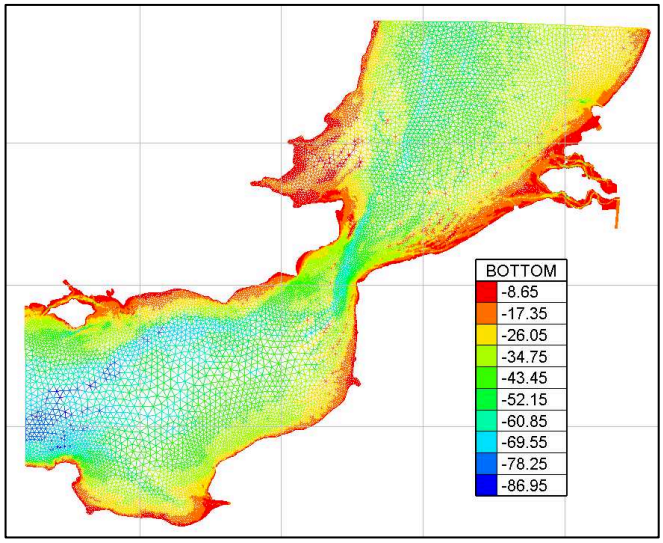

Figure 1. Figure II-1: Mesh and bathymetry of the Kazno Model (bathymetry is relative to m MSL).

The total number of computational nodes is 22,941, with 43,156 triangular elements. To better represent the water quality process, the KaZNo model runs in 3-D mode with 12 vertical nodes (11 layers) using equivalent sigma coordinates (0, 0.1, 0.2…0.9 and 1.0 from bottom to top). The mesh resolution varies from 500 m near the coast to maximum 10 km in deep waters. The model bathymetry is adopted from the EMODNET 2018 dataset with a spatial resolution of 1/16 × 1/16 arc minutes (circa 115 × 115 meters).

The hydrodynamic condition (water level and velocity) at the northern and western offshore boundary sections are computed by the in-house 2D barotropic model continental shelf model iCSM [4, 5] The hourly salinity and temperature data at the offshore boundary are provided by Copernicus Marine (https://resources.marine.copernicus.eu/product-detail/NWSHELF_MULTIYEAR_PHY_004_009/INFORMATION). Daily data of river discharge and nutrient concentration (NH4, etc) [8] are imposed at the river boundaries of Rhine, Scheldt and Seine.

The meteorological surface forcing includes the space- and time varying wind (at 10-meter height), air pressure at MSL, 2-meter air temperature, relative humidity and cloud cover, which are provided by the ERA5 hourly dataset of European Centre for Medium-range Weather Forecasting (ECMWF).

The model runs for the entire year of 2015. The initial condition of salinity and temperature are also taken from data by Copernicus Marine.

The hydrodynamic parameter settings of the KaZNo model are summarized in Table I.

Table I Model parameters.

Parameter	**Description**
Time Step	120 s
Number of vertical levels	10
Version TELEMAC	v8.1goblinshark
Salt transport	On
Wind	On
Roughness formula	Nikuradse law
Bed roughness value	Space varying roughness field
Option for the treatment of tidal flats	1: equations solved everywhere with correction on tidal flats
Treatment of negative depths	2: flux control
Free surface gradient compatibility	0.9
Vertical turbulence model	2: MIXING LENGTH
Minxing length model	3: Bakhmetev distribution
Horizontal turbulence model	4: Smagorinski
Scheme for advection of velocities	1: characteristic method
Scheme for advection of tracers	13: Leo Postma for tidal flats
Solver for Propagation	7: GMRES
Scheme for diffusion of tracers	0: No diffusion (see section III.D) + set_dif.f for vertical diffusion.

III. CODE CHANGES TO RUN AED-2

A couple of changes were implemented to TELEMAC-#D in order to be able to perform the study.

A. Meteorlogical input

In TELEMAC, there are two different models for the atmospheric exchange, a linearized model, which uses the water temperature at the surface and the air temperature (at an elevation of 2m above the sea), and a full energy balance, which uses air temperature, air pressure, nebulosity and relative humidity as input parameters. The model domain in the current study is quite large, meaning that it is likely that substantial spatial variation occurs in these parameters. However, for nebulosity and relative humidity, it is currently only possible to use a time series without spatial variation. Therefore, some code was added to allow these variables to be read. Also, a modification was made to the source code, because the atmospheric pressure in TELEMAC uses a different unit in different modules: Pa is used for the hydrodynamic calculation in TELEMAC-2D and TELEMAC-3D, whereas hPa is used for the atmospheric exchange modelling in WAQTEL.

A large number of meteorological variables for a full year, leads model to large input files when the data is interpolated to the mesh. However, the resolution of the meteorological input data (from ERA-5) is substantially coarser than the mesh resolution of the TELEMAC model. Reading the meteo data at the original mesh, rather than on the TELEMAC mesh, can reduce the file size of the meteorological data substantially. Therefore, a modification was implemented to the

`find_variable.f` subroutine that is used in TELEMAC to read data from Selafin files, which allows the use of input data with a mesh that is different from the computational mesh. Data from the meteo file are automatically interpolated to the computational mesh using linear interpolation. In order to ease the implementation, and in order to prevent the large time loss during partitioning input files in PARTEL, the full meteorological mesh is read by all parallel processors.

Finally, the code was adapted to read a spatially varying Secchi depth from the WACGEO file, which is then used in the energy balance for calculating the water temperature. For the moment, the spatially varying Secchi depth is only used in the calculation of the water temperature, and not yet for the water quality calculation in AED2. In the later case, changes in the light penetration due to the presence of algae are taken into account is combination with a spatially constant background turbidity. It is planned to include the spatial variation of the background Secchi depth on the water quality calculations in a later stage. It is also planned to couple the calculation of the Secchi depth to the calculation of cohesive sediment concentrations that are calculated using GAIA.

B. Implicitation of the source terms

In the original implementation of TELEMAC-3D coupled to AED2, all source terms were discretised explicitly in time:

$$\frac{c^{n+1} - c^n}{\Delta t} + ADV + DIFF = S(c^n)$$

Here, c^{n+1} and c^n are the concentrations of the water quality variables at time steps n+1 and n respectively, Δt is the time step, ADV and $DIFF$ are the advection and diffusion terms, which we will not consider here, and $S(c^n)$ is the source term. This method is conditionally stable, but with a time step criterion, which is roughly given by:

$$\Delta T < -c^n / S(c^n)$$

It is easy to show that larger time steps lead to the occurrence of negative concentrations, which then will lead to problems in the calculation of the sources in AED2 in the next time step. In order to prevent instabilities, the numerical discretisation was changed to an implicit discretisation using Patankar's [9] method:

$$\frac{c^{n+1} - c^n}{\Delta t} + ADV + DIFF = \frac{S(c^n)}{c^n} c^{n+1},$$

which is based on the assumption that $\frac{c^{n+1}}{c^n} \approx 1$. Using this method, it was found that the stringent time step limit that were found with the original implementation indeed disappeared, thus allowing for time steps of the order of minutes (they are now limited by the hydrodynamic processes), whereas previously the maximum time step was of the order of seconds. This code change has been included in the official TELEMAC release v8p3.

C. Drying-flooding

When the first test runs were performed, the model crashed rapidly. After investigating the instabilities, it appeared that these are related to the calculation of source terms and surface boundary conditions for water quality and temperature on cells with small water depths. Therefore, a threshold water depth was implemented, currently set to 0.1 m, below which, no water quality calculations are calculated using AED2, and below which surface boundary conditions and source terms are not applied in the tracer equation in TELEMAC-3D. An additional change was made to the code of the NERD scheme, as still some crashes occurred, related to tracer transport on areas with very small water depths ($O(10^{-3}$ m)), where concentrations of tracers (like dissolved oxygen) all of a sudden increased rapidly. In order to overcome this issue, the code of `cvdf3d.f` was changed, such that for nodes with a water depth lower than 0.01 m, the tracer concentration does not change due to advection[8]. After these modifications, the water quality model could be run for a full year period, without any crashes.

D. Settling velocity improvements

In the original implementation of the coupling, a separate settling routine (called `SETTLING`) was included in the module `t3d_aed2.F90`. However, it appeared that the changes in the concentrations due to the settling of water quality constituents, where later overwritten in the advection diffusion module. Instead of debugging this routine, it was chosen to use the existing settling functionalities (developed for sediment) in TELEMAC-3D. The code was modified, such that the settling velocities coming from AED2 are copied to the variable containing the settling velocities in TELEMAC-3D (called WCHU), which has a default value of 0.0 m/s (no settling). In this way, the `set_dif.f` subroutine, for which a version including source terms and surface boundaries was previously developed [10], can be used to calculate the vertical settling and vertical diffusion of the water quality variables. When then the horizontal diffusion is switched off, which typically leads to very limited changes in the results, because the used advection schemes in TELEMAC are rather diffusive, the simulations are speedup substantially.

IV. WATER TEMPERATURE CALIBRATION

Knowing the importance of sea water temperature on driving water quality processes, an accurate representation of sea water temperature is necessary prior to perform water quality modelling. The measureddata of sea water temperature collected at a number of stations at the Belgian Coastal Zone (Figure 2) from Meetnet Vlaamse Banken, are used for the sea water temperature calibration.

[8] Additionally, tests were performed setting the fluxes to and from dry nodes (defined as cells with a water depth lower than 1 cm) to zero. The advantage of this approach is that the tracer mass is fully conserved. It appeared that in these simulations the maximum occurring tracer values decreased, leading to an improved model stability. However, the decrease was substantially less, and very high tracer values were still encountered on dry areas. Therefore, this method was not used further.

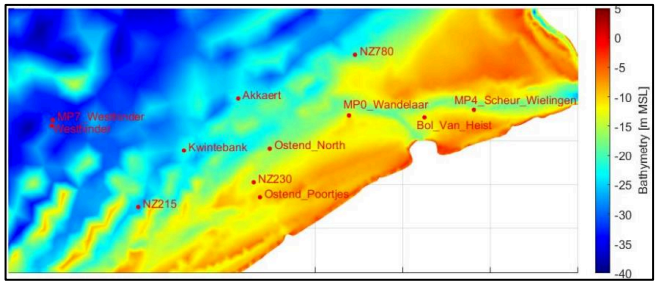

Figure 2. Figure IV-1: Measurement stations of sea water temperature in the Belgian coastal zone.

The calibration is firstly carried out for ATMOSPHERE-WATER EXCHANGE MODEL = 1 (linearised formula at the free surface), for which the optimal calibration parameter C_ATMOS (coefficient to calibrate the atmosphere-water exchange model) is found to be 0.0035.

For ATMOSPHERE-WATER EXCHANGE MODEL = 2 (model with complete energy balance), the most sensitive parameter is found to be the Secchi depth. Other parameters such as coefficients of aeration formula, coefficients for calibrating atmospheric radiation, coefficients for calibrating surface water radiation, coefficient of clouding rate etc are found to have a limited impact on the sea water temperature. The space varying Secchi depth map are adopted from [6] and is implemented in the KaZNo model.

After calibration, the KaZNo model reproduces sea water temperature in the North Sea reasonably well, with an average root mean square error (RMSE) for the sea water temperature of 0.8° C with both ATMOSPHERE-WATER EXCHANGE MODEL of 1 and 2 (Figure 3 and Table II). Time series plots are shown for the measurement station at Akkaert and Westhinder (Figure 4 and Figure 5). The yearly patterns of the sea water temperate variations are well captured by the KaZNo model.

It is also noticeable that with ATMOSPHERE-WATER EXCHANGE MODEL = 2, the daily variation of sea water temperature is better simulated, which might be important for the sea water quality modelling. Therefore, the water quality modelling will proceed with ATMOSPHERE-WATER EXCHANGE MODEL = 2.

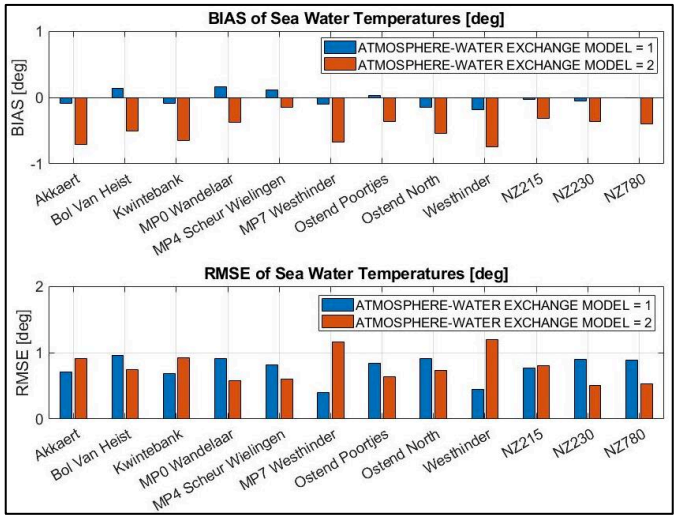

Figure 3. Figure IV-2: Bias and RMSE of the sea water temperature with ATMOSPHERE - WATER EXCHANGE MODEL = 1 and 2.

Table II RMSE of sea water temperature [deg C] with atmosphere - water exchange model = 1 and 2.

Stations	**atmosphere - water exchange model = 1**	**atmosphere - water exchange model = 2**
Akkaert	0.7	0.9
Bol Van Heist	1.0	0.7
Kwintebank	0.7	0.9
MP0 Wandelaar	0.9	0.6
MP4 Scheur Wielingen	0.8	0.6
MP7 Westhinder	0.4	1.2
Ostend Poortjes	0.8	0.6
Ostend North	0.9	0.7
Westhinder	0.4	1.2
NZ215	0.8	0.8
NZ230	0.9	0.5
NZ780	0.9	0.5
Average	**0.8**	**0.8**

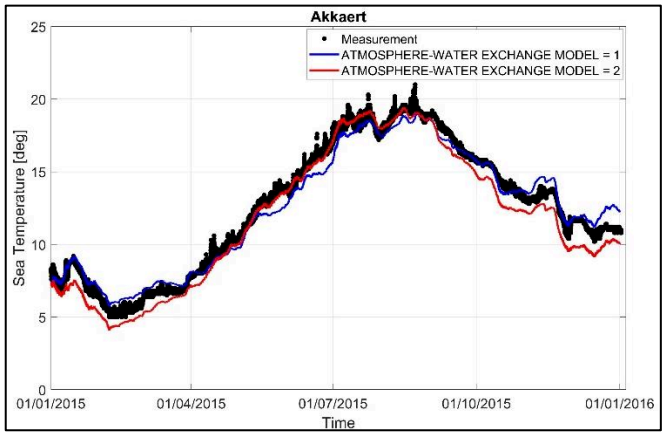

Figure 4. Figure IV-3: Comparison of measured and modelled sea water temperature at Akkaert

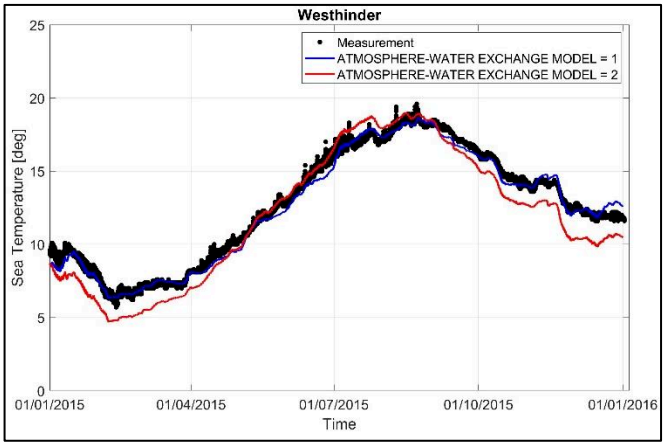

Figure IV-4: Comparison of measured and modelled sea water temperature at Westhinder .

V. PRELIMINARY RESULTS WATER QUALITY MODELLING

To numerically reproduce the nutrient cycle and primary production in the North Sea the Aquatic EcoDynamics (AED2) model was used [7]. AED2 is a biochemical library that consists of various modules that allow to simulate different processes that play a role in the biochemical cycle of an aquatic ecosystem. In Table III the modules used in the present study are presented, along with the simulated variables of each module.

Table III AED2 modules and the simulated parameters used in the present model to study water quality in North sea

Module	**Simulated variable**
sedflux	oxygen sediment flux
Oxygen	Dissolved oxygen
Carbon	Inorganic carbon
Silica	Silica
Nitrogen	Ammonium
	Nitrate
Phosphorus	Phosphate
Organic matter	Particulate organic carbon (POC)
	Particulate organic nitrogen (PON)
	Particulate organic phosphorus (POP)
	Dissolve organic carbon (DOC)
	Dissolve organic nitrogen (DON)
	Dissolve organic phosphorus (DOP)
Phytoplankton	Diatoms
	Phaeocystis
Zooplankton	Copepods

In the North Sea, two phytoplankton groups are dominant and used in the present model: diatoms and phaeocystis. Diatoms are typically related with lower optimum water temperatures, whereas phaeocystis colonies are linked to higher ones [1]. Moreover, Copepods grazing only on diatoms are included in some of the sensitivity runs performed in the framework of the present study.

For the initialization of the model, representative values of oxygen, nutrient and chlorophyll-a concentration were used, based on measurement data collected from Belgian Marine Data Center (BMDC, https://www.bmdc.be/NODC/search_data.xhtml;jsessionid=k7Wb3MSNEd58EOEg-D4zbZJnaJKbOGnKOzVQMRu.teuthida) for the year 2015 at different locations in front of the Belgian coast zone. The exact locations of the BMDC measurement points are shown in Figure 6

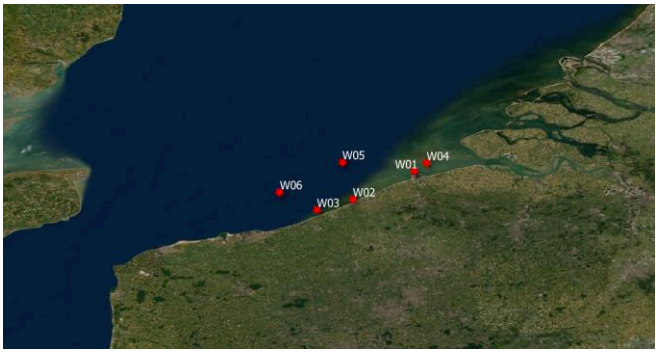

Figure 5. Figure V-1: Measurement stations of nutrients and chlorophyll-a concentration.

The main challenge for the calibration of the water quality model, is the large number of calibration parameters (more than 100). However, in the present study the calibration is focused on the most sensitive ones as identified from a previous sensitivity analysis. In addition, some parameters for the oxygen and nutrient were also manipulate (eg oxygen sediment flux, reaction rate of nitrification and reaction rate of denitrification). However, their influence on the results was less evident. The range of the calibration parameters is selected based on literature [1, 7].

As mentioned above the calibration of the water quality model is quite challenging and the available measurements limited. In this paper, calibration is mainly focused on the time evolution of chl-a concentration at the North Sea. In Figure 6 to Figure 11 the preliminary results in terms of surface chl-a concentration over an entire year, obtained from four different sensitivity runs are shown. The presented time series are extracted at the measurements points shown in Figure 6. An overview of the sensitivity runs performed in this study is presented in Table IV. The first three runs indicate the influence of silica uptake and Copepods grazing on the chl-a concentration. More specifically, in run01 silica uptake is not taken into account and the zooplankton module is not active. In run02, the silica uptake for diatoms is activated. Run03 is similar to run01 but Copepods grazing is considered only on diatoms. It can be noticed that silica uptake and the presence of zooplankton lead to a decrease of chlorophyll-a. Therefore, in run04, where both silica uptake and zooplankton are activated, the basic calibration parameters for the phytoplankton groups have been adjust to better reproduce the phytoplankton bloom.

Table IV Overview of the sensitivity runs performed

Runs	Activated modules	
run01	Sedflux oxygen carbon Organic matter	Nitrogen Phosphorus Phytoplankton
run02	Sedflux oxygen carbon Organic matter	Nitrogen Phosphorus Silica Phytoplankton
run03	Sedflux oxygen carbon Organic matter	Nitrogen Phosphorus Phytoplankton Zooplankton
run04	Sedflux oxygen carbon Organic matter	Nitrogen Phosphorus Silica Phytoplankton Zooplankton

For the validation of the numerical model, the obtained results are compared with both BMDC measurements and satellite data provided by Copernicus (https://marine.copernicus.eu/). It is worth noting that for year 2015 the available BMDC measurements are limited. Furthermore, an inconsistency can be observed between the two data sets. Based on BMDC data, the phytoplankton bloom occurs at the end of March whereas the satellite data suggest that the bloom occurs in the second half of April. Since satellite data is less scarce, they are here considered as more relevant for the validation of the model.

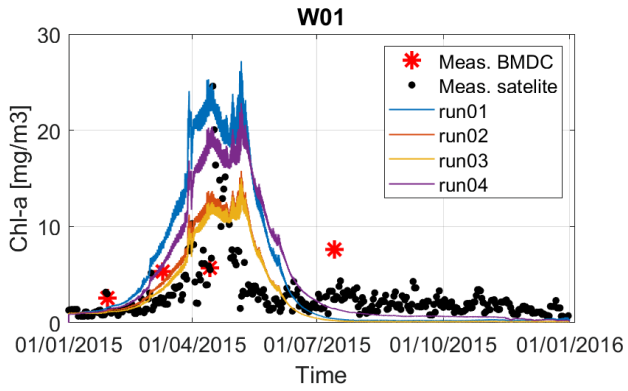

Figure 6. Figure V-2 Comparison of model output and measured data (both BMDC and satellite data) in terms of chl-a concentration for 2015, at the measurements point W01.

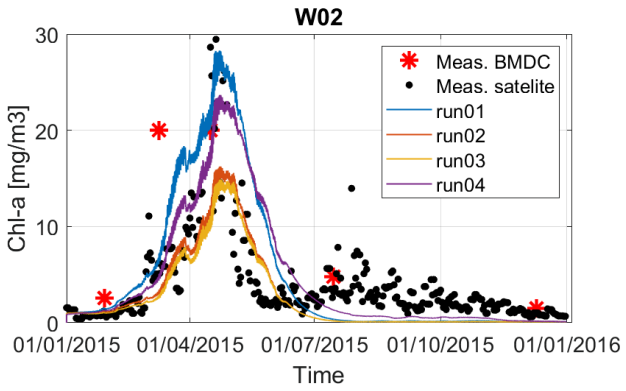

Figure 7. Figure V-3 Comparison of model output and measured data (both BMDC and satellite data) in terms of chl-a concentration for 2015, at the measurements point W02.

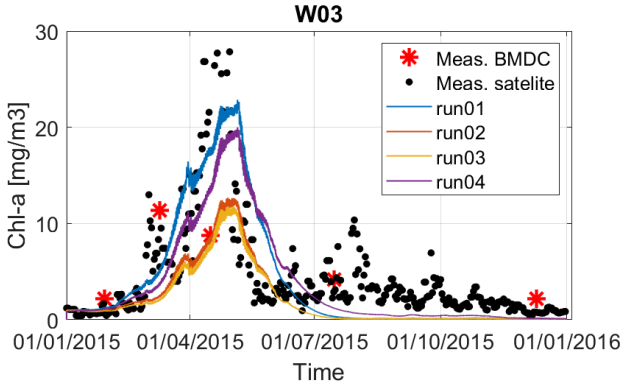

Figure 8. Figure V-4 Comparison of model output and measured data (both BMDC and satellite data) in terms of chl-a concentration for 2015, at the measurements point W03.

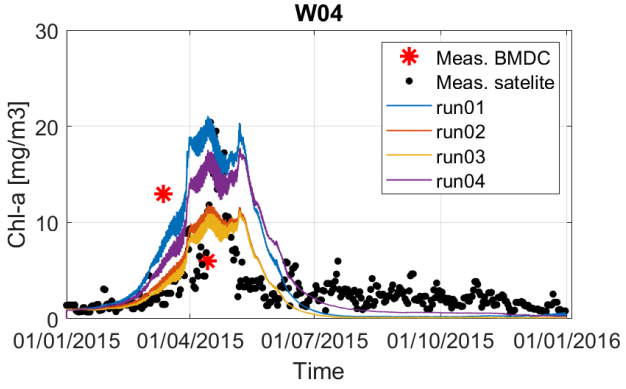

Figure 9. Figure V-5 Comparison of model output and measured data (both BMDC and satellite data) in terms of chl-a concentration for 2015, at the measurements point W04.

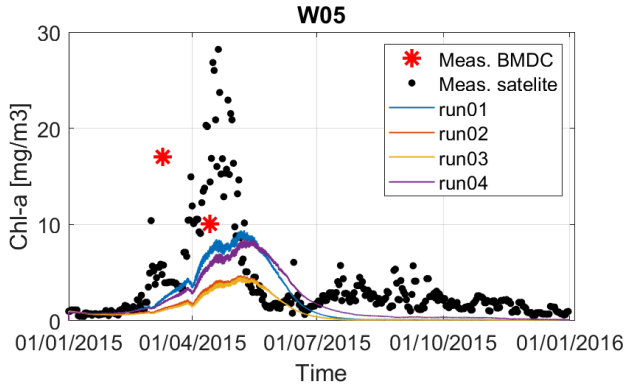

Figure 10. Figure V-6 Comparison of model output and measured data (both BMDC and satellite data) in terms of chl-a concentration for 2015, at the measurements point W05.

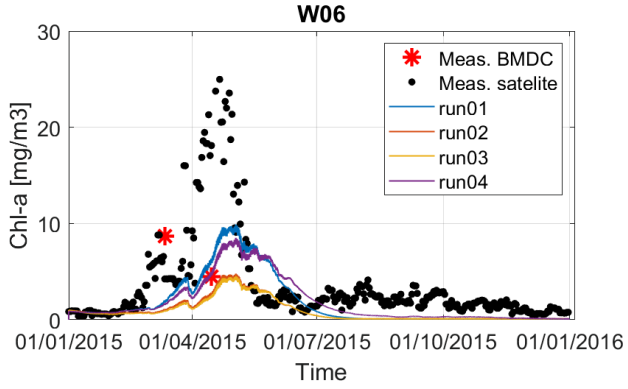

Figure 11. Figure V-7 Comparison of model output and measured data (both BMDC and satellite data) in terms of chl-a concentration for 2015, at the measurements point W05.

It can be observed that the model results are in good agreement with the satellite data, for the stations located closer to the coast. The chl-a peak during the second half of April is well represented as well as the limited availability of phytoplankton biomass the rest of the year. However, an noticeable underestimation of chl-a is observed at the stations W05 and W06 located more offshore. This may be related to the fresh water plumes generated in the mouth of Scheldt and Rhine river. Fresh water is one of the main carries of nutrients into the North Sea which are necessary for phytoplankton growth. It seems that in the model the fresh water zone is too small, which may be related to the treatment of the lateral boundary conditions. Further work is planned in the future to improve this issue.

The nitrate and phosphate concentration at stations W02 and W03 are also shown in Figure 12 to Figure 15. The nutrients dynamics reproduced by the numerical model are consistent with the patterns of the phytoplankton biomass. The phytoplankton growth observed in the second half of April consumes the stock of nutrients in the water column (particularly of nitrate). However, it can be observed that nitrate concentration do not recover after the decay of the phytoplankton. Thus, nitrate concentration is very low at the end of the simulated year. This issue may be related to the offshore BC conditions, for which it is difficult to prescribe correct values due to the lack of available data. One of the possible solutions to overcome this issue is to apply zero-gradient boundary conditions for tracers, which allow the nutrients at the boundary to adapt to the nutrient concentrations inside the domain. A more detailed validation of the nutrient dynamics is planned in the future.

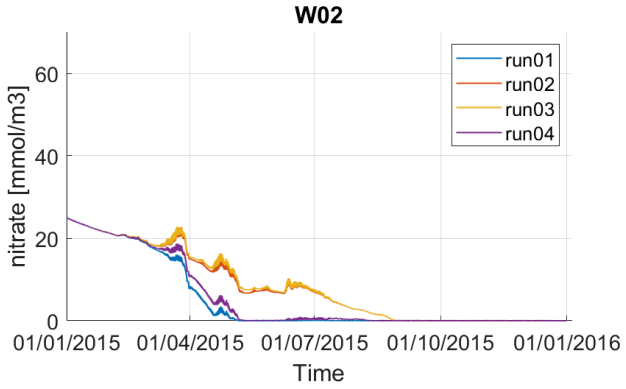

Figure 12. Figure V-8 Model results of nitrate concentration for the four sensitivity runs, at station W01.

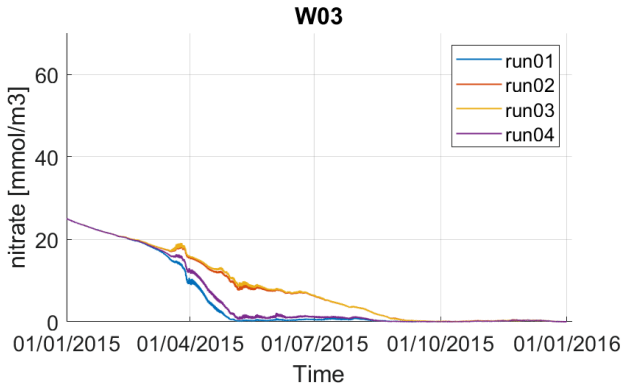

Figure 13. Figure V-9 Model results of nitrate concentration for the four sensitivity runs, at station W02.

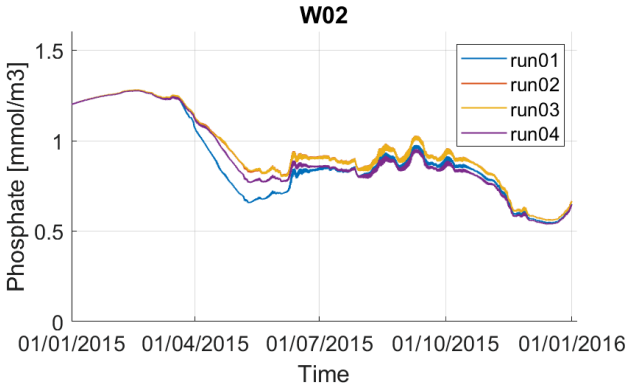

Figure 14. Figure V-10 Model results of phosphate concentration for the four sensitivity runs, at station W01.

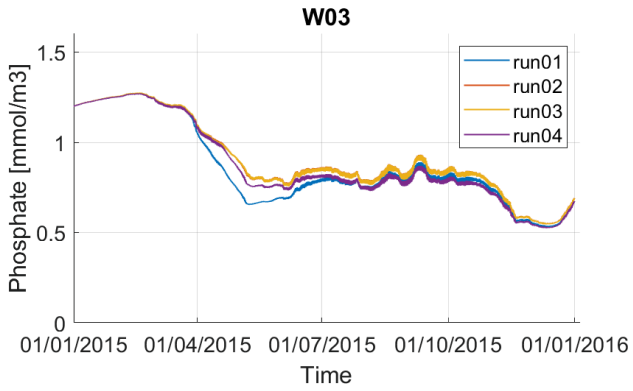

Figure 15. Figure V-11 Model results of phosphate concentration for the four sensitivity runs, at station W02.

VI. SUMMARY AND CONCLUSIONS

In this work, TELEMAC-3D coupled to the AED2 library were used in the KaZNo model to simulate the thermal dynamics and biochemical cycle in the North Sea for the year 2015. However, in order to perform this study a couple of modification were required in TELEMAC-3D. A brief description of the implemented changes are given in the paper.

Due to the high importance of the water temperature in the biochemical cycle of an aquatic ecosystem this work is initially focused on temperature calibration. Two different atmospheric exchange models were used. A linearized model, which uses the water temperature at the surface and the air temperature at an elevation of 2m above the sea and a more complex model, in which the complete energy balance is taken into account. Both models showed a very good performance based on measurement data of sea water temperature from the Meetnet Vlaamse Banken, collected at a number of stations at the Belgian Coastal. The averaged RMSE was around 0.8ºC, for both atmospheric models.

In terms of chlorophyll-a concentration the model results show a correct simulation of the phytoplankton growth compared to the available satellite data. Phytoplankton biomass starts growing in March and reaches its peak at the second half of April. The rest of the year chl-a concentration remains low. It is also indicated that for 2015 the simulated nutrient cycle is consistent with the patterns of the phytoplankton biomass.

A future goal of the present work is to further calibrate the nutrient cycle and zooplankton grazing. However, a necessary condition for the further calibration of the model is the availability of monitoring data. In addition, in order to improve the distribution of the chl-a concentration offshore further work is required for the better representation of the fresh water plume in the mouth of Scheldt and Rhine river. To do so a new zero-gradient boundary conditions for tracers will be applied. Finally, the use of a large number of racers (around 25) leads to substantial calculation times. In order to speed up the model, faster advection schemes for tracers are needed. Therefore, alternative advection schemes, based on the characteristic method, but with correction to ensure mass conservations are currently being implemented in TELEMAC-3D.

REFERENCES

[1] C. Lancelot, Y. Spitz, N. Gypens, K. Ruddick, S. Becquevort,V. Rousseau, G. Lacroix, and G. Billen. “Modelling diatom and Phaeocystis blooms and nutrient cycles in the Southern Bight of the North Sea: the MIRO model”. Marine Ecology Progress Series, vol. 289, pp. 63-78, March 2005.

[2] H.J. Lenhart, D.K. Mills, H. Baretta-Bekker, S.M. Van Leeuwen, J. Van Der Molen, J.W. Baretta, M. Blaas, X. Desmit, W. Kühn, G. Lacroix, and H.J. Los, “Predicting the consequences of nutrient reduction on the eutrophication status of the North Sea,” Journal of Marine Systems, vol. 81(1-2), pp. 148-70, April 2010.

[3] J.P. Ducrotoy, M. Elliott, and V.N. de Jonge, V.N., “The north sea,” Marine pollution bulletin, 2000, vol. 41(1-6), pp.5-23.

[4] K. Chu, W.A. Breugem and B. Decrop, “Improvement of a Continental Shelf Model of the North Sea”. TELEMAC User Conference, Antwerp, Belgium, 2020.

[5] K. Chu, W.A. Breugem and B. Decrop, “Automatic calibration of a continental shelf model of the North Sea using data assimilation algorithm”. Proc. 39th IAHR World Congr. Int. Assoc. Hydro-Environ. Eng. Res, 2022.

[6] K. Muylaert, M. Tackx, W. Vyverman, “Phytoplankton growth rates in the freshwater tidal reaches of the Schelde estuary (Belgium) estimated using a simple light-limited primary production model”. Hydrobiologia, vol. 540(1) pp.127-40, May 2005.

[7] M.R. Hipsey, L.C. Bruce, and D.P. Hamilton, “Aquatic Ecodynamics (AED) Model Library: Science Manual,” October 2013.

[8] Series E. OSPAR Integrated Report 2003 on the Eutrophication Status of the OSPAR Maritime Area Based Upon the First Application of the Comprehensive Procedure.

[9] S.V. Patankar, “Numerical heat transfer and fluid flow”. CRC press, 2018.

[10] W.A. Breugem, “Ongoing developments in TELEMAC and TOMAWAC at IMDC”. In Online proceedings of the papers submitted to the 2020 TELEMAC-MASCARET User Conference, pp.115-121, October 2020.

Open water swimming in urban areas *E. coli* distribution with TELEMAC-3D

Natalia Angelotti[1,2], Arthur Guillot Le-Goff[1], Rémi Carmigniani[2], Brigitte Vinçon-Leite[1]
natalia.angelotti-de-ponte-rodrigues@enpc.fr, Champs-sur-Marne, France
[1]: LEESU, Ecole des Ponts ParisTech, UPEC, Champs-sur-Marne, France
[2]: LHSV, Ecole des Ponts ParisTech, EDF R&D, Chatou, France

Abstract – **Swimming in urban open waters is increasingly popular. In Paris, a bathing area is open during summer in La Villette Basin, our study site. To control sanitary risks, the European Bathing Water Directive (2006/7/EC) classifies the water quality according to thresholds of indicators of pathogenic microorganisms, the faecal indicator bacteria (FIB), such as *E. coli*. The reference FIB enumeration methods take more than 24 h.**

To obtain, in due time, information on the sanitary conditions in the bathing area, in this study, two issues were considered.

On the one hand, for assessing more rapidly the microbiological level, a relationship between bacterial activity and fluorescent dissolved organic matter (FDOM) can be used. Here, *E. coli* was estimated from a relationship with tryptophan-like fluorescence (TLF) established for La Villette system.

On the other hand, the thermal stratification of the water column observed during summer heat waves can impact the spatiotemporal distribution of FIB, in water bodies with low current speed. The three-dimensional hydrodynamic model TELEMAC-3D was run to predict the space and time evolution of *E. coli*. To reproduce the thermal stratification in the basin, WAQTEL thermal process was activated. TLF data measured upstream were used as an input for the simulations.

Two periods of ten days were simulated. In the first period (12-22 September 2021), including a heavy rain event, five field measurements of *E. coli* were available. The model results were converted from TFL to *E. coli* and then compared to field data. There was a good agreement between them (RMSE = 197 MPN/100mL, r^2 = 0.74). The regulatory threshold was exceeded during four days and the bathing area would have had to be closed during this period.

The same *E. coli* input was used for a second simulation run during a heat wave period (13-23 July 2022). The thermal stratification was correctly reproduced. A slight lateral heterogeneity of *E. coli* distribution between left and right bank of the basin was simulated.

These preliminary results indicate the good capability of a warning system combining upstream continuous TLF monitoring with hydrodynamic modelling. It would support a better assessment of sanitary conditions in a bathing area and improve the accuracy on the duration of the regulatory threshold exceedance.

Keywords: thermal stratification, sanitary risk, bathing, open water, *E. coli*, faecal contamination, TELEMAC-3D.

I. INTRODUCTION

Open water sport events are increasingly popular in urban areas. Some open water competitions of the International Federation of Swimming are performed in urban freshwater bodies (FINA https://www.fina.org/open-water). For example, in July 2022, the second phase of Marathon Swim World Series took place in Paris, at the Ourcq Canal.

The prefectural decree of 1923, banning public swimming in the Seine River, is still in force today. An exception in Paris region, since 2017, is the public swimming area installed in La Villette Basin during summer.

Reintroducing urban bathing is part of environmental policies aimed at recovering the ecological quality of the river in wider Paris. Urban bathing mitigates the urban heat island effects of Paris and reduces the heat wave impact on the population. Furthermore, it is a way of reclaiming public space and reinforcing the links of the city dwellers with nature.

However, open water swimming can cause waterborne diseases. To control the sanitary risks, the European Directive of Bathing Waters 2006/7/EC [1] classifies the water quality in function of the concentrations of indicators of faecal contamination known as faecal indicator bacteria (FIB). Two bacteria are used as reference parameters in the European classification: *Escherichia coli* (*E. coli*) and intestinal enterococci (IE). For inland waters, the threshold for a sufficient water quality for bathing is 900 MPN/100mL for *E. coli* and 330 MPN/100mL for IE, both values based upon a 90-percentile evaluation. In this study, *E. coli* was used as a representative indicator of FIB. The reference method for *E. coli* enumeration, in the laboratory, has a long response time, taking from 24h to 48h [2].

In some watercourses, the analysis of the microbiological water quality is performed on a daily basis, upstream of the bathing area, in order to anticipate the decision of a closure of the bathing area. To improve the accuracy of the decision making and reduce the risk of having undetected contamination between two measurements, a more frequent monitoring time step is required.

The relationship between bacterial activity and fluorescent dissolved organic matter (FDOM) may provide a high-frequency assessment of the microbiological water quality. A possible indicator of *E. coli* is a fluorescence

signal known as tryptophan-like fluorescence (TLF) or peak T [3]–[5].

In water bodies of low current speeds, which is frequently the case in bathing areas, a thermal stratification is observed during summer in the water column. In turn, it impacts current speeds and, consequently, the spatiotemporal distribution of FIB [6].

This work focused on monitoring and estimating sanitary conditions in an urban bathing area, Bassin de La Villette (Paris, France), aiming to anticipate a possible closure of the site and its duration. More precisely, the objective was to predict *E. coli* concentration at the bathing area. A three-dimensional hydrodynamic model, TELEMAC-3D, was used to predict spatiotemporal distribution of *E. coli* from the upstream measurement point to the bathing area. The WAQTEL thermal module was activated to reproduce the thermal stratification on the basin. To have a few-hour forecast of the sanitary risk at the bathing area, real-time data from the upstream point were used as an input. *E. coli* values were inferred from the TLF measurements through the relationship established for La Villette system.

II. MATERIAL AND METHODS

A. Study site and field data

La Villette system is located in the north-east of Paris. It is composed of a canal of 25 m wide and 800 m long and a basin of 75 m wide and 700 m long, where the bathing area is located (Figure 1).

The upstream point, point A, is equipped with a vertical chain of temperature and conductivity sensors located at three depths and a water level sensor. The downstream point, point B, is also equipped with a "three depth" sensor vertical chain for temperature and conductivity measurements. The measurement time step is 20 min.

At points A and B, sampling of surface water (0.40 m depth) was performed for fluorescence measurements. From 30th June to 20th September 2021, 17 grab samples were collected at each point.

During the same period, surface water sampling for FIB and fluorescence measurements was performed at point C. Point C is located in the middle of the system, at the end of the canal (Figure 1). Five episodes were sampled, two of dry weather and three of rainy weather. Hourly samples were taken automatically for 24 hours, from 9h to 9h the day after. All the samples were then mixed to obtain mean daily samples. During the dry weather episodes, two daily samples were obtained. For the rain episodes, the duration of the first one was two days (two samples) and the duration of the other two was three days (2x3 samples). A total of ten mean daily samples were collected.

FDOM and *E. coli* concentrations in the samples were measured at the laboratory. *E. coli* was measured according to ISO 9308-3 method. The uncertainty on *E. coli* data is around 25%.

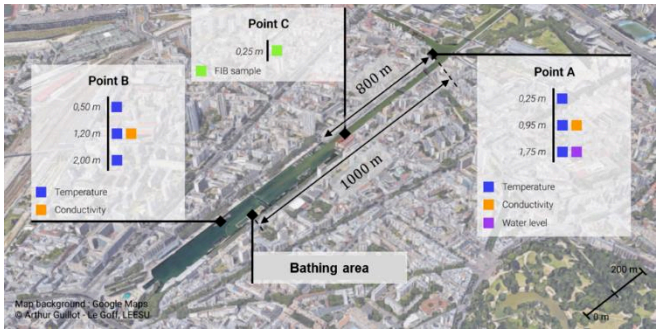

Figure 1. Location of the measuring stations at La Villette

FDOM measurements were performed on a Cary Eclipse Fluorescence Spectrophotometer (Agilent Technologies). For each sample, a simultaneous scan of excitation wavelength from 200 to 700 nm with 5-nm intervals and emission wavelength from 250 to 750 nm with 2-nm intervals was performed. The processing of the EEM spectra was conducted according to [7]. Data are expressed in Raman Units (RU) according to [8]. The TLF values, corresponding to the wavelength range 275 nm – 340 nm, respectively for Excitation and Emission wavelengths [9], were used to find a relationship with *E. coli* data.

B. E. coli estimation

The relationship between TLF and *E. coli* was established through the data of the 10 samples collected between June and September 2021 in La Villette basin. The range of *E. coli* data was from 98 to 1400 MPN/100mL. The range of TLF data was from 0.13 to 0.75 RU. The obtained linear relationship ($r^2 = 0.64$, $p = 4.10^{-5}$) is given by (1).

$$[E.\ coli] = 1381 \cdot \mathrm{TLF} \quad (1)$$

[*E.coli*] in MPN/100mL and TLF in RU.

C. Hydrodynamic model

The simulations were run using the v8p3 version of TELEMAC-3D on a Linux operating system. BlueKenue (3.3.4) was used for the preparation of geometry and mesh files and for the visualisation of the results.

1) Modelling domain

The domain goes from the canal round-about upstream to the downstream end of La Villette Basin (Figure 1). The 3D grid is composed by 10 layers of 0.30 m of depth and an average edge length of 5 m. The simulation results for the temperature and *E. coli* concentration at the surface and at the bottom layers are compared to field data at 0.5 m and 2.0 m, respectively.

The time-step of the model computation is of 20 s. The time step of the result output is 10 min

2) Hydrodynamic and heat exchange model

The thermal process was activated in WAQTEL module, considering the heat exchange of water with the atmosphere.

The lateral boundaries are defined as a solid wall. The upstream and downstream boundary conditions are defined

as open boundaries, upstream with prescribed water elevation and water temperature and downstream, prescribed flowrate.

To compute the heat exchange with the atmosphere, hourly meteorological data (wind speed and direction, air temperature, atmospheric pressure, relative humidity, cloud cover, and rainfall) are required. They were obtained from Le Bourget airport station, the nearest Météo France station (around 9 km in the North-East), excepted for cloud cover which is not available at Le Bourget. We used cloud cover from the Orly meteorological station (around 17 km in the South).

For upstream boundary conditions, water temperature and water elevation measured at point A were used.

Downstream, the outlet flowrate, Q, was computed using the water level measurements at the upstream point (point A) according to the Manning-Strickler equation (2).

$$Q(h) = K_S \cdot S_{tot} \cdot R_H^{2/3} \cdot i^{1/2} \quad (2)$$

Where Q (m^3/s) is the outlet flowrate, K_S ($m^{1/3}/s$) is the Strickler coefficient; S_{tot} (m^2), the total underwater section, R_H (m), the hydraulic radius, and i (m/m) the hydraulic slope.

The hydraulic radius (R_H) and the underwater section (S_{tot}) were computed using the water elevation, h and geometric data of the system obtained from a technical report [10]. Considering the macrophytes on the bed of the canal, a value of 2 $m^{1/3}/s$ for K_S was adopted.

The vertical turbulence model was Nezu and Nakagawa mixing length, with Viollet's damping function. The horizontal turbulent viscosity was considered constant. The Secchi depth was 0.9 m, derived from field data.

3) Microbiological input data

The TLF values obtained from the FDOM measurements at point A were linearly interpolated to an hourly time step. They were used as upstream input data, uniformly distributed on the water column, in the simulations. TLF was considered as a passive tracer.

4) Data processing

MATLAB (R2021b) was used for the preparation of input data and processing of simulation results. The model performance was assessed through two indicators, root mean square error (RMSE) and Pearson correlation coefficient (r).

D. Simulation periods

Two simulation periods were run. The first simulated period was 12-22 September 2021. It included a rainfall episode on 14th and 15th of September, with a total rain height of 28 mm in 48 hours. The results obtained for this period will illustrate the performance of the model to simulate the microbiological contamination level.

The second simulation period was 13-23 July 2022, a period of very high air temperature. Here, the impact of thermal stratification on a possible microbial contamination will be assessed.

III. RESULTS AND DISCUSSION

A. 12-22 September 2021

This period included a heavy rainfall episode on 14th and 15th of September, with a total rain height of 28 mm in 48 hours. Seven measurements of the microbiological indicator, TLF, were available during the period (Figure 2a). Before the rain event, the TLF level was around 0.14 RU. A value of 0.70 RU was observed on September 16th after the rain and TLF remained around 0.75 RU for 5 days, until September 20th, when it started to decrease (0.20 RU on 21st September). In parallel, 5 mean daily data of *E. coli* measured at point C were available (Figure 2b). The total number of available TLF and *E. coli* data are summarized in Table I.

To provide the upstream input of the microbiological indicator, TLF data were linearly interpolated at an hourly time step. The TLF simulation results were then converted in *E. coli* unit (MPN/100mL) using (1). Simulated *E. coli* was compared to the field data measured at point C.

For water temperature, model results and field data (Figure 3) were compared at the bathing area (point B). A good agreement was obtained, with RMSE of 0.66, 0.57, 0.53 °C and r^2 of 0.73, 0.74, 0.79 for the surface, middle and bottom layers, respectively.

Table I Number of TLF and E. coli data at each point

Period	**Point A**		**Point C**	
	TLF	***E. coli***	***TLF***	***E. coli***
12-22 September 2021	7	-	5	5

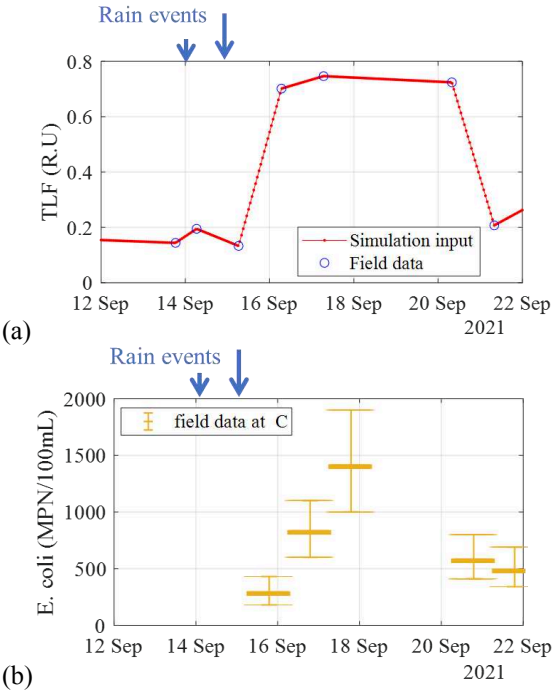

Figure 2. TLF as microbiological input at point A (a) and *E. coli* daily data at point C (b)

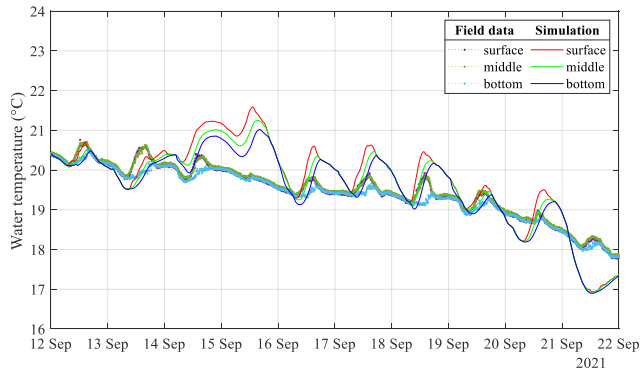

Figure 3. Water temperature at point B from 12 to 22/09/2021 – Field data and model results

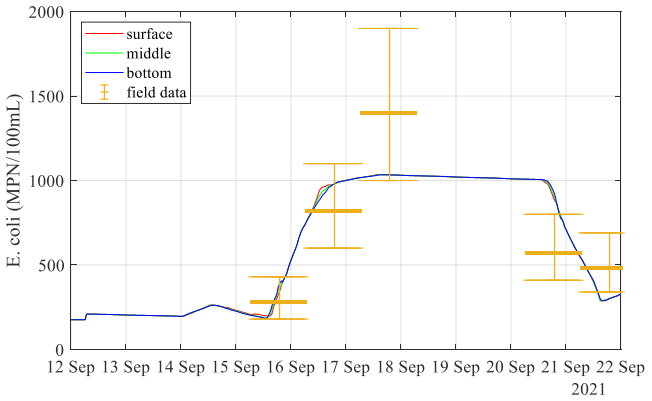

Figure 4. *E. coli* at point C – Simulation results and daily mean field data

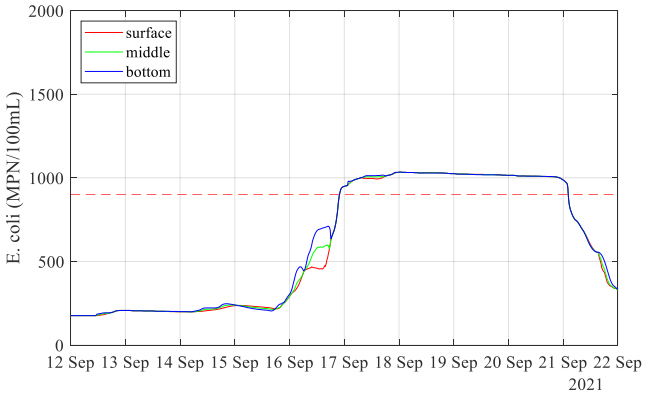

Figure 5. Simulation results of *E. coli* at point B

Over the whole period, the water column was slightly stratified during daytime, and was mixed during the night, with a temperature difference between the surface and the bottom layers of 0.21°C according to the field data and 0.34°C according to the model results.

To assess the microbiological results, the model output of TLF values were firstly converted to *E. coli* unit and then compared the field data measured at point C (Figure 4). The simulation results were within the uncertainty range of *E. coli* data. The agreement between the model results and the field data was very close, with a RMSE of 225 MPN/100mL and r^2 of 0.67.

The time evolution of *E. coli* at point B was then obtained from the TLF results (Figure 5) and compared to the sufficient quality threshold for bathing (900 MPN/100mL). The threshold was overpassed from the 17th to 20th September included, when the bathing area should be closed (it was the case!).

B. 13-23 July 2022

During this period, very high air temperature was recorded, with a maximum of 39.8 °C on 19th July. No *E. coli* data are available for this episode. For that reason, the data measured during the rain event of September 2021 were used to assess the impact of thermal stratification on *E. coli* distribution.

At the bathing area (point B), the water temperature range was [24.0 - 26.1 °C] for the field data and [22.9 - 26.8 °C] for the simulation results (Figure 6). There was a good agreement between model and data, with RMSE of 0.41, 0.47, 0.42 °C and r^2 of 0.70, 0.59, 0.66, respectively for the surface, middle and bottom layers.

From July 13th to 20th, the water column was stratified during daytime and mixed during the night. After July 20th, the stratification vanished. Over the stratified period, the maximum temperature difference between surface and bottom layers had a mean value of 0.97 °C for field data and of 0.91°C for model results. Over the whole period, the temperature difference between the bottom and the surface layers showed good agreement between field data and simulation results (RMSE = 0.19 °C and r^2 = 0.69).

The lateral heterogeneity of *E. coli* distribution at the basin area is illustrated on Figure 7. On July 17th at 13h00 (Figure 7 left), higher concentration reached earlier at left bank than at right bank. At the end of the simulated period, on July 22nd (12h00), *E. coli* spatial distribution also displayed heterogeneity between right and left banks (Figure 7 right) on July 22nd (12h00).

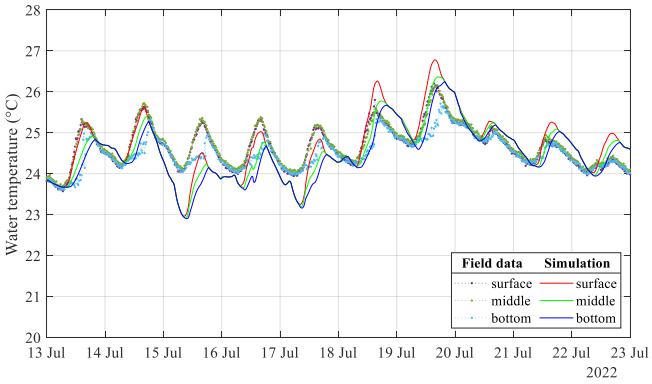

Figure 6. Water temperature at point B from 13 to 23/07/2022 – Field data and model results

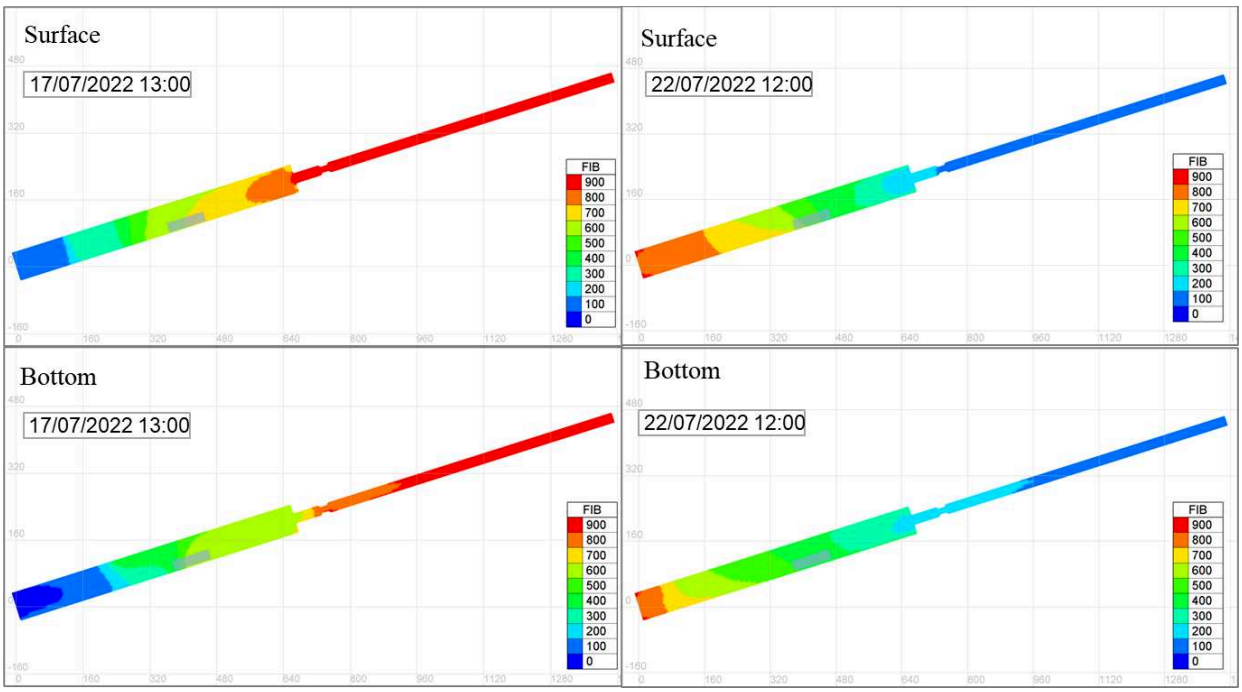

Figure 7. Spatio-temporal distribution of *E. coli* on the surface and bottom layers on July 17th at 13h00 (left) and on July 22nd at 12h00 (right)

IV. CONCLUSION

A monitoring system combined with model simulations was developed for the urban bathing area of Bassin de La Villette (Paris, France). The objective was to predict the overpassing of *E. coli* threshold for sufficient bathing water quality. The three-dimensional hydrodynamic model TELEMAC-3D was used to simulate *E. coli* spatial temporal distribution, from the upstream measurement point to the bathing area. The WAQTEL thermal module was activated to reproduce the thermal stratification on the basin.

Fluorescent dissolved organic matter (FDOM) was measured in grab samples, in parallel to *E. coli* enumeration. A relationship between *E. coli* and tryptophan-like-fluorescence (TLF) was established. As it is possible to monitor FDOM *in situ*, in the future, *E. coli* could be continuously estimated in Bassin de La Villette from its relationship with TLF values.

The first simulated period (12-22 September 2021) included a heavy rain episode. The model was able to simulate adequately the time evolution of *E. coli* level: increase of the concentration after the rain and decrease five days later. The regulatory threshold was exceeded, and the bathing area would have had to be closed. According to the model results, the closure should have occurred two days earlier (September 16th) than according to the field data (September 18th).

A second simulation was run during a heat wave (13-23 July 2022). The thermal stratification was correctly reproduced. During this period, a slight lateral heterogeneity of *E. coli* distribution between left and right bank of the basin was simulated.

The transfer time between points A and B estimated by the model varied between 11h 30 min and 16h 40 min. These results indicate that combining upstream continuous TLF monitoring with hydrodynamic modelling would allow to predict the exceedance of the regulatory threshold for water quality in a downstream bathing area. It would support the decision making on the closure/opening of the bathing area.

ACKNOWLEDGEMENT

This work is part of the OPUR project. The authors would like to thank our colleagues from ENPC/LEESU, particularly Philippe Dubois, for all support given with the implementation and maintenance of the measuring system, as well as Mohamed Saad, for the field campaigns.

We thank Manel Naloufi, Claire Therial and Françoise Lucas, from UPEC/LEESU, for the microbiological analysis and *E. coli* enumeration of samples from La Villette.

REFERENCES

[1] EU, 'Directive 2006/7/EC of the European Parliament and of the Council of 15 February 2006 concerning the management of bathing water quality and repealing Directive 76/160/EEC'. Feb. 15, 2006. Accessed: Nov. 16, 2020. [Online]. Available: https://eur-lex.europa.eu/legal-content/GA/TXT/?uri=CELEX:32006L0007

[2] ISO, 'ISO 9308-3:1998 - Water quality — Detection and enumeration of *Escherichia coli* and coliform bacteria — Part 3:

Miniaturized method (Most Probable Number) for the detection and enumeration of E. coli in surface and waste water', *ISO*, 1998.

[3] S. Nowicki, D. J. Lapworth, J. S. T. Ward, P. Thomson, and K. Charles, 'Tryptophan-like fluorescence as a measure of microbial contamination risk in groundwater', *Science of The Total Environment*, vol. 646, pp. 782–791, Jan. 2019, doi: 10.1016/j.scitotenv.2018.07.274.

[4] J. P. R. Sorensen *et al.*, 'Real-time detection of faecally contaminated drinking water with tryptophan-like fluorescence: defining threshold values', *Science of The Total Environment*, vol. 622–623, pp. 1250–1257, May 2018, doi: 10.1016/j.scitotenv.2017.11.162.

[5] A. Baker, S. A. Cumberland, C. Bradley, C. Buckley, and J. Bridgeman, 'To what extent can portable fluorescence spectroscopy be used in the real-time assessment of microbial water quality?', *Science of The Total Environment*, vol. 532, pp. 14–19, Nov. 2015, doi: 10.1016/j.scitotenv.2015.05.114.

[6] N. Angelotti, B. Vinçon-Leite, and R. Carmigniani, 'Hydrodynamic modelling for early warning of sanitary risks in open swimming waters', in *Proceedings of the papers submitted to the 2020 TELEMAC-MASCARET User Conference*, Oct. 2021, pp. 175–180.

[7] K. R. Murphy, C. A. Stedmon, D. Graeber, and R. Bro, 'Fluorescence spectroscopy and multi-way techniques. PARAFAC', *Anal. Methods*, vol. 5, no. 23, p. 6557, 2013, doi: 10.1039/c3ay41160e.

[8] A. J. Lawaetz and C. A. Stedmon, 'Fluorescence Intensity Calibration Using the Raman Scatter Peak of Water', *Appl Spectrosc*, vol. 63, no. 8, pp. 936–940, Aug. 2009, doi: 10.1366/000370209788964548.

[9] P. G. Coble, 'Characterization of marine and terrestrial DOM in seawater using excitation-emission matrix spectroscopy', *Marine Chemistry*, vol. 51, no. 4, pp. 325–346, Jan. 1996, doi: 10.1016/0304-4203(95)00062-3.

[10] SAFEGE, 'Elaboration d'un profil de baignade pour une baignade publique sur le bassin de la Villette à Paris. Rapport de phase 1: Etats des lieux'. Mairie de Paris-Suez, 2017.

Micropollutant and sediment interaction models using WAQTEL-MICROPOL module

Zied AMAMA[1], Florent TACCONE[1], Philippe CIFFROY[1]
zied.amama@edf.fr
[1]: EDF R&D National Laboratory for Hydraulics and Environment (LNHE)

Abstract – **The MICROPOL sub-module of WAQTEL simulates the exchanges of micropollutants between three compartments of the water column: Water (dissolved form), suspended sediment (adsorbed) and bed sediments (deposited). Micropollutant transport is mainly impacted by sediment processes (transport, deposition, and resuspension) and chemical reactions (sorption, desorption and decay) in 2D/3D. This article presents recent model development allowing to simulate transport of micropollutant considering one or two-step adsorption/desorption reversible reactions. In the first case, the dissolved form of micropollutant exchanges through direct adsorption or desorption with suspended sediments, forward and reverse kinetics being pseudo-1st order. In the second case, slowly reversible internal sediment sites are considered as an additional micropollutant tracer, exchanging concentration with surfacic sediment sites, internalisation and externalisation kinetics being pseudo-1st order. This new version of MICROPOL was integrated into the TELEMAC system and validated with analytical solutions on multiple test-cases available on the TELEMAC validation manual. A real study case of the use of this WAQTEL module in the Loire Estuary is also presented. A fixed concentration of sediment and micropollutant was injected in the upstream boundary condition, decay and kinetic parameters were chosen to study the impact of the different model hypothesis available in the MICROPOL settings.**

Keywords: Micropollutant, Sediment transport, pollutant transport, WAQTEL-MICROPOL.

I. INTRODUCTION

Hydrodynamic modelling is an effective tool to assist decision making related to continuous or accidental micropollutant release. Model complexity must be adjusted to match intricated settings such as uneven topography, stratified water bodies or interactions between multiple components. Evaluating the effect of sediments on pollutant transport in 2D or 3D is necessary to accurately locate pollutant concentrations [1]. Previous studies were made on the subject using the TELEMAC system for bacterial [2] and radionuclide [3] release models, on account of the high spatiotemporal resolution and user-defined processes.

The MICROPOL sub-module of WAQTEL simulates the evolution of micropollutants (metals or radioelements) and their interaction with sediments (suspended or deposited). Concentrations of particles (pollutants or sediments) are represented as advected tracers in the water column. In the V8P3 version of TELEMAC, WAQTEL-MICROPOL module was able to correctly model micropollutant transport in 2D using 1st order kinetic exchanges. The 3D model could not properly model sediment settling, erosion of bed sediments and carried unstable operations on pollutant tracers. TELEMAC solves tracer advection diffusion equation:

$$F(C) = \frac{\partial C}{\partial t} + \boldsymbol{U}.\boldsymbol{\nabla C} - \nabla.(\mathrm{k}\boldsymbol{\nabla}\mathrm{C}) = S, \qquad (1)$$

with $C(x;y;z;t)$ is the tracer concentration, t is time, $(x;y;\ z)$ the coordinates, k the diffusion coefficient (m^2/s), U the velocity vector (m/s), $S(x;y;\ z;\ t)$ the internal source term.

Suspended Particulate Matter (SPM) can adsorb micropollutants in rivers and estuaries [4]. In WAQTEL, suspended sediments are advected and dispersed as tracers while bed sediments remain stationary. Two main sedimentary physical phenomena can occur depending on the sediment and water conditions: settling in smooth waters and erosion/re-suspension in high flow areas ([6], [7] and [8]). Combining micropollutant and sediment transport, TELEMAC considers 5 tracers:

- suspended matter (SS),
- bottom sediments (SF),
- dissolved species of micropollutant (C),
- the fraction of micropollutant adsorbed on suspended particulate matter (C_{ss}),
- the fraction of micropollutant adsorbed on bottom sediments (C_{ff}).

Whether in suspension or deposited on the bottom, the matter is a passive tracer: in other words, it does not influence the flow (no feedback). This hypothesis involves that the deposits depth must be negligible compared to the water depth (the bed is assumed to be unmodified).

There is no direct adsorption/desorption of dissolved micropollutants on the deposited matter, only on SPM (the model assumes a preponderance of water – SPM exchanges over direct water – bottom sediment exchanges). Contaminated particles from SPM can deposit in bottom sediments.

Multiple models can be used to predict the micropollutant interactions at the interface water-SPM particles. The most common model uses the "equilibrium" approach, where interactions are considered instantaneous. Those models are

well-suited for chronic continuous contaminations with small spatiotemporal variations. However, more complex models are required when facing acute pollution events. Considering one or two-step kinetic exchanges can have a large impact on the concentration's outcome, in view of the fact that sorption speed of micropollutant on SPM depends on the pollutant and sediment characteristics. Accurately representing kinetic models in the 2D and 3D components of the TELEMAC system would then allow studies of SPM-micropollutant interactions on large-scale high-resolution cases. It is also essential to study the impact of choosing more complex models on the propagation of pollutants.

The aim of this paper is firstly to present the model development of 2D and 3D SPM-micropollutant interactions, validation test-cases were then used to verify this model. Lastly, the model was tested on a real test-case scenario in the Loire estuary, this allowed the comparison of simple one-step reversible kinetic model and more complex two-step reversible model.

II. MODEL DESCRIPTION

A. *Suspended matter*

The model describing the evolution of SPM and bottom sediments involved in MICROPOL is a classic representation of the deposition laws and re-suspension of cohesive SPM [5], that are the laws of Krone [6] and Partheniades [7], [8]. Both processes require the knowledge of characteristic constants:

- deposition occurs when bottom shear stress τ_b, which varies according to the flow conditions, becomes lower than a threshold value τ_s, known as the critical shear stress for sedimentation. It is then assumed that the SPM settles at a constant velocity w (known as the settling velocity or velocity of sedimentation),
- re-suspension occurs when a threshold τ_r, known as the critical shear stress for re-suspension, is exceeded. Its importance is weighted by a constant e, the rate of erosion characteristic of deposited SPM (also known as the Partheniades constant).

These phenomena translate into the following expressions of deposition flux SED and erosion RS (kg/m²/s):

$$SED = \begin{cases} w.SS\left(1-\frac{\tau_b}{\tau_s}\right) & \text{if } \tau_b < \tau_s \\ 0 & \text{if } \tau_b \geq \tau_s \end{cases}, \quad (2)$$

$$RS = \begin{cases} e\left(\frac{\tau_b}{\tau_r}-1\right) & \text{if } \tau_b > \tau_r \\ 0 & \text{if } \tau_b \leq \tau_r \end{cases}. \quad (3)$$

The bottom shear stress τ_b (in Pa) is given by

$$\tau_b = \frac{1}{2}\rho C_f U^2 \quad (4)$$

with C_f the friction coefficient, ρ the density of water and U^2 the square of the velocity. The equations of the evolution of SPM tracers (variable SS) and bottom sediments (variable SF) write as follows:

- First tracer: suspended particulate matter

$$F(SS) = \frac{RS-SED}{h}. \quad (5)$$

With F as defined in equation (1).

- Second tracer: fixed bottom sediments

$$\frac{\partial(SF)}{\partial t} = SED - RS. \quad (6)$$

The model relating to SPM has four parameters: the velocity of sedimentation w, the erosion rate e, the critical shear stress for deposition τ_s and the critical shear stress for erosion τ_r.

B. *Micropollutants*

1) One-step reversible model

The model representing the evolution of micropollutants assumes that the transfers of micropollutants (radioelement, metal) between the dissolved and particulate phases correspond to either direct adsorption or ionic exchanges modelled by a reversible reaction, of pseudo-1st kinetic order [9]. In the case of direct adsorption, the reaction can be represented in the form of the following chemical equation:

$$R + \cdot - S \underset{k_{-1}}{\overset{k_1}{\rightleftharpoons}} R - S \quad (7)$$

with R the micropollutant in dissolved form, $-S$ the surface site associated with SPM, $R-S$ the adsorbed micropollutant. It is a reversible reaction, controlled by adsorption (k_1 in m³/kg/s) and desorption velocities (k_{-1} in s^{-1}). It leads to an equilibrium state, and then a distribution of micropollutants between the dissolved and particulate phase described by the distribution coefficient K_d (in m³/s):

$$K_d = \frac{[R-S]}{[R]} = \frac{k_1}{k_{-1}}, \quad (8)$$

where $[R]$ is the activity (or concentration of micropollutant) in dissolved phase (in Bq/m³ or kg/m³), $[R-S]$ is the activity (or concentration of micropollutant) associated to SPM (in Bq/kg or kg/kg). Once adsorbed, the fixed micropollutants act like SPM (deposition, re-suspension) and can then produce areas of polluted sediment. The model includes an exponential decay law (radioactive decay type) of micropollutant concentrations in each compartment of the modelled ecosystem, through a constant written L (expressed in s^{-1}). One-step reversible model can be schematically represented as in Figure 1:

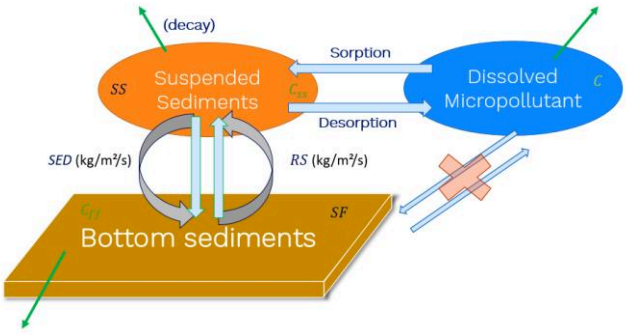

Figure 1. One-step reversible model exchanges.

2) Two-step reversible model

A new feature in MICROPOL allows the user to consider a two successive-step reversible model. In this case, a second reaction of pseudo-1st order introducing a slowly reversible site is considered [10]. This new reaction can be represented by the following chemical equation:

$$R-S+\cdot-S_2 \underset{k_{-2}}{\overset{k_2}{\rightleftharpoons}} R-S_2+\cdot-S \qquad (9)$$

with $R-S_2$ the adsorbed micropollutant bound to slowly reversible sites $-S_2$ of the suspended particle. It is a reversible reaction, controlled by adsorption (k_2 in s^{-1}) and desorption velocities (k_{-2} in s^{-1}). It leads to an equilibrium state, and then a distribution of micropollutants between the "non-specific" and "specific" sites ($-S$ and $-S_2$ respectively) described by the distribution coefficient K_{d2}:

$$K_{d2} = \frac{[R-S_2]}{[R-S]} = \frac{k_2}{k_{-2}}, \qquad (10)$$

where $[R-S_2]$ is the activity (or concentration of micropollutant) in the internal "specific" sites (in Bq/kg or kg/kg), $[R-S]$ is the activity (or concentration of micropollutant) associated to SPM surfacic "non-specific" sites (in Bq/kg or kg/kg). Two-step reversible model can be schematically represented as in Figure 2:

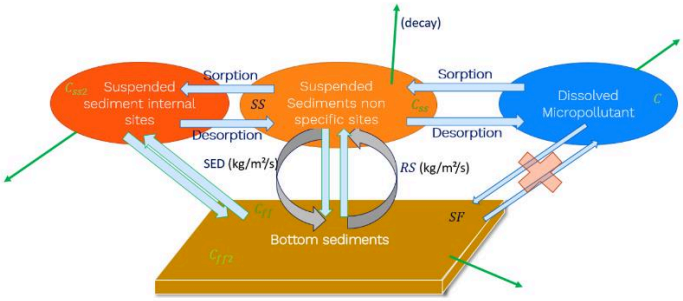

Figure 2. Two-step reversible model exchanges.

3) Equations

The system includes an equation for each micropollutant phase, namely 5 tracers:

- C : concentration of micropollutants in water (Bq/m^3),
- C_{ss1}: concentration of micropollutants adsorbed on SPM "non-specific sites" (Bq/m^3),
- C_{ff1}: concentration of micropollutants adsorbed on bottom sediments "non-specific sites" (Bq/m^2),
- C_{ss2}: concentration of micropollutants adsorbed on SPM "specific sites" (Bq/m^3),
- C_{ff2}: concentration of micropollutants adsorbed on bottom sediments "specific sites" (Bq/m^2).

The unit of concentration chosen for the demonstration is Bq/m^3, but it could also be written in kg/m^3 (for example, in the case of a metal). The internal sources for sediment tracers SS and SF are the same as in the previous section.

Taking the two-step reversible model into account leads to the following equations for each micropollutant phases:

- Third tracer: dissolved micropollutant:

$$F(C) = -k_1.SS.C + k_{-1}.C_{SS1} - L.C. \qquad (11)$$

- Fourth tracer: micropollutant associated to SPM "non-specific" sites

$$F(C_{ss1}) = k_1.SS.C - k_{-1}.C_{ss1} + \frac{\frac{RS}{SF}C_{ff1} - \frac{SED}{SS}C_{ss1}}{h} - k_2.C_{ss1} + k_{-2}.C_{ss2} - L.C_{ss1}. \qquad (12)$$

- Fifth tracer: micropollutant associated to bottom sediments "non-specific" sites

$$\frac{\partial C_{ff1}}{\partial t} = \frac{SED}{SS}C_{ss1} - \frac{RS}{SF}C_{ff1} - k_2.C_{ff1} + k_{-2}.C_{ff2} - L.C_{ff1}. \qquad (13)$$

- Sixth tracer: micropollutant associated to SPM "specific" sites

$$F(C_{ss2}) = \frac{\frac{RS}{SF}C_{ff2} - \frac{SED}{SS}C_{ss2}}{h} + k_2.C_{ss1} - k_{-2}.C_{ss2} - L.C_{ss2}. \qquad (14)$$

- Seventh tracer: micropollutant associated to bottom sediments "specific" sites

$$\frac{\partial C_{ff2}}{\partial t} = \frac{SED}{SS}C_{ss2} - \frac{RS}{SF}C_{ff2} + k_2.C_{ff1} - k_{-2}.C_{ff2} - L.C_{ff2}. \qquad (15)$$

Terms with SF as denominator are nullified when SF is close to 0. Two-step kinetic exchanges tracers C_{ss2}, C_{ff2} and parameters k_2 and k_{-2} are nullified when the keyword KINETIC EXCHANGE MODEL is set to the value 1 (default).

Therefore, there are five parameters of the micropollutant model: the distribution coefficient at equilibrium K_d between the dissolved and particulate non-specific phase, the kinetic constant of desorption k_{-1} between the dissolved and particulate non-specific phase, the distribution coefficient at equilibrium K_{d2} between the "non-specific" and "specific" sites, the kinetic constant of desorption k_{-2}, and the exponential decay constant L (radioactive decay, for example).

III. TEST CASES

Multiple test cases for WAQTEL-MICROPOL module are now available on the V8P4 version of the TELEMAC system. The MICROPOL model was compared to analytic solutions in the case of a simple basin at rest for 2D and 3D models. More advanced interactions are also qualitatively studied to ensure that exchange processes are consistent.

A. 2D Basin at rest

In 2D, a basin at rest is considered (length and width = 10 m) with flat bathymetry and elevation at 0 m. The triangular mesh is

composed of 272 triangular elements and 159 nodes as in Figure 3.

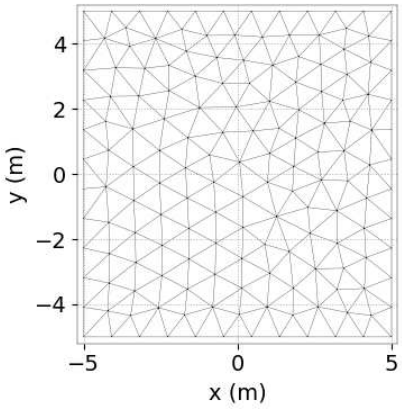

Figure 3. 2D square basin at rest mesh.

The initial conditions, settling velocity w (m/s) and the exponential decay constant L (s-1) are adapted in each test case in order to individually model sedimentation, sorption, desorption and decay. The distribution coefficient K_d (L/g) is set at a value of 1 and the constant of kinetic desorption k_{-1} at the value of 2.5E-7 s^{-1} for all test cases. All other parameters are taken with the default values in the WAQTEL STEERING FILE. The time step is 1h = 3,600 s for a simulated period of 3,200 h ≃ 133 days.

The first test case is a simple sorption with no sedimentation or erosion: initial tracer conditions $(SS, SF, C, C_{ss}, C_{ff})$ = (1, 0, 1, 0, 0) and parameter values (w, L) = (0, 0). An analytical solution can be calculated in the case of simple steady hydrodynamic conditions using (11) and (12). In the case where the settling velocity w is nil, there is no sediment evolution, and the exchanges remain exclusively in the micropollutant tracers. By setting the initial concentration of micropollutants adsorbed by SPM (C_{ss}) at 1 Bq/m3 and 0 otherwise, an analytical solution under these conditions is:

$$\begin{cases} C_{ss}(t) = \frac{SS_0}{SS_0+1}(1 - e^{-k_{-1}(SS_0+1)t}) \\ C(t) = \frac{1}{SS_0+1}(SS_0 + e^{-k_{-1}(SS_0+1)t}) \end{cases} \quad (16)$$

Figure 4 shows the comparison between simulated simple sorption and the analytic solution (16).

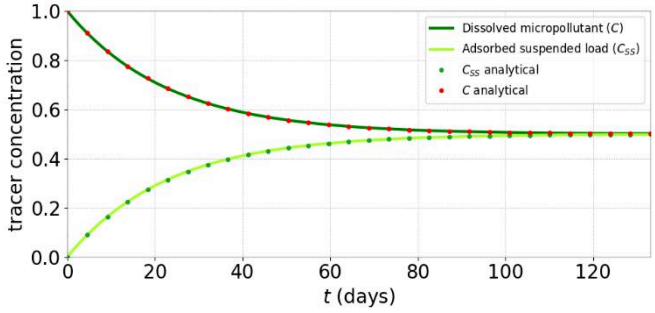

Figure 4. Tracer evolution on simple sorption test case.

The second test case evaluates deposition of SPM in the basin at rest: $(SS, SF, C, C_{ss}, C_{ff})$= (1, 0, 0, 0, 0) and (w, L) = (4E-7, 0). An analytical solution can be calculated in the case of simple steady hydrodynamic conditions using (5) and (6). With a unitary constant water depth (h = 1 m) and no erosion (U = 0 m/s) the deposition flux SED follows:

$$SED = w.SS, \quad (17)$$

and the suspended sediment concentration (SS) is:

$$SS(t) = SS_0 e^{-wt}. \quad (18)$$

Similarly, the bottom sediments follow:

$$SF(t) = SF_0 + SS_0(1 - e^{-wt}). \quad (19)$$

Figure 5 shows that simple sediment is modelled correctly according to the analytic solution (18) and (19).

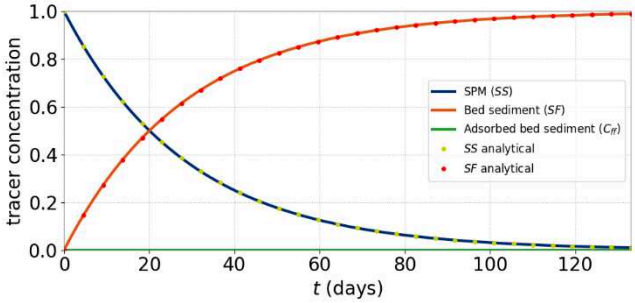

Figure 5. Tracer evolution on simple sedimentation test case.

When combining the first two test cases (sorption and sedimentation), we can qualitatively assess that the model correctly represents more complex dynamics with: $(SS, SF, C, C_{ss}, C_{ff})$ = (1, 0, 1, 0, 0) and (w, L) = (4E-7, 0). Under steady hydrodynamic conditions, the model reaches an equilibrium state when all sediments are deposited as shown in Figure 6.

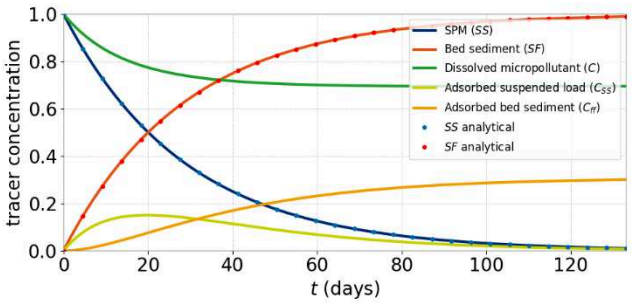

Figure 6. Tracer evolution on sedimentation and sorption test case.

Decay and desorption can also be studied in the fourth test case: $(SS, SF, C, C_{ss}, C_{ff})$ = (1, 0, 0, 1, 0) and (w, L) = (4E-7, 1.13E-7). Once the suspended sediment tracer is fully deposited, concentrations of micropollutants in water and in bed sediments decreases with the appropriate rate as shown in Figure 7.

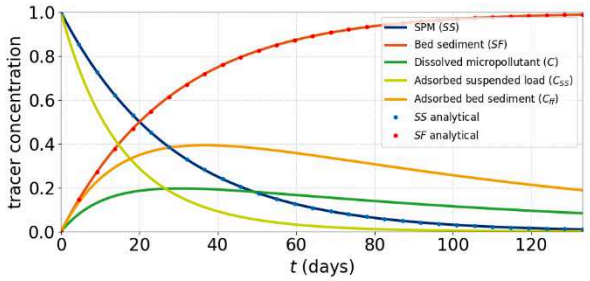

Figure 7. Tracer evolution on sedimentation and sorption test case with decay.

Two-step reversible model can be activated by setting the keyword KINETIC EXCHANGE MODEL = 2 in the WAQTEL STEERING FILE. In the next test cases, the distribution coefficients K_d and K_{d2} are set at a value of 2 L/g and 2. The sorption reaction rates k_1 and k_2 are set at a value of 0.1 L.g^{-1}.s^{-1} and 0.1 s^{-1}. All other parameters are taken with the default values in the WAQTEL STEERING FILE. The initial water depth is 1 m with a fluid at rest. The initial values for tracers are homogeneous in each test cases.

In the case where the settling velocity w is nil, there is no sediment evolution, and the exchanges remain exclusively in the micropollutant tracers in the water column. By setting the initial concentration of micropollutants in the water (C) at 1 Bq/m^3 and 0 otherwise, an analytical solution under these conditions is:

$$\begin{cases} C(t) = \frac{1}{7}(1 + (3+\sqrt{2})e^{\frac{-3+\sqrt{2}}{10}t} + (3-\sqrt{2})e^{-\frac{3+\sqrt{2}}{10}t}) \\ C_{ss1}(t) = \frac{1}{7}(2 - (1-2\sqrt{2})e^{\frac{-3+\sqrt{2}}{10}t} - (1+2\sqrt{2})e^{-\frac{3+\sqrt{2}}{10}t}) \\ C(t) = \frac{1}{7}(4 - (2+3\sqrt{2})e^{\frac{-3+\sqrt{2}}{10}t} - (2-3\sqrt{2})e^{-\frac{3+\sqrt{2}}{10}t}) \end{cases} \quad (20)$$

This analytical solution corresponds to a simple sorption using two-step kinetic scheme with no sedimentation or erosion with $(SS, SF, C, C_{SS1}, C_{ff1}, C_{ss2}, C_{ff2})$ = (1, 0, 1, 0, 0, 0, 0) and (w, L) = (0, 0). Figure 8 shows the comparison between simulated simple sorption and the analytic solution (16).

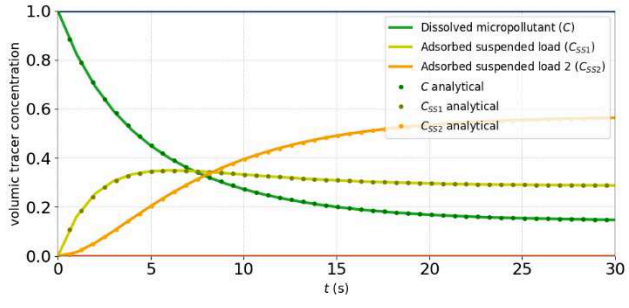

Figure 8. Tracer evolution on simple sorption test case using two-step reversible model.

The two-step reversible model can be used to model more complex transfers. In this second test case, both desorption of micropollutants from SPM toward dissolved form, deposition, and decay are evaluated with $(SS, SF, C, C_{ss1}, C_{ff1}, C_{ss2}, C_{ff2})$ = (1, 0, 0, 1, 0, 0, 0) and (w, L) = (4E-7, 1.13E-7). Once the suspended sediment tracer is fully deposited, concentrations of micropollutants in water and bed sediments specific and non-specific sites decreases with the appropriate rate as shown in Figure 9.

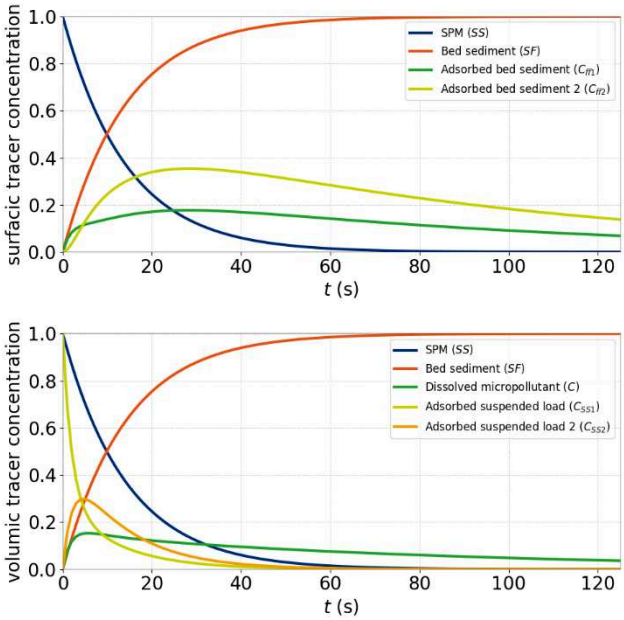

Figure 9. Tracer evolution on sedimentation and desorption test case with decay using two-step reversible model.

B. 3D Basin with various hydrodynamic conditions

Exchanges between suspended sediments and bed sediments are studied here. A concentration of suspended sediment is initially placed on top of the water column and settling, and deposition processes are observed. A 50 m long and 2.5 m wide rectangular basin at rest is considered with flat bathymetry and elevation at 0 m. Five superimposed layers are regularly spaced vertically. The triangular mesh is composed of 500 triangular elements and 306 nodes as showed in Figures 10 and 11.

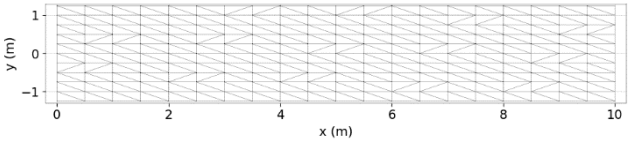

Figure 10. Horizontal mesh

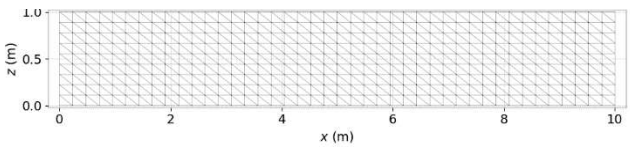

Figure 11. Vertical mesh.

In this test case, only suspended sediments (SS) and bed sediments (SF) are studied. The settling velocity w is set at 4.E−3 m/s in the WAQTEL STEERING FILE. The initial water depth is 1 m with a fluid at rest. The initial value for

the suspended sediment tracer is set at a concentration of 1 kg/m3 in the top layer (z = 1 m) as in Figure 12. The bed sediment tracer is initially set to zero. The time step is 1 s for a simulated period of 1,000 s ≈ 17 min.

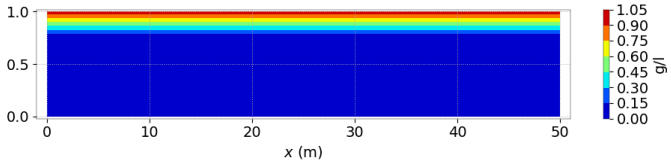

Figure 12. Suspended sediment initial concentrations.

Figure 13 shows the suspended sediment (SS) (kg/m3) and bed sediment (SF) (kg/m2) evolution along time at different water depths. The blue dashed line represents the water depth divided by the sediment settling velocity, it can help to estimate the time magnitude for the SPM to reach the bottom layer.

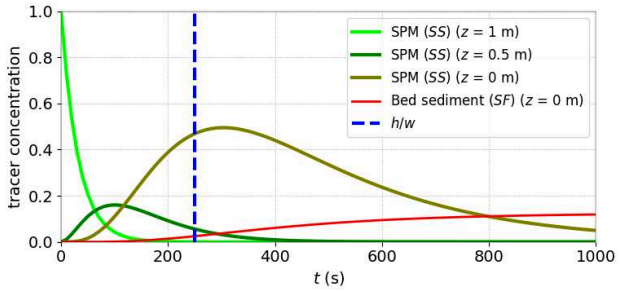

Figure 13. Suspended sediment and bed sediment evolution.

At t = 1,000 s only residual suspended sediments are still being deposited in the bottom layer as in the vertical cross section of Figure 14.

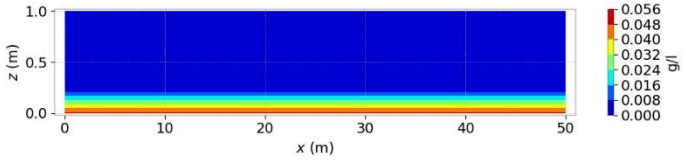

Figure 14. Suspended sediment concentrations at t = 1000 s.

In the next test case, an initial bump of bed sediment is placed at the bottom layer under a constant water velocity, erosion process is observed. The mesh is identical as the previous test case, except it is vertically divided in 10 superimposed layers. The settling velocity w is set at 0.02 m/s in the WAQTEL STEERING FILE. Critical shear stresses of resuspension and sedimentation τ_r and τ_s are set to 0.01 Pa. The erosion rate (or Partheniades constant) e is set at 1.E-3 kg/m^2/s. The initial water depth is 1 m. The initial values for the suspended sediment tracer is set to zero and the initial values of the bed sediment are placed as a polynomial concentration:

$$SF(t=0) = \max(0{,}5(x-7)(3-x)). \qquad (21)$$

For the solid walls, a slip condition is used. Upstream flowrate equal to 1.5 m^3/s is imposed. Downstream, the water level boundary condition is equal to 1 m.

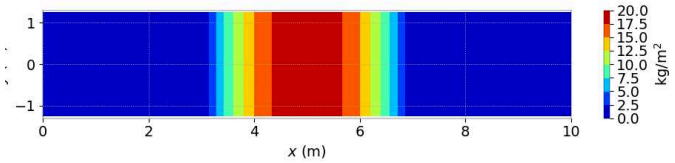

Figure 15. Bed sediment initial concentrations.

The time step is 0.1 s for a simulated period of 150 s. Figures 16 and 17 show the suspended sediment (SS) and bed sediment (SF) evolution along time on a vertical cross section and bed sediment final concentrations.

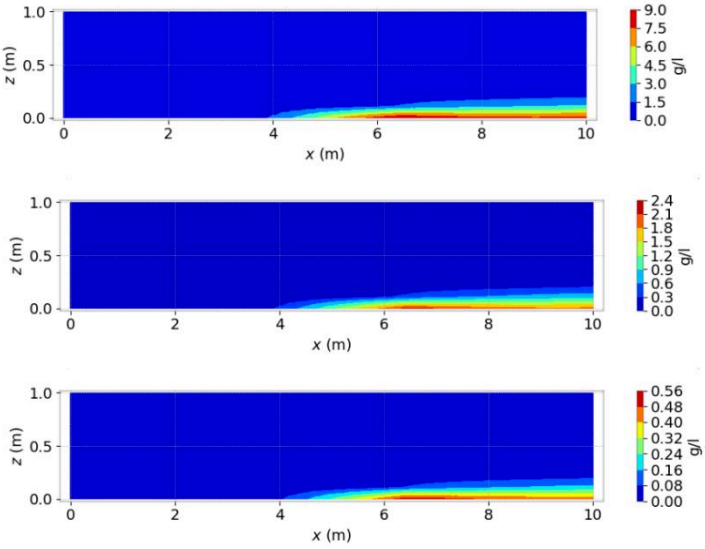

Figure 16. Suspended sediment concentrations at t = 5, 75 and 150 s.

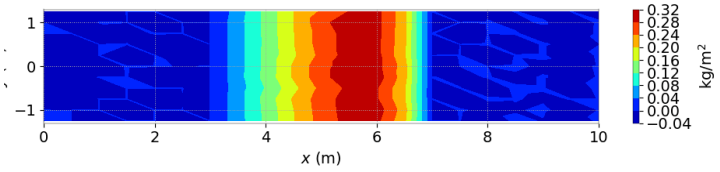

Figure 17. Bed sediment final concentrations.

Having verified that sediment and erosion processes are now properly represented, micropollutant transport can be studied as in the 2D test cases.

Decay and desorption can also be studied in the next test case in 3D: $(SS, SF, C, C_{ss}, C_{ff})$ = (1, 0, 0, 1, 0) and (w, L) = (0,07,8.3E-3). Once the suspended sediment tracer is fully deposited, concentrations of micropollutants in water and in bed sediments decreases with the appropriate rate as shown in Figure 18.

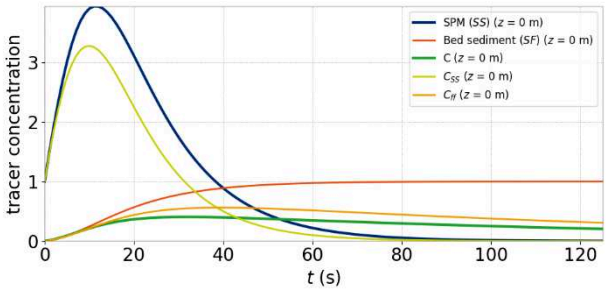

Figure 18. Tracer evolution on sedimentation and desorption test case with decay in 3D.

Depending on the bottom layer thickness, suspended sediments concentration accumulates before reaching the bed sediment layer.

Next test case uses two-step reversible model with distribution coefficients K_d and K_{d2} set at a value of 2 L/g, sorption reaction rates k_1 and k_2 set at a value of 0.1 L.g^{-1}.s^{-1}, sediment settling velocity w to 4E-7 m/s and exponential decay constant L to 1.13E-7 s^{-1}. Initial concentrations are as follows: $(SS, SF, C, C_{ss1}, C_{ff1}, C_{ss2}, C_{ff2})$ = (1, 0, 0, 1, 0, 0, 0). Figure 19 illustrate the evolution of surfacic (top) and volumic tracer concentrations. The model was able to simulate the exchanges between specific and non-specific sites along with desorption of micropollutant towards the dissolved form, sedimentation process and decay.

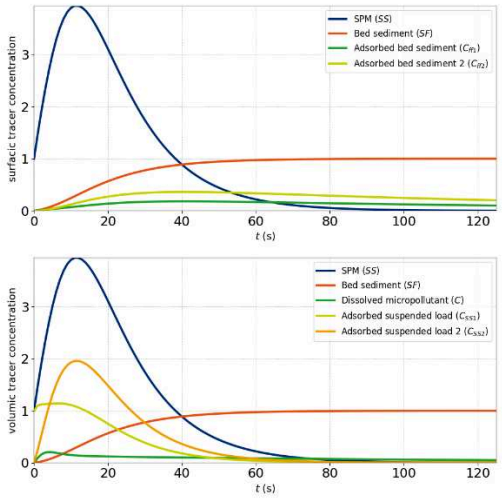

Figure 19. Tracer evolution on sedimentation and desorption test case with decay using two-step reversible model in 3D.

IV. REAL CASE: LOIRE ESTUARY

The model was tested on the Loire Estuary domain coupling TELEMAC-2D and WAQTEL module. The study area extends from 40 km upstream of the Saint-Nazaire Port and up to 100 km offshore. In view of limiting computing costs, the grid was refined in the Loire riverbed and coarsened on Atlantic Ocean side. For all simulations, a numerical time step of 5 s was considered. A triangular mesh of 45 000 nodes and 90 000 elements was mapped on a 100 m resolution bathymetric dataset as shown in Figure 20.

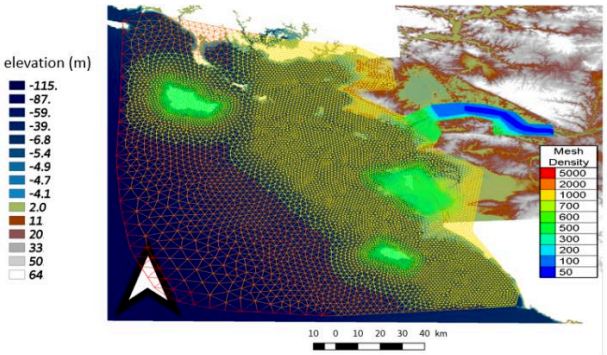

Figure 20. Model mesh and bathymetry.

The hydrodynamic model solves shallow water equations in the non-conservative form using finite element method. A Strickler law of bottom friction was chosen with a coefficient of 50 m$^{1/3}$ s^{-1}. Sediment settling velocity was set at the value of 0.4 cm/h, sedimentation critical shear stress and critical stress of resuspension were respectively set at 0.1 and 0.5 Pa. A constant prescribed flowrate of 900 m^3/s was imposed on the upstream boundary condition. A semi-diurnal tidal flow is introduced by means of a sinusoidal free surface elevation in time with a mean value of 3 m and an amplitude of 2 m. A first run with no micropollutant concentration was used to reach a stable periodic state on a one-year period. In Figure 21 is presented the spatial distribution and time evolution of suspended sediment and bed sediments at five locations. These locations are near the upstream boundary condition (+35km), in the riverbed (+26km, +18km), at the estuary (Saint-Nazaire) and offshore (+15km).

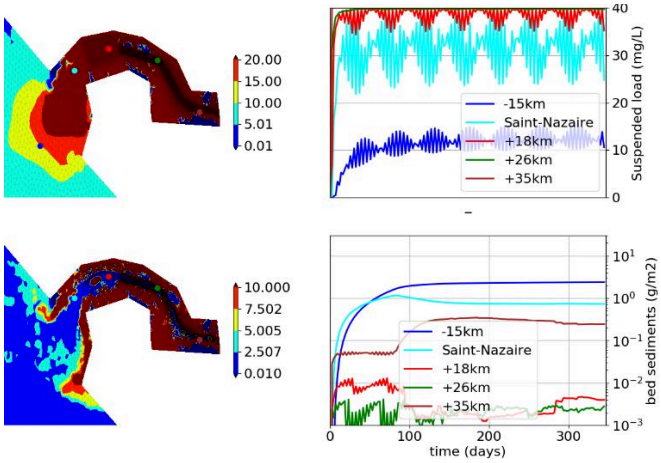

Figure 21. Sediment initialisation in the Loire estuary.

After this initialisation, a micropollutant discharge was injected as an upstream boundary condition with a concentration of 100 L^{-1}. In this case, the micropollutant can be viewed as any type of contaminant. The exponential decay constant was set at the value of 7.3E-10 s^{-1}, the distribution coefficient at 63 L/g, and the kinetic desorption coefficient at the value of 4.E-4 s^{-1}. The choice of these parameters is aimed to replicate the characteristics magnitude measured of ^{137}Cs in the Loire Estuary in [11]. Transport, sorption, and deposition of micropollutant was observed on a period of 4

days. Figure 22 demonstrate the model ability to simulate the transfers of micropollutant to sediments while being advected by the river. It was observed that dissolved concentrations were reduced by the presence of sediments. In this case, the low sediment settling velocity and the short simulation duration only allowed a small fraction of micropollutant to be deposited in the bottom sediments.

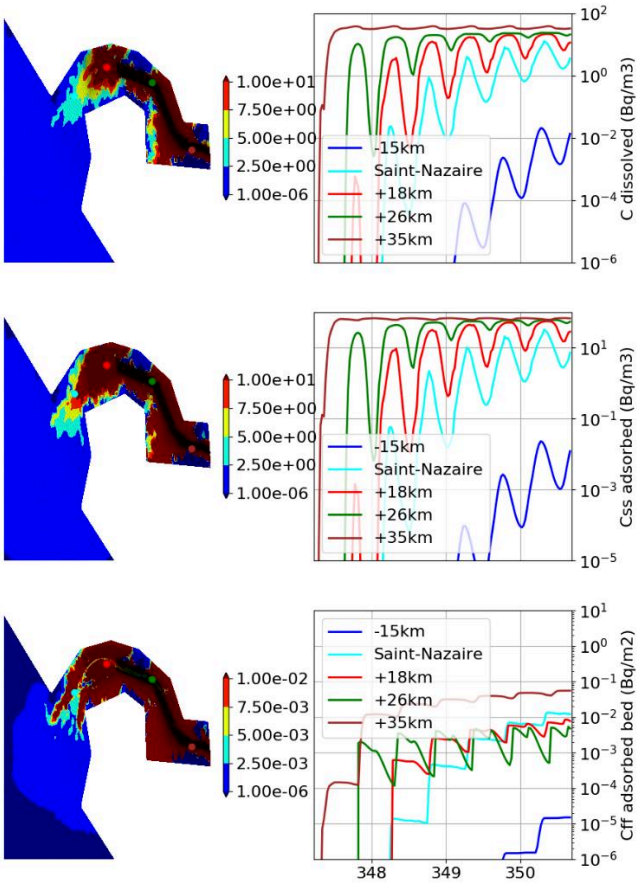

Figure 22. Micropollutant concentrations in dissolved form, adsorbded by suspended load and deposited in bed sediments. Colormaps show the final concentrations in the estuary.

As a way to assess the impact of considering two-step reversible model for micropollutant and sediment interactions, another test case was implemented with the same hydrodynamic and sediment parameters. In this case however, the two-step reversible option was activated, and two new parameters were added: The second distribution coefficient K_2 was set at the value of 2.5, and the kinetic desorption coefficient k_{-2} at the value of 2.E-5 s^{-1}. Propagation of micropollutant was observed on the same time scale as before on Figure 23.

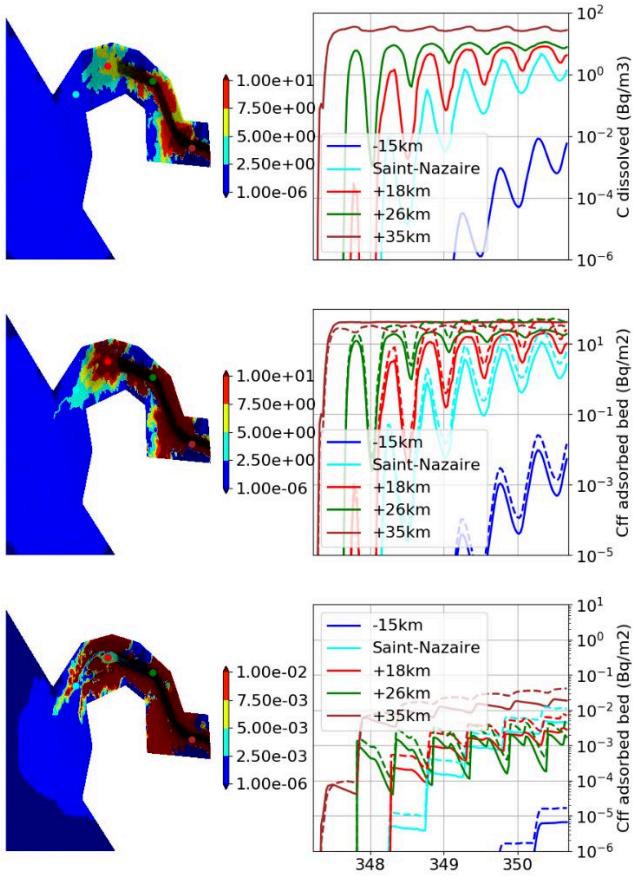

Figure 23. Micropollutant concentrations in dissolved form, adsorbded by suspended load and deposited in bed sediments in sediment surfacic sites (colored lines) and internal sites (dashed lines). Colormaps show the final concentrations in the estuary.

A qualitative analysis of the two previous figures shows that considering the two-step reversible model reduces the spatial dispersion of micropollutant and their concentration in surfacic sites. As expected, the micropollutant are transferred towards sediment "specific" sites, thus reducing dissolved concentrations in the water column. Comparison of final concentrations between one-step and two-step kinetic exchange models are shown in Table I. Final concentrations in the points distant from the inlet were more impacted by the different models. At some points, the concentrations were reduced by up to two-thirds.

Table I Dissolved micropollutant concentration comparison at the five study points.

Points	One-step reversible model		Two-step reversible model		Relative differences
	Final concentration C_{f1}	*Dilution coefficient* $C_i/C_{f1}{}^a$	*Final concentration* C_{f2}	*Dilution coefficient* $C_i/C_{f2}{}^a$	$\frac{C_{f2}-C_{f1}}{C_{f1}}$ (%)
-15 km	2.2E-02	4.5E+03	9.0E-03	1.1E+04	-59%
Saint-Nazaire	4.3	2.3E+01	1.57	6.4E+01	-63%
+18 km	1.5E+01	6.7	5.3	1.9E+01	-65%

Points	One-step reversible model		Two-step reversible model		Relative differences
	Final concentration C_{f1}	*Dilution coefficient* $C_i/C_{f1}{}^a$	*Final concentration* C_{f2}	*Dilution coefficient* $C_i/C_{f2}{}^a$	$\frac{C_{f2}-C_{f1}}{C_{f1}}$ (%)
+26 km	2.2E+01	4.5	8.1	1.2E+01	-63%
+35 km	3.4E+01	2.9	2.8E+01	3.6	-18%

a. $C_i = 100\ L^{-1}$ the injected concentration at the inlet

V. Conclusions And Perspectives

The goal of this study was to present and assess the developments of pollutant and sediment interactions in the TELEMAC system and to experiment on different modelling approaches.

In this paper, the implementation of the WAQTEL-MICROPOL module of TELEMAC is presented on theoretical and real test-cases. It was demonstrated that the TELEMAC software can now model conservative sediment and micropollutant transport in 2D and 3D with decay law and using one or two step reversible model. The test case on the Loire Estuary demonstrated that the model is usable on more complex domains and for intricated boundary conditions. Moreover, the results demonstrated that the model selection has a great impact on the final concentrations. Considering one or two pollutant sites in sediments affect the transfer rates from dissolved form to adsorbed micropollutant state.

This work provides a basis for further usage of the WAQTEL-MICROPOL model, while demonstrating application of the documentation test case and an application on a fictive scenario. The model developed is now ready to be tested on industrial and scientific studies.

Some additional work could improve the model by implementing salinity laws and concentration laws for sensitive parameters, namely the distribution coefficient and the kinetic desorption velocity. Another development could see the link between the sediments of this module and the sediments used in the GAIA module.

References

[1] L. Koziy, V. Maderich, N. Margvelashvili, and M. Zheleznyak. "Three-dimensional model of radionuclide dispersion in estuaries and shelf seas." in Environmental Modelling & Software, 1998, pp 413-420.

[2] L. A. Van, K. D. Nguyen, F. Le Marrec and A. Jairy. "Development of a Tool for Modeling the Fecal Contamination in Rivers with Turbulent Flows—Application to the Seine et Marne Rivers (Parisian Region, France). " in *Water*, 2022.

[3] V. Bacchi, P. Tassi. "Three-dimensional Modelling of Radionuclides Dispersion in a Marine Environment with Application to the Fukushima Dai-ichi Case." in Environmental Modeling & Assessment, 2019, pp 457-477.

[4] P. Ciffroy, C. Moulin, and J. Gailhard. "A model simulating the transport of dissolved and particulate copper in the Seine river." in Ecological Modelling, 2000, pp 99-117.

[5] "WAQTEL Technical manual, Version v8p3", 2021.

[6] R.B. Krone. "Flume studies of transport of sediment in estrarial shoaling processes." in Hydr. Engr. and Samitary Engr. Res. Lab., Univ. of California, 1962.

[7] Partheniades, E. "Erosion and deposition of cohesive soils. " In Journal of the Hydraulics Division, 1965, pp 105-139.

[8] Partheniades, E. "A study of erosion and deposition of cohesive soils in salt water. " University of California, Berkeley, 1962.

[9] P. Ciffroy. "Les échanges de radioéléments à l'interface eau-matières en suspension. principe théorique et équations d'un modèle descriptif. bilan des expérimentations in situ. " Technical report, EDF DER-ENV, 1995.

[10] P. Ciffroy, J.M. Garnier, and M.K. Pham. "Kinetics of the adsorption and desorption of radionuclides of co, mn, cs, fe, ag and cd in freshwater systems: experimental and modelling approaches." in Journal of environmental radioactivity, 2001, pp 71–91.

[11] P. Ciffroy, J.M. Garnier, and L. Benyahya, "Kinetic partitioning of Co, Mn, Cs, Fe, Ag, Zn and Cd in fresh waters (Loire) mixed with brackish waters (Loire estuary): experimental and modelling approaches. " in Marine Pollution Bulletin, 2003, pp 626-641.

Process based model for riverine plastic fluxes

Wilhem Riom[1], Nithin Achutha Shettigar[1], Erik Toorman[1]
wilhem.riom@kuleuven.be, Leuven, Belgium
[1] Hydraulics Laboratory, Department of Civil Engineering, KU
Leuven, Kasteelpark Arenberg 40, Box 2448, 3001 Leuven, Belgium

Abstract - **Plastic pollution in the sea and oceans is an increasing concern, especially when considering its impact on the biome, biota and eventual hazardous consequences on human activities and health. Rivers are the major pathways for plastic and microplastics (MP, size <5mm) exportation toward the ocean. Adopting modelling approaches may increase our understanding of this pathway as well as the distribution and fate of MPs in the environment. Eulerian approaches permit to account for plastic concentration, number of particles or mass, temporal and spatial evolution and is appropriate for smaller particles. A coupled TELEMAC-2D+GAIA only allows to model settling particles as sediments preventing to account for the full range of plastic particles behaviour (buoyant and settling). The LABPLAS (Land-Based Solutions for Plastics in the Sea) project aims at developing a three-layered model representing microplastics dispersal and interaction with their environment over riverine and coastal areas. In this model MPs are modelled as tracers transported at three levels: at the surface, in suspension and as bedload. Material exchanges between floating and suspended layers are possible through a buoyant and a mixing flux. This three-layered module was developed based on the existing TELEMAC-2D+GAIA code and results in mass-conservative and coherent results when applied to simple flumes with and without flow. However, the presented implementation induces non negligeable mass creation (or losses) when the domain includes inter tidal areas. The full schematised module is visible in Figure 1.**

Keywords: pollution, microplastics, freshwater, coastal water, tracers, TELEMAC-2D, GAIA.

I. INTRODUCTION

The, largely acknowledged, extent of plastic pollution in the marine environment [1] has for main origin, land-based sources with debris mostly being conveyed by freshwater discharges [2]. Understanding rivers pollution levels and export mechanisms is thereby, crucial to capture the full scope of plastic waste at sea [3]. Within the LABPLAS project, a process-based model for riverine plastic fluxes is under development. This model must faithfully represent both horizontal transport and the complex vertical settling of plastics. Indeed, the plastic waste shows large polydispersity in term of shape, size, density and thus buoyancy is the main driver governing the vertical dispersion (suspension in the water column, settling towards the bottom or buoyancy at the surface) of plastic particles both at sea [4] [5] and in freshwater [6]. Complementary mechanisms such as biofouling [7], weathering [8], mechanical stresses [9] and interactions with sediments flocs [10] may alter plastic particle and hence their fate in waterways. These mechanisms altogether, may explain why normally buoyant plastics (PE and PP) were found at the bottom of the Elbe River during a sampling campaign [11]. Based on the TELEMAC system, and specifically TELEMAC-2D and GAIA, for coupled depth averaged flows with sediment transports, this paper presents the theorization and validation of a three-layer model allowing the transport of microplastics over three layers: at the surface, in suspension and in the bedload.

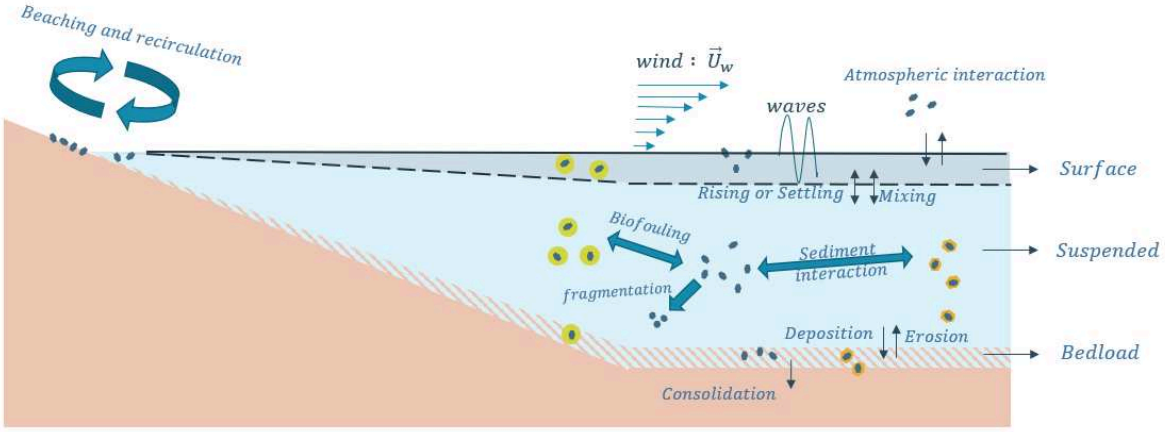

Figure 12. Schematic representation of the three-layered model

II. THEORY AND MODEL IMPLEMENTATION

A. Model description

The proposed three-layer model has been developed according to how TELEMAC-2D and GAIA are already coupled for sediments transport. A class of sediment can evolve in suspension and/or in one or several bed layers. Here, a class of plastic can be transported in suspension, in the bedload and at the surface of the water.

This section describes the theory behind the horizontal transport equation in the water column (suspension and surface) and the vertical transfer of mass. The horizontal bedload transport and vertical exchanges between suspension and the bedload is kept as already implemented in GAIA [12]. Plastic classes will be designated by the term tracer as the following theory is not limited to plastic particles only.

Considering a fluid of viscosity ν_{ts} in a shallow water flow, solved by TELEMAC-2D. The free surface elevation is $h = h(x,y,t)$, and the depth-averaged velocity field is $\boldsymbol{u_s}$=$(u_s, v_s)(x,y,t)$, with, x, y and t respectively the space and time variables. Suspended tracers transport follows the 2D advection-diffusion equation (1).

$$\frac{\partial hC_s}{\partial t} + \frac{\partial hu_s C_s}{\partial x} + \frac{\partial hv_s C_s}{\partial y} = \frac{\partial}{\partial x}\left(h\frac{\nu_{ts}}{S_c}\frac{\partial C_s}{\partial x}\right) + \frac{\partial}{\partial y}\left(h\frac{\nu_{ts}}{S_c}\frac{\partial C_s}{\partial y}\right) + M + B + E - D \quad (1)$$

with $S_c = 0.7$ the turbulent Schmidt number developed in [13] and [14], E and D, are respectively the erosion and deposition fluxes between the suspended layer and the bed which are handled by Gaia [15]. M and B are the mixing and buoyant fluxes between the suspended and surface layer. They are introduced next.

A surface layer, of zero thickness, is introduced and characterized by a fluid viscosity, ν_{tf}, and a surface velocity field $\boldsymbol{u_f} = (u_f, v_f)(x,y,t)$ function of the shallow-water velocity $\boldsymbol{u_s}$ and of a given vertical velocity profile (e.g. constant, linear, logarithmic, power-law). In this study, for simplification purposes, the profile is considered constant. This surface layer can transport tracers of concentration, $C_f(x,y,t)$, following the advection-diffusion equation under its non-conservative form (2):

$$\frac{\partial C_f}{\partial t} + \frac{\partial u_f C_f}{\partial x} + \frac{\partial v_{tf} C_f}{\partial y} = \frac{\partial}{\partial x}\left(\frac{\nu_{tf}}{S_c}\frac{\partial C_f}{\partial x}\right) + \frac{\partial}{\partial y}\left(\frac{\nu_{tf}}{S_c}\frac{\partial C_f}{\partial y}\right) - \frac{(M+B)}{h} \quad (2)$$

where the mixing, M and buoyancy, B allow coupling between (1) and (2) through vertical mass transfer between the surface and the suspension layer. The fluxes exist for buoyant and settling classes of tracers. B represents the vertical movement of particles due to their buoyancy. It is defined here following the Partheniades approach. Equations (3) and (4) present respectively this flux for a settling tracer, of positive settling velocity $w_s > 0$, and for a buoyant tracer class ($w_s < 0$).

$$B = p_f w_s C_f \quad (3)$$

$$B = -p_s w_s C_s \quad (4)$$

where p_f and p_s are probability function taken equal to the unit h. If the tracer class is buoyant, B will add mass in the surface layer while removing mass from the suspended layer.

Usually, the mixing flux, M, counterbalance the rising or settling and allows equilibrium of the vertical concentration distribution. Mixing is important in affecting the vertical distribution of plastic in water [9] [5]. Indeed, vertical turbulent mixing dampens the buoyant vertical transfer. Equation (5) shows it usual definition with a continuous concentration, C, and viscosity, ν_t, over the vertical axis z.

$$M = \frac{\nu_t}{S_c}\frac{\partial C}{\partial z} \quad (5)$$

However, to match our three-layered model, one can approximate the vertical derivative by its first order as in (6):

$$M = \frac{\nu_{tf}}{S_c}\frac{C_f - C_s}{h} \quad (6)$$

We choose here the viscosity at the surface and the free surface elevation, h as characteristic distance for the derivative. In (2), and (6), h is chosen as characteristic height for the mass transfer, another distance may be a lead for improvement. Using an exponential vertical profile for the buoyant plastic concentration could be directly inspired from [10]. Using a Rouse profile may be directly applicable to settling plastic classes. In equation (1), the erosion and deposition fluxes are only defined if the tracer is settling. Hence, buoyant plastics are assumed to never reach the bottom without considering other factors (e.g. biofouling, sediments interaction) that will change their settling.

As the surface layer is assumed to have no thickness, the surface tracers concentration dimension is a surface mass ($[M][L]^{-2}$). This causes dimensional issues with the presented definition of the equations. This will be dealt with directly in the implementation section.

B. Implementation

1) New variables

The way that the surface layer was added into the TELEMAC-2D code is first, by declaring the following sets of variables:

- The surface velocity field called U_SURF, V_SURF and a new surface viscosity field named VISCT_SURF. These variables are identical in format and shape to their existing counterpart.

- A set of tracers for the surface concentrations: one for the previous calculation step TN_SURF and one for the current one: T_SURF. These tracers are created identical in size to TN and T which become here the suspended tracer concentration. This allows to conserve the coupling between suspended concentration, dealt with in TELEMAC-2D, and bedload mass, solved by GAIA.
- The settling velocity although considered here constant in space, was adapted in format to allow spatial variations. This will become useful at later stage of the module development where local variation of the settling velocity may occur due to spatial biological variations.
- Variables related to the boundary conditions of the suspended tracers were also duplicated and named just by juxtaposing the suffix "_SURF" after their name.
- TEXP_SURF, TIMP_SURF, TSCEXP_SURF respectively the explicit, implicit and punctual source of mass for the surface layer were implemented as clones of TEXP, TIMP and TSCEXP.

The interesting modified or added variables are autonomously exited in the resulting selafin file: if n tracers are followed through a simulation, then the output selafin file will have n+2 new fields: VELOCITY SURF U, VELOCITY SURF V, T_SURF 1, T_SURF 2, …, T_SURF N.

2) Algorithmic resolution

This section focuses on the numerical solution of the quantities introduced in the module. It is supposed that all the quantities at timestep N are known. Table I shows the order of the calculation to derive the quantities at time $N+1$. No changes were done to how Telemac2D and Gaia are coupled. From this table, the coupling is assured by steps 3 and 5. However, this coupling must assure adequation between the dimensions of the numerical counterpart of equations (1) and (2).

3) Vertical fluxes implementation

The buoyant flux is added in the numerical counterpart of equations (1) and (2) either implicitly or explicitly depending on the buoyancy of the tracer class and the concerned layer. The implementation is summarized in Table II. Where SM, SMH and SMI are respectively the explicit non conservative, conservative and implicit source or sink terms added in the numerical advection-diffusion equations. SM and SMH are added as such while for SMI and a tracer F, the added term is $\frac{SMI\,F}{H}$, with H, the numerical variable designating the free surface elevation. To ease the numerical implementation, the mixing flux is divided in two fluxes: one depends on the suspended concentration while the other depends on the surface concentration (see (7)). For a given layer, this flux is now made of two independent terms. Table III shows the implementation method of these terms into the numerical equations.

$$M = \frac{\nu_{tf}}{S_c}\frac{C_f - C_s}{h} = \frac{\nu_{tf}}{S_c}\frac{C_f}{h} - \frac{\nu_{tf}}{S_c}\frac{C_s}{h} \qquad (7)$$

ν_t is the turbulent viscosity of the interface, taken equal to its value in the surface layer.

Table I Module order of resolution

Step	***Resolution***	*Derived variable*
1.	Solve the Saint-Venant Equation.	U^{N+1}, V^{N+1}, H^{N+1}
2.	Derive the surface velocity and the surface turbulent viscosity.	U_SURF^{N+1}, V_SURF^{N+1}, $HUCT\_SURF^{N+1}$
3.	Calculate the fluxes from bedload to suspension and surface to suspension.	$TEXP, TIMP, TSCEXP$
4.	*Solve the advection-diffusion of the suspended concentration*	C_s^{N+1}
5.	*Calculate the fluxes from suspension to surface.*	$TEXP\_SURF$, $TIMP\_SURF$, $TSCEXP\_SURF$
6.	*Solve the advection diffusion of the surface layer*	C_f^{N+1}
7.	*Calculate the fluxes from suspension to bedload*	*GAIA*
8.	Solve bedload transport.	

Table II Buoyant flux numerical implementation

Buoyancy/Layer	**Suspended** step 3.	**Surface** step 5.
Settling $w_s > 0$	$\boldsymbol{SMH} = +\frac{p_s w_s C_f^{N+1}}{h^2}$	$\boldsymbol{SMI} = -p_f w_s$
Buoyant $w_s < 0$	$\boldsymbol{SMI} = -p_s w_s$	$\boldsymbol{SM} = -p_s w_s C_s^{N+1}$

Table III Mixing flux numerical implementation

Layer	$\frac{\nu_{tf}}{S_c}\frac{C_s}{h}$	**Flux**	$\frac{\nu_{tf}}{S_c}\frac{C_f}{h}$	**Flux**
Suspended step 3.	*Sink*	$\boldsymbol{SMI} = -\frac{\upsilon_t}{Sc}$	*Source*	$\boldsymbol{SMH} = +\frac{\upsilon_t}{Sc}\frac{C_f^{N+1}}{h^2}$
Surface step 5.	*Source*	$\boldsymbol{SM} = +\frac{\upsilon_t}{Sc}\frac{C_s^{N+1}}{h}$	*Sink*	$\boldsymbol{SMI} = -\frac{\upsilon_t}{hSc}$

One can notice that when a term is a source of mass, then it is added explicitly while when it is a sink for concentration,

it is added implicitly. The fractional/variational resolution of the layer concentration evolution may induce mass creation or losses during the numerical solving. The final balance of mass must be verified over different tests cases and for different type of tracers.

III. VALIDATION METHODOLOGY

A. Test cases: hydrodynamic and forcing

The model mass conservation is assessed over three test cases based on two different meshes. The first two cases use an identical mesh and simply test the masses transfer over a basic rectangular flume with and without flow. For both cases, the initial free surface elevation is constant and fixed at $11m$. The flume width is of $80.89m$ while its length of $281.53m$. In the first scenario, all the boundaries are closed resulting in an immobile water tank. In the second scenario a constant flow, $Q = 50m^3/s$ and elevation $h = 11m$ are imposed upstream at $X = 0m$ and downstream at $X = 281.53m$ over a limited part of the lateral boundary. The upstream and downstream liquid boundaries do not cover the full lateral extent of the domain. That way, a non-uniform velocity field is created inside the domain.

A triangular mesh of 1100 nodes is used to discretize the domain. Figure 2 shows the velocity field in the flume for the second test case and after 2 hours. For these two scenarios we use a time step for the resolution of $15s$.

The third test case is here to assess how tidal flats will affect the mass transfer of the module. Thus, the focus is taken on a larger zone. The domain extends 15-km in x wise and 7-km y wise. The bottom elevation evolves linearly from $-50m$ at $X = 0$ to $+10m$ at $X = 15km$ while remaining constant in the y-direction. The triangular mesh discretizing the domain is made of ~12400 nodes of equal size around 100m. Initially, the water is immobile with a constant and null free surface elevation.

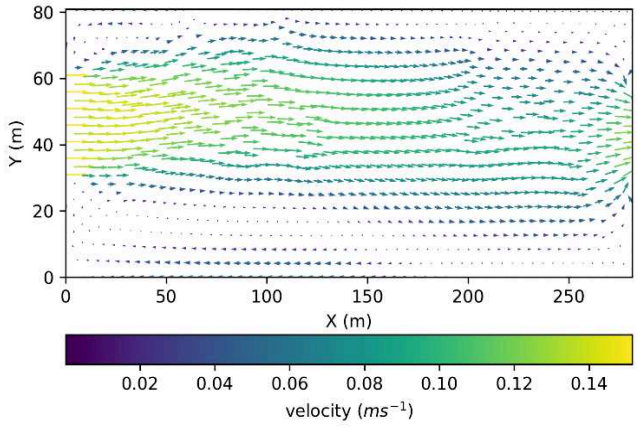

Figure 2. Second test case depth-averaged velocity after 2 hours of simulation. The bottom depth is homogenous and the free surface elevation remains constant at 11m. Initially, the water is still, a constant discharge of $50m^3s^{-1}$ forces the domain upstream (30≤Y≤60m) and downstream (35≤Y≤60m). All the boundaries are closed for the tracers.

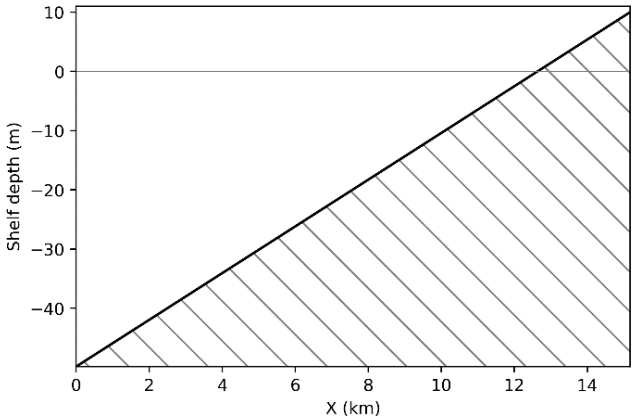

Figure 3. Longitudinal cross section of third test case with bathymetry. The left boundary represents the deep sea while the right one is the coastline. The depth goes linearly from -50m, at X=0m, to 10m at X=15km. The sea boundary is forced with a sea surface wave of amplitude 0.3m and period 12h. All the boundaries are closed for the tracers. The grey horizontal line is the initial water elevation.

The model is forced at $X = 0$ by a sinusoidal wave of amplitude 0.3m and period of 12 hours. This model, with its bathymetry and forcing is a schematization of a North Sea coastline under the main tidal component M2. For the three scenarios, the domain is always closed for tracer allowing easier comparison between initial and final mass. A constant turbulent viscosity for the surface and the suspended layer of $10^{-6}m^2/s$ is used. The bottom friction is characterized by a constant Chézy coefficient of $65m^{1/2}/s$.

While the wave equation solves the shallow water flow [16] [17], the classical resolution method is used for the tracer advection diffusion. For all the three scenarios, the bedload is made of a unique layer without cohesive sediments. Bedload transport is allowed following van Rijn's equation. Its validity range for particle size matches the size of particles generally sampled in the North Sea or its major influents. No erosion is permitted from the bottom thanks to the definition of a high critical shear stress.

B. Initial condition on tracers and buoyancy.

A unique class of plastic is inputted in the models. This class is defined as non-cohesive sediment and characterized by a constant absolute settling velocity of $|w_s| = 1.10^{-3}m/s$. For all three test cases, three scenarios are tested with varying initial conditions and buoyancy:

- Initial mass in the **surface layer** with **settling** plastic ($w_s > 0$). Surface plastics are expected to be transferred into suspension and then in the bedload.
- Initial mass in the **suspended layer**, with **settling** plastic ($w_s > 0$). Tracers will go directly into the bedload layer. Only a minimal fraction of the initial mass will go into the surface due to mixing. The rest of the exchanges follows what is already implemented in Telemac2D and Gaia.
- Initial mass in suspension, with **buoyant** plastic ($w_s < 0$). Plastic mass will go from suspension to the floating

layer with turbulent mixing dampening the buoyancy flux.

The simulations are run until vertical mass equilibrium is reached.

IV. RESULTS

A. Mass conservation

For the first two test cases and for all three scenarios, the model converges towards the expected and aforementioned behaviours. For test case 1 and for the three scenarios, the relative evolution of plastic mass in respect of time is represented in figure 4. The final mass creation or loss is shown in Table IV for the first two test cases.

For the first scenario, shown in Figure 4a, mass is transferred from the surface layer to the suspension and then reaches the bottom layer where it is kept. The total mass creation is equal to 0.136% for all scenarios where suspended and surface layer have exchanges. When comparing the time taken by the mass transfer with the time for a particle, with the given settling velocity w_s, to travel $11m$, Δt, (represented by the vertical grey line), one can notice that for scenario (a), at Δt maximal suspended mass is reached. Furthermore, the time needed by the simulation to reach full mass transfer to the bottom is approximatively twice Δt. This stems from the characteristic length chosen for the buoyant fluxes definition which is h for fluxes from floating to suspension and suspension towards bed.

This could be modified by assuming that floating particles travel a smaller vertical distance before reaching the suspension layer. In Figure 4b, the initial mass is set to the suspended layer and is totally transferred to the bedload. Figure 4c shows identical behaviour except that, as buoyant, the mass is transferred accordingly towards the surface. At Δt, around 60% of the initial mass have been transferred. Scenario (b) creates a negligible amount of mass as fluxes are mostly handled by Telemac2D and Gaia and can be taken as reference for the mass conservation of the module. The two vertical exchanges and their implementation introduces a mass creation of 0.1%. There is limited however not negligeable error in the mass conservation. One could wonder which of the exchange is responsible for this divergence.

Table IV Relative final mass for the test case 1 and 2. The mass are rounded up to three decimals.

	Mass lost / created (%)	
Scenario / test cases	**Test case 1**	**Test case 2**
(a)	0,136	0,136
(b)	$\mathbf{1.5\ 10^{-5}}$	$\mathbf{9.4\ 10^{-4}}$
(c)	0,136	0,136

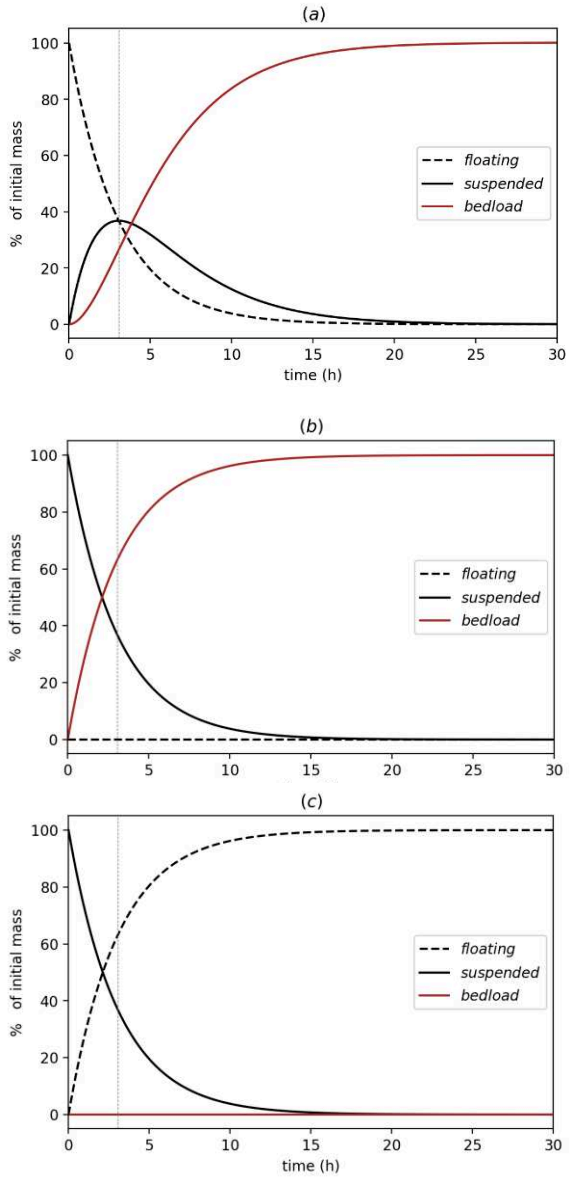

Figure 4. Relative mass evolution of the three layers in test case 1 for scenarios (a), (b) and (c) in vertical order. The vertical grey line at $t = \Delta t \sim 3h$ represents the time for a particle, with the given settling velocity, to travel the water depth of 11m.

B. Implicitation for vertical mixing fluxes

To identify the source of the created mass, the buoyant or the mixing flux, additional calculations were performed with changes in the fluxe implementation. Three configurations were observed. The first one is the implicit-explicit expression of the buoyant and mixing fluxes, seen in Table II and III. The second configuration removes the mixing fluxes while the last one considers an only explicit implementation for the turbulent fluxes. Table V summarizes the results on mass creation.

Table V Table V Relative final mass for different implementation of the vertical fluxes for test case 1 and 2

Flume	Test case:	1	2		
	Mixing fluxes implementation:	*Implicit explicit*	*none*	*explicit*	*Implicit explicit*
Mass difference (%)	*(a)*	0.136	0.136	0.136	0.136
	(b)	$\mathbf{1.6\ 10^{-5}}$	$\mathbf{1.0\ 10^{-3}}$	$\mathbf{1.0\ 10^{-3}}$	$\mathbf{1.0\ 10^{-3}}$
	(c)	0.136	$\mathbf{4.10^{-3}}$	0.136	0.136

No significant changes were observed when using an explicit implementation of the vertical mixing fluxes. For scenario (a), mixing has limited influence since mass is rather quickly transferred towards the suspension and then the bottom. In the other hand, in scenario (c), the mixing exchanges are more significant since the mass settles in the surface layer with continuous mixing with the suspension. For all configurations with mixing fluxes, the mass creation is of the same order. However, when there is no mixing and for scenario (c) mass creation drops significantly to reach the level of mass created in scenario (b). The combined turbulent and buoyant fluxes induce limited mass creation. Thereafter, the implicit-explicit implementation will be kept as providing more stability to the equations especially over tidal flats.

C. *Tidal flats*

Over test case 3 and for scenarios (a), (b) and (c) the model's advection diffusion equation does not converge anymore due to the inter tidal area located between kilometres 12 and 13 of the schematized shelf. However, functioning over tidal flats is crucial for the intended use of the final process-based model. Thus, to overcome this divergence, two solutions artificially removing the dry elements from the calculation of the vertical fluxes were investigated.

The first one, α, keeps the same implementation as before. It uses the NERD scheme for the resolution of the advection of tracers with free surface gradient correction and a minimum threshold, $h_{\lim}$, on the free surface elevation to define the mixing and buoyant fluxes. Several different limit values were tested and their respective results in term of convergence and final mass conservation are shown in table VI.

The second option, named β, is to use masking of the dry elements along with the LIPS scheme for the advection. Mass conservation of this method is shown in the same table. In both cases, the explored solution is not ideal as adding sharp limits, such as clipping on the elevation, results in the creation or removal of mass. For configuration α, the model was converging only when $h_{\lim} > 0$. Full explicit implementation of the mixing fluxes did not allow convergence of the model in neither of the tidal flat configuration. Here again, there is limited mass creation for scenario (b) and all configuration, due to the limited exchanges between the surface and the suspended layers. However, for the other scenarios, the created/lost mass in not negligible anymore and reaches the order of one percent to divergence, especially when the elevation threshold becomes too low for configuration (c). Configuration α with a high enough threshold (0.1m) seems to limit mass creation for all scenarios. Configuration β does not allow convergence for (a) and (c). The issues that arise with tidal flats are challenging and requires further in-depth study.

D. *Implicitation for tracers concentration*

Another lead was explored to reduce the mass creation in cases with and without tidal flats: eventual implication of the concentrations in the fractional resolution of the concertation at a given time step. Once step 4 of the resolution is reached (Table VI), instead of using the newly obtained suspended concentration to calculate the explicit fluxes of the surface layer an implication on C_s^N and C_s^{N+1} is used with a factor θ. Thus, the used concentration is T, obtained from (8).

Table VI Table VI Final mass creation / losses on the third test case with tidal flats and for the two different implementations. Different thresholds were tested for the first configuration α

Test case 3		α			β
$h_{\lim}$ (m)		0.1	0.05	0.01	
Mass difference (%)	*(a)*	-0.949	-0.592	8.231	120.259
	(b)	-0.097	-0.097	-0.096	-0.100
	(c)	0.833	1.666	1.24e18	diverge

$$C_s = \theta C_s^N + (1-\theta) C_s^{N+1} \quad (8)$$

This configuration was tested for different values of the implication factor ($0 \leq \theta \leq 1$) and for test case (c). Indeed, for this test case, the tracer class is buoyant linked with an explicit expression of the buoyant flux.

Furthermore, due to the fractional resolution method, the surface tracer concentration at time N is not kept in memory when calculating the floating concentration at time N+1. For test case 3, the results are based on tidal flat configuration α with a limit threshold of 0.1m. Table VII present the results for different implication factors. There is significant improvement when the implication factor is null for test case (2) without tidal flats while limited progress for the test case (3). When C_s^N, suspended concentration of the last time step, is used to calculate the source and sink terms for the surface layer.

Table VII Implication of suspended concentration influence on final mass

Test case – configuration (c)	Mass created / lost (%)		
	$\theta = 1$	$\theta = 0.5$	$\theta = 0$
2-Flume	0.136	0.068	0.003
3-Coast	0.833	0.769	0.731

V. Conclusion

A newly developed three-layer module for TELEMAC-2D and GAIA, for a full process-based model for riverine plastic fluxes has been developed and tested for simple schematized cases.

The proposed numerical implementation of an additional surface layer and the implied vertical fluxes results in limited mass creation in a simple flume without tidal flats for both buoyant and settling plastic classes. For tidal flats, convergence is guaranteed only when imposing a strict limit on the free surface elevation for the vertical fluxes to exist. This strict limit generates significant mass creation that may be containable with manual optimization of the threshold or other implementations. Tidal flats consideration appears rather challenging but are crucial for the intended use of the full model (i.e. dealing with beached plastics) and the author hope that future work on that topic may help to improve the results.

The next step to be investigated and implemented are the different processes affecting riverine plastic (i.e. fragmentation, erosion, biofouling and sediment interaction) for each of them, theoretical or empirical laws must be deduced based on literature, observations or experiments and implemented inside the module. Then drift from external parameters such as wind or waves could also be added as a correction of the surface velocity. Finally, as the control of the presented module is (for now) hard coded using Fortran files, the user friendliness of the module would be considerably improved by the reading of a steering file for monitoring plastics in the simulation.

Acknowledgement

This work is carried out in the framework of the EU H2020 LABPLAS project (www.LABPLAS.eu) and the Flemish SBR PLUXIN project funded through VLAIO and the Flemish Blue Cluster (www.PLUXIN.be).

References

[1] Law, K. L. (2017). Plastics in the Marine Environment. *Annual review of marine science*, *9*, 205-229.

[2] Schmidt, C., Krauth, T., & Wagner, S. (2017). Export of plastic debris by rivers into the sea. *Environmental science & technology*, *51*(21), 12246-12253.

[3] Schöneich-Argent, R. I., Dau, K., & Freund, H. (2020). Wasting the North Sea?–A field-based assessment of anthropogenic macrolitter loads and emission rates of three German tributaries. *Environmental Pollution*, *263*, 114367.

[4] Kooi, M., Reisser, J., Slat, B., Ferrari, F. F., Schmid, M. S., Cunsolo, S., Brambini, R., Noble, K., Linders, T.E.W., Schoeneich-Argent, R. & Koelmans, A. A. (2016). The effect of particle properties on the depth profile of buoyant plastics in the ocean. *Scientific reports*, *6*(1), 1-10.

[5] Reisser, J., Slat, B., Noble, K., Du Plessis, K., Epp, M., Proietti, M., ... & Pattiaratchi, C. (2015). The vertical distribution of buoyant plastics at sea: an observational study in the North Atlantic Gyre. *Biogeosciences*, *12*(4), 1249-1256.

[6] Waldschläger, K., & Schüttrumpf, H. (2019). Effects of particle properties on the settling and rise velocities of microplastics in freshwater under laboratory conditions. *Environmental science & technology*, *53*(4), 1958-1966.

[7] Fischer, R., Lobelle, D., Kooi, M., Koelmans, A., Onink, V., Laufkötter, C., ... & van Sebille, E. (2022). Modeling submerged biofouled microplastics and their vertical trajectories. *Biogeosciences Discussions*.

[8] Jahnke, A., Arp, H. P. H., Escher, B. I., Gewert, B., Gorokhova, E., Kühnel, D., ... & MacLeod, M. (2017). Reducing uncertainty and confronting ignorance about the possible impacts of weathering plastic in the marine environment. *Environmental Science & Technology Letters*, *4*(3), 85-90.

[9] Kukulka, T., Proskurowski, G., Morét-Ferguson, S., Meyer, D. W., & Law, K. L. (2012). The effect of wind mixing on the vertical distribution of buoyant plastic debris. *Geophysical Research Letters*, *39*(7).

[10] Andersen, T.J., Rominikan, S., Olsen, I.S., Skinnebach, K.H., Fruergaard, M., 2021. Flocculation of PVC microplastic and fine-grained cohesive sediment at environmentally realistic concentrations. *Biological Bulletin* 240, DOI:10.1086/712929.

[11] Scherer C, Weber A, Stock F, Vurusic S, Egerci H, Kochleus C, Arendt N, Foeldi C, Dierkes G, Wagner M, Brennholt N, Reifferscheid G. (2020) Comparative assessment of microplastics in water and sediment of a large European river. Sci Total Environ. 2020 Oct 10;738:139866. doi: 10.1016/j.scitotenv.2020.139866.

[12] Audouin, Y., Benson, T., Delinares, M., Fontaine, J., Glander, B., Huybrechts, N., ... & Walther, R. (2019). Introducing GAIA, the brand new sediment transport module of the TELEMAC-MASCARET system. In *XXVIth TELEMAC-MASCARET User Conference, 15th to 17th October 2019, Toulouse*.

[13] Domercq, P., Praetorius, A., & MacLeod, M. (2022). The Full Multi: An open-source framework for modelling the transport and fate of nano-and microplastics in aquatic systems. *Environmental Modelling & Software*, *148*, 105291.

[14] Toorman, E.A. (2008). Vertical mixing in the fully developed turbulent layer of sedi- ment-laden open-channel flow. J. Hydraul. Eng. 134 (9), 1225–1235 .

[15] Toorman, E.A. (2009). Errata and addendum for “Vertical mixing in the fully devel- oped turbulent layer of sediment-laden open-channel flow”by EA Toorman. J. Hydraul. Eng. 135 (6), 538 -538

[16] Hervouet, J. M., & Razafindrakoto, E. (2005). The wave equation applied to the solution of Navier-Stokes equations in finite elements. *WIT Transactions on the Built Environment*, *78*.

[17] Hervouet, J. M. (2007). *Hydrodynamics of free surface flows: modelling with the finite element method*. John Wiley & Sons.

Modelling particle size distribution in TELEMAC-2D with Population Balance Method

Nithin Achutha Shettigar[1], Wilhem Riom[1], Qilong Bi[1,2], Erik A. Toorman[1]
nithinachutha.shettigar@kuleuven.be
[1]: Hydraulics Laboratory, KU Leuven, Belgium
[2]: Flanders Hydraulics Research, Antwerp, Belgium

Abstract – **Modelling transport of microplastic particles in aquatic environments is challenging owing to the heterogeneity of the particles. Conventional Lagrangian and Eulerian modelling approaches come with the restriction of defining singular particle properties. Drawing inspiration from other scientific disciplines, particle heterogeneity is addressed in this work using population balance equations (PBE) with the method of moments solution. As a first step, a wide size range of microplastics is considered as internal coordinate of the number density function (NDF). The moment transport equation includes source and sink terms of erosion and deposition respectively. The method is implemented in the TELEMAC-2D and WAQTEL environments. The test case of a channel with steady state flow and erosion and deposition zones is implemented. The results of the model show physically meaningful NDFs after episodes of erosion and deposition. Further model development is planned to include the integral source and sink terms such as aggregation and breakage of flocs of microplastic and sediment particles.**

***Keywords*:** microplastics, deposition, erosion, method of moments, number density function, Telemac2D.

I. INTRODUCTION

Drastic increase in the use of plastics without proper disposal mechanisms has resulted in large quantities of plastic litter ending up in the open environment [1]. Often rivers play a crucial role in transporting plastic litter from inland to the marine environment [2]. Once disposed in the open environment, plastic litter undergoes a slow but continuous change in its size, shape and strength [3][4]. This results eventually in the apparition and multiplication of microplastic. Microplastic are generally described in the literature as plastic litters of size 5 mm or less [5]–[7]. Plastic litter of a few nanometres are also detected in many parts of the world, including on top of the glaciers [8]. This makes microplastics very challenging to track.

Modelling tools are often employed to simulate plastic litter transport pathways in the fluvial, marine and estuarian systems. Coupled hydrodynamic and Lagrangian particle tracking models can reveal the transport trajectories of plastic litter. This approach has led to claims of floating garbage patches in several parts of the world oceans [9]. However, Lagrangian models track the individual particles which requires large computational resources in order to track realistic plastic concentrations [8][9]. Moreover, the Lagrangian approach is not ideal to model the processes of plastic transport such as – deposition, erosion, aggregation, breakdown, etc. On the contrary, the Eulerian approach deals with particle mass or volumetric concentrations; therefore, modelling realistic plastic concentrations is convenient with the Eulerian approach. A major weakness of both the Lagrangian and Eulerian approach is the need for multiple classes (few tens) to address heterogeneity of plastic litter in the aquatic environment, in other word, the variety of the size, shape and density [9]. In the Eulerian approach, for each different property of the plastic, a different particle class must be defined. In order to model a wide size range – from few nanometres to few millimetres – several size classes must be defined. This requires high computational resources. A sophisticated approach exists to address this issue. Population Balance Equations (PBE) with the Method of Moments (MoM) are often used in the chemical, biochemical and industrial engineering to model the bubble size distribution in chemical applications, flocs size distribution in wastewater treatment processes, particle size distribution in the grinding process, etc [12]. In the next section the PBE approach and the mathematical model of the PBE applied to microplastic transport in aquatic environment is explained.

II. POPULATION BALANCE EQUATION

The PBE approach describes the spatial and temporal evolution of the number density function (NDF) associated with a particle population. While NDF evolves continuously due to phenomena of advection and diffusion, it can also evolve discontinuously due to aggregation, breakage, etc. [13]. In the PBE approach, a particle population is either a discrete or a continuous entity which interacts with their environment which is a continuous phase. The particle populations are defined by an array which contains both internal and external coordinates. An internal coordinate describes the properties of the particle population in the state space and an external coordinate is used to describe the particle location in the physical space [12]. The internal coordinates may include the particle's size, volume, mass or the chemical composition [14]. The mathematical expression of PBE applied to a system with a particle population in a carrier fluid consists of the Navier-Stokes equations (or other shallow water simplification) for the carrier fluid and a spatial transport equation (e.g. advection and diffusion), source terms (e.g. dissolution, deposition), integral terms

(e.g. aggregation and breakage) for the particle population [14]. In this paper, the transport of the microplastics in the liquid media is studied with a focus on the erosion and deposition as sink and source terms. Further, the size of the microplastics alone is defined as the internal coordinate of the NDF. The tested model is a 2D hydrodynamic model coupled with a PBE-based particle transport model.

The evolution of the NDF of a discrete phase of particles in a continuous medium is expressed in the following form [15]:

$$\frac{\partial hn}{\partial t} + \frac{\partial}{\partial x}(\mathrm{hU}\, n) + \frac{\partial}{\partial y}(\mathrm{hV}\, n) - \frac{\partial}{\partial x}\left(hD_x \frac{\partial n}{\partial x}\right) - \frac{\partial}{\partial y}\left(hD_y \frac{\partial n}{\partial y}\right) = S_o - S_i \quad (1)$$

where:

- $n(\xi; x, y, t)$ = number density function $[number/m^3]$ or $[1/m^3]$;
- ξ = internal coordinate of NDF e.g. particle size;
- x, y = spatial coordinate;
- U, V = depth-averaged velocities in x & y directions;
- D_x, D_y = turbulent dispersion coefficients in x & y directions;
- S_o, S_i = sink term and source term respectively e.g., aggregation, breakage, erosion, deposition, etc.

Several methods of solving PBE can be found in the literature. The class or sectional method works by discretizing the internal coordinate space into intervals (classes or sections), transforming the PBE into a set of macroscopic balance equations in the physical domain [16]. However, a large number of scalars (i.e., classes) are required to maintain reasonable accuracy [17].

In the Monte Carlo method, a finite sample of the population is used to track its evolution under the influence of growth and disintegration mechanisms with probabilities proportional to the corresponding rates [18]. However, because of the large number of scalars required, incorporating these methods into CFD codes is also computationally challenging.

An effective and more elegant solution is found through the Method of Moments (MoM). A discrete set of moment values carry the NDF information. The low order moment values are related to the mean, variance, skewness and flatness of the statistical distributions described by the NDFs [19]. In contrast to the method of classes and the Monte Carlo method, MoM is appropriate for use with CFD codes because the internal coordinates are integrated, requiring only a small number of scalars (i.e., lower order moments) at each grid point [17].

A. Method of Moments

In the case of a multivariate NDF i.e., a NDF with several internal coordinates (ξ), the k^{th} order moment (M_k) of the NDF is expressed as:

$$M_k(x, y, t) = \int_{\Omega_\xi} n(\xi; x, y, t)\, \xi_1^{k_1} \xi_2^{k_2} \dots \xi_M^{k_M}\, d\xi \quad (2)$$

where Ω_ξ represents the internal coordinate space of all the possible sizes ξ. The array $k = (k_1, k_2, \dots k_M)$ represents the order of the moment values with respect to all the internal coordinate values (ξ) taken into account [20]. In the case of single internal coordinate ξ which assumes only $\mathbb{R}^+$ (non-negative real numbers), the above moment expression reduces to:

$$M_k(x, y, t) = \int_0^{+\infty} n(\xi; x, y, t)\, \xi^k\, d\xi \quad (3)$$

The NDF transport equation (1) can be modified into a moment transport equation by multiplying it with the ξ^k and integrating over $[0, +\infty)$ [13].

$$\frac{\partial M_k}{\partial t} + \frac{\partial}{\partial x}(U\, M_k) + \frac{\partial}{\partial y}(\mathrm{V}\, M_k) - \frac{\partial}{\partial x}\left(D_x \frac{\partial M_k}{\partial x}\right) - \frac{\partial}{\partial y}\left(D_y \frac{\partial M_k}{\partial y}\right) = \int_0^{+\infty} S_o\, \xi^k\, d\xi - \int_0^{+\infty} S_i\, \xi^k\, d\xi \quad (4)$$

The solution of (4) is advantageous as the moment values hold quantities with physical meaning and therefore are measurable. M0, M1 and M2 represent the total number of particles, total length and total area respectively [21]. This overcomes difficulty of validation through the NDF, as the NDF itself is not measured in most cases but its integral quantities are measured such as total mass, total volume, etc. However, the challenge is to express the sink and source terms in moment values, which leads to closure problem.

This is addressed by means of quadrature approximation. In the Quadrature Method of Moments (QMOM), N-node Gaussian quadrature is employed to approximate the integrals in the moment transport equations for the solution of a univariate PBE. The algorithm calculates the N abscissas and N weights of the quadrature from the 2N transported moments [16]. The NDF is approximated with the discrete weighted sum of Dirac δ functions, uniquely found by means of moment inversion algorithms [13]:

$$n(\xi; x, y, t) \approx \sum_{i=1}^{N} w_i(x, y, t)\, \delta[\xi - \xi_i(x, y, t)] \quad (5)$$

which implies the moment approximation as:

$$M_k(x, y, t) \approx \sum_{i=1}^{N} w_i(x, y, t)\, \xi_i^k(x, y, t) \quad (6)$$

The abscissas $\xi_i(x, y, t)$ and the weights $w_i(x, y, t)$ are derived from the lower order moments. For a NDF approximation of order N, only the first $2N$ moments are essential [22]. In the next section, an alternative MoM-Extended Quadrature Method of Moments (EQMOM) is explained, which is the focus of the current work.

B. EQMOM procedure

In the QMOM procedure, the approximation of the NDF at certain values of the internal coordinate (ξ) can be problematic in cases where a population is diminishing continuously (for example, pure settling). An alternative MoM for such case is EQMOM which utilises continuous kernel density functions (KDF) in the place of Dirac δ functions. Several existing works have used different KDFs as applicable to the physical processes involved. Most widely reported are the Gaussian distribution with infinite support $(-\infty, \infty)$, gamma and log-normal distributions with semi-infinite positive support $[0, \infty)$ and beta distribution with finite support [0,1] [16]. The mathematical expressions of the EQMOM approximation of the NDF is:

$$n(\xi; x, y, t) \approx p_N(\xi; x, y, t) = \sum_{i=1}^{N} w_i \, \delta_\sigma(\xi, \xi_i) \tag{7}$$

where w_i and ξ_i are the weights and abscissae of the non-negative KDF. N is the number of KDFs used to approximate the NDF.

In the case where σ tends to zero, in other words the population is diminishing to few particle sizes, the KDF $\delta_\sigma(\xi, \xi_i)$ tends to a Dirac δ function, w_i are the non-negative weights and ξ_i are the respective quadrature abscissae [13]. The first step in the numerical procedure of solving EQMOM is the selection of an appropriate KDF. This choice has to be made based on the distribution of the NDF in question. From the knowledge of the size distribution of the plastic particles found in nature [7], we select the log-normal KDF. Therefore the δ function can be defined as [23]:

$$\delta_\sigma(\xi, \mu) = \frac{1}{\xi\sigma\sqrt{2\pi}} \exp\left(-\frac{(\ln\xi - \mu)^2}{2\sigma^2}\right); \xi, \sigma \in \mathbb{R}^+, \mu \in \mathbb{R} \tag{8}$$

where μ and σ are the mean and standard deviation of the natural logarithm of the log-normally distributed variable ξ. The integer moments of order k of the log-normal distribution is given by the Mellin transform [23]:

$$M_k(x, y, t) = exp\left(k\mu + \frac{k^2\sigma^2}{2}\right) \tag{9}$$

One-node case – One-node case uses one subordinate KDF to represent the whole distribution. To take bimodal (or higher) behaviour of NDF into account, using two-node (or more) is required. The one node (N=1) approximation of the NDF is the simplest case of EQMOM, which needs only the first $2N + 1 = 3$ moments to be solved [16]. In this case the approximated NDF is given as [23]:

$$\begin{aligned} n(\xi; x, y, t) \approx P_1(\xi; x, y, t) &= w_1 \delta_\sigma(\xi, \xi_1) \\ &= \frac{w_1}{\xi\sigma\sqrt{2\pi}} exp\left(-\frac{(\ln\xi - \xi_1)^2}{2\sigma^2}\right) \end{aligned} \tag{10}$$

The first three moments can be defined with (10) as follows:

$$\begin{cases} M_0 = w_1 \\ M_1 = w_1 \, e^{(\xi_1 + \sigma^2/2)} \\ M_2 = w_1 \, e^{(2\xi_1 + 2\sigma^2)} \end{cases} \tag{11}$$

Equation (12) can be analytically solved to find the values of w_1, ξ_1 and σ:

$$\begin{cases} w_1 = M_0 \\ \xi_1 = \ln\left(\dfrac{M_1^2}{M_0\sqrt{M_0 M_2}}\right) \\ \sigma = \sqrt{2\ln\left(\dfrac{\sqrt{M_0 M_2}}{M_1}\right)} \end{cases} \tag{12}$$

C. Erosion and deposition terms in the MoM framework

The fully unsteady and non-equilibrium 2D sediment transport equation is written in terms of the sediment concentration C as:

$$\begin{aligned} &\frac{\partial hC}{\partial t} + \frac{\partial}{\partial x}(\mathrm{hU}\, C) + \frac{\partial}{\partial y}(\mathrm{hV}\, C) - \\ &\frac{\partial}{\partial x}\left(hD_x \frac{\partial C}{\partial x}\right) - \frac{\partial}{\partial y}\left(hD_y \frac{\partial C}{\partial y}\right) = \\ &\mathrm{E} - \mathrm{D} \end{aligned} \tag{13}$$

where D = deposition rate and E = resuspension rate, both with units $[kg/m^2 s]$.

The existing sediment transport models define the erosion and deposition rates in two categories, i.e., cohesive and non-cohesive cases. A choice must be made regarding which category to be applied to the microplastic case. In order to avoid investigating through tens of empirical formulations of erosion rates under the non-cohesive category and to be able to express these rates in terms of moments of NDF, the formulation under the cohesive sediment category is adapted.

The erosion rate and deposition rate for cohesive sediments are specified as:

$$\begin{aligned} E &= \begin{cases} \mathrm{e}\, C_{bed}\left(\dfrac{\tau_b}{\tau_R} - 1\right) & \text{if} \quad \tau_b > \tau_R \\ 0 & \text{if} \quad \tau_b \le \tau_R \end{cases} \\ D &= \begin{cases} w_s \; C_{sus}\left(1 - \dfrac{\tau_b}{\tau_S}\right) & \text{if} \quad \tau_b < \tau_S \\ 0 & \text{if} \quad \tau_b \ge \tau_S \end{cases} \end{aligned} \tag{14}$$

where:

- C_{sus} = sediment concetration in suspension $[kg/m^3]$;
- C_{bed} = sediment concetration in the bed layer $[kg/m^3]$;
- w_s = sediment settling velocity $[m/s]$;
- e = erosion rate $[\mathrm{m}/s]$;
- τ_b = bed shear stress $[\mathrm{N}/m^2]$;
- τ_R = critical shear stress of resuspension $[\mathrm{N}/m^2]$;
- τ_S = critical shear stress of sedimentation $[\mathrm{N}/m^2]$;

The above formulation expressed in terms of sediment concentration needs to be adapted for the moment transport problem. The same formulation can be rewritten in terms of moment values. The moment erosion rate (E_k) and depsoition rate (D_k) are then expressed as:

$$E_k = e_\mathrm{k}\, M_{k_{bed}}\left(\frac{\tau_b}{\tau_R} - 1\right) \tag{15}$$

$$D_k = w_{s_k} M_{k_{sus}} \left(1 - \frac{\tau_b}{\tau_s}\right)$$

where:

- $M_{k_{sus}}$, $M_{k_{bed}}$ = moment value M_k in the suspension load and bottom material respectivbely with units of 3 lower order moments being $[1/m^3], [1/m^2], [1/m]$;
- w_{s_k} = moment settling velocity $[\mathrm{m/s}]$;
- e_k = moment erosion rate $[\mathrm{m/s}]$;

Settling velocity of the k^{th} order moment w_{s_k} is expressed in the form:

$$w_{s_k} = \frac{1}{M_k} \int_0^{+\infty} \xi^k \, w_s(\xi) \, n \, d\xi \tag{16}$$

where $w_s(\xi)$ is the size dependent settling velocity e.g. Stokes equation. The above expression is essentially a weighted average of settling velocity. The erosion rate e_k is not defined in a similar integral term, instead its values are assumed irrespective of the particle size.

The resulting 2D moment transport equation is expressed as:

$$\frac{\partial h\, M_k}{\partial t} + \frac{\partial}{\partial x}(\mathrm{hU}_k\, M_k) + \frac{\partial}{\partial y}(\mathrm{hV}_k\, M_k) - \frac{\partial}{\partial x}\left(hD_x \frac{\partial M_k}{\partial x}\right) - \frac{\partial}{\partial y}\left(hD_y \frac{\partial M_k}{\partial y}\right) = E_k - D_k \tag{17}$$

III. TEST CASE: FLUME MODEL

A. Model implementation

A test case is developed in TELEMAC-2D to verify the use of PBE-MoM with erosion and deposition terms. In this regard, the modelling features available in WAQTEL – MICROPOL are utilised. WAQTEL is a water quality modelling package of the TELEMAC system (TMS) [24]. MICROPOL is a module under WAQTEL which allows modelling the evolution of the micro-pollutants e.g., heavy metals in three components of an aquatic system – water, suspended particulate matter and bottom material. Each of these components are a homogenous class. MICROPOL employs 5 tracer classes – suspended sediment (SS), bottom sediment (SF), dissolved micropollutant (C), micropollutant fraction adsorbed by suspended sediment (C_{ss}) and micropollutant fraction adsorbed by bottom sediment (C_{sf}). The SS and SF comply to the classical sedimentary physics i.e., deposition and resuspension as in case of cohesive sediments. These two processes are defined by the law of Krone and Partheniades respectively. One of the key assumptions made in MICROPOL is that SS and SF are passive tracers i.e., they do not have impact on the flow (no feedback). Therefore the bed elevation is kept unmodified during the simulation [25]. While MICROPOL is designed to be used for the micropollutant evolution, we make use of only the sediment modelling aspects to implement the PBE-MoM. The reason for this is the simplicity of the sediment transport implementation in MICROPOL and bed elevation being unmodified. At this stage, the transformation of bottom material moment values to the bed elevation is not yet determined. As a result, MICROPOL is a convenient candidate for the PBE-MoM implementation with few modifications.

As described under section II.B, in a one-node case the first three lower order moments are sufficient to reconstruct the NDF. These three moment values are treated as suspended and bottom material in MICROPOL model. In other words, the three moment values are specified for suspended class and three moments for the deposition class, resulting in a total of 6 tracers. We introduce these 6 tracers in the MICROPOL model along with the associated parameter sets. The nomenclature of the 6 moments are given in Table I. As explained in the section II.C, each of the suspended and bottom material moment values have source and sink terms i.e., erosion and deposition fluxes. The nomenclature of the parameter sets associated with erosion and deposition fluxes is given in Table II.

Table I Nomenclature of the 6 tracer introduced in MICROPOL model

Indices of unique tracers	Description
SS_M0, SS_M1, SS_M2	Moments M0, M1, M2 respectively in suspension load
SF_M0, SF_M1, SF_M2	Moments M0, M1, M2 respectively in bottom material

Table II Nomenclature of the parameters associated with 6 tracer introduced in MICROPOL model

Parameter	Description
ERO_M0, ERO_M1, ERO_M2	Erosion rate of moment M0, M1, M2 respectively
TAUS_M0, TAUS_M1, TAUS_M2	Critical shear stress of sedimentation of moment M0, M1, M2 respectively
TAUR_M0, TAUR_M1, TAUR_M2	Critical shear stress of resuspension of moment M0, M1, M2 respectively
VITCHU_M0, VITCHU_M1, VITCHU_M2	Settling velocity of moment M0, M1, M2 respectively

B. Hydrodynamic model setup

The model domain is a 50 m long and 2.5 m wide rectangular channel. The bottom elevation reduces gradually from 0 m at the flow inlet to -0.05 m at the flow outlet. The model is provided with an initial condition of 0.47 m water depth. A prescribed flowrate of 1 m^3/s is assigned at the channel inlet, while at the outlet a prescribed elevation of 0.47 m is assigned. A warming up model simulation of 500 s is carried out to create a steady state flow in the channel. The result of this simulation at t = 500 s is used as restart for the further model simulations, results of which are further presented. The further simulation and the hydrodynamic setup are given in Table III. The resulting flow pattern in the channel is a steady state flow with higher bed shear stress at the flow inlet and lower at the flow outlet. This is utilised for a further erosion and deposition behaviour criterion.

Initial moment values M0, M1, M2 are specified over the entire domain for the bottom material only. On the other hand, moment values for the suspended load are prescribed with the channel inflow from t = 0 s to t = 60 s. The values of initial bottom material moments and prescribed suspended load moments are given in Table IV. The calculation of these moment values is detailed under the following section.

Table III imulation and hydrodynamic model setup

Simulation time setup	
number of time steps	5000
time step	0.1 s
Hydrodynamic setup	
prescribed flowrates	0.0; 1.0 m^3/s (outflow boundary; inflow boundary)
prescribed elevations	0.47; 0.0 m (outflow boundary; inflow boundary)
option for liquid boundaries	2; 1 (Thompson method; strong setting)
law of bottom friction	Manning's law
friction coefficient	0.018
type of advection	1; 5; 4 (Method of characteristics for velocity; PSI distributive scheme for depth; N distributive scheme for tracer)
diffusion of tracers	$\frac{1}{h}\ div\ (hv\ \overrightarrow{grad}(T))$
Turbulence model	Constant viscosity
coefficient for diffusion of tracers	1.E-6

Table IV Initial and prescribed moment values

initial bottom material moment values	SF_M0 SF_M1 SF_M2	0.5146 $1/m^3$ 3.576E-4 $1/m^2$ 8.294E-7 1/m
prescribed suspended load moment values	SS_M0 SS_M1 SS_M2	0.5146 $1/m^3$ 3.576E-4 $1/m^2$ 8.294E-7 1/m

C. *PBE-MoM model setup*

The values of the moments M0, M1, M2 given in Table IV are estimated from the NDF associated with field measurements of microplastic particles. These field measurement are carried out under the Flemish project – PLUXIN [26]. Measurement data is collected at the Wintam area of the Scheldt river [27]. The NDF of 4,737 particles is shown in Figure 1, along with its reconstructed fit. The particles are grouped in size bins and corresponding NDF is found. Then Riemann integral with 25 bins is applied to calculate the moment value. As explained in the section II.B, the calculated moments are used to derive the parameters w_1, ξ_1 and . Next, these parameters are used to reconstruct the NDF. The mismatch between the measured and reconstructed NDF is caused by the choice of the integral approximation used to calculate the moment values. The resulting moments M0, M1, M2 are presented in Table IV. From here on, the units of M0, M1 and M2 are omitted as they remain consistent i.e., $1/m^3$, $1/m^2$ and 1/m respectively. The reconstructed NDF corresponds to mean size = 695 µm, median size = 380 µm and mode size = 114 µm.

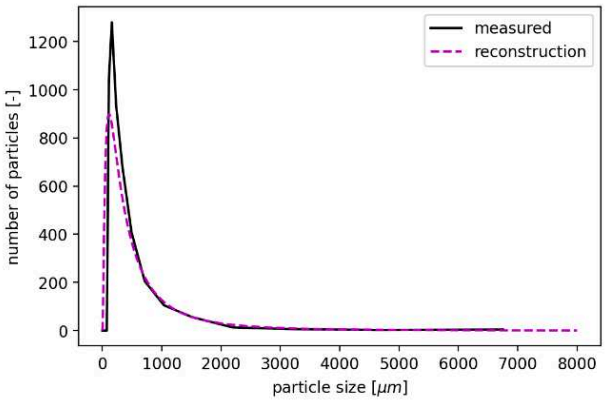

Figure 1. Measured and approximated log-normal fit of the NDF

The settling velocities w_{s_k} for the moment values are calculated as formulated in (5). The size dependent settling velocity is calculated with Stokes' equation. The initial moment values are used for the calculation of settling velocities and these settling velocities are kept constant during the simulation. As in the case of the moment value calculation, a Riemann integral with 25 bins is applied. The resulting settling velocities of the moments M0, M1, M2 are presented in Table V. In the absence of the integral size dependent formulation for the erosion rate, the initial moment values themselves are assigned to the erosion rates e_k. This implicitly allows erosion of scaled-down NDF from the bottom material at each timesteps when bed shear stress exceeds the critical shear stress of resuspension.

The critical shear stresses for resuspension and deposition are selected in order to have two distinct zones in the channel domain – an erosion zone and a deposition zone. The steady state flow allows for these zones to be static in time. The erosion zone is observed in the first 1/3rd length of the channel from the inflow boundary and the deposition zone in the last 1/3rd length of the channel (Figure 2). Further analyses on the moment and NDF evolution are carried out at two nodes roughly 14 m after the beginning of the respective zones. While the node 662 is at the end of erosion zone with a bed shear stress higher than the critical shear stress for resuspension = 2.68 N/m^2, node 840 is at the end of the deposition zone with a bed shear stress lower than the critical shear stress of deposition = 2.42 N/m^2.

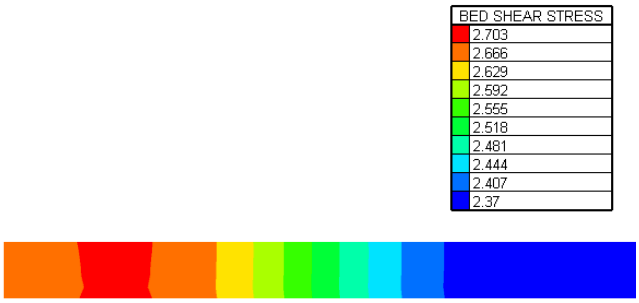

Figure 2. Bed shear stress (N/m^2) in the channel

Table V Parameters set corresponding to three moment values

PBE-MoM model parameters		
erosion rates of moments	ERO_M0	0.5146 m/s
	ERO_M1	3.576E-4 m/s
	ERO_M2	8.294E-7 m/s
settling velocity of moments	VITCHU_M0	0.083 m/s
	VITCHU_M1	0.387 m/s
	VITCHU_M2	0.756 m/s
critical shear stress of resuspension	TAUR_M0, TAUR_M1, TAUR_M2	2.68 N/m^2
critical shear stress of sedimentation	TAUS_M0, TAUS_M1, TAUS_M2	2.42 N/m^2

IV. RESULTS AND DISCUSSION

A. *Mass balance*

Firstly, the moment value conservation is checked. For this purpose, the model domain is transformed into a still basin case, by assigning all boundaries to be solid boundary. Only initial suspended load moment values (M0 = 0.5146, M1 = 3.576E-4, M2 = 8.294E-7) are imposed. This allows all the suspended moment values to be deposited as bottom material moments. The relative error after 500 s simulation is provided in Table VI. These Percentage errors show a good mass conservation of the moment values.

Table VI Mass conservation of moment values

Suspended load moments	Percentage error	Bottom material moments	Percentage error
SS_M0	-0.561E-13	SF_M0	-0.195E-10
SS_M1	0.572E-11	SF_M1	-0.138E-10
SS_M2	0.257E-8	SF_M2	-0.182E-10

B. *Moment evolution*

The moment values in suspension load as well in bottom material are further analysed over the simulation time. The evolution of moment values is shown for the two nodes with node index 662 and 840 in Figure 3.

Node 662, located at the end of the erosion zone, shows the expected behaviour in the moment values of suspension and deposition loads (Figure 3a). M0, which assumes a higher magnitude erosion rate, is intensively eroded due to the exceeded bed shear stress. However, both the M1 and M2 bed load moments do not show significant erosion as they assume erosion rates of 3 and 6 orders of magnitude less than that of M0. The eroded bed load moment is added to the suspended moments. In the M0 suspended load, we see that peak value is higher than 0.6 as compared to the prescribed M0 suspended load = 0.5146. However, this is not noticeable in the case of M1 and M2 in suspension load due to the aforementioned reasons.

Node 840, located at the end of the deposition zone, shows the deposition behaviour of the suspended load moment values (Figure 3b). It should be noted that M0 has the lowest settling velocity and M2 the highest settling velocity. This leads to M2 in the suspension load diminishing significantly in comparison to the other two moments as the bed shear stress stays below the critical shear stress for deposition. Consequently, the bed load moments also show a proportional increase in their values as suspended load moments are deposited to the bed layer. The highest gain in bed load moment is seen for M2 and the lowest one for M0.

C. *NDF evolution*

The transported moment values are transformed into a NDF in the post-processing as briefed in section II.B. The initial moment values result in a mean particle size of 695 µm, which is reflected in the bed layer NDF as shown in Figure 4a. Only a few time steps are selected for Figure 4 such that a moment set at that time at the corresponding node results in a valid NDF. The size range of the NDF are trimmed until 2000 µm, instead of full scale up to 8000 µm as meagre changes are observed at larger size range.

At node 662, located at the end of erosion zone, the bed load NDF is progressively diminishing in its peak particle number as well as the peak number is shifting towards larger particle size (Figure 4a). This is reflected in the mean particle size presented along with each subplot. This shows that the moment value erosion is reflecting the smaller particle erosion which leads to NDF skewing more towards the larger particle. It should be noted that the chosen erosion rate parameters for the moments implicitly favours the erosion of smaller particles. The suspended load NDF shows higher particle number i.e., ~1500 than the prescribed value which is ~900 (Figure 4a), which is due to the addition of eroded material to suspension. The mean size in suspended NDF is remarkably lower than the prescribed value i.e., 695 µm, also caused by the addition of eroded smaller size particles to the suspension.

At node 840, located at the end of the deposition zone, the bottom material NDF is gradually gaining the larger particle sizes reflected in the increasing number on the particles in larger size range (Figure 4b). Also, the NDF of the suspended load is gradually skewed toward the smaller size in coherence with the changes in bottom material NDF. It should be noted that the NDF of the suspended load has a mean size much lower than the prescribed value of 695 µm, as a portion of heavier particles have already settled in the deposition zone before reaching the node 840 (Figure 4b).

The NDFs of the suspended and bottom material do not show significant changes in the larger size range (>2000 µm) due to the fact that log-normal KDF is used for approximating the NDF. Log-normal distribution by its characteristics tend to zero at the larger size range. When significant changes at the larger size range is expected, more than one subordinate KDF would be required.

a)

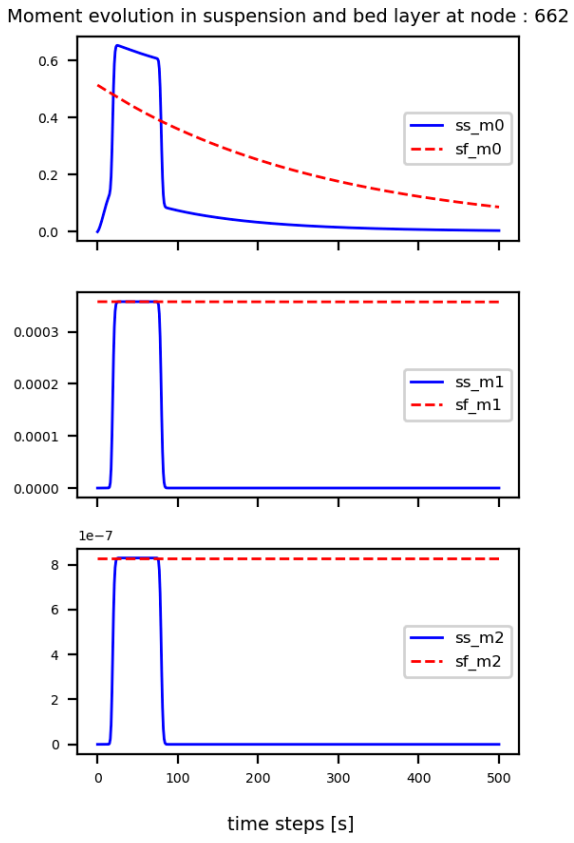

b)

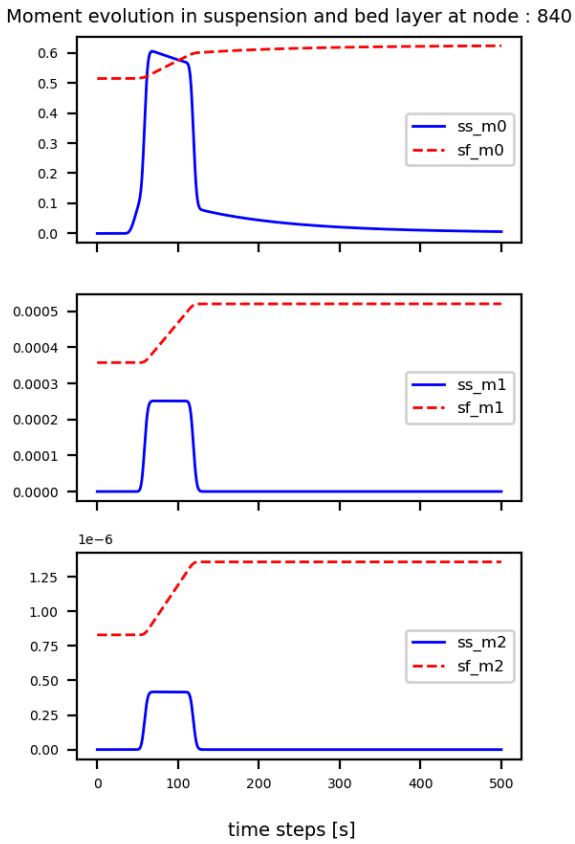

Figure 3. Moment evolution of suspended load and bottom material at two nodes a) 662 (erosion zone) and b) 840 (depostion zone). First, second and third row of plots show evolution of M0, M1 and M2 respectively.

a)

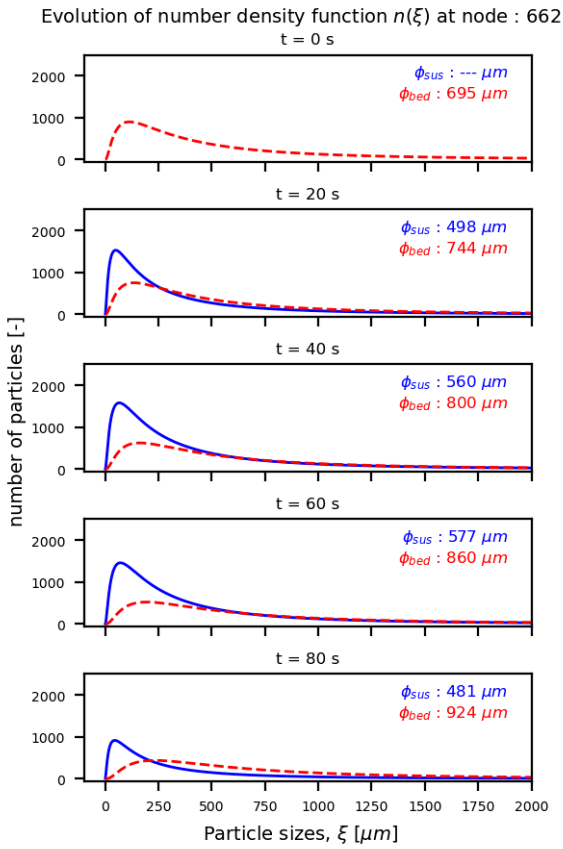

b)

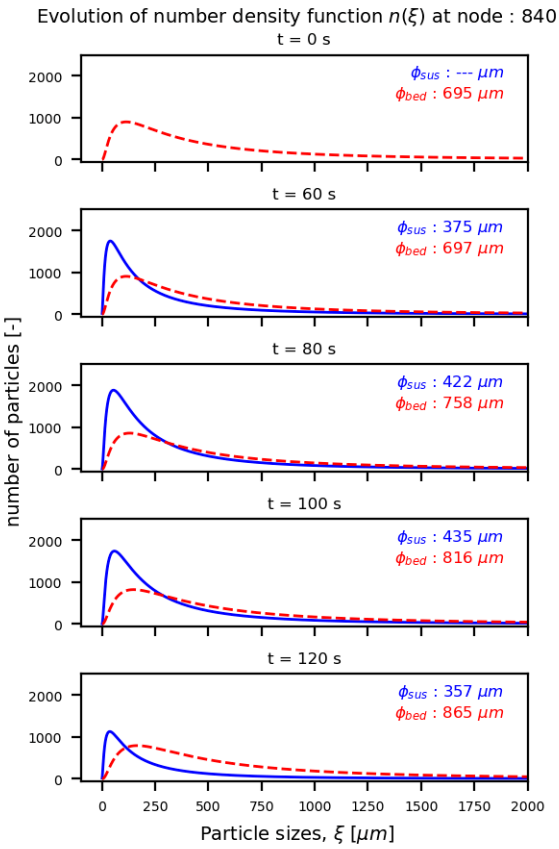

Figure 4. NDF evolution at two nodes a) 662 (erosion zone) and b) 840 (depostion zone) for selected time steps. The mean particle size of the NDF in the suspension load and bottom material are denoted as ϕ_{sus} and ϕ_{bed}.

V. CONCLUSIONS

In this study, a first attempt is made to include erosion and deposition terms in the framework of PBE-MoM. The MICROPOL module of the WAQTEL modelling package is utilised for implementing the PBE-MoM. The use of the EQMOM procedure to model the evolution of the moments and subsequently of the NDF are discussed. A procedure has been developed to determine the initial moment values as well as a post-processing technic for reconstruction of the NDF. In spite of the limited knowledge of the parameter values for erosion and deposition fluxes in MoM, physically meaningful results are obtained. The evolution of the NDF as a result of erosion and deposition are discussed and results are justified. However, the authors recognise the need for the validation of the results against measured data. In the absence of measured NDF datasets, the model needs to be first validated against concentration of suspended and deposited load. Further it is recommended that deposited bottom material moments would be transformed into mass and volumetric concentration, which can lead to the computation of bed elevation changes using the Exner equation. Apart from erosion and deposition, microplastics very likely undergo the process of flocculation with sediment and subsequent breakage of the flocs. This needs to be treated as additional source and sink terms to model the microplastic transport in aquatic environment. This would also need redefining the NDF such that both sediment and microplastic are taken into account. This is possible with multivariate NDFs and by employing more than one kernel density function to approximate the NDF. The implementation of additional source and sink terms would need reconstruction of the NDF at every time step and at every computational node. This would require efficient integral approximation methods to be implemented within the TELEMAC computation environment. Considering all the additional and unique computational requirements of PBE-MoM in TELEMAC, it is recommended to implement a standalone module.

ACKNOWLEDGEMENT

This work is carried out in the framework of the Flemish SBR PLUXIN project funded through VLAIO and the Flemish Blue Cluster (www.pluxin.be) and the EU H2020 LABPLAS project (www.LABPLAS.eu).

REFERENCES

[1] C. Lorenz *et al.*, "Spatial distribution of microplastics in sediments and surface waters of the southern North Sea," *Environ. Pollut.*, vol. 252, pp. 1719–1729, 2019, doi: 10.1016/j.envpol.2019.06.093.

[2] N. De Troyer, "Occurrence and distribution of microplastics in the Scheldt river," 2015.

[3] T. Maes *et al.*, "Microplastics baseline surveys at the water surface and in sediments of the North-East Atlantic," *Front. Mar. Sci.*, vol. 4, no. MAY, pp. 1–13, 2017, doi: 10.3389/fmars.2017.00135.

[4] M. Claessens, S. De Meester, L. Van Landuyt, K. De Clerck, and C. R. Janssen, "Occurrence and distribution of microplastics in marine sediments along the Belgian coast," *Mar. Pollut. Bull.*, vol. 62, no. 10, pp. 2199–2204, 2011, doi: 10.1016/j.marpolbul.2011.06.030.

[5] A. Malli, E. Corella-Puertas, C. Hajjar, and A. M. Boulay, "Transport mechanisms and fate of microplastics in estuarine compartments: A review," *Mar. Pollut. Bull.*, vol. 177, no. February, p. 113553, 2022, doi: 10.1016/j.marpolbul.2022.113553.

[6] H. A. Leslie, S. H. Brandsma, M. J. M. van Velzen, and A. D. Vethaak, "Microplastics en route: Field measurements in the Dutch river delta and Amsterdam canals, wastewater treatment plants, North Sea sediments and biota," *Environ. Int.*, vol. 101, pp. 133–142, 2017, doi: 10.1016/j.envint.2017.01.018.

[7] K. Aoki and R. Furue, "A model for the size distribution of marine microplastics: a statistical mechanics approach," *PLoS One*, vol. 16, no. 11, Mar. 2021, doi: 10.1371/journal.pone.0259781.

[8] P. Pastorino *et al.*, "High-mountain lakes as indicators of microplastic pollution: current and future perspectives," *Water Emerg. Contam. Nanoplastics*, vol. 1, no. 1, p. 3, Feb. 2022, doi: 10.20517/WECN.2022.01.

[9] A. S. Mountford and M. A. Morales Maqueda, "Eulerian Modeling of the Three-Dimensional Distribution of Seven Popular Microplastic Types in the Global Ocean," *J. Geophys. Res. Ocean.*, vol. 124, no. 12, pp. 8558–8573, 2019, doi: 10.1029/2019JC015050.

[10] L. Khatmullina and I. Chubarenko, "Transport of marine microplastic particles: Why is it so difficult to predict?," *Anthr. Coasts*, vol. 2, no. 1, pp. 293–305, 2019, doi: 10.1139/anc-2018-0024.

[11] F. Guerrini, L. Mari, and R. Casagrandi, "A coupled Lagrangian-Eulerian model for microplastics as vectors of contaminants applied to the Mediterranean Sea," *Environ. Res. Lett.*, vol. 17, no. 2, 2022, doi: 10.1088/1748-9326/ac4fd9.

[12] D. Ramkrishna and M. R. Singh, "Population balance modeling: Current status and future prospects," *Annu. Rev. Chem. Biomol. Eng.*, vol. 5, pp. 123–146, 2014, doi: 10.1146/annurev-chembioeng-060713-040241.

[13] A. Passalacqua, F. Laurent, E. Madadi-Kandjani, J. C. Heylmun, and R. O. Fox, "An open-source quadrature-based population balance solver for OpenFOAM," *Chem. Eng. Sci.*, vol. 176, pp. 306–318, 2018, doi: 10.1016/j.ces.2017.10.043.

[14] T. T. Nguyen, F. Laurent, R. O. Fox, and M. Massot, "Solution of population balance equations in applications with fine particles: Mathematical modeling and numerical schemes," *J. Comput. Phys.*, vol. 325, pp. 129–156, 2016, doi: 10.1016/j.jcp.2016.08.017.

[15] X. Shen, E. A. Toorman, M. Fettweis, B. J. Lee, and Q. He, "Simulating multimodal floc size distributions of suspended cohesive sediments with lognormal subordinates: Comparison with mixing jar and settling column experiments," *Coast. Eng.*, vol. 148, no. August 2018, pp. 36–48, 2019, doi: 10.1016/j.coastaleng.2019.03.002.

[16] M. Shiea, A. Buffo, M. Vanni, and D. Marchisio, "Numerical Methods for the Solution of Population Balance Equations Coupled with Computational Fluid Dynamics," *Annu. Rev. Chem. Biomol. Eng.*, vol. 11, no. 1, pp. 339–366, Jun. 2020, doi: 10.1146/annurev-chembioeng-092319-075814.

[17] D. L. Marchisio, R. D. Vigil, and R. O. Fox, "Implementation of the quadrature method of moments in CFD codes for aggregation - breakage problems," *Chem. Eng. Sci.*, vol. 58, no. 15, pp. 3337–3351, 2003, doi: 10.1016/S0009-2509(03)00211-2.

[18] K. Lee and T. Matsoukas, "Simultaneous coagulation and break-up using constant-N Monte Carlo," *Powder Technol.*, vol. 110, no. 1–2, pp. 82–89, 2000, doi: 10.1016/S0032-5910(99)00270-3.

[19] M. Pigou, J. Morchain, P. Fede, M. Penet, and G. Laronze, "New developments of the Extended Quadrature Method of Moments to solve Population Balance Equations," *J. Comput. Phys.*, vol. 365, pp. 243–268, 2018, doi: 10.1016/j.jcp.2018.03.027.

[20] A. Buffo, M. Vanni, and D. L. Marchisio, "On the implementation of moment transport equations in OpenFOAM: Boundedness and realizability," *Int. J. Multiph. Flow*, vol. 85, pp. 223–235, 2016, doi: 10.1016/j.ijmultiphaseflow.2016.06.017.

[21] X. Shen and J. P. Y. Maa, "Modeling floc size distribution of suspended cohesive sediments using quadrature method of moments," *Mar. Geol.*, vol. 359, pp. 106–119, 2015, doi: 10.1016/j.margeo.2014.11.014.

[22] D. L. Marchisio, J. T. Pikturna, R. O. Fox, R. D. Vigil, and A. A. Barresi, "Quadrature method of moments for population-balance equations," *AIChE J.*, vol. 49, no. 5, pp. 1266–1276, May 2003, doi: 10.1002/aic.690490517.

[23] E. Madadi-Kandjani and A. Passalacqua, "An extended quadrature-based moment method with log-normal kernel density functions," *Chem. Eng. Sci.*, vol. 131, pp. 323–339, 2015, doi: 10.1016/j.ces.2015.04.005.

[24] "WAQTEL user manual v8p1," 2020.

[25] "WAQTEL technical manual v8p1," 2020.

[26] "PLUXIN." https://www.pluxin.be/nl.

[27] G. Everaert *et al.*, "Plastic baseline (t0) measurement in the scope Flemish Integral Action Plan on Marine Litter (OVAM)," Flanders Marine Institute, Ostend, Belgium, 2020.

Coupling between a large scale model Mercator and a coastal TELEMAC-3D flow model for the Martinique island

Catherine VILLARET[1], Ludivine GOUJON[1], Cristele CHEVALIER[2]
[1]: MOBIDYC (contact@mobidyc.fr)
[2]: MIO, University of Aix Marseille

Abstract – **A meso-scale TELEMAC-3D model has been developed for the Martinique island, including salinity and temperature induced stratification effects. A methodology has been developed in order to force the 3D flow model with the Mercator global model. The TELEMAC-3D flow model results have been compared with the Mercator model and discrepancies obtained between the two models are analysed.**

Keywords: TELEMAC-3D, Sargassum transport, Mercator.

I. INTRODUCTION

The floating Sargassum seaweed has been stranded in a massive and almost continuous way along the Caribbean coasts for several years. This massive stranding of seaweeds impacts the lives of riverine populations. The rapid degradation of these seaweeds following stranding events is responsible for the emission and dispersion in the atmosphere of large amounts of hydrogen sulphide gas (H_2S), combined with other toxic gases (chlorides, NH_3, …)., which is a major issue for the living population.

The Martinique island is particularly impacted, with several million tons per year washed onshore, with a negative socio-economic impact on tourism, fishing, and health. The objective of this project is to examine the feasibility of the TELEMAC system to be applied as a forecasting management tool to predict the risks of sargassum stranding and associated H_2S emissions as well as evaluate mitigation solutions, like sargassum dam barriers, in order to limit the sargassum impact on the coast.

We present here:

- an analysis of the processes responsible for the stranding of sargassum algae and H_2S emission,
- a TELEMAC-3D meso-scale flow model which has been developed for the Martinique island and coupled to the global ocean model Mercator,
- a local scale TELEMAC-2D flow model, including near shore processes, which has been used for sargassum transport modelling by adapting the existing algae module.

II. MET-OCEANIC CONDITIONS

A. Meteo conditions

Weather conditions have been downloaded from the ERA5 model of ECMWF for the period (2018-2021). This provides global wind, waves and atmospheric pressure data on a 30 km grid and hourly estimates. This meteorological data set has been used to impose the atmospheric forcing in the TELEMAC model.

Local meteorological stations (e.g. Le Vauclin, Fort de France, …) can be purchased from Meteo France, so monthly meteorological reports were used.

According to the yearly bulletins emissions from Meteo France, two seasons can typically be observed:

- a dry season during the winter and spring, dominated by the fairly constant Eastern wind regime with typical mean value of 7m/s (20 to 30 km/h).
- a humid season during the summer and fall, characterized by a diminution of the Alize regime and more perturbated storm conditions with hurricane and tropical storms.

B. Tides and Current conditions

The Martinique island is under the influence of both tides and global ocean circulation.

- The North equatorial Current reaches the Antilles Island with a flux globally aligned with the wind circulation (Eastern direction).
- Tides conditions are characterized by a fairly small amplitude and mixte semi-diurnal to diurnal signal and fairly weak currents (0.1 to 0.3 m/s).

C. Wave conditions

Wave data from the reseau CANDHIS have been collected and analysed at the North of Martinique (Basse Pointe) and southern tip (Ste Lucie).

Waves come generally from the Est to North-East with a significant wave height of less than 2m, with a mean value of 1.6m for a pic period of 8.5s.

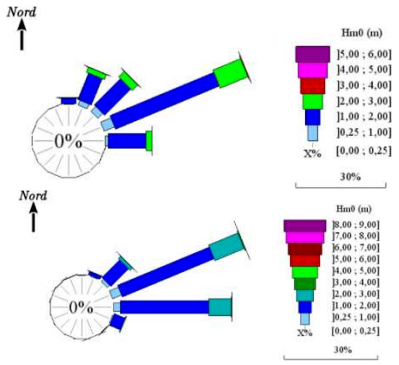

Figure 1. Wave distribution at Basse Terre (top Figure) and Ste Lucie (bottom Figure) [1]

III. SARGASSUM TRANSPORT PROCESSES

A. *Sargassum origin*

The Sargasso Sea (or large floating patches of seaweeds) was formed as a result of the agglomeration of pelagic sargassum species, Sargassum *fluitans* and S. *natans*, and drifting waste, stabilized in the Atlantic Ocean North of Brazil. However, since 2011, a new sargassum sea appeared in the subtropical Atlantic. Floating algae mats of large dimensions ranging from a few square meters to strips that stretches for several kilometers are then observed to be transported by surface currents and deposit in massive and recurrent event along the shoreline. Sargassum strips are schematized on Figure 2 (left).

B. *Satellite observations – video recording*

The geo-referenced tiles produced by the Sentinel (II and III) and Modis satellites can be used to give the position and the biomass of Sargassum seaweed rafts. Those images will be used to initialize the algae mats in the algae transport module. An example is shown on Figure 2.

In addition, video recording of sargassum stranding on shore are also available in order to validate the modelling approach.

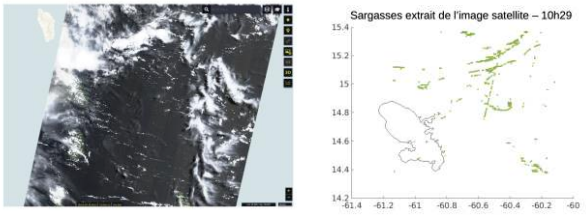

Figure 2. An example of a satelitte image (Sentinel II) and interpreted in terms of sargassum rafts positions the 07/07/2022

C. *Statistical analysis of H_2S Emissions*

The Eastern coastline of Martinique is particularly impacted (Figure 3) and various sites have been identified where H_2S emissions have been recorded by Madininair.

A preliminary statistical analysis of H_2S emissions and modelling has been performed in order to identify the most impacted along the Eastern coastline. Figure 4 highlights the high variability in the observed H_2S emissions (year 2020 and 1st semester of 2021) and the most impacted area to stranding events like the Fregate and Vauclin beaches.

This statistical analysis has shown that Sargassum stranding along the Eastern coastline occurs predominantly under southerly current conditions and for moderate wave conditions from East.

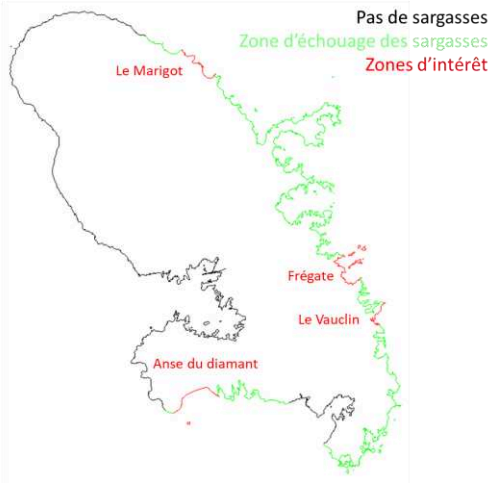

Figure 3. The Martinique coastline – indicating the zones of interest [1]

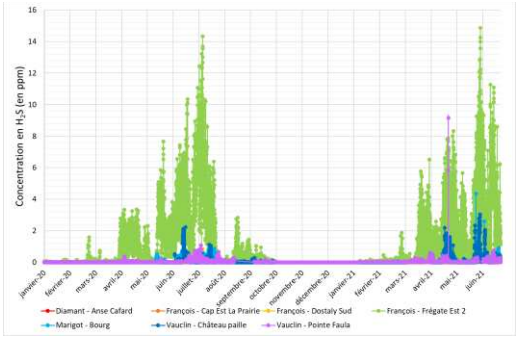

Figure 4. Statistical Analysis of H_2S emissions at Fregate and Vauclin showing the intermittency of the H_2S emissions, highlighting the most risky areas like Vauclin and Fregate [1].

IV. MARTINIQUE COASTAL FLOW MODEL

A. *Data collection*

The Martinique coastline and bathymetry has been downloaded from the SHOM data base. Two sets of bathymetry have been combined as summarized in Table I: a high resolution LITTO3D bathymetry (resolution 1m) and the DEM of the HOMONIM project (resolution 100m).

The meteorological data has been downloaded from Copernicus web site using the ERA5 monthly averaged data on single levels from 1979 to present [6].

For the boundary conditions, a global large-scale model is required to impose the flow, temperature and salinity along the offshore boundary of the local model.

Two global ocean models, the HYCOM model and the Mercator model, have been developed including atmospheric

forcing and density effects (as well as other bio-chemical processes) and assimilation techniques but only the Mercator model is maintained at present. So, the Mercator model results (including 43 planes in the vertical (50 planes maximum)) have been downloaded from the Copernicus [6] data base for years 2020 and 2021.

Table I Summary of data sets

DATA	**Bathymetry Data**		
	Data source	***Spec***	***format***
Large scale Bathymetry	2018 (projet HOMONIM)	Dx = 0.001° (100 m) Martinique and Guadeloupe	xyz
Coastal Bathymtry	LITTO3D	Dx=1 m Martinique	xyz
Shoreline	HISTOLIT		shp
Meteorologial 2021	Copernicus.eu	wind (10 m) & atm. Pressure	nc
Global Ocean MERCATOR	Copernicus.eu	*1/12° Physics Analysis and Forecast*	nc

B. *Computational domain – Mesh generation*

The computational domain includes the whole Martinique island with an offshore maritime boundary located at about 60 km from the shoreline in deep water (1000 to 3000 water depth) and forms an ellipsoid shape of 135 kmx100 km.

The mesh is refined in the nearshore zone along the Southern and Eastern coastline (less than 50m) and using a coarser mesh size along the western coastline. In areas of interest i.e., Vauclin Bay and Simon Bay (Le François), the mesh is refined down to less than 10 m.

The mesh size increases progressively with bathymetry up to 2.5 km in the outer maritime boundary.

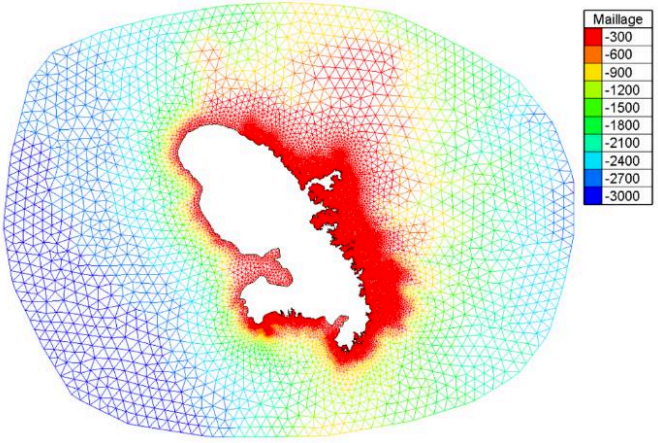

Figure 5. Glogal mesh [1]

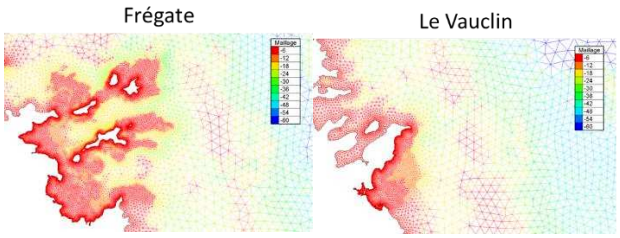

Figure 6. Zoom on the zones of interest (Vauclin Bay, Fregate) [1]

The final mesh size has been generated using Blue Kenue and is shown in Figures 5 and 6.

C. *Meteorological forcing*

Three successive steps were necessary to generate an atmospheric data file interpolated on the geometry file. We used here the v8p3r1 python scripts library:

- The script “converter.py ecmwf2srf” has been used to convert the NetCDF atmospheric data in a slf format. The original NetCDF atmospheric data is in latitude longitudinal coordinates and covers a domain between 14 and 16° latitude. It was required to substract -360° to the longitudes such that the domain covers the range -422° t -420° (instead of -62° to -60°).
- The file has then been transformed in cartesian coordinates (UTM 20N) using the script “run_telfile.py alter –ll2utm”.
- The output file was then interpolated on the TELEMAC mesh to generate the atmospheric file using the script “converter.py generate_atm”.

D. *Boundary conditions file*

The TELEMAC-3D coastal flow model is interfaced with the Global Ocean 1/12° Mercator model which is a reference model for flow predictions offshore Martinique (like the MOTHY alert system provided by Meteo France and used by DEAL for sargasso alert bulletin emissions [2]).

The existing python scripts within the TELEMAC system were provided for the HYCOM model which is no longer maintained and therefore could not be applied for recent events (after 2018). Matlab scripts were developed to interpolate the Mercator model results on the TELEMAC grid. More details can be provided and the scripts made available upon request.

A comparison between TELEMAC and Mercator was made at various points along the boundary and shows that the Mercator conditions is perfectly satisfied (Figure 7).

As shown on Figure 8 (bottom figures), the density is fairly uniform under 50 m whereas strong gradients are well captured by TELEMAC in the surface layer.

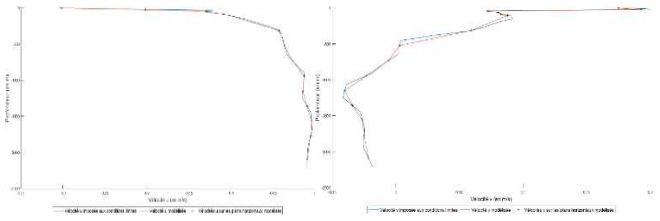

Figure 7. Comparison between the Mercator model to the TELEMAC flow velocity at a boundary point (N°76) on the North Eastern side [1]

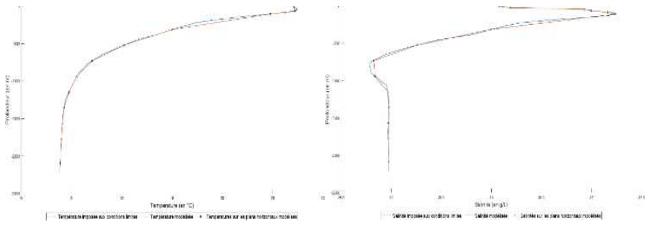

Figure 8. Comparison between the Mercator model to the TELEMAC salinity and temperature profile at a boundary point (N°76) on the North Eastern side [1]

E. TELEMAC-3D Flow modelling

The TELEMAC-3D flow model has been applied for a number of 15 planes in the vertical, using sigma transformation. The mesh resolution is increased at the surface in order to capture the near surface gradients (as shown on Figure 9).

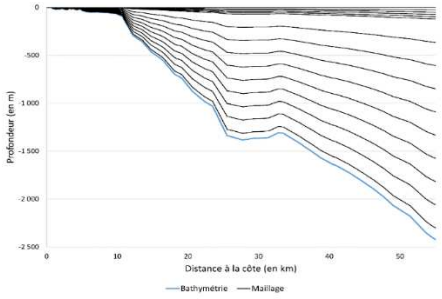

Figure 9. Vertical mesh variation [1]

The impact of the thermocline and salinity stratification are included by use of a mixing length model including wind effects – Queutin N°5 – and applying the Munk and Anderson damping function.

F. TELEMAC-3D and Mercator model comparison

The TELEMAC model results have been compared to the Mercator model at a selected number of points within the computational domain. An example of the results after 3 days of simulation (starting from an initial uniform velocity and density profile). The velocity profile is shown in Figure 10 where TELEMAC results are in red, and the Mercator model shown in blue. The extraction point is located offshore Anse du Diamant in water depth of 100 m. In this coastal area, we can observe some discrepancies: the Mercator model overestimates the near bed gradients in comparison to the TELEMAC model (see Figure 11).

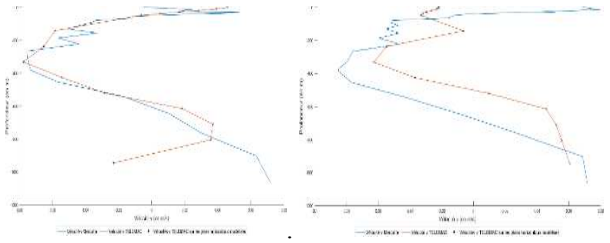

Figure 10. Comparison between the Mercator model (blue) and TELEMAC (red) for velocity profiles at a 100 m deep point (offshore anse du Diamant) [1].

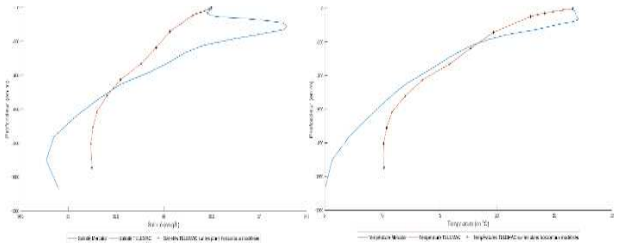

Figure 11. Comparison between the Mercator model (blue) and TELEMAC (red) for temperature and salinity [1]

G. Future work

TELEMAC-3D model results are found to deviate from Mercator particularly in the near shore area and the reasons for these discrepancies need to be further investigated (better resolution in the nearshore region in TELEMAC or some other issues).

V. A 2D COASTAL INCLUDING SARGASSUM TRANSPORT

In addition to the 3D flow model, a TELEMAC-2D tidal flow model and a TOMAWAC wave model were developed using the same 2D grid. Our objective was:

- Assess the impact of tides in the nearshore area in comparison to the global flow model results.
- Assess the role of waves and waves induced currents in the transport processes.
- Examine the feasibility of existing 2D algae algorithm to represent sargassum transport processes [5].

Preliminary results show that all existing 2D algae transport algorithm give similar results offshore but still need to be adapted to account for onshore stranding.

VI. Conclusions - Future Work

This is a preliminary feasibility study towards the development of a fully predictive 3D model for the stranding of sargassum on the shore of Martinique.

Our interest is now to include near-shore processes and implement the existing algae models which have been developed in 2D [5] in order to represent the sargassum transport from offshore to nearshore following the procedure described in previous transport model using the Mercator surface velocity field [3]. A summary of the overall methodology is summarized in Figure 12.

Acknowledgements

Thanks to Carole Boulanger from Madininair for providing the H_2S data.

Thanks to BRGM for providing video recording at local sites.

References

[1] Goujon L. (2022, août). Dynamique d'échouement des sargasses en Martinique : mise en place d'un système de prévision courte échelle et aide au positionnement des barrages anti-sargasses (Mémoire de fin d'études). ENGEES, & ENTPE.

[2] DEAL de la Martinique. Le bulletin de prévision des échouages de sargasses.

[3] Jouanno, J., Benshila, R., Berline, L., Soulié, A., Radenac, M. H., Morvan, G., Diaz, F., Sheinbaum, J., Chevalier, C., Thibaut, T., Changeux, T., Menard, F., Berthet, S., Aumont, O., Ethé, C., Nabat, P., & Mallet, M. (2021). A NEMO-based model of Sargassum distribution in the tropical Atlantic : description of the model and sensitivity analysis (NEMO-Sarg1.0). Geoscientific Model Development, 14(6), 4069 4086.J. Clerk Maxwell, A Treatise on Electricity and Magnetism, 3rd ed., vol. 2. Oxford: Clarendon, 1892, pp.68–73.

[4] Bouvier, C., de Cathelineau, T., & Valentini, N. (2020, février). *Suivi de la dynamique des échouages des sargasses sur le littoral martiniquais : développement et application des algorithmes* (BRGM/RP-69651-FR). Bureau de recherches géologiques et minières BRGM.

[5] Joly, A. (2011, 14 décembre). Modelisation of the diffusive transport of algal blooms in a coastal environment using a stochastic method. Université Paris-Est.

[6] CMEMS, Global Ocean Wind L4 Reprocessed 6 hourly Observations.

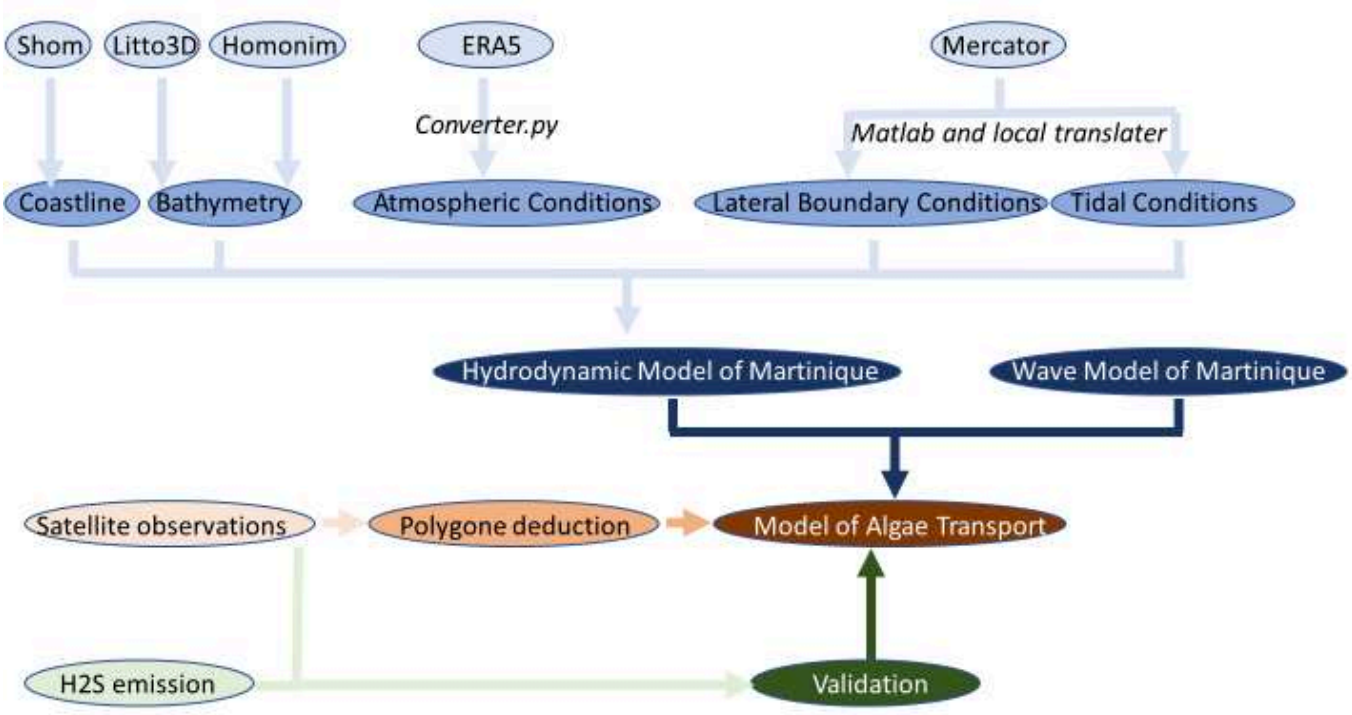

Figure 12. Summary of the ovearall modelling strategy

Development of a shape optimisation module for TELEMAC-2D: application to the excavation of a reservoir

Laure Géroudet[1], Matthieu Sécher[1], Thomas Viard[1], Cédric Goeury[2], Fabrice Zaoui[2]
laure.geroudet@edf.fr

[1]: EDF CIH La Motte Servolex, France
[2]: EDF R&D LNHE Chatou, France

Abstract – **Reshaping part of the riverbed is sometimes considered as a solution to prevent issues such as risks of flooding or reservoir capacity decrease. Searching for the best compromise between gains and excavation costs by testing a diversity of scenarios can be time consuming, with no insurance that the optimum solution is found.**

The search for an optimised shape can however be automated using optimisation tools. A shape optimisation python module is here developed to facilitate and strengthen the determination of the best riverbed shape, for TELEMAC-2D studies. It includes the OptimStudy class, which handles the whole shape optimisation process, and offers different optimisation strategies.

The OptimStudy class was used to optimise the excavation in a reservoir. The new shape of the reservoir was defined using 5 parameters: the bank slope, the channel width, and 3 parameters that define the evolution of the bathymetry in the centre of the channel.

An experimental design (by using optimised Latin Hypercube Sample method) was first conducted to explore the parametric field. The analysis of the results allowed to appreciate the relative influence of the parameters and to locate the ranges of the parameters that minimise a cost function. This offered the possibility to reduce the complexity and the extent of the investigation for the optimisation. The results of the experimental design also provided important information about the magnitude and variations of the cost function in the parametric field, which was used to balance their relative importance in the global cost function defined for the optimisation.

An excavation optimisation was then performed using the 3DVAR algorithm of the ADAO module. This work provided a feasible solution to prevent overflow risks while minimising excavation costs.

Keywords: channel shape, optimisation, TELEMAC-2D, PYTHON, ADAO.

I. INTRODUCTION

Sediment deposits in channels and reservoirs often cause water level rise, increasing the risk of flooding and overtopping. Removal of some of the sediments by dredging in the riverbed is sometimes considered, and a trade-off between excavation costs and gains in terms of water elevation and/or reservoir capacity must be decided. Because of the many parameters determining the excavation shape, and the complexity of the cost criteria, searching for the best compromise can be time consuming. The number of excavation scenarios explored is then limited, and the best excavation solution found may be far from the real optimum.

Fortunately, the search for the optimum excavation shape can be automated through shape optimisation algorithms. The field of optimisation has developed significantly over the last decades, thanks to important developments in computational capabilities, data and methods. At EDF R&D, shape optimisation has already been used together with hydraulic models for calibrating a fish passage [1] and for optimising spillways design [2].

A shape optimisation python module was developed to facilitate and strengthen the determination of the best riverbed shape, for TELEMAC-2D studies. The developed scripts include the OptimStudy class, which handles the pre-processing of TELEMAC files, the simulation run, and the cost estimation to be used in an optimisation process.

Section II introduces the developed shape optimisation module. The OptimStudy class was used to optimise the excavation in a dam reservoir. The results of this example are presented in section III. Eventually, section IV highlights future directions of development for the shape optimisation module.

II. SHAPE OPTIMISATION MODULE

A. Shape optimisation principles

Shape optimisation consists in determining the shape parameters that minimise a cost function. This automated search implies that the optimised shape can be described by a set of parameters, and that it is possible to associate a cost (flooding risk, economic cost, difference with observations) to any set of parameters.

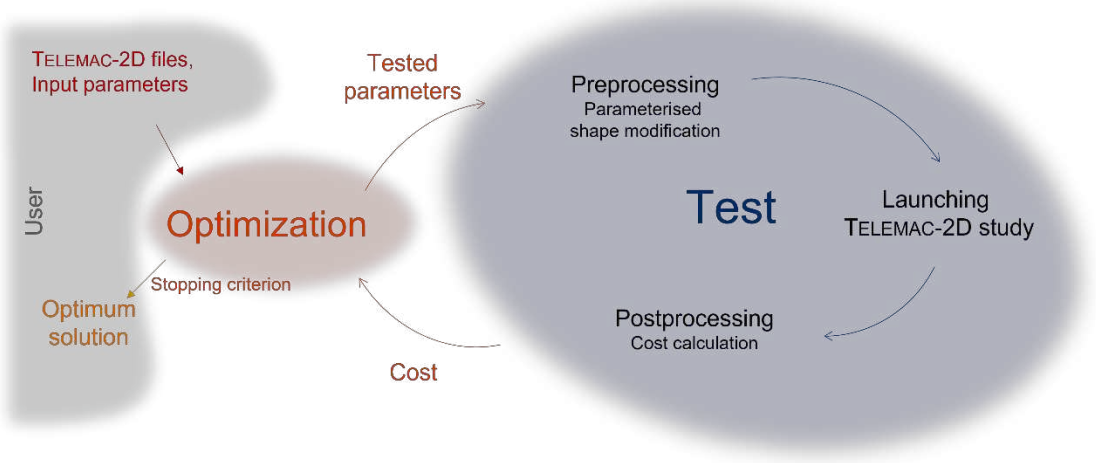

Figure 1. Overview of the organisation of the processes used for shape optimisation.

The optimisation process also relies on the communication between a test procedure (in blue on Figure 1) and an optimisation algorithm (in red on Figure 1). The algorithm prescribes the set of parameters to be tested and analyses its associated cost. From this analysis, a new set of parameters is determined. The test procedure handles pre-processing, model simulation and post-processing, computing a cost for any tested set of parameters.

The user controls the shape optimisation by providing input parameters (the optimisation parameters themselves, their ranges of validity, the files needed to run the TELEMAC-2D study, etc.), including a stopping criterion. When this stopping condition is met, the optimisation process stops and returns the optimum solution to the user.

B. Aims of the developed module

The developed shape optimisation module aims at facilitating the use of shape optimisation for TELEMAC-2D studies. A major part of the development concerned the excavation shape parameterisation and the handling of pre- and post-processing. This was made in a generic way, with the perspective of facilitating their use and adaptation to other shape optimisation problems in TELEMAC-2D studies.

The second axis of development concerned the organisation of the scripts in a tool that, from a limited number of input parameters, manages the whole shape optimisation process. The OptimStudy class was created for this purpose.

Moreover, quality standards (such as Python Pep8) were followed, and the scripts were organised in such a way that future development is facilitated. New test functions, as well as new optimisation methods can be included.

C. Preexisting tools

- Various python modules and scripts already exist for the pre- and post-processing of TELEMAC-2D files. The work presented here relies a lot on these existing tools:
  - The pre- and post-processing functions developed for the shape optimisation module use the TelemacFile class from the data-manip module of TELEMAC, and other scripts that enable the modification of TELEMAC variables (bottom friction, bottom, ...) from contour shapefiles.
  - The TelemacCas class, from the execution module of TELEMAC, is used to handle the files needed for the TELEMAC-2D simulation.
  - A python module has already been developed to study channel erosion [3]. Many of these scripts have been adapted to enable their use in a more general framework, including reservoir excavation.
  - Several optimisation tools have been developed by EDF R&D and were integrated to the shape optimisation module [4][5].

D. Overview of the OptimStudy functionalities

The OptimStudy class instantiates an optimisation study object. This object has specific attributes (e.g. TELEMAC-2D steering file, parameters for shape optimisation, optimum solution parameters and cost, name of output files etc.). A diversity of actions (i.e. methods) can be applied to modify these attributes, and are listed below:

(pre-processing)

- Modify the value of a TELEMAC-2D variable (bottom friction, water depth, ...) in a zone defined by a shape contour
- Modify the value of a TELEMAC-2D parameter in a TELEMAC-2D file (steering file, culvert file, ...)
- Modification of the bathymetry

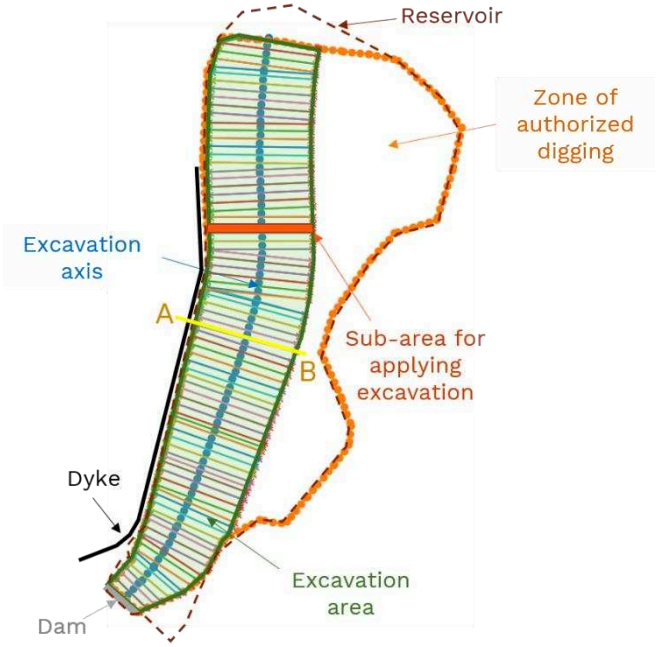

Figure 2. Visualisation of the area where excavation is allowed (orange), hydraulic axis for excavation (blue), and area where excavation is applied (green). The dam and dyke that close the reservoir are also represented here. The parameters taken for this excavation example, also used in Figure 3, 4 and 5, differ from the application optimum solution.

(post-processing)

- Statistical analysis of an experimental design results
- Cost functions (RMSE, volume of excavation, overtopping)
- Data plotting

(optimisation process)

- Running a TELEMAC-2D study
- Test functions, which can be used both for shape optimisation or parameter calibration
- Experimental design build up and run
- Parameter calibration
- Shape optimisation
- Build up and use of a metamodel for optimisation

E. Excavation shape parameterisation

In order to allow its use in a variety of channel shape studies, the excavation shape parameterisation was made generic.

The excavation zone is determined from (1) a polygon (defined in a geographical shapefile), which defines the area where excavation is allowed, (2) the channel hydraulic axis (also defined in a geographical shapefile), and (3) a channel width parameter, that can be varied by the user (Figure 2).

The excavation shape also depends on a banks slope parameter, and the bottom profile at the channel centre is determined from 5 other parameters (Figure 3):

- The bottom value at the most downstream point;
- A series of intermediate points whose distances from downstream determine the locations of slope discontinuities;
- The values of the bottom slope from downstream to the first intermediate point, and then between pairs of successive intermediate points must also be provided;

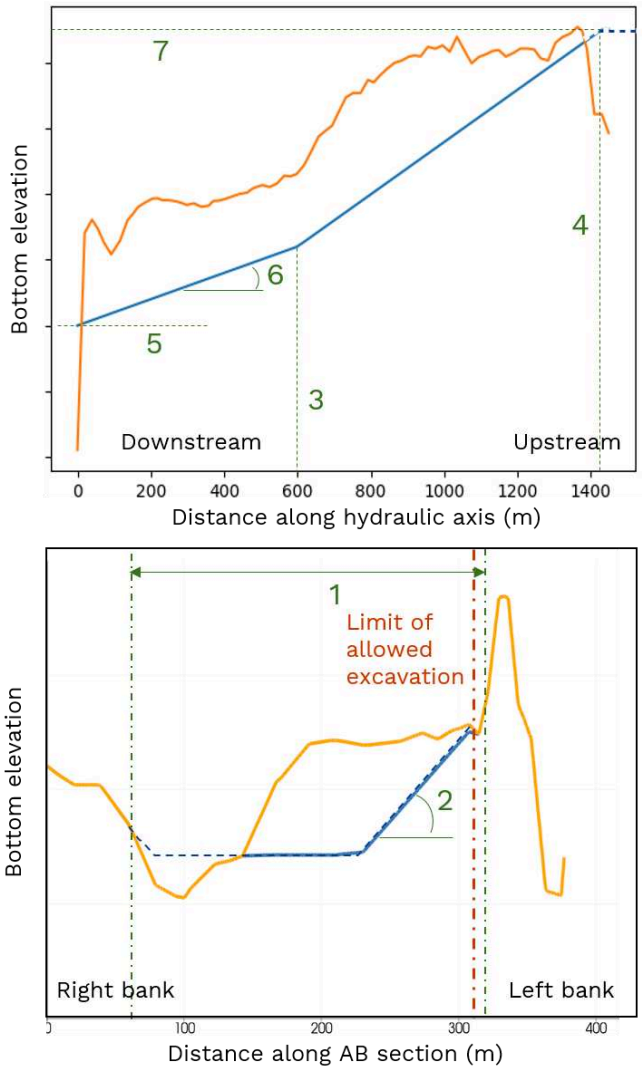

Figure 3. Bottom elevation profiles along the excavation axis (top) and the section AB (see Figure 2) of the reservoir (bottom). The calculated (dashed line) and applied (plain line) excavation are also plotted in blue. Green numbers enable visualisation of the parameters that influence the excavation bottom: (1) channel width, (2) banks slope, (3) Position of an intermediate point, (4) Length of excavation area, (5) downstream bottom elevation, (6) bottom slope in the downstream part of the excavation area (7) upstream bottom elevation.

- The length of the portion of the hydraulic axis where excavation is applied; and
- The bottom elevation value at the most upstream point (optional parameter i.e. default is the actual bottom elevation value at this point);

F. Shape test-function

The test function used for shape optimisation follows these successive actions to associate a cost to any set of shape parameters:

- Determine the shape of the excavation from the shape parameters. The excavation zone is divided in several zones (Figure 2);
- Apply excavation to the TELEMAC geometry file (and to the previous computation file), gradually from downstream to upstream. The TELEMAC field *BOTTOM* is modified where the excavation bathymetry is deeper than the actual one (Figure 4);
- Modify the value of the TELEMAC field *BOTTOM FRICTION* where the bathymetry was modified (optional) (Figure 5);
- Run the TELEMAC simulation (includes modifications of the TELEMAC steering file and handling of the TELEMAC files required for the simulation);
- Extract a cost criteria or observation from the results; and
- Combine cost criteria in a global cost value (see an example of global cost-function in section III.A.1).

III. APPLICATION

A. Presentation of the example case

As an application, we consider the case of an excavation in a reservoir. The scenario is presented in Figure 2: A reservoir is closed with a dam downstream. On the right bank, a dyke retains water in the reservoir, and is used for flood protection. The value of the flow discharge imposed at the intake of the reservoir is significant enough to cause overtopping on this dyke. The goal of shape optimisation, in this case, is to determine the shape of the excavation in the reservoir that would prevent from risks of overtopping and flooding, while limiting the excavation costs. Two cost criteria are therefore defined: the excavation volume (which is determinant for excavation costs), and the importance of overtopping, estimated as the integral of water depth along the dyke.

For every combination of shape parameters tested during the experimental design and the optimisation process, a TELEMAC-2D simulation is performed, and results are analysed for determining the cost associated with the set of parameters.

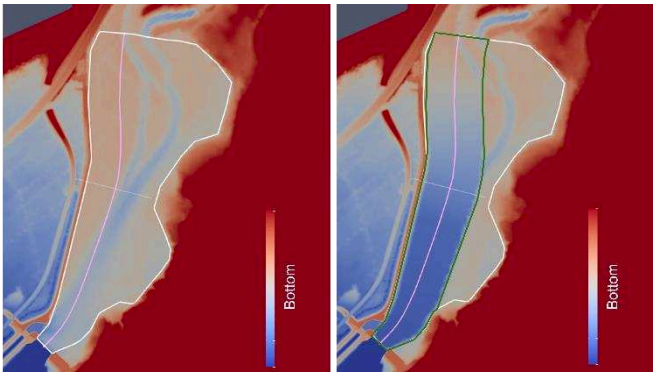

Figure 4. Application of the excavation to the TELEMAC BOTTOM field value. Left: initial bottom elevation, right: bottom elevation after the excavation was applied. The area where excavation is allowed, the excavation axis and the area where excavation is applied are plotted respectively in white, light pink and green.

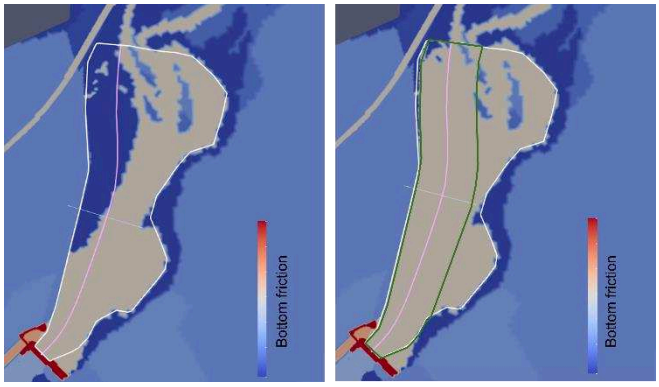

Figure 5. Modification of the TELEMAC BOTTOM FRICTION field value, according to effective excavation. Left: initial bottom friction, right: bottom friction after the excavation was applied. The area where excavation is allowed, the excavation axis and the area where excavation is applied are plotted respectively in white, light pink and green.

The boundary conditions used for these hydraulic simulations are (1) constant discharge flow upstream and (2) constant water elevation downstream. The initial conditions are taken from a previous computation file, which corresponds to the case of a steady state regime within the reservoir, using the original bathymetry (no excavation), with constant flow and constant water elevation set upstream and downstream respectively.

We first chose to use the same entrance flow in this previous computation as in the simulations for testing excavation shapes. However, because of water receding issues on the dyke (see appendix), we preferred to use a low entrance flow for the setup of initial conditions, insuring the absence of non-physical overtopping.

B. Excavation shape design

The contour of the zone where dredging is allowed, and the hydraulic axis taken for this study are presented on Figure 2. Among the shape parameters that define the excavation shape (Figure 3), two are set constant: the distance between the most downstream and upstream points (i.e. length of the excavation zone) is maximum, and the bottom elevation value at the most upstream point is set to

the maximum of actual bottom values in the upstream reservoir cross section. Using this value for upstream bottom elevation prevents from sharp bottom variations at the edges of the digging area.

The five other parameters are varying over a range of values defined by lower and upper bounds for each parameter: The downstream bottom elevation value is bounded by the geometry of the dam, and by the actual bottom elevation in the reservoir. The channel width ranges from that of the dam to that of the central part of the reservoir. The position of the slope discontinuity is set up inside the middle third of the hydraulic axis, to lower risks of getting torrential conditions in the upstream part of the reservoir. With the same flow regime constraints in mind, the slope in the downstream part of the reservoir ranges from 0 to 2%. The banks slope maximum is set up to respect the stability slope of wet sand and the minimum for banks slope is taken so the defined bottom profile is always reached at the excavation zone centre.

C. *Optimisation strategy*

We first conduct an experimental design to explore the parametric field. The main goal was to get insights on the variations of the two cost criteria over the set of parameters and on the relative influences of the shape parameters.

A mathematical optimisation is then conducted using the gradient descent algorithm 3DVAR from ADAO (https://pypi.org/project/adao/) [9] to determine an optimal excavation solution.

D. *Experimental design*

The experimental design (created using optimised Latin Hypercube Sample method [6][7][8]) is composed of 1,000 parameters combinations. Using linux-bash scripts that allow running several TELEMAC-2D simulations on a cluster, the 1,000 experiments were launched in blocks of 20 simulations, with a maximum of 4 blocks launched simultaneously (limitation due to fair use rules of EDF's supercomputers). Each simulation is run on 36 processors in 1h30 (with a mesh containing about 300,000 nodes, and for a simulated time of 3 hours). Running all the experiments took less than one day of computation.

For each experiment, both the excavation volume and the integral of the water depth along the dyke are calculated. The correlation coefficients between shape parameters and these two cost-criteria highlight which parameters have the greatest influence (Table I). The two parameters that have the greatest influence on the magnitude of overtopping are the downstream bottom elevation and the slope in the downstream part of the reservoir. The excavation volume is also greatly influenced by these two parameters, and by the channel width.

Table I Correlation coefficients[9] of shape parameters with cost criteria.

		Cost criteria	
		Excavation volume	***Integral of water depth along the dyke***
Shape parameters	***Channel width***	**0.134**	-0.01
	Banks slope	0.032	-0.074
	Position of slope discontinuity	-0.007	0.035
	Downstream bottom elevation	**-0.384**	**0.945**
	Downstream bottom slope	**-0.712**	**0.254**

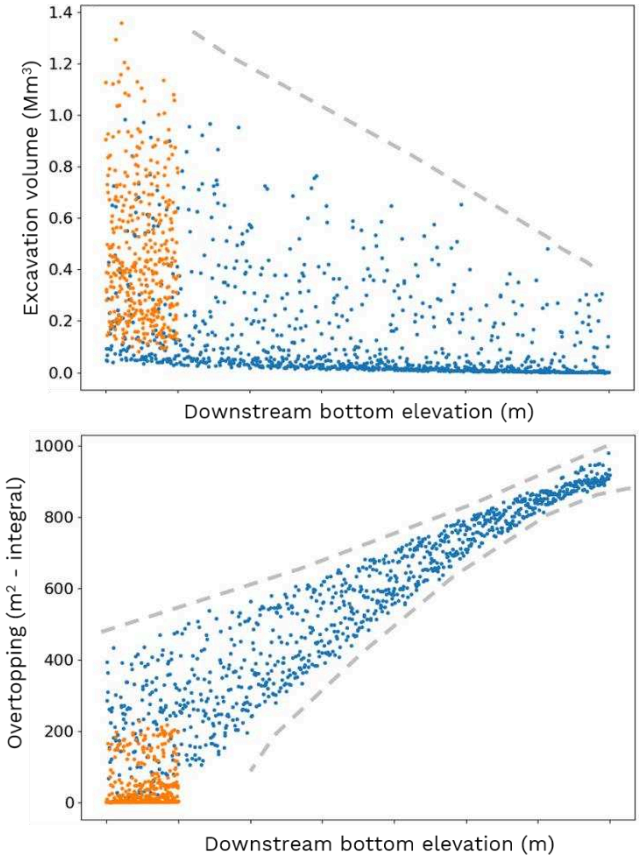

Figure 6. Volume of excavation (top) and Integral of water depth along the dyke (bottom) cost criteria as functions of the downstream bottom elevation. Blue points: initial experimental design, orange points: complementary experimental design. Dashed grey line: possible emplacement of the limit of the area where solutions exist.

On Figure 7 both cost criteria are plotted as functions of the downstream bottom elevation, for the 1,000 experiments. The range of excavation volume values obtained is restricted as the downstream bottom elevation increases, which is consistent with the way the excavation shape is determined. The results also show the strong correlation between downstream elevation and overtopping. The field of solutions seems to be framed by two limits (grey dashed lines) beyond which no solution exists under the given conditions. Besides,

[1] [9] The correlation coefficient of two variables is the ratio between their covariance and the product of their mean values

the range of downstream bottom elevation values associated with solutions with little or no overtopping is very limited. This parameter is therefore highly constrained by the objective of limiting overtopping.

Results on cost-criteria evolution as a function of the 4 other parameters allowed to constrain the downstream slope parameter values to the 0 – 1% range. The lesser influence of the three other parameters is also confirmed. The ranges of values to be used for optimisation can also be slightly constrained for these parameters.

A second experimental design in the restrained parametric field was launched and complements the results of the first experimental design (orange dots in Figure 6).

Figure 7 shows the excavation volume for each experiment as a function of the overtopping integral. Results point out that there exist excavation solutions that greatly limit overtopping and are associated with excavation volumes of less than 400,000m^3.

E. Optimisation

1) Cost-function

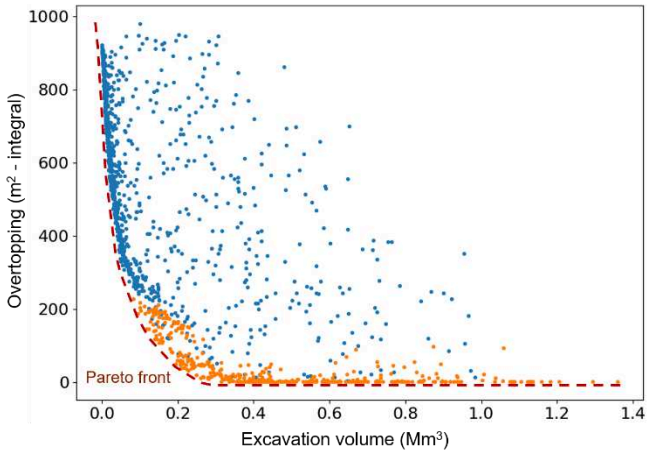

Figure 7. Overtopping cost criteria vs Excavation volume for every experiments of the initial (blue) and complementary (orange) experimental designs. The red line indicates the possible emplacement of the Pareto front of the best compromises.

Figure 7 shows that the overtopping criterion ranges from 0 to about 1,000m^2, while the excavation volume ranges up to 1.4Mm^3.

For this application example, we assume that limiting overtopping is a priority over the cost, and that a value of 1m^2 for overtopping is equivalent in terms of (theoretical) cost to an excavation volume of 1Mm^3. Using such a balance of the cost criteria to design the global cost function (1) favours solutions with limited overtopping. Among those solutions, those with limited excavation volumes are then preferred.

$$Cost = \frac{S_{overtopping}}{c_1} + \frac{V_{excavation}}{c_2} \quad (1)$$

with $c_1 = 1\text{m}^2$, $c_2 = 10^6\,\text{m}^3$

The global cost function defined in (1), is used to calculate the costs associated with the experimental plan solutions. The best solution from the experimental plan is associated with a cost of 0.38 (Table II). We expect to improve these results by using shape optimisation to find an excavation solution associated with an even lower cost.

Table II Best excavation solutions given by the different optimisation strategies.

Optimisation strategy	Cost (1)	Excavation volume (m^3)	Overtopping (m^2)
Experimental design	0.378	~378000	(0)10^{-7}
3DVAR (case 1)	0.498	~484000	1.37 10^{-2}
3DVAR (case 2)	0.357	~357000	(0)10^{-3}
GENOP + Metamodel	0.584	~410	1.73 10^{-1}

The overtopping cost criteria corresponds to the integral of water depth along the dyke.

2) Optimisation method

We use the optimisation algorithm 3DVAR, from the ADAO module [9]. This algorithm minimises a variational function J, which depends on (1) an initial guess on the parameters, (2) an observation (or target), and (3) two error matrices that represent the trust in the initial guess and in the observation. These parameters, and a stopping criterion, are provided by the user.

The 3DVAR algorithm conducts minimisation by a gradient descent process. The variations of the cost function in the proximity of the current set of parameters are evaluated. From this information, the parametric evolution that would minimise the cost function is estimated, and a new set of parameters is selected. The process goes iteratively, until the cost function variations in the proximity of the new set of parameters are negligible, or a maximum number of iterations was reached. This optimisation process usually converges rapidly to an optimum. However, this optimum may not be global, but local.

3) Scenarios

This algorithm was applied to the example case using two different initial guesses. The first initial set of parameters was taken within the parametric area for which overtopping is minimum, using the experimental plan results on parameters influence. The optimisation process is expected to minimise the excavation volume, starting from this initial parametric combination. The second initial set of parameters was taken in the very proximity of the best solution of the experimental plan. The optimisation parameters used for these two optimisation scenarios are given in Table III.

Table III Parameters used for optimisation with 3DVAR (ADAO).

Parameter	Value
Observation (target)	0
Error on observation	1e-4
Error on initial guess	1e3
Increment for gradient calculation	1e-2
Stopping criteria	Cost increment tolerance = 1e-3 Maximum number of iterations = 20

4) Results

Figure 8 presents the evolution of the cost function and of one of the parameters along with the optimisation process (scenario 1). The optimisation process converges rapidly to the solution (in about 10 iterations).

The optimum solutions obtained for both scenarios are presented in Table II. The cost obtained for the scenario 2 optimum solution is 0.36, which is better than the cost of the experimental plan best solution.

The optimum sets of parameters, although corresponding to minima of the cost function, are different. This highlights the presence of several local optima in the cost function. Because of the complexity of the cost function, there is no insurance that the optimum solution obtained for scenario 2 is a global optimum.

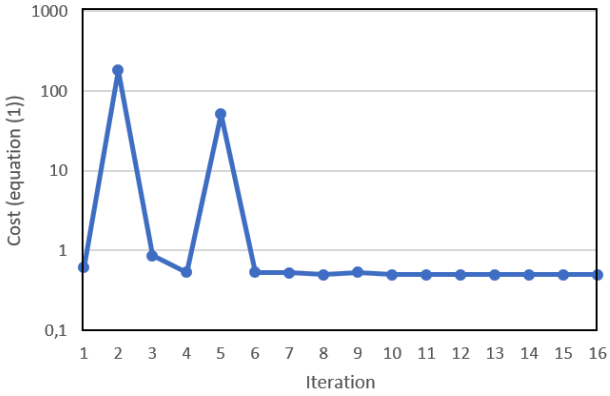

Figure 8. Cost (1) evolution along the optimisation process.

5) Optimum solution

The optimum solution obtained for this study is presented in Figure 9. Overtopping is almost absent, and only concerns the upstream extremity of the dyke. The flow in the reservoir concentrates in the channel that was created by the excavation. At the dam downstream, the flow was increased by 1,000 m^3/s due to the excavation.

The excavation volume associated with this solution nears 360,000 m^3. This information can be used to estimate the economic cost associated with this solution, and compare the dredging scenario with other solutions (e.g. dyke elevation increase).

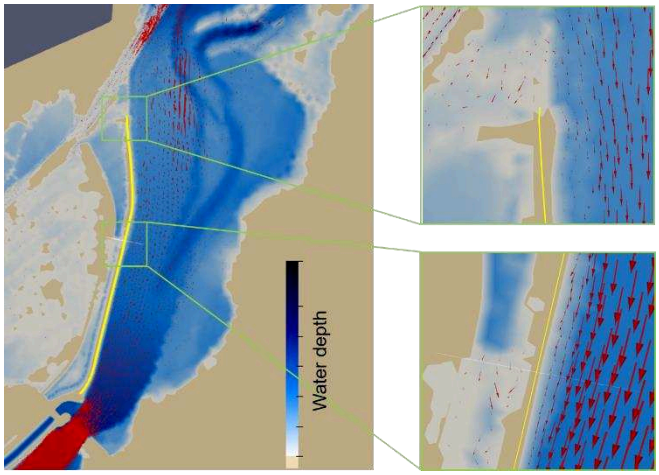

Figure 9. Map of the water depth (blue color scale) and of the velocity (red arrows) for the optimum excavation scenario. The dyke location is indicated with the yellow line.

IV. DISCUSSION

A. Other optimisation strategies

1) Genetic algorithm coupled with a metamodel

The complexity of the cost-function, with several local optima, limits the efficiency of using a gradient descent algorithm (such as 3DVAR) to find the optimum solution. Other optimisation methods exist, including methods that follow the evolution of a population and do not require any information on the cost-function variations, such as genetic algorithms [10].

The advantage of the population-based optimisation methods is its strong efficiency in finding the global optimum of a cost-function. However, they require important computation resources.

A genetic optimisation algorithm (GENOP, developed by EDF-R&D and taken from the Scilab optim_ga module) is included in the OptimStudy class.

To limit the needs in terms of computational resources, the test function, which here includes a TELEMAC-2D simulation, can be replaced by a model of its outputs, i.e. a metamodel. This metamodel is built from a series of experiments for which both the shape parameters and the associated cost are known. It gives an approximation of the cost for any set of parameters in the parametric field, and requires negligible resources.

A metamodel for the application case was built by Kriging from part of the results of the experimental design [11][12]. The remaining experiments were used to test and validate the metamodel. This metamodel was then used together with a genetic algorithm for the search of the optimum solution.

For the application case presented here, we however did not get a better solution using this optimisation strategy. The efficiency of this method was indeed limited here by the complexity of the cost-function variations, that the metamodel did not entirely captured. In particular, the

locations of the optima according to the metamodel did not match those of the real cost-function.

These results could be improved by using other cost-functions, and by improving the metamodel build up technique.

2) Multi-objective optimisation

In this article, we applied shape optimisation using a global cost-function that combines the two cost-criteria. On Figure 7, a limit beyond which no solution seems to exist is visible (highlighted by the dashed red line on Figure 7). This limit is the Pareto front of the two cost criteria, i.e. the line regrouping the optimum compromises, according to the importance given to each criterion (e.g. [5]). Obtaining more details on this front would make it easier to arbitrate the choice of the solution that should be implemented to limit overtopping.

Multi-objective optimisation techniques exist and enable the search for the best compromises taking into account several cost-criteria separately (e.g. [5][13]). The Pareto front of the best solutions could be determined using such techniques, and will be included in future developments of the shape optimisation module.

B. Shape optimisation interest for Telemac-2D studies

1) Performances

The experimental design and the shape optimisation using the 3DVAR algorithm both gave very good compromises for the application case. The best solution from the experimental design is close to that obtained from shape optimisation. The fact that shape optimisation only slightly improved the compromise obtained with the experimental plan is linked with two observations:

- A high number of experiments was used for the experimental plan. Moreover, a second experimental design was conducted on a restricted area of the parametric field, where cost optima were expected. The parametric field was therefore well represented, making it possible to find a very good compromise even without using optimisation algorithm.
- Results highlighted that the cost-function variations are complex, and that several local minima exist. In these conditions, the efficiency of gradient descent algorithms in searching for the optimum solution is limited. The best solution obtained here may therefore not be the real optimum scenario.

For the application presented here, shape optimisation initiated from the area where optimum solutions were expected, gave worse results than the experimental plan. This is again tightly linked with the complex behaviour of the cost function and the good precision of the experimental plan. In this case, using a high precision experimental design would have been an adequate strategy for searching for the best excavation scenario. For other shape optimisation problems, the best optimisation strategy could be different, especially if time and computational resources are constrained.

2) Time and computational resources

For the application presented here, only one day was necessary to run the 1,000 experiments of the experimental design (first set of experiments). This was possible due to substantial computational resources available at EDF. With limited resources, the time needed would have been much more important. Contrarily, the shape optimisation process using the 3DVAR algorithm from ADAO, which required the sequential run of 120 simulations in several days but used much reduced computational resources.

For future applications, the choice between shape optimisation and automated experimental design should depend on several criterion:

- Expected precision on the optimal solution
- Available time and computational resources
- A priori knowledge on the cost-criteria variations and amplitude over the parametric field

VI. PERSPECTIVES

Future development will concern the following directions:

- Improvement of the metamodel building method and use.
- Extension of the current tool to enable multi-objective optimisation studies
- Adaptations for TELEMAC models calibration
- Adaptation to other shape optimisation problems.
- Application of the optimisation techniques to other modelling tools.

Last but not least, it should be noted that there are no plans to share this module with the community. Nevertheless, it would be possible to use this work to propose a generic Python Class in TELEMAC to set up this kind of numerical study.

REFERENCES

[1] C. Goeury, F. Zaoui, Y. Audouin, P. Prodanovic, J. Fontaine, P. Tassi, R. Ata, “Finding good solutions to Telemac optimization problems with a metaheuristic”, 25th Telemac-Mascaret User Conference, Norwich, UK, October 2018. *(references)*

[2] O. Fatna, Y. Bercovitz, C. Goeury, F. Zaoui, “Shape optimization of spillways design using a gradient base algorithm”, Advances in hydroinformatics, models for complex and global water issues – Practices and expectations, pp. 705-718, September 2022.

[3] E. Valette, M. Sécher, “Method to integrate a simplified erosion channel during flood in reservoir simulation with Telemac”, 26th Telemac-Mascaret User Conference, Toulouse, France, October 2019.

[4] C. Goeury, Y.Audouin, F. Zaoui, “Interoperability and computational framework for simulating open channel hydraulics: Application to sensitivity analysis and calibration of Gironde Estuary Model”, Environmental Modelling Software, vol. 148, 105243, 2022

[5] F. Zaoui, C. Goeury, Y. Audouin, “A metamodel of the Telemac errors”, 26th Telemac-Mascaret User Conference, Toulouse, France, October 2019.

[6] McKay, M.D., Beckman, R.J., Conover, W.J. "A Comparison of Three Methods for Selecting Values of Input Variables in the Analysis of Output from a Computer Code". Technometrics. American Statistical Association. 21 (2): 239–245, May 1979.

[7] F. A. C. Viana, "Things you wanted to know about the Latin Hypercube Design and were afraid to ask", 10th World Congress on Structural and Multidisciplinary Optimization, Orlando, Florida, USA, pp. 1-9, 2013

[8] . Kirkpatrick, S., Gelatt Jr, C. D., Vecchi, M. P., "Optimization by Simulated Annealing". Science. 220 (4598): 671–680, 1983,

[9] Argaud, J.-P., EDF R&D, "ADAO, a module for Data Assimilation and Optimization", http://salome-platform.org/, 2022

[10] Golberg D., "Genetic Algorithms in Search, Optimization, and Machine Learning", Addison-Wesley Professional, 1989.

[11] D. G. Krige, "A statistical approach to some mine valuation problems on the Witwatersrand", Journal of the Chemical, Metallurgical and Mining Society of South Africa, vol. 52, pp. 119-139, 1951

[12] G. Matheron, "Principles of Geostatistics", Economic Geology, vol 58(8), pp. 1246-1266, 1963

[13] K. Deb, A. Pratap, S. Agarwal, T. Meyarivan, "A fast and elitist multiobjective genetic algorithm: NSGA-II", IEEE Transactions on Evolutionary Computation, vol. 6 (2), pp. 182-197, 2002

APPENDIX

TELEMAC receding procedure issue

The initial conditions used for hydraulic simulations were at first taken from an equivalent hydraulic simulation with the actual bottom elevation, at steady state. In these initial conditions, overtopping was present all along the dyke. During hydraulic simulations with a modified bottom elevation, the water levels decreased in the reservoir and above the dyke. For some of the experiments, water levels in the reservoir at steady state were lower than the dyke elevation, even close to the dyke (Figure 10). Water elevation however never reached zero over the dyke (the remaining water depth was a few mm).

In order to get rid of the remaining (non-physical) water at the top of the dyke, the threshold depth for receding procedure was increased from 3 cm to 10 cm, with no success. The solution adopted afterwards was to initiate the hydraulic simulations with much lower water level conditions (corresponding to steady state with a much lower entrance flow).

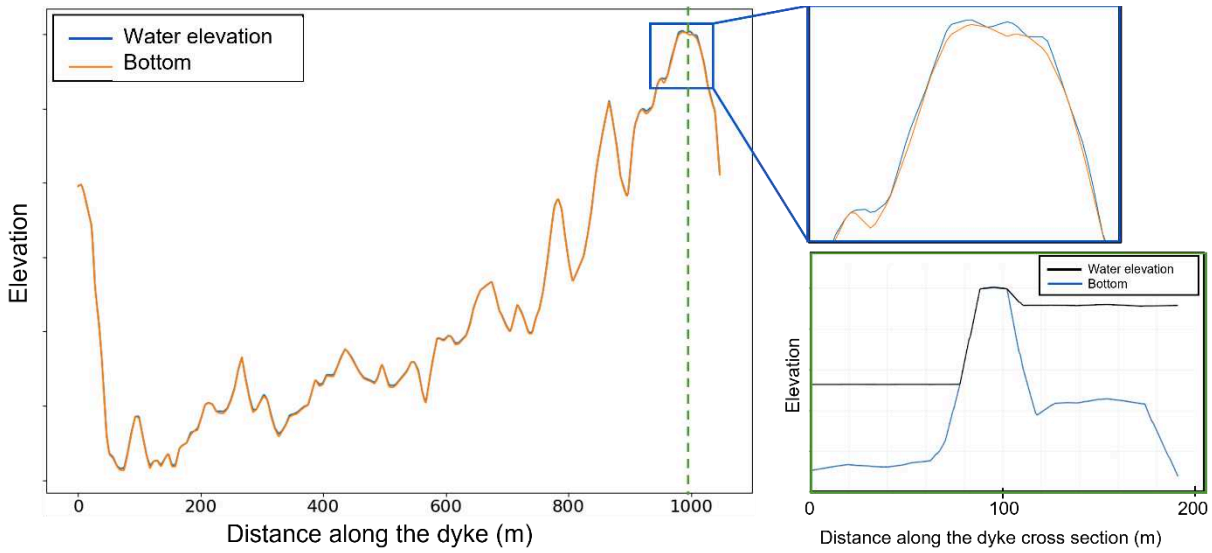

Figure 10. Bottom and water elevation along the dyke (left). Top right: zoom on part of the dyke. Bottom right: bottom and water elevations along a cross section orthogonal to the dyke. The emplacement of the cross section is indicated in the left panel with the dashed green line.

River Dynamics Forecasting using TELEMAC, Earth Observation and AI

Mariana Damova, Stanko Stankov
mariana.damova@mozajka.co, Sofia, Bulgaria
stanko.stankov@mozajka.co, Sofia, Bulgaria
Mozaika, Ltd.
http://www.mozajka.co

Abstract – **The changes in the runoff and alluvial outflow lead to changes in the slope, the depth, meandering, the width of the riverbed and the vegetation. Being able to predict the changed of the river dynamics is of crucial importance for the sustainable monitoring, maintenance and operation of rivers.**

We adopt deep learning architectures pipeline consisting of GAN, CNN and LSTM to actually generate forecasts for river discharge, water level and sediment deposition by using historic satellite data of the meteorological features listed above, and in-situ measurements for water level, discharge and turbidity. To leverage the applicability of the forecasts on the river morphology in integrated models, we calibrate hydrodynamic models using TELEMAC-2D, and we demonstrate how the fusion of a complex EO4AI method and geometry mapping produces a solution for a real user need of being aware of upcoming changes in the navigable channel of the downstream of the Danube. The satellite data are provided by ADAM via the NoR service of ESA.

We provide comparison between the generated hydrodynamic models with real and with forecasted river data, and analyse them. Finally, we demonstrate a visualisation of the forecasted pathway on a GIS component using OpenLayers.

Keywords: hydrodynamic modelling, TELEMAC, deep learning, earth observation, AI, forecast, GIS visualisation, navigable channel.

I. INTRODUCTION

The changes in the runoff and alluvial outflow lead to changes in the slope, the depth, meandering, the width of the riverbed and the vegetation. The bed load and the suspended load can change the morphology of the riverbed as a result of high runoff. This has a direct impact on the determination of the channel in navigable rivers. That is why it is of great importance for assisting the maintenance of the navigable rivers to provide with instruments to predict the modifications in the river morphology that will potentially impact the channel. To address this problem, it is necessary to forecast the sediment deposition amounts and the river runoff and to determine how they will change the river morphology. Predicting sediment deposition potential depends on a variety of meteorological and environmental factors like turbidity, surface reflectance, precipitations, snow cover, soil moisture, vegetation index. Satellite data offer rich variety of datasets, supplying this information.

We adopt deep learning architectures pipeline consisting of Generative adversarial networks (GAN), Convolutional Neural Networks (CNN) and Long Short Term memory (LSTM), further described below, to generate forecasts for river discharge, water level and sediment deposition by using historic satellite data of the meteorological features listed above, and in-situ measurements for water level, discharge and turbidity. To leverage the applicability of the forecasts on the river morphology in integrated models, we calibrate hydrodynamic models using TELEMAC-2D, and we demonstrate how the fusion of a complex EO4AI method, a method that makes use of earth observation data to train AI models, conversely to the usually employed in earth observation methods using AI models in order to better detect objects or phenomena on earth through earth observation – AI4EO[10] - and geometry mapping produces a solution for a real user need, such as being alerted of upcoming changes in the navigable channel of the downstream of the Danube. The structure of the paper is as follows: first we present the adopted method, then we describe the data that have been used for the experiments to demonstrate the method, third we outline the experiments and the experiment results, including GIS (Geographical Information System) visualization of the forecasted navigable channel, finally we discuss related work and conclude.

II. METHOD

We address the problem of river dynamics prediction by forecasting the river discharge and the sediment deposition amounts and then proceed to hydrodynamic modelling with TELEMAC-2D by using the forecast data, the river bathymetry including sediment sizes. (see Figure 1)

[10] Satellite data provide a very rich source of information about the earth. However, they are not perfect. That is why a big segment of the research dedicated to earth observation is concerned with developing AI methods that will improve and maximize the Earth observation using satellite data. This field of research is referred to with AI4EO. In our approach we are using satellite data of meteorological features to train AI methods and obtain predictions for their behavior. This field of research is referred to with EO4AI, and is in its early stages of development.

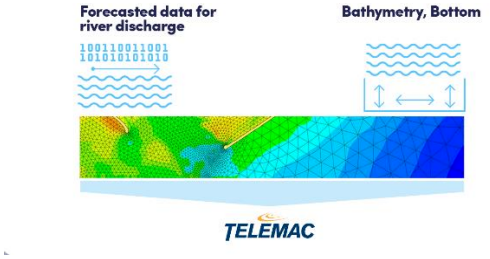

Figure 1. Figure 13 Forecast of river dynamics

For the forecasts we adopt a pipeline of deep learning architectures consisting of GAN, CNN and LSTM by using historic satellite data of meteorological features, that have impact on the river dynamics, such as precipitations and soil moisture, and in-situ measurements for the hydraulic input feature to be forecasted e.g. water level, discharge and turbidity (see Figure 2)**.**

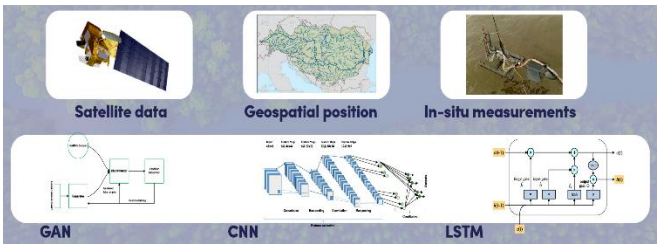

Figure 2. Figure 14 Forecast pipeline of NN

A. Generative adversarial network (GAN)

A generative adversarial network (GAN) [1] is a type of construct in neural network technology that offers a lot of potential in the world of artificial intelligence. It is composed of two neural networks: a generative network and a discriminative network (see Figure 2). The discriminator function compares real data with generated sample data optimizing the model towards reaching a state of no discrepancy. Thus, the one network generates data, e.g. models a transform function that takes a variable and produces another variable following the target distribution and the other network is a discrepancy evaluator that models a discrepancy function that returns the probability of a generated data to be true. The benefits of adopting GANs are that they generate data that looks similar to original data. If a GAN is given an image, then it will generate a new version of the image which looks similar to the original image. Similarly, it can generate different versions of the text, video, audio. However, they are much harder to train since it is needed to provide different types of data continuously to check if it works accurately or not.

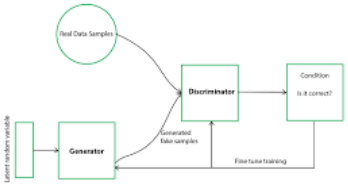

Figure 3. Figure 15 Generative adversarial network architecture

We use GAN to address one specificity of satellite data to be inconsistent, e.g. they do not produce harmonized timeseries, for example daily data, as no data as being provided for some days. But to run neural network architecture to generate forecasts using satellite data, we need consistent timeseries. So, GAN is the first step of our pipeline. It harmonizes the timeseries of the satellite data by generating the missing values in the timeseries.

B. Convolutional neural networks (CNN)

CNN [2] is a type of artificial neural network used for descriptive and generative tasks very often adopted in computer vision. The term "convolutional" means mathematical function derived by integration from two distinct functions. It includes rolling different elements together into a coherent whole by multiplying them. CNNs are made from neurons with trainable weights where each neuron receives input data and takes a weighted sum over them and passes it through an activation function returning the output (see Figure 4.

The convolution applies a kernel [19] over the input data, performing elementwise multiplication with the part of the input that is currently on, after that it sums up the result into a single value (see Figure 4).

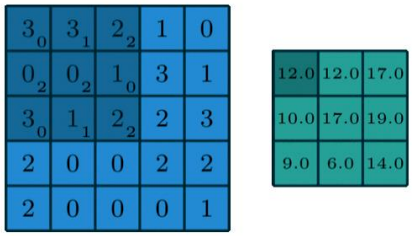

Figure 4. Figure 16: Convolution

After the convolutional layer in CNNs a pooling layer is applied [4]. This layer is responsible for reducing the size of the convoluted feature. It is used to decrease the computation power. There are two types of pooling layers – max pooling and average pooling. They are used to extract the average values or the max values from a kernel (see Figure 5).

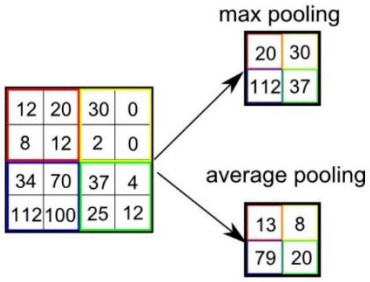

Figure 5. Figure 17: Pooling layer

CNN architectures are used for generating forecasts (see Figure 6)

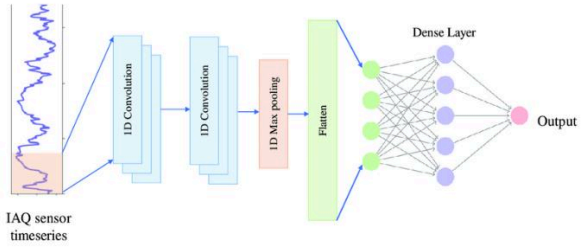

Figure 6. Figure 18: Convolutional neural network used for forecasting

The benefits of adopting CNNs are mainly the high accuracy in tasks that require image recognition and the weight sharing. The disadvantages of adopting CNNs are the need of large datasets to obtain good performance, and long training time, that typically requires a specialized hardware (GPU) to speed up the training process.

CNNs are used as a first step in order to optimally consume the geopositioned input data, as they are effective with geospatial data.

C. *Long Short Term Memory (LSTM)*

LSTM [5] is a type of Recurrent Neural Networks (RNN) model [6] to remember each information throughout time, which is very helpful in any time series predictor. Recurrent Neural Networks (RNN) are designed to recognize sequence patterns and stock markets [7] (see Figure 7).

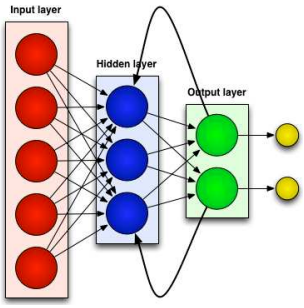

Figure 7. Figure 19: RNN architecture

Instead of neurons, LSTM networks have memory blocks that are connected through layers (see Figure 7). A block has components that make it smarter than a classical neuron and a memory for recent sequences. A block contains gates that manage the block's state and output. A block operates upon an input sequence and each gate within a block uses the sigmoid activation units to control whether they are triggered or not, making the change of state and addition of information flowing through the block conditional. There are three types of gates within a unit: 1) Forget Gate: conditionally decides what information to throw away from the block. 2) Input Gate: conditionally decides which values from the input to update the memory state. 3) Output Gate: conditionally decides what to output based on input and the memory of the block.

The advantages of using LSTMs can be summarized in the following points:

- They can remember each information throughout time, which is very useful for time series predictions
- Native Support for Sequences. LSTMs are a type of recurrent network, and as such are designed to take sequence data as input, unlike other models where lag observations must be presented as input features.
- Multivariate Inputs. LSTMs directly support multiple parallel input sequences for multivariate inputs, unlike other models where multivariate inputs are presented in a flat structure.
- Vector Output. Like other neural networks, LSTMs are able to map input data directly to an output vector that may represent multiple output time steps.

D. *ConvLSTM*

In the adopted architecture, the forecast model of our solution includes both CNNs and LSTMs [8]. Firstly, convolutional layers are used for feature extraction on the input data and are combined with a LSTM layer allowing the architecture to support sequence prediction (see Figure 7).

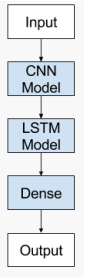

Figure 8. Figure 20: ConvLSTM architecture

ConvLSTMs are used when the input is 2D structure such as image, or 1D as word, sentence or some other sequential input data with the task for classification or forecast. The advantages of using ConvLSTM architectures are that they achieve high accuracy, they operate with input data in 1D, 2D or 3D and since they contain both CNN and LSTM layers they can look back and forward on 1D.

E. *The open TELEMAC system*

TELEMAC-2D is a well-known and established hydrodynamic model solving the shallow water equations. It is used to simulate free-surface flows in two dimensions of horizontal space. At each point of the mesh, the program

calculates the depth of water and the two velocity components. It can perform simulations in transient and permanent conditions. The algorithms used by TELEMAC-2D are extremely efficient and are constantly being improved in order to incorporate the latest developments made in the field of numerical computations. TELEMAC-2D meet the specific requirements of each model: specification of initial conditions or complex boundary conditions, links up with other modelling systems, allow the introduction of new functions.

As shown on Figure 9 we combine the physical model of the river bathymetry and sediments with the forecasted water data for river discharge and water level, employing the Composite Modelling (CM) method that is defined as the integrated and balanced use of physical and numerical models [9]. It is important to emphasize the novelty of our approach to make use of forecast hydraulic input data instead of using hydrological formulas in TELEMAC to obtain the river dynamics prediction.

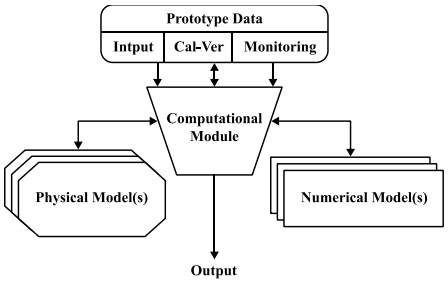

Figure 9. Figure 21 Model integration leading to an integrated model11

III. DATA

Predicting discharge, water level and sediment deposition depends on a variety of meteorological and environmental factors such as precipitations, snow cover, soil moisture, vegetation index, turbidity, surface reflectance. Satellite data offer rich variety of datasets, supplying this information. That is why we make use of satellite data to feed our forecast models with this kind of information. In addition, we make use of in-situ measurements for discharge, water level and turbidity for the forecast models, as well as gain size and bathymetry for the hydrodynamic modelling.

The data used for the experiments and the forecasting prototype as presented below.

A. Satellite data

The satellite data are provided by ADAM (http://adamplatform.eu). ADAM allows accessing a large variety of multi-year global geospatial collections enabling data discovery, visualisation, combination, processing and download. It permits to exploit data from global to local scale. Table I shows the satellite datasets that are provided and made use of in our experiments. The data collections have been selected in order to guarantee:

- - full coverage of the project spatial domain
- - the best available spatial resolution per time
- - data availability for at least 10 years.

Table I Satellite data collections

Meteorological Feature	**Satellite Data Collection**
Temperature	MODIS land surface temperature day
Soil Moisture	SMOS
	CCI Soil Moisture
precipitation	imerg liquid precipitation daily
	imerg liquid precipitation 30 min
	imerg solid precipitation daily
	imerg solid precipitation 30 min
Snow cover	MODIS Snow cover
Solar irradiance	MSG Downwelling Shortwave Surface Flux
vegetation index	MODIS NDVI
	Sentinel 2 NDVI
Copernicus water turbidity	MSI based 300m (CLMS)
	OLCI based 300m (CLMS)
MODIS surface reflectance	MODIS based 250m

The core of ADAM is a Data Access System (DAS), a software module that manages a large variety of geospatial information that feature different data format, geographic / geometric and time resolution. It allows accessing, visualising, sub-setting, combining, processing, downloading all data sources simultaneously. The DAS exposes OGC Open Search (CSW-compliant) and Web Coverage Service (WCS 2.x) interfaces that allow discovering available collections and subset them in any dimension with a single query.

B. In-situ measurements

As the experimental setting of our work was the Danube River, the in-situ measurements were taken from measurement points on the Bulgarian segment of the Danube. They are outlined below.

Historic daily measurements for water discharge in cm^3/s, water levels in m and water temperature in ^oC are provided for the period 2015-2020 by the National Agency for Exploration and Maintenance of the Danube River from the hydrometric stations Lom (km 743,300), Svistov (km 554,300), and Silistra (km 375,500). The current daily measurements from 2021 of the same categories are being collected from the site of the Agency on a daily basis.

[11] Gerritsen, H., Sutherland, J., Deigaard, R., Sumer, B.M., Fortes, J, Sierra, J-P and Prepernau, U, (2009). Guidelines for Composite Modelling of the Interactions Between Beaches and Structures. Final Report, September, 66 pages, (HYDRALAB-III Deliverable JRA1.4).

The turbidity and grain size historic data daily sampling from the same hydrometric stations are provided for the period 2015-2020 inclusively by The National Institute for Meteorology and Hydrology. The turbidity [g/l] is being determined via laboratory analysis in The National Institute for Meteorology and Hydrology.

For the purposes of the geometry modelling of the Danube River, to address the use case for predicting of the navigable channel on the Danube River, the bathymetry of the Bulgarian segment of Danube River has been provided by the National Agency for Exploration and Maintenance of the Danube river.

IV. Experiments and Results

Experiments have been carried out with different ConvLSTM architectures. The best performing one turned out to be the one using two convolutional layers. We show the results of the generation of missing data with GAN, and the ConvLSTM architecture with two convolutional layers. Subsequently, we show the results of the river dynamics prediction with the adopted method using TELEMAC 2D.

A. Missing data generation with GAN

The missing data generation with GAN was carried out with daily satellite data timeseries from 2014-2019 and the tests were the daily timeseries from 2020. The results are shown on Table II. It is evident that the precision of the generated missing data is very satisfactory with MinMae score close to 0. It is important to point out that the spatial resolution for the satellite data in the reported experiments was 1.1 km.

Table II Missing data generation results

Meteolological feature	**Satellite dataset name**	**MinMae**
Soil moisture	ESACCI-SOILMOISTURE-L3S-SSMV-COMBINED_4326_025	0
Liquid precipitations	IMERG_DAY_LIQUID_SCALED_4326_01	0,92
Snow cover	MODIS_SNOW_4326_001	0,73
NDVI	MOD13_NDVI_4326_005	0,05
Solid precipitations	IMERG_DAY_ICE_SCALED_4326_01	0,07
Reflectance	MODIS based ISMoSeDe_reflectance	0,04

B. Forecast with ConvLSTM

The forecasting experiments were carried out with the harmonized satellite data, as described in the previous subsection, and with in-situ measurements for discharge, water level and turbidity as per the description in section III. Table III below shows the annual average deviation in the results for discharge, water level and turbidity for the three hydrometric posts on the Danube with a model calibrated to generate forecast for 7 days ahead. The experiments are carried out with daily historic data from 2014-2019 and the test is performed on year 2020.

Table III Forecast performance

Feature	**Deviation**		
	Lom	**Svishtov**	**Silistra**
Turbidity (NTU)	0,01	0,02	0,04
Discharge (cm3/sec)	224,70	181,70	86,90
Water level (cm)	26,74	20,40	18,83

Figure 10 shows the performance of the discharge forecast compared to real measurements for 30 days ahead for the three hydrometric stations on the Danube.

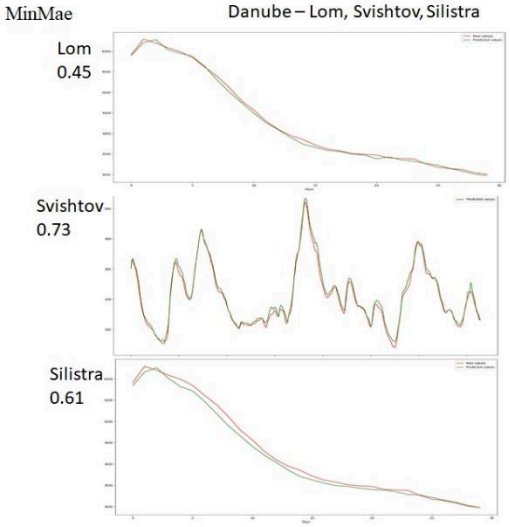

Figure 10. Figure 10 Forecast performance for 30 days ahead

Here we also notice that the performance is satisfactory.

C. River dynamics prediction with TELEMAC D

TELEMAC simulation is performed for the critical areas around the hydrometric points Lom, Svishtov and Silistra. We have used the bathymetry of the critical areas to draw the mesh, in-situ measurements for substrate and the forecasted data for discharge and water level, as turbidity was not relevant for the type of river segments of interest.

For the simulation a time step value of 10 and Nikuradse for the law of bottom friction. The liquid boundary is represented with three parameters – time, free surface and discharge measured in s, m and m^3/s. The temporal resolution of the simulation is one day, represented in seconds (0-86400 seconds). We introduce the forecasted value for discharge and calculate the free surface from the forecasted water levels using the following formula:

$$Fs = wl/100 + K$$

where wl is the forecasted water level and K is the station elevation.

The created output file is shown on Figure 11

```
# liquid boundary file
#REFDATE 2020-01-01 00:00:00
T SL(1) Q(2)
s  m  m^3/s
0.000000 9.08 6268.0
86400.000000 9.299999999999999 5643
172800.000000 9.59 5668.0
259200.000000 9.52 5530.0
345600.000000 9.43 5332.0
432000.000000 9.36 5039.0
518400.000000 9.25 4668.0
604800.000000 9.07 4317.0
691200.000000 8.899999999999999 412
777600.000000 8.68 3963.0
864000.000000 8.43 3817.0
950400.000000 8.25 3705.0
```

Figure 11. Figure 11 Liquid boundary file with forecasted data

The generated 6 features: riverbed, velocity U, velocity V, friction velocity, surface elevation, and water depth are produced. Figure 12 shows the predicted riverbed for the critical area around Svishtov, and Figure 13 shows the comparison between the real and predicted depth for January 2020 for the critical area around Svishtov for 1, 10, 20 and 30 days ahead.

The precision in the prediction of the depths is evident from the similarity of the images. It is important to point out that we do not observe deterioration of the performance results as the prediction period increases to 30 days.

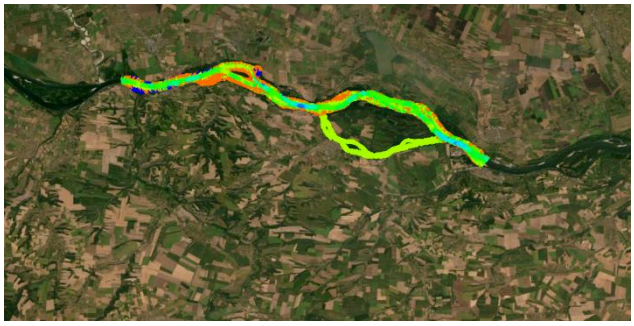

Figure 12. Figure 12 Predicted riverbed of a critical area around Svishtov

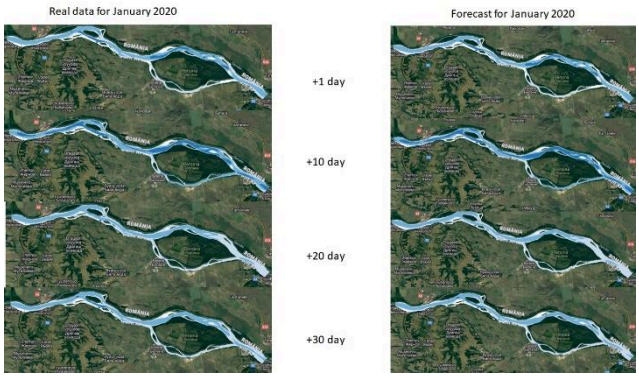

Figure 13. Figure 13 Comparison of real vs predicted depth of a critical area around Svishtov

Based on the forecasted data as TELEMAC output we proceeded to the generation of the forecasted navigable channel by identifying the middle path on the XY axis as shown on Figure 14.

Figure 14. Figure 14 Visualization of the forecasted fairway on the critical area of Svishtov

V. RELATED WORK

Hydrodynamic modelling [9] forms the basis for many modelling studies, whether sediment transport, morphology, waves, water quality and / or ecological changes are being investigated. Research is being carried out to improve the representation of tides, waves, currents, and surge in coastal waters. A variety of coastal models are available, and the modelling techniques have become sufficiently mature [10]. Composite Modelling (CM) is defined as the integrated and balanced use of physical and numerical models [11]. Our approach blends the CM method and demonstrates how it can be applied to hydrodynamic modelling.

River dynamics has been observed and forecasted with various mathematical models. They are gaining popularity for solving a wide range of natural fluid mechanical problems. When it comes to free-flow currents and sediment transport processes in open channels, single-dimensional (1D) and two-dimensional (2D) digital models are widespread. To the best of our knowledge our approach is the first to attempt to forecast river dynamics by inserting forecasts of hydraulic input into TELEMAC. Moreover, the forecasts of the hydraulic input are produced by means of using historic satellite data of meteorological features and in-situ measurements from given hydrometric stations. This constitutes a cutting-edge novel method in the field of hydrodynamic modelling.

VI. CONCLUSION AND FUTURE WORK

We presented a method for predicting river dynamics using TELEMAC, AI and Earth observation. It consists of producing TELEMAC simulation by using forecasted measurements for discharge and water level. For the forecast we adopt neural networks pipelines and historic satellite data with meteorological information and in-situ measurements.

The satellite data input to the neural network is harmonized in a first processing step also using neural networks - GAN. We succeed to obtain very good forecasting results that are consequently blended in the TELEMAC simulations, based on which we are capable to derive hands-on determination and visualization of forecasted fairway. We have demonstrated how the fusion of a complex EO4AI method and geometry mapping produces a solution

for a real user need of being aware of upcoming changes in the river fairway of the downstream of the Danube. To the best of our knowledge our approach is the first to make use of forecast hydraulic input data to produce a hydrodynamic simulation with TELEMAC. Our results demonstrate the viability and robustness of our method. Our plans are to integrate the method in our e-Infrastructure for monitoring dams and rivers for sustainable development – ISME-HYDRO (http://isme-hydro.com).

ACKNOWLEDGEMENT

This work has been carried out within ESA Contract No 4000133836/21/NL/SC. For the hydrodynamic modelling we received training and consulting from IMDC for which we thank Alexander Breugem, Theofano Koutrouveli, Boudewijn Decrop.

REFERENCES

[1] https://machinelearningmastery.com/what-are-generative-adversarial-networks-gans/

[2] https://towardsdatascience.com/a-comprehensive-guide-to-convolutional-neural-networks-the-eli5-way-3bd2b1164a53

[3] https://towardsdatascience.com/intuitively-understanding-convolutions-for-deep-learning-1f6f42faee1

[4] https://www.analyticsvidhya.com/blog/2021/05/convolutional-neural-networks-cnn/

[5] https://wiki.pathmind.com/lstm

[6] https://stackabuse.com/time-series-analysis-with-lstm-using-pythons-keras-library/

[7] https://towardsdatascience.com/understanding-recurrent-neural-networks-the-prefered-neural-network-for-time-series-data-7d856c21b759

[8] https://machinelearningmastery.com/cnn-long-short-term-memory-networks/

[9] http://www.coastalwiki.org/wiki/Modelling_coastal_hydrodynamics

[10] Chau, KW Modelling for coastal hydraulics and engineering, Taylor and Francis Ltd., 231 pp., 2010.

[11] Gerritsen, H., Sutherland, J., Deigaard, R., Sumer, B.M., Fortes, J, Sierra, J-P and Prepernau, U, (2009). Guidelines for Composite Modelling of the Interactions Between Beaches and Structures. Final Report, September, 66 pages, (HYDRALAB-III Deliverable JRA1.4).

[12] Barthel, V and E.R. Funke. Hybrid modelling as applied to hydrodynamic research and testing. In: Recent Advances in Hydraulic Physical Modelling, R. Martins (Ed), NATO ASI Series E: Applied Sciences – vol. 165, Kluwer Academic Publishers, 1989.

[13] Oumeraci, H. Strengths and Limitations of Physical Modelling in Coastal Engineering - Synergy Effects with Numerical Modelling and Field Measurements. Proc. of the Hydralab -Workshop on Experimental Research and Synergy Effects with Mathematical Models, Eds.: K.-U. Evers, J. Grune, A. van Os, Coastal Research Centre, Hannover, 1999.

[14] https://www.mikepoweredbydhi.com/download/mike-2016/mike-11?ref=%7B181C63FF-2342-4C41-9F84-F93884595EF3%7D

[15] https://webspace.clarkson.edu/~wwu/CCHE1D.html

[16] https://www.usbr.gov/tsc/techreferences/computer%20software/models/srh1d/index.html

Automatic calibration of a tidal estuary model of the Scheldt using data assimilation algorithm

Kai Chu[1], W.A. Breugem[1], Li Wang[1], Thom Wolf[1], Theofano Koutrouveli[1], Boudewijn Decrop[1]
kai.chu@imdc.be, Antwerp, Belgium
[1]: IMDC N.V.

Abstract – **A tidal estuary model of the Scheldt is developed in TELEMAC-3D. The model is calibrated on bottom roughness using an automatic procedure. The Python module TELAPY, is online coupled with the Python ADAO library from the SALOME platform. The 3D-Variational data assimilation algorithm is adopted to improve water level predictions along the estuary. The automatic calibration routine steers iterative runs, after each of which the bottom roughness is updated based on the minimization of a cost function. After automatic calibration, the model reproduces the hydrodynamics in the Scheldt Estuary accurately. For instance, the averaged root-mean-square-error (RMSE) of the water level is reduced to 12 cm and the M2 tidal amplitude is accurately reproduced. The Scheldt model is also validated for stormy period and validated against ADCP transect data. Therefore, the Scheldt model is considered as a reliable and efficient tool for various applications in the estuary.**

Keywords: Automatic calibration, tidal estuary, TELEMAC-3D, Scheldt, ADAO, TELAPY.

I. INTRODUCTION

The Scheldt is a tidal estuary situated in the Netherlands and Belgium, with a tidal reach up to 160 km upstream from the mouth near Vlissingen (The Netherlands). The Scheldt estuary has important environmental and commercial values. An accurate prediction of the tidal propagation along the estuary has numerous applications. Process-based numerical models, which include the most important processes and parameters for tidal predictions, have widely been adopted for this purpose.

Model calibration is often referred to as finding the optimal set of model parameters, which provide an accurate description of the system behaviour. It is normally achieved by confronting model predictions with measurements representing the system. Model calibration is an essential modelling step, but manual calibration often requires significant time and effort without guarantee of finding the optimal solution. Recently, automatic calibration of numerical models has shown its capacity in obtaining the optimal parameter settings in a fraction of the time needed for manual calibration. In the TELEMAC community, several studies [1,3,4,5] have shown successful calibration of TELEMAC models in both tidal rivers and the North Sea. All these studies have shown the potential of automatic model calibration in oceanic, estuarine and coastal waters.

In this study, a TELEMAC-3D hydrodynamic model is set up for the Scheldt Estuary. Tidal propagation is typically calibrated by adjusting the bottom roughness, which is performed in an automated manner in the present study. The Python module TELAPY, is coupled online with a Python library called ADAO (A module for Data Assimilation and Optimization) [2] from the SALOME platform [3]. The 3D-Variational data assimilation algorithm [6] is adopted to perform automatic model calibration. This algorithm compares time-series of water levels predicted by the Scheldt model to measurement data at 22 stations throughout the estuary, leading to a cost function which is subject to minimization. Twelve roughness polygons are selected for the Scheldt model domain, which is a compromise between model accuracy and computational efforts. The automatic calibration routine steers iterative runs, after each of which, the bottom roughness is updated based on the minimization of the cost function. After 75 iterations, an optimal bottom roughness field is found, which provides the lowest cost function.

After automatic calibration, the model is further validated for a stormy period and validated against ADCP transect data, showing that the model reproduces the hydrodynamics in the Scheldt Estuary accurately.

The Scheldt model is a very computationally efficient model. With a time step of 30 seconds, a simulation of 28 days period takes only 6.25 hours of computation time using 48 computational cores. Therefore, it is a reliable and efficient tool for various applications in the estuary, such as operational forecasting, sediment transport calculations [7] and transportation of macroplastics [8] etc.

II. ABBREVIATIONS AND CONVENTIONS

The used abbreviations are summarized in Table I. The following conventions are followed in this paper:

- Times are represented in UTC.
- The coordinate reference system, used by the model and for presentation of the model output is RD (Rijksdriehoekscoördinaten), expressed in meters.
- The vertical reference level used in the model is TAW which is 2.35m below NAP.
- Current directions refer to the direction to which the flow is directed: e.g. a current direction of 90°N means that the currents are directed towards the East.

- Wind directions refer to the direction the wind is coming from: e.g. a wind direction of 90°N means that the wind is coming from the East.
- SI units are used.

Table I Used abbreviations

ADAO	A module for Data Assimilation and Optimization
ADCP	Acoustic Doppler Current Profiler
API	Application Program Interface
HIC	Hydrological Information Centre
HMCZ	Hydro Meteo Centrum Zeeland
iCSM	IMDC Continental shelf Model of the North Sea
NAP	Normaal Amsterdams Peil (Dutch vertical reference level)
RD	Rijksdriehoekscoördinaten (Dutch horizontal system)
RMAE	Relative Mean Absolute Error
RMSE	Root Mean Square Error
RWS	Rijkswaterstaat
TAW	Tweede Algemene Waterpassing (Belgian vertical reference level)
UTC	Universal Time Coordinate

III. MODEL SETUP

A. *Mesh and Bathymetry*

The mesh of the Scheldt model covers the estuary mouth and the entire Scheldt River (Figure 1). The mesh resolution gradually decreases from ~450 m near the offshore boundary to ~3.5 m in the upper river tributaries. The total number of computational nodes is 143,872, with 260,595 triangular elements in a horizontal plane. To better represent the flow patterns, the Scheldt model runs in 3-D mode with 5 vertical nodes using sigma coordinates at (0, 0.12, 0.3, 0.6 and 1.0 from bottom to top).

The mesh is made such that it is aligned with the flow lines of the water movement inside the estuary, e.g. using soft-lines along the channel to guide the generation of the mesh. In the upstream parts, channel meshes are used to structure the triangles of the mesh in such a way that they better follow the channel geometry and the flow direction.

The bathymetric data of 2019 are used, which are identical to the data described in [9]. The data is formatted as combigrids (combination between LIDAR and Bathy data into one consistent dataset). The dataset has a spatial resolution of 5 m.

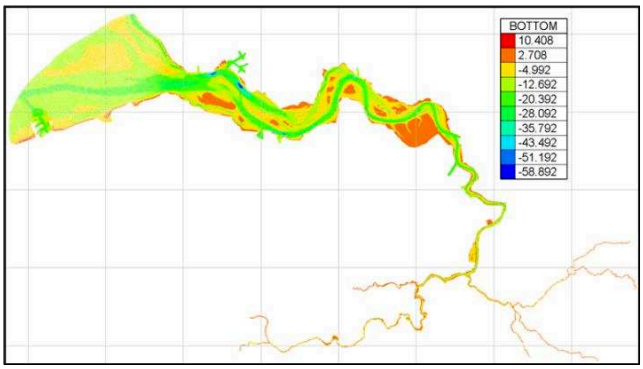

Figure 1. Mesh and bathymetry (m TAW) of the Scheldt model.

B. *Boundary and Initial Condition*

The model contains one open boundary at the mouth of the Western Scheldt and eight upstream boundary sections. At the downstream boundary, time series of water levels and depth-averaged velocities are imposed from the in-house iCSM model [10]. Recently, the iCSM was automatically calibrated [5] on bottom friction on the platform of SALOME-Hydro with three-dimensional variational assimilation (3D-Var). The iCSM model accurately reproduce the hydrodynamics in the North Sea. For instance, the root mean square error (RMSE) of the water levels along the Belgian coastal zone is 10 cm. The RMSE of the velocity magnitude in the Belgian Coastal Zone (determined form stationary velocity measurements) is of the order 0.1 m/s, which is considered as top-of-range numerical model accuracy.

The water levels and velocities computed by iCSM are interpolated on the open sea boundary nodes of the Scheldt model via an in-house boundary nesting tool. For the eight upstream boundaries, measured time series of river discharge (provided by HIC and RWS) and salinity (set to zero) are imposed.

The initial condition from the models comes from a two-day spin-up simulation for the water levels and velocities. The initial condition for the salinity was obtained from spatial interpolation of measurements data from point measurements along the Scheldt estuary.

C. *Wind*

Wind measurement data is available at Hansweert with time interval of 10 minutes (data source: HMCZ, https://waterberichtgeving.rws.nl/water-en-weer/dataleveringen/ophalen-opgetreden-data). The time series of wind measurement at Hansweert of 2019 are used to force the Scheldt model. Figure 2 shows the wind rose plot for the entire year of 2019. The dominant wind comes from the south-west direction with a typical wind speed between 6 - 12 m/s.

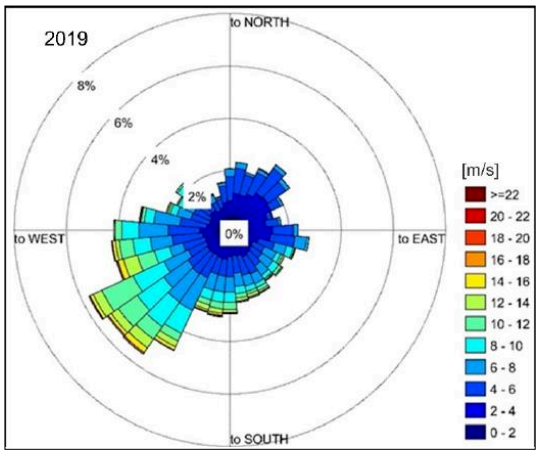

Figure 2. Wind rose for the entire year of 2019 at Hansweert.

D. *Parameter Settings*

The parameter settings of the Scheldt model are summarized in Table II.

Table II Model parameters of the Scheldt model.

Parameter	**Description**
Time Step	30 s
Initial condition	two-day spin-up
Number of vertical nodes	5
Version TELEMAC	v8.1goblinshark
Salt transport	On
Wind	On
Roughness formula	Nikuradse law
Bed roughness value	Space varying roughness field
Option for the treatment of tidal flats	1: equations solved everywhere with correction on tidal flats
Treatment of negative depths	2: flux control
Vertical turbulence model	6: GOTM (using K-epsilon model with second order closure for the buoyancy flux) [11].
Horizontal turbulence model	4: Smagorinsky
Scheme for advection of velocities	1: characteristic method
Scheme for advection of tracers	13: Leo Postma for tidal flats
Solver	7: GMRES
Scheme for diffusion of tracers	0: No diffusion horizontally. Vertical diffusion is calculated using the set_dif.f subroutine [12].

IV. MODEL CALIBRATION

A. *Modelling Period*

The model calibration period is 29 days from 22/03/2019 to 20/04/2019, which is a relatively calm period with an average wind speed of 4.3 m/s (Figure 3).

Thanks to the use of improved drying-flooding methods [13], the Scheldt model could run with a time step of 30 seconds which significantly increases the computational efficiency. For instance, it takes 6.25 hours for 29 days simulation on 48 cores.

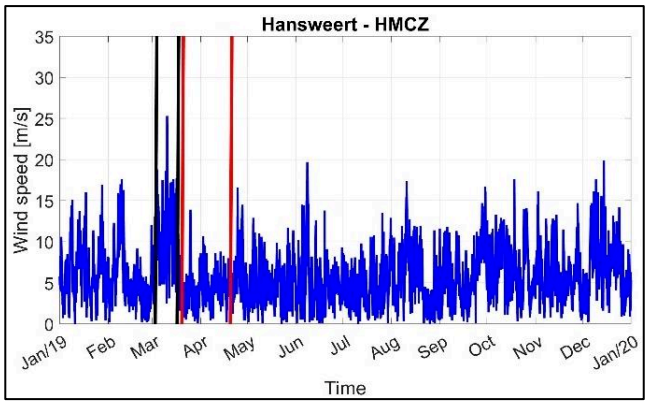

Figure 3. Time series of the wind speed at Hansweert. The calibration period (22/03 – 20/04/2019) is indicated by red lines.. The stormy period used for the validation (03/03 - 17/03/2019) is indicatedby black lines.

B. *Automatic calibration*

The objective of the automatic calibration is to improve water levels along the estuary predicted by the Scheldt model. The Python module TELAPY is coupled online to the Python ADAO library from the Salome-Hydro platform. The 3D-Variational data assimilation algorithm is adopted to execute the automatic model calibration. This algorithm compares time-series of water levels predicted by the Scheldt model to measurement data at 22 measurement stations along the river Scheldt (Figure 7 and Table III), leading to a cost function which is subject to minimization. The automatic calibration routine steers iterative runs, after each of which, the bottom roughness is updated based on the minimization of cost function.

The automatic model calibration is executed using the SALOME platform (https://www.salome-platform.org/), which is an open-source tool developed at EDF, which provides pre- and post-processing of model simulations, supports cascading and coupling of different software tools, modules and codes [14]. SALOME is based on an open and flexible architecture with reusable components, which can be used to construct a computation scheme assembling internal module or external codes through specific communication protocols [1]. In this study, the Scheldt model developed in TELEMAC-3D is coupled using the TelApy and dynamically linked to ADAO within SALOME (Figure 4).

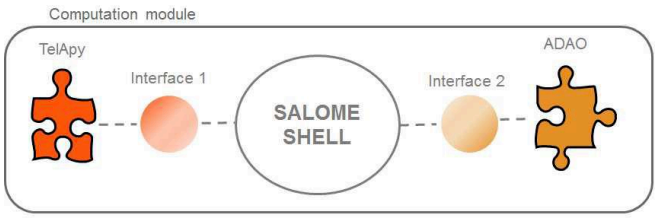

Figure 4. The SALOME composition linking TELAPY to ADAO, adopted after [1].

The TELAPY is an internally built-in component in the open-source TELEMAC system [15]. It is essentially a python module which wraps and controls TELEMAC simulations through a Fortran API (Application Program Interface). The API is used to steer a simulation while running a model. The TelApy component has the capability to be extended to new types of TELEMAC simulations including high performance computing for the computation of uncertainties, other optimization methods and coupling [3].

ADAO is a Python library (https://pypi.org/project/adao/) providing standard and advanced data assimilation and optimization algorithms on the SALOME platform [1]. ADAO can be easily coupled with other modules or external simulation codes, for instance TELEMAC-2D and TELEMAC-3D.

The automatic calibration is based on a 3D-Variational data assimilation scheme [6]. This method minimizes a cost function J(x) which describes the deviation between a model state and an observation as expressed in Eq. (1). The cost function is essentially a sum of squared differences between the observations and the corresponding model values:

$$J(x) = (x - x^b)^T B^{-1}(x - x^b) + (y^0 - H(x))^T R^{-1}(y^0 - H(x)) \quad (1)$$

where the vector x represents the parameters to be calibrated (bottom roughness in this study), x^b represents the prior knowledge of x (the background state, e.g. the initial guess); y^0 is the observation vector (time series of measured water levels in this study), H is an observation operator enabling the passage of the parameter space to the observation space (the TELEMAC-3D Scheldt model in this study) such that y = H(x). B, R are the so-called background and observation error covariance matrices respectively.

The first term in the right hand side of Eq. (1) is often referred to the 'penalty term' introduced by [16], meaning that additional cost is added to the cost function when the calibrated parameter x drifts away from the background state x^b. This is useful for fine-tune the calibration, when the modeler has high confidence in his initial guess x^b. In this study, the background error covariance B is set to a very large value (10^8) such that the 'penalty term' of the cost function is ignored.

The minimization of the cost function is based on the so-called constrained Broyden Fletcher Goldfarb Shanno Quasi-Newton method (c-BFGS-QN). Using this constrained optimization method makes it possible to impose boundaries during the search process of the model parameters, guaranteeing that only physically meaningful values are used. A detailed description of the BFGS is given by [1]. Thus, it will not be further discussed here.

As a preparation step for the auto-calibration, twelve roughness polygons are selected for the Scheldt model domain as shown in Figure 7. The number of polygons in use is a compromise between model accuracy and computational efforts. The selection of polygons is based on knowledge gained from manual calibration experience from the past. For instance if modelled water level behaves differently at two neighbouring stations with the same roughness values, those two stations shall be assigned to two different polygons. The bottom roughness in the model is calculated using the Nikuradse equation:

$$c_d = \left(\frac{\kappa}{\log\left(\frac{30h}{ek_s}\right)}\right)^2 \quad (2)$$

where C_d is the bed drag coefficient [-], h is the water depth [m]; κ is the Von Kármán constant of 0.41 [-]; e is Euler's constant of 2.71828, and k_s is the Nikuradse roughness value [m].

However the Nikuradse value k_s has a highly nonlinear relation with the drag coefficient C_d (see Eq. 2), meaning that the change in the water level as function of the roughness behaves differently for high Nikuradse values than for low Nikuradse values, and that the physically admissible range of Nikuradse values is rather large (it can vary from 0.1 cm to 10 cm). This will slow down the automatic calibration process. Therefore instead of directly calibrating k_s, we calibrated $\log_{10}$ (k_s), see relation in Figure 5. An initial guess of 0.03 m of Nikuradse value ($\log_{10}(k_s)$ = -1.52) is assumed for the automatic calibration. Note that although $\log_{10}(k_s)$ is calibrated, the model is still forced with k_s during the simulation.

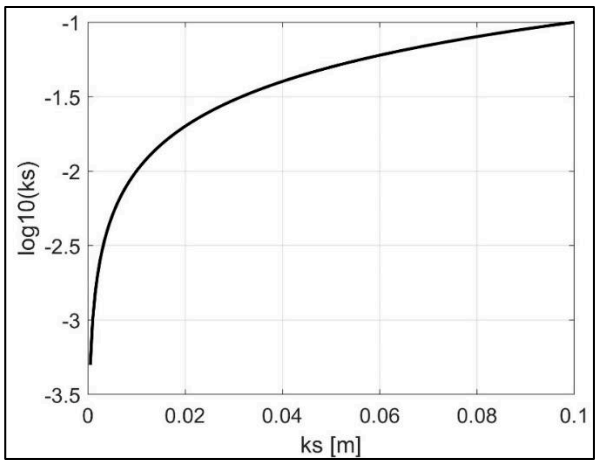

Figure 5. Relation between Nikuradse value (ks) and its transformation of log10(ks).

V. CALIBRATION RESULTS

Figure 6 illustrates the evolution of the cost function. After 75 iterations, an optimal bottom roughness field is found (Figure 7), leading to the lowest cost function.

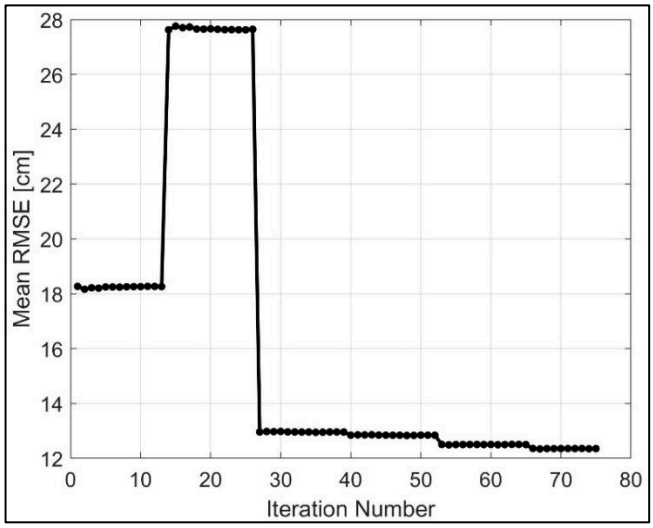

Figure 6. Evolution of mean RMSE during the automatic calibration.

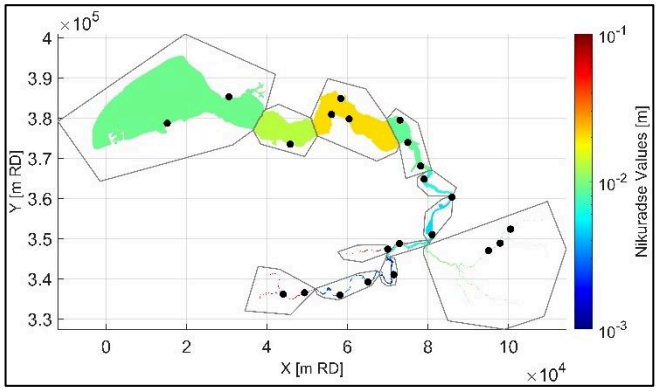

Figure 7. Roughness map showing the Nikurase values after automatic calibration. The 12 polygons in grey define different roughness zones. The black dots represent water level measurement stations as indicated in Table III.

Figure 8 shows that the RMSE of the water levels in general reduces after the automatic calibration, especially in the upstream part of the Scheldt estuary. Figure 9 shows that the M2 amplitude is very well reproduced. The full statistics of the water levels after the automatic calibration are referred to Table III. The average RMSE of the water level in the Scheldt estuary is reduced from 18 cm to 12 cm after automatic calibration.

Table III Statistics of water level after automatic calibration along the estuary (from downstream to upstream).

Stations	**Bias of the water level [cm]**	**RMSE of the water level [cm]**	**Bias of the M2 Amplitude [cm]**	**Bias of the M2 Phase [deg]**
Cadzand	0.5	9.9	-2.1	1.6
Vlissingen	-0.2	8.9	0.2	1.2
Terneuzen	-0.6	8.8	3.0	-1.4
Overloop Hansweert	-0.7	7.9	2.3	0.3
Hansweert	-1.7	8.2	2.5	-0.4
Walsoorden	-2.9	9.1	1.5	-0.1
Bath	2.0	10.0	1.1	0.3
Prosperpolder	4.8	10.7	1.8	-0.4
Liefkenshoek	-1.6	10.3	2.5	-0.7
Kallosluis	4.2	11.2	1.3	-0.4
Antwerpen	-1.3	10.9	2.0	-0.5
Hemiksem	-1.4	12.7	6.0	-1.6
Temse	-2.7	15.8	8.9	-2.8
Tielrode	-1.5	14.9	8.6	-1.7
Sint-Amands	-1.6	14.0	6.3	-2.1
Dendermonde	0.6	11.1	-3.5	1.6
Schoonaarde	-3.0	11.9	-3.3	3.5
Wetteren	-6.8	12.7	-1.6	2.2
Melle	-8.7	14.8	-1.5	2.1
Duffel	-2.5	12.5	-6.8	1.3
Lier Molbrug	-3.0	15.0	-7.9	6.1
Emblem	-22.9	30.4	1.3	-2.8
|Average|	**3.4**	**12.4**	**3.5**	**1.6**

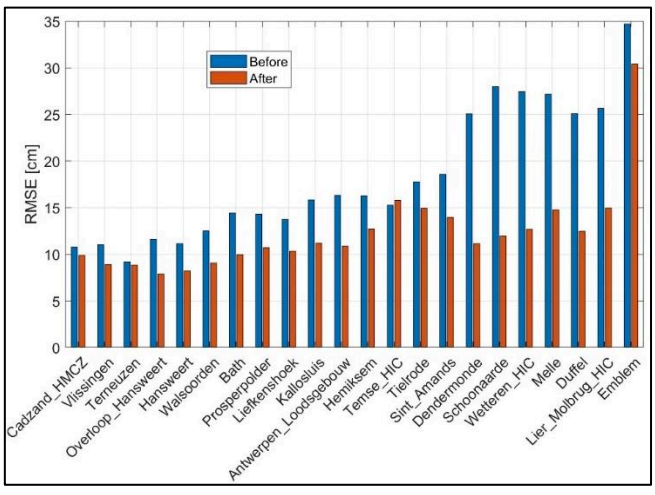

Figure 8. RMSE of the water level along the Scheldt before and after automatic calibration.

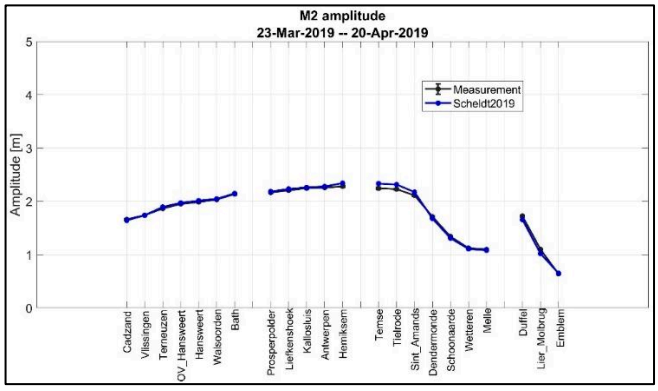

Figure 9. M2 amplitude of the Scheldt model after auto-calibration.

VI. Model Validation

A. *Validation for a stormy period*

The Scheldt model was run for a stormy period from 03/03/2019 to 17/03/2019. This period contains a maximum wind speed of 25 m/s and mean wind speed of 11 m/s (Figure 3).

Figure 10 presents the RMSE of the water level along the Scheldt Estuary during this stormy period, compared to the RMSE determined from the calibration period. In general, the model performance from the estuary mouth to Sint-Amands is comparable to the performance for calibration period (with a RMSE that is 2-3 cm larger). It is noticeable that the model performs slightly worse in the upstream part for this stormy period (e.g. the RMSE is more than 30 cm at Melle), which requires further investigation. It might be due to the uncertainties in the river discharge data at Melle, and/or the use of stationary wind data at Hansweert, which is quite far away from the upstream branches, for the entire model domain. It also worthwhile to mention that such a deviation is usually a classical diagnostic in data assimilation which can be considered as a positive systematic side-effect of using data assimilation framework.

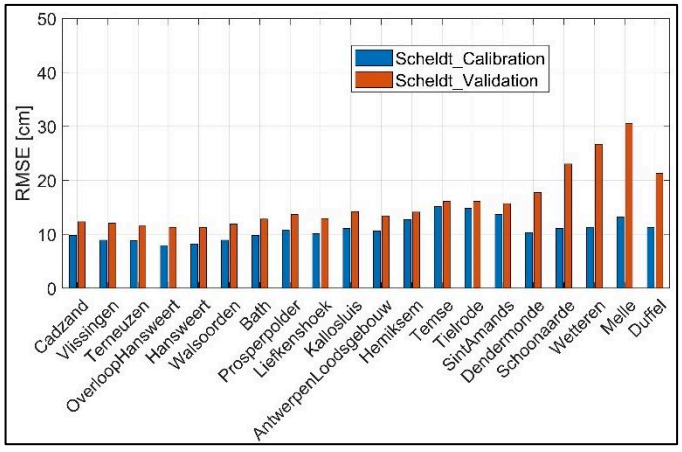

Figure 10. Comparison of the RMSE of the water levels along the Scheldt between the calibration period and the validation period.

B. *Validation on ADCP transect data*

The model is also validated against eleven ADCP transect data in the Western Scheldt as described in [7]. The measured tide during the through tide measurement campaigns are used to determine the modelling period using the comparable tide analysis [17]. This is a method that allows the comparison of model results to measurements, which are outside of the simulation period. In this method, the water levels that occurred during the through tide measurement (ADCP) are compared to the water level measurements during the simulation period. Those tidal cycles that match best with the tidal cycles during the through tide measurement are selected and used for the model validation.

By using a model qualification based on the RMAE (Relative-Mean-Absolute Error), which includes the accuracy of both the velocity magnitude and direction, the comparison can be quantified (Table IV). Table V shows the RMSE and RMAE statistics of the simulated velocities during the eleven ADCP campaigns. All the eleven different transects show a RMAE with the qualification 'Good' or 'Excellent'. The average RMSE of the flow magnitude is 16.8 cm/s, which can be considered a good performance given that the average tidal peak velocity is 1.5 m/s. In general the flow pattern is adequately reproduced by the Scheldt model. Figure 11 shows the modelled and measured velocity field at Waarde during maximum ebb tide. Both flow magnitude and direction are well reproduced by the model.

Due to the lack of data, the Scheldt model is not validated for the Sea Scheldt and the Upper Sea Scheldt, which shall be further evaluated in the future.

Table IV Model qualification based on RMAE [18].

Model qualification	**RMAE [-]**
Excellent	<0.2
Good	0.2-0.4
Reasonable/fair	0.4-0.7
Poor	0.7-1.0
Bad	>1.0

Table V RMSE and RMAE of velocities along 11 ADCP transects. The campaign names indicate the location and date of the measurement.

Campaign	**RMSE [cm/s]**	**RMAE [-]**
R6_GatVanOssenisse_20120509	20.2	0.25
R6_Middelgat_20120508	21.5	0.35
Diepe_Put_Hansweert_20170720	21.5	0.22
Diepe Put Hansweert 20181214 Dwarsraai	18.6	0.28
Diepe Put Hansweert 20181214 Langsraaien	17.1	0.28
Diepe Put Hansweert 20181220 Dwarsraai	15.9	0.21

Diepe Put Hansweert 20181220 Langsraaien	13.3	0.18
Waarde_20060323_Neap	12.9	0.25
Waarde_20060928_Average	11.9	0.24
R5_SchaarVanWaarde_20130424	15.4	0.30
R5_Zuidergat_20130425	17.4	0.26
Average	**16.8**	**0.26**

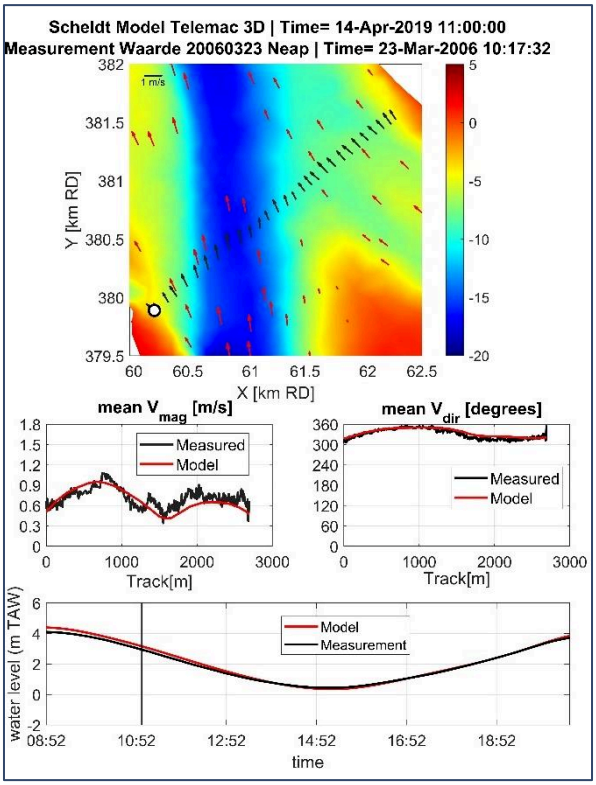

Figure 11. Modelled and measured velocity at Waarde during ebb.

VII. CONCLUSION

In the present study, a TELEMAC-3D hydrodynamic model is set up for the Scheldt Estuary. The bed roughness in the model is calibrated automatically using the 3D-Varational data assimilation algorithm, which compares time-series of the water levels from the Scheldt model and measurement data at 22 stations throughout the estuary, leading to a cost function which is subject to minimization. Twelve roughness polygons are selected for the Scheldt model domain. After 75 iterations, an optimal bed roughness field is found, leading to the lowest cost function. Using the bed roughness determined by the automatic calibration procedure, the model reproduces the hydrodynamics in the Scheldt Estuary accurately, with an average RMSE of the water levels of 12 cm.

The Scheldt model generally shows good predictive skills for a stormy period, that was selected for the validation, except at the upstream branches of the estuary. The reason for this needs further investigation in the future.

The model is also validated against measured velocity along ADCP transects, leading to an averaged RMSE of the flow magnitude of 0.16 m/s which is considered a good performance given that the average tidal peak velocity is 1.5 m/s.

ACKNOWLEDGEMENT

The present work is funded by the European Union's Horizon 2020 research and innovation programme under grant agreement No 728053-MarTERA, with the references HBC.2020.2954, under the frame of the Belgian Agentschap Innoveren en Ondernemen (VLAIO).

REFERENCES

[1] Poncot, A., Goeury, C., Argaud, J.P., Zaoui, F., Ata, R., and Audouin, Y. (2017): Optimal calibration of TELEMAC-2D models based on a data assimilation algorithm. Proceedings of the XXIVth TELEMAC-MASCARET User Conference, 17 to 20 October 2017, Graz University of Technology, Austria. Graz: Graz University of Technology. S. 73-80.

[2] ADAO, a module for Data Assimilation and Optimization, http://www.salome-platform.org/, 2022.

[3] Goeury, C., Zaoui, F., Audouin, Y., Prodanovic, P., Fontaine, J., Tassi, P., and Ata, R. (2018): Finding Good Solutions to Telemac Optimization Problems with a Metaheuristic. Proceedings of the XXVth TELEMAC-MASCARET User Conference, 9th to 11th October 2018, Norwich. Norwich: Centre for Environment, Fisheries and Aquaculture Science. S. 159-168.

[4] Bel, C., Jodeau, M., Tassi, P., Claude, N., and Haddad, H. (2019): Calibration and validation strategy for 2D hydrodynamic modelling: application to morphodynamics of a gravel-bed river with suspended sediments. In: XXVIth TELEMAC-MASCARET User Conference, 15th to 17th October 2019, Toulouse. https://doi.org/10.5281/zenodo.3611515.

[5] Chu K., Breugem W.A. & Decrop B. (2022). Automatic calibration of a continental shelf model of the North Sea using data assimilation algorithm. IAHR World Congr.

[6] Lahoz, W., Khattatov, B., and Menard, R. (Eds.), (2010). Data Assimilation: Making Sense of Observations. Springer.

[7] Wolf, T.; Breugem, W.A.; Chu, K.; Decrop, B.; Van Holland, G.; Plancke, Y.; Stark, J. (2021). Sediment transport modelling (TELEMAC-3D + GAIA) case study: sand disposals in the Western Scheldt, Proceedings of the papers submitted to the 2020 TELEMAC-MASCARET user conference - October 2021. pp. 49-57.

[8] Breugem,W.A.; Chu K.; Koutrouveli, T.; Decrop, B. (2022). Numerical modelling of plastic dispersion: a case study of the river Scheldt. IAHR World Congr.

[9] Vanlede J., Chu K., Smolders S., Decrop B. & Mostaert F. (2020). Update SCALDIS 2019: a 3D hydrodynamic model of the Scheldt Estuary: Calibration report. Version 3.0. FHR Reports, PA_016_1. Flanders Hydraulics Research: Antwerp.

[10] Chu K., Breugem A., Wolf T. & Decrop B. (2020). Improvement of a Continental Shelf Model of the North Sea. TELEMAC User Conference, Antwerp, Belgium.

[11] Lanckriet, Thijs; Breugem, Alexander; Decrop, Boudewijn (2018): Coupling TELEMAC-3D with the General Ocean Turbulence Model (GOTM). Proceedings of the XXVth TELEMAC-MASCARET User Conference, 9th to 11th October 2018, Norwich. Norwich: Centre for Environment, Fisheries and Aquaculture Science. S. 137-144.

[12] Breugem, W. Alexander (2020): Ongoing developments in TELEMAC and TOMAWAC at IMDC. Online proceedings of the papers submitted to the 2020 TELEMAC-MASCARET User

Conference October 2020. Antwerp: International Marine & Dredging Consultants (IMDC). S. 115-121.

[13] Breugem, W. Alexander (2022): Wetting and drying improvements in TELEMAC. Online proceedings of the papers submitted to the 2022 TELEMAC-MASCARET User Conference October 2022.

[14] Ribes A. & Caremoli C. (2007). Salome platform component model for numerical simulation. 31st Annu. Int. Comput. Softw. Appl. Conf. COMPSAC 2007, doi: 10.1109/COMPSAC.2007.185.

[15] Goeury C., Audouin Y. & Zaoui F. (2017). Telapy User's Manual.

[16] Parrish D.F. & Derber J.C. (1992). The National Meteorological Center's Spectral Statistical Interpolation Analysis System. Monthly Weather Review, 120, 1747-1763.. https://doi.org/10.1175/1520-0493(1992)120<1747:TNMCSS>2.0.CO;2.

[17] Vanlede, J.; Chu, Kai; Fonias, E. (2020): Introducing the VIMM toolbox for the (re)calibration of the SCALDIS model. Online proceedings of the papers submitted to the 2020 TELEMAC-MASCARET User Conference October 2020. Antwerp: International Marine & Dredging Consultants (IMDC). S. 153-158.

[18] Sutherland J. & Soulsby R. (2003). Use of model performance statistics in modelling coastal morphodynamics. Proc. Int. Conf. Coast. Sediments.

Enhancing Flood Forecasting with Dual State-Parameter Estimation and Ensemble-based SAR Data Assimilation

Thanh Huy Nguyen[1], Sophie Ricci[1], Andrea Piacentini[1], Raquel Rodriguez Suquet[2], Gwendoline Blanchet[2], Santiago Peña Luque[2] and Peter Kettig[2]

thnguyen@cerfacs.fr
[1]: CECI, CERFACS/CNRS UMR 5318, Toulouse, 31057, France
[2]: Centre National d'Etudes Spatiales (CNES), Toulouse, 31401, France

Abstract – **Ensemble data assimilation in flood forecasting depends strongly on the density, frequency and statistics of errors associated with the observation network. This work focuses on the assimilation of 2D flood extent data, expressed in terms of wet surface ratio, in addition to the in-situ water level data. The objective is to improve the representation of the flood plain dynamics with a TELEMAC-2D model and an Ensemble Kalman Filter (EnKF). The EnKF control vector is composed of friction coefficients and corrective parameters to the input forcing. It is augmented with the water level state averaged over selected subdomains of the floodplain. This work focuses on the 2019 flood event that occurred over the Garonne Marmandaise catchment. The merits of assimilating SAR-derived flood plain data complementary to in-situ water level observations are shown in the control parameter and observation spaces with 1D and 2D assessment metrics. It was also shown that the assimilation of Wet surface Ratio in the flood plain complementary to in-situ data in the river bed brings significative improvement when a corrective term on flood plain hydraulic state is included in the control vector. Yet, it has barely no impact in the river bed that is sufficiently well described by in-situ data. We highlighted that the correction of the hydraulic state in the flood plain significantly improved the flood dynamics, especially during the recession. This proof-of-concept study paves the way towards near-real-time flood forecast, making the most of remote sensing-derived flood observations.**

Keywords: Flooding, hydraulic modelling, data assimilation, dual state-parameter analysis, ensemble Kalman Filter, Remote Sensing, Garonne.

I. INTRODUCTION

The occurrence and intensity of natural disasters—among which flooding is one of the most common and costliest—has increased over recent decades, especially in the context of climate changes. In 2021 alone, the Emergency Event Database (EM-DAT) recorded 432 disastrous events related to natural hazards worldwide with 223 flood events having affected more than 100 million people and accounted for an economic loss of 74 billion USD. While hydrology and hydraulic numerical models play an essential role in flood forecasting, their capabilities remain limited due to uncertainties in their input data such rainfall, inflow, geometry of the catchment and the river (e.g. topographic errors from Digital Elevation Models (DEMs) and bathymetric errors) and hydraulic parameters (calibration of friction coefficients). Data assimilation is an efficient tool to reduce these uncertainties, by combining numerical model outputs with various Earth Observations from space or from in-situ measurements. The increasing volume of data from space missions provide heterogeneous and relevant data, such as altimetry (TOPEX/POSEIDON, Jason-1/2/3, ENVISAT, SARAL/ ALTIKA, Sentinel-3/6, SWOT), optical (Pléïades, Sentinel-2) and radar (Sentinel-1, TerraSAR-X). A conventional DA approach stands in the assimilation of water surface elevation data, either from in-situ time-series, from altimetry or retrieved from Synthetic Aperture Radar (SAR) images using river width information with complementary DEM data. An updated review from [1] provides the state-of-the-art on the assimilation of Earth Observation data with hydraulic models for the purpose of improved flood inundation forecasting.

SAR data provides an all-weather global imagery of continental waters depicted by low backscatter values resulting from the specular reflection of the incident radar pulses upon arrival at the water surfaces. While the assimilation of SAR-derived water level (WL) information is convenient as it deals with a diagnostic variable of the model, it depends on the usage of a DEM and thus may suffer from the lack of precision of high-resolution topographic data [2-4]. This constraint can be relaxed with the direct assimilation of SAR-derived flood probability maps or flood extent maps. Hostache *et al.* [5] presents the assimilation of SAR-derived flood probability maps with a Particle Filter (PF). For that matter, a probabilistic flood map is derived from SAR backscatter images using a Bayesian approach to assign a probability of flooded to its pixels, assuming that the prior probabilities for a backscatter value to be flooded or non-flooded follow two gaussian distributions, as detailed in [6]. Cooper *et al.* [7] proposed an observation operator that directly uses backscatter values from SAR images as observations in order to bypass the flood edge identification or flood probability estimation processes. Similarly to [5, 6], this approach also relies on the hypothesis that SAR images must yield distinct distributions of wet and dry backscatter values, which may not hold for real SAR data.

In this work, we propose to take into account the flood extent information derived from SAR S1 images, as wet surface ratios (WSR). This is the ratio between the number of wet pixels within a floodplain subdomain and the total number of pixels. An ensemble data assimilation (DA) approach to accommodate 2D WSR observations alongside in-situ water level time-series within an EnKF framework has been implemented on the TELEMAC-2D hydrodynamic model set up over the Garonne Marmandaise catchment. A dual state-parameter DA strategy is also carried out to reduce the uncertainties in friction coefficients, upstream forcing and hydraulic state considered as water level averaged over selected subdomains of the floodplain.

II. Study Area and Model

A. Shallow Water Equations in TELEMAC-2D

Free-surface hydraulic modelling is principally governed by the Shallow Water equations (SWE, also known as Saint-Venant equations derived from Navier-Stokes Equations), which express mass and momentum conservation averaged in the vertical dimension. In this work, the hydrodynamic numerical model TELEMAC-2D is used to simulate and predict the water level (denoted by H [m]) and velocity (with horizontal components denoted by u and v [m.s^{-1}]) from which flood risks can be assessed. It solves the SWE with an explicit first-order time integration scheme, a finite-element scheme and an iterative conjugate gradient method. A complete description of the underlying theoretical approach is provided in [8].

The 2D domain is described by a triangular mesh, in which each node associates with a topographical height. Different parameters are defined, including the friction coefficients, using Strickler formulation [9] denoted by K_s, defined uniformly over of a number of segments of the riverbed and over the whole floodplain. The mesh is constructed with three distinguished mesh types: (i) the riverbed with an oriented and fine mesh (max. triangle size 80 m) which guides the flows; (ii) the floodplain with an unstructured and coarse mesh (max. triangle size 150 m); and (iii) the dyke systems modelled by guidelines along which the mesh is very fine (max. triangle size 40 m). Beside topographic and bathymetric data, hydraulic models require a time-varying hydrograph of the inflow discharge at the upstream boundary, initial conditions, and outflow WL data or a rating curve at the downstream boundary.

B. Study Area and Event

The study area is the Garonne Marmandaise catchment (southwest France) which extends over a 50-km reach of the Garonne River between Tonneins and La Réole (Figure 1). This catchment has been equipped with infrastructures, and a progressively constructed system of dykes and weirs to protect the floodplains from flooding events such as the historic flood of 1875 and manage submersion and flood retention areas. Observing stations operated by the VigiCrue network (https://www.vigicrues.gouv.fr/) are located at Tonneins, Marmande, and La Réole (indicated as black circles).

A TELEMAC-2D model was developed and calibrated by EDF R&D [10] over this catchment, built on a mesh of 41,000 nodes using bathymetric cross-sectional profiles and topographic data [10]. A local rating curve at Tonneins is used to translate the observed WLs into a discharge time-series that is applied over the whole upstream interface (cyan arrow), including both river bed and floodplain boundary cells. Such a modeling strategy was implemented to allow for a cold start of the model with any inflow value. However, it prompts an artificial over-flooding of the upstream first meander, which remains for a period of time until the water returns to the river bed. On the other hand, the downstream BC at La Réole is described with a local rating curve built from gauge measurements. Over the simulation domain, the friction coefficient is defined over seven zones, K_{s_1} to K_{s_6} for the river bed and K_{s_0} for the entire floodplain, as illustrated in Figure 1 with solid-colored segments of the river bed and white region for the floodplain [11, 12]. The description of the friction coefficients is highly prone to uncertainties related to the zoning assumption, the calibration procedure, and the set of calibration events. In the absence of in-situ data in every river segment, their a priori values are set based on the calibration process from the original design by EDF.

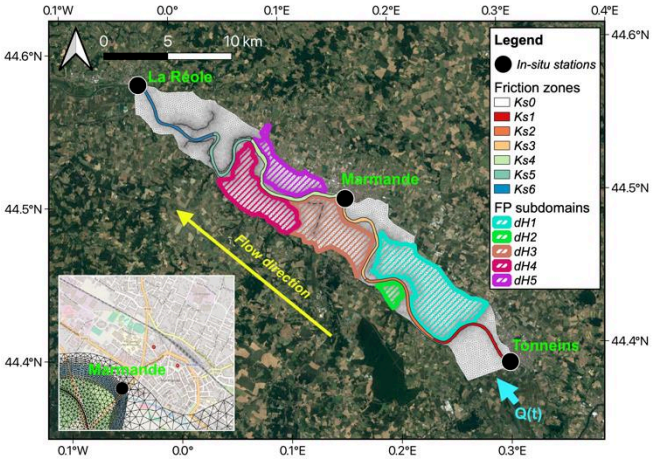

Figure 1. TELEMAC-2D Garonne Marmandaise model and control vector. Inset figure magnifies the impacted urban area around Marmande.

A significant flood event occurred in December 2019 has been studied in this research work. In-situ WL measured every 15 minutes at Tonneins, Marmande and La Réole from VigiCrue observing network are shown in Figure 2. This double-peak flood event was observed by eleven Sentinel-1 (S1) SAR images, provided by the constellation of S1-A and S1-B ascending and descending orbits, represented by the black vertical dashed lines. There are also two Sentinel-2 (S2) optical images available, represented by the red vertical dashed lines, near the first flood peak at 2019-12-15 12:05 and 2019-12-17 11:54 thus providing independent data for validation, with a cloud cover ratio of 40.6% and 11.3%, respectively. In this work, the S1-derived flood extent maps are used for the assimilation in combination with the in-situ WL observations whereas the S2-derived ones are only used for validation.

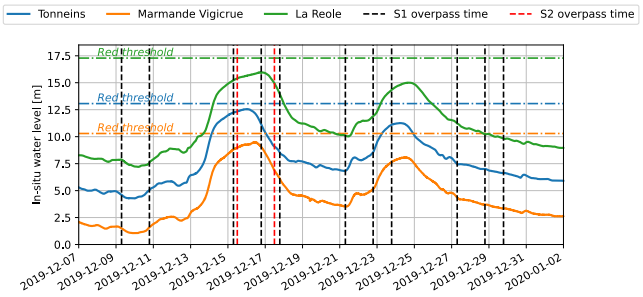

Figure 2. Water level time series at VigiCrue observing stations, and S-1 and S-2 overpass times.

III. METHOD

A. Data Assimilation

In this work, the WL time-series at the three VigiCrue stations (Tonneins, Marmande and La Réole) and the WSR computed over the five floodplain zones, are assimilated with the EnKF algorithm implemented on the TELEMAC-2D Garonne model. This allows for a sequential correction of the friction, the inflow discharge, and water level averaged over selected subdomains of the floodplain. For full description of the performed cycled EnKF, please refer to [13, 14].

B. Control Vector

Table I summarizes the variables included in the control vector of the EnKF. The friction coefficients are considered as random variables with a gaussian Probability Density Function (PDF) with mean and standard deviation estimated from the calibration process. The uncertainty in the upstream BC is also taken into account. Indeed, the limited number of in-situ observations also yields errors in the formulation of the rating curve that is used to translate the observed WLs into discharge, especially for high flows. Therefore, a multiplicative factor μ applied on the time-dependent discharge time-series is considered as a random variable with a gaussian PDF centered at 1.

In addition, in order to account for the evapotranspiration, ground infiltration and rainfall processes that are lacking in the TELEMAC-2D Garonne model, a state correction is implemented in the floodplain. Five subdomains (hereafter called *zones*) delineated in the floodplain beyond the dykes, involving a uniform WL correction over each zone, are added to the control vector. These state corrections $\delta H_{[1:5]}$ are considered as zero-mean gaussian random vectors. These zones were determined based on the description of the storage areas [10] and the dyke system of the catchment. It is worth-noting that the first storage area of the model, at the first meander near Tonneins, is excluded in this study because of the aforementioned artificial over-flooding effect. In addition, several storage areas near the downstream area are not considered, because these areas are not fully observed by S1, and spurious dynamics may be caused by the errors in topography near La Réole [10]. Over each of the five zones, the WSR between the area of observed wet surfaces and the total area of the zone is computed.

Table I Gaussian PDF of uncertain input variables.

Var-iables	Unit	Calibrated/ default value $\mathbf{x_0}$	Standard deviation $\boldsymbol{\sigma_x}$	95% confidence interval
K_{s_0}	$m^{1/3}s^{-1}$	17	0.85	17 ± 1.67
K_{s_1}	$m^{1/3}s^{-1}$	45	2.25	45 ± 4.41
K_{s_2}	$m^{1/3}s^{-1}$	38	1.9	38 ± 3.72
K_{s_3}	$m^{1/3}s^{-1}$	38	1.9	38 ± 3.72
K_{s_4}	$m^{1/3}s^{-1}$	40	2.0	40 ± 3.92
K_{s_5}	$m^{1/3}s^{-1}$	40	2.0	40 ± 3.92
K_{s_6}	$m^{1/3}s^{-1}$	40	2.0	40 ± 3.92
μ	-	1	0.06	1 ± 0.12
$\delta H_{[1:5]}$	m	0	0.25	0 ± 0.49

C. Experimental Setup

One free run (FR) and three DA experiments (IDA, IWDA, IHDA) were carried out (Table 1) with different configurations regarding the types of observations that are assimilated and the active components of the control vector. Two types of observations are considered: (i) in-situ WL observations at three VigiCrue stations Tonneins, Marmande and La Réole every 15 minutes, (ii) WSR measurements on the five floodplain zones (corresponding to $\delta H_{[1:5]}$) at the eleven S1 overpass times (Figure 2).

Table II Summary of the Free Run and DA experiment settings.

Exp.	DA	Assimilated observations	Nb of members	Control variables
FR	No	-	1	-
IDA	Yes	In-situ	75	$K_{s_0}, K_{s_{[1:6]}}, \mu$
IWDA	Yes	In-situ and WSR	75	$K_{s_0}, K_{s_{[1:6]}}, \mu$
IHDA	Yes	In-situ and WSR	75	$K_{s_0}, K_{s_{[1:6]}}, \mu, \delta H_{[1:5]}$

D. Results

In this section, quantitative performance assessments are carried out in the control and in the observation spaces by

(i) comparing the parameters yielded by the different DA analysis;

(ii) comparing the different analyzed WL time-series with synthetical or real in-situ observations;

(iii) comparing the different analyzed WSR with real or synthetical WSR observations in the floodplain;

(iv) evaluating the contingency maps and the overall Critical Success Index (CSI) and Cohen's kappa index (κ) with respect to the observed flood extent maps (S1-derived ones that were used to yield WSR, or S2-derived ones only used for validation). While CSI is conventionally the most widely used metric for this comparison, Cohen's kappa index provides a better overall metric with correctly predicted non-flooded pixels also being taken into account.

1) Results in the control space

The analyzed parameters from the different DA experiments are shown in Figure 3 where horizontal dashed lines stand for the default values $\mathbf{x}_0$ (Table I), blue curves for IDA, green curves for IWDA, and red curves for IHDA. Vertical lines show the acquisition time of the S1 images, providing WSR observations being assimilated in the IWDA and IHDA experiments.

The analyzed values for K_{s_k} (with $k \in [0,6]$) over the flood event are shown on the top panel in Figure 3. The analysis for the inflow correction μ and for δH_k^a with $k \in [1,5]$ (only by IHDA) are shown on panel in Figure 3. The bottom panel of Figure 3b displays the upstream forcing for referential purposes. First, it should be noted that for all DA experiments, the analysis values for the friction coefficients in the river bed and the floodplain remain within physical ranges. The analysis for IHDA is closer to that of IWDA, compared to IDA as they both assimilate in-situ and WSR data. The analyses in the 4th friction segment (i.e. K_{s_4}), which includes the Marmande in-situ station, are relatively close for IDA, IWDA and IHDA, showing that the assimilation of in-situ WLs at Marmande suffices to account for friction errors in this area. For the friction coefficients of the 5th and 6th river segments (i.e. K_{s_5} and K_{s_6}), the analysis is quite far from the calibrated values which is most likely due to the poor quality of the model topography in the downstream part of the domain, as well as the large misfit between the in-situ and the simulated WLs at La Réole. The analyses on μ are very similar among IDA, IWDA, and IHDA. This suggests that the in-situ WLs observed at upstream station Tonneins are enough to constrain the multiplicative correction to the inflow and that the use of additional data in the floodplain is unnecessary. Concerning the δH parameters controlled by IHDA, the mostly negative correction on all δH values increase (i.e. more water is removed in the corresponding floodplain zones) as the flood rises, especially at the flood peak, between the two peaks, and during the recess period in order to account for the TELEMAC-2D model's limitation in physical process to empty the floodplain.

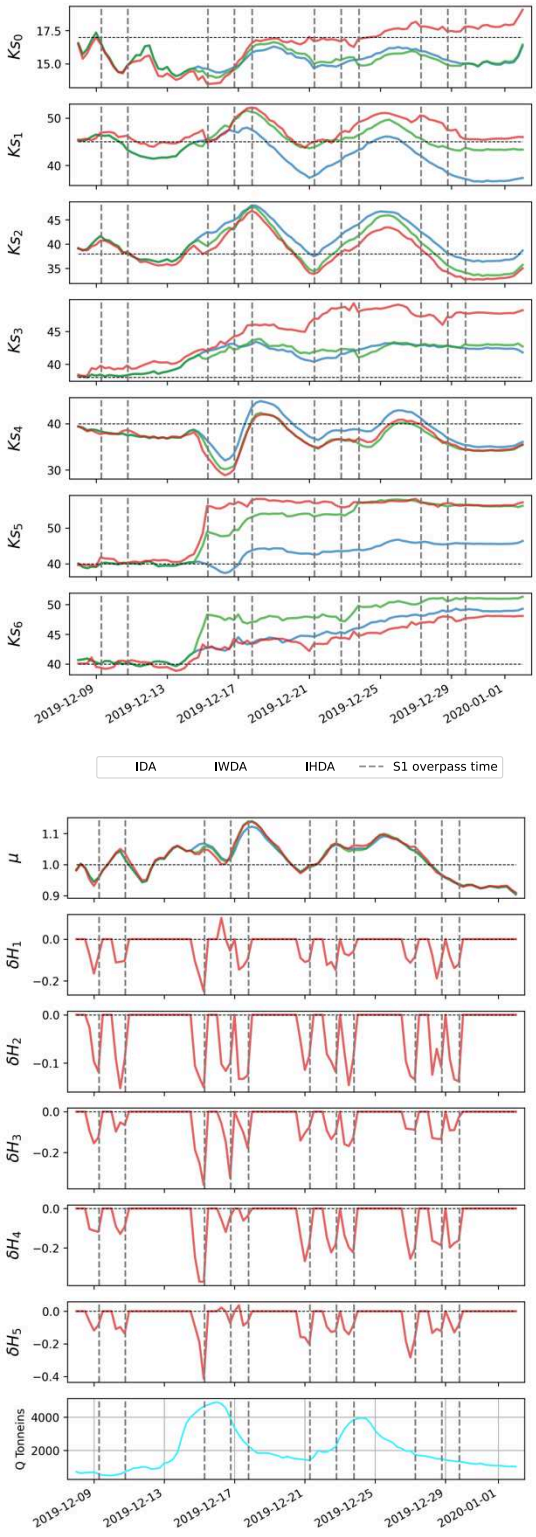

Figure 3. Evolution of controlled parameters for friction, multiplicative correction to the inflow, state correction in the floodplain. The last panel depicts the forcing inflow at Tonneins.

2) Results in the observation space: Water levels at observing stations

Table III Water level RMSE w.r.t. in-situ WL at VigiCrue observing stations. Lowest RMSE values are underlined.

Exp.	RMSE [m]		
	Tonneins	***Marmande***	***La Réole***
FR	0.129	0.220	0.318
IDA	<u>0.060</u>	<u>0.045</u>	<u>0.125</u>
IWDA	0.064	0.049	0.128
IHDA	0.064	0.051	0.138

The RMSEs computed over time for the 2019 event for the WLs from the FR, IDA, IWDA and IHDA, with respect to the observed WLs at Tonneins, Marmande, and La Réole are summarized in Table III. For each observing station, the lowest RMSE values are underlined, which show the slight advantage of IDA which only concerns the assimilation of the WLs at these observing stations. Figure 4 depicts the WLs simulated by FR (Figure 4a) and IHDA (Figure 4b) compared to the in-situ observations, in dashed curves. It is shown that all DA experiments succeed in significantly reducing the WL errors compared to those of FR. An important message is that the addition of WSR data does not bring significative improvement (nor does it degrade it) to the dynamics in the river bed that is already well described by in-situ data assimilation. The three DA experiment bring a significative improvement with respect to the Free run in the river bed. The reductions in RMSE with respect to FR amount to 50%, 77%, and 57%, respectively, at Tonneins, Marmande, and La Réole, with close values between IDA, IWDA, and IHDA. The RMSEs at Tonneins and Marmande remain under 6.5 cm for all DA experiments, whereas it is under 14 cm at La Réole.

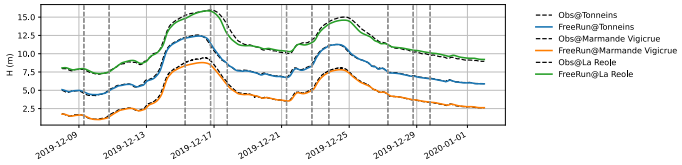

(a) FR (RMSE: 0.318, 0.129, 0.220)

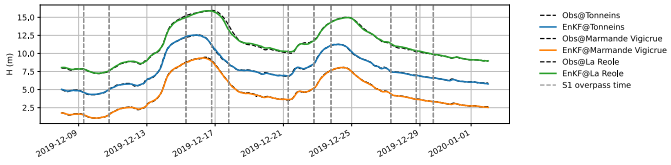

(b) IHDA (RMSE: 0.138, 0.064, 0.051)

Figure 4. Simulated WL compared to observations.

It should be noted that the best DA strategy according to in-situ WL RMSE is IDA (although slightly). The additional WSR observations in the floodplain (assimilated in IWDA and IHDA) leads to a smaller WL improvement from FR at observing stations than IDA does. It is highly probable that an extended control vector is necessary to account for model error in the river bed and in the flood plain. For instance, we could consider a finer zoning of friction in the floodplain, the addition of lateral tributaries that mainly carry a large volume of water for high flows, a more precise description of the topography in the floodplain, or an addition of physical processes in the SWE solver such as rain and evapotranspiration. A preliminary conclusion here is that the assimilation of data in the floodplain does not bring any significant improvement to the flood dynamics when only assessed in the river bed, through 1D metrics defined in the river bed.

3) Results in the observation space: WSR in the floodplain

The performance of the DA strategy is now assessed in the observation space of WSR, in the floodplain. The WSR in the five floodplain subdomains for the simulated WL in FR and the analyzed WL in the three DA experiments with a wet threshold of 5 cm are compared to the WSR computed from the observed S1-derived flood extent maps. The misfit between simulation and observation WSR values (i.e. observed WSR - simulated WSR) are shown in Figure 5, which allows to assess the performance of the simulation in terms of flood extent representation. The color codes for the experiments remain the same as in previous figures, i.e., FR in orange, IDA in blue, IWDA in green, and IHDA in red.

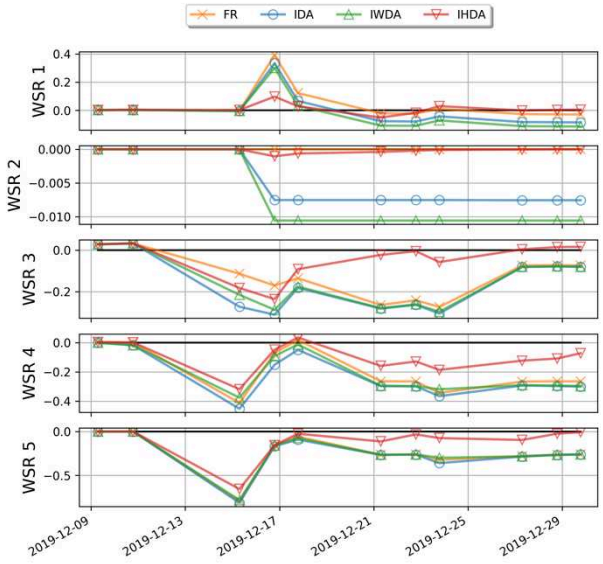

Figure 5. Errors between truth's WSR values and simulated WSR values in the 5 floodplain zones.

First, it can be noted that the analyses for IDA and IWDA do not bring much improvement in terms of flood extent representation with respect to FR. The improvement is much more evident for IHDA, as we can see it yields the smallest WSR misfits among the experiments. In particular, IHDA brings a significant improvement for the subdomains 1, 3, 4 and 5; whereas the misfits in subdomain 2 have already been small for FR, hence the contributions from IHDA are less obvious. Compared to IWDA, the assimilation of WSR by IHDA with the extended control vector brings an improvement in all subdomains, and thus allows the floodplain to be efficiently emptied after the flood peak.

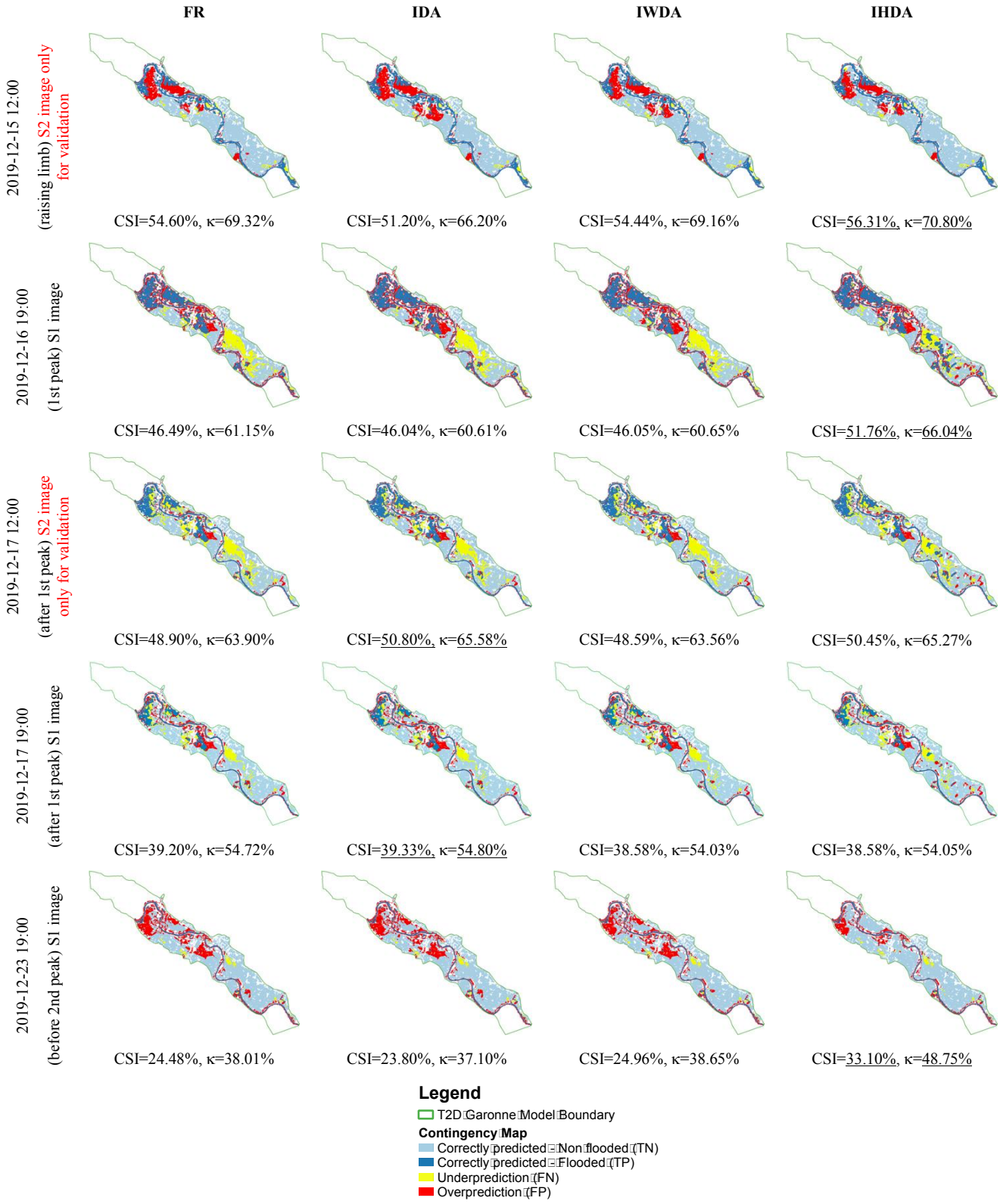

Figure 6. Contingency maps computed between simulated flood extent (from left to right: FR, IDA, IWDA and IHDA) with respect to S1-derived flood extent (row 2, 4 and 5) and S2-derived flood extent (rows 1 and 3). Highest CSI and κ scores are underlined.

A significant overprediction at the 3rd timestep, right before the first peak (2019-12-15 07:00), in subdomain 4 and 5 can be observed. This could stem from the characteristics of SAR backscatter which intensifies as the soil moisture increases due to rainfalls while the area has not been flooded.

At later moments during the flood, the correction of the hydraulic state in the floodplain for IHDA, during the recess of the first peak (between 2019-12-17 and 2019-12-21), allows for a better simulation of the second flood peak than in FR.

E. 2D validation with contingency maps, CSI and κ indices

2D validations are carried out by evaluating contingency maps comparing TELEMAC-2D water masks with S1-/S2-derived flood maps at their respective overpass times, and by quantitatively assessing the resulting CSI and the κ index scores. Figure 6 depicts the contingency maps based on the comparison of the TELEMAC-2D simulated flood extent maps from FR and DA experiments with respect to those derived from S1 or S2 images during the 2019 flood event. It should be stressed that S2 imagery data are not assimilated, they are only used for validation as independent data. The associated CSI and the κ indices are indicated on each contingency map. The contingency maps are shown from top to bottom, at satellite overpass time:

- at the rising limb of the first flood peak observed by S2 (2019-12-15 12:00),
- at first flood peak by observed S1 (2019-12-16 19:00),
- during the first falling limb observed by S2 (2019-12-17 12:00) and then by S1 (2019-12-17 19:00),
- before the second flood peak observed by S1 (2019-12-23 19:00).

From the first row in Figure 6, IHDA brings some improvements with respect to FR, IDA and IWDA before the flood peak, with relatively significant overprediction regions (red pixels) on subdomain 4 and 5 from all experiments can be observed on these first-row figures. It is coherent with the remark made on the WSR validation. At the first flood peak observed by S1 image (second row in Figure 6), IHDA allows better predictions of the flooded pixels (represented by dark blue pixels), mostly in subdomain 1. During the first flood recess (third and fourth row in Figure 6), the improvement brought by IHDA is not as visible as at the flood peak (second row). Relatively large amount of underprediction (yellow pixels) in the subdomains 1 and 3 remains significant which suggests a further improvement to be made concerning the topography and friction of these subdomains.

The added validation of the S2 image at 2019-12-17 12:00 (third row) provides an interesting remark. Indeed, the observed flood extent detected on this image is more similar to the one captured by the S1 image at 2019-12-16 19:00 (17 hours before) than to the one right afterward at 2019-12-17 19:00 (5 hours later). Such a non-linear situation, taking into account the fact that these three images were acquired in the span of 24 hours during the start of the falling limb, shows the different tendencies between the in-situ WL and the floodplain dynamics.

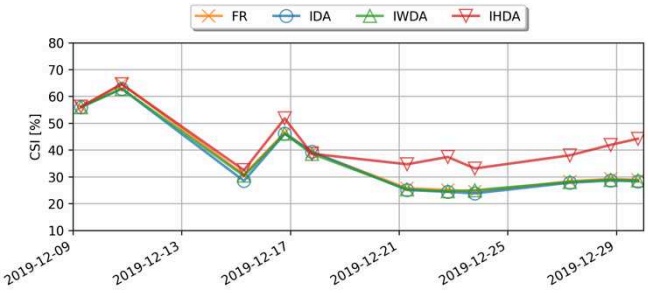

(a) CSI

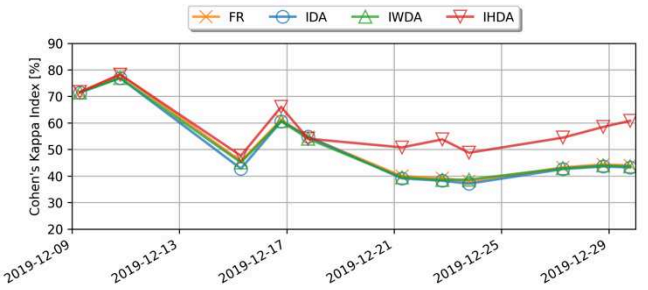

(b) Cohen's κ index

Figure 7. CSI and κ scores.

This emphasizes the complexity of the flood dynamics in the floodplain, and advocates for the further addition of the S2-derived flood observations in the DA. Such a combination of S1 and S2 images is rarely possible due to the unavailability of S2 images during a flood event because of cloud cover problem. Lastly, the 5th row of Figure 6 shows an overall improvement spread out over the five subdomains, as the amount of overprediction regions are significantly reduced. This is due to the state corrections applied at the timesteps between the two flood peaks. Figure 7 depicts the CSI (left column) and the κ index (right column) yielded by FR and DA experiments at all S1 overpass times for the 2019 event with the same color code used previously. These confirm the merits of the DA strategy in IHDA, especially for the representation of the floodplain dynamics and during flood recess.

IV. CONCLUSIONS AND PERSPECTIVES

This study presents the merits of assimilating 2D flood extent observations derived from remote sensing Sentinel-1 SAR images with an Ensemble Kalman Filter implemented on the 2D hydrodynamics model TELEMAC-2D. The flood extent information is expressed in terms of Wet Surface Ratio or WSR computed over defined sensitive subdomains of the floodplain. The WSR is assimilated jointly with in-situ water level observations. The study was carried out over the Garonne Marmandaise catchment, focusing on the flooding event in 2019. Four experiments were realized; one in free run mode and three in DA mode. The control vector gathers

friction and forcing correction, and is augmented with correction of the hydraulic state in subdomains of the floodplains (IHDA experiment) that constitute the innovative strategy of this work. All of the DA experiments were implemented by a cycled EnKF with an 18-hour assimilation window sliding with 6-hour overlapping. The simulation results were comprehensively assessed with 1D and 2D metrics with respect to assimilated data as well as with respect to independent flood extent, derived from Sentinel-2 optical imagery data.

The first DA experiment (IDA) involves only in-situ observations whereas the second one (IWDA) assimilates both in-situ observations and WSR observations derived from 2D S1 flood extent maps. These two experiments focus on the sequential correction of friction coefficients and inflow discharge. The spotlight of the article is the IHDA experiment, which not only assimilates both types of observations (similar to IWDA), but also handles a dual state-parameter estimation within the EnKF, by treating inflow discharge and friction coefficients as well as the hydraulic state variable in five particular floodplain subdomains, representing evapotranspiration and/or ground infiltration processes that are unavailable in the TELEMAC-2D model.

We have shown that the assimilation of in-situ data in IDA significantly improves the simulation in the river bed, yet, the dynamics in the floodplain remains incorrect with a significant underestimation of the flood. Indeed, the in-situ observations located in the river bed, do not provide information on the dynamics in the floodplain. The assimilation of WSR data in the floodplain, in IWDA, brings no significant improvement in the river bed and no significant improvement in the flood plain when only upstream forcing and friction coefficients are corrected in the river bed. Indeed, the dynamics of the floodplain is not sensitive to model parameters that are accounted for in its limited control vector (i.e. river bed friction and discharge). In order to allow for the improvement of the dynamics in the flood plain, the assimilation of WSR data must be associated to the augmentation of the control vector with the hydraulic state in the flood plain. More specifically, it was shown that the correction of the augmented control vector in IHDA allows to better represent the flood peak and to efficiently dry out the floodplain during the recess period. From FR to IHDA, the RMSE computed with respect to in-situ data in the river bed is reduced by up to 77-80% at Marmande, whereas the CSI computed with respect to remote-sensing flood extent maps is improved by up to 5.27 percentage points for this flood event. This study confirms the assertion that a densification of the observing network, especially in the floodplain, with remote sensing data and advanced DA strategy, allows to improve the representation of the dynamics of the flow in the floodplains.

This work relies on the implementation of an advanced DA strategy for TELEMAC-2D, especially the development of the observation operator dedicated to WSR, as well as the definition of the associated augmented control vector. Yet, it should be noted that the definition of the subdomains in the floodplain over which the hydraulic state is uniformly corrected, requires a deep understanding of the dynamics of the flood, and is thus not straightforward. This aspect could be further investigated, for instance based on a global sensitivity analysis with respect to the hydraulic state but also to other sources of uncertainty such as topography, especially in the downstream area. Indeed, the same dual state-parameter estimation approach could be applied to correct the bathymetry and topography provided that the size of the uncertainties is reduced, for instance working with a spatially uniform correction or a correction that is only projected onto a limited number of principal components of the errors. In this perspective, we aim to consider using high- and very-high-resolution topography as additional inputs to the model. The use of other imagery datasets (e.g. Landsat-8 and Landsat-9) can also be investigated. In the present work, the combination between remote-sensing data with regards to S1 and S2 data requires further investigation as it seems that the improvements made using S1-derived flood extent maps does not necessarily lead to an improvement with regards to S2-derived flood extents. This could stem from the differences between the S1 and S2 measurement, and the flood extent mapping algorithm. In addition, the identification of S1 or S2 exclusion maps—which signify the reliability of the detected flooded and non-flooded regions—should also be considered taking into account the limitations of each data source.

Lastly, a major perspective of this work stands in the potential non-gaussianity of the WSR observations. This limitation can amount to a loss of optimality of the EnKF which relies on the assumption that the observational error follows a gaussian distribution. On-going work, based on a rich literature based on a change of variable to transform the non-gaussian error into gaussian errors (widely known as Gaussian anamorphosis) is ongoing and yields promising early results.

ACKNOWLEDGEMENT

This work was supported by CNES, CERFACS and SCO-France. The authors gratefully thank the EDF R&D for providing the Telemac-2D model for the Garonne River, and the SCHAPI, SPC Garonne-Tarn-Lot and SPC Gironde-Adour-Dordogne for providing the in-situ data.

REFERENCES

[1] Dasgupta, A., Hostache, R., Ramsankaran, R. A. A. J., Grimaldi, S., Matgen, P., Chini, M., ... & Walker, J. P. (2021). Earth Observation and Hydraulic Data Assimilation for Improved Flood Inundation Forecasting. In *Earth Observation for Flood Applications* (pp. 255-294). Elsevier.

[2] Giustarini, L., Matgen, P., Hostache, R., Montanari, M., Plaza, D., Pauwels, V. R. N., ... & Savenije, H. H. G. (2011). Assimilating SAR-derived Water Level Data into a Hydraulic Model: A Case Study. *Hydrology and Earth System Sciences*, 15(7), 2349-2365.

[3] García-Pintado, J., Mason, D. C., Dance, S. L., Cloke, H. L., Neal, J. C., Freer, J., & Bates, P. D. (2015). Satellite-supported Flood Forecasting in River Networks: A Real Case Study. *Journal of Hydrology*, 523, 706-724.

[4] Matgen, P., Montanari, M., Hostache, R., Pfister, L., Hoffmann, L., Plaza, D., ... & Savenije, H. H. G. (2010). Towards the Sequential Assimilation of SAR-Derived Water Stages Into Hydraulic Models using The Particle Filter: Proof Of Concept. *Hydrology and Earth System Sciences*, 14(9), 1773-1785.

[5] Hostache, R., Chini, M., Giustarini, L., Neal, J., Kavetski, D., Wood, M., ... & Matgen, P. (2018). Near-Real-Time Assimilation of SAR-derived Flood Maps for Improving Flood Forecasts. *Water Resources Research*, 54(8), 5516-5535.

[6] Giustarini, L., Hostache, R., Kavetski, D., Chini, M., Corato, G., Schlaffer, S., & Matgen, P. (2016). Probabilistic Flood Mapping using Synthetic Aperture Radar Data. *IEEE Transactions on Geoscience and Remote Sensing*, 54(12), 6958-6969.

[7] Cooper, E. S., Dance, S. L., García-Pintado, J., Nichols, N. K., & Smith, P. J. (2019). Observation Operators for Assimilation of Satellite Observations in Fluvial Inundation Forecasting. *Hydrology and Earth System Sciences*, 23(6), 2541-2559.

[8] Hervouet, J. M. (2007). *Hydrodynamics of Free Surface Flows: Modelling with the Finite Element Method*. John Wiley & Sons.

[9] Gauckler, P. (1867). *Etudes Théoriques et Pratiques sur l'Ecoulement et le Mouvement des Eaux*. Gauthier-Villars.

[10] Besnard, A., & Goutal, N. (2011). Comparison between 1D and 2D Models for Hydraulic Modeling of a Floodplain: Case of Garonne River. *Houille Blanche-Revue Internationale De L'Eau*, (3), 42-47.

[11] Nguyen, T. H., Delmotte, A., Fatras, C., Kettig, P., Piacentini, A., & Ricci, S. (2021). Validation and Improvement of Data Assimilation for Flood Hydrodynamic Modelling Using SAR Imagery Data. In *Proceedings of the 2020 TELEMAC-MASCARET User Conference,* October 2021 (pp. 100-108).

[12] Nguyen, T. H., Ricci, S., Fatras, C., Piacentini, A., Delmotte, A., Lavergne, E., & Kettig, P. (2022). Improvement of Flood Extent Representation with Remote Sensing Data and Data Assimilation. *IEEE Transactions on Geoscience and Remote Sensing*, DOI: 10.1109/TGRS.2022.3147429.

[13] Nguyen, T. H., Ricci, S., Piacentini, A., Fatras, C., Kettig, P., Blanchet, G., Pena Luque, S., & Baillarin, S. (2022). Assimilation of SAR-derived Flood Observations for Improving Fluvial Flood Forecast. In *Proceedings of the 14th International Conference on Hydroinformatics (HIC2022)*, July 2022. arXiv:2205.08471.

[14] Nguyen, T.H., Ricci, S., Piacentini, A., Fatras, C., Kettig, P., Blanchet, G., Pena Luque, S., & Baillarin, S., (2022). Dual State-Parameter Assimilation of SAR-derived Wet Surface Ratio for Improving Fluvial Flood Reanalysis. *Earth and Space Science Open Archive*, doi:10.1002/essoar.10511831.1.

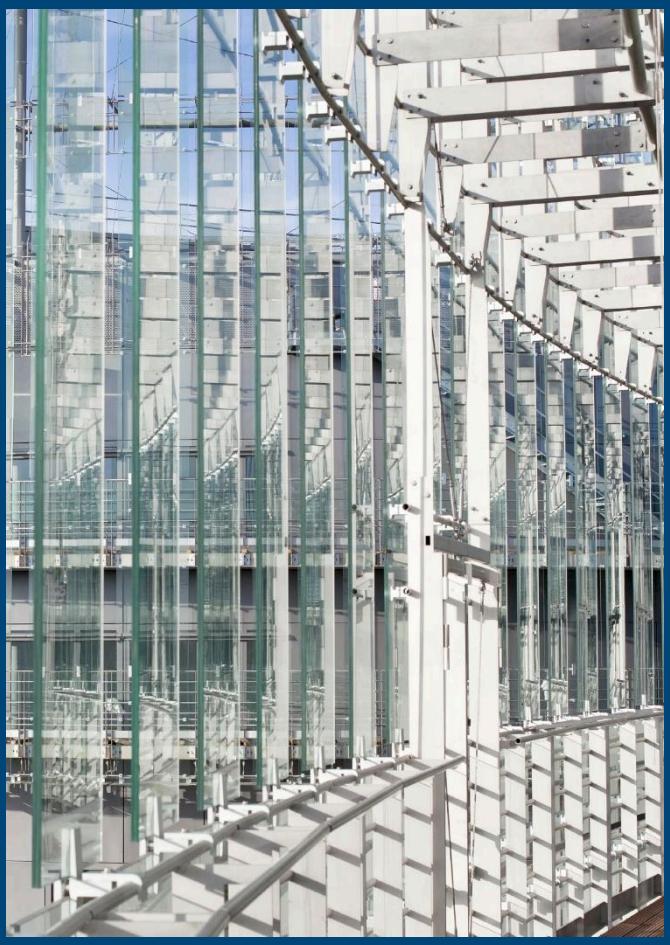

Proceedings of the

XXVIIIth TELEMAC User Conference

18-19 October 2022, Paris-Saclay

EDF Direction Recherche et Développement
EDF Lab Paris-Saclay
7 boulevard Gaspard Monge
91120 Palaiseau